

Metal-cyclam based Metal-Organic Frameworks for CO₂ Chemical Transformations

Jie Zhu

Dissertation submitted to the faculty of the Virginia Polytechnic Institute and State University in partial fulfillment of the requirements for the degree of

Doctor of Philosophy

In

Chemistry

Amanda J. Morris, Chair

Brenda S.J. Winkel

Harry C. Dorn

Louis A. Madsen

Brian E. Hanson

Karen J. Brewer

April 1, 2018

Blacksburg, Virginia

Keywords: metal-organic frameworks, MOFs, cyclam, CO₂ fixation, cycloaddition, gas adsorption, electrochemistry, catalysis, electrocatalysis, Ruthenium, photodynamic therapy, PDT

Metal-cyclam based Metal-Organic Frameworks for CO₂ Chemical Transformations

Jie Zhu

Abstract

Designing new materials for CO₂ capture and utilization is one of the most challenging research topics. Metal-organic frameworks (MOFs) are one of the most efficient CO₂ adsorbents, as well as an emerging class of heterogeneous catalysts for CO₂ chemical transformations. Highlighted by their high content of active centers, large internal surface areas, tunable pore size, and versatile chemical functionalities, MOFs can serve as highly stable and reusable heterogeneous catalysts and provide a great platform to explore the structure-function relationships for transforming CO₂ into useful chemicals. In this dissertation, we aim to develop a new class of metal-cyclam based robust MOFs as porous materials for CO₂ uptake as well as efficient catalysts for CO₂ chemical transformations, including CO₂ chemical fixation, CO₂ photo- and electroreduction.

Chapter 1 introduces the concept and main challenges of CO₂ capture and conversion. The potential of metal-cyclam complexes as molecular catalysts for CO₂ conversion is also mentioned. The current state of the art in designing stable MOFs and azamacrocyclic-based MOFs is briefly discussed. Finally, the strategies, challenges and future outlook of using MOF as catalysts in CO₂ chemical transformation are summarized.

Metal-organic frameworks (MOFs) as highly ordered, tunable hybrid materials have shown great promise in photon collection, energy transfer and photocatalytic reactions. In Chapter 2, the fundamental principles of energy transfer in the condensed phase are summarized, and a series of studies in light-harvesting, excited state quenching and photo-excited reactivity occurring within ruthenium-polypyridyl-doped zirconium MOFs are reviewed. The application of MOFs in energy conversion devices such as dye-sensitized solar cells (DSSC) is also discussed.

Chapter 3 reports two new robust 3D porous metal-cyclam based Zr-MOFs, VPI-100 (Cu) and VPI-100 (Ni) with potential as heterogeneous catalysts for CO₂ chemical fixation. The frameworks are prepared by a modulated synthetic strategy and the structure highlighted by eight-connected Zr₆ clusters and metallocyclams as organic linkers. The VPI-100 MOFs exhibit excellent chemical stability in various organic and aqueous solvents over a wide pH range and show high CO₂ uptake capacity (up to ~9.83 wt% adsorption at 273 K under 1 atm). Moreover, VPI-100 MOFs demonstrate some of the highest reported catalytic activity values (turnover frequency and conversion efficiency) among Zr-based MOFs for the chemical fixation of CO₂ with epoxides. The MOFs, which bear dual catalytic sites (Zr and Cu/Ni), enable chemistry not possible with the cyclam ligand under the same conditions and can be used as recoverable stable heterogeneous catalysts without losing performance.

A follow-up study of CO₂ chemical fixation using Hf analogs of VPI-100 is presented in Chapter 4. Structural characterization and catalytic performance of Hf-VPI-100 are summarized. Moreover, a detailed comparison of VPI-100 and Hf-VPI-100 is made. *In situ* powder X-ray diffraction (PXRD), quartz crystal microbalance (QCM) and diffuse reflectance infrared Fourier transform spectroscopy (DRIFTS) have been used to probe the interaction between the guest molecules (CO₂/epoxide) and Hf-VPI-100. For CO₂, no specific chemical binding sites in MOFs has been observed and the uptake of CO₂ does not change the crystal structure of Hf-VPI-100. Both QCM and DRIFTS revealed the irreversible binding between the framework and 1,2-epoxybutane. The epoxide uptake per unit cell of VPI-100 MOFs and diffusion coefficients have been calculated by QCM analysis.

Transition metal complexes capable of visible light-triggered cytotoxicity are appealing potential candidates for photodynamic therapy (PDT) of cancer. In Chapter 5, two monometallic polyazine complexes, [(Ph₂phen)₂Ru(dpp)]²⁺ and [(Ph₂phen)₂Os(dpp)]²⁺ (Ph₂phen = 4,7-diphenyl-1,10-phenanthroline; dpp = 2,3-bis(2-pyridyl)pyrazine), were synthesized, characterized and studied as light activated drugs to kill rat malignant glioma F98 cells. Both compounds display strong absorption in visible

spectrum, oxygen-mediated DNA and BSA photocleavage and significant photocytotoxicity under blue light irradiation along with negligible activity in the dark. The compounds show approximately five-fold higher cytotoxicity compared the traditional chemotherapeutic drug, cisplatin. Furthermore, $[(\text{Ph}_2\text{phen})_2\text{Os}(\text{dpp})]^{2+}$ shows promising photocytotoxicity in F98 rat malignant glioma cells within the phototherapeutic window with an IC_{50} value of $(86.07 \pm 8.48) \mu\text{M}$ under red light (625 nm) irradiation.

In Chapter 6, the mixed-metal supramolecular complex, $[(\text{Ph}_2\text{phen})_2\text{Ru}(\text{dpp})\text{PtCl}_2]^{2+}$, was found to display significant DNA modification, cell growth inhibition, and toxicity towards F98 malignant glioma cells following visible light irradiation. The design of this complex has a significantly higher potential for membrane permeability than three other FDA-approved anti-cancer agents, including cisplatin, and exhibited a dramatic ten-fold higher uptake by F98 cells than cisplatin in a two-hour window. Based on studies with a rat glioma cell line, the compound has very low cytotoxicity in the dark, but results in substantial cell death upon light treatment. The complex is thus among the first to exhibit all the hallmarks of a very promising new class of PDT agents.

Metal-cyclam based Metal-Organic Frameworks for CO₂ Chemical Transformations

Jie Zhu

Abstract

(General Audience)

Increased carbon dioxide (CO₂) emissions have triggered a series of environmental effects, including global warming and ocean acidification. Scientists are trying to develop new materials to capture and convert CO₂ into useful chemical products. However, the main challenge is that CO₂, the gas generated upon burning fossil fuels, has strong C=O bonds that are hard to break. In other words, it is too stable to be easily changed into other compounds. A class of highly porous materials known as metal-organic frameworks (MOFs) possess significant potential for CO₂ adsorption uptake and chemical fixation. MOFs are metal ions or clusters held together by organic linkers to make highly ordered, crystalline 3D structures with tunable porosity and functionality. The design and synthesis of MOFs is similar to playing with Legos at the molecular level; you need to pick the right pieces (metal nodes and linkers) to get your desired structure. In this dissertation, we aim to develop a new class of macrocycle complexes based stable MOFs as porous materials for CO₂ uptake as well as efficient catalysts for CO₂ chemical transformations.

We have developed two new stable three dimensional porous frameworks, VPI-100 (Cu) and VPI-100 (Ni) as catalysts for CO₂ chemical fixation. The new 3D robust MOFs named VPI-100 (VPI = Virginia Polytechnic Institute) are assembled by the reaction of zirconium oxo clusters and linkers bearing metal complexes. Using the metal complexes as the linker provides additional metal active sites in the framework that can act as accessible catalytic centers for CO₂ conversion. The VPI-100 MOFs are not only able to convert CO₂ to cyclic carbonates (important industrial chemicals) in high efficiency (~98%), but also can be reused for multiple cycles. The heterogeneous catalyst can be easily recovered from the reaction mixture by centrifugation and the active metal centers

are earth-abundant transition metals (Cu and Ni), which are cost effective. Additionally, VPI-100 MOFs also show high CO₂ uptake capacity (up to ~10 wt%) at ambient pressure. Since the MOFs can enhance the local concentration of CO₂ around the active catalytic centers located inside the pores of the framework, these materials could be used as catalysts for flow chemistry, which is widely used in industry.

We further investigated the CO₂ chemical fixation using Hf analogs of VPI-100. Structural characterization and catalytic performance of Hf-VPI-100 are summarized. Moreover, a detailed comparison of VPI-100 and Hf-VPI-100 is made. Different analytical techniques have been used to further understand the reaction mechanism as well as the interaction between the CO₂/epoxide and the frameworks. These insights would help us to design new MOFs as better catalysts for practical applications.

Acknowledgments

Firstly, I would like to express my sincere gratitude and appreciation to my research advisor, Professor Amanda Morris. Without her guidance and mentorship, I cannot be where I am. I still remember when we met to talk about my project, I knew nothing about cyclam or CO₂ chemical transformations. Three and half years later, my thesis title is “Metal-cyclam based MOFs for CO₂ chemical transformations.” Thank you, Dr. Morris. Thank you for accepting me to join your group during my difficult time. Thank you for always be there for your student and trying to help as much as you can. Thank you for allowing me to follow my interests in science and encouraging me to set up the collaborations with many other great scientists. During my Ph.D. journey, I always enjoyed talking with you about chemistry, hearing your interesting life stories and learning to be better in presentation and writing skills. As a Chinese proverb said, “一日为师，终身为父。” I will always be grateful and honored to be your academic child.

I would also like to acknowledge the late Professor Karen Brewer, who mentored me for my first two years after I joined graduate school. She was very encouraging and supportive not only in research but also in life. She was a role model and taught me how to think in other people's shoes. The experience in her group helped me to become more independent and mature as a chemist and the life lesson I learned from her will benefit me all the time.

I owe much appreciation to my other committee members, Professors Brenda Winkel, Harry Dorn, Louis Madsen and Brian Hanson. Thanks Dr. Winkel for serving as the corresponding author for our paper in *Chem. Commun.*. We could not have published that paper without your help. It was always very delightful to have a conversation with you (in person or even just by email). I always amazed by your character (encouraging, thoughtful and leadership) and wish I could learn that from you. I am glad that I took the advice from Dr. Brewer to add you as my committee member in the first place. Thank

you Dr. Dorn for being the mentor and great friend for me and my wife, Tina. During our ORP class I found you knowledgeable and creative in science. I admired you for being so passionate about chemistry. To be honest, I am a big fan of yours. Thanks Dr. Madsen for your critical and helpful insights in my project. I learned a lot from your feedback, and it was a great pleasure to work with you as one of the TAs in your class. I always enjoyed the conversation with you. Thanks to Dr. Hanson for his help and suggestions. I learned how to read literature critically in his organometallic class, and that benefited me and developed my critical thinking for research. Again, for my committee members, I appreciate your time, efforts, encouragements and suggestions.

I am also incredibly thankful for my research collaborators. I thank Dr. Wenqian Xu at Argonne National Lab for solving the structure of our new MOFs by powder X-ray diffraction. He is also an excellent host for our two onsite trips to Argonne National Lab. Many thanks to Dr. Sanjaya Senanayake, who initiated our collaboration with Wenqian and hosted my visit to Brookhaven National Lab. Thanks Dr. John Robertson for providing the opportunity to explore cell studies in those photodynamic therapy projects. Thanks Dr. Jeffery Parks, Dr. Carla Slebodnick, Dr. Mehdi Ashraf-Khorassani and Dr. N. Murthy Shanaiah for their help in ICP-MS, single crystal X-ray diffraction, HPLC-MS, and NMR, respectively.

My sincerest gratitude also goes to my talented colleagues and friends in the Morris lab, Brewer group, and chemistry department. I am lucky enough to work with four postdocs, Dr. Gerald Manbeck, Dr. Gilbert Kosgei, Dr. William Maza and Dr. Pavel Usov. Thank you for all your help and inspirations. Many thanks to Dr. Spencer Ahrenholtz, Dr. Charity Epley, Dr. Roberto Padilla, Dr. Elise Naughton, Dr. Theodore Canterbury, Dr. Yuming Dai, Dr. Xiangtao Meng, José Rodriguez Corrales, Jennifer Rowe, Shaoyang Lin, Meng Cai, Paula Celis-Salazar, Bradon Gibbons, Matthew Kessinger, Shaunak Shaikh and Ran Liu. Thank you for your support, helpful discussions and company through the long journey. Especially for those who worked with me during after hours, I gained a lot of motivation and strength instead of feeling alone because of you. I also would like to acknowledge one of my best friends, Dr. Zongmin Zhao, who

not only assisted me on the basketball court but also helped me with the protein gel analysis in those photodynamic therapy projects. To the eight undergraduates who worked with me, Kendall Shafran, Reece Prussin, Anthony Dominijanni, Eddie Jensen, Cole McManus, Tu Du, Yered Arias-Machain and Michael McHale, it is a great pleasure to mentor you and learn from your bright young minds. I am incredibly thankful to my high school chemistry teacher, Mrs. Suping Hong. Thank you for inspiring me and guiding my interests in chemistry. Beyond that, I am grateful to know all the wonderful friends I made along the Ph.D. journey.

Lastly, I would like to extend my appreciation and love to my family. My father, Dr. Dunru Zhu, who is also a chemistry professor, has been a great role model since I was a kid and always trying to lead me to this academic career path. Thank you for lighting up my interests in science. My mother, Zhaoxia Yu, who educated me to be nice, kind and helpful to others. To my wonderful wife, Dr. Tinghui Li, who is a great chemist and strong woman. We met in the graduate program of chemistry at Virginia Tech, and I am so happy that we could grow up together in graduate school. Thank you for your trust and belief in me. With your support and encouragement, I am fearless in pursuing my dream. I thank my grandparents and other family members for their love and support. Moreover, I would like to thank our dog, Potato, for being a good family member. I gratefully acknowledge all my friends I met, especially to Mingda Liu, who is fighting against Leukemia. I wish the best for him.

Looking back my six years Ph.D. journey, I found the experience is full of joys and tears, ups and downs. As my favorite quote from Romain Rolland said, “There is only one heroism in the world: to see the world as it is and to love it.” I appreciate all the life lessons I have learned from this unique journey. I am blessed to meet so many great scientists, mentors, friends, and colleagues. I am proud that I became a Hokie after my phone interview with Dr. Morris, and Blacksburg has become my second home. I love you all.

Table of Contents

Contents

Chapter 1 Introduction	1
1.1 Research motivation.....	1
1.2 CO ₂ capture and conversion.....	2
1.2.1 CO ₂ capture	2
1.2.2 CO ₂ chemical transformation	4
1.3 Metal cyclam complexes.....	5
1.4 Metal-organic frameworks.....	8
1.4.1 Famous MOFs	9
1.4.2. Designing stable MOFs	12
1.4.3 Azamacrocyclic-based Metal Organic Frameworks	15
1.5 MOFs for CO ₂ chemical transformations	21
1.5.1 MOFs for CO ₂ chemical fixation	22
1.5.2 MOFs for photocatalytic CO ₂ reduction	29
1.5.3 MOFs for electrochemical CO ₂ reduction.....	35
1.6 Reference	37
Chapter 2 Light-harvesting and energy transfer in ruthenium(II)-polypyridyl doped zirconium(IV) metal-organic frameworks: a look towards solar cell applications	44
2.1 Abstract	44
2.2 Introduction.....	44
2.3 Förster and Dexter Energy Transport in MOFs	46
2.3.1 Resonance Energy Transfer.....	46
2.3.2 Förster and Dexter Energy Transfer.....	47
2.4 Photophysical Properties of RuDCBPY-UiO-67 Powder	51
2.4.1 Two-State Model.....	52
2.4.2 ³ MLCT Quenching Mechanism- Förster Energy Transfer.....	55
2.4.3 Concentration Dependent Dimensionality of RET in Postsynthetically Doped RuDCBPY-UiO-67-DCBPY	57
2.5 MOFs for Solar Cell Applications	62
2.5.1 Photophysical Characterization of RuDCBPY-UiO-67 Thin Film.....	64

2.5.2 Light Harvesting for Energy Transfer	65
2.6 Summary and Concluding Remarks	69
2.7 Acknowledgement	71
2.8 Reference	71
Chapter 3 A New Class of Metal-Cyclam based Zirconium Metal-Organic Frameworks for CO₂ Adsorption and Chemical Fixation	75
3.1 Abstract	75
3.2 Introduction.....	75
3.3 Experimental Section	77
3.3.1 Materials and methods.....	77
3.3.2 Synthesis of 6,13-dicarboxy-1,4,8,11-tetrazacyclotetradecan)-copper (II) perchlorate [CuL(ClO ₄) ₂] (1).....	77
3.3.3 Synthesis of 6,13-dicarboxy-1,4,8,11-tetrazacyclotetradecan (L) (2).....	77
3.3.4 Synthesis of 6,13-dicarboxy-1,4,8,11-tetrazacyclotetradecan)-nickel (II) perchlorate [NiL(ClO ₄) ₂]·2H ₂ O (3).....	78
3.3.5 Synthesis of VPI-100 (Cu).	78
3.3.6 Synthesis of VPI-100 (Ni).....	78
3.3.7 Structure Determination and Refinement.....	78
3.3.8 Structure Confirmation and Phase Purity.....	79
3.3.9 Single-Crystal X-ray Diffraction.....	79
3.3.10 Attenuated Total Reflectance Fourier-Transform Infrared Spectroscopy (ATR-FTIR).	80
3.3.11 Thermogravimetric Analysis (TGA).	80
3.3.12 Sample Activation and N ₂ /CO ₂ Adsorption Measurement.....	80
3.3.13 X-ray Photoelectron Spectroscopy (XPS).....	81
3.3.14 Scanning electron microscopy imaging (SEM).....	81
3.3.15 Stability Tests.	81
3.3.16 Inductively Coupled Plasma-Mass Spectrometry (ICP-MS).	81
3.3.17 Catalytic cycloaddition of CO ₂ to epoxides.	82
3.4 Results and Discussion	82
3.4.1 Synthesis and Characterization.	82
3.4.2 Investigation of gas adsorption.....	91
3.4.3 Catalytic performance of VPI-100 MOFs for CO ₂ chemical fixation	95
3.5 Conclusion	98
3.6 Acknowledgements.....	99
3.7 References.....	99
3.8 Supporting Information.....	102

3.8.1 Ligand Synthesis and Characterization	102
3.8.2 Single-Crystal X-ray Crystallography.....	104
3.8.3 Structure determination and refinement of VPI-100 (Cu) and VPI-100 (Ni)	106
3.8.4 Characterization of VPI-100 (Cu) and VPI-100 (Ni).....	109
3.8.5 Experimental N ₂ adsorption isothermal analysis and theoretical CO ₂ isotherm fitting of VPI-100 (Cu) and VPI-100 (Ni).....	114
3.8.6 Catalyst studies of cycloaddition of CO ₂ to epoxides using VPI-100.....	116
3.8.7 References:	134
Chapter 4 Insights into Hf-VPI-100 for CO₂ Adsorption and Chemical Fixation	135
4.1 Abstract	135
4.2 Introduction.....	135
4.3 Results and discussion	137
4.3.1 Synthesis and characterization	137
4.3.2 Cycloaddition of CO ₂ and epoxides	140
4.3.3 Quartz Crystal Microbalance (QCM).....	143
4.3.4 <i>In situ</i> PXRD	146
4.4 Experimental	147
4.4.1 Materials	147
4.4.2 Synthesis.....	147
4.4.3 Characterization and analysis	148
4.5 Conclusion	150
4.6 Acknowledgements.....	150
4.7 Reference	151
4.8 Supporting Information.....	152
4.8.1 Structure determination and refinement of Hf-VPI-100 (Cu) and Hf-VPI-100 (Ni)	152
4.8.2 Characterization of Hf-VPI-100 (Cu) and Hf-VPI-100 (Ni).....	153
4.8.3 Catalyst studies of cycloaddition of CO ₂ to epoxides using Hf-VPI-100	156
Chapter 5 Visible Light-Induced Cytotoxicity of Ru,Os-Polyazine Complexes Towards Rat Malignant Glioma.....	164
5.1 Abstract	164
5.2 Introduction.....	164
5.3 Experimental Section	167
5.3.1 Materials and methods.....	167
5.3.2 Synthesis of [(Ph ₂ phen) ₂ Ru(dpp)](PF ₆) ₂ (1).....	168
5.3.3 Synthesis of [(Ph ₂ phen) ₂ Os(dpp)](PF ₆) ₂ (2).....	168
5.3.4 ESI-TOF Mass Spectrometry	169

5.3.5 High performance liquid chromatography-mass spectroscopy (HPLC-MS).....	169
5.3.6 Electrochemistry.....	170
5.3.7 Electronic Absorption Spectroscopy.....	170
5.3.8 DNA Gel Shift Assay.....	170
5.3.9 Protein Gel Shift Assay.....	170
5.3.10 Cell Culture.....	171
5.3.11 Photocytotoxicity.....	171
5.4 Results and Discussion.....	171
5.4.1 Synthesis.....	171
5.4.2 Electrochemistry.....	171
5.4.3 Electronic Absorption Spectroscopy.....	173
5.4.4 DNA gel shift assay.....	174
5.4.5 Protein gel shift assay.....	176
5.4.6 Cytotoxicity.....	177
5.5 Conclusions.....	179
5.6 Acknowledgements.....	179
5.7 References.....	180
5.8 Supporting Information.....	181
Chapter 6 Exploring the Activity of a Polyazine Bridged Ru(II)–Pt(II) Supramolecule in F98 Rat Malignant Glioma Cells	184
6.1 Abstract.....	184
6.2 Introduction.....	184
6.3 Experimental Section.....	186
6.3.1 Synthesis and characterization of [(Ph ₂ phen) ₂ Ru(dpp)PtCl ₂]Cl ₂	186
6.3.2 Partition coefficient.....	189
6.3.3 DNA Gel Shift Assay.....	190
6.3.4 Protein Gel Shift Assay.....	190
6.3.5 Cell culture.....	191
6.3.6 Cell uptake of Ru(II)-Pt(II) by F98 MG cells.....	192
6.3.7 Cytotoxicity and photocytotoxicity.....	192
6.3.8 Design of LED Array.....	194
6.4 Results and Discussion.....	196
6.5 Conclusions.....	201
6.6 Acknowledgements.....	201
6.7 References.....	202

Chapter 7 Conclusions and Future Work	204
7.1 Conclusions	204
7.2 Future work	205
7.2.1 Design new metal-cyclam based MOFs	205
7.2.2 How to synthesize MOF containing free-base cyclam ligand	206
7.2.3 The interaction between epoxide and MOFs	208
7.3 Reference:	209
Appendix A Energy Transfer in Metal Organic Frameworks	211
1. Introduction	211
1.1 Background information about energy transfer	211
1. Coupling Regimes	212
2. Coupling Mechanisms	214
2.1. Distance dependence of coupling mechanisms	215
Förster type integral, $(ai jb)$: Turning our attention to the Förster (or coulomb) term, the explicit forms of this integral is	217
1.2 Why MOFs	220
2. Lanthanide-based Luminescent MOFs	222
2.1 Energy transfer in Ln-node based MOF	226
2.2 Ln@MOF	241
2.3 Summary	244
3. Ru/Os based MOF	245
3.1 Ru/Os in Zn-node based MOFs	247
3.2 Ru(bpy) ₃ ²⁺ doped zirconium(IV) MOFs	255
3.3 Summary	259
4. Porphyrin and metalloporphyrins based MOFs materials	260
4.1 Porphyrin-based MOFs as crystalline powders	262
4.2 Porphyrin-based MOFs as thin films	269
4.3 Summary	273
5. Non-Porphyrinic, Organic Chromophore -based MOFs	274
5.1 Summary	282
6. Conclusions	283
7. Reference	283

Attributions

Chapter 2 of this dissertation is a reprint of a manuscript published in the Journal of Photochemistry and Photobiology A: Chemistry to which the author, Jie Zhu, contributed significantly. Writing assistance and editing were provided by Dr. William A. Maza and Dr. Amanda J. Morris.

Chapter 3 is a reprint of a manuscript published in the Journal of the American Chemical Society. Jie Zhu synthesized and characterized the materials and performed the major experiments. Dr. Pavel M. Usov performed stability test and partial catalytic experiments and assisted with manuscript writing and editing. Dr. Wenqian Xu determined the structure of VPI-100 MOFs by powder X-ray diffraction using synchrotron radiation. Paula J Celis-Salazar and Dr. Carla Selbodnick helped to resolve the structures of metal cyclam complexes using single crystal X-ray diffraction. Shaoyang Lin provided TGA data. Matthew C. Kessinger collected XPS data. Dr. Carlos Landaverde-Alvarado calculated the isosteric heats of CO₂ adsorption. Meng Cai performed SEM imaging experiments. Ann M. May helped with repeating ligand synthesis. Dr. Dunru Zhu provided data for variable temperature powder X-ray diffraction. Dr. Sanjaya D. Senanayake assisted in writing and editing. Dr. Amanda J. Morris, principle investigator (PI), supervised the research project, provided experimental management and assisted in writing and editing.

Chapter 4 is in preparation for submission for publication. Jie Zhu synthesized and characterized the materials and performed the major experiments. Jianzhao Liu performed the QCM measurements and analysis, and assisted with manuscript writing and editing. Yered Arias-Machain helped with the catalytic experiments and repeated the MOF synthesis. Shaoyang Lin provide TGA data. Meng Cai performed SEM imaging experiments. Matthew C. Kessinger collected XPS data. Dr. Wenqian Xu determined the structure of Hf-VPI-100 MOFs by powder X-ray diffraction using synchrotron radiation. Dr. Pavel M. Usov helped the MOF figures. Dr. Sanjaya D. Senanayake assisted with the DRIFTs experiments. Dr. Alan R. Esker helped with the analysis of QCM data. Dr. Amanda J. Morris, principle investigator (PI), supervised the research project, provided experimental management and assisted in writing and editing.

Chapter 5 is a reprint of a manuscript published in the Inorganica Chimica Acta. Jie Zhu synthesized and characterized the materials and performed the major experiments. Jie Zhu also served as

corresponding author. Anthony Dominijanni helped with the cell study. José Á. Rodríguez-Corrales collected data for DNA gel shift assay and assisted with manuscript writing and editing. Reece Prussin provide the device for photolysis cell study. Zongmin Zhao performed the protein gel shift assay. Tinghui Li helped with the graph abstract. Dr. John L Robertson and Dr. Karen J. Brewer supervised the research project and served as principle investigators (PIs).

Chapter 6 is a reprint of a manuscript published in the Chemical Communications. Jie Zhu synthesized and characterized the materials and performed the major experiments. José Á. Rodríguez-Corrales collected data for DNA gel shift assays and assisted with manuscript writing and editing. Reece Prussin and Anthony Dominijanni helped with the cell study. Zongmin Zhao performed the protein gel shift assay. Dr. Samantha L. Hopkins initiated this project with some preliminary data during her Ph.D. study. Dr. Brenda S.J. Winkel served as corresponding author and assisted in writing and editing. Dr. John L. Robertson and Dr. Karen J. Brewer supervised the research project and served as principle investigators (PIs).

Appendix A is a reprint of a manuscript published as book chapter in the world scientific to which the author, Jie Zhu, contributed significantly. Dr. Nicholas Mayhall and Shaunak Shaikh wrote section 1.1. Dr. Amanda J. Morris, principle investigator (PI), assisted in writing and editing.

Preface

During my graduate study at Virginia Tech, I have also been involved with several projects, resulting in other publications, which are beyond the scope of this dissertation. The following is the list of publications to date from my graduate work at Virginia Tech.

1. **Zhu, J.**; Usov, P. M.; Xu, W.; Celis-Salazar, P. J.; Lin, S.; Kessinger, M. C.; Landaverde-Alvarado, C.; Cai, M.; May, A. M.; Slebodnick, C.; Zhu, D.; Senanayake, S. D.; Morris, A. J., “A New Class of Metal-Cyclam based Zirconium Metal-Organic Frameworks for CO₂ Adsorption and Chemical Fixation”, *J. Am. Chem. Soc.*, **2018**, 140, 993-1003. (Chapter 3)
2. **Zhu, J.**; Shaikh, S.; Mayhall, N.; Morris, A. J., “Energy Transfer in Metal-Organic Frameworks. In Elaboration and Applications of Metal-Organic Frameworks, *World Scientific: 2018*; pp 581-654. (Appendix A)
3. **Zhu, J.**; Maza, W. A.; Morris, A. J. “Light-harvesting and Energy Transfer in Ruthenium(II)-polypyridyl Doped Zirconium(IV) Metal-Organic Frameworks: a Look towards Solar Cell Applications”, *J. Photochem. Photobiol., A*, **2017**, 344, 64-77. (Chapter 2)
4. **Zhu, J.**; Rodriguez-Corrales, J. A.; Prussin, R.; Zhao, Z.; Dominijanni, A.; Hopkins, S. L.; Winkel, B. S. J.; Robertson, J. L.; Brewer, K. J., “Exploring the Activity of a Polyazine Bridged Ru(II)-Pt(II) Supramolecule in F98 Rat Malignant Glioma Cells”, *Chem. Commun.*, **2017**, 53, 145-148. (Chapter 6)
5. **Zhu, J.**; Dominijanni, A.; Rodríguez-Corrales, J. Á.; Prussin, R.; Zhao, Z.; Li, T.; Robertson, J. L.; Brewer, K. J., “Visible Light-induced Cytotoxicity of Ru,Os–Polyazine Complexes towards Rat Malignant Glioma”, *Inorg. Chim. Acta*, **2017**, 454, 155-161. (Chapter 5)
6. Lin, S.; Ravari, A. K.; **Zhu, J.**; Usov, P.; Cai, M.; Ahrenholtz, S. R.; Pushkar, Y.; Morris, A. J., “Insight into Metal–Organic Framework Reactivity: Chemical Water Oxidation Catalyzed by a [Ru(tpy)(dcbpy)(OH₂)]²⁺-Modified UiO-67”, *ChemSusChem*, **2018**, 11, 464-471.
7. Rowe, J. M.; Soderstrom, E. M.; **Zhu, J.**; Usov, P. M.; Morris, A. J., “Synthesis, Characterization, and Luminescent Properties of Two New Zr(IV) Metal–Organic Frameworks Based on Anthracene Derivatives”, *Can. J. Chem.*, **2017**, 999, 1-6.
8. Zhao, Z.; Lou, S.; Hu, Y.; **Zhu, J.**; Zhang, C., “A Nano-in-Nano Polymer–Dendrimer Nanoparticle-Based Nanosystem for Controlled Multidrug Delivery”, *Mol. Pharmaceut.*, **2017**, 14, 2697-2710.
9. Usov, P. M.; Huffman, B.; Epley, C. C.; Kessinger, M. C.; **Zhu, J.**; Maza, W. A.; Morris, A. J., “Study of Electrocatalytic Properties of Metal-Organic Framework, PCN-223 for the Oxygen Reduction Reaction”, *ACS Appl. Mater. Interfaces*, **2017**, 9, 33539-33543.
10. Lin, S.; Pineda-Galvan, Y.; Maza, W. A.; Epley, C. C.; **Zhu, J.**; Kessinger, M. C.; Pushkar, Y.; Morris, A. J., “Electrochemical Water Oxidation by a Catalyst-Modified Metal–Organic Framework Thin Film”, *ChemSusChem*, **2017**, 10, 514-522. (**Cover Article**)
11. Usov, P. M.; Ahrenholtz, S. R.; Maza, W. A.; Stratakes, B.; Epley, C. C.; Kessinger, M. C.; **Zhu, J.**; Morris, A. J., “Cooperative Electrochemical Water Oxidation by Zr Nodes and Ni-porphyrin Linkers of a PCN-224 MOF Thin Film”, *J. Mater. Chem. A*, **2016**, 4, 16818-16823.

12. Li, T.; Murphy, S.; Kiselev, B.; Bakshi, K. S.; Zhang, J.; Eltahir, A.; Zhang, Y.; Chen, Y.; **Zhu, J.**; Davis, R. M.; Madsen, L. A.; Morris, J. R.; Karolyi, D. R.; LaConte, S. M.; Sheng, Z.; Dorn, H. C., “A New Interleukin-13 Amino-Coated Gadolinium Metallofullerene Nanoparticle for Targeted MRI Detection of Glioblastoma Tumor Cells”, *J. Am. Chem. Soc.*, **2015**, 137, 7881-78

Chapter 1 Introduction

1.1 Research motivation

According to BP energy review¹, 85% of global energy consumption was based on fossil fuels in 2016 (Figure 1.1). Consequently, the burning of fossil fuels is leading to the rise of anthropogenic CO₂ emission, which can cause a series of environmental problems including global climate change² and ocean acidification³. As observed by NOAA earth system research lab, the atmospheric CO₂ level has increased 30% over the period 1960~2018 (from 315 ppm to 408 ppm). At present rates of generation, atmospheric CO₂ is predicted to exceed 500 ppm in 2050 and will result in a 0.7 to 1.5 °C global temperature rise.⁴ Although renewable energy such as solar energy has shown great promise as an ideal solution for our energy needs, it is still very challenging to change the dominance of fossil fuel in the energy supply in the short term and the CO₂ emission is predicted to increase further.⁵ Implementation of carbon capture and sequestration technologies has been proposed as a means of enabling the continued use of fossil fuels.⁶ Therefore, there is urgent demand for developing new materials for CO₂ capture and conversion.

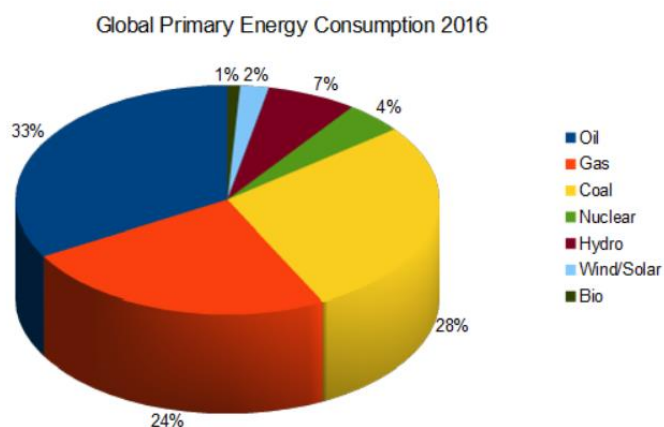


Figure 1.1 Global primary energy consumption by different sources in 2016. Reprinted with permission from ref.1.

1.2 CO₂ capture and conversion

1.2.1 CO₂ capture

One of the most promising strategies to reduce CO₂ emission is carbon capture and storage/sequestration (CCS). CCS is the process of capturing waste CO₂ from stationary point sources, such as fossil fuel power plants, and then sequestering it to underground geological formations (Figure 1.2). In fact, according to the Global CCS Institute in 2012, at least 16 industrial-scale projects were in operation or in construction, which could capture around 36 million tonnes CO₂ per year.⁶ The primary target for CCS technologies is to fit all coal and gas power plants by 2050 and reduce world CO₂ emissions from energy by 20%. However, CCS has been viewed as a costly venue, using 10% to 40% of the energy output from a power station to reduce the CO₂ emission, even as there is no set penalty for the release of CO₂ into the environment. Although there are still significant practical considerations associated with many other steps within CCS system, almost 70% of the cost of CCS is derived from the carbon capture step. Therefore, the greatest challenge for the implementation of CO₂ capture within power plants is to find new cost-effective materials that have suitable chemical and physical properties to be used in the real-world system.

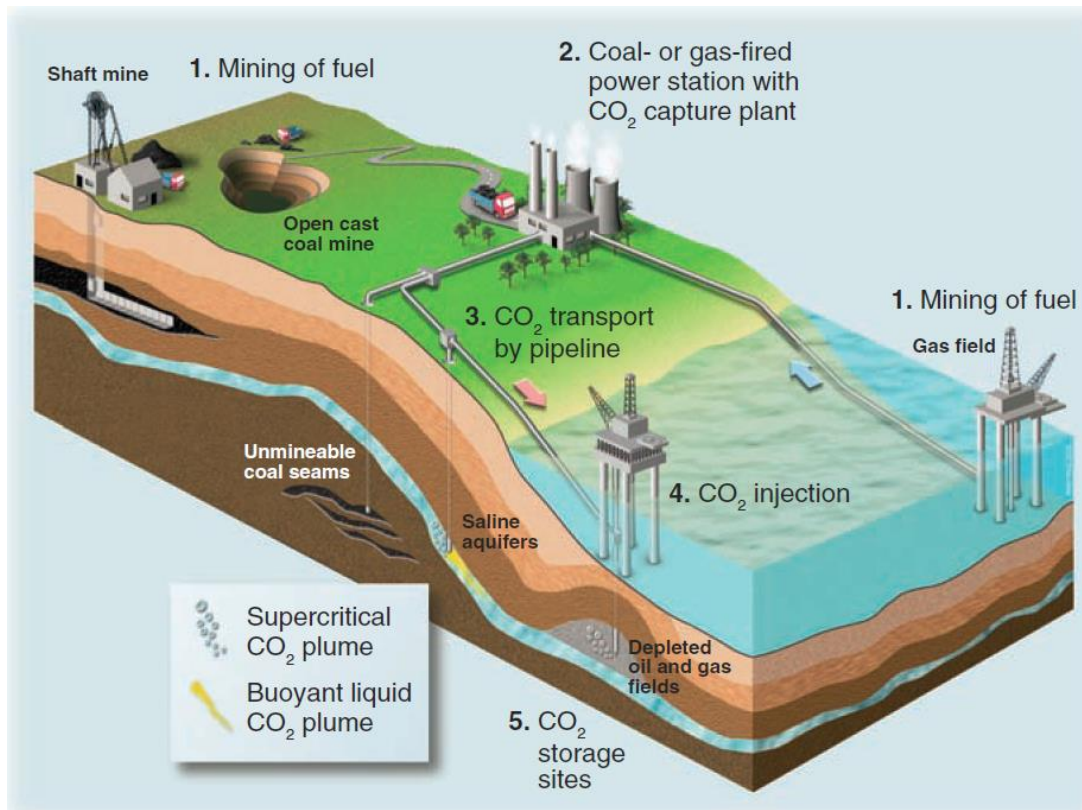


Figure 1.2 Diagrammatic representation of the life cycle chain of fossil fuel use. CO₂ separation and capture at power plants enables storage of CO₂ in porous rocks deep below ground. Adopted from ref. 6, Copyright 2009, Science.

In the context of fossil fuel power plants, three methods of CO₂ capture are currently being investigated. Post-combustion capture removes CO₂ from the flue gas after combustion of the fuel in the air. Pre-combustion capture chemically strips off the carbon, leaving hydrogen to burn, and oxyfuel combustion burns coal or gas in the denitrified air to yield on CO₂ and water. The development of CO₂ capture materials requires the consideration of numerous performance parameters, which must be finely adjusted depending on the type of CO₂ capture and the specific configuration of the power plant. Generally speaking, the ideal CO₂ capture materials should high selectivity towards CO₂, high stability under the capture and regeneration conditions, and effective CO₂ uptake at high density. Currently, the main existing CO₂ capture materials that have been used in industrial scale are aqueous alkanolamine solutions and porous solids, such as zeolites and activated carbons. Nonetheless, none of the materials fulfill all of the criteria mentioned above, which highlights the urgent need for new substances. In this regard, other types of porous materials are emerging as potential adsorbents for CO₂

capture applications, including covalent-organic frameworks (COFs),⁷ amine-grafted silicas,⁸ microporous organic polymers⁹ and metal-organic frameworks (MOFs).¹⁰ Among those, MOFs are arguably one of the most promising next-generation materials for CO₂ capture, although more research is needed to further optimize MOF properties for CCS.

1.2.2 CO₂ chemical transformation

Besides CCS, an alternative strategy to reduce CO₂ emission is making use of the potential chemical transformations of CO₂ to produce valuable carbon-based chemicals. Although such approaches would not be a viable long-term strategy owing to the tremendous scale of worldwide CO₂ emissions (ca. 30 Gt per year which can easily saturate the market for any desired chemicals), converting a considerable fraction of the emissive CO₂ can offer some recompense to the development of CCS technologies. Indeed, instead of treating CO₂ as a waste, it represents an important, non-toxic, abundant, and cheap C1 feedstock.

Carbon dioxide is a non-polar, linear molecule representing carbon in its highest oxidation state and is highly thermodynamically stable. Converting CO₂ to target compounds such as fuels requires significant energy input to overcome the thermodynamic barrier, and kinetic barriers necessitate the use of catalysts to limit overpotentials and promote product selectivity¹¹. For example, the one-electron reduction of CO₂ to CO₂^{•-} has a very high thermodynamic threshold, as evidenced by the reduction potential of -1.9 V vs. NHE. In contrast, however, with the presence of proton sources, proton-coupled, multielectron reduction reactions are more favorable in terms of electrochemical thermodynamics, and the more desirable products such as formic acid, formaldehyde, and methanol can be produced (Table 1.1)⁴. While proton coupled electron transfer (PCET) make those transformations more thermodynamically favorable, they also require an efficient catalyst¹² to selectively reduce CO₂ over H⁺ and to improve the slow kinetics of these processes. Therefore, it is clear that catalyst development for CO₂ chemical transformation is the key to solve the problem.

Table 1.1 Electrochemical reduction of CO₂ in the presence of a proton source (aqueous solutions, pH 7, vs. NHE)

Selected reduction reaction of CO ₂	E°/V
CO ₂ + e ⁻ → CO ₂ ^{-•}	-1.90
CO ₂ + 2H ⁺ + 2e ⁻ → CO + H ₂ O	-0.53
CO ₂ + 2H ⁺ + 2e ⁻ → HCO ₂ H	-0.61
CO ₂ + 6H ⁺ + 6e ⁻ → CH ₃ OH + H ₂ O	-0.38
CO ₂ + 8H ⁺ + 8e ⁻ → CH ₄ + 2H ₂ O	-0.24

1.3 Metal cyclam complexes

Cyclam (1,4,8,11-tetraazacyclotetradecane), first synthesized in 1937¹³, is one of the most studied and used macrocyclic polyamides. The 14-membered macrocyclic structure (Figure 1.3), characterized by four secondary amine group, exhibits rich coordination chemistry with different transition metals including Ni, Cu, Co, Cr, Ru, Cd, and Zn. Depending on the spatial alignment of the NH protons, there are five possible configurations of metal cyclam complexes: RSRS, RSRR, SSRR, RSSR, and RRRR, designated to *trans*-I to *trans*-V, respectively (Figure 1.3)¹⁴. Cyclam has applications in a wide variety of areas including catalysis¹⁵, bioinorganic¹⁶, biomimetic and medicine¹⁷⁻¹⁸. Moreover, the structural and chemical properties of cyclam can be altered by chemical modification on the macrocyclic ring with different substituents, which further extend the application of those cyclam derivatives¹⁸⁻²⁰. For my research, we are particularly interested in their role as catalysts in redox reactions, especially towards CO₂ reductions.

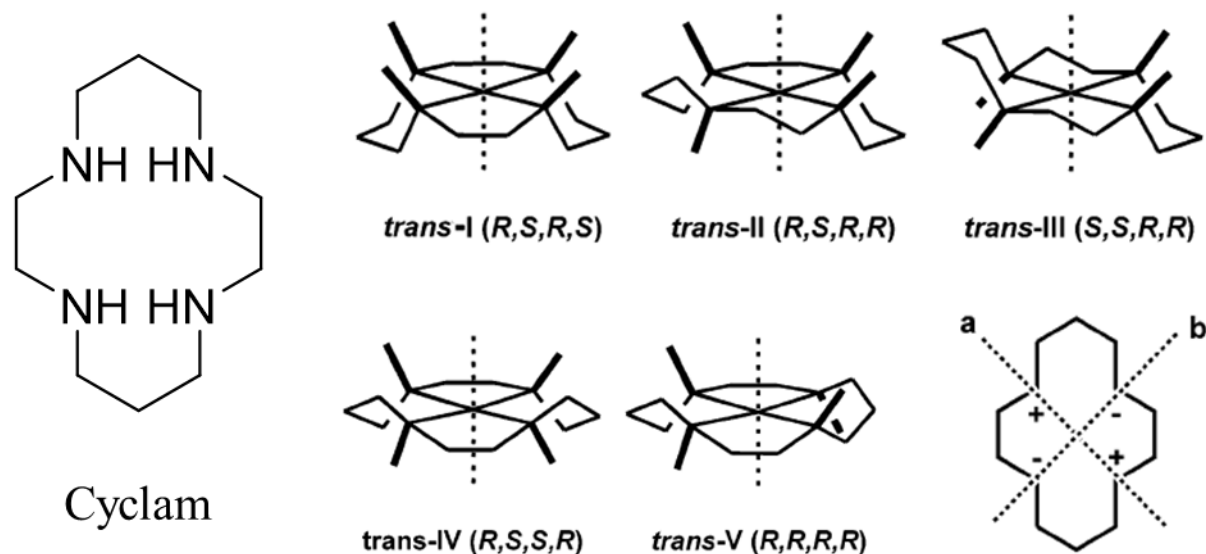
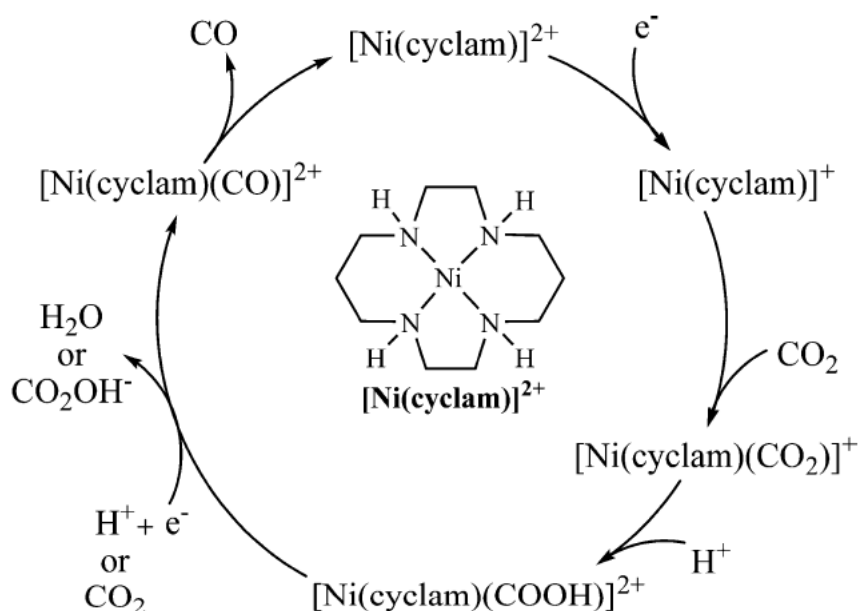


Figure 1.3 Five possible configurations of metal cyclam complexes, showing the different alignments of the NH protons and chirality at the N atoms. The folding of the *trans-V* configuration along axes *a* or *b* to give the *cis-V* configuration is shown in the bottom right (+ indicated NH proton above the cyclam plane, - below). Modified from ref.14 with permission. Copyright 2002, American Chemical Society.

$\text{Ni}(\text{cyclam})^{2+}$ and its derivatives have been recognized as highly selective catalysts for electrochemical CO_2 reduction in aqueous solution using mercury as working electrode²¹⁻²². CO was the main product for the reduction and the catalysts have shown remarkable stability. No significant degradation of $\text{Ni}(\text{cyclam})^{2+}$ was observed after 10,000 electrocatalytic cycles and the turnover frequency was $\sim 10^3$ mol of CO produced per mole of nickel complex in one hour.²² A mechanistic study using CV, polarography, and electrocapillarity indicated that the $\text{Ni}(\text{I})$ -cyclam adsorbed complex on Hg was the active catalyst.²³ Both $\text{Ni}(\text{II})$ - and $\text{Ni}(\text{I})$ - cyclam can adsorb on Hg, and the oxidation states of the adsorbed complexes depend on the electrode potentials. The surface concentration of catalytic $\text{Ni}(\text{I})$ - cyclam decreases gradually with a decrease in the potential and desorbs completely at potential more negative than -1.7 V under CO or CO_2 . The desorption of $\text{Ni}(\text{I})$ -cyclam is due to the formation of $\text{Ni}(\text{I})$ -cyclam-CO by the reaction of $\text{Ni}(\text{I})$ -cyclam in solution with electrocatalytically generated CO from CO_2 .²³ Using electrochemistry and infrared spectroelectrochemistry (IR-SEC) the Kubiak group observed that the formation of deactivated species, $\text{Ni}(\text{I})$ -cyclam-CO, is a major limitation for higher catalytic currents, while adding a CO scavenger leads to a substantial increase (up to 10 times) in the catalytic current for CO_2 reduction.²⁴ The proposed CO_2 reduction catalytic

cycle is summarized in scheme 1.1. Density functional theory (DFT) calculations also probed the optimized geometry for the $[\text{Ni}(\text{cyclam})(\text{CO})]^+$ species²⁴⁻²⁵. Other molecular materials that are structurally similar to Ni(II)cyclam have also been studied as electrocatalysts for CO_2 reduction at the mercury working electrode, which further highlights the importance of surface geometries for the adsorbed catalytic active species and electronic effects on the cyclam backbone²⁶⁻²⁷.

Scheme 1.1 Proposed CO_2 reduction catalytic cycle for $[\text{Ni}(\text{cyclam})]^{2+}$. Reprint from ref.24 with permission. Copyright 2015, American Chemical Society.



Considering that the utilization of mercury electrodes is not environmental friendly, CO_2 electroreduction catalyzed by Ni-cyclam complexes on non-mercury electrodes has also been explored. $\text{Ni}(\text{cyclam})^{2+}$ still can reduce CO_2 to CO using glassy carbon as the working electrode with less catalytic activity that has been observed on mercury electrodes.²⁸ Coated with other substrates, such as a Nafion film²⁹, metal oxide³⁰ or a poly-(allylamine) (PALA) backbone³¹, Ni-cyclam complex also demonstrates some effective electrocatalytic activity for CO_2 reduction. If the geometry of adsorbed Ni(I)cyclam on a Hg surface can be mimicked by chemical modification on the cyclam backbone, it would be a step closer to a more environmentally benign catalyst system.

1.4 Metal-organic frameworks

Metal-organic frameworks (MOFs), also known as porous coordination polymers (PCPs), are crystalline porous materials constructed by linking metal-based nodes (single ions or clusters) and organic linkers to form one-, two-, or three-dimensional coordination networks. Although the research on coordination polymers traces back to 1965³², the more descriptive term MOFs was introduced in 1995³³ and is now widely accepted. Characterized by their wide range of well-defined and tailorable pore sizes, pore geometries, high void fractions and large surface areas, MOFs have become one of the most exciting materials in porous materials science. The surface area of such hybrid crystalline materials can be as high as 10,000 m²/g³⁴, which substantially exceeds those of traditional porous materials such as zeolites (ca.1000 m²/g) and activated carbons (3500 m²/g)³⁵. According to the Cambridge Structural Database (CSD), the number of existing MOFs passed 70,000 in 2017 and more than 20,000 different MOFs have been reported and studied in the past decade³⁶. This large number of MOFs has been obtained by combining roughly 100 different nodes with approximately 1000 different ditopic or polytopic organic linkers. Considering that more than 100 million organic compounds have been synthesized so far, which are all, in principle, suitable as MOF linkers after appropriate functionalization, there is virtually no upper limit to the number of possible structures.³⁷

Originally explored for applications in gas storage^{10, 38-39} and separation⁴⁰⁻⁴³, MOF applications⁴⁴ have expanded to many different areas including catalysis⁴⁵⁻⁴⁶, drug delivery⁴⁷⁻⁴⁸, light harvesting⁴⁹⁻⁵¹, and energy transfer⁵²⁻⁵³. Diverse synthetic approaches have made it feasible to precisely control over the assembly of these high-ordered porous materials⁴⁴. MOF chemistry has developed to the point where the composition, structure, functionality, porosity, and metrics of a metal-organic structure can be designed for specific applications. An area of focus for my research involved the design and study of novel MOF materials as catalysts for CO₂ chemical transformations.

1.4.1 Famous MOFs

Among the large number of reported MOFs, few MOFs are well-studied. MOF-5, debatably the most famous MOF, is the first reported robust and highly porous MOF with x-ray single crystal structure determination and low-temperature, low pressure gas sorption properties⁵⁴. The framework comprises $Zn_4O(CO_2)_6$ octahedral secondary building units (SBUs) linked by six ditopic 1,4-benzenedicarboxylate (BDC^{2-}) ligands to form a cubic structure (Figure 1.4). Later, a family of 16 cubic MOFs – IRMOF-1 (also known as MOF-5) to IRMOF-16 – with the same topology (isorecticular) was prepared³⁸. This development not only highlighted the potential for expanding and functionalizing MOFs for applications in gas storage and separation but also proved that the concept of isorecticular expansion is synthetically feasible.

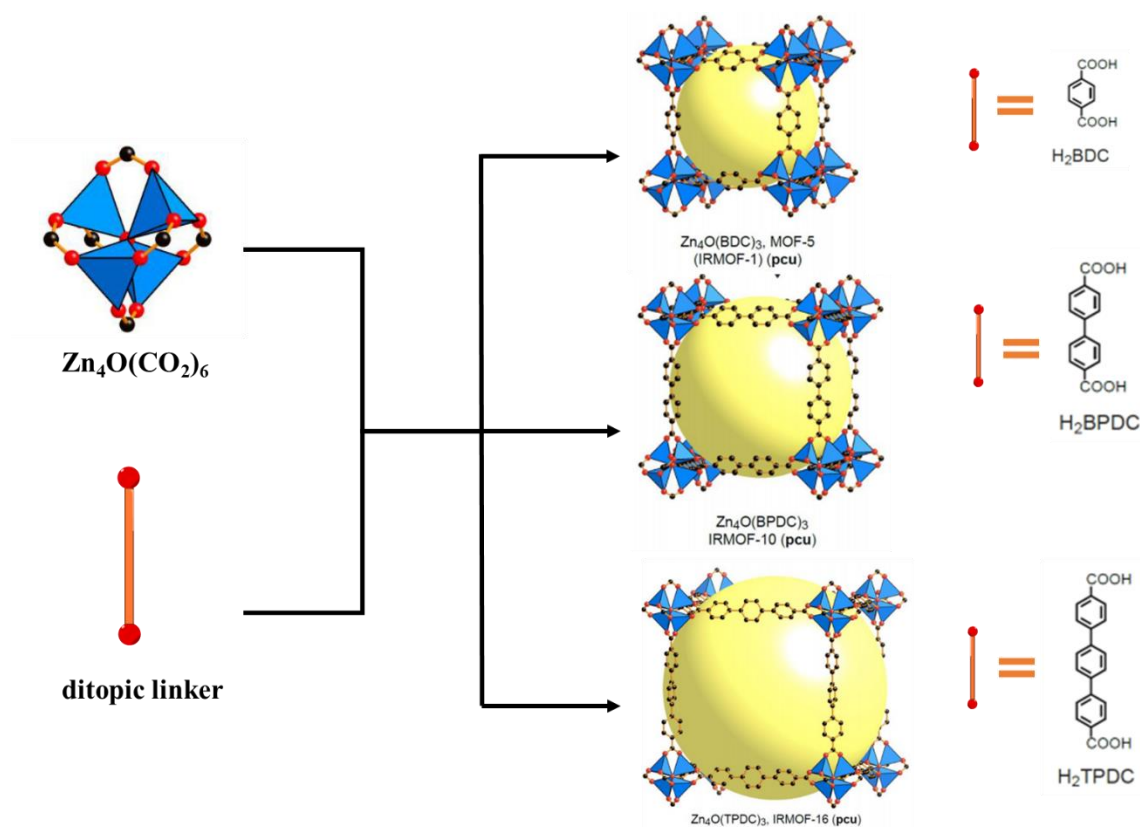


Figure 1.4 The schematic representation of isorecticular expansion of metal-organic frameworks with pcu nets. The same inorganic SBUs combined with ditopic organic linkers in different length to obtain IRMOF-1 (MOF-5), IRMOF-10 and IRMOF-16. The large yellow sphere represents the largest sphere that would occupy the cavity. Atom colors; C, black; O, red; Zn, blue polyhedra. Hydrogen atoms are omitted for clarity. Modified from ref. 44 with permission. Copyright 2013, Science.

HKUST-1⁵⁵ [where HKUST = Hong Kong University of Science and Technology; $Cu_3(BTC)_2$; BTC^{3-} = benzene-1,3,5-tricarboxylate] is one of the most studied MOFs,

exhibiting cubic, twisted boracite topology composed of a dinuclear Cu paddlewheel $[\text{Cu}_2(\text{CO}_2)_4]$ SBUs and a tritopic linker, BTC^{3-} . Similar to the example of MOF-5 mentioned above, several isorecticular structures have been made by expansion with organic linkers, including TATB^{3-} [4,4',4''-(1,3,5-triazine-2,4,6-triyl)tribenzoate], and BBC^{3-} [4,4',4''-(benzene-1,3,5-triyl-tris(benzene-4,1-diyl))tribenzoate] linkers (Figure 1.5). More interestingly, the as-synthesized form of the framework contains bound solvent molecules on the axial coordination sites of each Cu^{2+} metal center, which can subsequently be removed to create the open metal sites or replaced by other guest molecules. Indeed, these sites have been shown to act as Lewis acid sites⁵⁶⁻⁵⁷. The discovery unlocks the opportunity to explore the catalytic reactivity related to inorganic nodes, instead of treating them as the inert framework-building components. What is more, the HKUST-1 structure type can be prepared using a variety of metal ions ($\text{M} = \text{Cr}$, Fe , Zn , Mo and Ru)⁵⁸⁻⁶², even with mixed-metal species⁶³ or mixed-valence metal ions⁵⁹,
64.

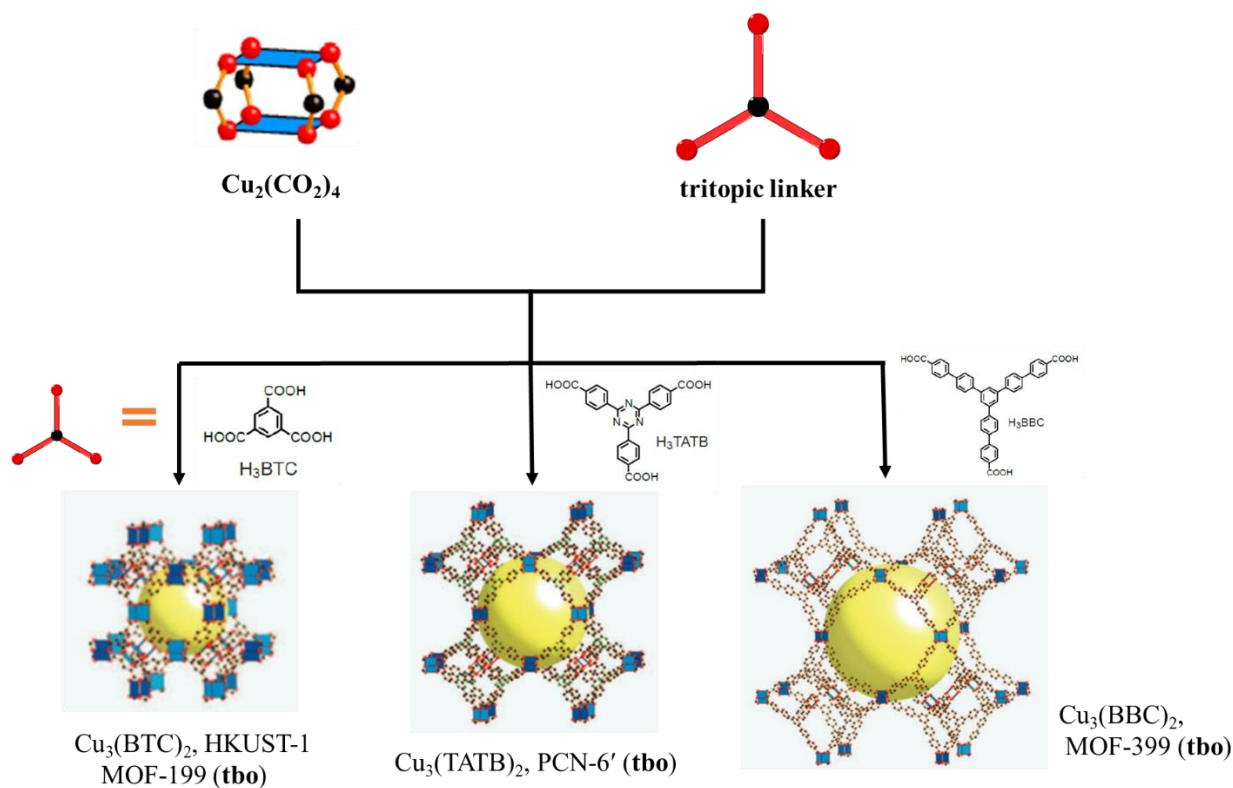


Figure 1.5 The schematic representation of isorecticular expansion of metal-organic frameworks with **tbo** nets. The same inorganic SBUs combined with different tritopic organic linkers to obtain HKUST-1, PCN-6, and MOF-399. The large yellow sphere represents the largest sphere that would occupy the cavity. Atom colors; C,

black; O, red; Cu, blue polyhedra. Hydrogen atoms are omitted for clarity. Modified from ref. 44 with permission. Copyright 2013, Science.

There are many other famous MOFs, such as MIL-101, ZIF-8, and CPO-27/MOF-74 (Figure 1.6), which have been well studied in different areas. One interesting fact about those MOFs is that they are all commercially available, although no particularly industrial applications have been developed for those structures. I could write more about those MOFs and go on with many more examples, however, as Voltaire put it “le secret d’ennuyer est celui de tout dire (The secret of being a bore is to tell everything).” Instead, I would like to summarize the MOFs with benchmark records for different properties and applications as shown in Table 1.2.

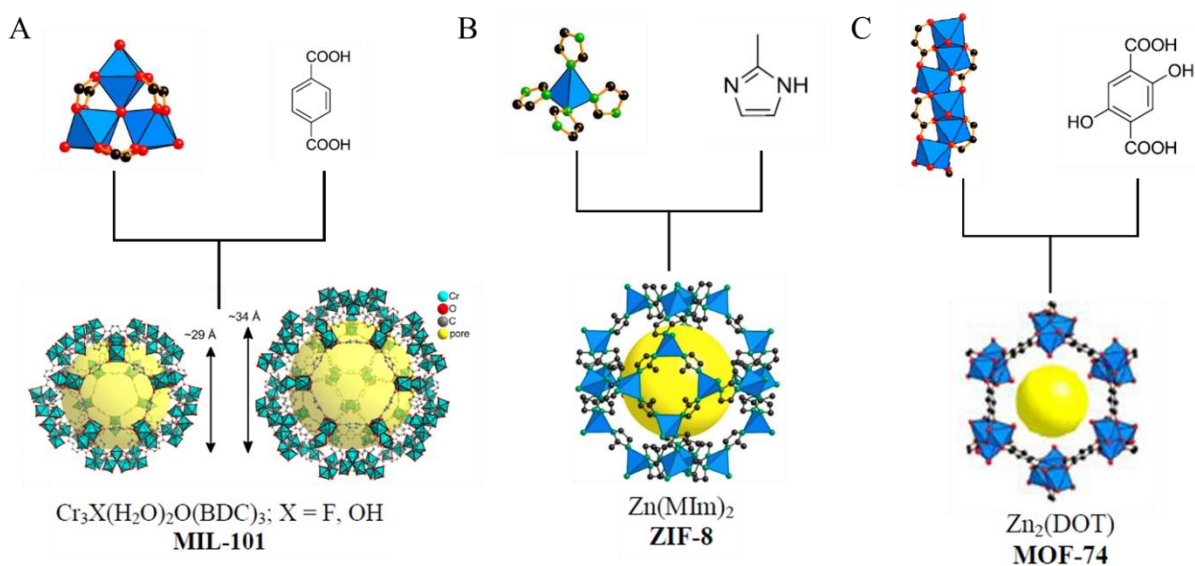


Figure 1.6 Inorganic secondary building units, organic linkers and crystal structures of representative MOFs (A) MIL-101; (B) ZIF-8; (C) MOF-74 (Zn). Modified from ref.44 with permission. Copyright 2013, Science.

Table 1.2 MOFs exhibit the lowest and highest values for the indicated property.

Property	MOF	Record value
Lowest density	NU-1301 ⁶⁵	0.124 g/cm ³
<i>Highest reported value</i>		
Pore aperture	IRMOF-74-XI ⁶⁶	98 Å
Number of organic linkers	MTV-MOF-5 ⁶⁷	8
Degrees of interpenetration	Ag ₆ (OH) ₂ (H ₂ O) ₄ (TIPA) ₅ ⁶⁸	54
BET surface area	NU-110 ³⁴	7140 m ² /g

Pore volume	NU-110 ³⁴	4.40 cm ³ /g
Excess hydrogen uptake (77 K, 56 bar)	NU-100 ⁶⁹	9.0 wt%
Excess methane uptake (298 K, 35 bar)	UTSA-76a ⁷⁰	211 cm ³ /cm ³
Methane working capacity(298 K, 35 bar)	Co(BDP) ³⁹	155 cm ³ /cm ³
Excess carbon dioxide uptake (298 K, 50 bar)	MOF-200 ⁷¹	2347 mg/g
Low pressure carbon dioxide uptake (298 K, 1 bar)	Mg ₂ (dobdc) ⁷²	379 mg/g
Proton conductivity (98% relative humidity, 60 °C)	Im-Fe-MOF ⁷³	1.21x10 ⁻² S/cm ⁻¹
Charge mobility	Zn ₂ (TTFTB) ⁷⁴	0.2 cm ² /V•s

1.4.2. Designing stable MOFs

A drawback of MOFs has long been their limited chemical and thermal stability. Indeed, the robustness and reactivity of a framework is mainly dependent on its metal-ligand interactions, where the metal nodes are often vulnerable to ligand substitution by water or other nucleophiles, meaning that the framework may collapse in hydrated environments. Other frameworks may collapse upon thermal or vacuum treatment or simply over time. This instability limits the practical applications of many MOFs. Based on the fundamentals of MOF stability, stable MOFs are classified into two categories: high-valency metal-carboxylate frameworks and low-valency metal-azolate frameworks⁷⁵⁻⁷⁶. Specifically, we are interested in designing stable frameworks by building strong metal-ligand bonding⁷⁷ between high-valent metal ions (such as Ti⁴⁺, Zr⁴⁺, Al³⁺, Fe³⁺, and Cr³⁺) with carboxylate-based ligands. The design principle is consistent with Pearson's hard/soft acid/base (HSAB) theory⁷⁸, where carboxylate-based ligands serve as hard bases, and high-valent metal cations serve as hard acids.

Tetravalent metal (Ti⁴⁺, Zr⁴⁺, Hf⁴⁺ or Ce⁴⁺) and carboxylate linker-based MOFs have drawn particular attention in MOF research due to their exceptional chemical and thermal stability. Among them, Zr-MOFs⁷⁹ with various compositions and structural types are the most studied and developed subgroups. Instead of covering all the Zr-MOFs in this section, I would like to introduce some representative structures of Zr-MOFs. The first

example of the Zr-MOF, $Zr_6(\mu_3-O)_4(\mu_3-OH)_4(BDC)_6$ (UiO-66, where UiO = University of Oslo, Figure 1.7), was reported in 2008⁸⁰. It is constructed from 12 connected $[Zr_6(\mu_3-O)_4(\mu_3-OH)_4(COO)_{12}]$ clusters (SBUs) (Figure 1.7A) and linear dicarboxylate linkers (1,4-benzene-dicarboxylate, BDC). Within the octahedral cluster, six vertices are occupied by Zr^{4+} and eight triangular faces are alternatively capped by four μ_3-OH and four μ_3-O . Each cluster is fully coordinated by 12 carboxylate groups to form $[Zr_6(\mu_3-O)_4(\mu_3-OH)_4(COO)_{12}]$ SBU with the O_h -symmetry. Each BDC^{2-} links two SBUs to build a 3D **fcu** network with tetrahedral (Figure 1.7B) and octahedral cages (Figure 1.7C), where each octahedral cage is connected to eight tetrahedral cages through sharing triangular windows. The structure of UiO-66 exhibits exceptional thermal stability (up to 540 °C) and chemical stability. Two isostructural MOFs, UiO-67 and UiO-68, were also synthesized at the same time by the elongation of linkers (Figure 1.7D).

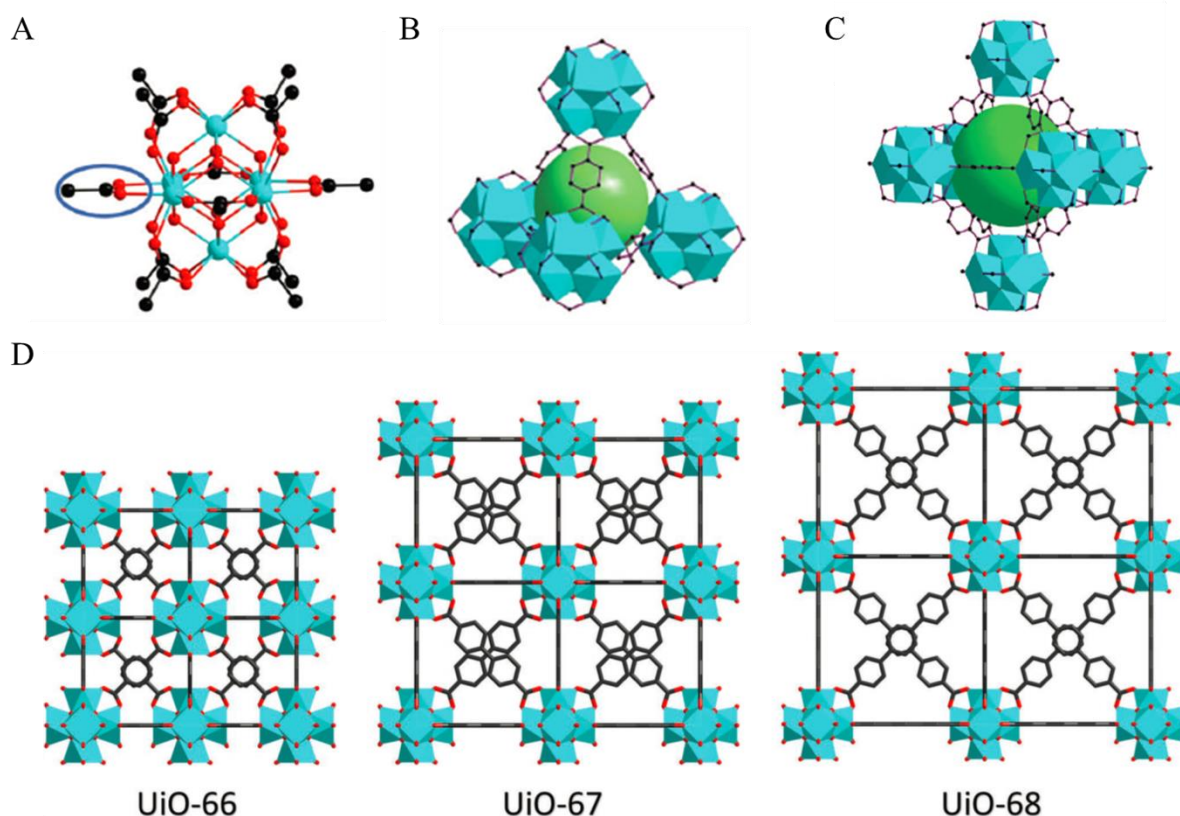
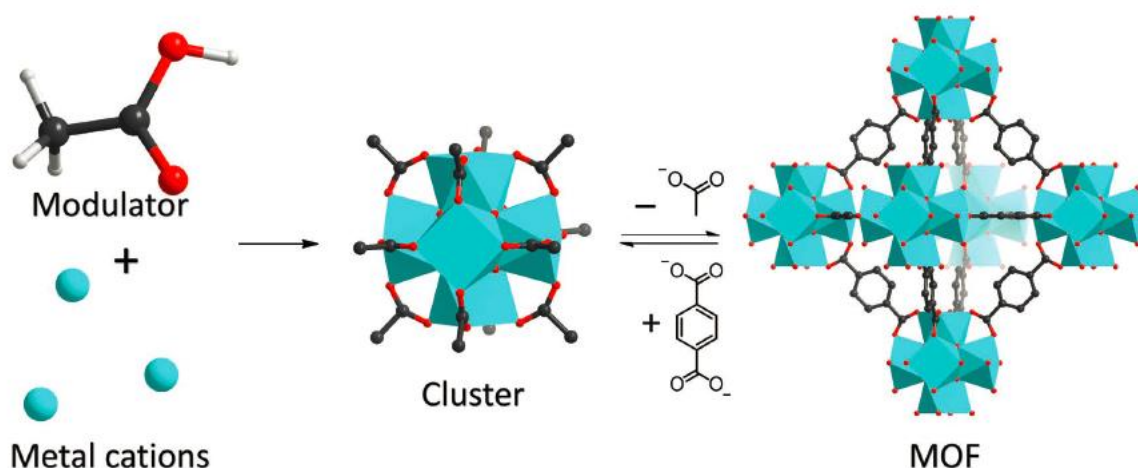


Figure 1.7 (A) The 12-connected $[Zr_6(\mu_3-O)_4(\mu_3-OH)_4(COO)_{12}]$ in UiO-66; (B) tetrahedral cage in UiO-66; (C) octahedral cage in UiO-66; (D) structures of UiO-66, 67 and 68. Modified from ref.75 with permission. Copyright 2018, Wiley.

Three years after the discovery of UiO-66, Schaate et al. reported the modulated synthetic strategy to prepare Zr-MOFs with controllable particle sizes in 2011⁸¹.

Modulated synthesis refers to the regulation of the coordination equilibrium by the modulator which either competitively coordinates with the metals or suppresses the deprotonation of the linkers (Scheme 1.2). As a result, the competitive reaction can reduce the rate of nucleation and slow down crystal growth to help produce highly crystalline products. With modulated synthesis, single crystals of UiO-68-NH₂ were obtained and solved by single-crystal X-ray diffraction (XRD), providing the first single crystal structure of a Zr-MOF. The study dramatically accelerated the development of Zr-MOF because single crystalline samples allow facile and precise structural determination by single-crystal XRD. Following this work, more Zr-MOFs were synthesized, and their applications were extensively explored.

Scheme 1.2 Representative scheme for modulated synthesis. Reprinted from ref. 75. Copyright 2018, Wiley.



Numerous isostructural analogues of UiO-66 have been reported, Zr-MOFs containing similar $[\text{Zr}_6(\mu_3\text{-O})_4(\mu_3\text{-OH})_4]$ core with different connection numbers were obtained. The first 8-connected $[\text{Zr}_6(\mu_3\text{-O})_4(\mu_3\text{-OH})_4(\text{OH})_4(\text{H}_2\text{O})(\text{COO})_8]$ cluster was observed in PCN-222 (Figure 1.8A), in which four equatorial carboxylates were replaced by four pairs of the terminal $-\text{OH}/\text{H}_2\text{O}$ ligands⁸². Following this work, other structures based on similar 8-connected Zr-clusters and square planar (NU-1000, Figure 1.8B)⁸³, tetrahedral (PCN-521)⁸⁴, or linear carboxylate linkers (PCN-700)⁸⁵ were discovered. Although the connection number is decreased, the stability of those 8-connected Zr-MOFs is not compromised. For example, both PCN-222 and NU-1000 can maintain high crystalline and surface area in concentrated HCl solutions. Instead, the coordinative unsaturated Zr-

nodes also allow further modification with external ligands or metals, providing a versatile platform for different applications⁸⁵⁻⁸⁶. 6-connected $[\text{Zr}_6(\mu_3\text{-O})_4(\mu_3\text{-OH})_4(\text{OH})_6(\text{H}_2\text{O})_6(\text{COO})_6]$ clusters⁸⁷⁻⁸⁹ and 10-connected $[\text{Zr}_6\text{O}_4(\text{OH})_4(\text{tdc})_5(\text{CH}_3\text{COO})_2(\text{H}_2\text{O})_2]$ ⁹⁰ MOF were also documented, demonstrating structural and functional diversity without losing stability as 12-connected Zr-MOFs. In these studies, analogues based on Hf were often isolated as isostructural materials and usually used to increase the Lewis acidity of the node for specific catalytic reactions⁹¹.

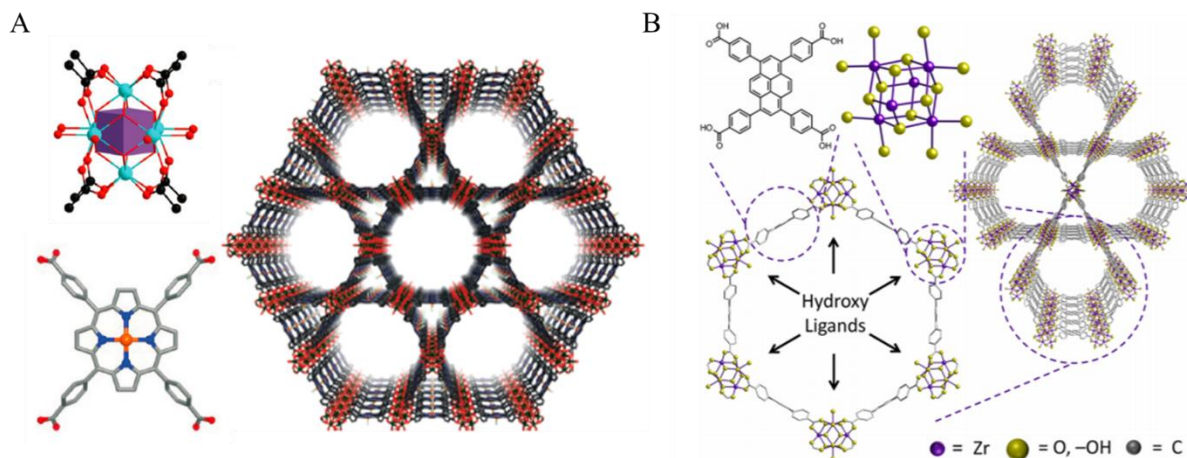


Figure 1.8 (A) The node, ligand and MOF structure of PCN-222(Fe); (B) The node, ligand and MOF structure of NU-1000. Modified from ref. 82 and ref. 83 with permission. Copyright 2012, Wiley and Copyright 2013, American Chemical Society.

1.4.3 Azamacrocyclic-based Metal Organic Frameworks

Polyazamacrocycles denote as a class of macrocyclic ligands that can be used as organic building blocks for MOFs. Incorporation of azamacrocycles in the MOF architectures provides the opportunity to import N-donors, advance topological diversity, and impart potential hierarchical porosity associated with macrocycles.⁹² Directly employing azamacrocycles as organic linkers for constructing MOFs can be very challenging, mainly because of the lack of coordination sites to form the extended framework and various conformations of N₄ azamacrocycles. The reported azamacrocycles-based MOFs can be divided by two design strategies: 1. employing discrete transition metal-azamacrocyclic complexes as organic linkers where the metal core can coordinate with other co-linkers to form the extended framework. 2. Using functionalized derivatives of azamacrocycles where synthetic modification via N-

alkylation can integrate pendant arms bearing coordination sites, such as carboxylates, phosphonate, nitriles etc.⁹³

1.4.3.1 Metal-azamacrocyclic complexes based MOFs

The earliest reported azamacrocyclic-based MOFs were synthesized by Choi et al. in 1988. Two 2D networks with brick wall and honeycomb structures were prepared by the Ni(II)-macrocyclic complex containing hydroxyl pendent chains and 1,3,5-benzenetricarboxylate (BTC³⁻).⁹⁴ Each Ni(II)-macrocyclic binds two BTC³⁻ in *trans* position and each BTC³⁻ coordinates three Ni(II)-macrocyclic units via C₁ symmetry in brick wall structure and C₃ symmetry in honeycomb structure. Six macrocycles and six tridentate ligands form the simplest cavity of the 2D networks (Figure 1.9). In 2005, the same research group reported a 2D network of threefold parallel interwoven (6,3) nets that were constructed by Ni(II) cyclam complex and 1,3,5-tris[2-(4-carboxyphenyl)-1-ethynyl]benzene. This MOF structure contains triangle voids of effective cavity size 18.4 × 14.7 × 9.5 Å³ and 35% free crystal volume.

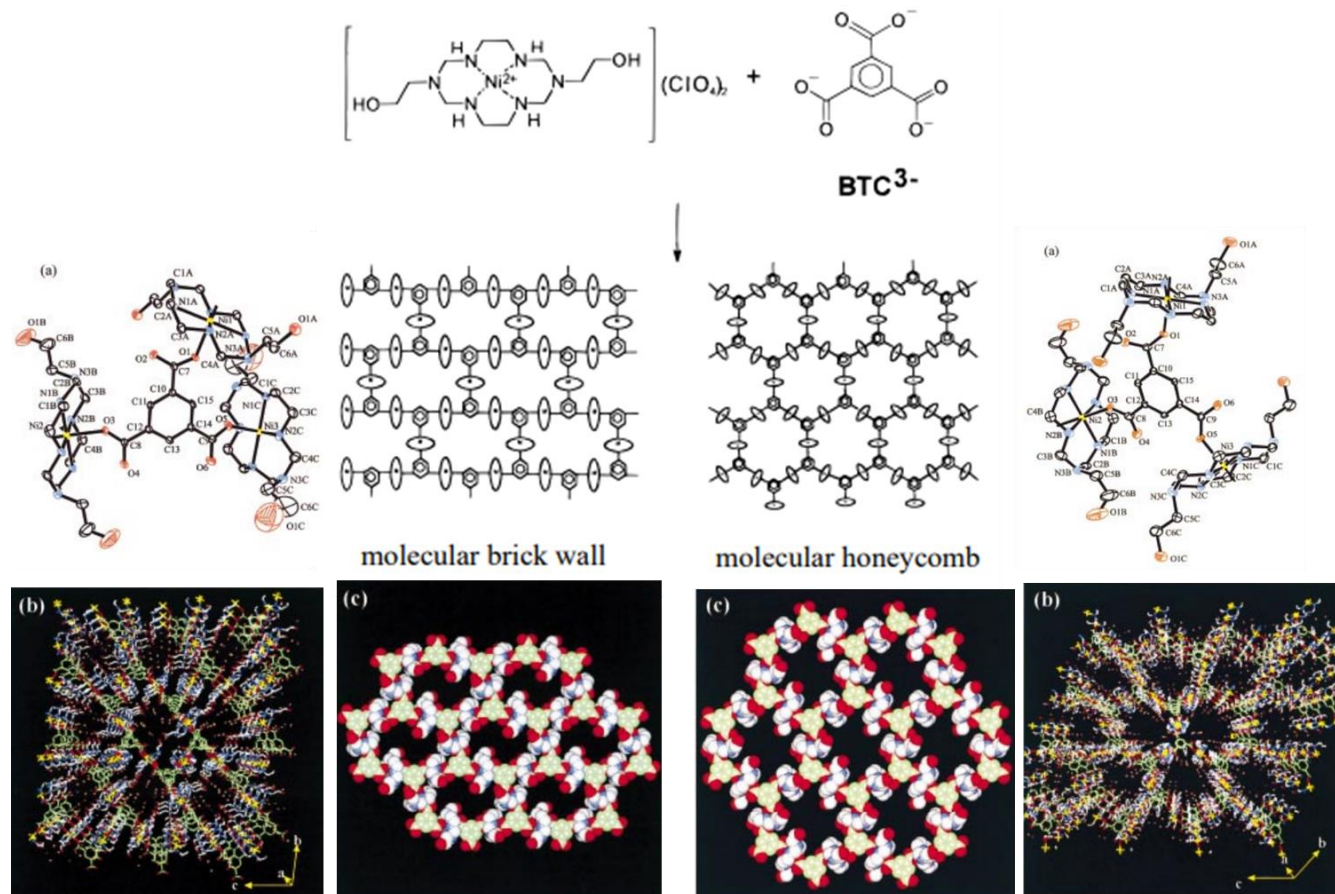


Figure 1.9 Azamacrocyclic MOFs formed using Ni(II)-1,3,5,8,10,12-hexaazacyclotetradecane-3,10-diethanol macrocyclic complex with BTC³⁻. Modified with the permission from ref. 94. Copyright 1998 American Chemical Society.

3D pseudo-MOF type structures can be constructed by 1D coordination polymer chains through supramolecular interactions. As demonstrated by Suh et al., a robust metal-organic open framework, [Ni(cyclam)(bpydc)]·5H₂O, is constructed by linear chains made of Ni(II)-cyclam and 2,2'-bipyridyl-5,5'-dicarboxylate (bpydc²⁻) (Figure 1.10A).⁹⁵ The coordination polymer chains extended in three different directions and stacked to form 1D channels that are filled with water molecules, which can be removed completely or reabsorbed with the retention of the single crystallinity. A similar structure was obtained with a Ni(II)-cyclam derivative complex alongside 4,4'-biphenyldicarboxylate (bpdc). The resulting framework [$\{\text{Ni}(\text{C}_{10}\text{H}_{26}\text{N}_6)\}_3(\text{bpdc})_3\} \cdot 2 \text{C}_5\text{H}_5\text{N} \cdot 6\text{H}_2\text{O}$] exhibited 1D channels with honeycomb openings of an effective 7.3 Å pore size (Figure 1.10B). The MOF served as a redox catalyst for the synthesis of silver nanoparticles at room temperature.⁹⁶

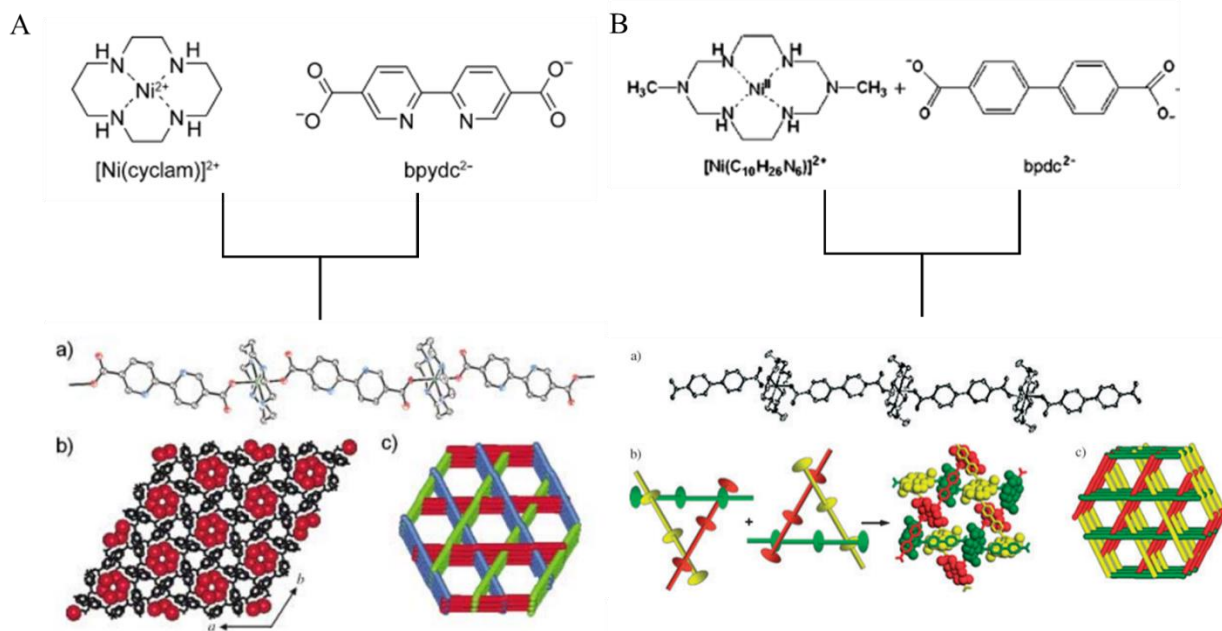


Figure 1.10 X-ray structure of (A) [Ni(cyclam)(bpydc)]·5H₂O; (B) [$\{\text{Ni}(\text{C}_{10}\text{H}_{26}\text{N}_6)\}_3(\text{bpdc})_3\} \cdot 2 \text{C}_5\text{H}_5\text{N} \cdot 6\text{H}_2\text{O}$]. Reprint with permission from ref.95 and ref. 96. Copyright 2004, Wiley and Copyright 2005, Wiley.

In addition to 1D linear coordination polymer chains, 2D and 3D MOF structures have also been discovered using metal-cyclam and co-linkers. A one pot reaction between the [Mo^{IV}(CN)₈]⁴⁻ and [Cu(cyclam)]²⁺ complex in aqueous solution yields a 2D cyano-

bridged coordination polymer $[\text{Cu}(\text{cyclam})]_2[\text{Mo}(\text{CN})_8] \cdot 10.5\text{H}_2\text{O}$. The framework composed by neutral zigzag sheet layers connected by hydrogen bonding.⁹⁷ Utilization of tetrahedral bridging ligand with metal cyclam complex tends to produce the diamond-like structure. In 2005, Suh and coworkers obtained an 8-fold interpenetrating diamondoid network, $[\text{Ni}(\text{cyclam})_2][\text{TCM}] \cdot 2\text{DMF} \cdot 10\text{H}_2\text{O}$ from the self-assembly of Ni(II)-cyclam and tetrakis[4-(carboxyphenyl)oxamethyl] methane (TCM) in DMF/water (Figure 1.11A).⁹⁸ In 2016, Almási et al. reported a four-fold interpenetrated diamondoid structure $\{[\text{Zn}_2(\mu_4\text{-MTB})(\kappa^4\text{-CYC})_2] \cdot 2\text{DMF} \cdot 7\text{H}_2\text{O}\}_n$ (Figure 1.11B) using cyclam, zinc salt and tetrahedral methanetetra benzoate (MTB^{4-}).⁹⁹

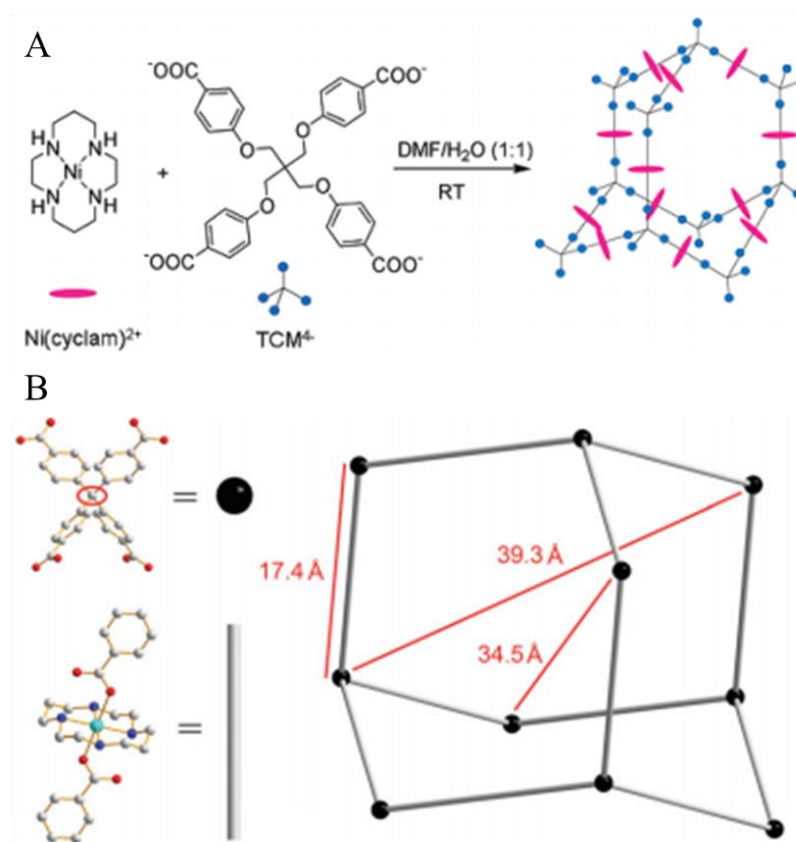


Figure 1.11 The synthetic scheme of $[\text{Ni}(\text{cyclam})_2][\text{TCM}] \cdot 2\text{DMF} \cdot 10\text{H}_2\text{O}$ (A) and $\{[\text{Zn}_2(\mu_4\text{-MTB})(\kappa^4\text{-CYC})_2] \cdot 2\text{DMF} \cdot 7\text{H}_2\text{O}\}_n$ (B). Reprint with permission from ref. 98 and ref. 99. Copyright 2005, American Chemical Society and Copyright 2016, Royal Society of Chemistry.

As demonstrated by these examples, the strategy employing discrete transition metal-azamacrocyclic complexes has certain limitations to deliver the functional diversity in designed frameworks: 1. It is hard to predict the topology and structure of designed MOFs. 2. To obtain extended framework, secondary linker other than macrocyclic

ligands is commonly used. 3. The dimension, pore size of the prepared structure is highly depended on the structure of co-linkers. 4. The metal center of azamacrocyclic complexes participated in the structural backbone of the framework, consequently precluding guest binding and subsequent metal-mediated reactivity.

1.4.3.2 Functionalized azamacrocyclic based MOFs

Instead of directly using metal-azamacrocyclics as linear linkers, macrocyclic ligands can be modified as polydentate structural building unit via N-alkylation of coordination capable pendant arms. Functionalized derivatives of azamacrocyclics often still form a metal-azamacrocyclic complex *in situ* or by design before crystallization of an extended framework. Coordination of the functional moieties such as carboxylates, phosphonate, and nitriles to metal ion or metal cluster may lead to intriguing 3D structures, and in some cases, other secondary co-ligands may be introduced to further increase the structural diversity.

In 2012, Zhu et al. reported isostructural prismatic crystals of $[\text{Eu}_2\text{Zn}_3(\text{TETA})_3(\text{H}_2\text{O})_4] \cdot 12\text{H}_2\text{O}$ and $[\text{Gd}_2\text{Cu}_3(\text{TETA})_3(\text{H}_2\text{O})_2] \cdot 6\text{H}_2\text{O}$ using 1,4,8,11-tetraazacyclotetradecane-1,4,8,11-tetraacetic acid (H_4TETA) as a bifunctional organic linker. The two MOFs are first reported 3d-4f heterometallic azamacrocyclic ligand based MOFs.¹⁰⁰ The frameworks featured with a distorted octahedral metal macrocyclic complex, wherein the metal coordinates with the four nitrogens and two carboxylates on the pendant arms. The mononuclear $[\text{M}(\text{TETA})]^{2-}$ complexes exhibited two kinds of connection models to lanthanide ions to give rise to 3D pillared-layer frameworks with highly solvent accessible volume. In 2013, a lead based MOF $[\text{Pb}_2(\text{TETA})] \cdot 6\text{H}_2\text{O}$ was prepared by the hydrothermal reaction using same macrocyclic ligand (TETA). The 3D frameworks were formed via cross-linked 1D chains of lead atoms two carboxylate oxygens and two amino nitrogens from a single TETA^{4-} ligand along with two carboxylate oxygens from the other two different TETA^{4-} ligands.¹⁰¹

Another commonly-used functionalized azamacrocyclic linker is 1,4,7,10-tetraazacyclododecane-N,N',N'',N'''-tetra-p-methylbenzoic acid (tactmb). In 2012, Ma and coworkers reported a twofold interpenetrating microporous MOF (MMCF-1, Metal-

Macrocyclic Framework) from the self-assembly of the tactmb ligand with Cd(II) under solvothermal conditions.¹⁰² MMCF-1 crystallized in the space group $P2_1/c$ with an asymmetric unit containing two unique Cd atoms. The first seven coordinated Cd atom connects with six oxygen atoms of three carboxylate groups from three different tactmb ligands and one oxygen atom from the coordinated water. The other Cd atom is six coordinated to the four nitrogens of a macrocycle and the oxygen atoms of a separate tactmb (Figure 1.12). MMCF-1 demonstrated good thermal stability up to 320 °C and interesting selective uptake of CO₂ over N₂. The solvothermal reaction of tactmb with copper nitrate affords [Cu₂(Cu-tactmb)(H₂O)₃(NO₃)₂], MMCF-2 (Figure 1.12),¹⁰³ which crystallized in the $Pm\bar{3}m$ space group. The framework exhibits an nbo topology arising from two different types of 4-connected square planar nodes, copper paddlewheels, and the Cu-metallated tactmb ligand. MMCF-1 demonstrated excellent catalytic performance in CO₂ chemical fixation at room temperature under 1 atm. In 2013, Maspoch et al. utilized the azamacrocyclic ligand 1,4,7,10-tetraaza-cyclododecane-1,4,7,10-tetramethylene-phosphonic acid to produce the bimetallic MOF [GdCu(DOTP)Cl]4.5H₂O. The potential contrast agent was reportedly stable in both physiological saline solution and cell culture media, not cytotoxic, and miniaturize to the nanoscale as stable colloids. Relaxometry studies show a non-pH dependent maximum in r_1 relaxivity of 15 mM⁻¹s⁻¹ at 40 MHz and at high field (500 MHz) $r_1 = 5$ mM⁻¹s⁻¹.¹⁰⁴

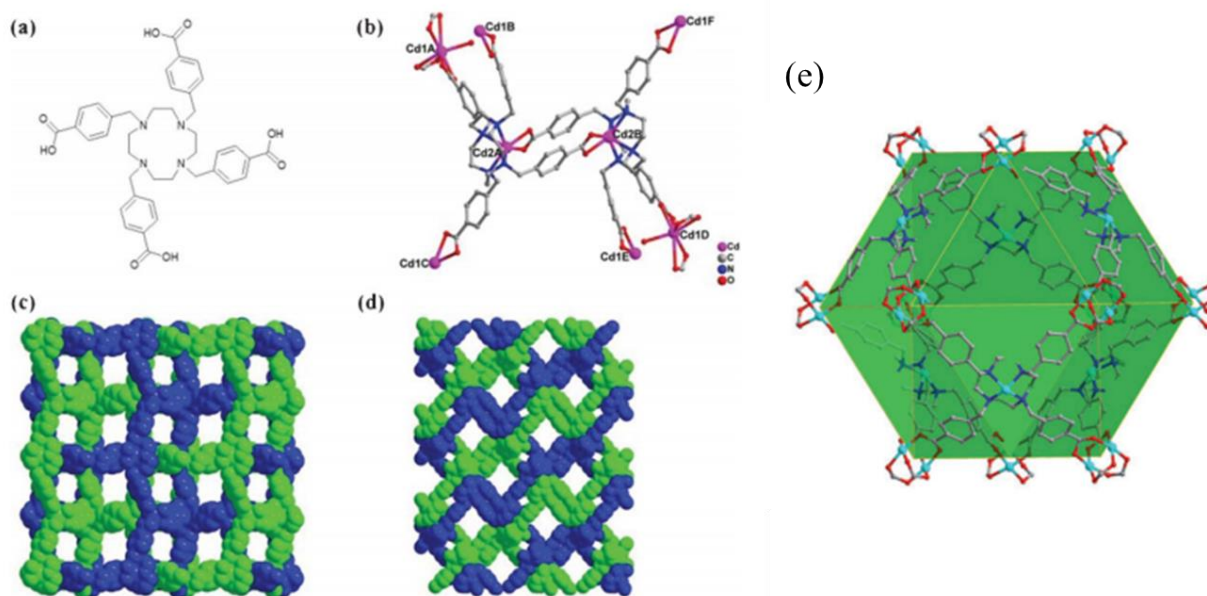


Figure 1.12 (a) The tactmb ligand; (b) the coordination unit of MMCF-1; (c) the two-fold interpenetrating structure viewed from the b direction; (d) the two-fold interpenetrating structure viewed from the c direction; (e) the structure of MMCF-2. Reprint with permission from ref. 102 and ref. 103. Copyright 2012, Royal Society of Chemistry and Copyright 2014, Wiley.

As discussed in the above mentioned examples, functionalized macrocyclic ligands are flexible linkers offering multiple favorable conformations of similar energies to promote structural diversity yet increase the difficulty for crystallization with different metal ions. Moreover, the synthetic modification of the azamacrocycles usually altered the electronic properties of the parent ring molecules, which made it challenging to maintain structural related chemical properties. Therefore, it requires the rational design of new entrants to this type of materials to achieve the full potential of azamacrocyclic-based MOFs.

1.5 MOFs for CO₂ chemical transformations

The grand challenge with current state of the art catalysts for CO₂ chemical transformations is embedded in the fact that no single system can independently control and optimize the interplay between activity, selectivity, and efficiency. In this context, MOFs have become promising candidates for CO₂ applications because of four crucial features. The first is that the desired properties of MOF can be achieved by rationally and systematically modulate the porous, crystalline structures. A large number of available frameworks provide a great platform for the designed MOFs to serve specific end function. Second, the marriage of molecular chemistry with reticular chemistry has led to molecular-level control and atomically precise chemical transformations to be carried out within extended frameworks. Third, the high porosity and surface areas, in some cases, high CO₂ adsorption uptake, can significantly enhance the local concentration of CO₂ around catalytic reaction centers within the confined pores of the framework. Indeed, the frameworks can act as a well-defined porous “nanoreactor” for CO₂ transformations. The fourth crucial feature is that the MOF materials established great benefits from “heterogeneity within order”, whereby structural and chemically different components are brought together to function synergistically.¹⁰⁵⁻¹⁰⁶ In this section, I will highlight the recent discoveries in the area of the CO₂ chemical transformation using MOFs as heterogeneous catalysts. The specific reactions are summarized into three main categories: chemical fixation, photocatalytic reduction, and electrochemical reduction.

1.5.1 MOFs for CO₂ chemical fixation

As mentioned in section 1.2.2, CO₂ can be treated as an important C1 chemical resource for the synthesis of valuable chemicals. In particular, extensive research studies have been focused on developing MOFs as heterogeneous catalysts for cycloaddition of CO₂ into epoxides.¹⁰⁷⁻¹⁰⁹ The mechanism for the cycloaddition of CO₂ to epoxides typically involves an acid catalyst (such as a metal ion or a proton) that coordinates to the epoxide as the first step to activate the epoxide, followed by nucleophilic attack by the co-catalyst (typically a tetraalkylammonium halide) to form a halo-alkoxide. The halo-alkoxide intermediate further reacts with CO₂ through cycloaddition to form cyclic carbonate with regeneration of the tetraalkylammonium halide co-catalyst (Figure 1.13).^{108, 110} In general, the reported MOFs that catalyze CO₂ addition to epoxides are categorized into three scenarios based on the different catalytic sites: structural MOF defects, open metal sites from metal node (SBU) and/or linkers, and co-catalyst functionalized MOFs.

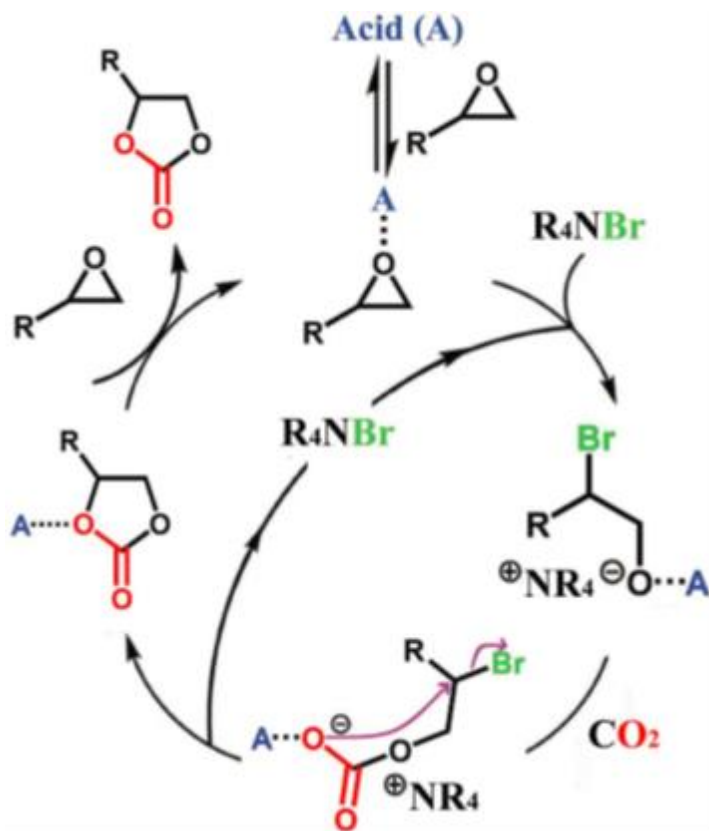


Figure 1.13 Proposed mechanism for the acid (A)-catalyzed cyclic carbonate synthesis from epoxides and CO₂ in the presence of a tetraalkyl ammonium halide (bromide). Reprint with permission from ref. 108. Copyright 2016, Wiley.

1.5.1.1 Defect-driven catalysis

The earliest reports of MOFs used for cycloaddition of CO₂ to epoxides were solely based on structural defect sites. In 2009, Song and co-workers reported MOF-5 as the catalyst for cycloaddition of CO₂ and epoxides in the presence of a quaternary ammonium salt co-catalysts.¹¹¹ It was discovered that MOF-5/n-Bu₄NBr catalytic system led to a very high yield of propylene carbonate (97.6%) and was reused for three cycles without losing catalytic activity. It is worth noting that percentage yields (as opposed to percentage conversion) are often provided for propylene oxide because it is highly volatile (boiling point = 34°C) and cannot be separated upon CO₂ decompression after the reaction. Although no active site was directly evidenced, the authors attributed the reactivity to defects at the Zn₄O cluster sites and also demonstrated that both MOF-5 and n-Bu₄NBr co-catalyst were essential for product formation.

In 2012, ZIF-8 was reported as an effective catalyst for cycloaddition of CO₂ and epichlorohydrin to form chloropropene carbonate.¹¹² As a result of surface defects, ZIF-8 contains both Lewis acid sites from zinc ions and base sites from the imidazole nitrogen atoms, the framework demonstrated high catalytic activity in epichlorohydrin conversion (up to 98.2% at 100 °C) without co-catalyst under solvent free system. To improve the selectivity and yield, ZIF-8 was functionalized with ethylene diamine. This post-synthetic modification successfully increased CO₂ adsorption and catalytic conversion yield. However, the amine-functionalized ZIF-8 catalysts lost their crystallinity and dramatically decreased catalytic performance after the first cycle. Similar research by Yang and co-workers investigated the catalytic behavior of ZIF-68 for the synthesis of styrene carbonate from CO₂ and styrene oxide.¹¹³ ZIF-68 demonstrated remarkable catalytic activity for CO₂ cyclic addition reactions at 120 °C and 1 MPa CO₂. Notably, the catalytic performance of ZIF-8 showered lower activity than ZIF-69 under same conditions. Both frameworks were reused for three times without any significant loss in catalytic activity.

In general, these MOF catalysts with active catalytic defect sites usually require high temperature, and pressure conditions for the cycloaddition reaction and this process may not be preferred when applied on a large scale. Therefore, it is a challenge to develop MOFs catalysts to promote this reaction under milder conditions.

1.5.1.2 MOFs with active catalytic nodes

MOFs nodes with accessible and coordinately unsaturated sites could function as Lewis acid sites to activate the epoxide substrates, but these reaction systems usually require a co-catalyst such as Lewis base to open the epoxide ring. Examples of MOFs with catalytically active metal centers including M-MOF-74, HKUST, MOF-505, Hf-NU-1000, Cr- and Fe-MIL-101, geo-MOF-1 and Ni-TCPE1.¹⁰⁸ It is important to note that these metal clusters are multinuclear complexes rather than mononuclear species, which leads to additional factors other than Lewis acidity alone that determine the catalytic activity.

In 2014, Guillerme and co-workers used an 18-connected yttrium cluster $[Y_9(\mu_3\text{-OH})_8(\mu_2\text{-OH})_3(\text{O}_2\text{C-})_{18}]^{2-}$ to prepare a MOF with (3,18)-connected *gea* topology. The crystalline powders were obtained by solvothermal reaction between 1,3,5-benzene(tris)benzoate (H_3BTB) and $\text{Y}(\text{NO}_3)_3 \cdot 6\text{H}_2\text{O}$ in DMF and water. X-ray structural analysis revealed that the anionic yttrium cluster is an 18-connected node linked to 18 tridentate BTB ligands to obtain a 3D porous framework (Figure 1.14).¹¹⁴ Considering its great thermal stability and high surface area, *gea*-MOF-1 was explored as the heterogeneous catalyst for cycloaddition reactions. The reactions were tested using the epoxide (100 mmol), *gea*-MOF-1 (60 mg, 0.15 mmol yttrium), $n\text{-Bu}_4\text{NBr}$ (0.15 mmol) at 120 °C and 20 bar CO_2 for 6 h without any solvent. The conversion yield to propylene carbonate was 88% and remained high at 77% after the third recycling. However, the homogeneous catalyst $\text{YCl}_3/ n\text{-Bu}_4\text{NBr}$ demonstrated 10 times higher turnover frequency than *gea*-MOF-1, indicating the effect of mass-transport limitations and less Lewis acid (Y^{3+}) sites in MOF. Compared with the heterogeneous system, $\text{Y}_2\text{O}_3/ n\text{-Bu}_4\text{NBr}$, *gea*-MOF-1 showed better catalytic performance, which highlighted the importance of accessible Lewis acid (Y^{3+}) sites and large surface area of MOF.

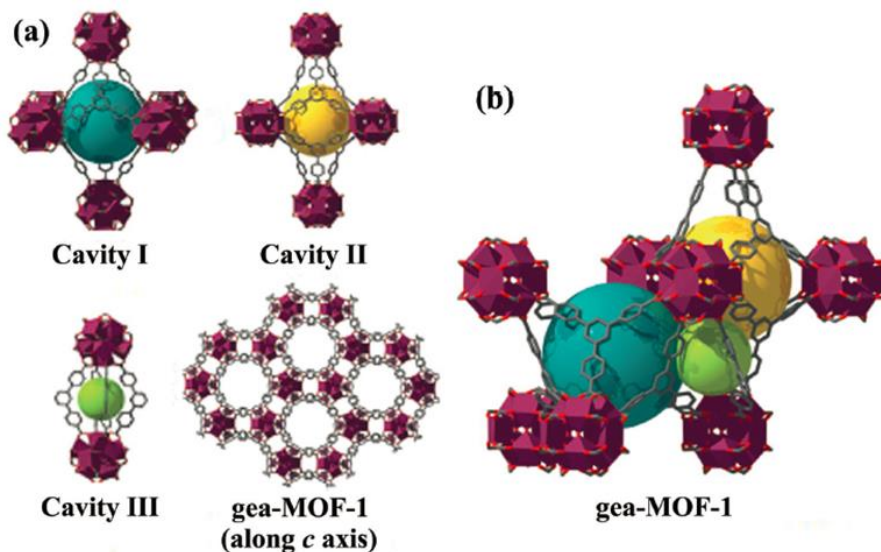


Figure 1.14 a) Structural representations of gea-MOF-1 with three types of cavity. b) The packing of these cavities in gea-MOF-1. The hydrogen atoms are omitted for clarity. Color code: Re, purple; C, grey; O, red. Reproduced with permission from ref.114. Copyright 2014, Nature Publishing Group.

Beyzavi et al. reported a Hf-based MOF, Hf-NU-1000, as an excellent catalyst for the cycloaddition reaction of CO₂ to epoxide under mild conditions.⁹¹ The MOF was prepared via the solvothermal synthesis of HfOCl₄•8H₂O and 1,3,6,8-tetrakis(p-benzoic acid)pyrene (H₄TBAPyr), affording the yellow microcrystalline product. The node consists of Hf₆ cluster capped by eight bridging carboxylate-containing linkers, which is indeed coordinately unsaturated. The Hf-NU-1000 demonstrated highly efficient catalytic activity for the quantitative cycloaddition of styrene oxide using CO₂ at 1 atm and room temperature after 56 h. The great catalytic activity was attributed to the –OH groups at the nodes via a Brønsted acid pathway, as simulation indicated that the hydroxyl protons of Hf-NU-1000 are slightly more acidic than those of the Zr⁴⁺ analog NU-1000. As a result, under the same conditions, NU-1000 was only yielded 46% conversion. Although Hf-Nu-1000 has demonstrated the highest conversion yield for cycloaddition of styrene oxide under mild condition, it is worth noting that the reaction was performed in extremely small scale: 0.2 mmol epoxide (22 μL), 0.02 mmol tetrabutylammonium bromide (6.5 mg), 5.6 mg Hf-NU-1000 (0.008 mmol –OH) and 400 μL acetonitrile. Therefore, the quantitative conversion yield does not have too much significance towards practical applications.

1.5.1.3 MOFs with catalytically active nodes and linkers

Aiming at increasing the density of Lewis acid sites, researchers have utilized Lewis acid containing linkers (organometallic linkers) and active nodes to construct MOFs as catalysts featured with dual catalytic metal centers. One good example of those MOFs is MMCF-2 reported from Gao and coworkers.¹¹⁵ As mentioned in section 1.4.3.2, the Cu^{2+} is not only used to form the Cu_2 -paddlewheel nodes but also to *in situ* metalates the azamacrocyclic complex. Therefore, the framework has high concentration of Cu^{2+} centers (18 Cu^{2+} sites per cuboctahedral cage), which is 50% higher than its parent MOF 505 (12 Cu^{2+} sites). Consequently, MMCF-2 produced much higher yield (95.4%) of propylene carbonate than that using MOF-505 (48%) under the mild conditions of 1 bar CO_2 and room temperature. Similar catalytic performance has been observed in MMPF-9 from the same group, where Cu metallated porphyrin was used as the organometallic linkers. Again, the high density of copper sites in MMPF-9 exhibited excellent catalytic activity for cycloaddition of propylene oxides and CO_2 under 1 atm and room temperature.¹¹⁶ Both MMCF-2 and MMPF-9 showed significantly higher catalytic activity than HKUST-1, a benchmark copper paddlewheel MOF. In addition, other metalloporphyrin MOFs, PCN-224 (Co)⁸⁸ and MMPF-18,¹¹⁷ showed outstanding catalytic properties.

Metallosalen molecules have also been employed in MOFs to offer a second Lewis acid catalytic site apart from the metal nodes. Ren et al. used a nickel salphen complex, Ni- H_2L , as a bridging metalloligand to build an extended framework with Cd^{2+} .¹¹⁸ The presence of Cd^{2+} and Ni^{2+} was proved to provide synergistic and additive activation effects, leading to an enhanced catalytic activity compared with the catalytic control system. The MOF could also be reused at least for three cycles, with no significant change in conversion yield and crystallinity.

To sum up, MOFs with dual catalytic metal sites can significantly increase the density of catalytic sites within the framework. Therefore, the higher yield under milder reaction conditions can be achieved, with the tradeoff of longer reaction time and the requirement of co-catalyst.

1.5.1.4 MOFs with functional linkers

As discussed, the cycloaddition reaction between CO₂ and epoxides required Lewis acid sites (originated from defects or open metal sites in MOFs) and co-catalyst such as tetraalkyl ammonium halides to facilitate the formation of intermediate. One interesting approach is to design MOFs with incorporated Lewis acid sites from the metal nodes and co-catalysts organic molecules as linkers to serve as dual functional MOFs, which would be sufficient enough as catalysts for CO₂ fixation reaction. More specifically, Lewis base functional groups such as amine have been introduced into the organic linker, which can coordinate with metal clusters modifying the result MOFs with acid-based pairs. A tentatively proposed mechanism for forming cyclic carbonates in one catalyst system with acidic and basic sites has shown in Figure 1.15.¹⁰⁹

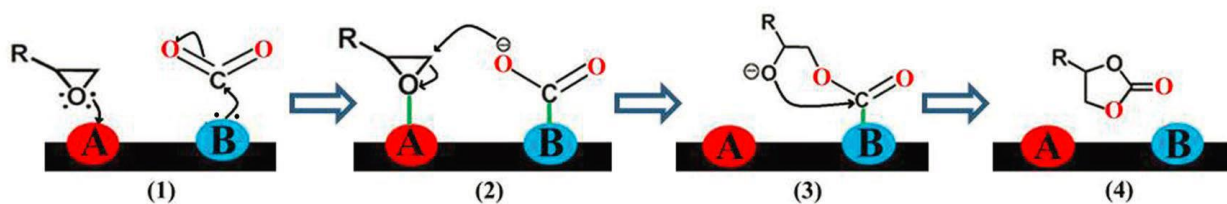


Figure 1.15 The proposed mechanism for catalysts with both a Lewis acid (LA) and Lewis basic (LB) pair catalyzing cyclic carbonate from epoxides and CO₂. Reprint with permission from ref. 109. Copyright 2015, Frontiers.

Lescouet and co-workers explored the key role of an amine-functionalized MIL-68(In)-NH₂ for the cycloaddition reaction.¹¹⁹ MIL-68(In)-NH₂ acid-base pairs derived from the indium clusters and the amino-terephthalate ligand. Significant higher conversion yield has been obtained from the amine-functionalized MIL-68(In)-NH₂ than that of MIL-68(In) in the synthesis of styrene carbonate from styrene oxide at 150 °C and 8 bar CO₂ for 8 h. Similarly, UiO-66-NH₂ also showed higher catalytic performance than the original UiO-66 with a styrene oxide conversion of 70% and 48%, respectively under 8 bar CO₂ pressure heated at 100 °C for one hour.¹²⁰ It can be summarized that MOFs with acid-base pair can increase catalytic activity by introducing weak basic sites in the framework. On the other hand, strong basic sites were found not as beneficial for the catalysis reaction presumably due to the slow desorption of the reaction products.

Besides using pre-designed functionalized linkers, various catalytically active groups can also be introduced into MOFs by post-synthetic modification techniques or mixed ligand approaches. For instance, quaternary ammonium salt functional groups were successfully incorporated into IRMOF-3 by post-synthetic modification, which can enhance the catalytic activity.¹²¹ A similar approach has also been applied to ZIF-90¹²²⁻¹²³ and MIL-101. Ma and co-workers reported two MOFs, MIL-101-N(n-Bu)₃Br and MIL-101-P(n-Bu)₃Br, by post-synthetic modification on the parent MIL-101-NO₂ (Figure 1.16a).¹²⁴ These MOFs exhibited great catalytic performance for the CO₂ cycloaddition reaction under mild and co-catalyst free condition. This was mainly attributed to the synergetic effect of containing both Lewis acid sites (Cr³⁺) and co-catalysts (Br⁻ ions from IL functionalization). Control experiments were performed to synthesize propylene carbonate using some benchmark MOFs under the same conditions, as shown in Figure 1.16b, those bifunctional catalysts MIL-101-N(n-Bu)₃Br and MIL-101-P(n-Bu)₃Br outperformed unfunctionalized MOFs.

Based on the above discussion, it is easy to conclude that MOFs exhibit high catalytic performance and show serious potential application for CO₂ chemical fixation. High yields and conversions under moderate conditions for cycloaddition to epoxide have been achieved by using different types of MOFs. Although the reaction mechanism has been proposed to guide the rational design and modification for the development of MOF catalysts, direct evidence of reaction intermediate and identification of active catalytic sites are still missing and rarely explored. Moreover, the epoxide is a high-energy starting material, and many other simple molecules (such as DMF) can also act as the catalyst for cycloaddition reaction.

Recyclability tests have also been reported, where most MOF catalysts were shown to maintain their activity and crystal integrity for 3 to 5 cycles. However, to fully assess the potential MOF catalysts, a higher number of cycles is required, while monitoring not only the changes in the crystal structure but also the changes in the morphology, surface area and chemical composition over time. The desired MOF catalyst system for CO₂ chemical fixation would have high catalytic performance including high conversion

yield, turnover number and selectivity with excellent recyclability under mild conditions, especially under similar conditions as flow chemistry. Indeed, recent study using MIL-101(Cr) has demonstrated the successful synthesis of propylene carbonate from the continuous flow of CO₂ and epoxide.¹²⁵ In a broad sense, the future directions to explore MOF catalysts for different CO₂ based organic transformations other than cycloaddition of CO₂ and epoxide, such as use CO₂ as monomer in copolymerization reactions with olefin or cyclic CO₂ carboxylation of alkyne-containing molecules.

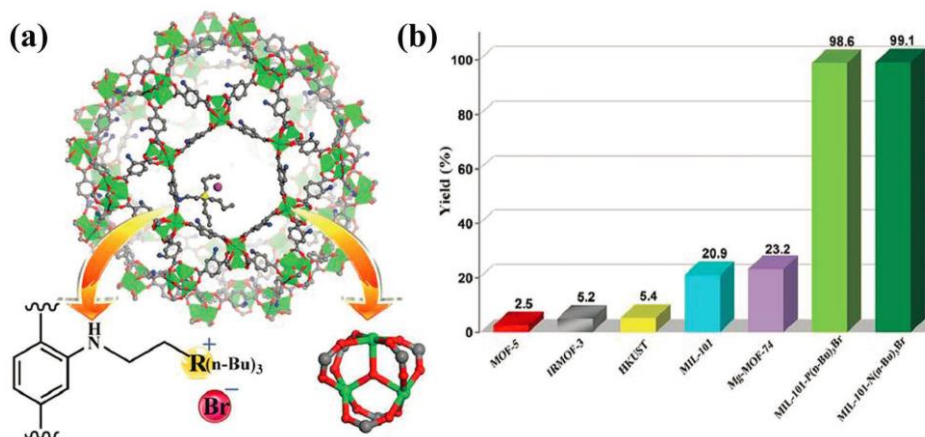


Figure 1.16 a) The structures of the heterogeneous catalysts: MIL-101-N(n-Bu)₃Br and MIL-101 P(n-Bu)₃Br. Atom color: Cr (green), C (gray), O (red), N (blue), Br (amaranth), and R = N or P). b) The yield of propylene carbonate from the cycloaddition of propylene oxide and CO₂ catalyzed by different MOF catalysts. Reprint with permission from ref. 124. Copyright 2015, Royal Society of Chemistry.

1.5.2 MOFs for photocatalytic CO₂ reduction

Molecular photocatalytic CO₂ reduction catalysts are highly selective but mainly limited for practical use by low efficiency and activity.¹¹ A strategy to take advantage of their selectivity, while enhancing their stability at the same time, is to spatially isolate them to eliminate the catalyst deactivation pathways such as dimerization. To accomplish this, molecular catalysts can be incorporated into the solid support, and MOFs are ideal platforms because of their high ordered crystalline structures, high surface area and high density of accessible active sites.

The first example of photoreduction in MOFs was accomplished with modified UiO-67 by integrating a well-known molecular catalyst, Re^I(bpy)CO₃Cl, into the backbone of the framework.¹²⁶ This photoactive MOF was used to reduce CO₂ to CO with a turnover number (TON) of 5 in 6 hours and a CO₂/H₂ selectivity of 10. The main drawback of this

system was the activation under ultraviolet light. The effects of catalyst loading on activity was also investigated in the same system of UiO-67 with $-\text{Re}(\text{CO})_3\text{Cl}$ catalyst bound to the linker, where a relatively low loading of 13% was found to be optimal. The activity was enhanced seven times by growing the Re-incorporated MOF on Ag nanocubes to spatially subject the photoactive MOF to intensified electric fields due to surface plasmons.¹²⁷ A similar approach has also been explored using different molecular catalysts. Kubiak, Cohen, and coworkers reported a Mn(I)-incorporated UiO-67 MOF as the efficient catalyst for CO_2 reduction to formate with the presence of Ru(II) photosensitizer under visible light irradiation (Figure 1.17A). The turnover number reached approximate 110 in 18 h and the catalytic activity outperformed the homogeneous reference systems. It is noteworthy that the TON was only reduced 25% when the CO_2 was diluted to 5% with Ar, with a concomitant drastic improvement in selectivity.¹²⁸ Kitagawa and co-workers introduced the molecular catalyst $[\text{Ru}(\text{II})(\text{H}_2\text{bpydc})(\text{terpy})(\text{CO}))(\text{PF}_6)_2]$ (denoted as H_2RuCO) via post-synthetic exchange into the UiO-67 framework forming Zrbpdc/RuCO photocatalyst (Figure 1.17B).¹²⁹ The resulting material was found to be a good CO_2 adsorbent and to exhibit high catalytic activity for CO_2 photoreduction to CO, HCOOH, and H_2 . Especially when the CO_2 concentration was lower than 20% in a CO_2/Ar gas mixture, the MOF catalyst showed higher catalytic performance than the discrete Ru based molecular catalyst. The difference was attributed to the synergistic effect between the adsorption sites and catalytically-active sites in Zrbpdc/RuCO.

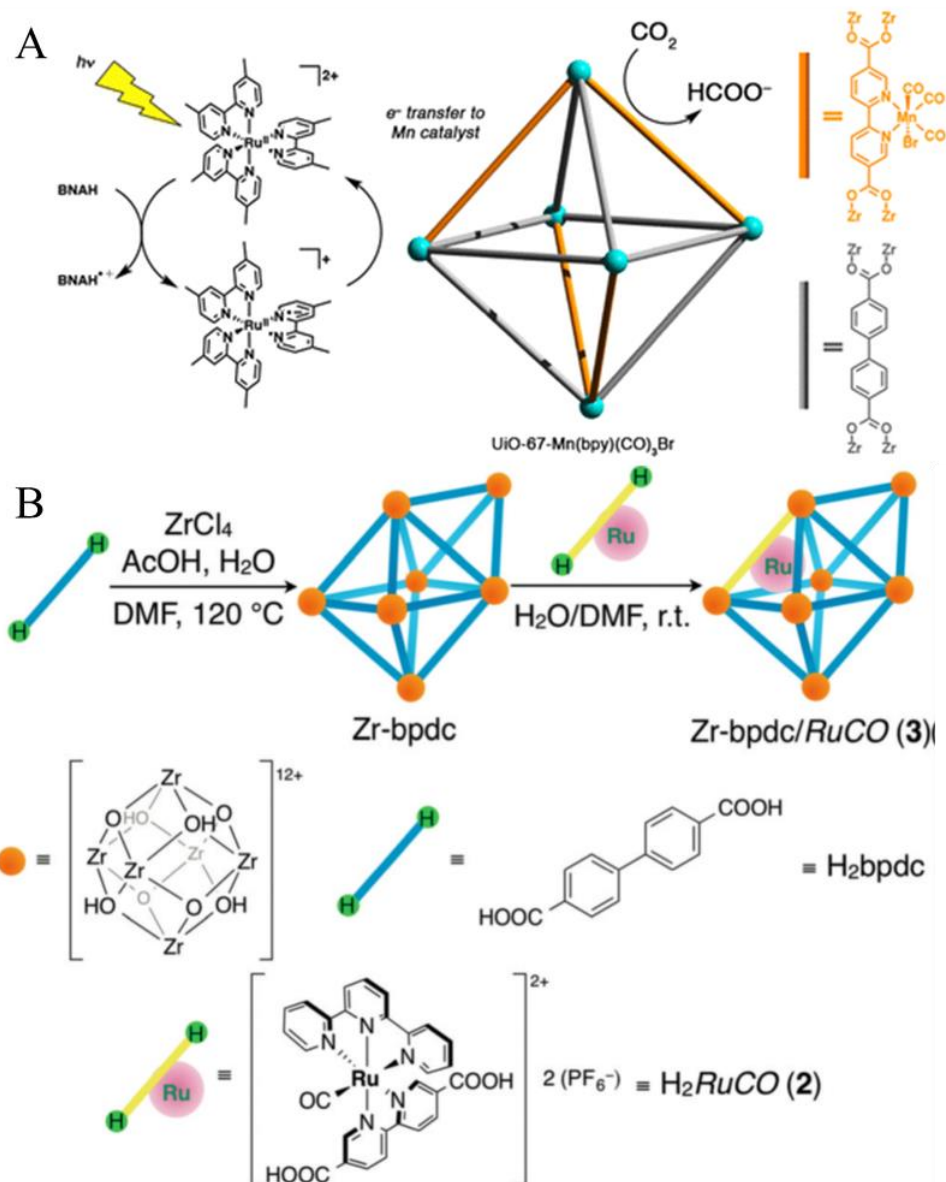


Figure 1.17 (A) Reaction scheme of Mn(I)-incorporated UiO-67 MOF as the photoactive catalyst. (B) Synthetic scheme of Zrbpdc/RuCO photocatalyst. Reprint with permission from ref. 128 and ref.129. Copyright 2015, American Chemical Society and Copyright 2016, Wiley.

Photoactive MOFs can also be designed by judicious choice of metal clusters and organic linkers. Metal nodes composed by redox active metals can serve as catalytic reaction centers. Moreover, the HOMO-LUMO gap of designed MOF materials can be engineered by tailoring the MOF backbone to ensure that the optical properties of framework match the proper range of light absorption. A good example would be the investigation of MIL-125 (Ti) and its amine functionalized derivative, NH₂-MIL-125, for photocatalytic reduction of CO₂.¹³⁰ The original MOF MIL-125 (Ti) has an absorption band edge at 350 nm only allowing photocatalysis to take place in the UV region. The

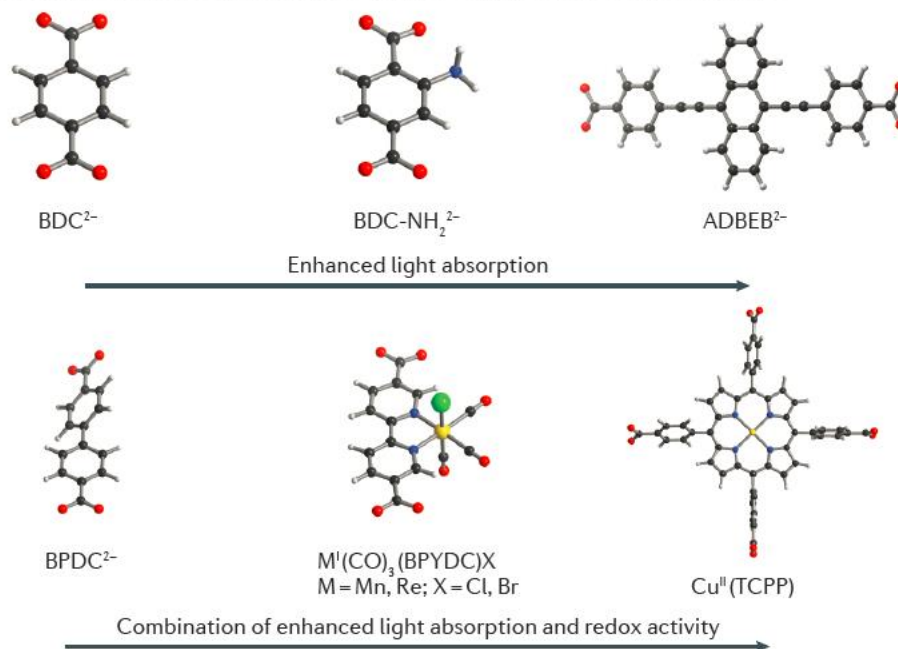
isorecticular functionalized analogue, NH₂-MIL-125 (Ti), adsorbed visible light with the band edge extending to 550 nm. Therefore, NH₂-MIL-125 (Ti) exhibited visible light activity towards the conversion of CO₂ into formate, with a yield of 8.14 μmol over the course of 10 hours irradiation, while no formate was produced using MIL-125(Ti) under the same conditions. The ligand to metal charge transfer (LMCT) between amine functionalized linker to Ti⁴⁺ clusters played an important role in the catalyst process, as evidenced by the observation of color change from bright yellow to green upon excitation with visible light. The color change was attributed to the reduction of Ti⁴⁺ to Ti³⁺, where with the introduction of CO₂, the color reverted from green to the original bright yellow as Ti³⁺ was oxidized to Ti⁴⁺, upon the process of electron transfer to CO₂. Similar electron transfer process has also been observed in photocatalytic CO₂ reduction using amino-functionalized NH₂-UiO-66 (Zr). The involvement of Zr(III) in the photocatalytic CO₂ reduction was confirmed by electro Spin Resonance (ESR) spectroscopy.¹³¹ Another Zr-based MOF, NNU-28, is the benchmark MOF catalyst for photoreduction of formate without an additional homogeneous photosensitizer. This framework showed a TON of 18 and generated 26.4 μmol formates over the course of 10 hours under visible light irradiation. The high catalytic efficiency was attributed to the dual catalytic centers of the anthracene linker and the metal cluster that comprise the framework.¹³²

Additionally, MOFs combined with nanoparticles and inorganic semiconductors can form hybrid materials for photocatalytic CO₂ reduction. In this approach, a core-shell motif could be used or the nanoparticle may be bound to the MOF surface. This core-shell material has been achieved with TiO₂ nanoparticles as the shell and HKUST-1 as the core. This hybrid material combines the high selectivity of HKUST-1 for CO₂, improving CO₂ conversion and reducing the production of H₂, with effective charge separation between the nanoparticles and the MOF.¹³³ A hybrid photocatalyst UiO-66/CNNS has also been reported by an electrostatic self-assembly synthesis between positively charged UiO-66 and negatively charged carbon nitride nanosheet (CNNS). UiO-66/CNNS demonstrated higher photocatalytic activity for the production of CO than

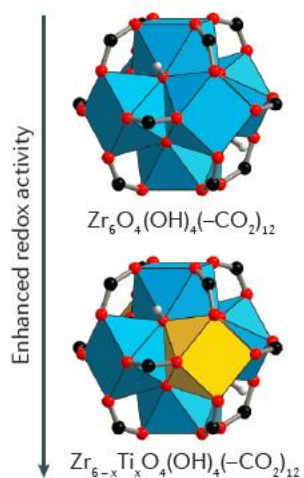
UiO-66/bulk carbon nitride (CN) mixture and bulk CN alone. The system also showed good stability up to three photocatalytic cycles without losing the activity.¹³⁴

In summary, the variety of systems used and the products obtained show the versatility and future potential of MOFs for photocatalysis. To date, different strategies to improve the photochemical reduction of CO₂ have been summarized in Figure 1.18, including the use of varying SBUs and linkers, grafting the active site onto the linker (and the combination of these two as the source of active sites), and composite materials with nanoparticles. An ideal future system has been depicted in Figure 1.19. In this desired MOF system, several components are critical for photocatalytic CO₂ reduction. (1) A high density of open metal sites, functioning as the active sites, are needed. The metal species must be chosen judiciously (for example, Fe, Co or Cu) to facilitate efficient electron transfer to adsorbed CO₂ substrates, which could solve the problems of low activity and selectivity. (2) The MOF backbone must be appropriately conjugated and functionalized to absorb visible light more efficient. (3) The MOF backbone must also have high charge carrier mobility by choosing coordinating groups that ensure proper frontier orbital overlap and redox matching between the organic linker and the SBU. (4) Charge carrier recombination must be minimized to break the rate-limiting step that has plagued other photocatalytic systems.

a Linker-based strategies for improving photophysical properties of MOFs



b SBU-based strategies



c 'Heterogeneity within order'

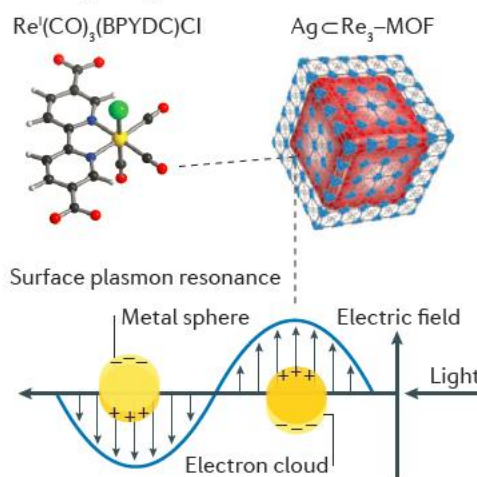


Figure 1.18 Strategies for improving photochemical CO_2 reduction. Photochemical CO_2 reduction performance can be improved by modification of the linker or the secondary building unit (SBU), or by introducing heterogeneity within ordered metal–organic framework (MOF) structures. Reprinted with the permission from ref. 106. Copyright 2016, Nature.

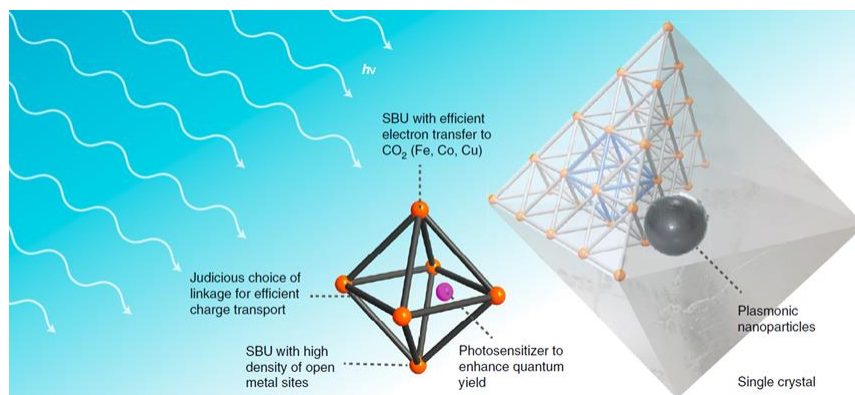


Figure 1.19 The ideal MOF system for photocatalytic CO₂ reduction. Reprinted with the permission from ref. 106. Copyright 2016, Nature.

1.5.3 MOFs for electrochemical CO₂ reduction

Instead of relying on sunlight as the energy source in photocatalysis, electrocatalysis is an alternative process of CO₂ reduction that involves a current applied through a voltage bias. A few MOFs have been investigated for CO₂ electrocatalytic reduction mainly because most MOFs have low electronic conductivity and limited stability under electrocatalysis conditions.

The first report of electrocatalytic CO₂ reduction with a MOF was performed using a Cu(II) rubeanate framework containing coordinatively unsaturated metal sites.¹³⁵ Formic acid was formed as the only CO₂ reduction product with a TON consistently larger than that of a Cu electrode. The high selectivity was attributed to the relative weak adsorption of CO₂ to the Cu(II) site in the MOF when compared with the adsorption strength of CO₂ to metallic Cu. Despite the high selectivity for the conversion of CO₂, a Faradaic efficiency of only 30% was achieved, with a large amount of hydrogen formed as the by-product. In 2012, Kumar and coworkers used uniformed films of HKUST-1 for CO₂ reduction in DMF.¹³⁶ The use of non-aqueous solvent leads to the production of oxalic acid with 90% selectivity, which was proposed to occur by dimerization of CO₂. The Faradaic efficiency was relatively low (51%). Similar to the previous example, no characterization of MOF was performed before and after the electrocatalytic reaction. Therefore, the actual role of MOF in the electrocatalytic process and stability of those systems remained unclear.

An aluminum porphyrin-based MOF, $\text{Al}_2(\text{OH})_2\text{TCPP-Co}$, comprising cobalt porphyrin active sites was employed for electrocatalytic reduction of CO_2 to CO (Figure 1.20).¹³⁷ Thin film of the MOF were directly grown on a conductive carbon disk electrode via atomic layer deposition (ALD). The use of thin films allows both mass and charge transfer to be optimized by controlling the thickness of the film. Indeed, selective CO_2 reduction to CO was achieved with a TON of 1400 over 7 hours and a Faradic efficiency of 76% in aqueous solutions. It was further demonstrated by *in situ* spectroelectrochemical experiments that Co(II) was reduced to Co(I) as part of the catalytic cycle.

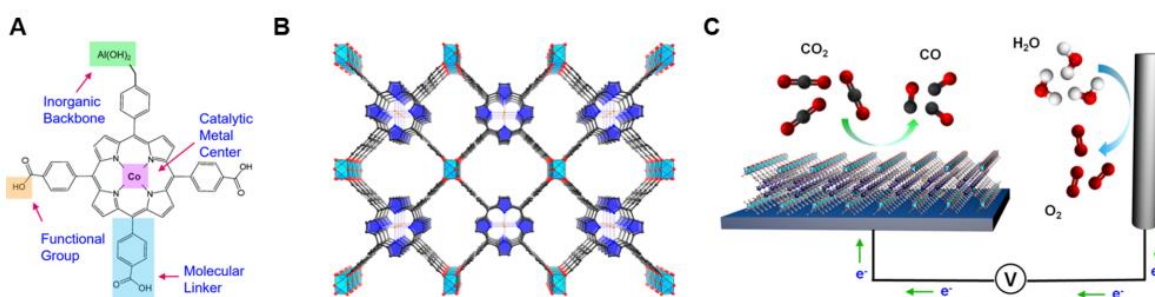


Figure 1.20 A) The modulation of metal centers, molecular linkers, and functional groups at the molecular level. B) The 3D structure of $\text{Al}_2(\text{OH})_2\text{TCPP-Co}$. C) The MOF is integrated with a conductive substrate to generate a functional CO_2 electrochemical reduction system. Reprinted with permission from ref. 137. Copyright 2015, American Chemical Society.

The thin film MOF approach was extended to iron porphyrin-based MOF-525 [$\text{Zr}_6\text{O}_4(\text{OH})_4(\text{TCPP-Fe})_3$].¹³⁸ The thin films of this MOF were electrophoretically deposited on an electrode to maximize the areal density of the active sites while achieving the necessary electronic contact with the electrode. The Zr-based framework was found to convert CO_2 to CO in a tetrabutylammonium hexafluorophosphate/DMF electrolyte solution with a TON of 272 over the course of 4 hours, although H_2 was produced in a 1:1 ratio with CO . Addition of 2,2,2-trifluoroethanol as a weak Brønsted acid increased current densities, leading to a TON of 1,520 over 3.2 hours, again with high H_2 production. The active center was assumed to be Fe(0) because catalytic currents were noted at more positive potentials than that of the Fe(I/0) redox couple.

To sum up, currently reported MOF systems for electrocatalytic CO_2 reduction have achieved in high turnover number with low overpotentials, moderate selectivity and

precise control in the thickness and orientation of thin films. However, few impactful examples have been successfully performed for electrocatalytic reduction of CO₂ and mainly limited to porphyrin based MOFs. Detailed mechanism studies of the electrocatalytic process should be thoroughly investigated, and the limited recyclability and stability for those electrocatalytic active MOFs should be addressed in the future research.

1.6 Reference

1. Dale, S., BP Statistical Review of World Energy June 2017. BP: 2017.
2. Stocker, T., Climate Change 2013, "The Physical Science Basis," Working Group I.
3. Orr, J. C.; Fabry, V. J.; Aumont, O.; Bopp, L.; Doney, S. C.; Feely, R. A.; Gnanadesikan, A.; Gruber, N.; Ishida, A.; Joos, F., Anthropogenic ocean acidification over the twenty-first century and its impact on calcifying organisms. *Nature* **2005**, *437* (7059), 681.
4. Finn, C.; Schnittger, S.; Yellowlees, L. J.; Love, J. B., Molecular approaches to the electrochemical reduction of carbon dioxide. *Chemical Communications* **2012**, *48* (10), 1392-1399.
5. Pachauri, R. K.; Reisinger, A., IPCC fourth assessment report. *IPCC, Geneva* **2007**, 2007.
6. Haszeldine, R. S., Carbon Capture and Storage: How Green Can Black Be? *Science* **2009**, *325* (5948), 1647-1652.
7. Rabbani, M. G.; El-Kaderi, H. M., Template-free synthesis of a highly porous benzimidazole-linked polymer for CO₂ capture and H₂ storage. *Chemistry of Materials* **2011**, *23* (7), 1650-1653.
8. Hicks, J. C.; Drese, J. H.; Fauth, D. J.; Gray, M. L.; Qi, G.; Jones, C. W., Designing adsorbents for CO₂ capture from flue gas-hyperbranched aminosilicas capable of capturing CO₂ reversibly. *Journal of the American Chemical Society* **2008**, *130* (10), 2902-2903.
9. Cooper, A. I., Conjugated microporous polymers. *Advanced Materials* **2009**, *21* (12), 1291-1295.
10. Sumida, K.; Rogow, D. L.; Mason, J. A.; McDonald, T. M.; Bloch, E. D.; Herm, Z. R.; Bae, T.-H.; Long, J. R., Carbon Dioxide Capture in Metal–Organic Frameworks. *Chemical Reviews* **2012**, *112* (2), 724-781.
11. Morris, A. J.; Meyer, G. J.; Fujita, E., Molecular approaches to the photocatalytic reduction of carbon dioxide for solar fuels. *Accounts of chemical research* **2009**, *42* (12), 1983-1994.
12. Qiao, J.; Liu, Y.; Hong, F.; Zhang, J., A review of catalysts for the electroreduction of carbon dioxide to produce low-carbon fuels. *Chemical Society Reviews* **2014**, *43* (2), 631-675.
13. Alphen, v., *Rec. Trav. Chim.* **1937**, *56*, 343.
14. Liang, X.; Parkinson, J. A.; Parsons, S.; Weishäupl, M.; Sadler, P. J., Cadmium Cyclam Complexes: Interconversion of Cis and Trans Configurations and Fixation of CO₂. *Inorganic Chemistry* **2002**, *41* (17), 4539-4547.
15. Schneider, J.; Jia, H.; Muckerman, J. T.; Fujita, E., Thermodynamics and kinetics of CO₂, CO, and H⁺ binding to the metal centre of CO₂ reduction catalysts. *Chemical Society Reviews* **2012**, *41* (6), 2036-2051.
16. Cho, J.; Sarangi, R.; Nam, W., Mononuclear Metal–O₂ Complexes Bearing Macrocyclic N-Tetramethylated Cyclam Ligands. *Accounts of Chemical Research* **2012**, *45* (8), 1321-1330.
17. Liang, X.; Sadler, P. J., Cyclam complexes and their applications in medicine. *Chemical Society Reviews* **2004**, *33* (4), 246-266.
18. Kent Barefield, E., Coordination chemistry of N-tetraalkylated cyclam ligands—A status report. *Coordination Chemistry Reviews* **2010**, *254* (15), 1607-1627.
19. Hubin, T. J.; Amoyaw, P. N. A.; Roewe, K. D.; Simpson, N. C.; Maples, R. D.; Carder Freeman, T. N.; Cain, A. N.; Le, J. G.; Archibald, S. J.; Khan, S. I.; Tekwani, B. L.; Khan, M. O. F., Synthesis and antimalarial activity of metal complexes of cross-bridged tetraazamacrocyclic ligands. *Bioorganic & Medicinal Chemistry* **2014**, *22* (13), 3239-3244.
20. Lindoy, L. F.; Park, K.-M.; Lee, S. S., Metals, macrocycles and molecular assemblies - macrocyclic complexes in metallo-supramolecular chemistry. *Chemical Society Reviews* **2013**, *42* (4), 1713-1727.

21. Beley, M.; Collin, J.-P.; Ruppert, R.; Sauvage, J.-P., Nickel(II)-cyclam: an extremely selective electrocatalyst for reduction of CO₂ in water. *Journal of the Chemical Society, Chemical Communications* **1984**, (19), 1315-1316.
22. Beley, M.; Collin, J. P.; Ruppert, R.; Sauvage, J. P., Electrocatalytic reduction of carbon dioxide by nickel cyclam²⁺ in water: study of the factors affecting the efficiency and the selectivity of the process. *Journal of the American Chemical Society* **1986**, *108* (24), 7461-7467.
23. Fujihira, M.; Hirata, Y.; Suga, K., Electrocatalytic reduction of CO₂ by nickel (II) cyclam: Study of the reduction mechanism on mercury by cyclic voltammetry, polarography and electrocapillarity. *Journal of Electroanalytical Chemistry and Interfacial Electrochemistry* **1990**, *292* (1-2), 199-215.
24. Froehlich, J. D.; Kubiak, C. P., The Homogeneous Reduction of CO₂ by [Ni(cyclam)]⁺: Increased Catalytic Rates with the Addition of a CO Scavenger. *Journal of the American Chemical Society* **2015**, *137* (10), 3565-3573.
25. Song, J.; Klein, E. L.; Neese, F.; Ye, S., The Mechanism of Homogeneous CO₂ Reduction by Ni(cyclam): Product Selectivity, Concerted Proton–Electron Transfer and C–O Bond Cleavage. *Inorganic Chemistry* **2014**, *53* (14), 7500-7507.
26. Schneider, J.; Jia, H.; Kobiro, K.; Cabelli, D. E.; Muckerman, J. T.; Fujita, E., Nickel (II) macrocycles: highly efficient electrocatalysts for the selective reduction of CO₂ to CO. *Energy & Environmental Science* **2012**, *5* (11), 9502-9510.
27. Fujita, E.; Haff, J.; Sanzenbacher, R.; Elias, H., High Electrocatalytic Activity of RRSS-[NiIIIHTIM](ClO₄)₂ and [NiIIDMC](ClO₄)₂ for Carbon Dioxide Reduction (HTIM= 2, 3, 9, 10-Tetramethyl-1, 4, 8, 11-tetraazacyclotetradecane, DMC= C-meso-5, 12-Dimethyl-1, 4, 8, 11-tetraazacyclotetradecane). *Inorganic Chemistry* **1994**, *33* (21), 4627-4628.
28. Froehlich, J. D.; Kubiak, C. P., Homogeneous CO₂ Reduction by Ni(cyclam) at a Glassy Carbon Electrode. *Inorganic Chemistry* **2012**, *51* (7), 3932-3934.
29. Jarzębińska, A.; Rowiński, P.; Zawisza, I.; Bilewicz, R.; Siegfried, L.; Kaden, T., Modified electrode surfaces for catalytic reduction of carbon dioxide. *Analytica chimica acta* **1999**, *396* (1), 1-12.
30. Neri, G.; Walsh, J. J.; Wilson, C.; Reynal, A.; Lim, J. Y. C.; Li, X.; White, A. J. P.; Long, N. J.; Durrant, J. R.; Cowan, A. J., A functionalised nickel cyclam catalyst for CO₂ reduction: electrocatalysis, semiconductor surface immobilisation and light-driven electron transfer. *Physical Chemistry Chemical Physics* **2015**, *17* (3), 1562-1566.
31. Saravanakumar, D.; Song, J.; Jung, N.; Jirimali, H.; Shin, W., Reduction of CO₂ to CO at Low Overpotential in Neutral Aqueous Solution by a Ni (cyclam) Complex Attached to Poly (allylamine). *ChemSusChem* **2012**, *5* (4), 634-636.
32. Janiak, C., Engineering coordination polymers towards applications. *Dalton Transactions* **2003**, (14), 2781-2804.
33. Yaghi, O. M.; Li, H., Hydrothermal Synthesis of a Metal–Organic Framework Containing Large Rectangular Channels. *Journal of the American Chemical Society* **1995**, *117* (41), 10401-10402.
34. Farha, O. K.; Eryazici, I.; Jeong, N. C.; Hauser, B. G.; Wilmer, C. E.; Sarjeant, A. A.; Snurr, R. Q.; Nguyen, S. T.; Yazaydin, A. Ö.; Hupp, J. T., Metal–Organic Framework Materials with Ultrahigh Surface Areas: Is the Sky the Limit? *Journal of the American Chemical Society* **2012**, *134* (36), 15016-15021.
35. Gómez-Gualdrón, D. A.; Moghadam, P. Z.; Hupp, J. T.; Farha, O. K.; Snurr, R. Q., Application of Consistency Criteria To Calculate BET Areas of Micro- And Mesoporous Metal–Organic Frameworks. *Journal of the American Chemical Society* **2016**, *138* (1), 215-224.
36. Moghadam, P. Z.; Li, A.; Wiggin, S. B.; Tao, A.; Maloney, A. G. P.; Wood, P. A.; Ward, S. C.; Fairen-Jimenez, D., Development of a Cambridge Structural Database Subset: A Collection of Metal–Organic Frameworks for Past, Present, and Future. *Chemistry of Materials* **2017**, *29* (7), 2618-2625.
37. Wilmer, C. E.; Leaf, M.; Lee, C. Y.; Farha, O. K.; Hauser, B. G.; Hupp, J. T.; Snurr, R. Q., Large-scale screening of hypothetical metal–organic frameworks. *Nature Chemistry* **2011**, *4*, 83.
38. Eddaoudi, M.; Kim, J.; Rosi, N.; Vodak, D.; Wachter, J.; O’Keeffe, M.; Yaghi, O. M., Systematic Design of Pore Size and Functionality in Isoreticular MOFs and Their Application in Methane Storage. *Science* **2002**, *295* (5554), 469-472.
39. Mason, J. A.; Oktawiec, J.; Taylor, M. K.; Hudson, M. R.; Rodriguez, J.; Bachman, J. E.; Gonzalez, M. I.; Cervellino, A.; Guagliardi, A.; Brown, C. M.; Llewellyn, P. L.; Masciocchi, N.; Long, J. R., Methane storage in flexible metal–organic frameworks with intrinsic thermal management. *Nature* **2015**, *527*, 357.

40. Brown, A. J.; Brunelli, N. A.; Eum, K.; Rashidi, F.; Johnson, J. R.; Koros, W. J.; Jones, C. W.; Nair, S., Interfacial microfluidic processing of metal-organic framework hollow fiber membranes. *Science* **2014**, *345* (6192), 72-75.
41. Peng, Y.; Li, Y.; Ban, Y.; Jin, H.; Jiao, W.; Liu, X.; Yang, W., Metal-organic framework nanosheets as building blocks for molecular sieving membranes. *Science* **2014**, *346* (6215), 1356-1359.
42. Banerjee, D.; Simon, C. M.; Plonka, A. M.; Motkuri, R. K.; Liu, J.; Chen, X.; Smit, B.; Parise, J. B.; Haranczyk, M.; Thallapally, P. K., Metal-organic framework with optimally selective xenon adsorption and separation. *Nature Communications* **2016**, *7*, ncomms11831.
43. Li, J.-R.; Sculley, J.; Zhou, H.-C., Metal-Organic Frameworks for Separations. *Chemical Reviews* **2012**, *112* (2), 869-932.
44. Furukawa, H.; Cordova, K. E.; O’Keeffe, M.; Yaghi, O. M., The Chemistry and Applications of Metal-Organic Frameworks. *Science* **2013**, *341* (6149).
45. Zhang, T.; Lin, W., Metal-organic frameworks for artificial photosynthesis and photocatalysis. *Chemical Society Reviews* **2014**, *43* (16), 5982-5993.
46. Lee, J.; Farha, O. K.; Roberts, J.; Scheidt, K. A.; Nguyen, S. T.; Hupp, J. T., Metal-organic framework materials as catalysts. *Chemical Society Reviews* **2009**, *38* (5), 1450-1459.
47. Huxford, R. C.; Della Rocca, J.; Lin, W., Metal-organic frameworks as potential drug carriers. *Current Opinion in Chemical Biology* **2010**, *14* (2), 262-268.
48. Rocca, J. D.; Liu, D.; Lin, W., Nanoscale Metal-Organic Frameworks for Biomedical Imaging and Drug Delivery. *Accounts of chemical research* **2011**, *44* (10), 957-968.
49. Zhang, X.; Ballem, M. A.; Hu, Z.-J.; Bergman, P.; Uvdal, K., Nanoscale Light-Harvesting Metal-Organic Frameworks. *Angewandte Chemie International Edition* **2011**, *50* (25), 5729-5733.
50. So, M. C.; Wiederrecht, G. P.; Mondloch, J. E.; Hupp, J. T.; Farha, O. K., Metal-organic framework materials for light-harvesting and energy transfer. *Chemical Communications* **2015**, *51* (17), 3501-3510.
51. Zhu, J.; Maza, W. A.; Morris, A. J., Light-harvesting and energy transfer in ruthenium(II)-polypyridyl doped zirconium(IV) metal-organic frameworks: A look toward solar cell applications. *Journal of Photochemistry and Photobiology A: Chemistry* **2017**, *344*, 64-77.
52. Williams, D. E.; Shustova, N. B., Metal-Organic Frameworks as a Versatile Tool To Study and Model Energy Transfer Processes. *Chemistry – A European Journal* **2015**, *21* (44), 15474-15479.
53. Zhu, J.; Shaikh, S.; Mayhall, N. J.; Morris, A. J., Energy Transfer in Metal-Organic Frameworks. In *Elaboration and Applications of Metal-Organic Frameworks*, World Scientific: 2018; pp 581-654.
54. Li, H.; Eddaoudi, M.; O’Keeffe, M.; Yaghi, O. M., Design and synthesis of an exceptionally stable and highly porous metal-organic framework. *Nature* **1999**, *402*, 276.
55. Chui, S. S.-Y.; Lo, S. M.-F.; Charmant, J. P. H.; Orpen, A. G.; Williams, I. D., A Chemically Functionalizable Nanoporous Material [Cu₃(TMA)₂(H₂O)₃]_n. *Science* **1999**, *283* (5405), 1148-1150.
56. Alaerts, L.; Séguin, E.; Poelman, H.; Thibault-Starzyk, F.; Jacobs, P. A.; De Vos, D. E., Probing the Lewis Acidity and Catalytic Activity of the Metal-Organic Framework [Cu₃(btc)₂] (BTC=Benzene-1,3,5-tricarboxylate). *Chemistry – A European Journal* **2006**, *12* (28), 7353-7363.
57. Dhakshinamoorthy, A.; Alvaro, M.; Garcia, H., Aerobic Oxidation of Benzylic Alcohols Catalyzed by Metal-Organic Frameworks Assisted by TEMPO. *ACS Catalysis* **2011**, *1* (1), 48-53.
58. Lu, J.; Mondal, A.; Moulton, B.; Zaworotko, M. J., Polygons and Faceted Polyhedra and Nanoporous Networks. *Angewandte Chemie International Edition* **2001**, *40* (11), 2113-2116.
59. Xie, L.; Liu, S.; Gao, C.; Cao, R.; Cao, J.; Sun, C.; Su, Z., Mixed-Valence Iron(II, III) Trimesates with Open Frameworks Modulated by Solvents. *Inorganic Chemistry* **2007**, *46* (19), 7782-7788.
60. Kramer, M.; Schwarz, U.; Kaskel, S., Synthesis and properties of the metal-organic framework MO₃(BTC)₂ (TUDMOF-1). *Journal of Materials Chemistry* **2006**, *16* (23), 2245-2248.
61. Murray, L. J.; Dinca, M.; Yano, J.; Chavan, S.; Bordiga, S.; Brown, C. M.; Long, J. R., Highly-Selective and Reversible O₂ Binding in Cr₃(1,3,5-benzenetricarboxylate)₂. *Journal of the American Chemical Society* **2010**, *132* (23), 7856-7857.
62. Kozachuk, O.; Yussenko, K.; Noei, H.; Wang, Y.; Walleck, S.; Glaser, T.; Fischer, R. A., Solvothermal growth of a ruthenium metal-organic framework featuring HKUST-1 structure type as thin films on oxide surfaces. *Chemical Communications* **2011**, *47* (30), 8509-8511.
63. Gotthardt, M. A.; Schoch, R.; Wolf, S.; Bauer, M.; Kleist, W., Synthesis and characterization of bimetallic metal-organic framework Cu-Ru-BTC with HKUST-1 structure. *Dalton Transactions* **2015**, *44* (5), 2052-2056.

64. Ahmed, A.; Robertson, C. M.; Steiner, A.; Whittles, T.; Ho, A.; Dhanak, V.; Zhang, H., Cu(i)Cu(ii)BTC, a microporous mixed-valence MOF via reduction of HKUST-1. *RSC Advances* **2016**, *6* (11), 8902-8905.
65. Li, P.; Vermeulen, N. A.; Malliakas, C. D.; Gómez-Gualdrón, D. A.; Howarth, A. J.; Mehdi, B. L.; Dohnalkova, A.; Browning, N. D.; O’Keeffe, M.; Farha, O. K., Bottom-up construction of a superstructure in a porous uranium-organic crystal. *Science* **2017**, *356* (6338), 624-627.
66. Deng, H.; Grunder, S.; Cordova, K. E.; Valente, C.; Furukawa, H.; Hmadeh, M.; Gándara, F.; Whalley, A. C.; Liu, Z.; Asahina, S.; Kazumori, H.; O’Keeffe, M.; Terasaki, O.; Stoddart, J. F.; Yaghi, O. M., Large-Pore Apertures in a Series of Metal-Organic Frameworks. *Science* **2012**, *336* (6084), 1018-1023.
67. Deng, H.; Doonan, C. J.; Furukawa, H.; Ferreira, R. B.; Towne, J.; Knobler, C. B.; Wang, B.; Yaghi, O. M., Multiple Functional Groups of Varying Ratios in Metal-Organic Frameworks. *Science* **2010**, *327* (5967), 846-850.
68. Wu, H.; Yang, J.; Su, Z.-M.; Batten, S. R.; Ma, J.-F., An Exceptional 54-Fold Interpenetrated Coordination Polymer with 103-srs Network Topology. *Journal of the American Chemical Society* **2011**, *133* (30), 11406-11409.
69. Farha, O. K.; Özgür Yazaydın, A.; Eryazici, I.; Malliakas, C. D.; Hauser, B. G.; Kanatzidis, M. G.; Nguyen, S. T.; Snurr, R. Q.; Hupp, J. T., De novo synthesis of a metal-organic framework material featuring ultrahigh surface area and gas storage capacities. *Nature Chemistry* **2010**, *2*, 944.
70. Li, B.; Wen, H.-M.; Wang, H.; Wu, H.; Tyagi, M.; Yildirim, T.; Zhou, W.; Chen, B., A Porous Metal-Organic Framework with Dynamic Pyrimidine Groups Exhibiting Record High Methane Storage Working Capacity. *Journal of the American Chemical Society* **2014**, *136* (17), 6207-6210.
71. Furukawa, H.; Ko, N.; Go, Y. B.; Aratani, N.; Choi, S. B.; Choi, E.; Yazaydın, A. Ö.; Snurr, R. Q.; O’Keeffe, M.; Kim, J.; Yaghi, O. M., Ultrahigh Porosity in Metal-Organic Frameworks. *Science* **2010**, *329* (5990), 424-428.
72. Bao, Z.; Yu, L.; Ren, Q.; Lu, X.; Deng, S., Adsorption of CO₂ and CH₄ on a magnesium-based metal organic framework. *Journal of Colloid and Interface Science* **2011**, *353* (2), 549-556.
73. Zhang, F.-M.; Dong, L.-Z.; Qin, J.-S.; Guan, W.; Liu, J.; Li, S.-L.; Lu, M.; Lan, Y.-Q.; Su, Z.-M.; Zhou, H.-C., Effect of Imidazole Arrangements on Proton-Conductivity in Metal-Organic Frameworks. *Journal of the American Chemical Society* **2017**, *139* (17), 6183-6189.
74. Narayan, T. C.; Miyakai, T.; Seki, S.; Dincă, M., High Charge Mobility in a Tetrathiafulvalene-Based Microporous Metal-Organic Framework. *Journal of the American Chemical Society* **2012**, *134* (31), 12932-12935.
75. Yuan, S.; Feng, L.; Wang, K.; Pang, J.; Bosch, M.; Lollar, C.; Sun, Y.; Qin, J.; Yang, X.; Zhang, P.; Wang, Q.; Zou, L.; Zhang, Y.; Zhang, L.; Fang, Y.; Li, J.; Zhou, H. C., Stable Metal-Organic Frameworks: Design, Synthesis, and Applications. *Advanced Materials* **0** (0), 1704303.
76. Bosch, M.; Zhang, M.; Zhou, H.-C., Increasing the stability of metal-organic frameworks. *Advances in Chemistry* **2014**, *2014*.
77. Devic, T.; Serre, C., High valence 3p and transition metal based MOFs. *Chemical Society Reviews* **2014**, *43* (16), 6097-6115.
78. Pearson, R. G., Hard and Soft Acids and Bases. *Journal of the American Chemical Society* **1963**, *85* (22), 3533-3539.
79. Bai, Y.; Dou, Y.; Xie, L.-H.; Rutledge, W.; Li, J.-R.; Zhou, H.-C., Zr-based metal-organic frameworks: design, synthesis, structure, and applications. *Chemical Society Reviews* **2016**, *45* (8), 2327-2367.
80. Cavka, J. H.; Jakobsen, S.; Olsbye, U.; Guillou, N.; Lamberti, C.; Bordiga, S.; Lillerud, K. P., A New Zirconium Inorganic Building Brick Forming Metal Organic Frameworks with Exceptional Stability. *Journal of the American Chemical Society* **2008**, *130* (42), 13850-13851.
81. Schaate, A.; Roy, P.; Godt, A.; Lippke, J.; Waltz, F.; Wiebcke, M.; Behrens, P., Modulated Synthesis of Zr-Based Metal-Organic Frameworks: From Nano to Single Crystals. *Chemistry A European Journal* **2011**, *17* (24), 6643-6651.
82. Feng, D.; Gu, Z. Y.; Li, J. R.; Jiang, H. L.; Wei, Z.; Zhou, H. C., Zirconium-Metalloporphyrin PCN-222: Mesoporous Metal-Organic Frameworks with Ultrahigh Stability as Biomimetic Catalysts. *Angewandte Chemie* **2012**, *124* (41), 10453-10456.
83. Mondloch, J. E.; Bury, W.; Fairen-Jimenez, D.; Kwon, S.; DeMarco, E. J.; Weston, M. H.; Sarjeant, A. A.; Nguyen, S. T.; Stair, P. C.; Snurr, R. Q.; Farha, O. K.; Hupp, J. T., Vapor-Phase Metalation by Atomic Layer Deposition in a Metal-Organic Framework. *Journal of the American Chemical Society* **2013**, *135* (28), 10294-10297.

84. Zhang, M.; Chen, Y. P.; Bosch, M.; Gentle, T.; Wang, K.; Feng, D.; Wang, Z. U.; Zhou, H. C., Symmetry-Guided Synthesis of Highly Porous Metal–Organic Frameworks with Fluorite Topology. *Angewandte Chemie* **2014**, *126* (3), 834-837.
85. Yuan, S.; Lu, W.; Chen, Y.-P.; Zhang, Q.; Liu, T.-F.; Feng, D.; Wang, X.; Qin, J.; Zhou, H.-C., Sequential Linker Installation: Precise Placement of Functional Groups in Multivariate Metal–Organic Frameworks. *Journal of the American Chemical Society* **2015**, *137* (9), 3177-3180.
86. Deria, P.; Mondloch, J. E.; Tylianakis, E.; Ghosh, P.; Bury, W.; Snurr, R. Q.; Hupp, J. T.; Farha, O. K., Perfluoroalkane functionalization of NU-1000 via solvent-assisted ligand incorporation: synthesis and CO₂ adsorption studies. *Journal of the American Chemical Society* **2013**, *135* (45), 16801-16804.
87. Furukawa, H.; Gándara, F.; Zhang, Y.-B.; Jiang, J.; Queen, W. L.; Hudson, M. R.; Yaghi, O. M., Water Adsorption in Porous Metal–Organic Frameworks and Related Materials. *Journal of the American Chemical Society* **2014**, *136* (11), 4369-4381.
88. Feng, D.; Chung, W.-C.; Wei, Z.; Gu, Z.-Y.; Jiang, H.-L.; Chen, Y.-P.; Darensbourg, D. J.; Zhou, H.-C., Construction of Ultrastable Porphyrin Zr Metal–Organic Frameworks through Linker Elimination. *Journal of the American Chemical Society* **2013**, *135* (45), 17105-17110.
89. Bon, V.; Senkowska, I.; Weiss, M. S.; Kaskel, S., Tailoring of network dimensionality and porosity adjustment in Zr- and Hf-based MOFs. *CrystEngComm* **2013**, *15* (45), 9572-9577.
90. Bon, V.; Senkowska, I.; Baburin, I. A.; Kaskel, S., Zr- and Hf-Based Metal–Organic Frameworks: Tracking Down the Polymorphism. *Crystal Growth & Design* **2013**, *13* (3), 1231-1237.
91. Beyzavi, M. H.; Klet, R. C.; Tussupbayev, S.; Borycz, J.; Vermeulen, N. A.; Cramer, C. J.; Stoddart, J. F.; Hupp, J. T.; Farha, O. K., A Hafnium-Based Metal–Organic Framework as an Efficient and Multifunctional Catalyst for Facile CO₂ Fixation and Regioselective and Enantioselective Epoxide Activation. *Journal of the American Chemical Society* **2014**, *136* (45), 15861-15864.
92. Stackhouse, C. A.; Ma, S., Azamacrocyclic-based Metal Organic Frameworks: Design Strategies and Applications. *Polyhedron* **2018**.
93. Zhang, H.; Zou, R.; Zhao, Y., Macrocyclic-based metal-organic frameworks. *Coordination Chemistry Reviews* **2015**, *292*, 74-90.
94. Choi, H. J.; Suh, M. P., Self-Assembly of Molecular Brick Wall and Molecular Honeycomb from Nickel(II) Macrocyclic and 1,3,5-Benzenetricarboxylate: Guest-Dependent Host Structures. *Journal of the American Chemical Society* **1998**, *120* (41), 10622-10628.
95. Lee, E. Y.; Suh, M. P., A Robust Porous Material Constructed of Linear Coordination Polymer Chains: Reversible Single-Crystal to Single-Crystal Transformations upon Dehydration and Rehydration. *Angewandte Chemie International Edition* **2004**, *43* (21), 2798-2801.
96. Moon, H. R.; Kim, J. H.; Suh, M. P., Redox-Active Porous Metal–Organic Framework Producing Silver Nanoparticles from AgI Ions at Room Temperature. *Angewandte Chemie International Edition* **2005**, *44* (8), 1261-1265.
97. Larionova, J.; Clérac, R.; Donnadiou, B.; Willemin, S.; Guérin, C., Synthesis and Structure of a Two-Dimensional Cyano-Bridged Coordination Polymer [Cu(cyclam)]₂[Mo(CN)₈]·10.5H₂O (Cyclam = 1,4,8,11-Tetraazacyclodecane). *Crystal Growth & Design* **2003**, *3* (2), 267-272.
98. Kim, H.; Suh, M. P., Flexible Eightfold Interpenetrating Diamondoid Network Generating 1D Channels: Selective Binding with Organic Guests. *Inorganic Chemistry* **2005**, *44* (4), 810-812.
99. Almasi, M.; Zelenak, V.; Zukal, A.; Kuchar, J.; Cejka, J., A novel zinc(ii) metal-organic framework with a diamond-like structure: synthesis, study of thermal robustness and gas adsorption properties. *Dalton Transactions* **2016**, *45* (3), 1233-1242.
100. Zhu, X.-D.; Lin, Z.-J.; Liu, T.-F.; Xu, B.; Cao, R., Two Novel 3d-4f Heterometallic Frameworks Assembled from a Flexible Bifunctional Macrocyclic Ligand. *Crystal Growth & Design* **2012**, *12* (10), 4708-4711.
101. Zhu, X.-D.; Tao, T.-X.; Zhou, W.-X.; Wang, F.-H.; Liu, R.-M.; Liu, L.; Fu, Y.-Q., A novel lead(II) porous metal–organic framework constructed from a flexible bifunctional macrocyclic polyamine ligand. *Inorganic Chemistry Communications* **2014**, *40*, 116-119.
102. Gao, W.-Y.; Niu, Y.; Chen, Y.; Wojtas, L.; Cai, J.; Chen, Y.-S.; Ma, S., Porous metal-organic framework based on a macrocyclic tetracarboxylate ligand exhibiting selective CO₂ uptake. *CrystEngComm* **2012**, *14* (19), 6115-6117.

103. Gao, W. Y.; Chen, Y.; Niu, Y.; Williams, K.; Cash, L.; Perez, P. J.; Wojtas, L.; Cai, J.; Chen, Y. S.; Ma, S., Crystal Engineering of an nbo Topology Metal–Organic Framework for Chemical Fixation of CO₂ under Ambient Conditions. *Angewandte Chemie International Edition* **2014**, *53* (10), 2615-2619.
104. Carné-Sánchez, A.; Bonnet, C. S.; Imaz, I.; Lorenzo, J.; Tóth, É.; Maspoch, D., Relaxometry Studies of a Highly Stable Nanoscale Metal–Organic Framework Made of Cu(II), Gd(III), and the Macrocyclic DOTP. *Journal of the American Chemical Society* **2013**, *135* (47), 17711-17714.
105. Diercks, C. S.; Liu, Y.; Cordova, K. E.; Yaghi, O. M., The role of reticular chemistry in the design of CO₂ reduction catalysts. *Nature Materials* **2018**, *17* (4), 301-307.
106. Trickett, C. A.; Helal, A.; Al-Maythaly, B. A.; Yamani, Z. H.; Cordova, K. E.; Yaghi, O. M., The chemistry of metal–organic frameworks for CO₂ capture, regeneration and conversion. *Nature Reviews Materials* **2017**, *2*, 17045.
107. Maina, J. W.; Pozo-Gonzalo, C.; Kong, L.; Schutz, J.; Hill, M.; Dumeé, L. F., Metal organic framework based catalysts for CO₂ conversion. *Materials Horizons* **2017**, *4* (3), 345-361.
108. He, H.; Perman, J. A.; Zhu, G.; Ma, S., Metal–Organic Frameworks for CO₂ Chemical Transformations. *Small* **2016**, *12* (46), 6309-6324.
109. Beyzavi, M. H.; Stephenson, C. J.; Liu, Y.; Karagiari, O.; Hupp, J. T.; Farha, O. K., Metal–Organic Framework-Based Catalysts: Chemical Fixation of CO₂ with Epoxides Leading to Cyclic Organic Carbonates. *Frontiers in Energy Research* **2015**, *2* (63).
110. North, M.; Pasquale, R.; Young, C., Synthesis of cyclic carbonates from epoxides and CO₂. *Green Chemistry* **2010**, *12* (9), 1514-1539.
111. Song, J.; Zhang, Z.; Hu, S.; Wu, T.; Jiang, T.; Han, B., MOF-5/n-Bu₄NBr: an efficient catalyst system for the synthesis of cyclic carbonates from epoxides and CO₂ under mild conditions. *Green Chemistry* **2009**, *11* (7), 1031-1036.
112. Miralda, C. M.; Macias, E. E.; Zhu, M.; Ratnasamy, P.; Carreon, M. A., Zeolitic Imidazole Framework-8 Catalysts in the Conversion of CO₂ to Chloropropene Carbonate. *ACS Catalysis* **2012**, *2* (1), 180-183.
113. Yang, L.; Yu, L.; Diao, G.; Sun, M.; Cheng, G.; Chen, S., Zeolitic imidazolate framework-68 as an efficient heterogeneous catalyst for chemical fixation of carbon dioxide. *Journal of Molecular Catalysis A: Chemical* **2014**, *392*, 278-283.
114. Guillerm, V.; WeselińskiŁukasz, J.; Belmabkhout, Y.; Cairns, A. J.; D'Elia, V.; WojtasŁukasz; Adil, K.; Eddaoudi, M., Discovery and introduction of a (3,18)-connected net as an ideal blueprint for the design of metal–organic frameworks. *Nat Chem* **2014**, *6* (8), 673-680.
115. Gao, W.-Y.; Chen, Y.; Niu, Y.; Williams, K.; Cash, L.; Perez, P. J.; Wojtas, L.; Cai, J.; Chen, Y.-S.; Ma, S., Crystal Engineering of an nbo Topology Metal–Organic Framework for Chemical Fixation of CO₂ under Ambient Conditions. *Angewandte Chemie International Edition* **2014**, *53* (10), 2615-2619.
116. Gao, W.-Y.; Wojtas, L.; Ma, S., A porous metal-metalloporphyrin framework featuring high-density active sites for chemical fixation of CO₂ under ambient conditions. *Chemical Communications* **2014**, *50* (40), 5316-5318.
117. Gao, W.-Y.; Tsai, C.-Y.; Wojtas, L.; Thiounn, T.; Lin, C.-C.; Ma, S., Interpenetrating Metal–Metalloporphyrin Framework for Selective CO₂ Uptake and Chemical Transformation of CO₂. *Inorganic Chemistry* **2016**, *55* (15), 7291-7294.
118. Ren, Y.; Shi, Y.; Chen, J.; Yang, S.; Qi, C.; Jiang, H., Ni(salphen)-based metal-organic framework for the synthesis of cyclic carbonates by cycloaddition of CO₂ to epoxides. *RSC Advances* **2013**, *3* (7), 2167-2170.
119. Lescouet, T.; Chizallet, C.; Farrusseng, D., The origin of the activity of amine-functionalized metal–organic frameworks in the catalytic synthesis of cyclic carbonates from epoxide and CO₂. *ChemCatChem* **2012**, *4* (11), 1725-1728.
120. Kim, J.; Kim, S.-N.; Jang, H.-G.; Seo, G.; Ahn, W.-S., CO₂ cycloaddition of styrene oxide over MOF catalysts. *Applied Catalysis A: General* **2013**, *453*, 175-180.
121. Kim, Y.-J.; Park, D.-W., Functionalized IRMOF-3: an efficient heterogeneous catalyst for the cycloaddition of allyl glycidyl ether and CO₂. *Journal of nanoscience and nanotechnology* **2013**, *13* (3), 2307-2312.
122. Jose, T.; Hwang, Y.; Kim, D.-W.; Kim, M.-I.; Park, D.-W., Functionalized zeolitic imidazolate framework F-ZIF-90 as efficient catalyst for the cycloaddition of carbon dioxide to allyl glycidyl ether. *Catalysis Today* **2015**, *245*, 61-67.

123. Tharun, J.; Bhin, K.-M.; Roshan, R.; Kim, D. W.; Kathalikkattil, A. C.; Babu, R.; Ahn, H. Y.; Won, Y. S.; Park, D.-W., Ionic liquid tethered post functionalized ZIF-90 framework for the cycloaddition of propylene oxide and CO₂. *Green Chemistry* **2016**, *18* (8), 2479-2487.
124. Ma, D.; Li, B.; Liu, K.; Zhang, X.; Zou, W.; Yang, Y.; Li, G.; Shi, Z.; Feng, S., Bifunctional MOF heterogeneous catalysts based on the synergy of dual functional sites for efficient conversion of CO₂ under mild and co-catalyst free conditions. *Journal of Materials Chemistry A* **2015**, *3* (46), 23136-23142.
125. James, B. R.; Boissonault, J. A.; Wong-Foy, A. G.; Matzger, A. J.; Sanford, M. S., Structure activity relationships in metal-organic framework catalysts for the continuous flow synthesis of propylene carbonate from CO₂ and propylene oxide. *RSC Advances* **2018**, *8* (4), 2132-2137.
126. Wang, C.; Xie, Z.; deKrafft, K. E.; Lin, W., Doping metal-organic frameworks for water oxidation, carbon dioxide reduction, and organic photocatalysis. *Journal of the American Chemical Society* **2011**, *133* (34), 13445-13454.
127. Choi, K. M.; Kim, D.; Rungtaweivoranit, B.; Trickett, C. A.; Barmanbek, J. T. D.; Alshammari, A. S.; Yang, P.; Yaghi, O. M., Plasmon-enhanced photocatalytic CO₂ conversion within metal-organic frameworks under visible light. *Journal of the American Chemical Society* **2016**, *139* (1), 356-362.
128. Fei, H.; Sampson, M. D.; Lee, Y.; Kubiak, C. P.; Cohen, S. M., Photocatalytic CO₂ Reduction to Formate Using a Mn(I) Molecular Catalyst in a Robust Metal-Organic Framework. *Inorganic Chemistry* **2015**, *54* (14), 6821-6828.
129. Kajiwarra, T.; Fujii, M.; Tsujimoto, M.; Kobayashi, K.; Higuchi, M.; Tanaka, K.; Kitagawa, S., Photochemical Reduction of Low Concentrations of CO₂ in a Porous Coordination Polymer with a Ruthenium(II)-CO Complex. *Angewandte Chemie International Edition* **2016**, *55* (8), 2697-2700.
130. Fu, Y.; Sun, D.; Chen, Y.; Huang, R.; Ding, Z.; Fu, X.; Li, Z., An Amine-Functionalized Titanium Metal-Organic Framework Photocatalyst with Visible-Light-Induced Activity for CO₂ Reduction. *Angewandte Chemie* **2012**, *124* (14), 3420-3423.
131. Sun, D.; Fu, Y.; Liu, W.; Ye, L.; Wang, D.; Yang, L.; Fu, X.; Li, Z., Studies on Photocatalytic CO₂ Reduction over NH₂-UiO-66(Zr) and Its Derivatives: Towards a Better Understanding of Photocatalysis on Metal-Organic Frameworks. *Chemistry – A European Journal* **2013**, *19* (42), 14279-14285.
132. Chen, D.; Xing, H.; Wang, C.; Su, Z., Highly efficient visible-light-driven CO₂ reduction to formate by a new anthracene-based zirconium MOF via dual catalytic routes. *Journal of Materials Chemistry A* **2016**, *4* (7), 2657-2662.
133. Li, R.; Hu, J.; Deng, M.; Wang, H.; Wang, X.; Hu, Y.; Jiang, H. L.; Jiang, J.; Zhang, Q.; Xie, Y., Integration of an inorganic semiconductor with a metal-organic framework: a platform for enhanced gaseous photocatalytic reactions. *Advanced Materials* **2014**, *26* (28), 4783-4788.
134. Shi, L.; Wang, T.; Zhang, H.; Chang, K.; Ye, J., Electrostatic Self-Assembly of Nanosized Carbon Nitride Nanosheet onto a Zirconium Metal-Organic Framework for Enhanced Photocatalytic CO₂ Reduction. *Advanced functional materials* **2015**, *25* (33), 5360-5367.
135. Hinogami, R.; Yotsuhashi, S.; Deguchi, M.; Zenitani, Y.; Hashiba, H.; Yamada, Y., Electrochemical reduction of carbon dioxide using a copper rubeanate metal organic framework. *ECS Electrochemistry Letters* **2012**, *1* (4), H17-H19.
136. Kumar, R. S.; Kumar, S. S.; Kulandainathan, M. A., Highly selective electrochemical reduction of carbon dioxide using Cu based metal organic framework as an electrocatalyst. *Electrochemistry Communications* **2012**, *25*, 70-73.
137. Kornienko, N.; Zhao, Y.; Kley, C. S.; Zhu, C.; Kim, D.; Lin, S.; Chang, C. J.; Yaghi, O. M.; Yang, P., Metal-Organic Frameworks for Electrocatalytic Reduction of Carbon Dioxide. *Journal of the American Chemical Society* **2015**, *137* (44), 14129-14135.
138. Hod, I.; Sampson, M. D.; Deria, P.; Kubiak, C. P.; Farha, O. K.; Hupp, J. T., Fe-Porphyrin-Based Metal-Organic Framework Films as High-Surface Concentration, Heterogeneous Catalysts for Electrochemical Reduction of CO₂. *ACS Catalysis* **2015**, *5* (11), 6302-6309.

Chapter 2 Light-harvesting and energy transfer in ruthenium(II)-polypyridyl doped zirconium(IV) metal-organic frameworks: a look towards solar cell applications

This chapter has been adapted from a published manuscript by [Zhu, J.](#); Maza, W. A.; and Morris, A. J. from the following reference: *Journal of Photochemistry and Photobiology A: Chemistry* **2017**, 344, 64-77. Reprinted with permission from the Elsevier copyright © 2017.

2.1 Abstract

Metal-organic frameworks (MOFs) as highly ordered, tunable hybrid materials for photon collection, energy transfer and photocatalytic reactions have raised great interest. Understanding the light-harvesting and exciton transport processes within well-defined 3D solid phases will result in the better design of highly efficient biomimetic chromophore arrays for artificial photosynthesis. In this review, we summarize the fundamental principles of energy transfer in the condensed phase and overview a series of studies in light-harvesting, excited state quenching and photo-excited reactivity occurring within ruthenium-polypyridyl-doped zirconium MOFs. The application of MOFs in energy conversion devices such as dye-sensitized solar cells (DSSC) is also discussed.

2.2 Introduction

With increased consumption of fossil fuels, the demand for finding and using sustainable clean energy sources, such as solar energy, has grown in the past decades. Although the energy which the sun provides is approximately 10,000 times greater than the world's present rate of energy consumption, the current devices for converting solar energy to electrical power/chemical energy suffer from low efficiency, high cost and/or limited scale.¹ Three-dimensional porous coordination polymers, known as metal-organic frameworks (MOFs), constructed by metal ions/clusters and organic bridging molecules, have shown promise for applications in artificial photosynthesis and photocatalysis owing to their rich electronic properties, structural diversity, and synthetic tunability.²⁻³ Incorporation of photoactive ligands into MOFs provides an attractive platform to study light harvesting, energy transfer, and photo-excited reactivity within highly ordered and well-defined architectures.⁴⁻⁷

MOFs as functional materials for solar light-harvesting could be employed as sensitizer agents providing excited state energy to a neighboring material, or, conversely, as the material to be sensitized. Molecular chromophores, such as porphyrins and Ru/Os tris-bipyridine transition metal complexes, have been used as building blocks in MOFs capable of donating and/or accepting excited-state energy or electrons as described above.^{4, 8-12} For example, Hupp and coworkers have reported two different

approaches to modifying porphyrin-based MOFs that display continuous absorption over the majority of the visible spectrum.^{4, 9} In one approach, they incorporated boron dipyrromethene (bodipy) and porphyrin complexes as complementary pairs of chromophores in the MOF material.¹³ The bodipy linkers absorb and emit in the green spectral region and serve as antenna chromophores for the excitation of porphyrinic struts via resonance energy transfer. By incorporation of the porphyrin units, the absorption of the bodipy-porphyrin-based (BOP) MOF crystals is extended even further into the visible range so that the MOF crystals appear nearly black compared to just the bodipy-only MOF material.⁴ Another strategy demonstrated by the Hupp group is the surface functionalization of porphyrin-based MOFs with quantum dots (QDs), which serves to enhance the light harvesting capability of the hybrid material. The QDs are highly absorbing in the near-UV to the visible region of the spectrum whereas the MOFs have smaller absorption cross-sections but absorb further in the visible to the near-IR region of the spectrum.⁹ Together, the light-harvesting efficiency of the hybrid material is, therefore, significantly improved. With CdSe/ZnS core/shell QDs chemically attached to the MOF surface, the QD-MOF hybrids could compensate for the relatively narrow absorption spectra of single-chromophore MOFs.⁹

Lin, Meyer and coworkers used Ru(bpy)₃²⁺/Os(bpy)₃²⁺-derivative linkers (bpy = 2,2'-bipyridine) and Zn²⁺-based connecting nodes to synthesize a phosphorescent MOF.⁷ Long excited-state lifetimes ($\tau \sim 375$ ns) were observed in crystals containing only Ru(bpy)₃²⁺. Upon doping the Ru(bpy)₃²⁺-Zn²⁺ MOF crystals with Os(bpy)₃²⁺ analog linkers, rapid quenching of photoexcited Ru(bpy)₃²⁺ due to energy migration to the Os(bpy)₃²⁺ trap sites was observed.^{7, 12} The sensitization of the Os(bpy)₃²⁺ complexes was proposed to occur via a Ru-to-Ru hopping mechanism to Os(bpy)₃²⁺ trap sites located up to 40 Å from the excited state Ru(bpy)₃²⁺ origin.⁷

Ru(bpy)₃²⁺ has also been incorporated into the porous, water stable framework UiO-67.¹⁴ By simple replacement of bipyridine ligands with 2,2'-bipyridyl-5,5'-dicarboxylic acid, Lin and co-workers doped Ru(bpy)₃²⁺ into UiO-67 MOFs and obtained as solid state photocatalysts. The photocatalytic activities of the designed MOF material were investigated in Aza-Henry reactions, oxidative coupling of amines and oxidation of sulfides as model reactions.¹⁴ The dependence of the photophysical behavior on Ru(bpy)₃²⁺ loading was later probed by our group.^{10, 15} The changes in excited state lifetimes and spectral differences observed with increasing dye concentration were attributed to dipole-dipole homogeneous resonance energy transfer (RET) and loading dependent differences in incorporation/encapsulation environments (*vide infra*).^{10, 15}

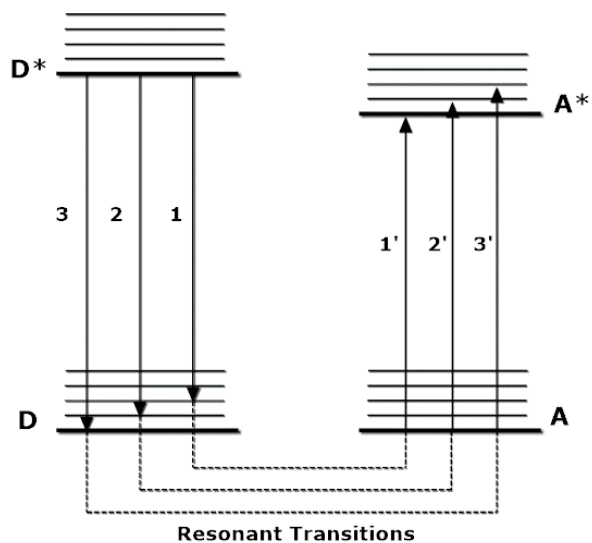
MOFs have been shown to function as sensitizers for applications in dye-sensitized solar cell (DSSC) devices of differing arrangements. For example, Cu-based MOF thin films prepared by porphyrinic linkers and Cu(II) connecting nodes have been shown to generate photocurrent in TiO₂ based solar cells.¹⁶⁻¹⁷ Although the cell performance of the Cu-MOF thin films was poor compared to conventional porphyrinic dye-based cells, statistically significant trends were observed upon increasing the surface content of the Cu-MOF indicating that MOFs, as highly ordered hybrid materials, afford exciting possibilities for harvesting photons and converting solar energy.

Excellent reviews have been written by Lin, Hupp and co-workers^{13, 18} discussing MOFs for photocatalysis and energy transfer. Therefore, in this perspective we have limited our focus to the work conducted on energy transfer in Ru(bpy)₃²⁺-doped UiO-67 frameworks with an eye towards highlighting their potential application for sensitized solar cells.^{10-11, 15, 19} For the most part, we discuss a) different synthetic approaches to doping Ru(bpy)₃ into UiO-67 class MOFs; b) the photophysical properties of the dopant within the MOF matrix and energy transfer mechanism studies performed on these doped MOFs and c) the application of these doped materials in photovoltaic devices.

2.3 Förster and Dexter Energy Transport in MOFs

2.3.1 Resonance Energy Transfer

Resonance energy transfer (RET) is a non-radiative process in which a portion of the excited state energy of a *donor* molecule or *sensitizer* is transferred to a neighboring ground-state acceptor molecule, thereby producing an excited-state acceptor and ground-state donor.²⁰⁻²² This transfer of energy occurs due to either an exchange mechanism (Dexter) or Coulombic coupling between the transition dipoles of the interacting molecules (Förster, Perrin, etc) (Scheme 2.1).²³⁻²⁴ Whereas the exchange mechanism occurs over short distances ($r_{DA} < 10 \text{ \AA}$), Coulombic coupling between donor (D) and acceptor (A) can occur over distances up to 100 \AA .



Scheme 2.1 Energy diagram depicting coupled transitions in resonance between an excited state energy donor fluorophore, D*, and quenching excited state energy acceptor, A.

There are three Coulombic coupling regimes that have been identified: a strong coupling, weak coupling, and very weak coupling (commonly referred to as the Förster limit) regimes. The strong and weak coupling regimes are characterized by a r^{-3} dependence on the rate of resonance energy transfer, k_{RET} , whereas Förster resonance energy transfer (or FRET) in the very weak coupling region is characterized by an r^{-6} dependence on k_{RET} .

2.3.2 Förster and Dexter Energy Transfer

Understanding the energy transfer processes in supramolecular architectures is an indispensable component to the appropriate design and application of those materials for solar energy conversion devices such as photovoltaics and photoelectrochemical cells. MOFs offer a rich diversity of unique platforms by which to study long-range energy transfer. By judicious choice of ligands and metal nodes, MOFs allow for precise control of distances and angles between chromophores and their alignment via crystal engineering.²⁵ Förster and Dexter resonance energy transfer mechanisms are the two most studied models for energy transfer in supramolecular light harvesting systems. The Förster model of resonance energy transfer (FRET) is dominated by weak long-range Coulombic dipole-dipole interactions. By contrast, Dexter resonance energy transfer (DRET) relies on stronger intermolecular interactions resulting in electron exchange due to donor-acceptor orbital overlap and is, therefore, only effective at short distances ($r < \sim 10\text{\AA}$). A visual representation of both FRET and DRET is given in Scheme 2.2. The Förster mechanism is only possible for symmetry allowed energy-transfer reaction while the Dexter mechanism plays an important role in depicting the energy transfer in which the spin state of the excited state may not be conserved.

In the very weak coupling regime, or Förster regime, intermolecular interactions are much weaker than electronic excitation energies for the $D \rightarrow D^*$ and $A \rightarrow A^*$ transitions. As a consequence, there is no perturbation to the experimentally observed absorption spectra. The efficiency of the Förster resonance energy transfer, FRET, is proportional to the degree of coupling between the $D^* \rightarrow D$ and $A \rightarrow A^*$ transition dipoles evaluated quantitatively as the overlap between emission spectra of the donor and absorption spectra of the acceptor molecule. This is expressed numerically as the overlap integral:

$$J = \frac{\int_0^\infty I_D(\lambda) \varepsilon_A(\lambda) \lambda^4 d\lambda}{\int_0^\infty I_D(\lambda) d\lambda} \quad (1)$$

where $I_D(\lambda)$ is the emission spectra of the donor and $\varepsilon_A(\lambda)$ is the extinction spectra of the acceptor. The overlap integral J gives a quantitative measure of the coupling between donor and acceptor transition dipole moments.

The energy transfer rate predicted by the Förster model is proportional to the inverse sixth power of the donor-acceptor distance (eq 2)

$$k_{ET} = k_D \left(\frac{R_0}{r} \right)^6 = \frac{1}{\tau_0} \left(\frac{R_0}{r} \right)^6 \quad (2)$$

where k_D is the emission rate constant of the donor in the absence of an adequate acceptor, τ_0 is the donor lifetime in the absence of quencher, r is the distance between donor and acceptor while R_0 is the Förster radius.²⁶ The Förster radius, R_0 is defined as the distance at which the efficiency of energy transfer is 50% and is directly proportional to the fluorescence quantum yield of the donor in the absence of acceptor, Φ_D , and the overlap integral, J , by the expression:

$$R_0 = \left[\frac{9000(I_n 10) \kappa^2 \Phi_D J}{128 \pi^5 N_A n^4} \right]^{1/6} \quad (3)$$

where κ^2 is a geometric parameter and describes the relative orientation between the donor and acceptor transition dipole moments, N_A is Avogadro's number, and n is the refractive index of the sample media. For an ensemble in which the donor and acceptor dipole moments are randomly distributed, sampling all possible orientations, the κ^2 parameter averages to $2/3$. However, for MOFs in which D and A are both incorporated into the framework of the material at fixed, r , and orientation with respect to each other, κ can be approximated as

$$\kappa = \cos \theta_{DA} - 3 \cos \theta_D \cos \theta_A \quad (4)$$

where θ_D and θ_A are the angles of the donor and acceptor transition moments, respectively, relative to the vector corresponding to the intermolecular separation distance between D and A. θ_{DA} is the angle between the donor and acceptor transition moment.

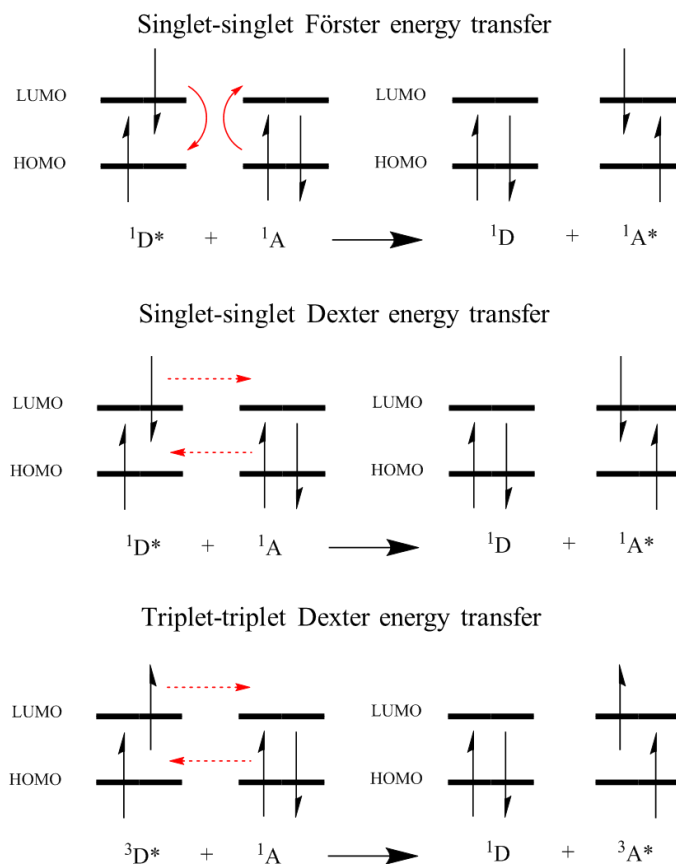
The Dexter energy transfer rate exhibits an exponential dependence on the donor-acceptor distance which can be written as (eq 5)

$$k_{ET} = k_o \exp \left[-\frac{2(r-r_o)}{L} \right] \quad (5)$$

where k_o is the limiting energy transfer rate at the intermolecular contact distance, r_o . r is the distance between donor and acceptor, r_o is analogous to the Förster radius and is the donor-acceptor distance at which the probability of RET is 50%, and L is the average Bohr radius of the interacting species.²⁷ Included in k_o is the Dexter overlap integral, J_{Dexter} ,

$$J_{Dexter} = \frac{\int I_D(\lambda) \epsilon_A(\lambda) d\lambda}{\int I_D(\lambda) d\lambda \int \epsilon_A(\lambda) d\lambda} \quad (6)$$

where J_{Dexter} ranges from zero to unity, so that the probability of DRET increases as the spectral overlap between the donor emission and the acceptor absorption increases.



Scheme 2.2 Förster and Dexter energy transfer mechanisms

From these models, it is clear that the rate and efficiency of energy transfer are primarily dependent on three physical variables. These are 1) the degree of overlap between the donor emission and acceptor absorption transition energies manifest by the spectral overlap between donor emission and acceptor absorption (quantified by J in equations 1 and 6), 2) the geometric orientation of the donor in relation to the acceptor within the MOF matrix – more specifically, the orientation between $D^* \rightarrow D$ and $A \rightarrow A^*$ transition dipoles, and finally 3) the distance between the donor and acceptor within the three-dimensional framework of the MOF, such that an increase in the inter-chromophores distance will effect k_{RET} negatively.

Therefore, in order to design MOF systems with improved resonance energy transfer capacity, the criteria above need to be considered. First, maximizing the degree of overlap between the emission spectrum of the donor and the absorption spectrum of acceptor to increases the magnitude of the Förster distance (eq 3), R_0 . By this means the probability of RET and the rate of energy transfer (eq 2) between donor and acceptor will be increased. Increasing the spectral overlap between the donor emission and acceptor absorption can be done by a number of different ways. In the case of heterogeneous RET, donor acceptor ligand pairs can be judiciously chosen such that their photophysical properties are appropriately matched. One good example for this strategy comes from the Hupp group's work with the design of BOP MOF.⁴ This pillared-paddlewheel type MOF was constructed by bidipy and metalloporphyrin struts, where the bodipy struts serve as antenna chromophores for the excitation of porphyrinic struts. Because of the good spectral overlap between the ligands, the nearly black BOP MOF material is not only capable of collecting most of light in visible range, but also demonstrates efficient rapid energy migration. Alternatively, the emission and absorption spectrum of heterogeneous or homogeneous donor-acceptor ligand pairs can be modified via covalent modification of the ligand structure by the addition of electron donating or withdrawing functional groups, varying the ligand symmetry, conjugation, and/or the rigidity of the chromophore. Other strategies include hydrogen bonding between the MOF-chromophores and a guest, ionization, and variation of the local environments of the MOF-chromophore by solvation, viscosity, etc.

The second and more complicated criterion to control is the orientation of the chromophores relative to each other. However, by controlling the position, orientation and transition dipole moments of the donor-acceptor MOF-chromophores in relation to each other, the κ^2 term in equation 3 can be maximized to lead the increase of k_0 term of equation 5. Therefore, the rate of energy transfer can be increased. In support of this strategy, Deria and coworkers recently reported the topological control over the photophysical properties of MOFs via modular inter-chromophoric orientation and interaction.²⁸ With the probe of computational and experimental data, they found that stronger inter-chromophore

interactions between chromophores oriented in MOF structures with smaller dihedral angles. The interactions lead to red shift in emission spectral and a faster emissive quenching rate. It is worthy to mention that while altering the angles between the chromophores, the donor-acceptor distance would vary accordingly, which leads us to the third criterion.

Lastly, it is easier, instead, to control the relative donor-acceptor distance by ligand modification and coordination geometry at the metal nodes of the MOF. For example, in order to decrease the distance between chromophores present in a layered framework, Hupp's group converted a pillared-paddlewheel, porphyrin-containing 3D MOF to a 2D framework via solvent-assisted linker exchange.²⁹ In addition to this work, our group explored the influence of chromophore concentration and thus spacing between those chromophores on the rate of RET in ruthenium (II) tris-(2,2'-bipyridine), Ru(bpy)₃²⁺ (bpy = bipyridine), doped zirconium frameworks. As expected, in both cases the frameworks that exhibited shorter chromophore to chromophore distances displayed faster rates of energy transfer.

A number of common chromophore RET pairs whose excited state properties and RET dynamics are well understood in solution have been chosen and exploited by incorporation into MOFs in order to elucidate the effect of the MOF matrix³⁰⁻³¹ in modulating RET for photochemical/photovoltaic applications. Some of these have already been briefly mentioned above. We have extensively studied the Ru(bpy)₃²⁺ transition metal complex³²⁻³³ and will now discuss our previous and current work on its ability to harvest light energy when incorporated into MOFs.

2.4 Photophysical Properties of RuDCBPY-UiO-67 Powder

UiO-67 is a water-stable framework containing Zr₆(μ₃-O)₄(μ₃-OH)₄ nodes connected by twelve 4,4'-biphenyldicarboxylate (BPDC) linkers (Figure 2.1A).³⁴ First developed at the University of Oslo in 2008, this Zr^{IV}-based MOF, and others like it, has attracted escalating research interest because of their robust thermal and chemical stability as well as its highly porous nature.³⁵ The structure contains pores with two distinct geometric environments: an octahedral cage of 16 Å diameter and a tetrahedral cage of 12 Å diameter (Figure 2.1B).³⁶⁻³⁷ UiO-67 provides a unique platform in which to incorporate classical organometallic photosensitizers such as [Ru(dcbpy)(bpy)₂]²⁺ (RuDCBPY) by the simple replacement of one the bipyridine ligands with 2,2'-bipyridyl-5,5'-dicarboxylic acid (DCBPY) (Figure 1B).¹⁴ Lin and co-workers were the first to report this mix-and-match synthetic strategy to dope different transitional metal molecular catalysts, including RuDCBPY, into the UiO-67 framework.¹⁴ The well-established and rich excited state properties of RuBPY and its derivatives along with their sensitivity to environmental stressors and confinement make them ideal photoactive transition metal complexes for doping within an MOF matrix in order to understand the nature of the environments within the MOF pores.^{7, 12, 38-40}

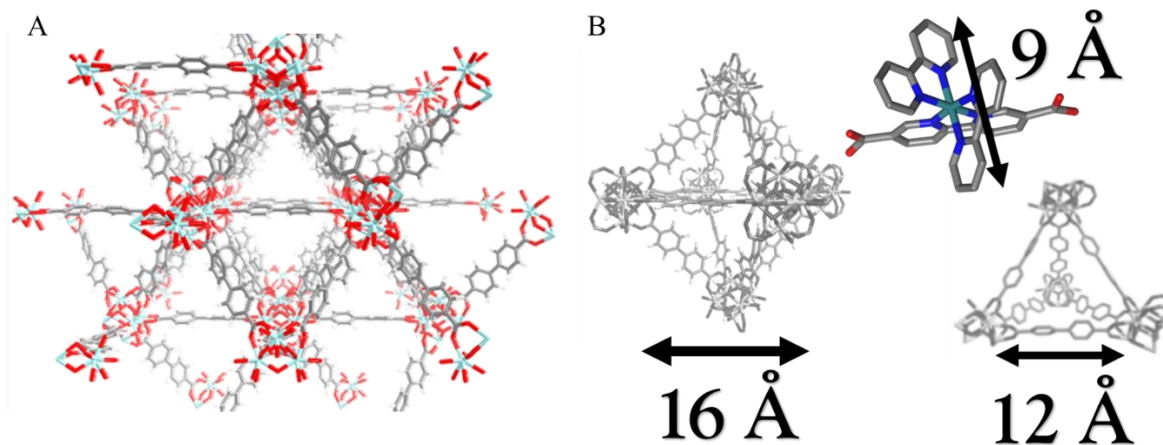


Figure 2.1 A) Crystal structure of UiO-67, $\text{Zr}_6(\mu_3\text{-O})_4(\mu_3\text{-OH})_4(\text{BPDC})_{12}$, where BPDC = biphenyldicarboxylic acid: black, carbon; red, oxygen; cyan, zirconium. B) Octahedral cavity (left), the tetrahedral cavity (right), RuDCBPY (middle). Adopted with the permission from Ref. 10. Copyright 2014 American Chemical Society.

2.4.1 Two-State Model

RuDCBPY-UiO-67 was prepared by a solvothermal reaction identical to the synthesis of UiO-67 except the addition of RuDCBPY in the reaction mixture. Specifically, ZrCl_4 was mixed with BPDC and RuDCBPY in DMF with the addition of benzoic acid as a modulator and the mixture heated at 120°C for 24 h (Figure 2.2A). The experimental PXRD of the doped material was in excellent agreement with PXRD patterns simulated from the previously reported structural data of the undoped UiO-67 (Figure 2.2B).⁴¹ The addition of varying amounts of RuDCBPY to the reaction mixture led to different doping concentrations varying from 2.6 *mm* to 44.7 *mm* (*mm* = millimolal).

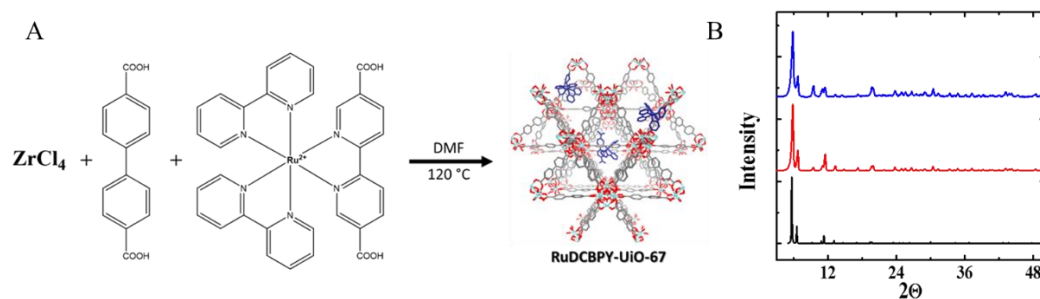


Figure 2.2 A) Synthetic diagram for RuDCBPY-doped UiO-67. B) PXRD patterns of UiO-67 (red) and RuDCBPY-UiO-67 (blue) powders along with the predicted pattern of UiO-67 (black). Adopted with the permission from Ref. 10. Copyright 2014 American Chemical Society.

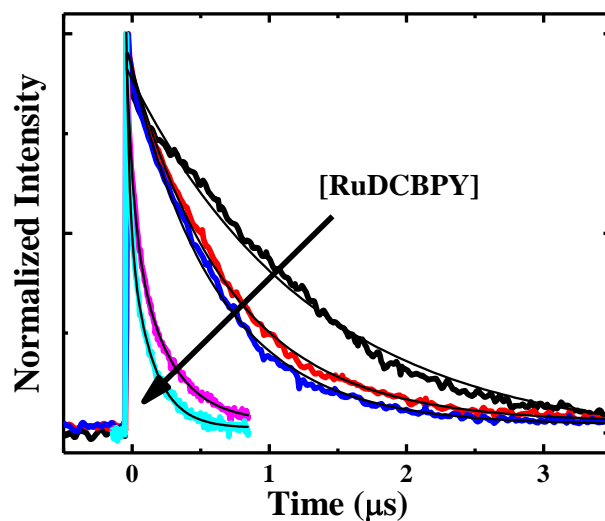
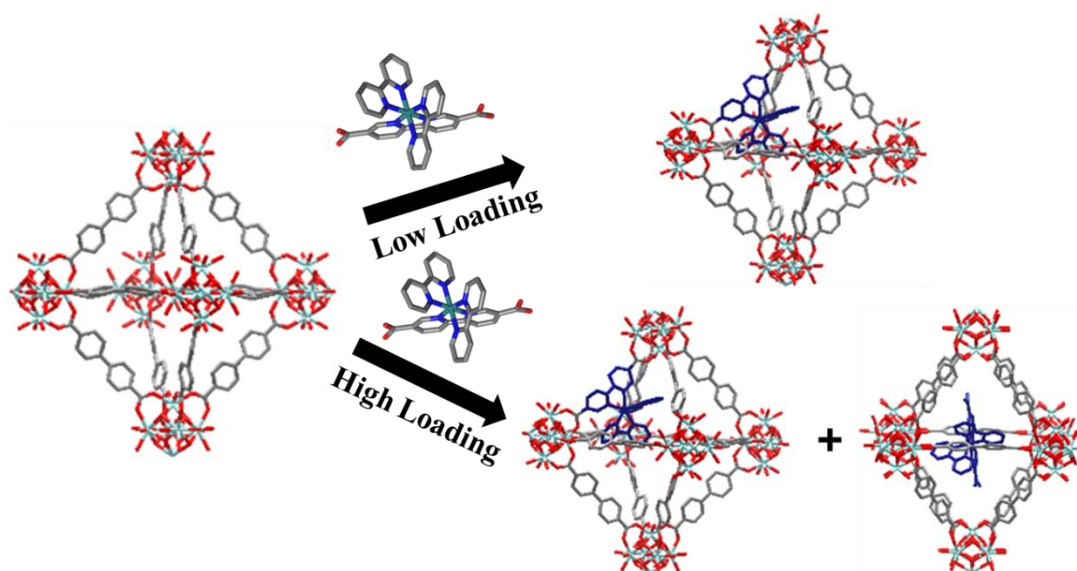
The steady-state diffuse reflectance of the RuDCBPY-UiO-67 powder showed an absorption maximum at 455 nm, which was attributed to a singlet metal-to-ligand charge transfer (¹MLCT) common to $\text{Ru}(\text{bpy})_3^{2+}$ and its derivatives.^{10, 38} This absorption band was observed to broaden with the increase of the loading percentage while the absorption maxima peak remained constant at all doping

concentrations. However, the energy of the emission maxima and excited state lifetimes were found to be quite sensitive to the concentration of RuDCBPY incorporated into UiO-67 (Figure 2.3). At low doping concentrations ($\leq 16.4 \text{ mm}$), the excited state properties of RuDCBPY in the MOF deviate markedly from those in aqueous solution but resemble those in DMF. To be specific, the emission maxima centered around 630 nm, slightly bathochromically shifted relative to RuDCBPY in DMF (625 nm).¹⁰ The emission decay can be adequately modeled using a single discrete exponential decay function with an observed lifetime of 1.4 μs , which is a longer lived excited state compared to RuDCBPY in DMF (890 ns) due to the fact that the chromophore is incorporated into a rigid matrix. Interestingly, at higher doping ($> 16.4 \text{ mm}$), the emission spectra demonstrated a bathochromic shift relative to the low doping materials displaying an emission maximum around 650 nm. The observed emission decays at high loading were biphasic with a concentration-dependent long lifetime component ($\tau \sim 165\text{-}210 \text{ ns}$) and a concentration independent short lifetime component ($\sim 24 \text{ ns}$) resembling the lifetime of RuDCBPY in water ($\sim 38 \text{ ns}$, Table 2.1).

A two-state model was proposed to explain the biphasic nature of the decay at high doping concentration. At low doping concentrations, RuDCBPY was said to preferentially occupy the larger octahedral cages of UiO-67 by incorporation into the backbone of the cage. As a result of residual solvothermal reaction solvent (i.e. DMF) residing in the pore, this population experiences a dimethylformamide (DMF)-like solvation environment. At higher doping concentrations, in addition to the *incorporation* of RuDCBPY into the backbone of the octahedral cavities, populations of *encapsulated* RuDCBPY were proposed to be found in separate octahedral UiO-67 cavities (Figure 2.4). Encapsulation is assumed to restrict the solvent (DMF) occupancy within the pore and the $\mu\text{-O}$ and $\mu\text{-OH}$ bridges of the Zr-nodes were thought to impose a polar water-like dielectric on RuDCBPY so that the solvation environment resembles that of bulk water. The result was emission spectra and lifetimes dominated by photophysical properties arising from a water-like environment. RuDCBPY in water has shorter emission lifetime ($\sim 38 \text{ ns}$) than in DMF, which is mainly due to the sensitivity to solvent (particularly to solution pH) arising from preferred localization of the $^3\text{MLCT}$ on the DCBPY ligand. Detailed studies of the photophysical properties of RuDCBPY have shown that the emission lifetime and quantum yield is not only pH dependent, but also influenced by the position of carboxylic acids in the 2,2'-bipyridine ligand. The lifetime of RuDCBPY decreases with lower pH because of the increased non-radiative decay. For protic chromophores it is well known that the rate of non-radiative decay increases with the oscillator strength of the H-bond, which dissipates the energy. Thus, at low pH (< 5), when dcbpy is protonated, O-H bonds serve as trap sites by increasing the non-radiative decay component of the $^3\text{MLCT}$ lifetime thereby decreasing the emission lifetime and quantum yield.

Table 2.1 Summary of fluorescence data

Sample	doping (mmolal)	Stretched exponential fit					Discrete exponential fit				
		τ (ns)	β	$\langle\tau\rangle$ (ns)	$\langle k\rangle$ (s^{-1})	f_1	τ_1 (ns)	f_2	τ_2 (ns)	$\langle\tau\rangle$ (ns)	$\langle k\rangle$ (s^{-1})
RuDCBPY-UiO67	2.6	--	--	--	--	--	--	1.0	1370 ± 30	1370	7.3×10^5
	6.8	--	--	--	--	--	--	1.0	720 ± 8	720	1.4×10^6
	16.4	--	--	--	--	--	--	1.0	645 ± 6	645	1.6×10^6
	20.6	107 ± 3	0.57 ± 0.01	390	5.8×10^6	0.42 ± 0.01	23 ± 2	0.58 ± 0.01	204 ± 4	121	8.3×10^6
	44.7	48 ± 2	0.53 ± 0.01	228	1.2×10^7	0.52 ± 0.01	24 ± 1	0.48 ± 0.01	168 ± 2	93	1.1×10^7
RuBPY in DMF	--	--	--	--	--	--	1.0	920 ± 10	916	1.1×10^6	
RuDCBPY in water	--	--	--	--	--	--	1.0	38 ± 1	38	2.6×10^7	
RuDCBPY in DMF	--	--	--	--	--	--	1.0	880 ± 10	880	1.1×10^5	

**Figure 2.3** Emission lifetime decays obtained at room temperature of RuDCBPY at various RuDCBPY loading: 3 mm (black), 7 mm (red), 16 mm (blue), 21 mm (pink), and 45 mm (light blue)**Figure 2.4** Two-state model of concentration dependent RuDCBPY doping behavior. Adopted with the permission from Ref. 10. Copyright 2014 American Chemical Society

2.4.2 ³MLCT Quenching Mechanism- Förster Energy Transfer

The concentration dependence of the long lifetime component observed for RuDCBPY-UiO-67 is indicative of a distance dependence on the self-quenching mechanism resulting from the interaction between RuDCBPY ³MLCT states in RuDCBPY-UiO67, either by energy transfer or electron transfer. An electron transfer mechanism was ruled out because it is energetically uphill ($\Delta E^\circ \approx -0.4$ V).^{10, 42} Also, diffusional or collisional quenching is improbable due to the incorporation of RuDCBPY into the framework of UiO-67, which restricts translational motion. Therefore, the large decrease in the RuDCBPY ³MLCT lifetime observed upon increasing the RuDCBPY concentration in RuDCBPY-UiO-67 was attributed to resonance energy transfer (RET). As mentioned in **Section 2**, homo- and heterogeneous energy transfer can occur by Coulombic interactions via an exchange or dipole-dipole reaction. In the dipole-dipole approximation described by Förster for very weak donor-acceptor interactions, the energy transfer rate, k_{RET} , is proportional to the inverse sixth power of the donor-acceptor distance as shown in eq 2. In the exchange mechanism of energy transfer k_{RET} falls off exponentially with respect to r as shown in eq 5. However, the results from fitting the data ruled out the exchange mechanism by following reasons.¹⁰ 1) The donor-acceptor distance at which the probability of RET is 50%, R_0 , is 33 Å, which is uncharacteristically long for an exchange mechanism ($R_0 < 15$ Å). 2) The data could not be adequately modeled by an exponential dependence on the concentration of RuDCBPY (which is proportional to r). Therefore, it is likely that homogeneous-energy transfer between RuDCBPY proceeds according to a dipole-dipole mechanism.



Ideally, depopulation of a ³MLCT on RuDCBPY(1) is coupled to the population of a ³MLCT on RuDCBPY(2) of the same lifetime as described in eq 7 (assuming both reactants RuDCBPY have similar environments so that their photophysical properties are the same). However, the observed decrease of the concentration dependent long lifetime component implied the existence of RuDCBPY trap sites and/or second population as shown in eq 8. Again, as previously described protonated carboxylic acids decrease the lifetime of carboxy-Ru(bpy)₃ derivatives (*vide supra*). Molecules on the surface of the MOF crystallites (and not fully incorporated into the framework) will have dangling –OH group which can serve as non-radiative decay trap states. In the low loading region (≤ 16.4 mm), the RuDCBPY on the surface of MOF with –OH group may act as trap sites. In the high loading region (> 16.4 mm), the emerging population of encapsulated RuDCBPY can also contribute to the decrease of excited state lifetime. Meanwhile, impurities, crystal lattice defects, or the resonant vibrations inherent

to the MOF may also act as energy traps also contributing to the decrease in the emission lifetime. However, the strong correlation between the decrease in excited state lifetime with increased doping concentration offers a strong argument for the dominance of homogeneous RET mechanism.

The emission lifetime data was fit to the Inokuti-Hirayama function, which is a generalized expression describing the effect of the donor emission lifetime (τ_0) on the acceptor concentration (C_A) and a distance dependent empirical term n (eq 9).⁴³

$$I(t) = I(t = 0) \exp \left[-\frac{t}{\tau_0} - \Gamma \left(1 - \frac{3}{n} \right) \left(\frac{C_A}{C_0} \right) \left(\frac{t}{\tau} \right)^{3/n} \right] \quad (9)$$

where⁴³

$$C_0 = \frac{3000}{4\pi N_A R_0^3} \quad (10)$$

$I(t)$ and $I(0)$ are the emission intensity at $t \neq 0$ and $t = 0$, respectively, C_A is the doping concentration, and C_0 is given by eq 10. R_0 is the Förster radius. The distance dependence term, n , takes on the values $n = 6, 8$ and 10 for dipole-dipole, dipole-quadrupole and quadrupole-quadrupole interactions, respectively. When $n = 6$, eq 9 reduces to the familiar form of Förster-type energy transfer, FRET (eq 11):

$$I(t) = I(t = 0) \exp \left[-\frac{t}{\tau_0} - 2 \left(\frac{C_A}{C_0} \right) \left(\frac{t}{\tau} \right)^{1/2} \right] \quad (11)$$

Fitting the decay data for RuDCBPY-UiO-67 at the doping concentration between 3 *mm* and 21 *mm* indicate $n = 3.5 \pm 0.3$ and $C_0 = 0.038 \pm 0.008$ *mm*, which correspond to a R_0 of 22 ± 5 Å based on eq 10. A $1/r^4$ distance dependency on the energy transfer rate suggests a dipole-dipole RET process lying on a continuum between the Perrin weak coupling and Förster very weak coupling regimes, which have been proposed by Kenkre and Knox.⁴⁴ This indicates stronger dipole coupling imparted by framework between the incorporated RuDCBPYs. The incorporated RuDCBPY in the MOF are locked into a specific geometry dictated by the crystal structure of the UiO framework. Such preferential orientation of chromophores enables dipole alignment, stronger dipole-dipole coupling, and longer range energy transfer. Lin and coworkers recently reported Förster energy transport of singlet excitons in two light-harvesting MOFs constructed from truxene derived ligands and zinc nodes.⁴⁵ They found that the usual nearest neighbor step-by-step exciton random hopping model given by DRET theory^{7, 46} was inadequate in describing the singlet energy transfer and exciton migration in the truxene-based MOFs. The migration distances of excitons were up to 43 and 48 nm, respectively. This study supports the

hypothesis that MOF incorporation can lead to long range energy transfer due to the orientation of chromophores within the designed framework.

It is worthy to mention that at high loadings ($> 16.4 \text{ mm}$), the emission decay using stretched exponential functions (also known as the Kohlrausch or Kohlrausch-Williams-Watts decay function) fits were equally good relative to the biexponential fits. The Kohlrausch decay function is expressed as

$$I(t) = A e^{-(t/\tau)^\beta} \quad (12)$$

where τ is the observed lifetime at the maxima of the distribution and β is a parameter related to the width and shape of the distribution and ranges between 0 and 1. Emission decays with a β of 1/2, 3/8 and 3/10 have been attributed to donor luminescence quenching via the dipole-dipole, dipole-quadrupole and quadrupole-quadrupole resonance energy transfer mechanisms, respectively.⁴³ At $\beta = 1$ the distribution becomes a δ -function, and therefore, eq 12 reduces to a discrete exponential.^{26, 47} Fitting the decay data for RuDCBPY-UiO-67 at high loading leads to $\beta = \sim 0.55$, which further confirm our hypothesis about the dipole-dipole resonance energy transfer for RuDCBPY in UiO-67.

2.4.3 Concentration Dependent Dimensionality of RET in Postsynthetically Doped RuDCBPY-UiO-67-DCBPY

To test the proposed two-state model, a post-synthetic approach was used in order to incorporate the transition metal complex directly into the backbone of UiO-67 MOF *in situ*.⁴⁸ First, UiO-67-DCBPY was prepared solvothermally using 2,2'-bipyridine-5,5'-dicarboxylic acid in the place of 4,4'-biphenyldicarboxylic acid, then post synthetically doped with RuDCBPY by incubating the material in an ethanolic solution containing ruthenium(II) bis-(2,2'-bipyridine) dichloride, $\text{Ru}(\text{bpy})_2\text{Cl}_2$. The concentration of RuDCBPY in the framework RuDCBPY-UiO-67-DCBPY can, therefore, be controlled by varying the concentration of $\text{Ru}(\text{bpy})_2\text{Cl}_2$ in the soaking solution (Figure 2.5A). PXRD patterns of UiO-67-DCBPY before and after RuDCBPY doping up to 141 mm indicated no loss of crystallinity of the sample or change in the overall structural morphology of the system. (Figure 2.5B)

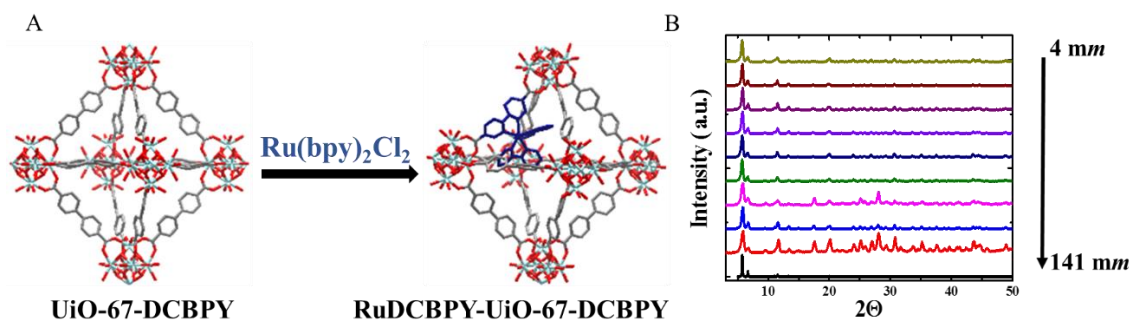
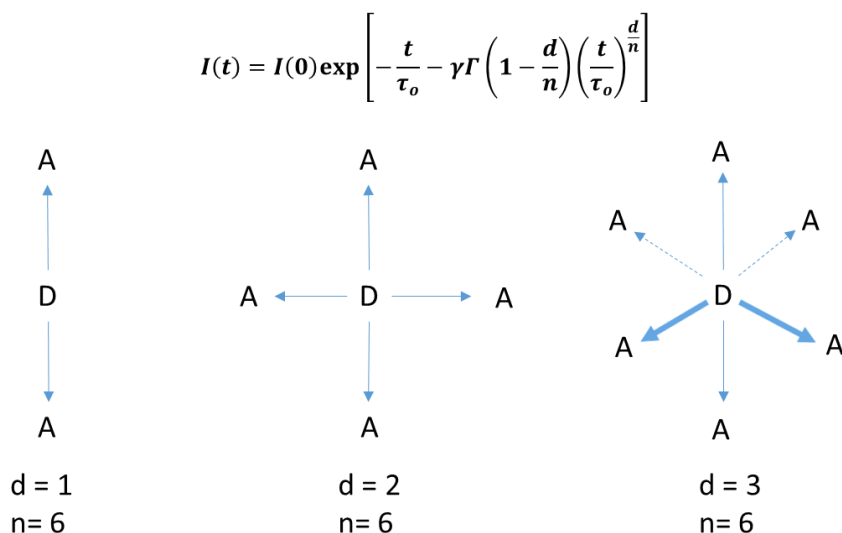


Figure 2.5 A) Schematic synthetic procedure for the post-synthetically approach of RuDCBPY-UiO-67-DCBPY. B) PXRD patterns of RuDCBPY-UiO-67-DCBPY as a function of loading. Adopted with the permission from Ref. 15. Copyright 2015 American Chemical Society.

Steady-state diffuse reflectance and emission spectra of RuDCBPY-UiO-67-DCBPY showed very little difference in the transition energies with increased doping. Diffuse reflectance spectra were found to display an absorption maximum at 450 nm, which is consistent with the ¹MLCT transition of RuDCBPY. The emission spectra display a maximum at ~610 nm, which was attributed to the ³MLCT of RuDCBPY. Emission lifetime decays of the RuDCBPY-UiO-67-DCBPY were observed to be monoexponential and relatively constant regardless of doping concentration. Interestingly, the emission lifetime of RuDCBPY-UiO-67-DCBPY at low doping concentrations (≤ 20 mm) was one magnitude shorter than that observed for RuDCBPY-UiO-67 ($\tau = 1.4$ μ s). While at higher doping concentrations, ³MLCT emission lifetime observed for RuDCBPY-UiO67-DCBPY resemble the slow emission lifetime component for RuDCBPY-UiO-67, with the absence of the fast component. Considering the *in situ* incorporated RuDCBPY presumably only leads to populations of *incorporated* RuDCBPY throughout the material, the previously two-state model of RuDCBPY occupancy in UiO-67 is not applicable; therefore, the data provided legitimacy to the previous two state model assumption (*vide infra*). Similar to RuDCBPY-UiO-67, a decrease in the RuDCBPY ³MLCT lifetime was observed upon the increase of RuDCBPY loading (Table 2.2).

Scheme 2.3 Schematic diagram for RET as predicted by the Klafter and Blumen model in one dimensional, two dimensional and three dimensions.



The emission decays were also fit to the Inokuti–Hirayama function (eq 9). The results obtained for the RuDCBPY-UiO-67-DCBPY samples suggests the r^{-4} distance dependence on the rate of dipole-dipole RET between RuDCBPY centers previously observed with the RuDCBPY-UiO-67 samples. As discussed before, it was argued that the degree of coupling between RuDCBPY centers lie somewhere

between the Perrin weak coupling and Förster very weak coupling regimes. It should be noted that the Inokuti-Hirayama model assumes that the RET interactions between the chromophores are random and uniform through three-dimensional and only apply to three-dimensional RET. For the doped RuDCBPY MOF system, a more generalized approach can be used if the distribution of RuDCBPY as fractal-like. The model suggested by Klafter and Blumen removes the *a priori* assumption that RET is three-dimensional and treats the dimensionality objectively (Scheme 2.3). That is to say, it is possible that the distribution of RuDCBPY in MOF is irregular resulting in isolated regions of densely populated chromophore so that the rate of energy transfer would depend on the fractal dimension \bar{d} , instead of the regular dimension d in Inokuti-Hirayama function. For FRET, the fractal dimension $\bar{d} \approx d$, and the Inokuti-Hirayama function (eq 9) takes the form:

$$I(t) = I(t=0) \exp \left[-\frac{t}{\tau_0} - \gamma \Gamma(1-\beta) \left(\frac{t}{\tau_0} \right)^\beta \right] \quad (13)$$

where

$$\beta = \frac{d}{n}$$

$\Gamma(t)$ is the gamma function

$$\Gamma(t) = \int_0^\infty x^{t-1} e^{-x} dx$$

and

$$\gamma = x_a (d/\bar{d}) V_d R_0^{\bar{d}} \Gamma(1-\beta)$$

In equation 13, n has the same distance dependent meaning as in the Inokuti-Hirayama model in equation 9, d is the regular dimension of the RET interaction, \bar{d} is the fractal dimension, and γ is related to the relative occupancy and positions of the donor and acceptors within the fractal space. V_d is the volume of the donor quenching sphere with dimension d , and x_a is the fraction of populated fractal sites. Equation 13 can be rearranged to a simpler form to yield eq 14

$$\ln \left[\frac{I(t=0)}{I(t)} \right] - \frac{t}{\tau_0} = \gamma \Gamma(1-\beta) \left(\frac{t}{\tau_0} \right)^\beta \quad (14)$$

Table 2.2 Fits of the emission lifetime decays to single exponential functions (τ_{obs}), the Inokuti-Hirayama function (eq 9), and the Klafter and Blumen function (eq 14).⁴⁹

	Loading		Single Exponential	Inokuti-Hirayama		Klafter and Blumen			Φ_{RET}	$r_{n=6}$ (Å) ^a
	(mm)	Ru/Zr ₆ -node	τ_{obs} (ns)	n	τ_0 (ns)	γ	β	$\bar{d}_{n=6}$		
RuDCBPY- UiO-67- DCBPY	1	0.031	126 ± 3	5.30	1665	2.74	0.155	0.93	0.91	22.4
	4	0.076	106 ± 7	4.37	910	2.69	0.119	0.71	0.92	21.7
	8	0.052	120 ± 3	4.92	1189	2.27	0.251	1.50	0.91	22.2
	17	0.164	106 ± 34	5.13	1352	2.44	0.262	1.57	0.92	21.7
	28	0.176	108 ± 16	5.19	1599	2.11	0.340	2.04	0.92	21.8
	52	0.380	70 ± 1	4.17	1736	2.33	0.391	2.35	0.95	20.2
	60	0.452	83 ± 10	4.27	1604	1.74	0.434	2.60	0.94	20.8

	80	0.566	78 ± 2	3.86	1706	1.82	0.380	2.28	0.94	20.6
	141	0.974	97 ± 11	5.58	2360	2.32	0.295	1.77	0.93	21.4
RuDCBPY- UiO-67⁵⁰	2.6	0.070	1370 ± 30	3.78	1722	-	-	-	0.02	62.4
	6.8	0.097	720 ± 8	3.53	1750	0.72	0.652	3.91	0.49	33.3
	16.4	0.160	645 ± 6	3.25	1673	0.94	0.621	3.73	0.54	32.1
	20.6	0.187	204 ± 4	5.46	992	0.94	0.607	3.64	0.85	24.6

^a using $R_0 = 33 \text{ \AA}$.

In this way, one can explicitly determine the dimensional interaction between chromophores under the common resonance coupling regimes, i.e. Dexter ($n = 3$), Förster or dipole-dipole ($n = 6$), dipole-quadrupole ($n = 8$), and quadrupole-quadrupole ($n = 10$). By fitting the RuDCBPY ³MLCT emission lifetime decays to eq 14 (Figure 2.6), it was found that γ was invariant to changes in RuDCBPY doping. In contrast, β increased from $\beta \approx 0.2$ at low RuDCBPY loading to $\beta \approx 0.4$ at higher loading. Neglecting the weaker $n = 8$ and $n = 10$ interactions, for the Förster-type dipole-dipole interaction, where $n = 6$, the dimensional factor d ranges from ~ 1 to 3 with increasing RuDCBPY concentrations. The average intermolecular distance between interacting RuDCBPY centers, r , can be estimated from eq 15,⁵¹

$$\Phi_{\text{RET}} = 1 - \frac{\tau}{\tau_0} = \frac{1}{1 + (r/R_0)^n} \quad (15)$$

Assuming that the distance dependence of k_{RET} is on the order of r^{-6} (Förster energy transfer), r is $21 \pm 0.8 \text{ \AA}$ on average in the concentration range studied where R_0 is $\sim 33 \text{ \AA}$.

The variation of d together with the r values from eq 15 are indicative of a concentration dependence on the dimensionality of RET where at low loading of RuDCBPY ($< 10 \text{ mm}$) RET is one-dimensional, at concentrations between ~ 10 and $\sim 50 \text{ mm}$ the RET was two-dimensional, and at a concentration above which a percolation limit is met the RET is then three-dimensional. (Figure 2.7)

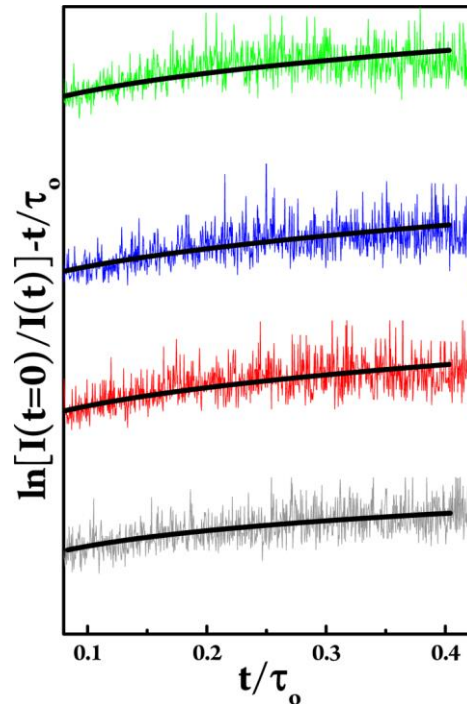


Figure 2.6 Klafter–Blumen plots for RuDCBPY-UiO-67-DCBPY ³MLCT emission lifetime decays at 8 mm (gray), 28 mm (red), 60 mm (blue), and 141 mm (green). The solid black lines represent best fits to the data using eq 14. Reprinted with the permission from Ref. 15. Copyright 2015 American Chemical Society.

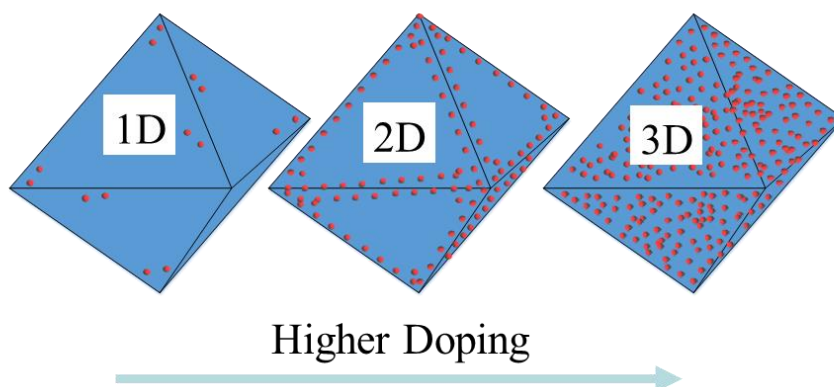


Figure 2.7 A schematic representation of fractal FRET in RuDCBPY-UiO-67-PS observed as a function RuDCBPY loading. Reprinted with the permission from Ref. 15. Copyright 2015 American Chemical Society.

To better understand the relationship between the dimensionality and doping concentration of the post-synthetically doped materials, inspired by Yan et al.'s work on IRMOF-10,⁵² confocal microscopy analysis was performed on RuDCBPY-UiO-67-DCBPY samples doped at 4, 28 and 141 mm. It was expected that the post-synthetic approach would form densely packed RuDCBPY centers at the outer layers of the MOF at low doping concentrations while populating more of the inner layers with increased doping. A three-dimensional rendering of the emission data along the z-axis indicates that the bands of higher emission intensity correspond to regions of increased RuDCBPY density along the edges of the crystal. (Figure 2.8D). Considerably less intensity, however, was observed within the internal bulk of the crystals indicating reduced RuDCBPY population in this region. In addition, the multiple bands observed along the middle of the crystal (along the z-axis) were observed to collapse into a single band corresponding to emission at a crystal vertex. Combining these observations with the fits of the emission lifetime decays, it was argued that a two-dimensional mechanism of FRET dominated the self-quenching reaction of RuDCBPY at low doping concentrations. The diffusion gradients of Ru(bpy)₂ populating the backbone of UiO-67-DCBPY during the post synthetic approach likely originate at the edges and vertices of MOF crystallites either due to the higher density of open channels leading to the interior of the crystal or the presence of higher concentrations of lattice defects in these regions. Once the precursors breach the solvent/crystal barrier, they are then free to diffuse throughout and occupy the interior layers of the MOF crystallites with increased loading, which eventually leads to three-dimensional FRET.

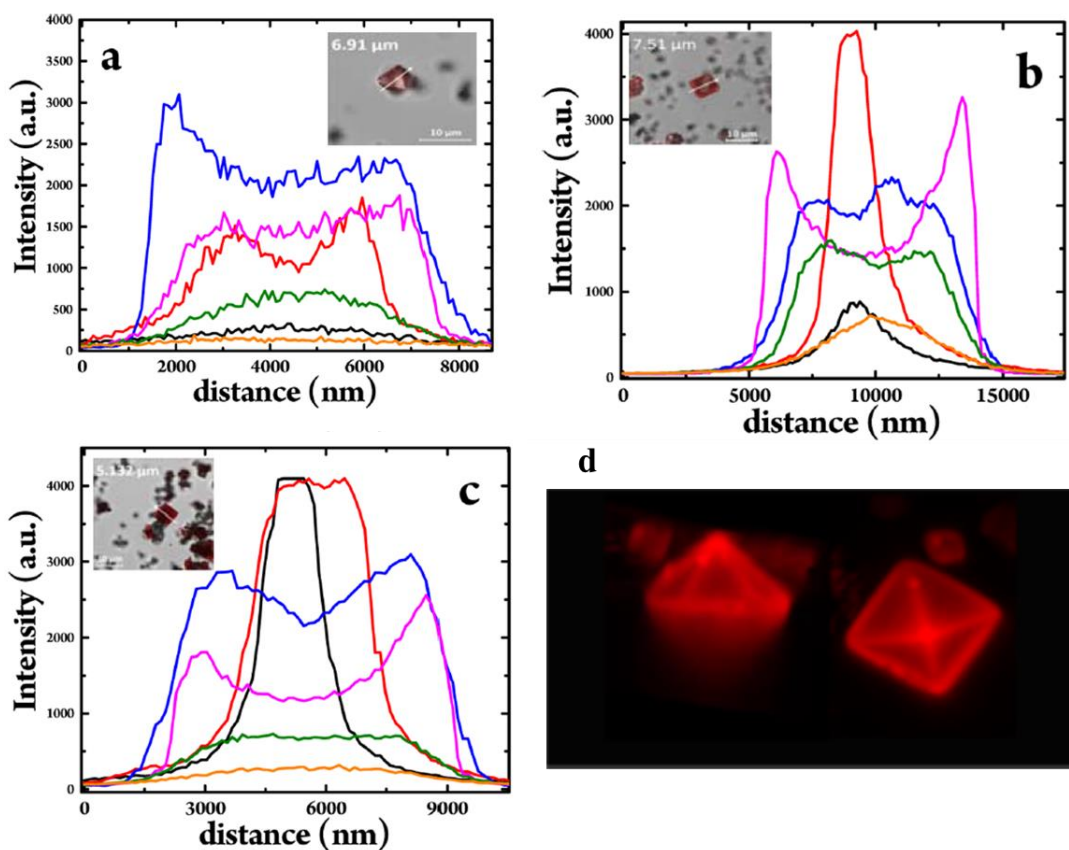


Figure 2.8 Spatial emission intensity profiles obtained by confocal emission microscopy of (a) 4 mm, (b) 28 mm, and (c) 141 mm RuDCBPY-UiO-67-DCBPY samples suspended in water as a function of incident excitation focal point position along the z-axis: (black) $\sim 1\mu\text{m}$, (red) $2\mu\text{m}$, (blue) $4\mu\text{m}$, (pink) $7\mu\text{m}$, (green) $10\mu\text{m}$, and (orange) $13\mu\text{m}$ from $z = 0\mu\text{m}$ position of the z-scan. Insets show the one-dimensional axis (white arrow) along the crystals corresponding to the data shown. (d) Three-dimensional rendering of confocal fluorescence microscopy images taken for single RuDCBPY-UiO-67-DCBPY crystals doped at 28 mm. Reprinted with the permission from Ref. 15. Copyright 2015 American Chemical Society.

2.5 MOFs for Solar Cell Applications

At a fundamental level photoactive MOFs offer novel insights into light harvesting and energy transfer in rigid three-dimensional isotropic solids; at an applied level, their properties may underpin the next generation of artificial photocatalytic and photovoltaic devices. Several different approaches have been investigated for MOFs as active materials in photovoltaic devices. These include the use of MOFs as an electrolyte additive⁵³, as the sensitizer material^{17, 19, 54-55}, as the support material⁵⁶ or as the photoanode material⁵⁷⁻⁵⁹. Nevruzoglu, *et al.* discovered that the use of UiO-67-DCBPY MOFs as a support material could improve the stability of $\text{Cu}_{2-x}\text{S}/\text{CdS}$ PV cells.⁵⁶ The Lewis-basic bipyridine moieties in MOF were exploited as supplementary Cu(I) ion storage sites needed due to a deficiency of Cu(I) ions caused by the diffusion from Cu_{2-x}S to the CdS phase.⁵⁶

Li *et al.* first reported the influence of coating a TiO₂ electrode with MOFs on the performance of DSC.⁵⁹ Taking advantage of the high porous nature of MOF, they successfully used ZIF-8 to increase the dye loading at the TiO₂ surface to improve the open-circuit potential of the PV device. Also, the interfacial MOF layer was thought to suppress the interfacial charge recombination due to its electrical insulating property.⁶⁰ However, the same insulating property could be the most challenging barrier of MOFs for their application as a light-harvesting sensitizer. In order for MOFs to be effective at harvesting and converting solar energy into electricity in PV devices, photo-induced charges must freely migrate within the frameworks to the donor (i.e., MOFs) and acceptor (mostly TiO₂ in DSSCs) interface and then efficiently be injected into the acceptor material.

Recently, it has been demonstrated that thin film of MOFs treated with iodine can be used as sensitizers to harvest solar radiation in TiO₂ based liquid junction solar cells.^{17, 57, 61} Han's group synthesized thin films of a cobalt-based MOF as a light-harvesting absorber in TiO₂-based solar cells by a layer-by-layer liquid epitaxy technique.⁶² They found that the hole doping of MOFs could facilitate the charge transfer across the TiO₂/MOF interface.⁶² Sun and coworkers reported a new class of Zn(II)porphyrin-based surface anchored MOF (SURMOF) thin films with an architecture employing a conductive polymer layer as top electrode to realize the photoelectric conversion.⁵⁵ By attachment of electron-donating groups (diphenylamine, DPA) into the primarily porphyrin-containing MOF skeletal backbone, the MOF thin films strongly enhanced the solar light absorption and generated higher photocurrent.⁵⁵ Similarly, we demonstrated that robust, stable and porous Ru-doped UiO-67 MOFs grown as thin films onto TiO₂-coated conductive surfaces (e.g. fluorine-doped tin oxide, FTO, coated glass slides) could be used as sensitizing materials in photovoltaic applications.⁶³

Fabrication of the photoactive MOFs as thin films on electrode surfaces is an attractive strategy for solar cell applications. As laid out in section 2, there are specific criteria for engineering efficient ET in MOFs. When moving to films, especially for solar cell applications, certain parameters must be considered in addition to chromophore orientation, chromophore to chromophore distance and spectral overlap. First, the thickness of the films should be precisely controlled by the synthetic approach. Second, exciton migration through the MOF thin film should be directional, displaying high efficiency and fast RET rate. Third, the exciton propagation distance should meet or exceed the MOF film thickness in order to maximize the accumulation of excited state energy at either the underlying electrode or external redox phase. Lastly, critical to sensitized solar cell architectures, the pore size of the MOF thin film material should be large enough that the redox mediator can diffuse freely throughout the structure but not too large as to hinder exciton mobility between the exciton pairs.

2.5.1 Photophysical Characterization of RuDCBPY-UiO-67 Thin Film

RuDCBPY-UiO-67 thin films were solvothermally prepared on fluorine-doped tin oxide (FTO) and glass slides.¹¹ Various doping concentrations were achieved by adding a different amount of RuDCBPY in the reaction mixture, similar to the aforementioned powder synthesis. The films were shown to be isostructural with UiO-67 and similarly doped RuDCBPY-UiO-67 powders (Figure 2.9). The photophysical properties of the film show significant line broadening of the diffuse reflectance spectra. Similar to the powders, a successive red shift of the emission maxima, and biphasic kinetics was observed with increased RuDCBPY doping of UiO-67 films above 10 mm. The two-lifetime components were consistent with the dual population of RuDCBPY previously proposed within the UiO-67 material: a population of RuDCBPY incorporated into the framework of UiO-67 replacing a bpdc ligand and a second population of RuDCBPY encapsulated within the octahedral cavities. The RuDCBPY dopant incorporated within the UiO-67 films were said to interact with each other and undergo self-quenching via the same resonance energy transfer mechanism observed in the powdered material. From emission lifetime and RET analysis, it was determined that the average distance between RuDCBPY was decreased in the film relative to similarly doped powders. For example, the average distance between interacting RuDCBPY at a doping concentration of 6.2 mm decreases to ~ 22 Å in the film from ~ 30 Å observed in a similarly loaded powder (doping concentration, 6.8 mm). This was attributed to an electrostatic effect upon formation of the framework due to increased charge at the bpdc self-assembled monolayer at the surface of the substrate.

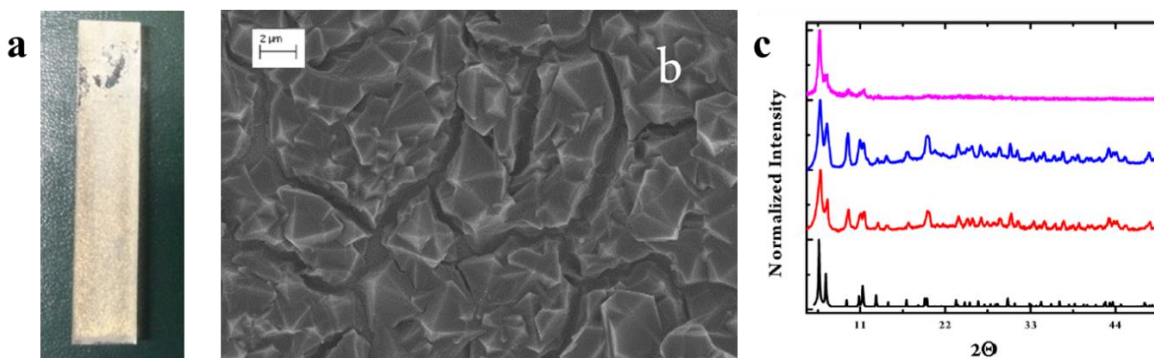


Figure 2.9 a,b) Picture and SEM images of a RuDCBPY-UiO-67 thin film on FTO. c) Experimental GIXD pattern of RuDCBPYUio67/FTO thin film (pink), the PXRD pattern of RuDCBPYUio67/FTO thin film scraped off the FTO substrate (blue), RuDCBPY-UiO67 powder (red), and the predicted pattern of UiO-67 from structural data (black, CCDC No. 889530) for comparison. Adopted with the permission from Ref. 11. Copyright 2014 American Chemical Society.

2.5.2 Light Harvesting for Energy Transfer

Since the RuDCBPY-UiO-67 could be grown on FTO-coated glass substrates without changing its excited state properties or dynamics, a series of RuDCBPY containing zirconium(IV)-based MOF were solvothermally grown as thin films onto TiO₂-coated FTO glass for photovoltaic applications. Two different methods were used to prepare the thin films: a) One-pot synthesis by incubation of ZrCl₄, DCBPY, and Ru(bpy)₂Cl₂ in DMF and heating at 120 °C for 24 h to yield RuDCBPY-UiO67-DCBPY-OP (OP = one pot), and b) post-synthetic modification of a UiO-67-DCBPY film by incubation in an ethanolic solution of Ru(bpy)₂Cl₂ to get RuDCBPY-UiO-67-DCBPY-PS (PS = post-synthetic). As mentioned above, the photophysics of RuDCBPY–UiO-67 thin films grown on FTO were shown to behave similarly to RuDCBPY–UiO-67 powders. A moderate photocurrent response was observed for all of the frameworks tested upon front-side illumination of MOFSCs TiO₂ cells constructed with a tetrabutylammonium iodide (TBAI) and iodine-based electrolyte in CH₃CN and platinum counter electrode (Figure 2.11&2.12). Short circuit current densities (J_{SC}) and open circuit potentials (V_{OC}) were found to range between ~-0.03 mA cm⁻² to ~-0.54 mA cm⁻² and ~-370 mV to ~-520 mV, respectively, leading to maximum observed power conversion efficiencies, η , of 0.125% (Table 2.3). RuDCBPY–UiO67–TiO₂ outperformed (higher J_{SC}, V_{OC} and η) the other constructs tested, while RuDCBPY–UiO67–DCBPY-PS–TiO₂ performed comparatively worse than the unmodified TiO₂ control. This was a strong indication that synthetic procedure has a direct impact on the observed photophysical properties. To be specific, 3D orientation and localization of RuDCBPY centers within the MOFs varied with the synthetic approach, leading to the different performance of MOFSCs.

In the post-synthetic approach, the formation of RuDCBPY centers *in situ* leads to denser population on the outer surface near the MOF-solution interface compared with the MOF-TiO₂ interface. This is mainly due to the inhibited penetration of RuDCBPY into the bulk of the crystalline material. As shown in Figure 2.10, the MOF-TiO₂ interface extends approximately 5 μ m from the underlying FTO electrode and exhibits complete penetration by the MOF crystallites in the mesoporous TiO₂ structure. However, pure MOF material extends beyond this for another ~ 2 μ m. With inefficient diffusion of RuDCBPY into the bulk of the MOF, the greatest population of chromophores is also approximately 2 μ m from the nearest TiO₂ nanoparticle. Therefore, the doped RuDCBPY are beyond the energy hopping/migration distance from the MOF-TiO₂ interface, which leads to the poor power conversion efficiencies (PCE). The observed PCE is less than that for TiO₂ alone, which can be attributed again to the blocking nature of the MOF film. The densely populated outer MOF surface closes off the MOF pores to redox mediator diffusion and limits charge carriers formed at the TiO₂ surface alone upon UV excitation. Although the power conversion efficiencies of the cells prepared here are less than 1%, the MOFSCs outperformed a

monolayer of the same dye on the surface of TiO_2 under the same conditions and, therefore, present a promising platform for photovoltaic applications.

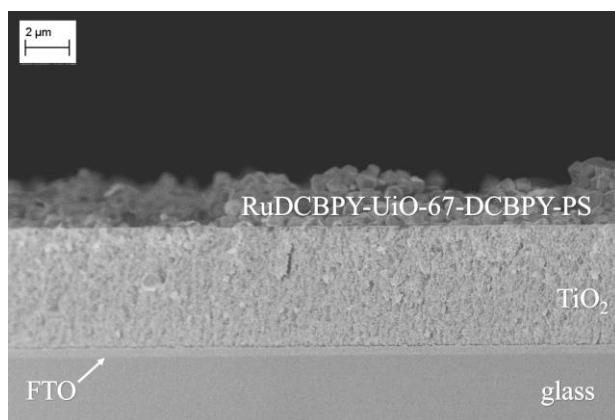


Figure 2.10 Side-on SEM image of a RuDCBPY-UiO-67-PS- TiO_2 assembly, which indicates that the MOF film can extend beyond the TiO_2 film by $\sim 2 \mu\text{m}$. Reprinted with the permission from Ref. 19. Copyright 2016 Royal Society of Chemistry.

Table 2.3 Summary of I-V Results

	J_{sc} (mA/cm^2)	V_{oc} (V)	FF	η (%)	
TiO_2	-0.132 ± 0.001	-0.451 ± 0.010	0.57 ± 0.05	0.034 0.011	\pm
RuDCBPY-UiO-67- TiO_2	-0.446 ± 0.097	-0.480 ± 0.019	0.55 ± 0.04	0.123 0.021	\pm
RuDCBPY-UiO-67-DCBPY-OP- TiO_2	-0.251 ± 0.025	-0.420 ± 0.026	0.44 ± 0.06	0.046 0.005	\pm
RuDCBPY-UiO-67-DCBPY-PS- TiO_2	-0.028 ± 0.005	-0.324 ± 0.035	0.41 ± 0.05	0.004 0.001	\pm

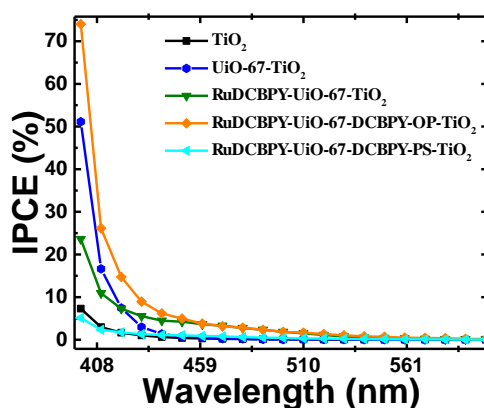


Figure 2.11 A) J-V curves of solar cells constructed with bare unmodified TiO_2 (black), undoped UiO-67- TiO_2 (blue), RuDCBPY-UiO-67- TiO_2 (green), RuDCBPY-UiO-67-DCBPY-OP- TiO_2 (orange) and RuDCBPY-UiO-67-DCBPY-PS- TiO_2 (cyan) in a tetrabutylammonium iodide (TBAI) and iodine-based electrolyte in CH_3CN and platinum counter electrode. B) Incident photon to current conversion

efficiency (IPCE) spectra. Adopted with the permission from Ref.19. Copyright 2016 Royal Society of Chemistry.

As illustrated in Figure 2.12B, there are at least three processes accounting for the observed photocurrent and excited state quenching dynamics upon illumination of the MOF.

1) Charge separation between the UiO-67 MOF backbone and TiO₂. The illumination of undoped UiO-67 with broadband light possibly results in BPDC-localized reactive singlet and/or triplet excited states which undergo charge separation at the MOF/TiO₂ interface. This is energetically plausible and computationally supported.⁶⁴⁻⁶⁵ Modest photocurrent upon one sun illumination of undoped UiO-67 grown on TiO₂ was observed in addition to slightly improved performance over unmodified TiO₂. However, since the contribution of the UiO-67 to the total photocurrent is minimal, with a PCE of ~0.05%, the dynamics of electron injection into TiO₂ by UiO-67 was not explored further.

2) Charge separation between RuDCBPY at or within the energy hopping distance from the MOF-TiO₂ interface and TiO₂. Upon excitation, the observed emission lifetime decays of the Ru-MOF/TiO₂ were fit to a biexponential decay model and showed a slow 100-300 ns phase and a fast 4 ns to 30 ns phase. The fast component of the emission decays (τ'_{obs}) is attributed to the quenching of the RuDCBPY excited states at or within the energy hopping distance (R_{hop}) from the MOF-TiO₂ interface by electron injection from RuDCBPY into TiO₂. The slow component (τ''_{obs}) is ascribed to homogeneous RET occurring within the MOF bulk at distances from the MOF-TiO₂ junction greater than the R_{hop} .

$$(\tau'_{\text{obs}})^{-1} = k_r + k_{\text{nr}} + k_{\text{hop}} \quad (16)$$

$$(\tau''_{\text{obs}})^{-1} = k_r + k_{\text{nr}} + k_{\text{hop}} + k_{\text{inj}} \quad (17)$$

The values from eq 16 for k_{inj} were obtained by assuming the sum of k_r , k_{nr} and k_{hop} were approximately equal to $(\tau'_{\text{obs}})^{-1}$ and are included in Table 2.4. The electron injection efficiency, Φ_{inj} , at the TiO₂-MOF interface is then defined as the product of τ''_{obs} and k_{inj} :

$$\Phi_{\text{inj}} = \tau''_{\text{obs}} k_{\text{inj}} \quad (18)$$

The magnitudes of k_{inj} and Φ_{inj} in Table 2.4 are indicative of strong coupling between RuDCBPY and TiO₂.

3) Energy transfer/hopping within the bulk of the MOF beyond the energy hopping diffusion length from the MOF-TiO₂ interface. The RuDCBPY centers found throughout the bulk of the material undergo homogeneous RET similar to previously discussed RuDCBPY-UiO-67. The average hopping distance, R_{hop} , is related to k_{hop} according to eq 19

$$k_{\text{hop}} = \frac{mD_{\text{RET}}}{R_{\text{hop}}^2} \quad (19)$$

where m is a dimensional factor ($m = 6$ for three-dimensional systems, $m = 4$ for two-dimensional systems, and $m = 2$ for one-dimensional energy hopping) and D_{RET} is the diffusion coefficient for energy migration (taken here to be $2 \times 10^{-6} \text{ cm}^2 \text{ s}^{-1}$ based on the triplet exciton diffusion rate of crystalline $\text{Ru}(\text{bpy})_3$ salts).⁶⁶ The R_{hop} values obtained with respect to 3D energy transfer throughout the films were around 14-25 nm and varied between the synthetic approaches. The average RuDCBPY intermolecular distance, $r \sim 20 \text{ \AA}$, was calculated from the value of R_{hop} and the energy transfer efficiency, Φ_{RET} , according to eq 18. From the results it was found that RuDCBPY centers located within the MOF matrix at distances greater than 25 nm from the MOF-TiO₂ interface could not participate in energy conversion by participating in energy transfer and electron injection into TiO₂. Therefore, in order to design a more efficient device using desired MOF thin film, it is very important to control film thickness that is within the R_{hop} distance ensuring all the incorporated chromophores result in transfer of excited state energy to MOF-TiO₂ interface.

Table 2.4 Summary of energy and electron transfer parameters obtained from photophysical data

	k_{hop} ($\times 10^6 \text{ s}^{-1}$)	k_{inj} ($\times 10^7 \text{ s}^{-1}$)	Φ_{RET}	Φ_{inj}	r (\AA)	R_{hop} (3D, \AA)	R_{hop} (2D, \AA)	R_{hop} (1D, \AA)
RuDCBPY-UiO-67-TiO ₂	1.86	2.59	0.72	0.91	24	254	207	147
RuDCBPY-UiO-67-DCBPY-TiO ₂ -OP	3.81	24.5	0.84	0.98	19	177	145	102
RuDCBPY-UiO-67-DCBPY-TiO ₂ -PS	6.28	6.99	0.89	0.91	16	138	113	80

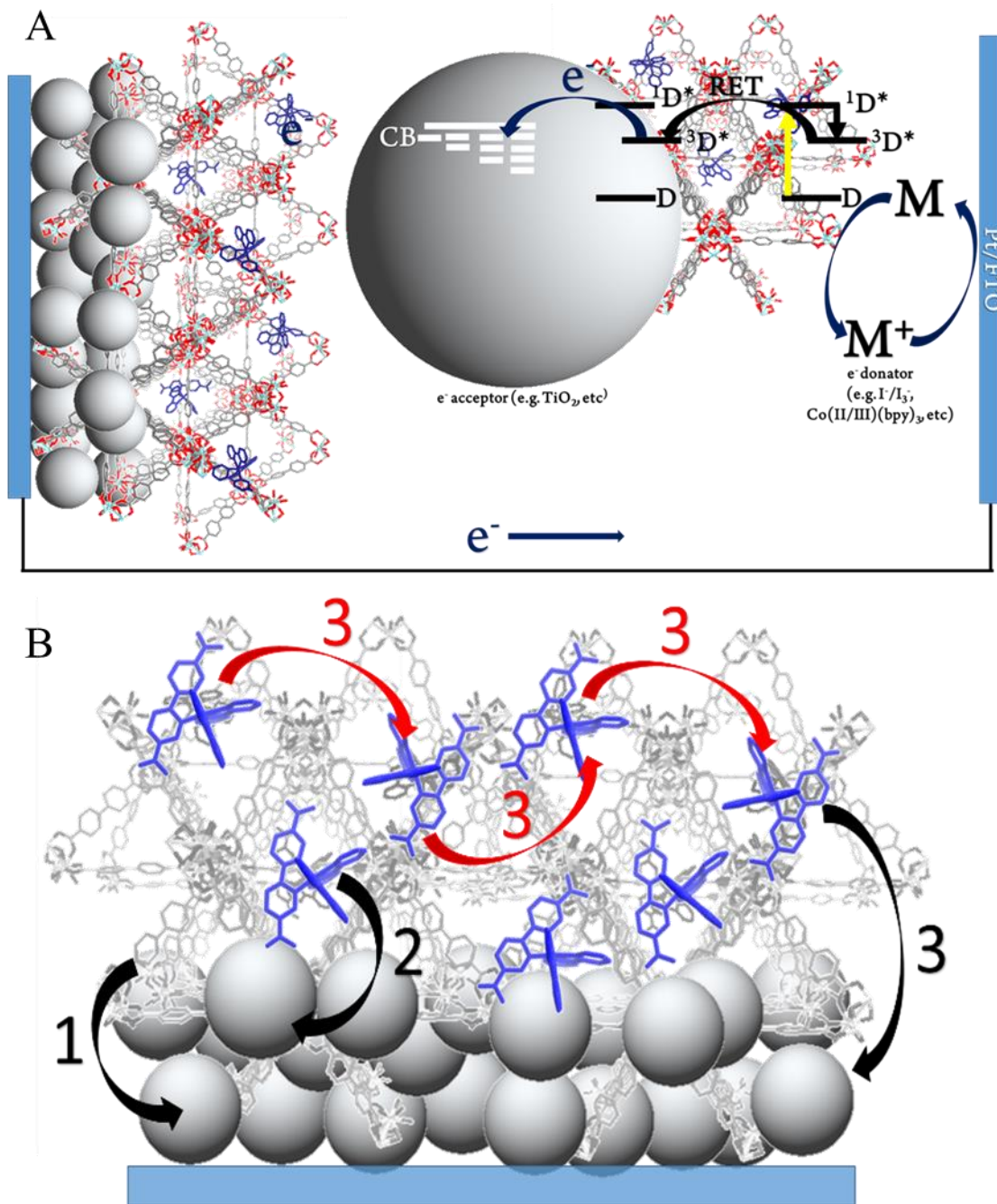


Figure 2.12 A) Ru-MOF sensitized solar cell. B) Potential processes contributing to the observed photocurrent for the RuDCBPY-MOF modified TiO₂ films: black arrows, indicate charge separation steps; red arrows are indicative of energy transfer/hopping. 1) Charge separation between the BPDC or DCBPY MOF ligands and TiO₂. 2) Charge separation between RuDCBPY centers within the MOF lying near or at the MOF/TiO₂ interface and the TiO₂. 3) Non-directional energy transfer/hopping between RuDCBPY centers within the MOF to the interface followed by electron injection into the TiO₂. Reprinted with the permission from Ref. 19. Copyright 2016 Royal Society of Chemistry.

2.6 Summary and Concluding Remarks

MOFs have been increasingly explored as functional materials in the fields of light harvesting, energy transfer, artificial photocatalysis, and photovoltaic devices. The main reason for this interest has

been the highly ordered and robust nature of MOFs providing tunable design, as well as control over the number density of light harvesting centers, and control over the mechanisms of intermolecular energy transfer and charge separation by appropriate design of the constituent MOF ligands. Based on the preliminary work from the Morris group, it has been demonstrated that the excited state behavior of Ru-polypyridyl photosensitizers immobilized in MOF crystalline networks is unique and requires further study. First, MOF incorporation increases the lifetime of RuDCBPY from 880 ns to 1370 ns when compared with RuDCBPY in a homogeneous DMF solution. Increased excited state lifetimes provide more time for exciton hopping events, thus result in longer range RET. Second, the observed $1/r^4$ distance dependence on the energy transfer rate fundamentally leads to longer range ET in MOFs. The cause of the unique distance dependence is not fully understood, but we hypothesize this is due to the orientation of the chromophore dipoles in the MOF and therefore, changes in κ (eq 3). Third, the synthetic approach has shown to have significant influence on RuDCBPY emission lifetime decay behavior. The behavior is proposed to result from the distribution of the chromophores in the framework. When the chromophores are distributed throughout the framework, RET occurs evenly in three-dimensions via an exciton hopping mechanism. However, when the chromophores cluster on the surface of the framework as a consequence of post-synthetic modification, concentration dependent dimensionality to exciton hopping, ranging from 1D at very low chromophore loading to 3D at higher loadings, is observed. In addition, the light harvesting and energy transfer properties exhibited by MOFs, like the RuDDBCPY doped UiO-67 MOF discussed here, lead to promising applications in photovoltaic devices. Although the efficiency of MOF-based devices is still lower than that of the current state-of-art dye-sensitized solar cells, understanding the origin of their limitations should lead to the intelligent design of later generation highly efficient MOFSCs. From our work on MOFSCs, it is clear that the efficiency of light harvesting by photoactive MOF thin films is dependent on the distribution of the chromophores throughout the photoactive layer, as well as the thickness of the photoactive material over electrode surface. Therefore, further study to control these factors will help propel the state-of-the-art into more commercially viable devices. However, some important questions need still be answered. These include 1) the role of MOF crystal-crystal (homogeneous) and MOF crystal-TiO₂ (heterogeneous) grain boundaries play in mitigating cell efficiency, 2) the effect of the “electrolyte” in the energetics and kinetics of energy transfer and electron transfer at the MOF-electrode interface, as well as 3) whether it is possible to design a multi-functional MOF containing electron shuttles or RET “stepping stones” involving complimentary heterogeneous modules resulting in a directional downhill energy cascade. Is it possible to design and produce photoactive MOF films in such a way as to diminish the loss of energy from RET cascade process? Answering these questions will aid in maturing the field of MOF-based

solar cells into a competitive class of photovoltaic devices for a wide range of technologically and industrially relevant applications.

2.7 Acknowledgement

This material is based upon work supported by U.S. Department of Energy, Office of Basic Energy Sciences under Award Number DE-SC0012446.

2.8 Reference

1. Grätzel, M., Photovoltaic and photoelectrochemical conversion of solar energy. *Philosophical Transactions of the Royal Society of London A: Mathematical, Physical and Engineering Sciences* **2007**, *365* (1853), 993-1005.
2. Yaghi, O. M.; O'Keeffe, M.; Ockwig, N. W.; Chae, H. K.; Eddaoudi, M.; Kim, J., Reticular synthesis and the design of new materials. *Nature* **2003**, *423* (6941), 705-714.
3. Zhou, H.-C.; Long, J. R.; Yaghi, O. M., Introduction to Metal–Organic Frameworks. *Chemical Reviews* **2012**, *112* (2), 673-674.
4. Lee, C. Y.; Farha, O. K.; Hong, B. J.; Sarjeant, A. A.; Nguyen, S. T.; Hupp, J. T., Light-Harvesting Metal–Organic Frameworks (MOFs): Efficient Strut-to-Strut Energy Transfer in Bodipy and Porphyrin-Based MOFs. *Journal of the American Chemical Society* **2011**, *133* (40), 15858-15861.
5. Zhang, X.; Ballem, M. A.; Hu, Z. J.; Bergman, P.; Uvdal, K., Nanoscale Light-Harvesting Metal–Organic Frameworks. *Angewandte Chemie International Edition* **2011**, *50* (25), 5729-5733.
6. Yan, D.; Tang, Y.; Lin, H.; Wang, D., Tunable Two-color Luminescence and Host–guest Energy Transfer of Fluorescent Chromophores Encapsulated in Metal–Organic Frameworks. *Scientific Reports* **2014**, *4*, 4337.
7. Kent, C. A.; Mehl, B. P.; Ma, L.; Papanikolas, J. M.; Meyer, T. J.; Lin, W., Energy Transfer Dynamics in Metal–Organic Frameworks. *Journal of the American Chemical Society* **2010**, *132* (37), 12767-12769.
8. So, M. C.; Jin, S.; Son, H.-J.; Wiederrecht, G. P.; Farha, O. K.; Hupp, J. T., Layer-by-Layer Fabrication of Oriented Porous Thin Films Based on Porphyrin-Containing Metal–Organic Frameworks. *Journal of the American Chemical Society* **2013**, *135* (42), 15698-15701.
9. Jin, S.; Son, H.-J.; Farha, O. K.; Wiederrecht, G. P.; Hupp, J. T., Energy Transfer from Quantum Dots to Metal–Organic Frameworks for Enhanced Light Harvesting. *Journal of the American Chemical Society* **2013**, *135* (3), 955-958.
10. Maza, W. A.; Morris, A. J., Photophysical Characterization of a Ruthenium(II) Tris(2,2'-bipyridine)-Doped Zirconium UiO-67 Metal–Organic Framework. *The Journal of Physical Chemistry C* **2014**, *118* (17), 8803-8817.
11. Maza, W. A.; Ahrenholtz, S. R.; Epley, C. C.; Day, C. S.; Morris, A. J., Solvothermal Growth and Photophysical Characterization of a Ruthenium(II) Tris(2,2'-Bipyridine)-Doped Zirconium UiO-67 Metal Organic Framework Thin Film. *The Journal of Physical Chemistry C* **2014**, *118* (26), 14200-14210.
12. Kent, C. A.; Liu, D.; Ito, A.; Zhang, T.; Brennaman, M. K.; Meyer, T. J.; Lin, W., Rapid energy transfer in non-porous metal-organic frameworks with caged Ru(bpy)₃²⁺ chromophores: oxygen trapping and luminescence quenching. *Journal of Materials Chemistry A* **2013**, *1* (47), 14982-14989.
13. So, M. C.; Wiederrecht, G. P.; Mondloch, J. E.; Hupp, J. T.; Farha, O. K., Metal-organic framework materials for light-harvesting and energy transfer. *Chemical Communications* **2015**, *51* (17), 3501-3510.
14. Wang, C.; Xie, Z.; deKrafft, K. E.; Lin, W., Doping Metal–Organic Frameworks for Water Oxidation, Carbon Dioxide Reduction, and Organic Photocatalysis. *Journal of the American Chemical Society* **2011**, *133* (34), 13445-13454.
15. Maza, W. A.; Padilla, R.; Morris, A. J., Concentration dependent dimensionality of resonance energy transfer in a postsynthetically doped morphologically homologous analogue of uiO-67 mof with a ruthenium (ii) polypyridyl complex. *Journal of the American Chemical Society* **2015**, *137* (25), 8161-8168.
16. Joyce, J. T.; Laffir, F. R.; Silien, C., Layer-by-Layer Growth and Photocurrent Generation in Metal–Organic Coordination Films. *The Journal of Physical Chemistry C* **2013**, *117* (24), 12502-12509.

17. Lee, D. Y.; Shinde, D. V.; Yoon, S. J.; Cho, K. N.; Lee, W.; Shrestha, N. K.; Han, S.-H., Cu-Based Metal–Organic Frameworks for Photovoltaic Application. *The Journal of Physical Chemistry C* **2014**, *118* (30), 16328-16334.
18. Zhang, T.; Lin, W., Metal-organic frameworks for artificial photosynthesis and photocatalysis. *Chemical Society Reviews* **2014**, *43* (16), 5982-5993.
19. Maza, W. A.; Haring, A. J.; Ahrenholtz, S. R.; Epley, C. C.; Lin, S. Y.; Morris, A. J., Ruthenium(ii)-polypyridyl zirconium(iv) metal-organic frameworks as a new class of sensitized solar cells. *Chemical Science* **2016**, *7* (1), 719-727.
20. Forster, T., *Zwischenmolekulare Energiewanderung Und Fluoreszenz. *Ann Phys-Berlin* **1948**, *2* (1-2), 55-75.
21. Forster, T., 10th Spiers Memorial Lecture - Transfer Mechanisms of Electronic Excitation. *Discuss Faraday Soc* **1959**, (27), 7-17.
22. Gadella, T. W. J., *FRET and FLIM techniques*. 1st ed.; Elsevier: Amsterdam ; Boston, 2009; p xxiii, 534 p., 44 p. of plates.
23. Valeur, B., *Molecular fluorescence : principles and applications*. Wiley-VCH: Weinheim ; New York, 2002; p xiv, 387 p.
24. Jameson, D. M.; Croney, J. C.; Moens, P. D. J., Fluorescence: Basic concepts, practical aspects, and some anecdotes. *Method Enzymol* **2003**, *360*, 1-43.
25. Williams, D. E.; Shustova, N. B., Metal–Organic Frameworks as a Versatile Tool To Study and Model Energy Transfer Processes. *Chemistry – A European Journal* **2015**, *21* (44), 15474-15479.
26. Valeur, B.; Berberan-Santos, M. N., *Molecular fluorescence: principles and applications*. John Wiley & Sons: 2012.
27. Dexter, D. L., A theory of sensitized luminescence in solids. *The Journal of Chemical Physics* **1953**, *21* (5), 836-850.
28. Deria, P.; Yu, J.; Balaraman, R. P.; Mashni, J.; White, S. N., Topology-dependent emissive properties of zirconium-based porphyrin MOFs. *Chemical Communications* **2016**, *52* (88), 13031-13034.
29. Goswami, S.; Ma, L.; Martinson, A. B. F.; Wasielewski, M. R.; Farha, O. K.; Hupp, J. T., Toward Metal–Organic Framework-Based Solar Cells: Enhancing Directional Exciton Transport by Collapsing Three-Dimensional Film Structures. *ACS Applied Materials & Interfaces* **2016**, *8* (45), 30863-30870.
30. Whittington, C. L.; Wojtas, L.; Gao, W.-Y.; Ma, S.; Larsen, R. W., A new photoactive Ru(ii)tris(2,2[prime or minute]-bipyridine) templated Zn(ii) benzene-1,4-dicarboxylate metal organic framework: structure and photophysical properties. *Dalton Transactions* **2015**, *44* (12), 5331-5337.
31. Kent, C. A.; Liu, D.; Meyer, T. J.; Lin, W., Amplified luminescence quenching of phosphorescent metal–organic frameworks. *Journal of the American Chemical Society* **2012**, *134* (9), 3991-3994.
32. Balzani, V.; Juris, A., Photochemistry and photophysics of Ru(II)□polypyridine complexes in the Bologna group. From early studies to recent developments. *Coordination Chemistry Reviews* **2001**, *211* (1), 97-115.
33. Thompson, D. W.; Ito, A.; Meyer, T. J., [Ru (bpy) 3] 2+* and other remarkable metal-to-ligand charge transfer (MLCT) excited states. *Pure and Applied Chemistry* **2013**, *85* (7), 1257-1305.
34. Cavka, J. H.; Jakobsen, S.; Olsbye, U.; Guillou, N.; Lamberti, C.; Bordiga, S.; Lillerud, K. P., A New Zirconium Inorganic Building Brick Forming Metal Organic Frameworks with Exceptional Stability. *Journal of the American Chemical Society* **2008**, *130* (42), 13850-13851.
35. Katz, M. J.; Brown, Z. J.; Colon, Y. J.; Siu, P. W.; Scheidt, K. A.; Snurr, R. Q.; Hupp, J. T.; Farha, O. K., A facile synthesis of UiO-66, UiO-67 and their derivatives. *Chemical Communications* **2013**, *49* (82), 9449-9451.
36. Bon, V.; Senkowska, I.; Weiss, M. S.; Kaskel, S., Tailoring of network dimensionality and porosity adjustment in Zr- and Hf-based MOFs. *CrystEngComm* **2013**, *15* (45), 9572-9577.
37. Chavan, S.; Vitillo, J. G.; Gianolio, D.; Zavorotynska, O.; Civalieri, B.; Jakobsen, S.; Nilsen, M. H.; Valenzano, L.; Lamberti, C.; Lillerud, K. P.; Bordiga, S., H2storage in isostructural UiO-67 and UiO-66 MOFs. *Physical Chemistry Chemical Physics* **2012**, *14* (5), 1614-1626.
38. Meyer, T. J., Photochemistry of metal coordination complexes: metal to ligand charge transfer excited states. In *Pure and Applied Chemistry*, 1986; Vol. 58, p 1193.
39. Barrett, S. M.; Wang, C.; Lin, W., Oxygen sensing via phosphorescence quenching of doped metal-organic frameworks. *Journal of Materials Chemistry* **2012**, *22* (20), 10329-10334.

40. Larsen, R. W.; Wojtas, L., Photoinduced inter-cavity electron transfer between Ru(II)tris(2,2'-bipyridine) and Co(II) tris(2,2'-bipyridine) Co-encapsulated within a Zn(II)-trimesic acid metal organic framework. *Journal of Materials Chemistry A* **2013**, *1* (45), 14133-14139.
41. Yang, Q.; Guillermin, V.; Ragon, F.; Wiersum, A. D.; Llewellyn, P. L.; Zhong, C.; Devic, T.; Serre, C.; Maurin, G., CH₄ storage and CO₂ capture in highly porous zirconium oxide based metal-organic frameworks. *Chemical Communications* **2012**, *48* (79), 9831-9833.
42. Creutz, C.; Chou, M.; Netzel, T. L.; Okumura, M.; Sutin, N., Lifetimes, spectra, and quenching of the excited states of polypyridine complexes of iron(II), ruthenium(II), and osmium(II). *Journal of the American Chemical Society* **1980**, *102* (4), 1309-1319.
43. Inokuti, M.; Hirayama, F., Influence of Energy Transfer by the Exchange Mechanism on Donor Luminescence. *The Journal of Chemical Physics* **1965**, *43* (6), 1978-1989.
44. Kenkre, V. M.; Knox, R. S., Theory of Fast and Slow Excitation Transfer Rates. *Physical Review Letters* **1974**, *33* (14), 803-806.
45. Zhang, Q.; Zhang, C.; Cao, L.; Wang, Z.; An, B.; Lin, Z.; Huang, R.; Zhang, Z.; Wang, C.; Lin, W., Förster Energy Transport in Metal–Organic Frameworks Is Beyond Step-by-Step Hopping. *Journal of the American Chemical Society* **2016**, *138* (16), 5308-5315.
46. Son, H.-J.; Jin, S.; Patwardhan, S.; Wezenberg, S. J.; Jeong, N. C.; So, M.; Wilmer, C. E.; Sarjeant, A. A.; Schatz, G. C.; Snurr, R. Q.; Farha, O. K.; Wiederrecht, G. P.; Hupp, J. T., Light-Harvesting and Ultrafast Energy Migration in Porphyrin-Based Metal–Organic Frameworks. *Journal of the American Chemical Society* **2013**, *135* (2), 862-869.
47. Berberan-Santos, M. N.; Bodunov, E. N.; Valeur, B., Mathematical functions for the analysis of luminescence decays with underlying distributions 1. Kohlrausch decay function (stretched exponential). *Chemical Physics* **2005**, *315* (1–2), 171-182.
48. Maza, W. A.; Padilla, R.; Morris, A. J., Concentration Dependent Dimensionality of Resonance Energy Transfer in a Postsynthetically Doped Morphologically Homologous Analogue of UiO-67 MOF with a Ruthenium(II) Polypyridyl Complex. *Journal of the American Chemical Society* **2015**, *137* (25), 8161-8168.
49. Klafter, J.; Blumen, A., Fractal behavior in trapping and reaction. *The Journal of Chemical Physics* **1984**, *80* (2), 875-877.
50. Maza, W. A.; Morris, A. J., Photophysical Characterization of a Ruthenium (II) Tris (2, 2'-bipyridine)-Doped Zirconium UiO-67 Metal–Organic Framework. *The Journal of Physical Chemistry C* **2014**, *118* (17), 8803-8817.
51. Yun, C. S.; Javier, A.; Jennings, T.; Fisher, M.; Hira, S.; Peterson, S.; Hopkins, B.; Reich, N. O.; Strouse, G. F., Nanometal Surface Energy Transfer in Optical Rulers, Breaking the FRET Barrier. *Journal of the American Chemical Society* **2005**, *127* (9), 3115-3119.
52. Tang, Y.; He, W.; Lu, Y.; Fielden, J.; Xiang, X.; Yan, D., Assembly of Ruthenium-Based Complex into Metal–Organic Framework with Tunable Area-Selected Luminescence and Enhanced Photon-to-Electron Conversion Efficiency. *The Journal of Physical Chemistry C* **2014**, *118* (44), 25365-25373.
53. Bella, F.; Bongiovanni, R.; Kumar, R. S.; Kulandainathan, M. A.; Stephan, A. M., Light cured networks containing metal organic frameworks as efficient and durable polymer electrolytes for dye-sensitized solar cells. *Journal of Materials Chemistry A* **2013**, *1* (32), 9033-9036.
54. Lee, D. Y.; Kim, E.-K.; Shin, C. Y.; Shinde, D. V.; Lee, W.; Shrestha, N. K.; Lee, J. K.; Han, S.-H., Layer-by-layer deposition and photovoltaic property of Ru-based metal-organic frameworks. *RSC Advances* **2014**, *4* (23), 12037-12042.
55. Liu, J.; Zhou, W.; Liu, J.; Fujimori, Y.; Higashino, T.; Imahori, H.; Jiang, X.; Zhao, J.; Sakurai, T.; Hattori, Y.; Matsuda, W.; Seki, S.; Garlapati, S. K.; Dasgupta, S.; Redel, E.; Sun, L.; Woll, C., A new class of epitaxial porphyrin metal-organic framework thin films with extremely high photocarrier generation efficiency: promising materials for all-solid-state solar cells. *Journal of Materials Chemistry A* **2016**.
56. Nevruzoglu, V.; Demir, S.; Karaca, G.; Tomakin, M.; Bilgin, N.; Yilmaz, F., Improving the stability of solar cells using metal–organic frameworks. *Journal of Materials Chemistry A* **2016**, *4* (20), 7930-7935.
57. Lopez, H. A.; Dhakshinamoorthy, A.; Ferrer, B.; Atienzar, P.; Alvaro, M.; Garcia, H., Photochemical Response of Commercial MOFs: Al₂(BDC)₃ and Its Use As Active Material in Photovoltaic Devices. *The Journal of Physical Chemistry C* **2011**, *115* (45), 22200-22206.
58. Kundu, T.; Sahoo, S. C.; Banerjee, R., Solid-State Thermolysis of Anion Induced Metal–Organic Frameworks to ZnO Microparticles with Predefined Morphologies: Facile Synthesis and Solar Cell Studies. *Crystal Growth & Design* **2012**, *12* (5), 2572-2578.

59. Li, Y.; Pang, A.; Wang, C.; Wei, M., Metal-organic frameworks: promising materials for improving the open circuit voltage of dye-sensitized solar cells. *Journal of Materials Chemistry* **2011**, *21* (43), 17259-17264.
60. Li, Y.; Chen, C.; Sun, X.; Dou, J.; Wei, M., Metal–Organic Frameworks at Interfaces in Dye-Sensitized Solar Cells. *ChemSusChem* **2014**, *7* (9), 2469-2472.
61. Liu, J.; Zhou, W.; Liu, J.; Howard, I.; Kilibarda, G.; Schlabach, S.; Couprie, D.; Addicoat, M.; Yoneda, S.; Tsutsui, Y.; Sakurai, T.; Seki, S.; Wang, Z.; Lindemann, P.; Redel, E.; Heine, T.; Wöll, C., Photoinduced Charge-Carrier Generation in Epitaxial MOF Thin Films: High Efficiency as a Result of an Indirect Electronic Band Gap? *Angewandte Chemie International Edition* **2015**, *54* (25), 7441-7445.
62. Lee, D. Y.; Lim, I.; Shin, C. Y.; Patil, S. A.; Lee, W.; Shrestha, N. K.; Lee, J. K.; Han, S.-H., Facile interfacial charge transfer across hole doped cobalt-based MOFs/TiO₂ nano-hybrids making MOFs light harvesting active layers in solar cells. *Journal of Materials Chemistry A* **2015**, *3* (45), 22669-22676.
63. Li, L.-L.; Diau, E. W.-G., Porphyrin-sensitized solar cells. *Chemical Society Reviews* **2013**, *42* (1), 291-304.
64. Flage–Larsen, E.; Røyset, A.; Cavka, J. H.; Thorshaug, K., Band Gap Modulations in UiO Metal–Organic Frameworks. *The Journal of Physical Chemistry C* **2013**, *117* (40), 20610-20616.
65. Yang, L.-M.; Ganz, E.; Svelle, S.; Tilset, M., Computational exploration of newly synthesized zirconium metal-organic frameworks UiO-66, -67, -68 and analogues. *Journal of Materials Chemistry C* **2014**, *2* (34), 7111-7125.
66. Ikeda, N.; Yoshimura, A.; Tsushima, M.; Ohno, T., Hopping and Annihilation of 3MLCT in the Crystalline Solid of [Ru(bpy)₃]X₂ (X = Cl⁻, ClO₄⁻ and PF₆⁻). *The Journal of Physical Chemistry A* **2000**, *104* (26), 6158-6164.

Chapter 3 A New Class of Metal-Cyclam based Zirconium Metal-Organic Frameworks for CO₂ Adsorption and Chemical Fixation

This chapter has been adapted from a published manuscript by [Zhu, J.](#); Usov, P. M.; Xu, W.; Celis-Salazar, P. J.; Lin, S.; Kessinger, M. C.; Landaverde-Alvarado, C.; Cai, M.; May, A. M.; Slebodnick, C.; Zhu, D.; Senanayake, S. D.; and Morris, A. J., from the following reference: *Journal of the American Chemical Society* **2017**. Reprinted with permission from the American Chemistry Society copyright © 2017.

3.1 Abstract

Metal-organic frameworks (MOFs) have shown great promise in catalysis mainly due to their high content of active centers, large internal surface areas, tunable pore size and versatile chemical functionalities. However, it is a challenge to rationally design and construct MOFs that can serve as highly stable and reusable heterogeneous catalysts. Here two new robust 3D porous metal-cyclam based zirconium MOFs, denoted VPI-100 (Cu) and VPI-100 (Ni), have been prepared by a modulated synthetic strategy. The frameworks are assembled by eight-connected Zr₆ clusters and metallocyclams as organic linkers. Importantly, the cyclam core has accessible axial coordination sites for guest interactions and maintains the electronic properties exhibited by the parent cyclam ring. The VPI-100 MOFs exhibit excellent chemical stability in various organic and aqueous solvents over a wide pH range, and show high CO₂ uptake capacity (up to ~9.83 % wt. adsorption at 273 K under 1 atm). Moreover, VPI-100 MOFs demonstrate one of the highest reported catalytic activity (TOF and conversion efficiency) among Zr-based MOFs for the chemical fixation of CO₂ with epoxides, including sterically hindered epoxides. The MOFs, which bear dual catalytic sites (Zr and Cu/Ni), enable chemistry not possible with the cyclam ligand under the same conditions and can be used as recoverable stable heterogeneous catalyst without losing performance.

3.2 Introduction

Metal-organic frameworks (MOFs), also referred to as multidimensional porous coordination polymers, are constructed from metal ions/clusters and organic linkers,¹⁻² and have wide-ranging applications, including gas storage and separation,³⁻⁵ sensing,⁶⁻⁷ drug delivery,⁸ and catalysis.⁹⁻¹² The extraordinary scope of available organic and inorganic components enables fine tuning of MOF structures and chemical properties, demonstrating the beauty of rational framework design via crystal engineering.¹³ The porous, highly ordered nature of these structures provides a unique platform to extend their applications as multifunctional hybrid materials.¹⁴⁻¹⁵ Generally, there are two strategies for

introducing the functional moieties into MOFs – design of an appropriate ligand or post-synthetic modification of existing frameworks.¹⁶

One of the highly desired MOF functionalities is organic linkers that can serve as secondary coordination sites for additional metal ions that do not directly construct the framework. Such metalloligands can support coordinatively unsaturated metal centers and endue the resultant MOF with unique set of reactivities difficult to attain otherwise. Cyclam (1,4,8,11-tetraazacyclotetradecane) is a 14-membered tetraamine macrocyclic ligand with rich coordination chemistry.¹⁷ This molecule features four secondary amine groups, which are capable of chelating various transition metal cations in a tetradentate fashion (*cis* or *trans*).¹⁸ The metal axial coordination sites can then bind different molecules and facilitate chemical or electrochemical transformations.¹⁹ For example, [Ni(cyclam)]²⁺ has been shown to be a low-cost, highly selective CO₂ electroreduction catalyst.²⁰⁻²² [Co(cyclam)]³⁺, on the other hand, can act as a photocatalyst for CO₂ reduction.²³⁻²⁴ Both complexes are promising candidates for CO₂ utilization applications.²⁵ *trans*-[Cr(cyclam)-(ONO)₂]⁺ is a known precursor complex for light-induced NO release, making it useful in many therapeutic areas.²⁶⁻²⁷ Motivated by the favorable properties of cyclam derivatives and their metal complexes, incorporation of these moieties into MOF structures has been explored in the literature.²⁸⁻³⁰ Cyclam containing MOFs have the potential to combine the unique reactivity described above with the high porosity and stability of MOFs in heterogeneous systems.

In order to tap the great potential held by cyclam-MOFs, two synthetic challenges must first be addressed. 1) MOF structures with open axial coordination sites must be developed. Thus far in reported cyclam-based MOFs, the core metal participated in the structural backbone of the framework, consequently precluding guest binding and subsequent metal-mediated reactivity.³¹⁻³⁴ 2) The synthetic modification of the parent cyclam molecule to incorporate MOF binding groups (carboxylic acids) must not electronically deactivate the compound. A common strategy is to bind the carboxylic groups to the coordinating amines. Such modification can reduce activity by altering the electron density on the central metal. Indeed, such a strategy has been used to incorporate a related macrocycle, cyclen, into MOFs.³⁵⁻³⁶ In this work, we address the challenges by, first, chemically modifying the cyclam periphery at the 6 and 13 positions. Such modification allows the cyclam to serve as a linear linker, while minimizing the electronic effects on the metal-tetraamine core. Second, the carboxylic acid substituents utilized are minimally flexible, which restricts the ability for the groups to interact with the metallic core of the same cyclam, as is commonly seen in reported structures.³¹⁻³⁴ Inspired by the outstanding chemical and thermal stability of Zr(IV)-based MOFs,³⁷⁻⁴¹ Zr(IV) is used in the construction of the metal nodes for the cyclam based MOFs.

By combining the versatility of metallocyclam motif with the durability of Zr-carboxylate structures, we report two new porous metal-cyclam based zirconium MOFs, $[\text{Zr}_6(\mu_3\text{-OH})_8(\text{OH})_8(\text{M-L})_4]$, where M = Cu(II) or Ni(II), L = 6,13-dicarboxy-1,4,8,11-tetraazacyclotetradecan, denoted as VPI-100 (Cu) and VPI-100 (Ni) (VPI = Virginia Polytechnic Institute), respectively. To the best of our knowledge, this is the first report of metal-cyclam based Zr-MOF, which exhibits extraordinary stability and promising catalytic activity. Unlike previously reported frameworks^{29-30, 42-43} featuring similar tetraamine linkers, the axial positions of metallocyclam are occupied by labile chloride ligands. The chloride ligands are readily displaced by the desired guest molecules without compromising the structural integrity of the material. This study undertakes a model approach for designing atomically precise Zr-based MOF with non-aromatic macrocyclic ligands, and opens a new window for the further development of metal-metallocyclam frameworks and their unique functionalities. This framework family could potentially feature a wide range of analogues, similar to the extensively studied metal-metalloporphyrin frameworks.⁴⁴

3.3 Experimental Section

3.3.1 Materials and methods. All chemicals were purchased from commercial sources and used without further purification unless otherwise mentioned. *Caution!* The perchlorate salts described are potentially explosive and should be handled with care and prepared in small quantities.

3.3.2 Synthesis of 6,13-dicarboxy-1,4,8,11-tetraazacyclotetradecan)-copper (II) perchlorate $[\text{CuL}(\text{ClO}_4)_2]$ (1). The Cu-based cyclam ligand $[\text{CuL}(\text{ClO}_4)_2]$ (1) was synthesized according to a literature procedure.⁴⁵ In a typical synthesis, the tetracarboxylate precursor $[\text{Cu}(\text{tetacH}_4)](\text{ClO}_4)_2$ (630 mg, 0.99 mmol) was added to 10 mL of 0.1 M HClO_4 solution and heated at reflux for 1 h. After the reaction mixture cooled down to room temperature (R.T.), 3 mL of 60 % HClO_4 was added and the solution refrigerated overnight. The product was filtered off as red crystalline solid (0.38 g, 46 % yield). The phase purity of (1) was verified by powder X-ray diffraction (PXRD).

3.3.3 Synthesis of 6,13-dicarboxy-1,4,8,11-tetraazacyclotetradecan (L) (2). The free-base ligand (2) was prepared by the demetallation of (1). The copper was removed by refluxing $[\text{CuL}(\text{ClO}_4)_2]$ (0.32 g, 0.58 mmol) in 20 mL of 37 % HCl for 1 h. The resultant white solid was filtered and washed with ethanol. After drying under vacuum, white powder (0.16 g, 95 % yield) was obtained. (ESI-MS: $[\text{M-H}]^+$ $m/z = 289.19$, $^1\text{H NMR}$, $^{13}\text{C NMR}$ and HSQC are shown in Figure S1, S2 and S3, respectively)

3.3.4 Synthesis of 6,13-dicarboxy-1,4,8,11-tetrazacyclotetradecan)-nickel (II) perchlorate $[\text{NiL}(\text{ClO}_4)_2] \cdot 2\text{H}_2\text{O}$ (3). The Ni based cyclam ligand $[\text{NiL}(\text{ClO}_4)_2] \cdot 2\text{H}_2\text{O}$ (3) was synthesized under solvothermal conditions. In a 20 mL vial, $\text{NiCl}_2 \cdot 6\text{H}_2\text{O}$ (70 mg, 0.295 mmol) and **L** (70 mg, 0.242 mmol) were dissolved in 5 mL H_2O with addition of 0.02 g NaOH (0.5 mmol). The vial was heated in a 100 °C oven for 6 h. After cooling to R.T., 2 mL of 60 % HClO_4 was added and the solution refrigerated overnight. The product was filtered off as orange crystalline solid: (38 mg, 26.9% yield). The phase purity of (3) was verified by PXRD.

3.3.5 Synthesis of VPI-100 (Cu). In an 8 mL vial, ZrCl_4 (14 mg, 0.06 mmol) was dissolved in 4 mL of dry DMF with 0.44 mL (200 eq.) of formic acid. The vial was heated in an 80 °C oven for 1 h. After cooling to R.T., $[\text{CuL}(\text{ClO}_4)_2]$ (33 mg, 0.06 mmol) was added and the solution was sonicated for 10 min. Then, the mixture was heated in a 120 °C oven for 24 h. After cooling to R.T., the resultant solid was isolated by centrifugation, washed with fresh DMF (3×1 mL) and acetone (3×1 mL). The powder was dried under vacuum at 60 °C. Violet crystalline powder was obtained (32 mg, 86 % yield). The phase purity of VPI-100 (Cu) was verified by PXRD.

3.3.6 Synthesis of VPI-100 (Ni). In an 8 mL vial, ZrCl_4 (14 mg, 0.06 mmol) was dissolved in 2 mL of dry DMF with 0.44 mL (200 eq.) of formic acid. In a separate vial, $\text{NiCl}_2 \cdot 6\text{H}_2\text{O}$ (14 mg, 0.06 mmol) and free-base ligand (2) (17.3 mg, 0.06 mmol) were added to 2 mL of dry DMF, and sonicated for 10 mins. Then, both vials were heated in an 80 °C oven for 1 h. The solutions were combined into one vial and heated in a 120 °C oven for 24 h. After cooling to R.T., the resultant solid was isolated by centrifugation, washed with fresh DMF (3×1 mL), and acetone (3×1 mL). The product was dried under vacuum at 60 °C. Light pink crystalline powders were obtained (22 mg, 60 % yield). The phase purity of VPI-100 (Ni) was confirmed by PXRD.

3.3.7 Structure Determination and Refinement. Both VPI-100 (Cu) and VPI-100 (Ni) were obtained as microcrystalline powders. Their structures were determined by means of the powder XRD technique using synchrotron radiation at Beamline 17-BM at Advanced Photon Source (APS) at Argonne National Laboratory (ANL). The X-ray wavelength was

0.45336 Å. Sample powder was packed in a 1.1 mm diameter Kapton capillary. 2-D diffraction data were collected with a PerkinElmer® flat panel amorphous Si area detector in the transmission geometry. Reduction of the 2D images to 1D XRD pattern of Intensity versus 2θ was carried out through the GSAS-II program.⁴⁶ XRD indexing and Rietveld analysis were performed with TOPAS version 5.

3.3.8 Structure Confirmation and Phase Purity. The phase purity of the synthesized MOF samples was analyzed on a Rigaku Miniflex diffractometer with a Cu(K α) radiation ($\lambda = 1.5418$ Å) over a 2θ range of 3-50° in continuous scanning mode (1.0°/min) and a resolution of 0.05°. The powder samples were loaded onto a zero-background Si (510) disk.

3.3.9 Single-Crystal X-ray Diffraction. Single-crystal X-ray data of [CuL(ClO₄)₂] (**1**) and [CuLCl₂] (**4**) were collected on a Rigaku Oxford Diffraction Gemini diffractometer equipped with a MoK α X-ray source ($\lambda = 0.71073$ Å), and a low temperature device operating at 100 K. X-ray data collection of [NiL(ClO₄)₂]·2H₂O (**3**) and [NiLCl₂]·2DMF (**5**) were performed on an Rigaku Oxford Diffraction Nova diffractometer operating with a CuK α radiation source ($\lambda = 1.5418$ Å). Collection temperature was 250 K for (**3**) and 100 K for (**5**). The data collection routine, unit cell refinement, and data processing were carried out with the program CrysAlisPro.⁴⁷ The structures were solved using SHELXT-2014⁴⁸ and refined using SHELXL-2014⁴⁹ via Olex2.⁵⁰ Molecular graphics generation was carried out using Olex2.⁵⁰ The final refinement model for all four structures involved anisotropic displacement parameters for non-hydrogen atoms. A riding model was used for all hydrogens not involved in hydrogen bonding. The H-atom position on the carboxylic acids were located from the residual electron density map and refined independently. The isotropic displacement parameters of the H-atom were constrained to 1.5U_{eq} of the attached O-atom.

Structure [CuL(ClO₄)₂] (**1**)

The sample crystalized as a pink plate (0.195×0.320×0.360 mm³). The Laue symmetry was consistent with the triclinic space groups P1 and P-1. The centrosymmetric space group P-1 was chosen.

Structure [NiL(ClO₄)₂] \cdot 2H₂O (**3**)

The sample crystallized as a yellow plate (0.039 \times 0.100 \times 0.214 mm³). The Laue symmetry and systematic absences were consistent with the monoclinic space group *P2₁/c*. A 2-position disordered model was used for the perchlorate with relative occupancies that refined to 0.585(12) and 0.415(12).

Structure [CuLCl₂] (**4**)

The sample crystallized as a purple plate (0.061 \times 0.104 \times 0.201 mm³). The Laue symmetry and systematic absences were consistent with the monoclinic space group *P2₁/n*.

Structure [NiLCl₂] \cdot 2DMF (**5**)

The sample crystallized as a colorless needle (0.16 \times 0.11 \times 0.05 mm³). The Laue symmetry was consistent with the triclinic space groups P1 and P-1. The centrosymmetric space group P-1 was chosen. The final refinement model involved anisotropic displacement parameters for non-hydrogen atoms.

3.3.10 Attenuated Total Reflectance Fourier-Transform Infrared Spectroscopy (ATR-FTIR). ATR-FTIR spectra were obtained on a Varian 670 FT-IR Spectrometer equipped with a diamond Specac Golden Gate attachment. All spectra were an average of 96 scans for powdered samples and were recorded from 4000 to 500 cm⁻¹ with 4 cm⁻¹ resolution. A background spectrum collected on air was subtracted from the sample spectra. The spectra were not corrected for the depth of wavelength penetration.

3.3.11 Thermogravimetric Analysis (TGA). A Q500 from TA Instruments was used to analyze thermal stability. Powder samples (~5 mg) were placed on an aluminum pan and heated at a rate of 10 °C/min under nitrogen atmosphere over the temperature range of 25–600 °C.

3.3.12 Sample Activation and N₂/CO₂ Adsorption Measurement. Before a gas sorption experiment, as-synthesized VPI-100 (Cu)/ VPI-100 (Ni) (~50 mg) samples were washed with DMF three times and acetone three times, followed by soaking in acetone for 3 days to allow solvent exchange. During the solvent exchange process, the acetone was decanted and replaced with fresh solvent 3 times every 24 h. After that, the MOF

powders were isolated by centrifugation. The resulting exchanged frameworks were activated under vacuum for 12 h, and then degassed under vacuum for 12 h at 100 °C prior to gas adsorption/desorption measurements.

3.3.13 X-ray Photoelectron Spectroscopy (XPS). The XPS spectra were collected on a PHI 5000 Vera Probe III spectrometer using an aluminum anode X-ray source (photon energy of 1486.6 eV). Survey and elemental spectra were collected using a 100 μm beam size and 25 W 15 kV source. The data were collected in the range of 1100-0 eV with a pass energy of 225 eV at a step size of 0.8 eV/step. Elemental spectra were collected at the following energy ranges using a pass energy of 69 eV and step size of 0.125 eV/step: N 1s (390-410 eV), Ni 2p_{3/2} (845-865 eV), Cu 2p_{3/2} (925-940 eV), and Zr 3d (174-194 eV). Each element was scanned at 15 sweeps except for the Cu, Ni, and N regions, which were scanned for 450 sweeps each. The pressure inside the sample chamber was kept below 1×10^{-7} Torr for all the measurements.

3.3.14 Scanning electron microscopy imaging (SEM). A LEO (Zeiss) 1550 field-emission scanning electron microscope, equipped with an in-lens detector, operating at 5.0 kV was used for high-resolution images of the MOF powders.

3.3.15 Stability Tests. For a solvent stability study, a small amount of freshly synthesized VPI-100 (Cu) and VPI-100 (Ni) (8–12 mg) was added into different vials containing 1 mL of solvent. The MOF powders were soaked for 24 h after which they were isolated by centrifugation, washed with fresh solvent three times, and dried under vacuum at room temperature. The resultant samples were analyzed by PXRD and compared to the pristine MOFs.

Thermal stability of VPI-100 (Cu) and VPI-100 (Ni) was assessed by variable temperature PXRD experiments. The measurements were performed using Bruker AXS D8 Advance powder diffractometer at 40 kV, 40 mA for Cu(K α) ($\lambda = 1.5406 \text{ \AA}$), with a scan speed of 0.2 s/step and a step size of 0.02°.

3.3.16 Inductively Coupled Plasma-Mass Spectrometry (ICP-MS). The MOF samples were digested in 70% nitric acid and heated at 90 °C for 1 h. After filtration through a syringe filter ($< 0.2 \mu\text{m}$), the solution was diluted with water so that the final concentration of

nitric acid was 7% by volume. All samples were analyzed for nickel/copper and zirconium content using a Thermo Electron X-Series ICP-MS in accordance with Standard Method 3125-B. The final results are the average of triplicate values.

3.3.17 Catalytic cycloaddition of CO₂ to epoxides. VPI-100 (Cu)/VPI-100 (Ni) (0.008 mmol), tetrabutylammonium bromide (99 mg, 0.31 mmol), and epoxide (31.1 mmol) were added to a 20 mL stainless steel Parr reactor. The sealed vessel was heated to 90 °C in a sand bath and charged with CO₂ (10 bar). After 6 h, the reactor was allowed to cool to R.T. and depressurized. A small aliquot was dissolved in CDCl₃ for ¹H NMR analysis to determine the conversion. The reaction solution was centrifuged to recover the catalyst. The recovered MOF powder was washed with CHCl₃ (3× 1 mL) and dried under vacuum. The sample was reused three times in the catalysis experiment for each substrate. The structural stability of the framework was confirmed by PXRD.

3.4 Results and Discussion

3.4.1 Synthesis and Characterization.

The first step in preparation of cyclam-based MOFs is the synthesis of the appropriate linkers. Condensation of bis(ethanediamine) complexes of copper(II) with formaldehyde and diethyl-malonic esters leads to the formation of 6,6,13,13-tetraester substituted cyclam complexes. The initially prepared tetraester complexes hydrolyze in base to the tetracarboxylate precursor [Cu(tetacH₄)](ClO₄)₂, which decarboxylates in acid to give the Cu-based cyclam ligand [CuL(ClO₄)₂] (**1**). This complex is demetallated in acid, allowing the isolation of free ligand (**2**), which can be remetallated with Ni(II). (Scheme S1)

In addition to [CuL(ClO₄)₂] (**1**) and [NiL(ClO₄)₂].2H₂O (**3**), two other metal-cyclam complexes, [CuLCl₂] (**4**) and [NiLCl₂].2DMF (**5**), have been obtained from the solvothermal reaction of metal chloride salt and the free ligand (**L**) in DMF. The metal cyclam complexes preferentially form the six-coordinate geometry around the metal center in the presence of Cl⁻ in DMF. The coordination bond of Cl⁻ with Cu²⁺/Ni²⁺ is perpendicular to the plane of four nitrogen atoms in the cyclam ring, where the ligand structure is consistent with that inside the MOF (*vide infra*). To expand on literature

reported structural data,⁴⁵ we present a detailed analysis of the four metal-cyclam complexes including unique crystal structures below.

Single-crystal X-ray diffraction studies revealed the structures of [CuL(ClO₄)₂] (**1**), [NiL(ClO₄)₂]·2H₂O (**3**), [CuLCl₂] (**4**) and [NiLCl₂]·2DMF (**5**). The crystallographic information for each compound is summarized in Tables S1 and S2 (Supporting information). As shown in Figure 3.1, all four structures exhibited the E(*trans*) arrangement of the carboxylic acid groups and the RRSS configuration of the coordinated secondary nitrogen centers, which is consistent with the thermodynamically stable geometry reported in [Ni(cyclam)](ClO₄)₂.⁵¹ For compounds **1**, **4** and **5**, the metal cation formed an octahedral coordination geometry, where four nitrogen atoms in the macrocyclic ring are located in the equatorial plane in addition to two labile ligands in axial positions. It is worth noting that coordinatively unsaturated metal sites were attained in compound **3**. The Ni-O (from ClO₄⁻) distance in compound **3** is longer than 3.15 Å, which is too long to be considered as a formal coordination bond. The preferred 4-coordination planar geometry on the central metal can be attributed to the bulky nature of the ClO₄⁻ ion and high perchloric acid concentration in solution.⁵²⁻⁵³

The Cu-N distances in **1** and **4** (the copper containing metallocyclams) are nearly identical (average 2.03 Å and 2.02 Å, respectively), while Cu-O distance in **1** and Cu-Cl distance in **4** are slightly longer at 2.44 Å and 2.84 Å, respectively. The Ni-N distance in **3** was found to be 1.94 Å, which is shorter than that found in **5** (2.06 Å). Meanwhile, the Ni-Cl bond length in the complex **5** was 2.49 Å, which is considerably shorter than that in Cu analogue, **4**. This effect was attributed to Jahn-Teller distortion of the coordination geometry of Cu²⁺ ion inside the cyclam ligand. The structures confirm the successful functionalization of the cyclam with carboxylic acid groups, enabling the metal-cyclam complexes to be further used as bridging linkers for the construction of MOFs.

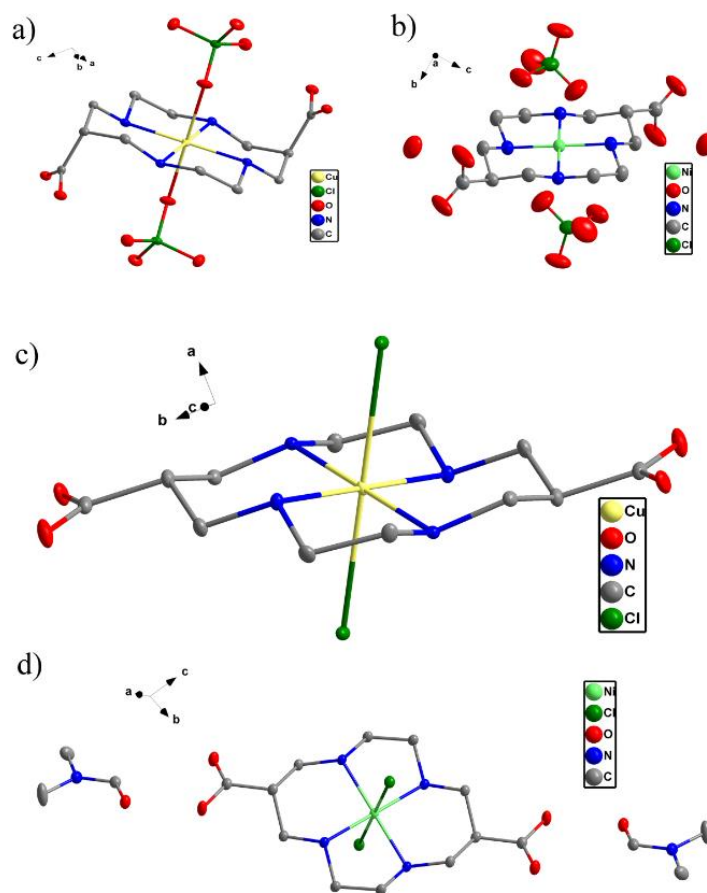


Figure 3.1 Anisotropic displacement ellipsoid drawing (30%) of (a) $[\text{CuL}(\text{ClO}_4)_2]$ (**1**), (b) $[\text{NiL}(\text{ClO}_4)_2] \cdot 2\text{H}_2\text{O}$ (**3**), (c) $[\text{CuLCl}_2]$ (**4**) and (d) $[\text{NiLCl}_2] \cdot 2\text{DMF}$ (**5**). Hydrogen atoms were omitted for clarity. Color scheme: C, grey; O, red; N, blue; Ni, light green; Cu, yellow; Cl, green.

Modulated syntheses³⁷ were used to obtain highly crystalline MOF powders from **1** and **2** (in the presence of NiCl_2). Both formic acid and acetic acid were found to be competent modulators, while benzoic acid was less suitable. This behavior could be due to different modulators would influence the crystal nucleation and growth rate differently in Zr(IV) based MOFs.⁵⁴⁻⁵⁵ Furthermore, it was essential to use a two-step solvothermal synthesis, as described in the Experimental Section for VPI-100 frameworks. Similar to the “controlled SBU” approach first reported by Férey *et al.*,⁵⁶⁻⁵⁷ the zirconium oxo-cluster was pre-assembled first. To do so, ZrCl_4 was reacted with modulator (e.g. formic acid) at elevated temperature. With the addition of the cyclam ligand and further increased reaction temperature, a direct ligand exchange between the monocarboxylates (formic acid) and the dicarboxylate linkers occurred to form the extended 3D frameworks. Without the pre-formation of the zirconium oxo-clusters, only amorphous product could

be obtained. These results revealed that the modulator behaved as a structure-directing agent.

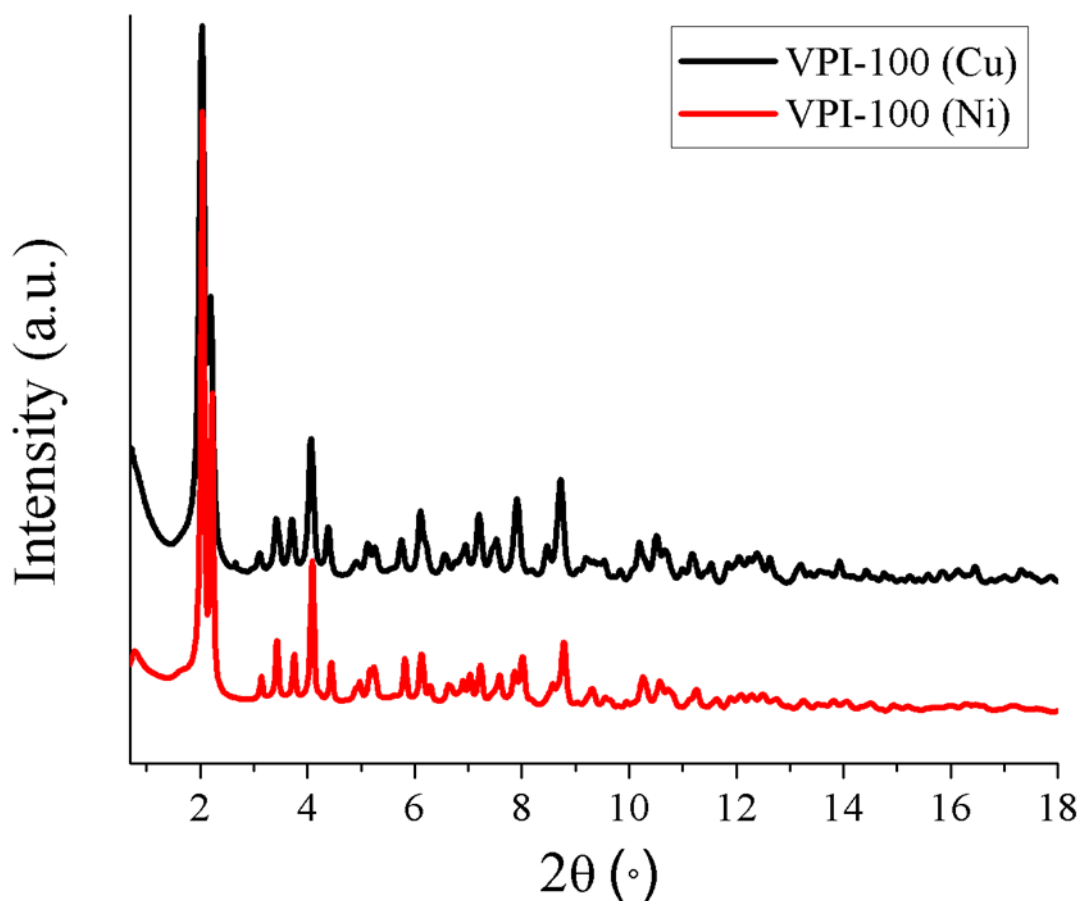


Figure 3.2 PXRD patterns of as synthesized VPI-100 (Cu) and VPI-100 (Ni) powders measured at room temperature. Black: VPI-100 (Cu); Red: VPI-100 (Ni).

Table 3.1 Crystallographic data for VPI-100 (Ni) and VPI-100 (Cu), and refinement statistic

	VPI-100 (Ni)	VPI-100 (Cu)
Space group	<i>I</i> 4/m	<i>I</i> 4/m
<i>a</i> (Å)	16.510(3)	16.721(3)
<i>c</i> (Å)	19.811(5)	19.704(5)
<i>V</i> (Å³)	5400(2)	5509(2)
Temperature (K)	298	298
Wavelength (Å)	0.45336	0.45336
2θ range (°)	1.5 to 18	1 to 18
Goodness of fit	4.16	5.58
R_p	0.0561	0.0598
R_{wp}	0.0742	0.0797

To determine the morphology of MOF particles, SEM was performed. The results revealed that the powder consists of quasi-spherical particles with the sizes of 100-300

nm (Figure S6), which were not suitable for single-crystal analysis. Therefore, their structures were determined from synchrotron PXRD. XRD indexing and Rietveld analysis was performed with TOPAS version 5. Figure 3.2 shows the XRD profiles of VPI-100 (Cu) and VPI-100 (Ni) at room temperature. Both patterns have intense low angle peaks, which are commonly seen in XRD of porous structures. The high similarity between the as-synthesized VPI-100 (Cu) and VPI-100 (Ni) patterns suggests they are isostructural. Crystallographic data for VPI-100 is summarized in Table 3.1. Further details about structure determination and refinement are summarized in the Supporting Information (Section 3).

VPI-100 (Cu) and VPI-100 (Ni) crystallize in the space group $I4/m$. In the structural models, each MOF node is comprised of a $Zr_6(\mu_3\text{-OH})_8(\text{OH})_8(\mu^2,\eta^2\text{-(O}_2\text{C)}_2\text{cyclam})_8$ cluster (Zr_6 -cluster) that is centered at I -lattice positions (i.e. unit cell origin and body center) with site symmetry $4/m$ (D_{4h}). Similar to 8-connected Zr_6 cluster in PCN-222⁵⁸ and NU-1000⁵⁹, the Zr-atoms of the Zr_6 -cluster occupy the corners of a distorted octahedron; each 8-coordinate Zr^{4+} has a distorted square antiprism geometry (Figure. 3.3A). The faces of the octahedron defined by the 6 Zr-atoms are capped by μ_3 -OH groups that fill 4 coordination sites around each Zr^{4+} . Eight cyclam ligands are coordinated to each cluster with each carboxylate bridging between an axial Zr^{4+} and equatorial Zr^{4+} of Zr_6 -octahedron. The coordination sphere around each equatorial Zr-atom is completed by two terminal -OH groups.

Each Zr_6 -cluster is linked to the eight nearest clusters via the eight cyclam ligands that lie parallel to the unit cell body diagonals (Figure 3.3B). The resulting 3D frameworks exhibit CsCl topology (Schläfli symbol of $4^{24}\cdot 6^4$). Disordered solvents and chloride ions occupy the pores. Because the PXRD data resolution is relatively low (~ 1.8 Å), the solvents and/ions content within the pores could not be definitively identified (see Supporting Information, Section 3). After removing the solvent/ion contents from pores, void calculation in Mercury⁶⁰ give a contact surface void volume of 2663.51 \AA^3 (48.3% of cell) and a solvent accessible void volume of 1306.03 \AA^3 (23.7% of cell) for VPI-100

(Cu). Corresponding volumes for VPI-100 (Ni) are 2569.44 Å³ (47.6%) and 1237.52 Å³ (22.9%).

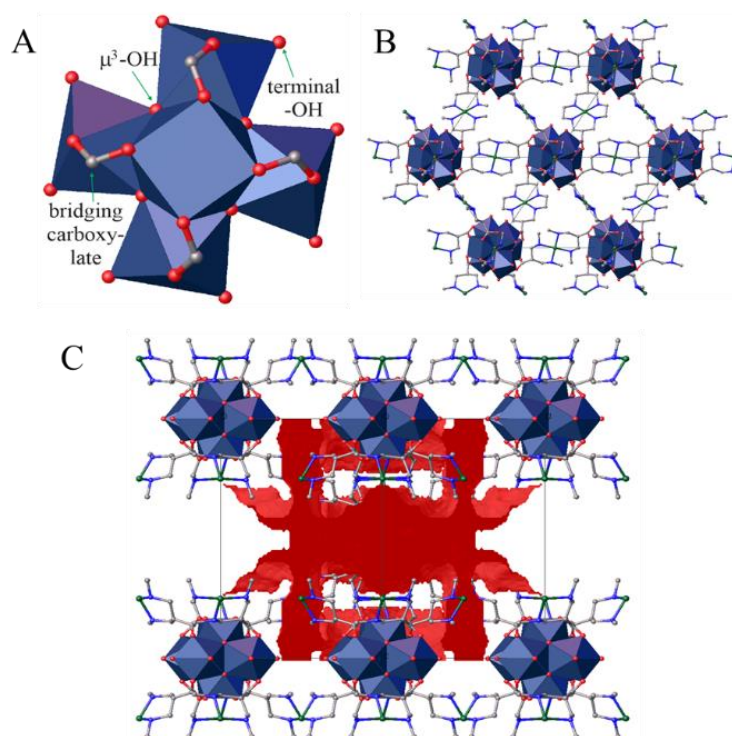


Figure 3.3 Structure of VPI-100 (Cu) (disordered solvent, chloride, and H-atoms are omitted for clarity). (A) Polyhedral drawing of the $Zr_6(\mu_3\text{-OH})_8(\text{OH})_8(\mu^2,\eta^2\text{-(O}_2\text{C)}_2\text{cyclam})_8$ cluster as viewed down [001] (i.e. the 4-fold axis). (B) Packing diagram viewed down [111] and depicting the cyclam linkers connecting the Zr_6 -clusters along the cell body diagonals. Six of the eight closest Zr_6 -clusters are depicted. The remaining two sit directly above and below the central Zr_6 cluster. (C) View down [110] depicting the pore space in the MOF.⁶¹ Color scheme: Zr, light blue; C, grey; O, red; N, blue; Cu, green.

The VPI-100 (Cu) and VPI-100 (Ni) powders were also characterized by XPS. The spectra revealed the oxidation states to be Zr(IV), Ni(II) and Cu(II) (Figures S7 and S8, SI). Further analysis on digested VPI-100 (Cu) and VPI-100 (Ni) powders *via* ICP-MS found that the Cu:Zr and Ni:Zr ratios are 0.63 and 0.69, respectively, which is consistent with the theoretical Cu(Ni):Zr ratio (2:3) based on the structural model, assuming 8 ligands and 2 Zr_6 clusters in one unit cell.

FTIR spectroscopy was used to investigate the metal coordination environment inside the cyclam ring and subsequent incorporation into the framework. In Figure S9, the vibrational spectra for the $[\text{CuL}(\text{ClO}_4)_2]$ (**1**), L (**2**) and $[\text{NiL}](\text{ClO}_4)_2$ (**3**) displayed several characteristic features. Peaks corresponding to the vibrational modes of the carboxylic acids occurred at 1708, 1724 and 1712 cm^{-1} , respectively. The high energy bands in the

range of 3000-3250 cm^{-1} can be attributed to the secondary amine in cyclam ring.⁶² The C-N stretching at 1076 cm^{-1} for **L** is shifted for $[\text{CuL}(\text{ClO}_4)_2]$ and $[\text{NiL}(\text{ClO}_4)_2]\cdot 2\text{H}_2\text{O}$ because of the coordination between the metal and cyclam.⁶²⁻⁶³ The spectra of VPI-100 (Cu) and VPI-100 (Ni) generally resemble those of the free metalloligands (Figure S10). The carboxylic acid stretches underwent a shift to lower energy (1602 cm^{-1} and 1592 cm^{-1} , respectively) attributed to the chelation of the oxygen atoms to the Zr_6 clusters in the MOF structure. After soaking in acetone for three days the peaks corresponding to DMF molecules could not be detected, indicating the successful removal of synthesis solvent from the pores of VPI frameworks.

The thermal stabilities of the MOFs were investigated by TGA and variable temperature PXRD measurements. Both MOF samples were activated by solvent exchange with acetone before the experiments. The weight loss below 100 °C in TGA curves of VPI-100 (Cu) and VPI-100 (Ni) was attributed to the removal of the adsorbed solvent molecules (Figure S11). The second loss occurred at 160 and 220 °C for the Cu and Ni analogues, respectively, which was assigned to the dehydroxylation of Zr_6 nodes. Above 300 °C the loss of the cyclam metalloligand was observed, leaving the final residue of metal oxides. Variable temperature PXRD results for VPI-100 frameworks (Figure 3.4 A and B) generally followed similar trends as in TGA. The minor change that occurred in the powder pattern from 8 to 12 ° above 100 °C was due to the removal of solvent molecules from the porous structure. The PXRD and N_2 adsorption isotherms (Figure S17) of VPI-100 (Cu) after the thermal treatment at 170 °C revealed that the samples retained their structural integrity and porosity. Above 190 °C however, the Cu analogue started to lose crystallinity, as evidenced by the disappearance of high angle diffraction peaks and overall peak broadening. The *ex-situ* PXRD experiment (Figure S12) confirmed that the change is permanent, and the MOF does not revert back to its starting structure after the exposure to 200 °C. Similar behavior has been observed in VPI-100 (Ni). While the Ni framework generally exhibited higher thermal stability with its PXRD patterns remaining relatively unchanged up to 220 °C. The BET surface area of VPI-100 (Ni) after thermal treatment at 220 °C decreased from 612 to 485 m^2/g (Table

S4)). The irreversibility of the structural changes has been further confirmed by *ex-situ* PXRD experiment (Figure S12). Above 300 °C the complete MOF decomposition was observed, which correlates well with the thermal decomposition of the metalloligand in the TGA data.

Despite the fact that VPI-100 MOFs were constructed from flexible cyclam-based linkers, both materials demonstrated excellent chemical stability in various organic and aqueous based solvents over a wide pH range. As shown by PXRD results (Figure 3.4 C & D), the MOFs maintained the PXRD patterns and excellent crystallinity after exposure to a wide variety of organic solvents, including acetone, methanol, ethanol, dichloromethane, chloroform, acetonitrile, tetrahydrofuran, ethyl acetate, toluene, pyridine and cyclohexane for 24 h. In order to further confirm the structural integrity of the frameworks, the synergistic analysis of VPI-100 MOFs after soaking in pyridine was investigated. The N₂ adsorption isotherms showed complete maintenance of the porosity (Figure S17), further demonstrating the frameworks stability. The TGA (Figure S18) indicate there is no significant change after the treatment, which is consistent with the unchanged PXRD patterns. All the organic solvents tested above are commonly used in guest exchange or post-synthetic modification procedures. As a result, these MOFs can be readily manipulated post-synthetically without substantial loss of their structures. In addition, the structural integrity of VPI-100 (Cu) and VPI-100 (Ni) was also retained in aqueous solutions under different pH conditions. After soaking the MOF samples for 24 h, the framework structures were preserved from 1 M HCl to pH 10 NaOH solution (Figure 3.4 E and F). It is interesting to note that small changes in PXRD patterns have been observed after soaking in 1 M HCl for both analogues, however, the change can be reversed by heating the MOFs in DMF at 120 °C for 16 h, mimicking the original synthetic conditions (Figure S13). Le Bail refinement also confirmed that after 1 M HCl treatment, the PXRD patterns could be fitted perfectly to the *I4/m* space group (Figure S14 and S16), although the unit cell parameters underwent a considerable change as summarized in Table S3. The change could be due to the framework flexibility facilitated by the non-aromatic nature and conformational flexibility of cyclam-based ligands. The

N₂ adsorption isotherms (Figure S17) and the TGA measurements (Figure S18) further confirmed the overall structural stability of the treated samples. It is noteworthy that VPI-100(Cu) was able to maintain crystallinity even after immersion into highly acidic mixtures (8 M HNO₃) for 24 h. Although changes have been observed in PXRD patterns, Le Bail refinement (Figure S15) confirmed the retention of the *I4/m* space group with longer c axis (21.435 Å) compared with the starting framework (19.704 Å). This change appears to be permanent and cannot be reversed as evidenced by the color change and crystallinity loss (Figure S13) after reactivation process. TGA data indicated decreased thermal stability after 8 M HNO₃ treatment. Gas sorption measurements (Figure S17) showed significantly decreased N₂ uptake and BET surface area, which could attribute to the structure collapse induced by the activation procedure before the measurements. The Ni analogue, on the other hand, was found to be less stable towards strong acids, with 6 M HCl and 8 M HNO₃, in particular, resulting in significant loss of crystallinity.

Similar to other reported Zr-MOFs,⁶⁴ VPI-100 (Cu) and VPI-100 (Ni) degraded in pH 7 phosphate solution, a commonly employed buffer. This effect was previously attributed to the strong interaction between phosphate ions and Zr₆ nodes. Moreover, the frameworks lost their crystallinity upon exposure to boiling H₂O for 24 h, which demonstrates the limits of these materials. Interestingly, while the VPI-100 (Ni) demonstrated better thermal stability than VPI-100 (Cu), the latter was more stable towards a wider variety of chemical environments. Overall, both frameworks exhibited excellent stabilities, comparable with other Zr-based MOFs.

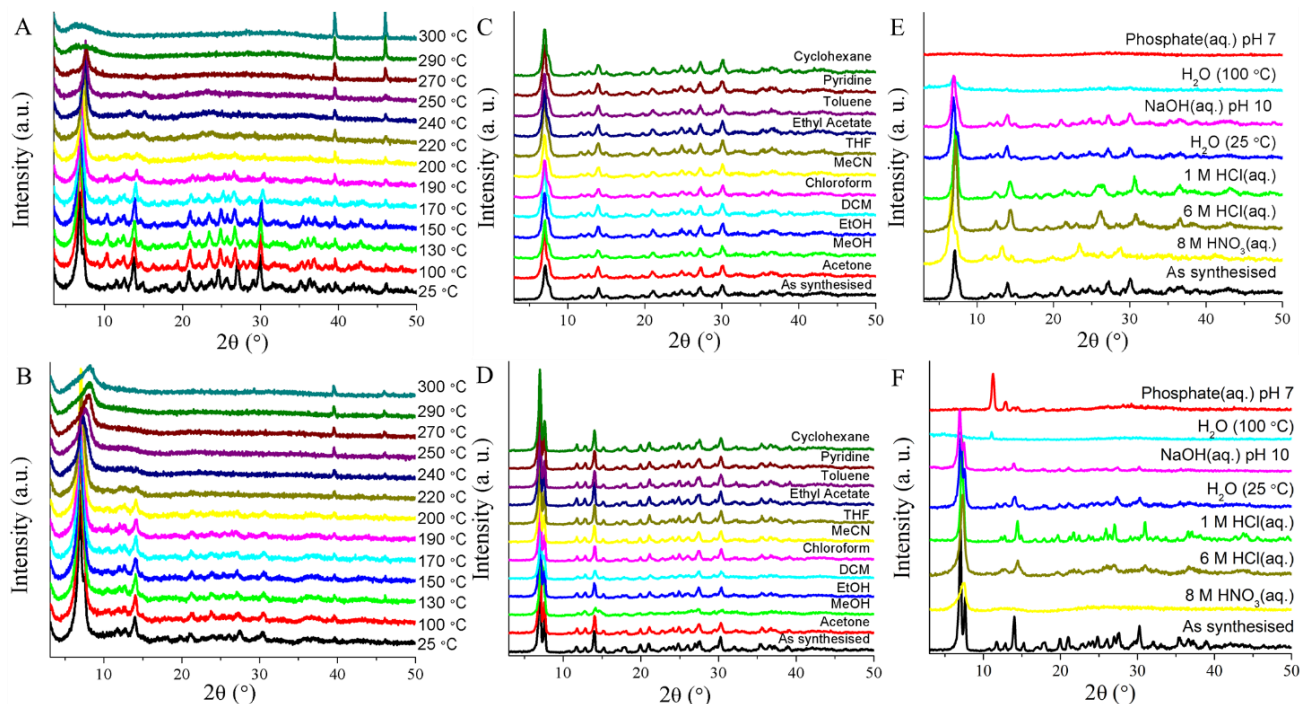


Figure 3.4 Variable temperature PXRD at the designated temperature of (A) VPI-100 (Cu) and (B) VPI-100 (Ni). PXRD patterns of (C) VPI-100 (Cu) and (D) VPI-100 (Ni) after exposure to different organic solvents; (E) VPI-100 (Cu) and (F) VPI-100 (Ni) after exposure to different aqueous solutions, compared to the as-synthesized sample.

3.4.2 Investigation of gas adsorption.

The permanent porosity of both VPI-100 MOFs was confirmed by nitrogen adsorption isotherm measurements taken at 77 K (Figure S12). The frameworks were exchanged with acetone for three days and activated at 100 °C under high vacuum prior to the measurements. The gas sorption data exhibited a reversible type II behavior and have a saturated uptake of 465 and 148 cm³ g⁻¹ for VPI-100 (Cu) and VPI-100 (Ni), respectively. Brunauer-Emmett-Teller (BET) surface areas of 398 and 344 m² g⁻¹ were obtained for VPI-100 (Cu) and VPI-100 (Ni). The total pore volume of the frameworks determined by single point method was found to be 0.312 and 0.228 cm³/g for VPI-100 (Cu) and VPI-100 (Ni), respectively. From FT and Monte Carlo simulations the pore width was calculated to be 6.37 Å for VPI-100 (Cu) and 5.77 Å for VPI-100 (Ni). The pore volumes and pore widths are consistent with the crystallographic data. The difference of BET and N₂ uptake between VPI-100 (Cu) and VPI-100 (Ni) might due to the partially remove of guest molecules in VPI-100 (Ni), therefore, a higher activation temperature has been performed on VPI-100 (Ni). Upon activation at 120 °C, VPI-100 (Ni) exhibited increased

BET surface area and N₂ uptake (Table 3.2 and Figure S12). The N₂ isotherms still followed a reversible type II behavior with the STP of 374 m² g⁻¹. The BET surface area increased to 612 m² g⁻¹, whereas the total pore volume and average pore width changed to 0.327 cm³/g and 8.16 Å. When similar higher temperature activation conditions were performed on the VPI-100 (Cu), it resulted in inferior adsorption properties as compared to those obtained with 100 °C activation. Furthermore, the VPI-100 (Cu) MOF lost crystallinity in the process. This behavior could be the result of lower thermal stability of the Cu analogue compared to the Ni, as revealed by the variable temperature PXRD experiments.

CO₂ sorption in the VPI-100 frameworks was investigated at 273 K and 296 K (Figure 3.5). Both MOFs exhibited a type I isotherm, which is indeed characteristic of microporous materials. VPI-100 (Cu) exhibits similar CO₂ uptake capacity as VPI-100 (Ni) under the same activation conditions, as shown in Table 2. For the Cu analogue, the CO₂ adsorption capacity at 296 K and 1 atm was 3.76 wt% (19.15 cm³/g at STP, 0.85 mmol/g), which increased to 6.65 wt% (33.85 cm³/g at STP, 1.51 mmol/g) when the temperature decreased to 273 K. While for VPI-100 (Ni), the CO₂ adsorption capacity at 296 K and 1 atm is 2.70 wt% (13.79 cm³/g at STP, 0.62 mmol/g), which increase to 5.52 wt% (28.20 cm³/g at STP, 1.26 mmol/g) when the temperature decreased to 273 K.

When VPI-100 (Ni) was activated at 120 °C, the CO₂ uptake capacity improved significantly, leading to 9.87 wt% adsorption (50.23 cm³/g at STP, 2.24 mmol/g) at 273 K and 1 atm. This effect could be attributed to a more efficient removal of guest molecules from the pore space and/or expansion of the framework under high temperature activation considering the flexibility of the cyclam. Compared with other cyclam related MOFs, the CO₂ uptake value of both VPI-100 MOFs is similar to previous reported Zn-cyclam based 1D material.³³ Moreover, PXRD measurements after gas sorption studies (Figure S13) confirmed that the framework still retained the crystallinity after the experiment.

The temperature dependence of the CO₂ adsorption isotherms enabled the evaluation of the isosteric heats of adsorption, reflecting the strength of interactions between the

frameworks and CO₂ molecule.⁶⁵⁻⁶⁶ The CO₂ adsorbed volume decreases as the temperature increased, confirming an exothermic nature to the adsorption process. CO₂ adsorption isotherms for the VPI-100 frameworks were fitted to the Langmuir-Freundlich isothermal model (equation 1) to determine the adsorbed gas volume as a function of pressure, and to study adsorption thermodynamics.

$$\frac{Q}{Q_m} = \frac{K_F P^{(1/t)}}{1 + K_F P^{(1/t)}} \quad (1)$$

In equation 1, Q is the moles of gas adsorbed, Q_m is the moles adsorbed at saturation, P is pressure, K_F is an affinity constant, and t is an index of heterogeneity ($0 < 1/t < 1$). The Langmuir-Freundlich equation can be rearranged and substituted into the Clausius-Clapeyron equation (equation 2) to determine the isosteric heats of adsorption, Q_{st} ,

$$\ln(P_i) = \frac{Q_{st}}{RT_i} + \frac{\Delta S}{R} \quad (2)$$

where P_i is the pressure for isotherm i , T_i is the temperature for isotherm i , R is the universal gas constant, and ΔS is entropy. The adsorption enthalpy values are negative throughout the adsorption due to the favorable interactions between CO₂ and the MOFs. The calculated values of Q_{st} at low surface coverage for VPI-100 (Ni), VPI-100 (Ni) activated at 120 °C, and VPI-100 (Cu) are -36.4 kJ/mol, -31.2 kJ/mol and -38.4 kJ/mol respectively. Those values are comparable with other frameworks containing open coordination metal sites, such as Ni-MOF-74 (-42 kJ/mol) and HKUST-1 (-35 kJ/mol).⁶⁷ The high heat adsorption enthalpy indicate strong interactions between the open metal sites and CO₂ in the frameworks. The sorption isotherms with the fits are shown in Figure 3.5 and the calculated parameters are summarized in Table S3.

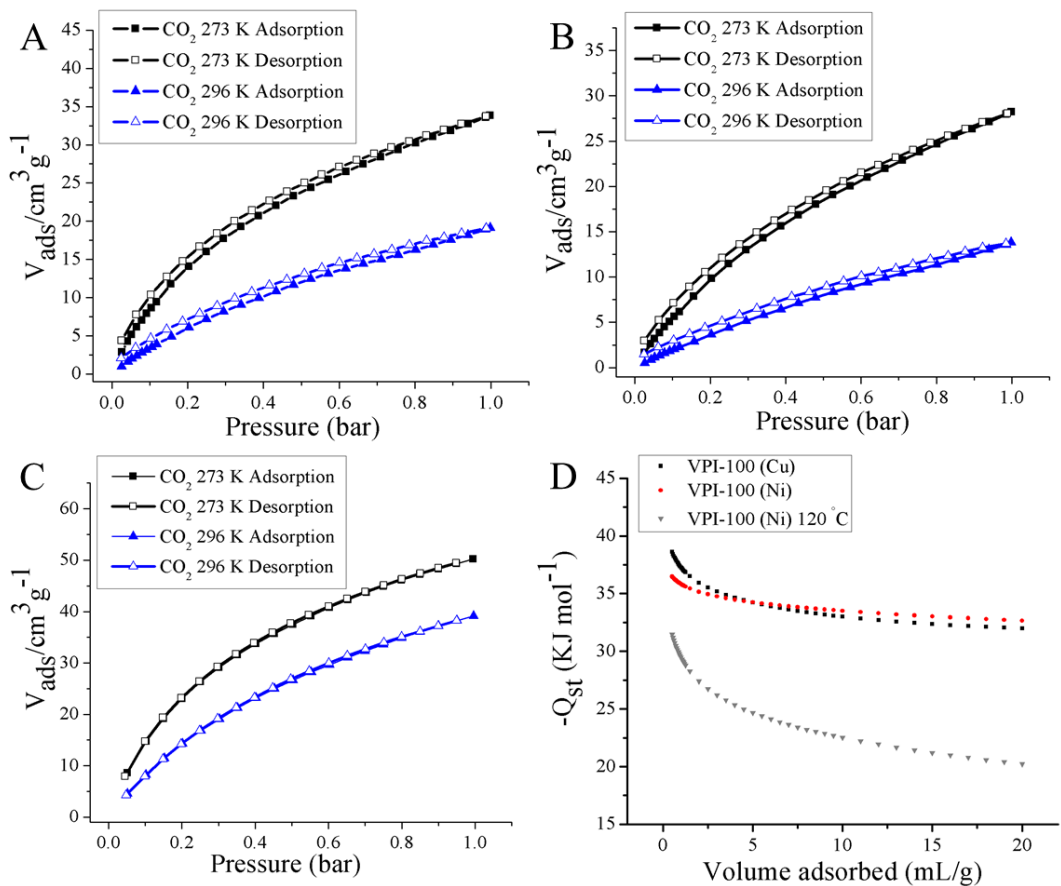


Figure 3.5 The CO₂ sorption isotherms of (A) VPI-100 (Cu), (B) VPI-100 (Ni) and (C) VPI-100 (Ni) activated at 120 °C at 273 K and 296 K, 1 atm. (D) CO₂ adsorption heat plots of VPI-100 frameworks.

Table 3.2 The summary of gas sorption properties of VPI-100 (Cu) and VPI-100 (Ni)

MOF	Activation Temperature	BET area (m ² /g)	CO ₂ sorption at 273 K under 1 atm		
			STP (cm ³ /g)	wt%	Q _{st} (kJ/mol)
VPI-100 (Cu)	100 °C	398	33.85	6.65	-38.4
VPI-100 (Ni)	100 °C	344	28.20	5.52	-36.4
	120 °C	612	50.23	9.83	-31.2

3.4.3 Catalytic performance of VPI-100 MOFs for CO₂ chemical fixation

Large quantities of CO₂, a main byproduct of the fossil fuel combustion, are released into the atmosphere every year. Therefore, it has been identified as an abundant, low cost chemical feedstock for the synthesis of a variety of important chemicals. In particular, cycloaddition reactions between CO₂ and epoxides are of great interest. The products of these transformations are organic cyclic carbonates, which are employed in several important applications, such as degreasers, polar aprotic solvents and electrolytes in lithium ion batteries.⁶⁸ In addition, CO₂ cycloaddition is considered as one of the most atom-economic reactions for artificial CO₂ fixation.⁶⁹

MOFs have been previously investigated as heterogeneous catalysts or co-catalysts for the production of cyclic carbonates from CO₂ and epoxides since they possess a number of favorable characteristics including high internal surface area, chemical tunability and high affinity for CO₂.⁷⁰⁻⁷² Notably, MOFs with open metal centers and coordinatively unsaturated metal nodes⁷³ serve as Lewis acidic catalysts for cycloaddition reactions. Characterized with dual Lewis acid catalytic metal sites, MOFs^{36, 74-75} like MMPF-9 and MMCF-2 have shown excellent catalytic performance due to the high density of Lewis acid sites in the structure. Metalloclamms have not previously been explored as catalysts in chemical fixation of CO₂ with epoxides. However, considering the Lewis acidic nature of both the potentially accessible Cu²⁺/Ni²⁺ metal active sites in the metalloclamms and the presence of coordinatively unsaturated Zr⁴⁺ sites in the equatorial plane of Zr₆ cluster in VPI-100 MOFs, their catalytic activity towards CO₂ cycloaddition to various organic epoxides was explored (summarized in Table 3.3). In a typical catalysis experiment, VPI-100 (0.008 mmol), tetrabutylammonium bromide (99 mg, 0.31 mmol), and epoxide (31.3

mmol) were added to an autoclave reactor. The reaction was carried out at 90 °C and 10 bar of CO₂ for 6 h, and the resulting mixture was analyzed by ¹H NMR to determine the yield and the purity of cycloaddition products (SI, section 6).⁷⁶ One of the common byproduct for this reaction is polycarbonate, which might have ¹H NMR peaks overlapping with cyclic carbonate. Therefore, gel permeation chromatography (GPC) was also used to analyze the reaction mixture. For all but one of the six catalytic reaction trials, we did not observe any polymers or oligomers. For one trial conducted with cyclohexane oxide as a substrate and VPI-100 (Ni) as the catalyst, a small amount (< 5%) of higher molecular weight product was detected.

Paralleled with the molecular metallocyclam species (Table S7), the VPI-100 MOFs demonstrated higher conversion yield for all three substrates as shown in Table 3.3. Although both [CuL(ClO₄)₂] (**1**) and [NiL(ClO₄)₂]·2H₂O (**3**) demonstrated improved conversion yield compared with the no co-catalyst control (Table S7), the catalytic performance of molecular catalysts was limited by their low solubility under such solvent-free conditions (<0.36 mM at 90 °C). In contrast, the designed MOFs heterogenized the cyclam catalysts while maintaining active site accessibility through porous structure, which circumvented the solubility issues.

Compared with related catalytic frameworks (Table S5), VPI-100 MOFs exhibited excellent catalytic activity under relatively mild conditions.⁷⁶⁻⁷⁷ Specifically, the reaction yields for cycloaddition of CO₂ with epichlorohydrin (6a) catalyzed by VPI-100 (Cu) and VPI-100 (Ni) are 94.3 (± 0.6) % and 97 (± 1) %, respectively. Furthermore, the corresponding turnover frequency (TOF) values of VPI-100 (Cu) and VPI-100 (Ni) are 72.3 ± 0.6 and 75 ± 1 h⁻¹, respectively, are among the highest of the previously reported values for MOFs. The impressive TOF values revealed a high reaction rate for the cycloaddition reaction with the presence of VPI-100 MOFs, which can be attributed to the synergistic effect of catalytic open metal sites of the cyclam ligand and unsaturated metal nodes. When the epoxide species is cyclohexene oxide (6c), VPI-100 MOFs established among the highest conversion yield at low catalyst loading (0.025 mol %) as compared with other reported MOFs (Table S6). In previous reports, the lower

conversion yields observed with 6c as compared to other epoxide substrates was attributed to the steric hindrance imparted by the cyclohexane ring. The higher conversion yields observed for VPI-100 could be due to the greater accessibility of the metal sites located in the cyclam ring (planar, far from nodes, not sterically confined).

Furthermore, the VPI-100 MOFs were easily recovered from the reaction mixture by centrifugation and reused for at least 3 cycles without substantial loss of catalytic activity. Although the overall quality of powder patterns has decreased with the noticeable broadening of the peaks, the MOFs largely retained their crystallinity after the catalytic cycles. The preservation of the framework structures was evidenced through the retention of the major PXRD peaks (Figure 3.6 and Figures S47-48). Le Bail refinement (Figures S50 and S51) further confirmed that the frameworks retained their space group symmetry as *I4/m*. A change in the unit cell parameters, however, was observed, the *a* axis elongated while the *c* axis contracted (Table S8). This change was attributed to the flexibility of the framework backbone. Alteration of the pore environment through incorporation of various guest molecules could therefore induce the structural modifications.

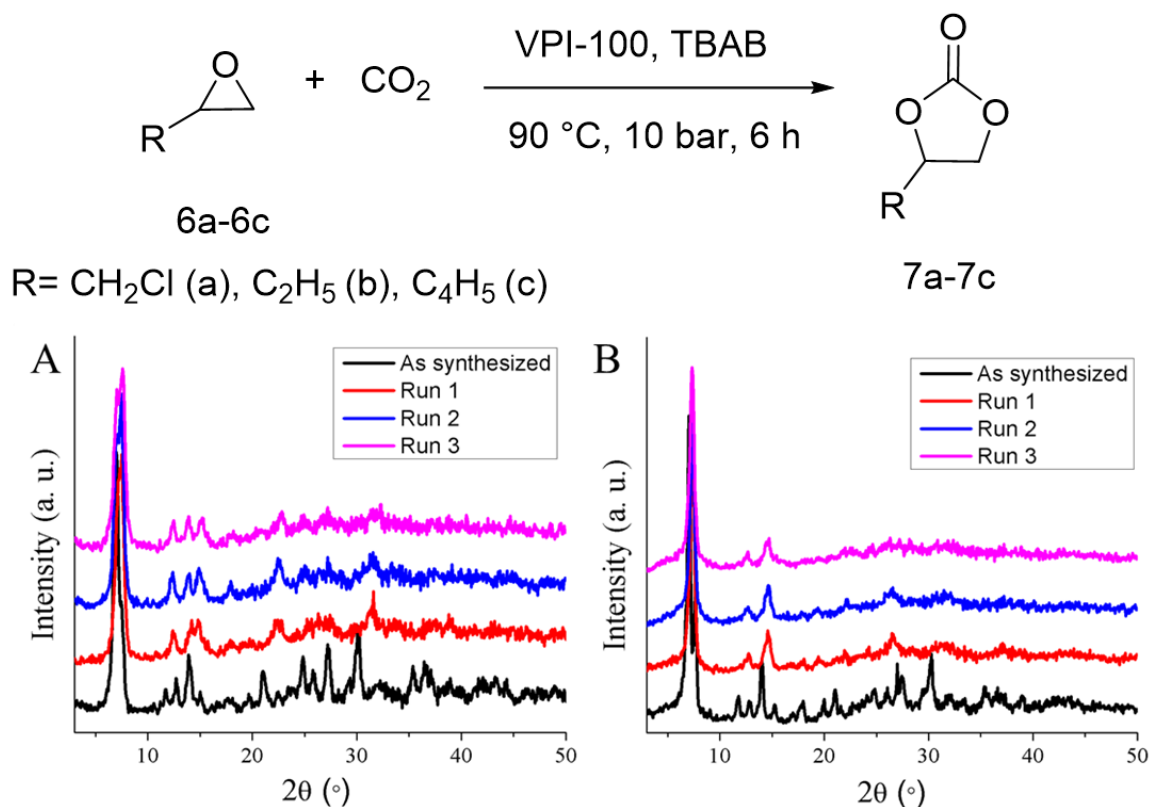
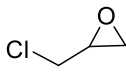
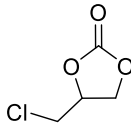
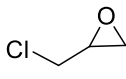
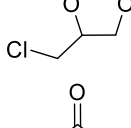
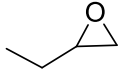
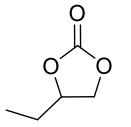
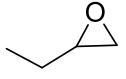
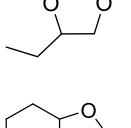
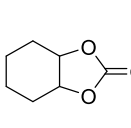
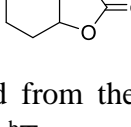


Figure 3.6 (Top) Reaction scheme of CO₂ and epoxide catalyzed by VPI-100 MOFs. (Bottom) PXRD patterns of A) VPI-100 (Cu) and B) VPI-100 (Ni) as synthesized and after three catalytic reaction cycles from 6a to 7a.

Table 3.3 Catalytic activities of VPI-100 MOFs: synthesis of cyclic carbonates from CO₂ and epoxides catalyzed by VPI-100.

Entry	Epoxide	Product	Catalyst	Conversion (%) ^a			TON ^b			TOF (h ⁻¹) ^c		
				R1 ^d	R2 ^d	R3 ^d	R1	R2	R3	R1	R2	R3
1			VPI-100 (Cu), TBAB	94	95	94	431	439	431	72	73	72
2			VPI-100 (Ni), TBAB	96	98	98	443	452	453	74	75	76
3			VPI-100 (Cu), TBAB	60	52	40	273	236	185	46	39	31
4			VPI-100 (Ni), TBAB	50	50	43	229	229	199	38	38	33
5			VPI-100 (Cu), TBAB	13	16	18	60	76	81	10	13	14
6			VPI-100 (Ni), TBAB	18	20	17	85	92	78	14	15	13

^aConversion evaluated from the ¹H NMR spectra by integration of epoxide versus cyclic carbonate peaks. (Figure S14-21) ^bTurnover number [product (mmol)/active site (mmol)], where “active site” is the sum of both the unsaturated Zr and Cu/Ni metal centers. ^cTurnover frequency [TON/ time (h)], ^d R1, R2 and R3 stands for 3 cycles for using same VPI-100 MOF materials as catalyst

ICP-MS analysis revealed the frameworks maintain the same Cu(Ni):Zr ratios before and after catalytic cycles, indicating that Cu/Ni did not leach from MOF. Additionally, for all the reaction mixtures, trace (less than 0.5% of the starting metal content of the MOF catalyst) Cu/Ni and Zr were detected. The Cu/Ni to Zr ratio for the solution content was consistent with that expected from the MOF molecular formula. Therefore, the presence of these metals was attributed to incomplete removal of MOF particles during the work-up of the reaction mixture, specifically during the catalyst isolation by centrifugation. Therefore, the catalytic reaction was, indeed, heterogeneous in nature.

3.5 Conclusion

In conclusion, a modulated synthetic approach has proved to be highly effective for the synthesis of a novel class of metallocyclam Zr-MOFs. To the best of our knowledge, this work represents the first example for the incorporation of metallocyclam-based ligands into highly robust Zr framework. The ligand design ensured that addition of carboxylic acid groups did not perturb the electronic structure of the chelated metal centers. More

importantly, the axial positions on the cyclam core were not permanently obstructed by ligands involved in supporting the framework structure. The VPI-100 MOFs exhibited remarkable chemical stability in a wide range of pH in aqueous and organic solutions. Moreover, these frameworks demonstrated high CO₂ uptake capacity up to ~9.83 wt% adsorption at 273 K under 1 atm and strong interaction between metal sites and CO₂, with heat adsorption values as high as 38.4 kJ/mol. More interestingly, VPI-100 MOFs demonstrated excellent catalytic efficiency (up to 98% conversion) for CO₂/epoxide coupling reaction as reusable heterogeneous catalysts. The immobilization of catalytically active metal centers in the MOF linker combined with the unsaturated metal nodes lead to a complimentary enhancement of catalytic efficiency. The cyclam MOF platform can be broadened to include other metals or cyclam derivatives, expanding their range of useful applications, akin to more established metalloporphyrin frameworks.

3.6 Acknowledgements

The authors would like to thank Dr. Jeffrey L. Parks for providing the ICP data. The authors are grateful to Ran Liu, Russell Snead for helpful discussion. This material is based upon work supported by the U.S. department of Energy, Office of Basic Energy Sciences under Award Number DE-SC0012445. Use of the Advanced Photon Source, an Office of Science User Facility operated for the U.S. Department of Energy (DOE) Office of Science by Argonne National Laboratory, was supported by the U.S. DOE under Contract No. DE-AC02-06CH11357. SDS was supported by the U.S. Department of Energy, Office of Science, Office of Basic Energy Sciences, and Catalysis Science Program under contract No. DE-SC0012704. D.-R. Zhu thanks the National Natural Science Foundation of China (No. 21476115) for financial support.

3.7 References

1. Zhou, H.-C.; Long, J. R.; Yaghi, O. M. *Chem. Rev.* **2012**, *112*, 673-674.
2. Kitagawa, S. *Chem. Soc. Rev.* **2014**, *43* (16), 5415-5418.
3. Ferey, G. *Chem. Soc. Rev.* **2008**, *37*, 191-214.
4. Li, J.-R.; Sculley, J.; Zhou, H.-C. *Chem. Rev.* **2012**, *112*, 869-932.
5. Qiu, S.; Xue, M.; Zhu, G. *Chem. Soc. Rev.* **2014**, *43*, 6116-6140.

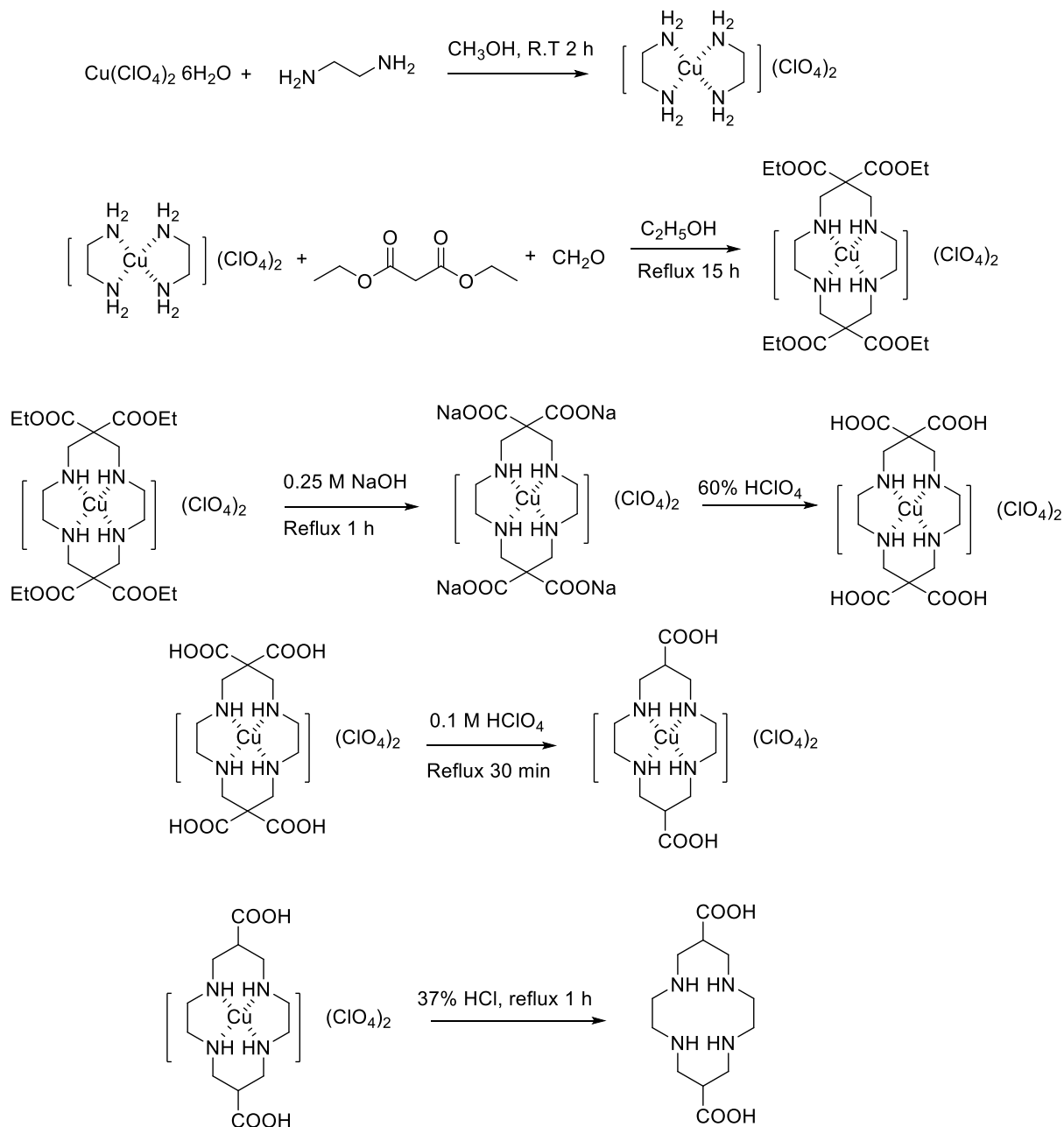
6. Hu, Z.; Deibert, B. J.; Li, J. *Chem. Soc. Rev.* **2014**, *43*, 5815-5840.
7. Kreno, L. E.; Leong, K.; Farha, O. K.; Allendorf, M.; Van Duyne, R. P.; Hupp, J. T. *Chem. Rev.* **2012**, *112*, 1105-1125.
8. Della Rocca, J.; Liu, D.; Lin, W. *Acc. Chem. Res.* **2011**, *44*, 957-968.
9. Liu, J.; Chen, L.; Cui, H.; Zhang, J.; Zhang, L.; Su, C.-Y., *Chem. Soc. Rev.* **2014**, *43*, 6011-6061.
10. Zhang, T.; Lin, W. *Chem. Soc. Rev.* **2014**, *43*, 5982-5993.
11. Usov, P. M.; Ahrenholtz, S. R.; Maza, W. A.; Stratakes, B.; Epley, C. C.; Kessinger, M. C.; Zhu, J.; Morris, A. J. *J. Mater. Chem. A* **2016**, *4*, 16818-16823.
12. Lin, S.; Pineda-Galvan, Y.; Maza, W. A.; Epley, C. C.; Zhu, J.; Kessinger, M. C.; Pushkar, Y.; Morris, A. J. *ChemSusChem* **2016**, *10*, 514-522.
13. Zhang, J.-P.; Liao, P.-Q.; Zhou, H.-L.; Lin, R.-B.; Chen, X.-M. *Chem. Soc. Rev.* **2014**, *43*, 5789-5814.
14. Jiang, J.; Zhao, Y.; Yaghi, O. M. *J. Am. Chem. Soc.* **2016**, *138*, 3255-3265.
15. Zhu, J.; Maza, W. A.; Morris, A. J. *Journal of Photochemistry and Photobiology A: Chemistry* **2017**, *344*, 64-77.
16. Cohen, S. M. *Chem. Rev.* **2012**, *112*, 970-1000.
17. Liang, X.; Sadler, P. J. *Chem. Soc. Rev.* **2004**, *33*, 246-266.
18. Kent Barefield, E. *Coord. Chem. Rev.* **2010**, *254*, 1607-1627.
19. Schneider, J.; Jia, H.; Muckerman, J. T.; Fujita, E. *Chem. Soc. Rev.* **2012**, *41*, 2036-2051.
20. Fisher, B. J.; Eisenberg, R. *J. Am. Chem. Soc.* **1980**, *102*, 7361-7363.
21. Schneider, J.; Jia, H.; Kobiros, K.; Cabelli, D. E.; Muckerman, J. T.; Fujita, E. *Energy Environ. Sci.* **2012**, *5*, 9502-9510.
22. Froehlich, J. D.; Kubiak, C. P. *J. Am. Chem. Soc.* **2015**, *137*, 3565-3573.
23. Ogata, T.; Yamamoto, Y.; Wada, Y.; Murakoshi, K.; Kusaba, M.; Nakashima, N.; Ishida, A.; Takamuku, S.; Yanagida, S. *J. Phys. Chem.* **1995**, *99*, 11916-11922.
24. Matsuoka, S.; Yamamoto, K.; Ogata, T.; Kusaba, M.; Nakashima, N.; Fujita, E.; Yanagida, S. *J. Am. Chem. Soc.* **1993**, *115*, 601-609.
25. Morris, A. J.; Meyer, G. J.; Fujita, E. *Acc. Chem. Res.* **2009**, *42*, 1983-1994.
26. De Leo, M.; Ford, P. C. *J. Am. Chem. Soc.* **1999**, *121*, 1980-1981.
27. Ostrowski, A. D.; Absalonsen, R. O.; Leo, M. A. D.; Wu, G.; Pavlovich, J. G.; Adamson, J.; Azhar, B.; Iretskii, A. V.; Megson, I. L.; Ford, P. C. *Inorg. Chem.* **2011**, *50*, 4453-4462.
28. Lee, E. Y.; Suh, M. P. *Angew. Chem., Int. Ed.* **2004**, *43*, 2798-2801.
29. Larionova, J.; Clérac, R.; Donnadiou, B.; Willemin, S.; Guérin, C. *Crystal Growth & Design* **2003**, *3*, 267-272.
30. Choi, H.-S.; Suh, M. P. *Angew. Chem., Int. Ed.* **2009**, *48*, 6865-6869.
31. Lee, E. Y.; Suh, M. P. *Angew. Chem.* **2004**, *116*, 2858-2861.
32. Martín-Caballero, J.; San José Wéry, A.; Reinoso, S.; Artetxe, B.; San Felices, L.; El Bakkali, B.; Trautwein, G.; Alcañiz-Monge, J.; Vilas, J. L.; Gutiérrez-Zorrilla, J. M. *Inorg. Chem.* **2016**, *55*, 4970-4979.
33. Almasi, M.; Zelenak, V.; Zukal, A.; Kuchar, J.; Cejka, J. *Dalton Trans.* **2016**, *45*, 1233-1242.
34. Kwag, J. S.; Kim, J. C.; Lough, A. J.; Lee, B. M. *Transition Met. Chem.* **2010**, *35*, 41-47.
35. Hawes, C. S.; Batten, S. R.; Turner, D. R. *CrystEngComm* **2014**, *16*, 3737-3748.
36. Gao, W.-Y.; Chen, Y.; Niu, Y.; Williams, K.; Cash, L.; Perez, P. J.; Wojtas, L.; Cai, J.; Chen, Y.-S.; Ma, S. *Angew. Chem., Int. Ed.* **2014**, *53*, 2615-2619.
37. Bai, Y.; Dou, Y.; Xie, L.-H.; Rutledge, W.; Li, J.-R.; Zhou, H.-C. *Chem. Soc. Rev.* **2016**, *45*, 2327-2367.
38. Banerjee, D.; Xu, W.; Nie, Z.; Johnson, L. E. V.; Coghlan, C.; Sushko, M. L.; Kim, D.; Schweiger, M. J.; Kruger, A. A.; Doonan, C. J.; Thallapally, P. K. *Inorg. Chem.* **2016**, *55*, 8241-8243.
39. Su, F.; Zhang, S.; Ji, H.; Zhao, H.; Tian, J.-Y.; Liu, C.-S.; Zhang, Z.; Fang, S.; Zhu, X.; Du, M. *ACS Sens.* **2017**, *2*, 998-1005.
40. He, T.; Ni, B.; Xu, X.; Li, H.; Lin, H.; Yuan, W.; Luo, J.; Hu, W.; Wang, X. *ACS Appl. Mater. Interfaces* **2017**, *9*, 22732-22738.
41. Gutov, O. V.; Bury, W.; Gomez-Gualdron, D. A.; Krungleviciute, V.; Fairen-Jimenez, D.; Mondloch, J. E.; Sarjeant, A. A.; Al-Juaid, S. S.; Snurr, R. Q.; Hupp, J. T.; Yildirim, T.; Farha, O. K. *Chem. Eur. J.* **2014**, *20*, 12389-12393.
42. Grancha, T.; Qu, X.; Julve, M.; Ferrando-Soria, J.; Armentano, D.; Pardo, E. *Inorg. Chem.* **2017**, *56*, 6551-6557.
43. Suh, M. P.; Choi, H. J.; So, S. M.; Kim, B. M. *Inorg. Chem.* **2003**, *42*, 676-678.

44. Gao, W.-Y.; Chrzanowski, M.; Ma, S. *Chem. Soc. Rev.* **2014**, *43*, 5841-5866.
45. Xin, L.; Curtis, N. F.; Weatherburn, D. C. *Transition Met. Chem.* **1992**, *17*, 147-154.
46. Toby, B. H.; Von Dreele, R. B. *J. Appl. Crystallogr.* **2013**, *46*, 544-549.
47. *CrysAlisPro Software System*, v1.171.38.43; Rigaku Corporation, Oxford, UK.: 2017.
48. Sheldrick, G. M. *Acta Crystallogr., Sect. A: Found. Adv.* **2015**, *71*, 3-8.
49. Sheldrick, G. M. *Acta Crystallogr., Sect. A: Found. Adv.* **2008**, *64*, 112-122.
50. Dolomanov, O. V.; Bourhis, L. J.; Gildea, R. J.; Howard, J. A.; Puschmann, H. *J. Appl. Crystallogr.* **2009**, *42*, 339-341.
51. Barefield, E. K.; Billo, E. J. *Acta Lett* **1984**, *81*, 9.
52. Billo, E. J. *Inorg. Chem.* **1984**, *23*, 236-238.
53. Barefield, E. K.; Bianchi, A.; Billo, E. J.; Connolly, P. J.; Paoletti, P.; Summers, J. S.; Van Derveer, D. G. *Inorg. Chem.* **1986**, *25*, 4197-4202.
54. Wißmann, G.; Schaate, A.; Lilienthal, S.; Bremer, I.; Schneider, A. M.; Behrens, P. *Microporous Mesoporous Mater.* **2012**, *152*, 64-70.
55. Hu, Z.; Castano, I.; Wang, S.; Wang, Y.; Peng, Y.; Qian, Y.; Chi, C.; Wang, X.; Zhao, D. *Cryst. Growth Des.* **2016**, *16*, 2295-2301.
56. Serre, C.; Millange, F.; Surblé, S.; Férey, G. *Angew. Chem., Int. Ed.* **2004**, *43*, 6285-6289.
57. Guillermin, V.; Gross, S.; Serre, C.; Devic, T.; Bauer, M.; Férey, G. *Chem. Commun.* **2010**, *46*, 767-769.
58. Feng, D.; Gu, Z.-Y.; Li, J.-R.; Jiang, H.-L.; Wei, Z.; Zhou, H.-C. *Angew. Chem., Int. Ed.* **2012**, *51*, 10307-10310.
59. Mondloch, J. E.; Bury, W.; Fairen-Jimenez, D.; Kwon, S.; DeMarco, E. J.; Weston, M. H.; Sarjeant, A. A.; Nguyen, S. T.; Stair, P. C.; Snurr, R. Q.; Farha, O. K.; Hupp, J. T. *J. Am. Chem. Soc.* **2013**, *135*, 10294-10297.
60. Macrae, C. F.; Bruno, I. J.; Chisholm, J. A.; Edgington, P. R.; McCabe, P.; Pidcock, E.; Rodriguez-Monge, L.; Taylor, R.; van de Streek, J.; Wood, P. A. *J. Appl. Crystallogr.* **2008**, *41*, 466-470.
61. Dolomanov, O. V.; Bourhis, L. J.; Gildea, R. J.; Howard, J. A. K.; Puschmann, H. *J. Appl. Crystallogr.* **2009**, *42*, 339-341.
62. Diaz F, G.; Clavijo C, R. E.; Campos-Vallette, M. M.; Saavedra S, M.; Diez, S.; Muñoz, R. *Vib. Spectrosc.* **1997**, *15*, 201-209.
63. Kavaklı, C.; Tuncel, S. A.; Salih, B. *Sep. Purif. Technol.* **2005**, *45*, 32-40.
64. DeCoste, J. B.; Peterson, G. W.; Jasuja, H.; Glover, T. G.; Huang, Y.-g.; Walton, K. S. *J. Mater. Chem. A* **2013**, *1*, 5642-5650.
65. Ahrenholtz, S. R.; Landaverde-Alvarado, C.; Whiting, M.; Lin, S.; Slebodnick, C.; Marand, E.; Morris, A. J. *Inorg. Chem.* **2015**, *54*, 4328-4336.
66. Landaverde-Alvarado, C.; Morris, A. J.; Martin, S. M. *J. CO2 Util.* **2017**, *19*, 40-48.
67. Sumida, K.; Rogow, D. L.; Mason, J. A.; McDonald, T. M.; Bloch, E. D.; Herm, Z. R.; Bae, T.-H.; Long, J. R. *Chem. Rev.* **2011**, *112*, 724-781.
68. Cokoja, M.; Bruckmeier, C.; Rieger, B.; Herrmann, W. A.; Kühn, F. E. *Angew. Chem., Int. Ed.* **2011**, *50*, 8510-8537.
69. Yoshida, M.; Ihara, M. *Chem. Eur. J.* **2004**, *10*, 2886-2893.
70. Beyzavi, M. H.; Stephenson, C. J.; Liu, Y.; Karagiari, O.; Hupp, J. T.; Farha, O. K. *Front. Energy Res.* **2015**, *2*.
71. He, H.; Perman, J. A.; Zhu, G.; Ma, S. *Small* **2016**, *12*, 6309-6324.
72. Maina, J. W.; Pozo-Gonzalo, C.; Kong, L.; Schutz, J.; Hill, M.; Dumez, L. F. *Mater. Horiz.* **2017**, *4*, 345-361.
73. Beyzavi, M. H.; Klet, R. C.; Tussupbayev, S.; Borycz, J.; Vermeulen, N. A.; Cramer, C. J.; Stoddart, J. F.; Hupp, J. T.; Farha, O. K. *J. Am. Chem. Soc.* **2014**, *136*, 15861-15864.
74. Zou, B.; Hao, L.; Fan, L.-Y.; Gao, Z.-M.; Chen, S.-L.; Li, H.; Hu, C.-W. *J. Catal.* **2015**, *329*, 119-129.
75. Gao, W.-Y.; Tsai, C.-Y.; Wojtas, L.; Thiounn, T.; Lin, C.-C.; Ma, S. *Inorg. Chem.* **2016**, *55*, 7291-7294.
76. Guillermin, V.; WeselińskiŁukasz, J.; Belmabkhout, Y.; Cairns, A. J.; D'Elia, V.; WojtasŁukasz; Adil, K.; Eddaoudi, M. *Nat. Chem.* **2014**, *6*, 673-680.
77. Feng, D.; Chung, W.-C.; Wei, Z.; Gu, Z.-Y.; Jiang, H.-L.; Chen, Y.-P.; Darensbourg, D. J.; Zhou, H.-C. *J. Am. Chem. Soc.* **2013**, *135*, 17105-17110.

3.8 Supporting Information

3.8.1 Ligand Synthesis and Characterization

The 6,13-dicarboxy-1,4,8,11-tetrazacyclotetradecan)-copper (II) perchlorate $[\text{CuL}(\text{ClO}_4)_2]$ and 6,13-dicarboxy-1,4,8,11-tetrazacyclotetradecan (L) ligands were synthesized based on previous reports¹ with minor modifications. The cyclam-based ligands can be obtained using a 5 steps synthetic route starting from Cu(II) perchlorate and ethylene diamine (Scheme S1).



Scheme S1. Synthetic scheme for the cyclam-based ligands.

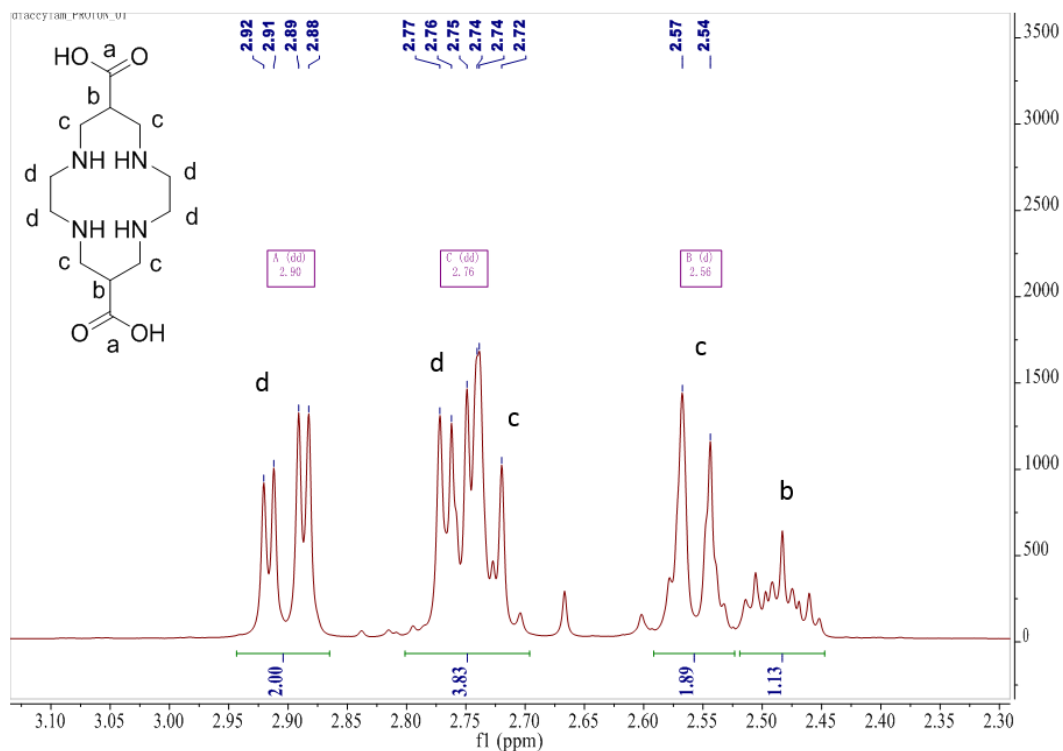


Figure S1. ¹H NMR spectrum of 6,13-dicarboxy-1,4,8,11-tetrazacyclotetradecan (**2**) in KOH/D₂O.

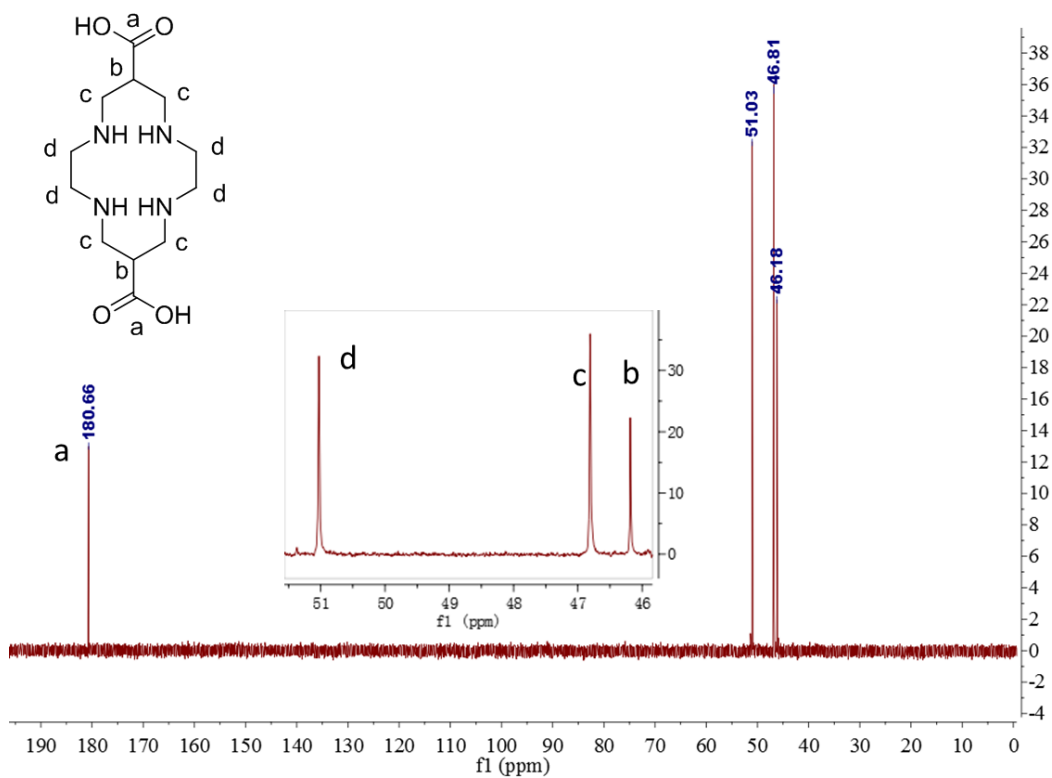


Figure S2. ¹³C NMR spectrum of 6,13-dicarboxy-1,4,8,11-tetrazacyclotetradecan (**2**) in KOH/D₂O.

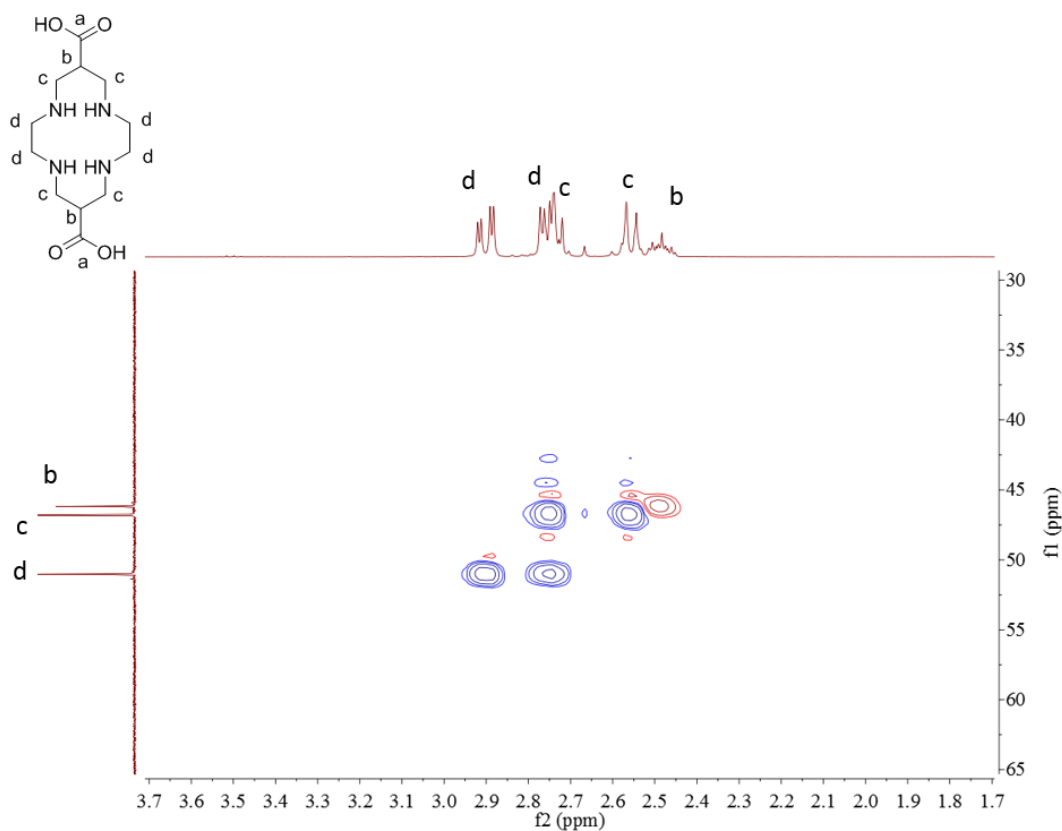


Figure S3. HSQC spectrum of 6,13-dicarboxy-1,4,8,11-tetrazacyclotetradecan (**2**) in KOH/D₂O.

3.8.2 Single-Crystal X-ray Crystallography

Table S1. Crystal data and structure refinements for [CuL(ClO₄)₂] (**1**) and [NiL(ClO₄)₂]·2H₂O (**3**).

	(1)	(3)
Compound name	[CuL(ClO ₄) ₂]	[NiL(ClO ₄) ₂]·2H ₂ O
Chemical formula	C ₁₂ H ₂₄ Cl ₂ CuN ₄ O ₁₂	C ₁₂ H ₂₈ Cl ₂ N ₄ NiO ₁₄
Formula mass	550.79	581.99
Crystal system	triclinic	monoclinic
Space group	P-1 (No.2)	P2 ₁ /n (No.14)
Wavelength/Å	0.71073	1.54184
a/ Å	8.5135(5)	8.5347(5)
b/ Å	9.7381(4)	15.2793(11)
c/ Å	13.3092(7)	8.7620(7)
α/deg	90.048(4)	90.00
β/deg	104.471(5)	103.592(8)

γ /deg	95.762(4)	90.00
Unit cell volume/ \AA^3	1062.61(10)	1110.59(14)
Z	2	2
μ /mm ⁻¹	1.347	4.193
Density/ g·cm ⁻³	1.721	1.740
T/K	101	250
2 θ range/deg	3.752 to 32.250	5.332 to 75.089
Reflections collected	11232	10087
Independent reflections	6900 [R(int) = 0.0348]	2266 [R(int) = 0.0526]
Goodness of fit	1.062	1.093
R indices [I > 2 σ (I)]	R1 = 0.0541	R1 = 0.0637
	wR2 = 0.1103	wR2 = 0.1593
R indices (all data)	R1 = 0.0784	R1 = 0.0720
	wR2 = 0.1221	wR2 = 0.1650

Table S2. Crystal data and structure refinements for [CuLCl₂] (**4**) and [NiLCl₂] \cdot 2DMF (**5**).

	(4)	(5)
Compound name	[CuLCl ₂]	[NiLCl ₂] \cdot 2DMF
Chemical formula	C ₁₂ H ₂₄ Cl ₂ CuN ₄ O ₄	C ₁₈ H ₃₈ Cl ₂ N ₆ NiO ₆
Formula mass	422.79	564.15
Crystal system	monoclinic	triclinic
Space group	P2 ₁ /n (No.14)	P-1 (No.2)
Wavelength/ \AA	0.71073	1.54184
a/ \AA	6.7984(4)	6.5665(3)
b/ \AA	9.7309(5)	8.8382(5)
c/ \AA	12.9543(7)	11.8641(5)
α /deg	90.00	71.886(4)
β /deg	93.913(5)	86.219(4)

γ/deg	90.00	73.762(5)
Unit cell volume/ \AA^3	854.98(8)	628.15(6)
Z	2	1
μ/mm^{-1}	1.613	3.462
Density/ $\text{g}\cdot\text{cm}^{-3}$	1.642	1.491
T/K	100	100
2θ range/deg	3.662 to 32.346	3.921 to 74.979
Reflections collected	9225	7818
Independent reflections	2782 [R(int) = 0.0449]	2563 [R(int) = 0.0468]
Goodness of fit	1.0860	1.0370
R indices [$I > 2\sigma(I)$]	R1 = 0.0405	R1 = 0.0356
	wR2 = 0.0758	wR2 = 0.0879
R indices (all data)	R1 = 0.0551	R1 = 0.0426
	wR2 = 0.0803	wR2 = 0.0935

3.8.3 Structure determination and refinement of VPI-100 (Cu) and VPI-100 (Ni)

XRD indexing and Rietveld analysis was performed with TOPAS version 5. Figure 3.2 shows the XRD profiles of VPI-100 (Cu) and VPI-100 (Ni) at room temperature. Both patterns have intense low angle peaks, which are commonly seen in XRD of porous structures. The high similarity between the as-synthesized VPI-100 (Cu) and VPI-100 (Ni) suggest they are of the same framework structure. Indexing of the two patterns both suggested a body-centered tetragonal lattice with unit cell parameters: $a \sim 17 \text{ \AA}$ and $c \sim 20 \text{ \AA}$. Considering the symmetry of Zr cluster and the cyclam ligand, it is natural to locate the Zr-cluster at the unit cell origin and thus at the body center and align the cluster's four-fold axis with the c-axis of the tetragonal unit cell. One cyclam ligand connects to both clusters at the origin and at the body center through the carboxylate at each end. In total, there are eight ligands and two Zr-clusters in one unit cell. The Zr-cluster is likely to be Zr_6 rather than Zr_8 , as the latter is bigger in size and does not leave enough room to accommodate the ligand in the unit cell. Chemical analysis from ICP-

MS showed a Ni/Zr ratio of 0.67 and a Cu/Zr ratio of 0.63, which corroborates the initial structure model assuming 8 ligands and 2 Zr_6 clusters in one cell which yields a theoretical Ni (Cu)/Zr ratio of 2/3. Out of 8 possible space groups, based on Laue symmetry and systematic absences, $I4/m$ was selected as it is congruent with the initial model and the symmetry of individual clusters and ligands. The Zr_6 cluster and the ligand were treated as rigid bodies in the Rietveld refinement with the Zr-O bond lengths and angles and the ligand torsion angles allowed to vary within reasonable ranges. Different conformations of the cyclam ligand resolved from the single crystal structure solutions were considered. The geometry presented in $[CuLCl_2]$ (**4**) and $[NiLCl_2] \cdot DMF$ (**5**) as shown in Figure 1 C & D gave the best fit. In the pores, oxygen atoms were used to model the various disordered solvent molecules. According to the synthesis procedure, DMF is expected in both MOFs but should be diffusely distributed and were not introduced in the models. Since the oxygen atoms in the pores represented all solvents and not just water, there was no concern when solvent oxygen atoms were close to each other or close to the equatorial oxygen of the Zr_6 cluster. The refinement model also suggested the presence of chloride, similar to the single crystal structures of the ligands presented. The diffraction pattern, however, is much lower resolution (only weak intensities above ~ 1.8 Å) than typically required for Rietveld analysis (1 Å). As a result, the Cl positions are ambiguous. In addition, there was correlation between modeling positions of the Cl and the solvent oxygens, contributing further to the ambiguity in the positions and contents of the pores. In the final refinement, Cl was restrained to Ni/Cu within a distance range of 2.2 to 4.2 Å and the N-Ni(Cu)-Cl angles were allowed a distortion within 10° from the right angle. The resulting M-Cl distances were ~ 3.1 Å for Ni-Cl and ~ 3.4 Å for Cu-Cl, larger than the observed in the single crystal structures of the ligands. Atomic displacement factors were initially allowed to vary within reasonable value ranges in order to fit the trend of the rapid decay of peak intensities going to high 2θ angles, and were eventually fixed in the final stages of the refinement. The refined structures were attached as CIFs. The fitted PXRD patterns are shown in Figures S4 and S5.

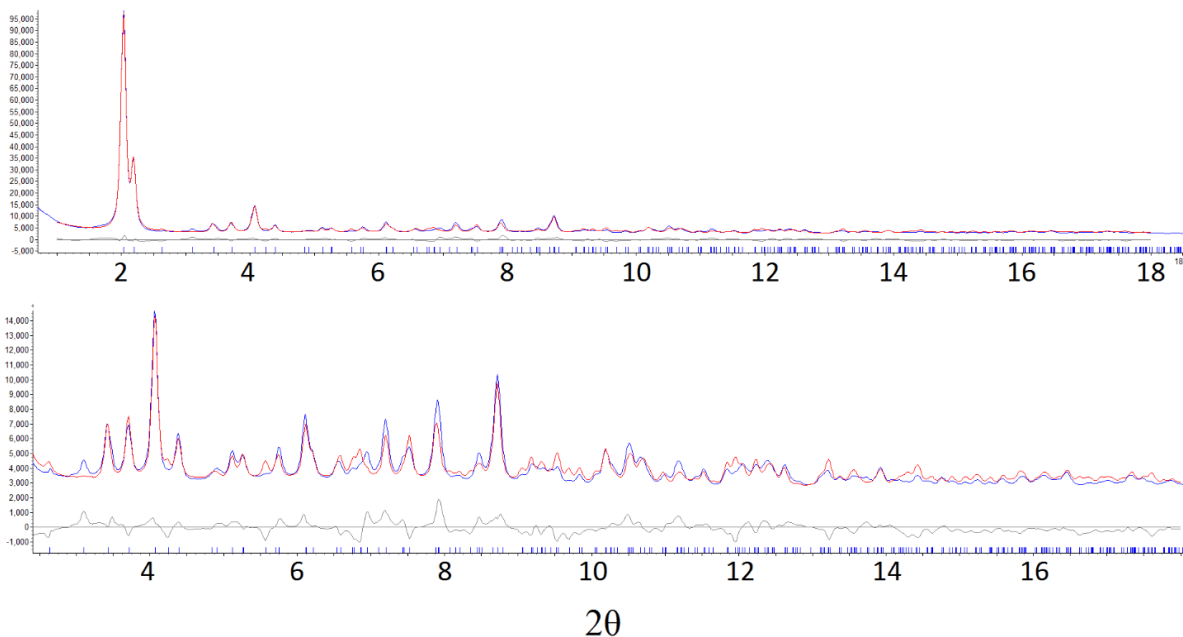


Figure S4. Refinement plots of VPI-100 (Cu) as synthesized under room temperature. The bottom panel is a zoomed-in view of the low intensity peaks in the top panel. The blue line is the observed curve, the red line is the calculated curve, the grey line is the fitted background line, and the grey line oscillating around 0 is the difference between the observed and the calculated.

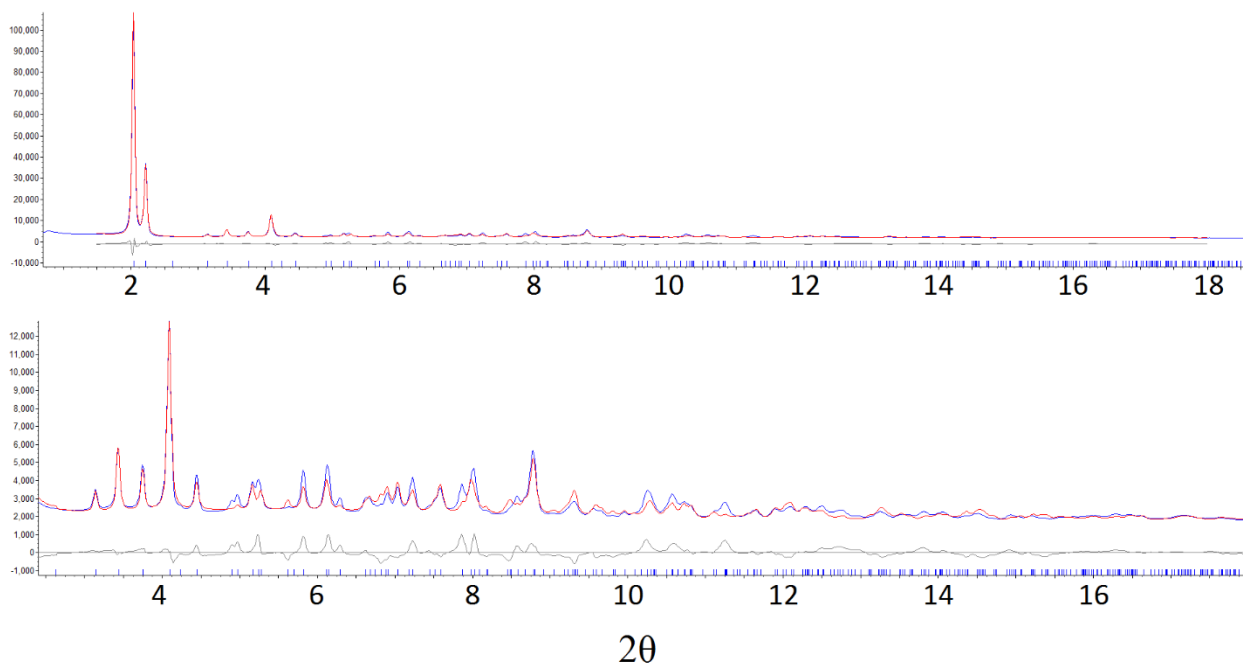


Figure S5. Refinement plots of VPI-100 (Ni) as synthesized under room temperature. The bottom panel is a zoomed-in view of the low intensity peaks in the top panel. The blue line is the observed curve, the red line is the calculated curve, the grey line is the fitted background line, and the grey line oscillating around 0 is the difference between the observed and the calculated.

3.8.4 Characterization of VPI-100 (Cu) and VPI-100 (Ni)

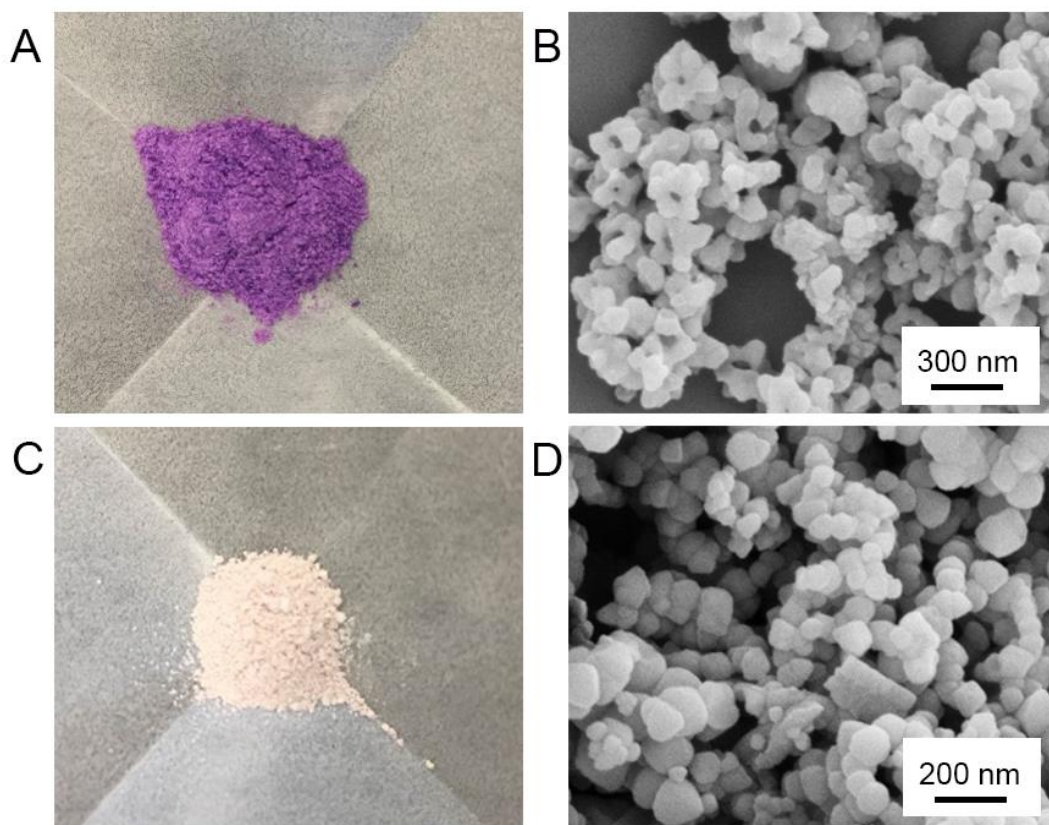


Figure S6. A) VPI-100 (Cu) powder. B) SEM image of the microcrystalline powder of VPI-100 (Cu). C) VPI-100 (Ni) powder. D) SEM image of the microcrystalline powder of VPI-100 (Ni).

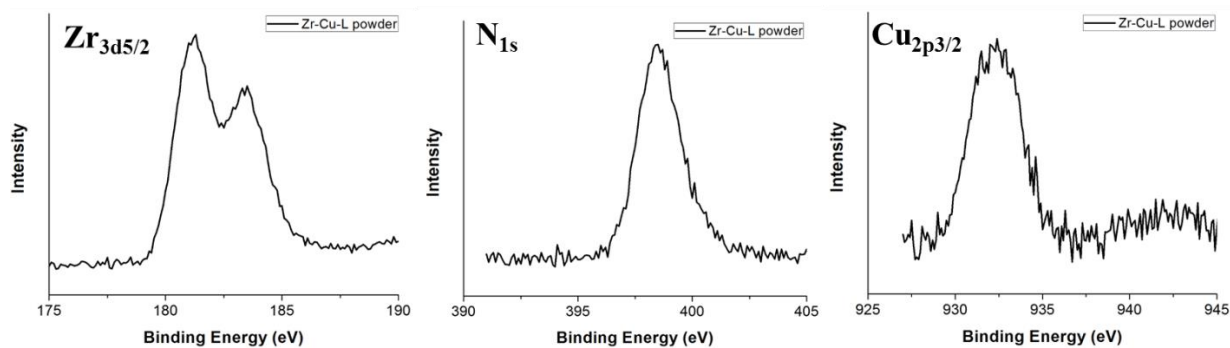


Figure S7. XPS spectrum of VPI-100 (Cu) powder displaying (left to right) Zr_{3d_{5/2}}, N_{1s} and Cu_{2p_{3/2}} binding energy regions.

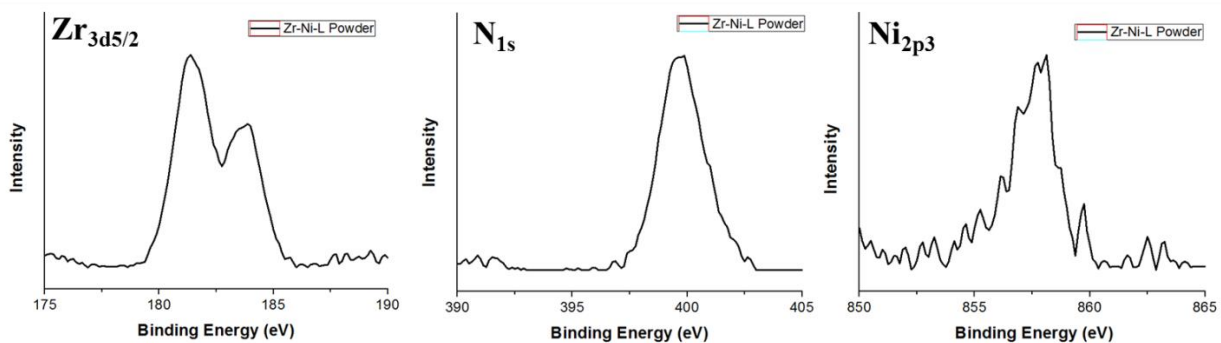


Figure S8. XPS spectrum of VPI-100 (Ni) powder displaying (left to right) Zr3d_{5/2}, N1s and Ni2p_{3/2} binding energy regions.

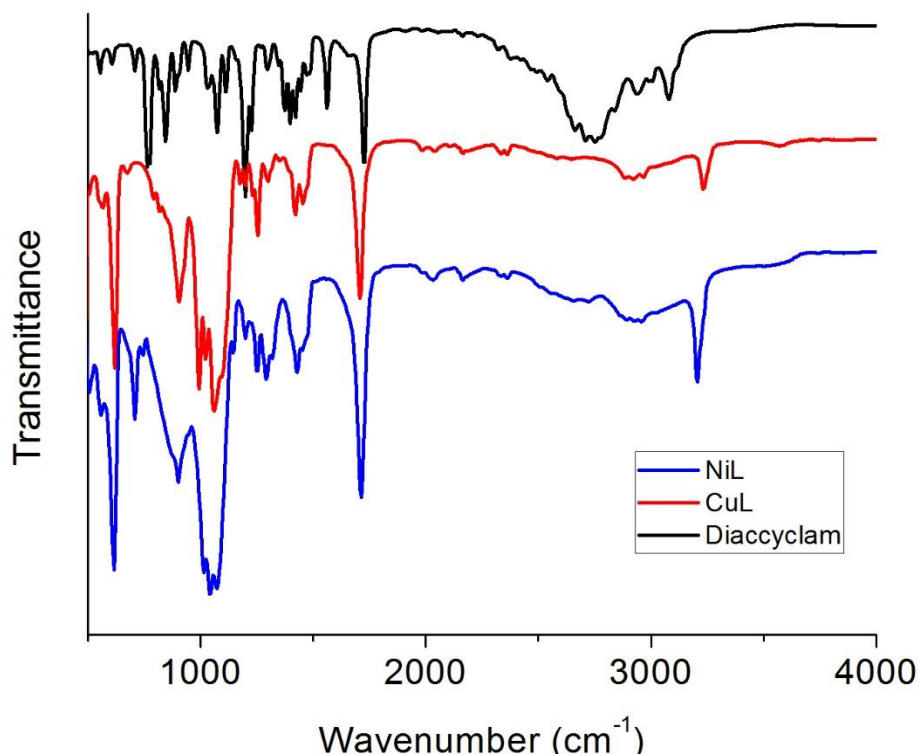


Figure S9. FTIR spectra of [CuL(ClO₄)₂] (1) (red), L (2) (black) and [NiL](ClO₄)₂ (3) (blue).

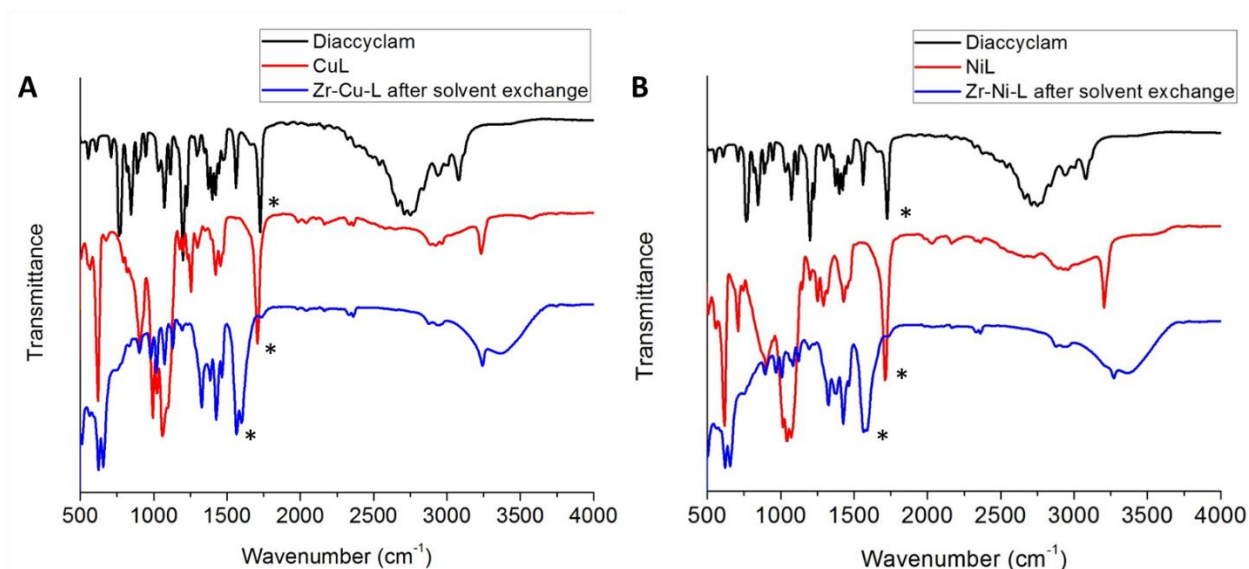


Figure S10. A) FTIR spectra of [CuL(ClO₄)₂] (1) (red), L (2) (black) and VPI-100 (Cu) (blue). B) FTIR spectra of [NiL](ClO₄)₂ (3) (red), L (2) (black) and VPI-100 (Ni) (blue). (*) indicate the peak position of carboxylate vibrational modes in the Diaccyclam.

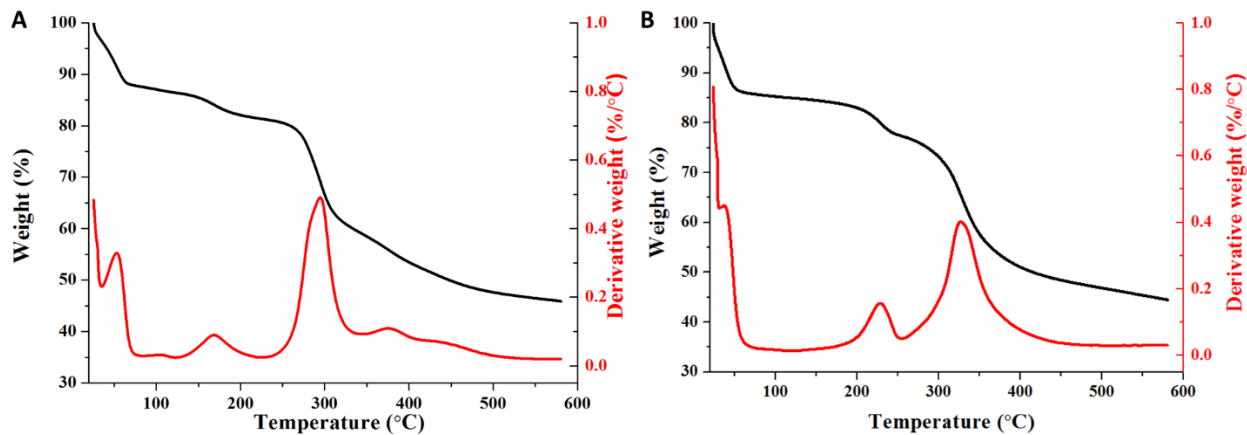


Figure S11. TGA curves of A) VPI-100 (Cu) and B) VPI-100 (Ni).

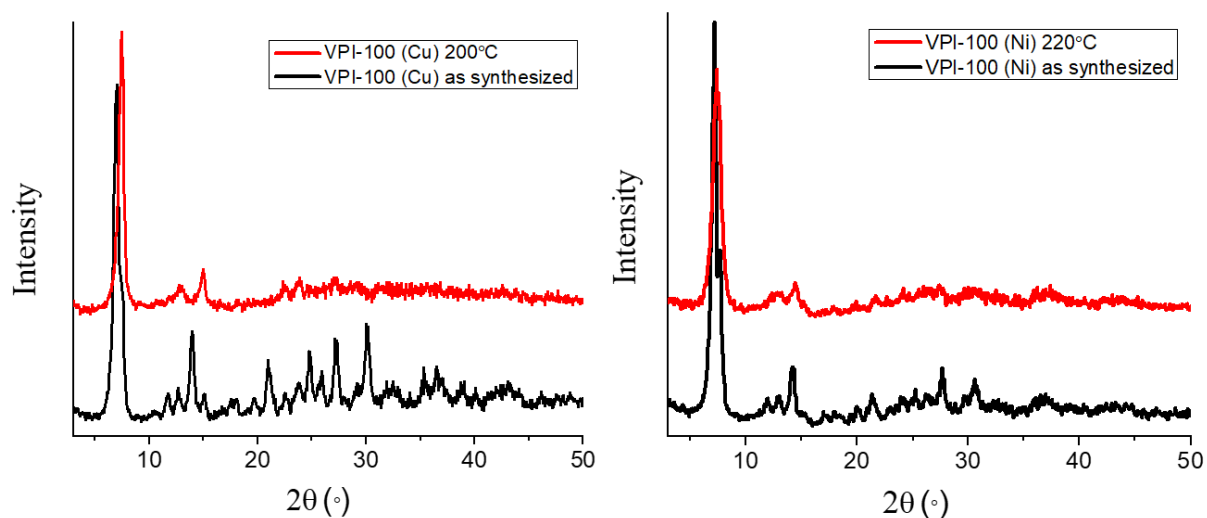


Figure S12. The *ex-situ* PXRD of A) VPI-100 (Cu) and B) VPI-100 (Ni) after thermal treatment.

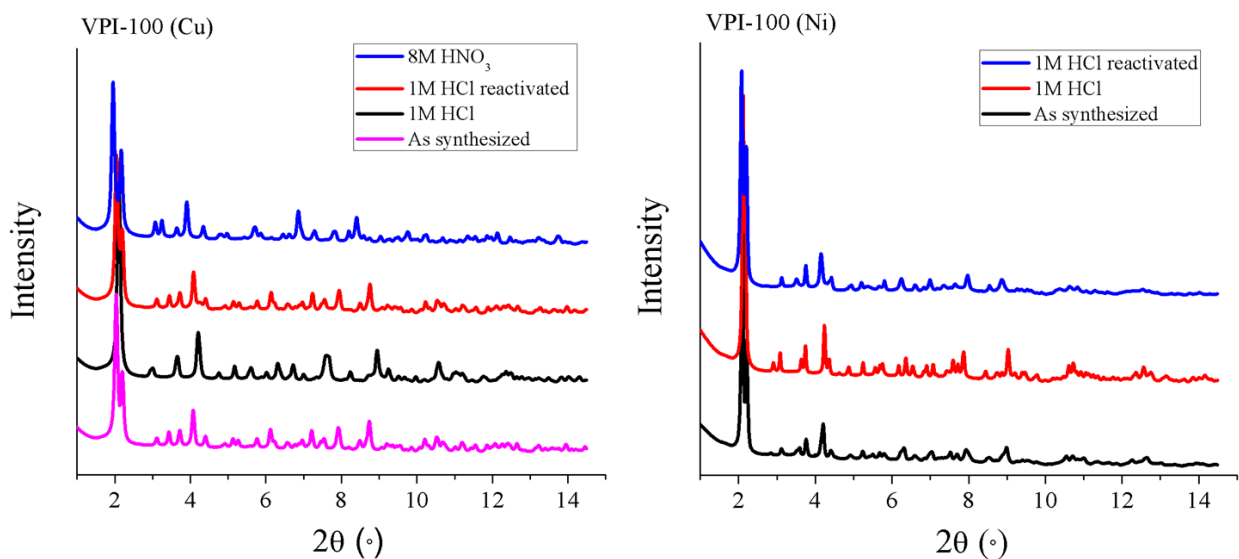


Figure S13. *in situ* synchrotron PXRD of VPI-100 after chemical treatment.

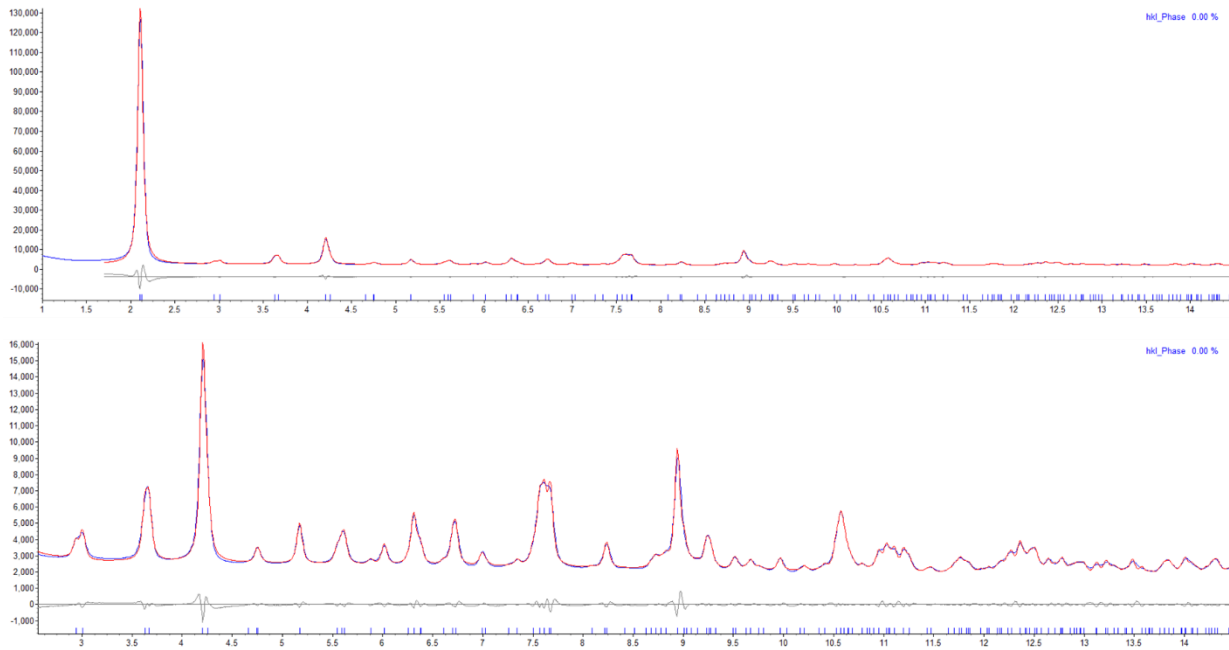


Figure S14. Le Bail refinement of VPI-100 (Cu) after 1M HCl treatment.

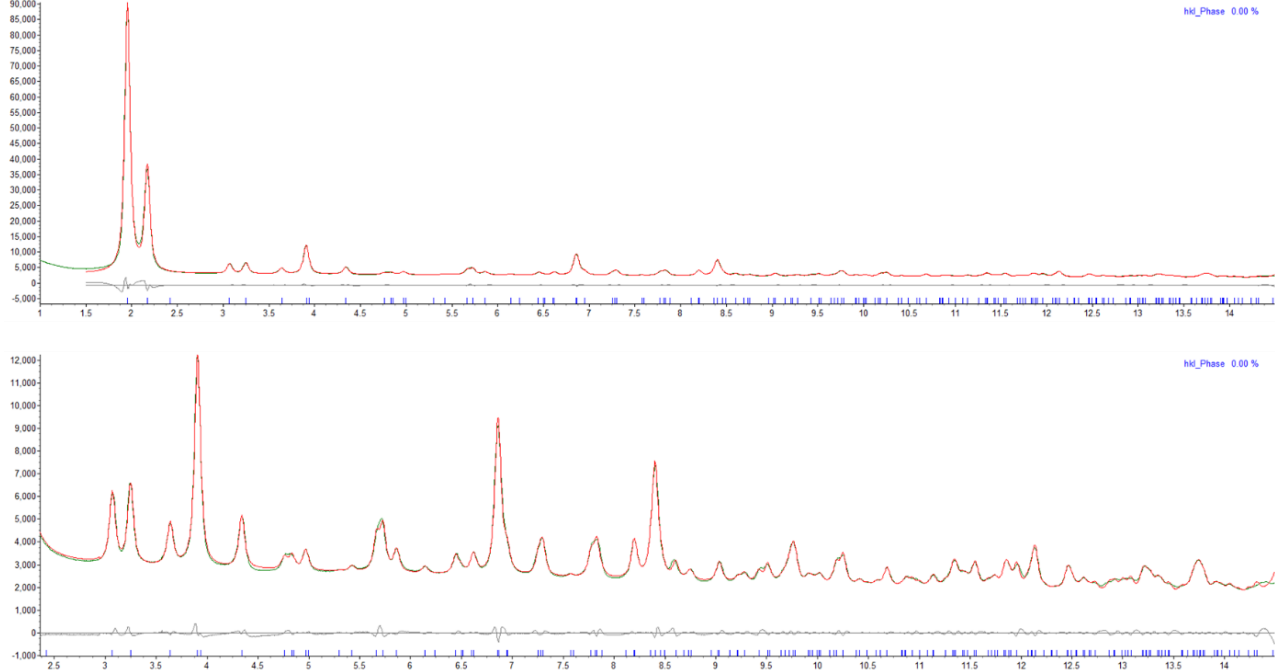


Figure S15. Le Bail refinement of VPI-100 (Cu) after 8M HNO₃ treatment.

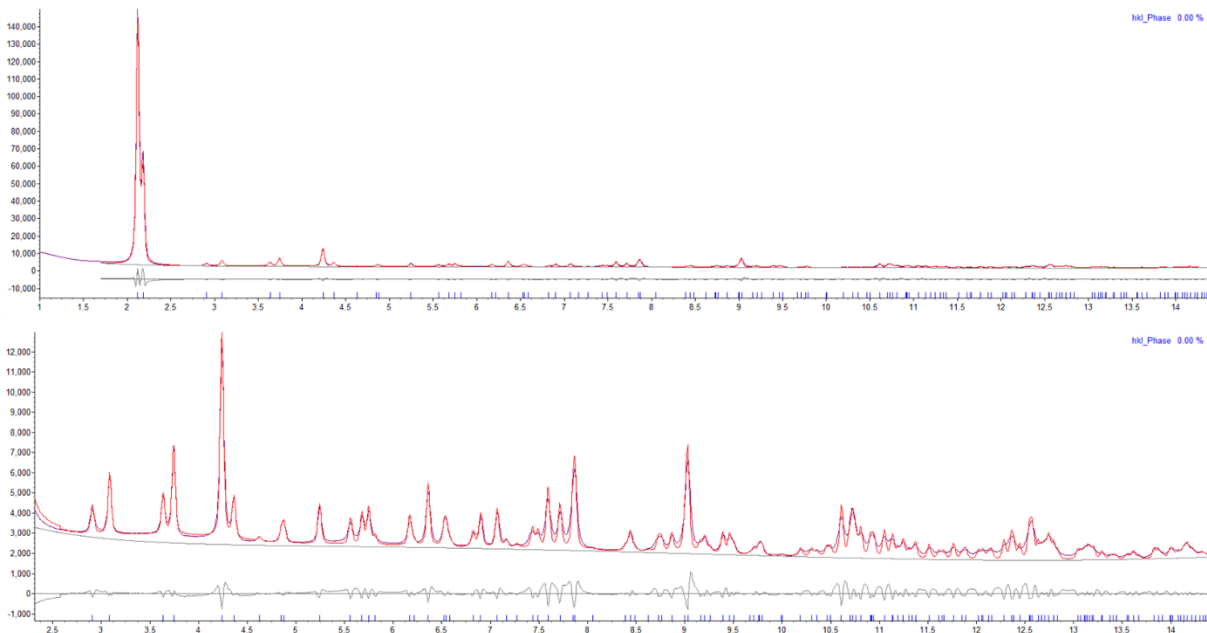


Figure S16. Le Bail refinement of VPI-100 (Ni) after 1M HCl treatment.

Table S3. Unit cell parameter after Le Bail refinement

	a (Å)	c (Å)
VPI-100 (Cu) 1M HCl	17.223	17.633
VPI-100 (Cu) 8M HNO ₃	16.881	21.435
VPI-100 (Ni) 1M HCl	16.798	17.823

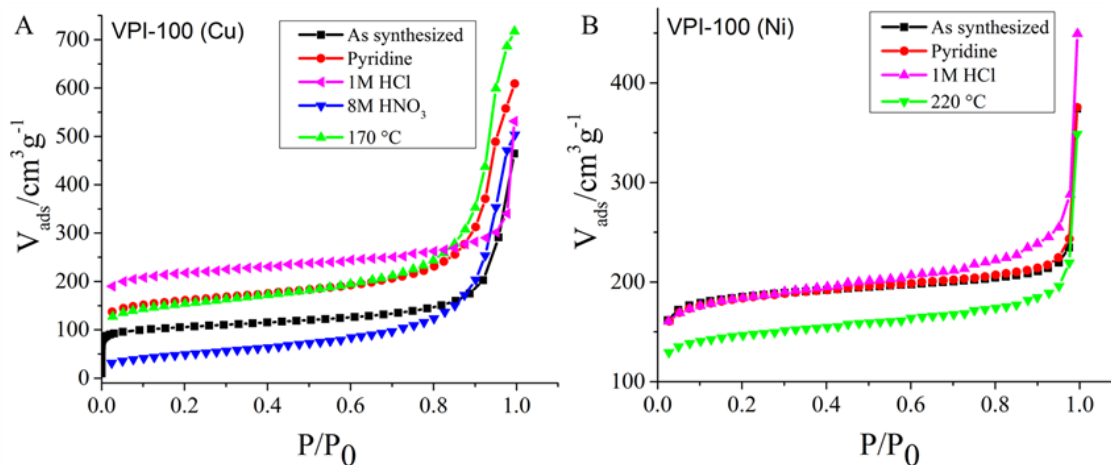


Figure S17. N₂ adsorption isothermal analysis after stability test of (A) VPI-100 (Cu) and (B) VPI-100 (Ni)

Table S4. BET of VPI-100 after stability test

VPI-100 (Cu)	BET surface area (m ² /g)	VPI-100 (Ni)	BET surface area (m ² /g)
--------------	--------------------------------------	--------------	--------------------------------------

as synthesized	398	as synthesized	612
pyridine	537	pyridine	607
1M HCl	613	1M HCl	609
8M HNO ₃	176	220 °C	485
170 °C	520		

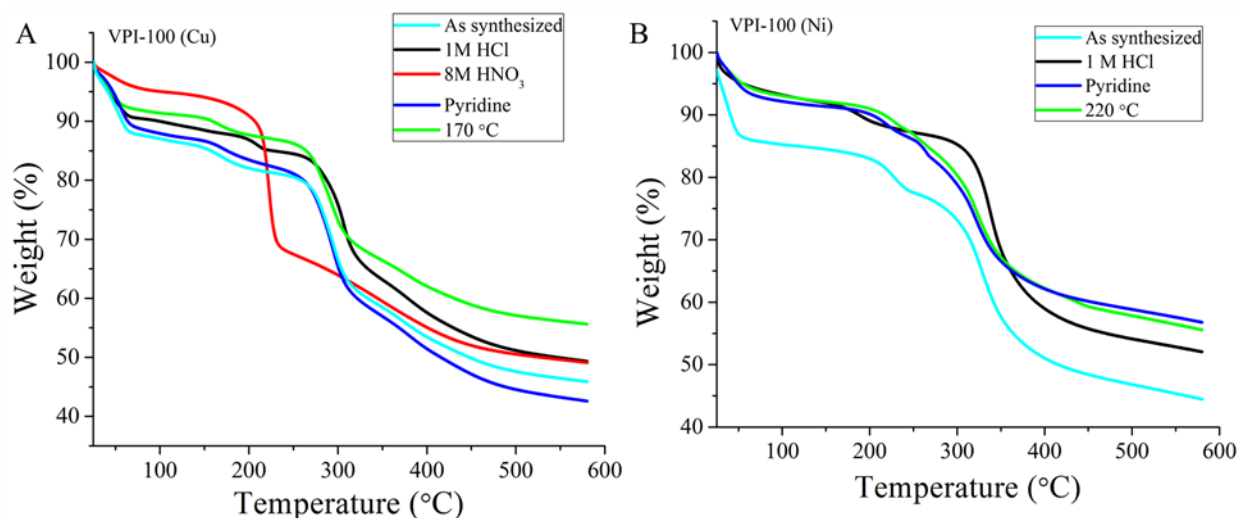


Figure S18. TGA of VPI-100 after stability test of (A) VPI-100 (Cu) and (B) VPI-100 (Ni)

3.8.5 Experimental N₂ adsorption isothermal analysis and theoretical CO₂ isotherm fitting of VPI-100 (Cu) and VPI-100 (Ni)

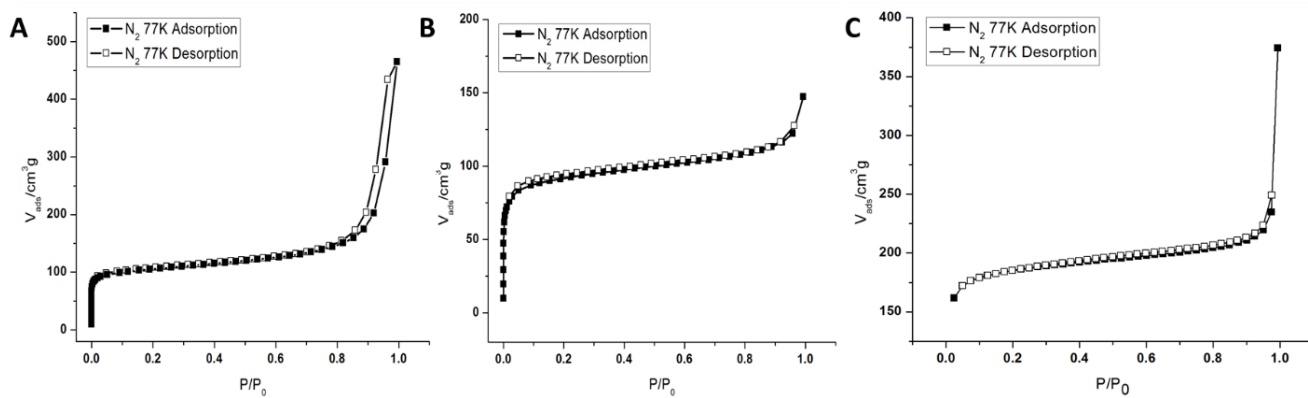


Figure S19. N₂ adsorption isotherms of (A) VPI-100 (Cu) and (B) VPI-100 (Ni) at 77 K, 1 atm after activation at 100 °C for 24 h. (C) N₂ adsorption isotherms of VPI-100 (Ni) after activation at 120 °C for 24 h.

Table S5. Summary of the parameters from Langmuir-Freundlich fit of CO₂ isotherm data at the designated temperature.

273 K			
MOF	<i>t</i>	<i>K_F</i> (KPa ⁻¹)	<i>Q_m</i> (ml/g)
VPI-100 (Cu)	1.222	0.020	71.698
VPI-100 (Ni)	1.120	0.011	70.477
VPI-100 (Ni) after activation at 120 °C	1.214	0.029	88.708
296 K			
MOF	<i>t</i>	<i>K_F</i> (KPa ⁻¹)	<i>Q_m</i> (ml/g)
VPI-100 (Cu)	1.156	0.007	65.917
VPI-100 (Ni)	1.088	0.003	70.785
VPI-100 (Ni) after activation at 120 °C	1.114	0.013	86.697

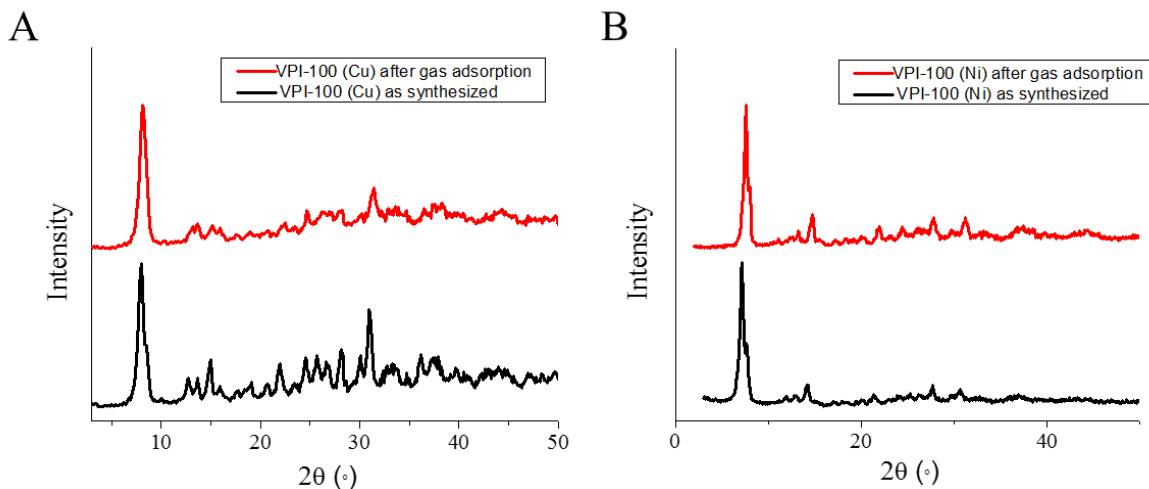
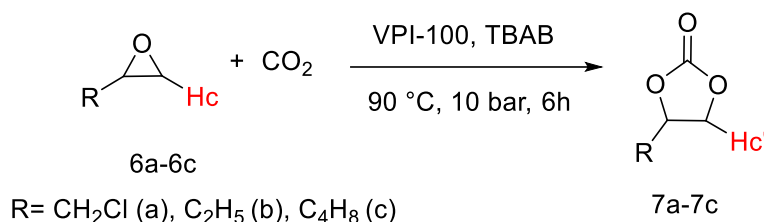


Figure S20. PXRD patterns of (A) VPI-100 (Cu) and (B) VPI-100 (Ni) before and after gas sorption measurements.

3.8.6 Catalyst studies of cycloaddition of CO₂ to epoxides using VPI-100

Determination of the conversion



Scheme S2. Synthesis of cyclic carbonates from CO₂ and epoxides catalyzed by VPI-100.

For each reaction, conversion was determined by comparison of the ¹H NMR integrals of the corresponding proton in the starting material (¹H_c) and in the product (¹H_{c'}) according to equation 1 and Supplementary Table 4.² Detailed spectrum of reaction mixture 7a has been shown as examples in Figures S14-21 below.

$$\text{Conversion} = \frac{I_{\text{Hc}'}}{(I_{\text{Hc}} + I_{\text{Hc}'})} \quad (1)$$

Table S6. Chemical shifts (δ, ppm) for the integrated proton in the epoxides and in the corresponding carbonates (in CDCl₃).

Epoxides	δH (CDCl ₃)(epoxide, ¹ H _c)	δH (CDCl ₃)(carbonate, ¹ H _{c'})
6a	2.65	4.35
6b	2.45	4.05

6c

3.05

4.65

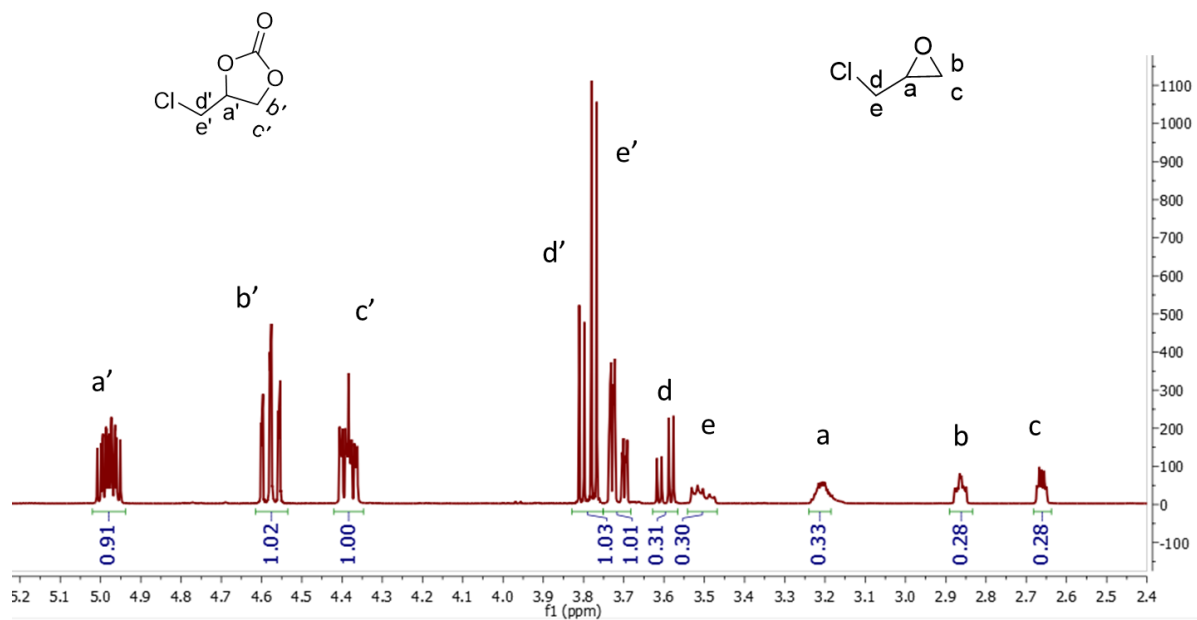


Figure S21. ¹H NMR (400 MHz, CDCl₃) spectrum of reaction mixture in Table S7 entry 1 only using TBAB as catalysts. Conversion = $1/1.28 = 78.1\%$

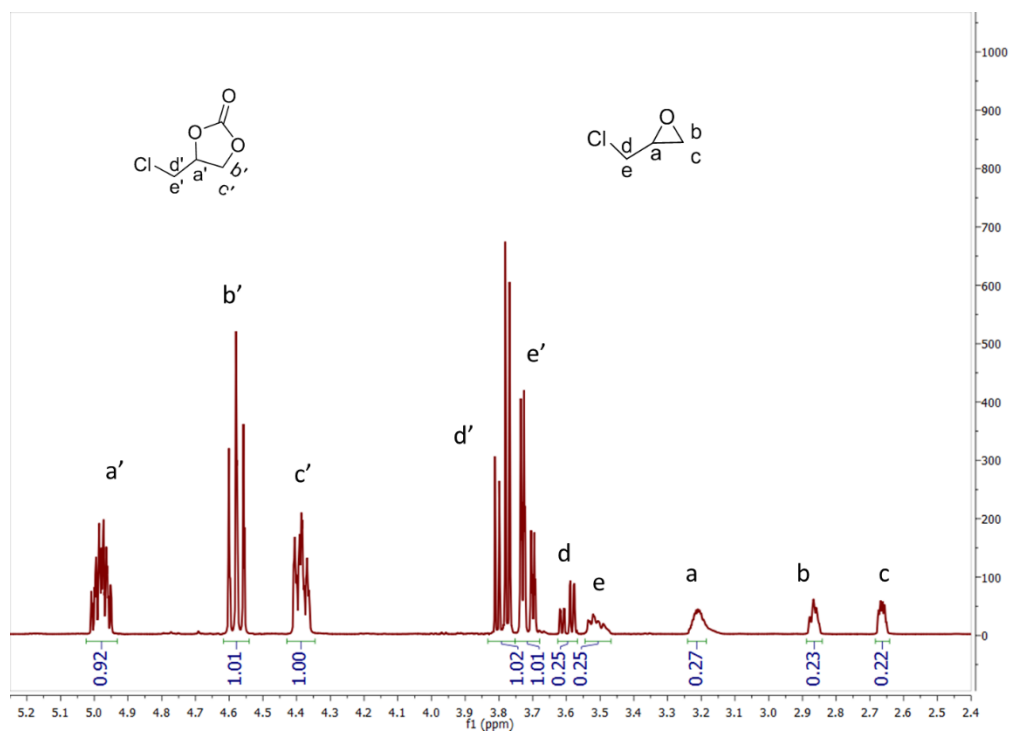


Figure S22. ¹H NMR (400 MHz, CDCl₃) spectrum of reaction mixture in Table S7 entry 2 using [CuL(ClO₄)₂] (**1**) and TBAB as catalysts. Conversion = $1/1.22 = 81.9\%$.

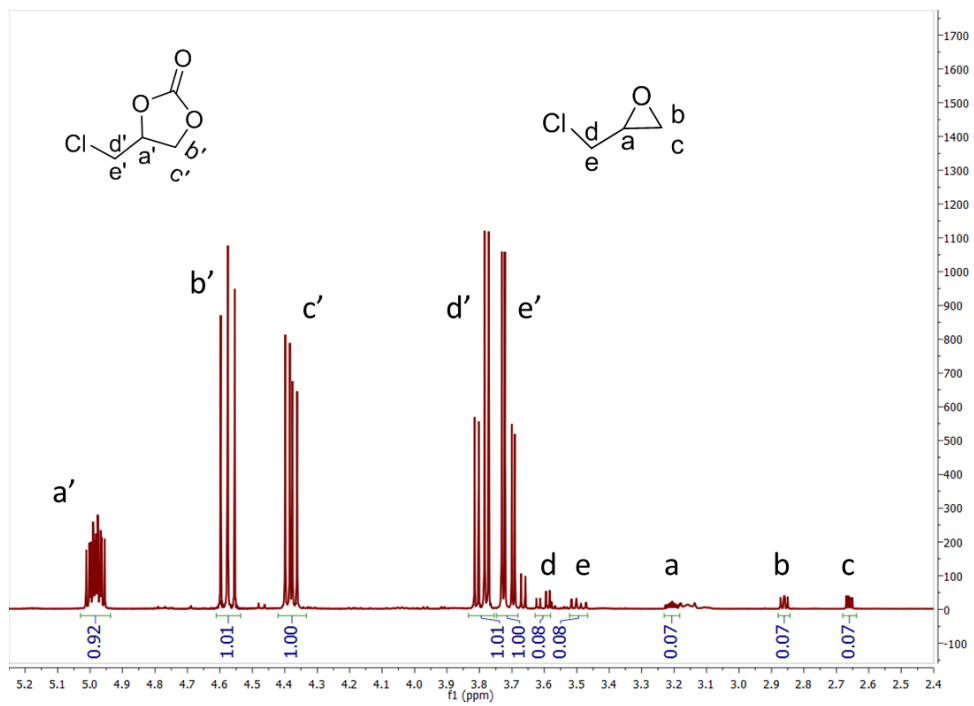


Figure S23. ^1H NMR (400 MHz, CDCl_3) spectrum of reaction mixture in Table 3 entry 1, run 1 using VPI-100 (Cu) and TBAB as catalysts. Conversion = $1/1.07 = 93.5\%$.

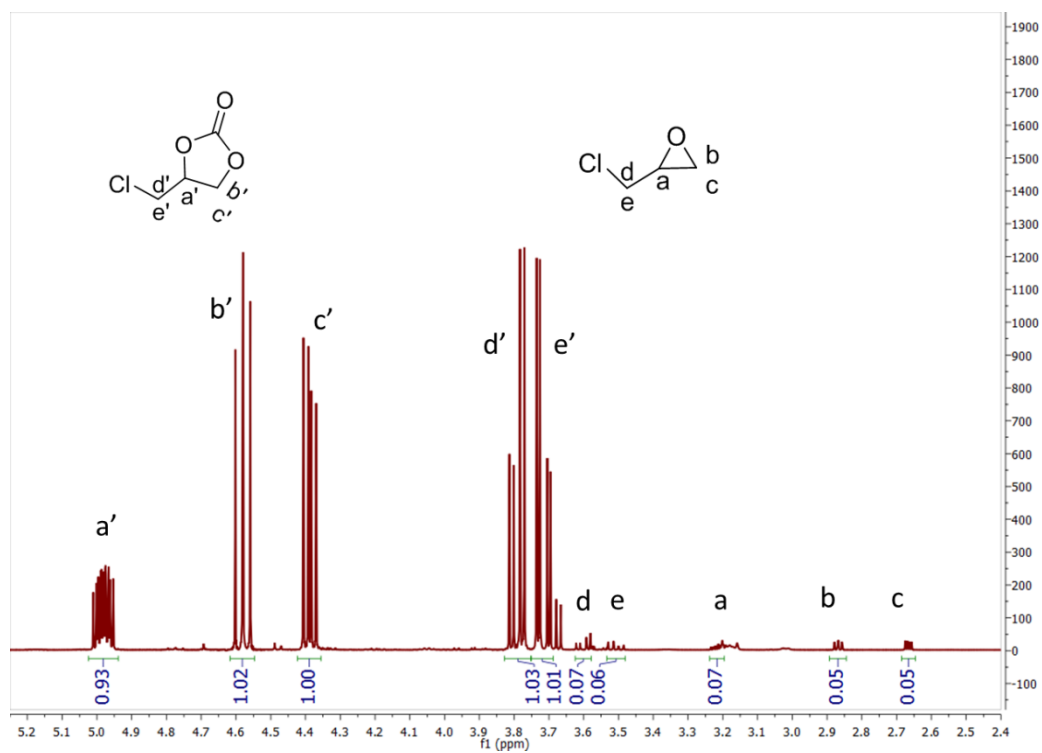


Figure S24. ^1H NMR (400 MHz, CDCl_3) spectrum of reaction mixture in Table 3 entry 1, run 2 using VPI-100 (Cu) and TBAB as catalysts. Conversion = $1/1.05 = 95.2\%$.

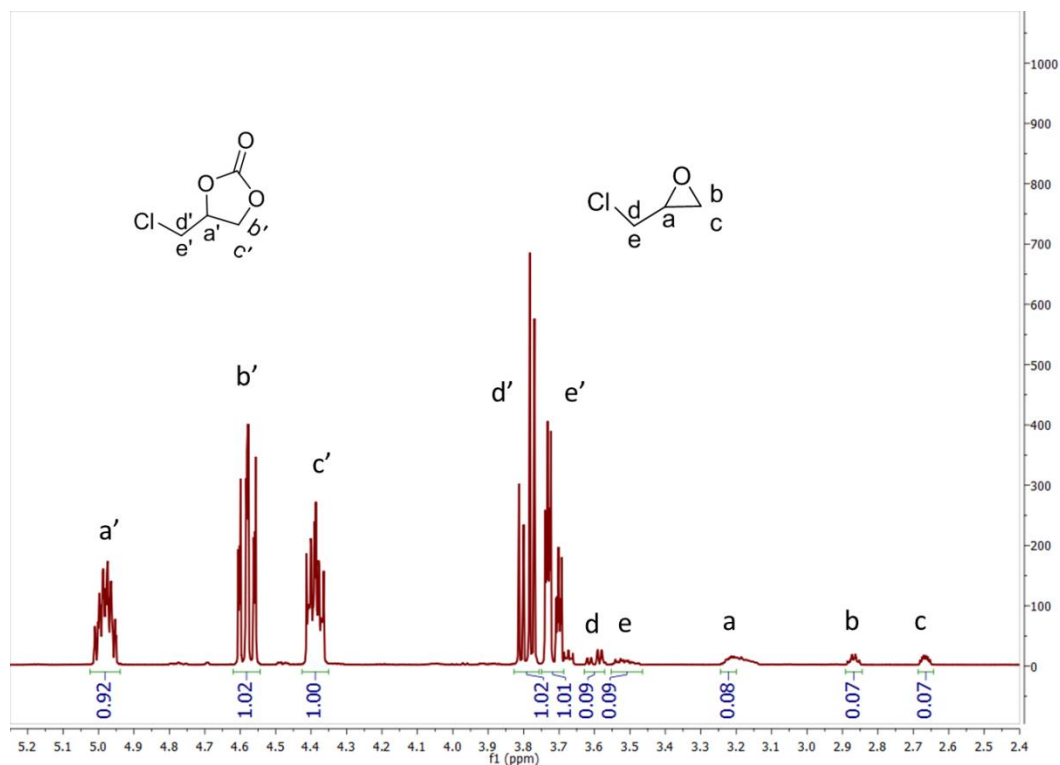


Figure S25. ¹H NMR (400 MHz, CDCl₃) spectrum of reaction mixture in Table 3 entry 1, run 3 using VPI-100 (Cu) and TBAB as catalysts. Conversion = 1/1.07 = 93.5%.

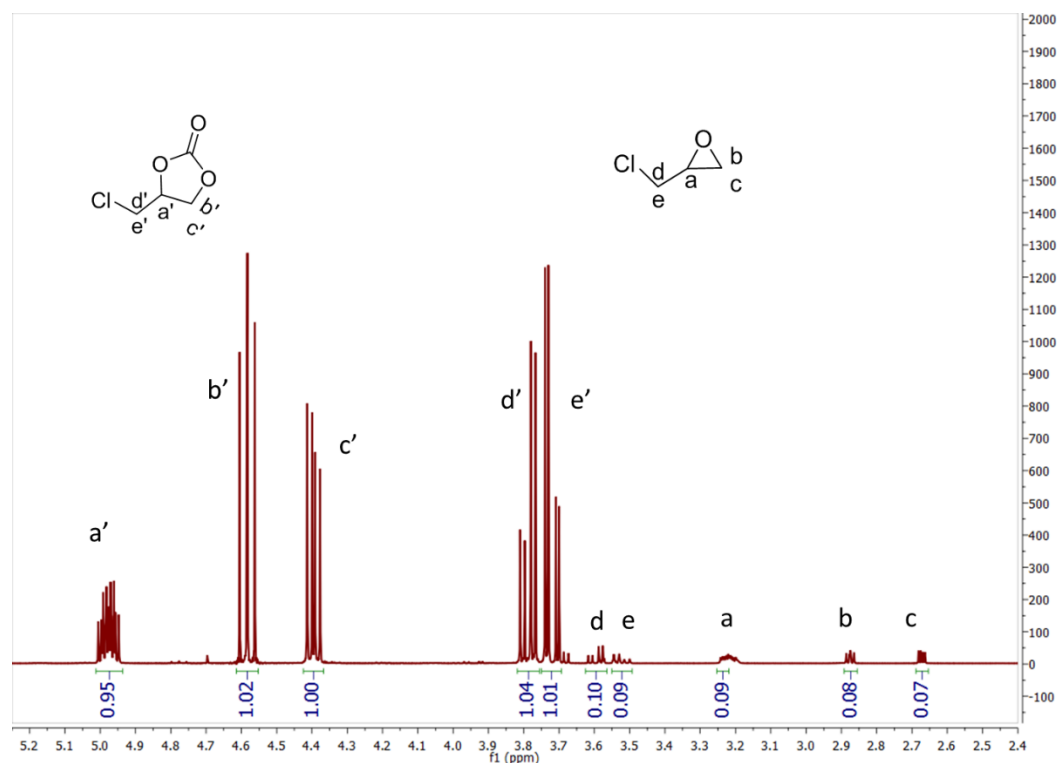


Figure S26. ¹H NMR (400 MHz, CDCl₃) spectrum of reaction mixture in Table S7 entry 3 using [NiL](ClO₄)₂ (**3**) and TBAB as catalysts. Conversion = 1/1.07 = 93.5%.

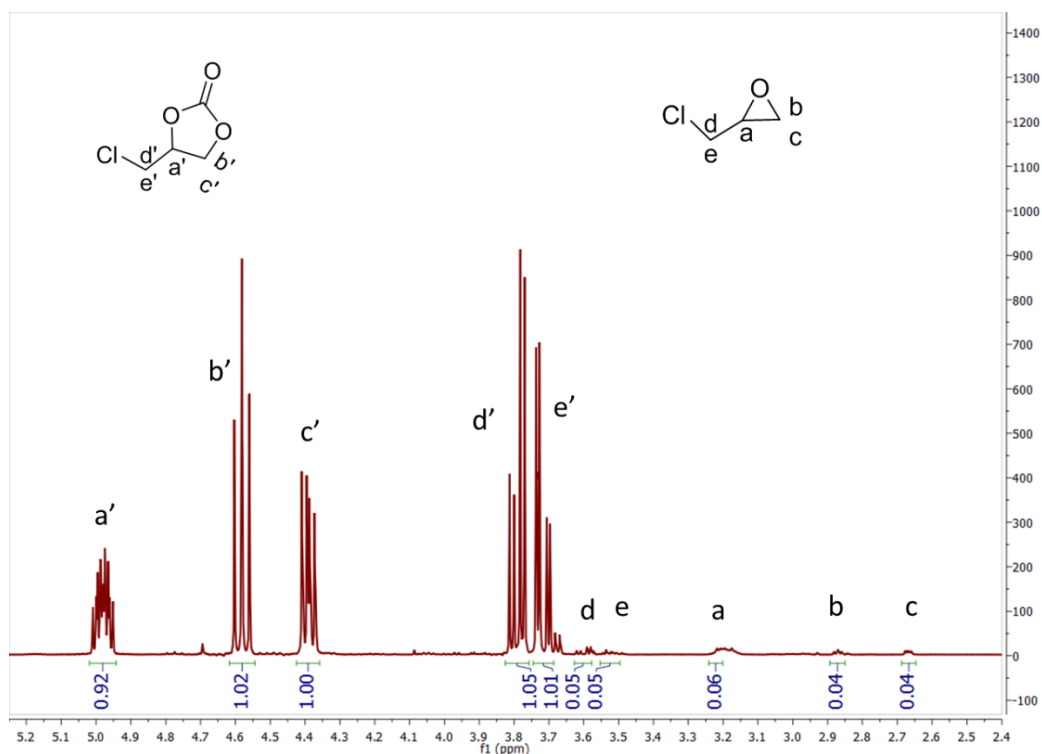


Figure S27. ¹H NMR (400 MHz, CDCl₃) spectrum of reaction mixture in Table 3 entry 2, run 1 using VPI-100 (Ni) and TBAB as catalysts. Conversion = $1/1.04 = 96.2\%$.

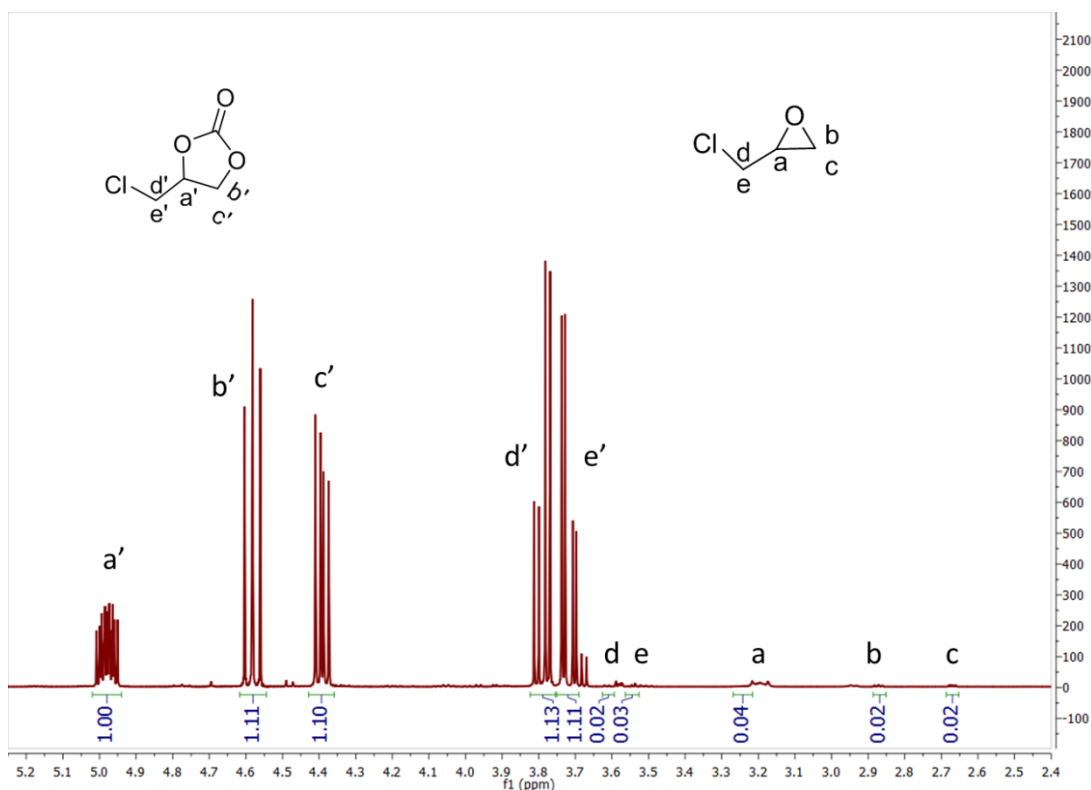


Figure S28. ¹H NMR (400 MHz, CDCl₃) spectrum of reaction mixture in Table 3 entry 2, run 2 using VPI-100 (Ni) and TBAB as catalysts. Conversion = $1.1/1.12 = 98.2\%$.

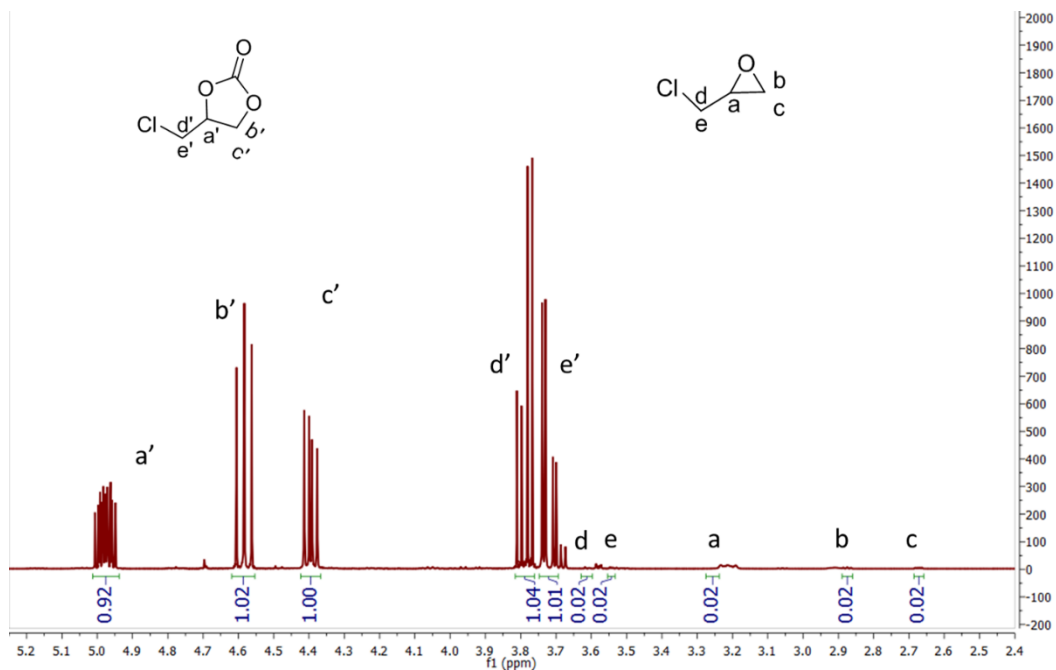


Figure S29. ^1H NMR (400 MHz, CDCl_3) spectrum of reaction mixture in Table 3 entry 2, run 3 using VPI-100 (Ni) and TBAB as catalysts. Conversion = $1/1.02 = 98\%$.

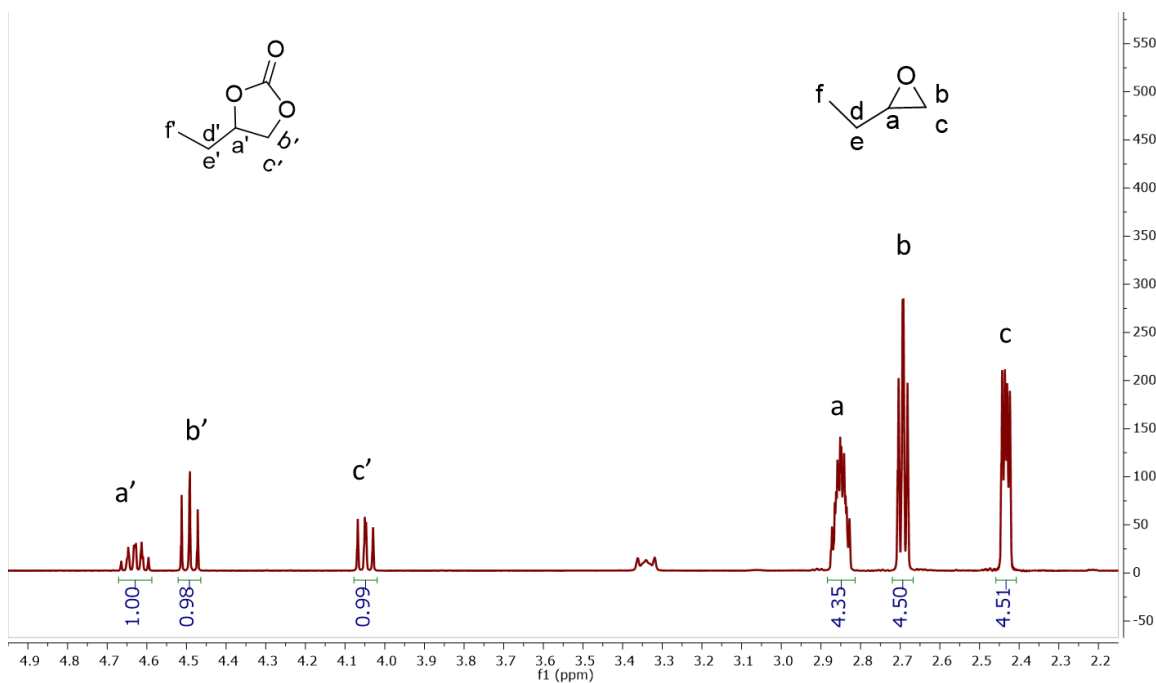


Figure S30. ^1H NMR (400 MHz, CDCl_3) spectrum of reaction mixture in Table S7 entry 4 only using TBAB as catalysts. Conversion = $0.99/5.50 = 18\%$.

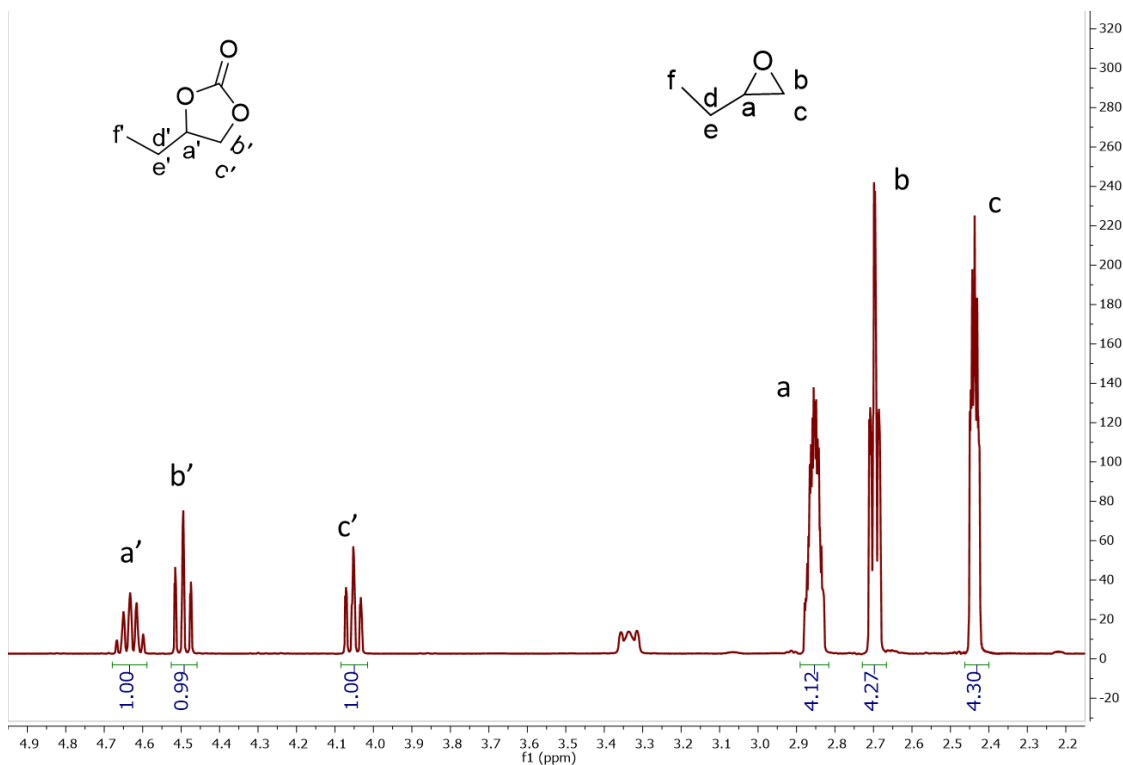


Figure S31. ^1H NMR (400 MHz, CDCl_3) spectrum of reaction mixture in Table S7 entry 5 using $[\text{CuL}(\text{ClO}_4)_2]$ (**1**) and TBAB as catalysts. Conversion = $1/5.30 = 18.9\%$

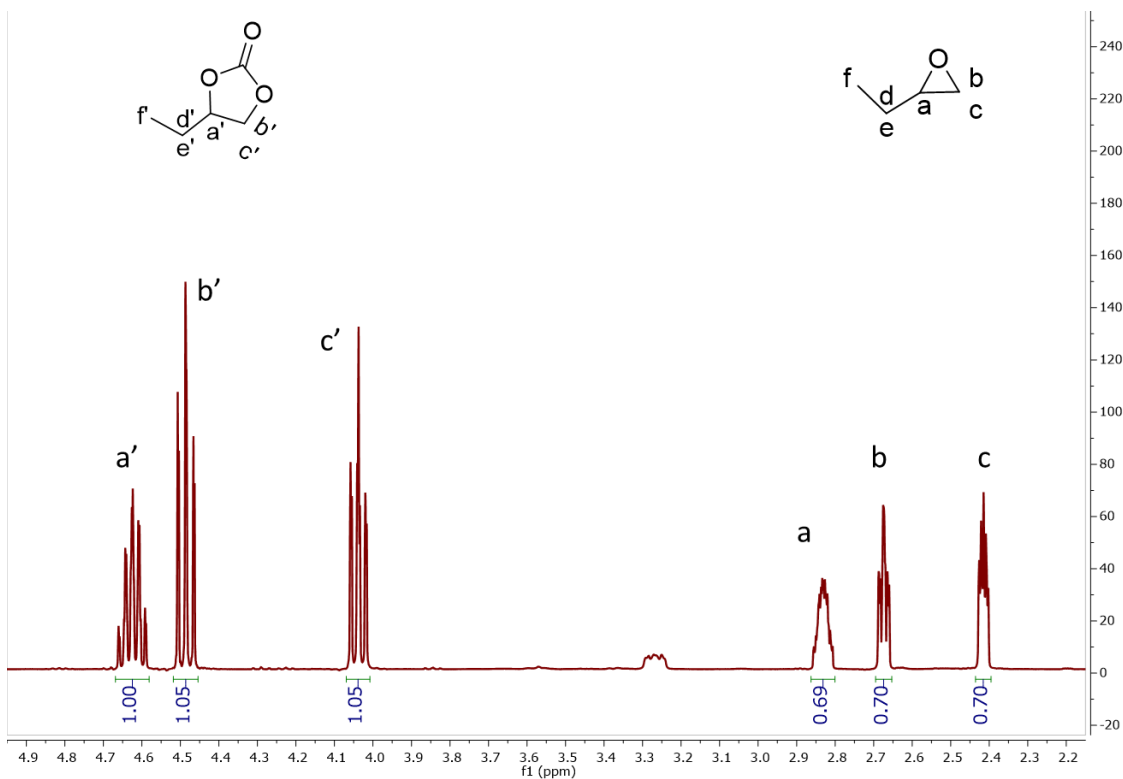


Figure S32. ^1H NMR (400 MHz, CDCl_3) spectrum of reaction mixture in Table 3 entry 3, run 1 using VPI-100 (Cu) and TBAB as catalysts. Conversion = $1.05/1.75 = 60\%$.

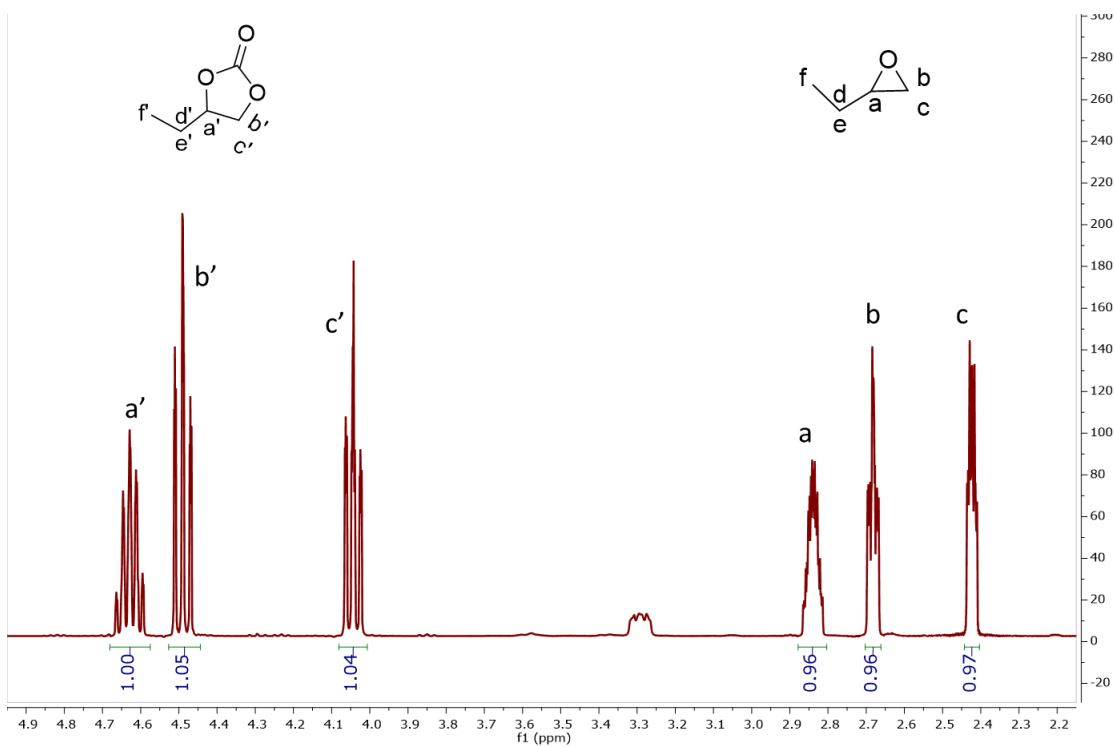


Figure S33. ¹H NMR (400 MHz, CDCl₃) spectrum of reaction mixture in Table 3 entry 3, run 2 using VPI-100 (Cu) and TBAB as catalysts. Conversion = 1.04/1.75 = 52%.

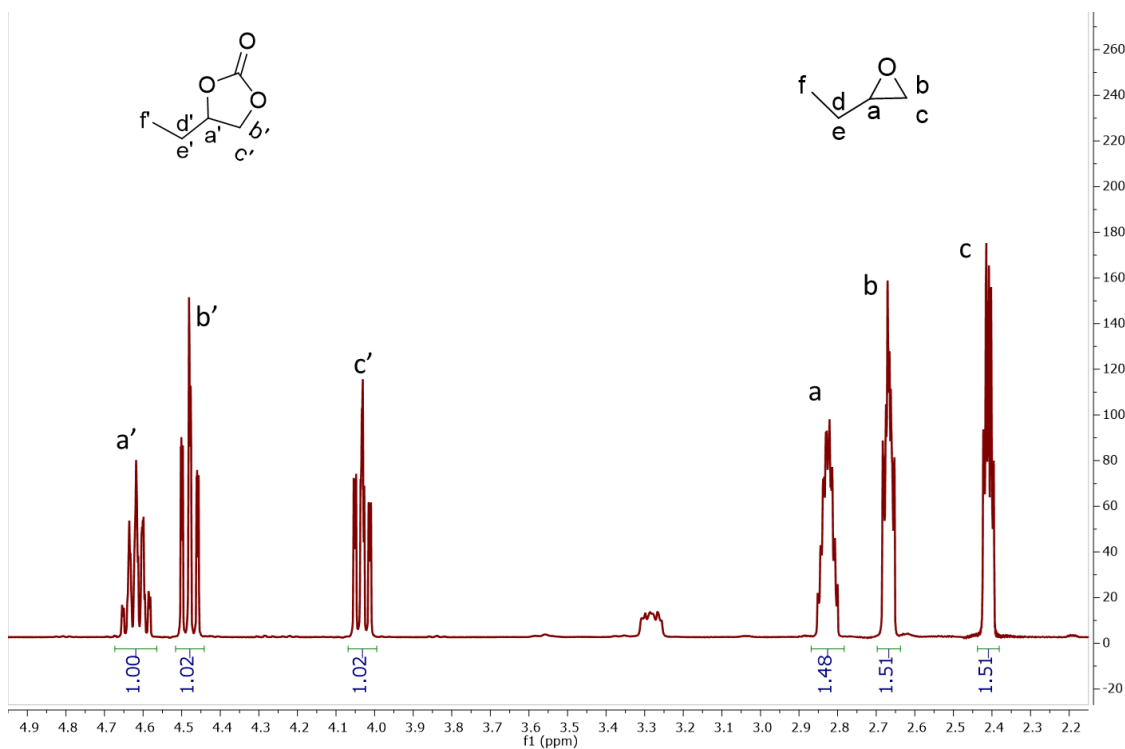


Figure S34. ¹H NMR (400 MHz, CDCl₃) spectrum of reaction mixture in Table 3 entry 3, run 3 using VPI-100 (Cu) and TBAB as catalysts. Conversion = 1.02/2.53 = 40%.

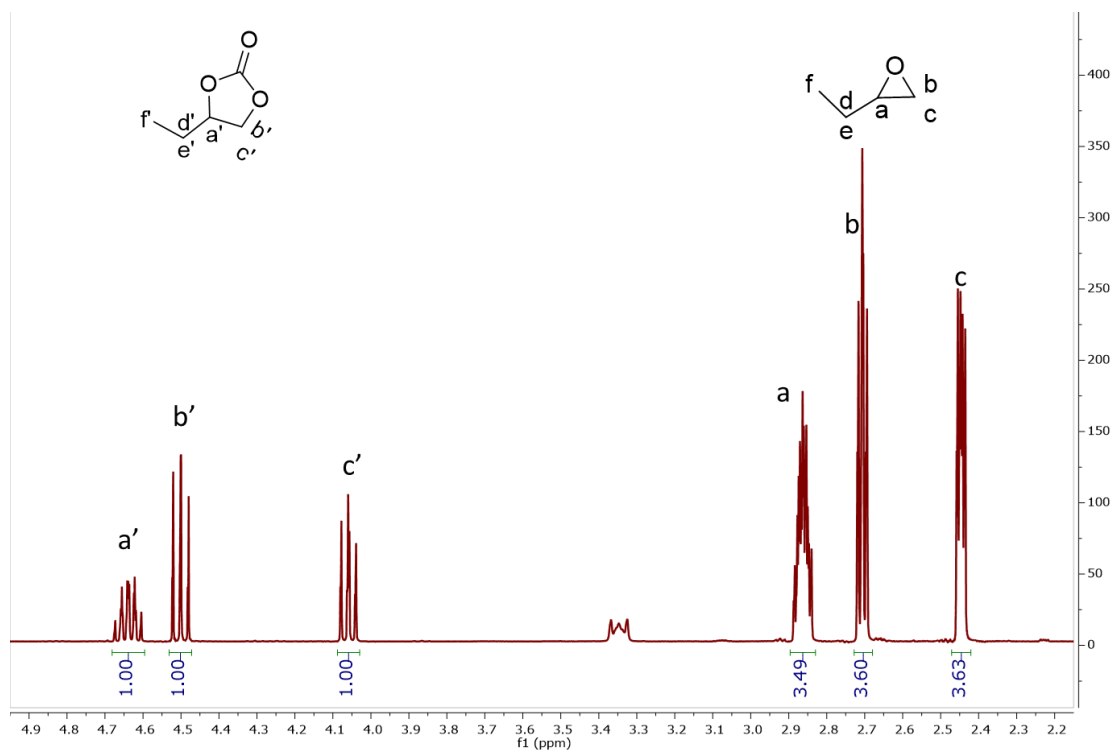


Figure S35. ^1H NMR (400 MHz, CDCl_3) spectrum of reaction mixture in Table S7 entry 6 using $[\text{NiL}](\text{ClO}_4)_2$ (**3**) and TBAB as catalysts. Conversion = $1/4.63 = 21.6\%$.

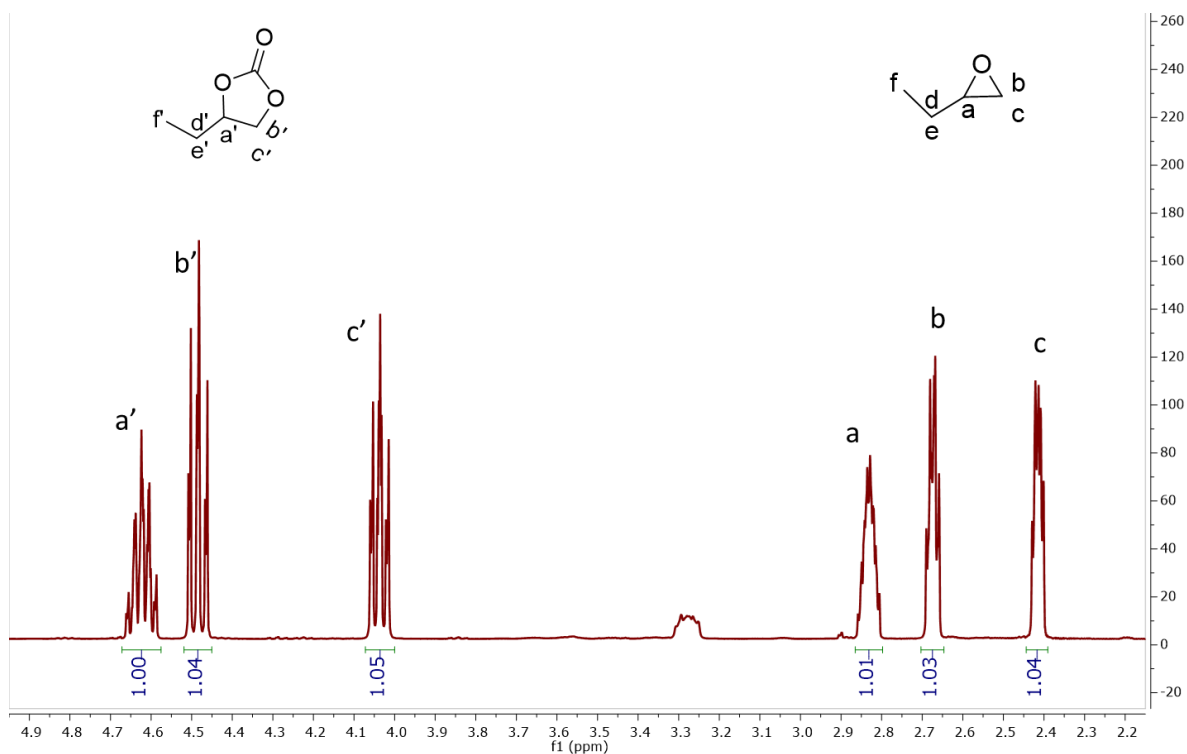


Figure S36. ^1H NMR (400 MHz, CDCl_3) spectrum of reaction mixture in Table 3 entry 4, run 1 using VPI-100 (Ni) and TBAB as catalysts. Conversion = $1.05/2.09 = 50\%$.

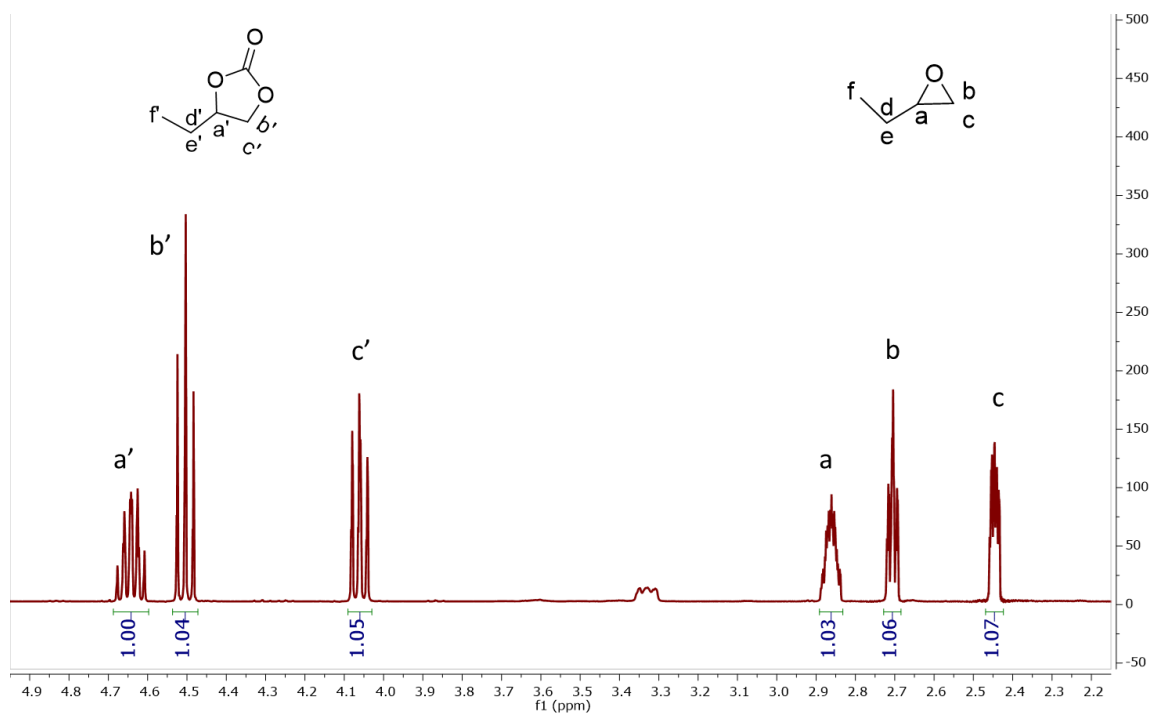


Figure S37. ¹H NMR (400 MHz, CDCl₃) spectrum of reaction mixture in Table 3 entry 4, run 3 using VPI-100 (Ni) and TBAB as catalysts. Conversion = 1.05/2.12 = 50%.

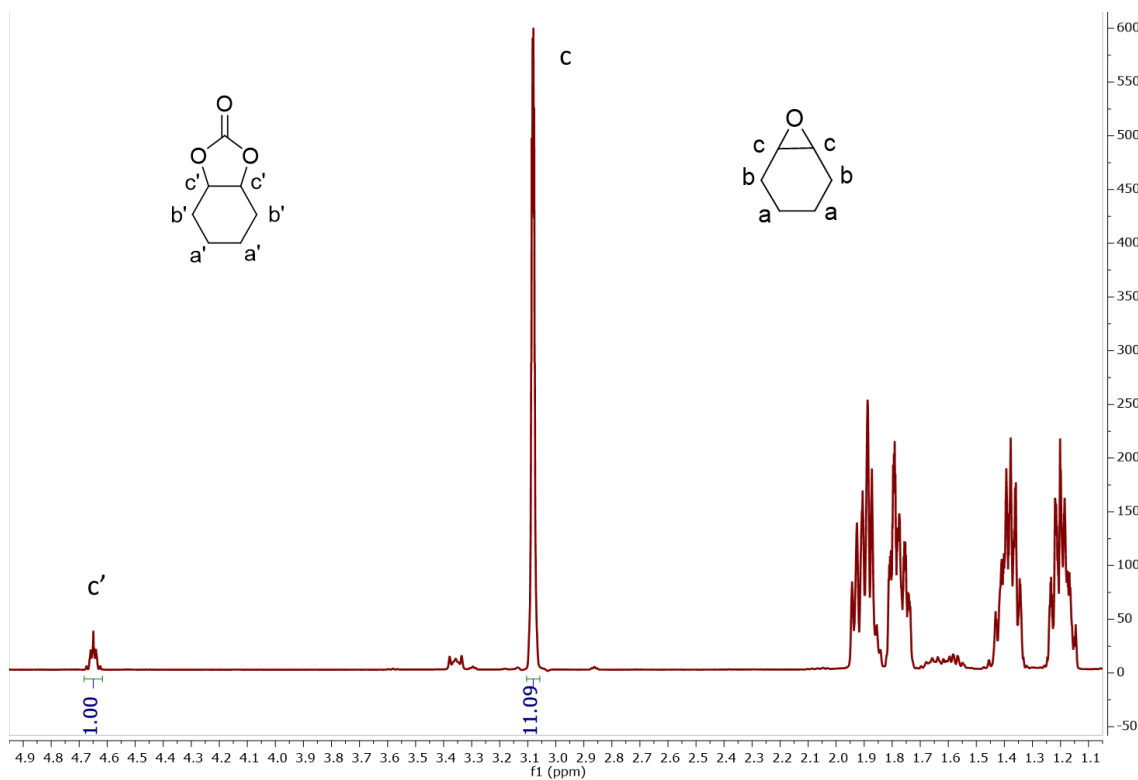


Figure S38. ¹H NMR (400 MHz, CDCl₃) spectrum of reaction mixture in Table S7 entry 7 using only TBAB as catalysts. Conversion = 1/12.09 = 8.3%.

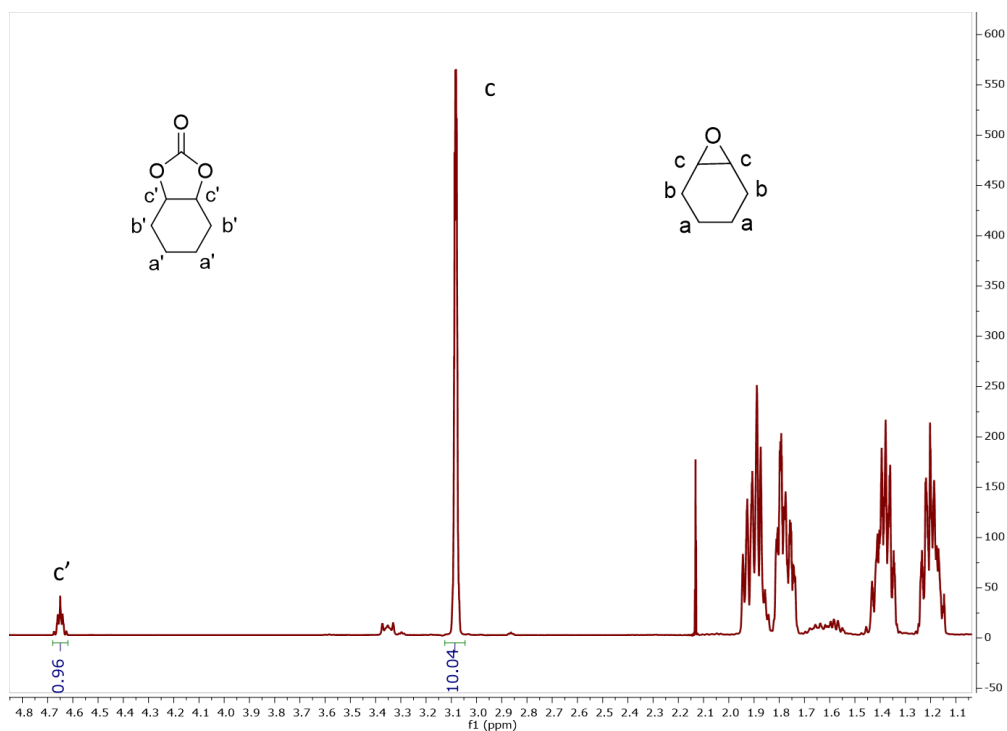


Figure S39. ¹H NMR (400 MHz, CDCl₃) spectrum of reaction mixture in Table S7 entry 8 using [CuL(ClO₄)₂] (**1**) and TBAB as catalysts. Conversion = 0.96/11 = 8.7%.

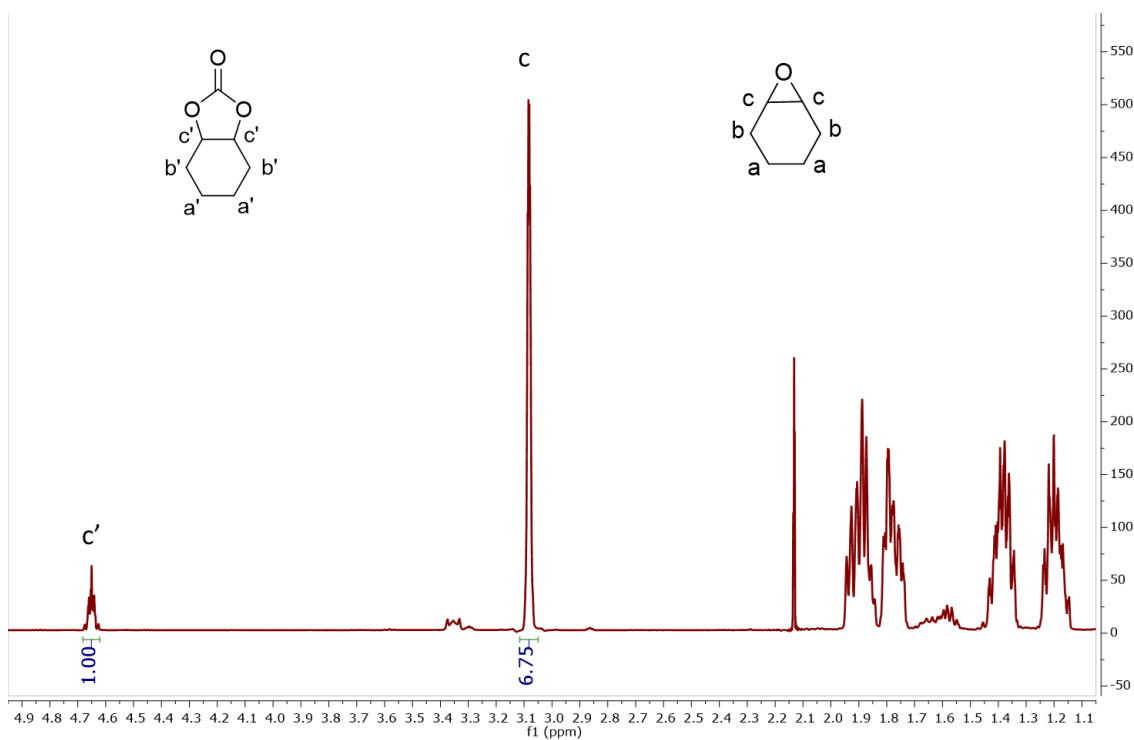


Figure S40. ¹H NMR (400 MHz, CDCl₃) spectrum of reaction mixture in Table 3 entry 5, run 1 using VPI-100 (Cu) and TBAB as catalysts. Conversion = 1/7.75 = 12.9%.

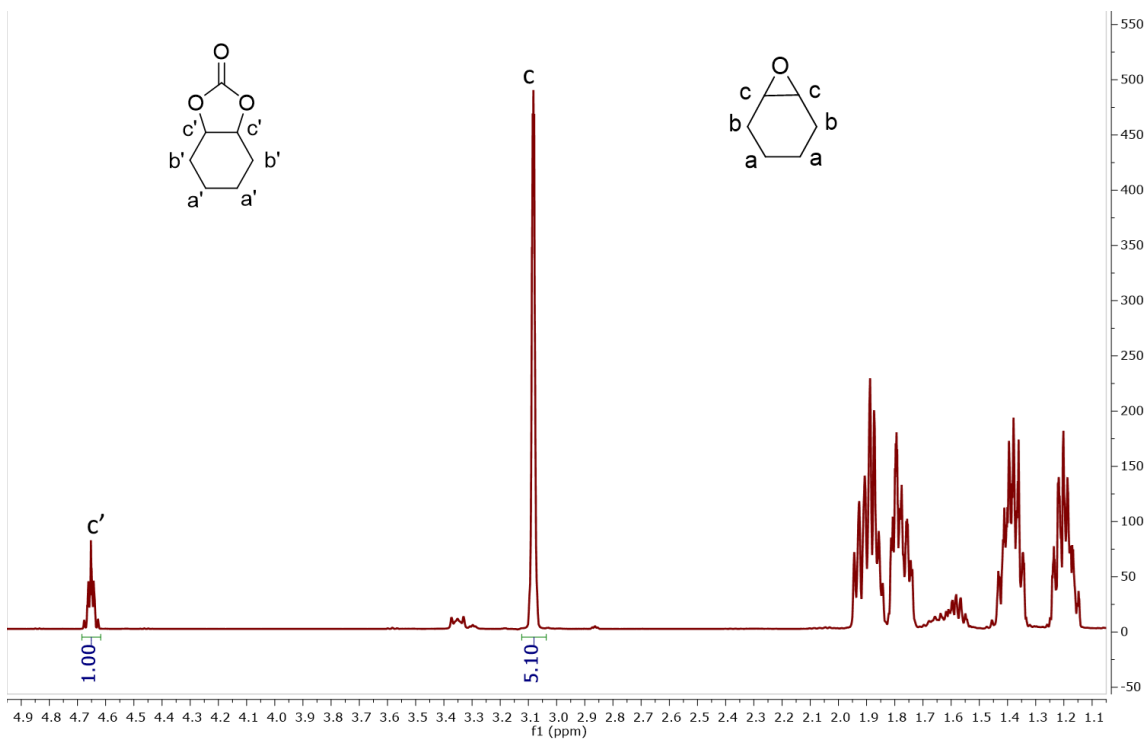


Figure S41. ^1H NMR (400 MHz, CDCl_3) spectrum of reaction mixture in Table 3 entry 5, run 2 using VPI-100 (Cu) and TBAB as catalysts. Conversion = $1/6.1 = 16.4\%$.

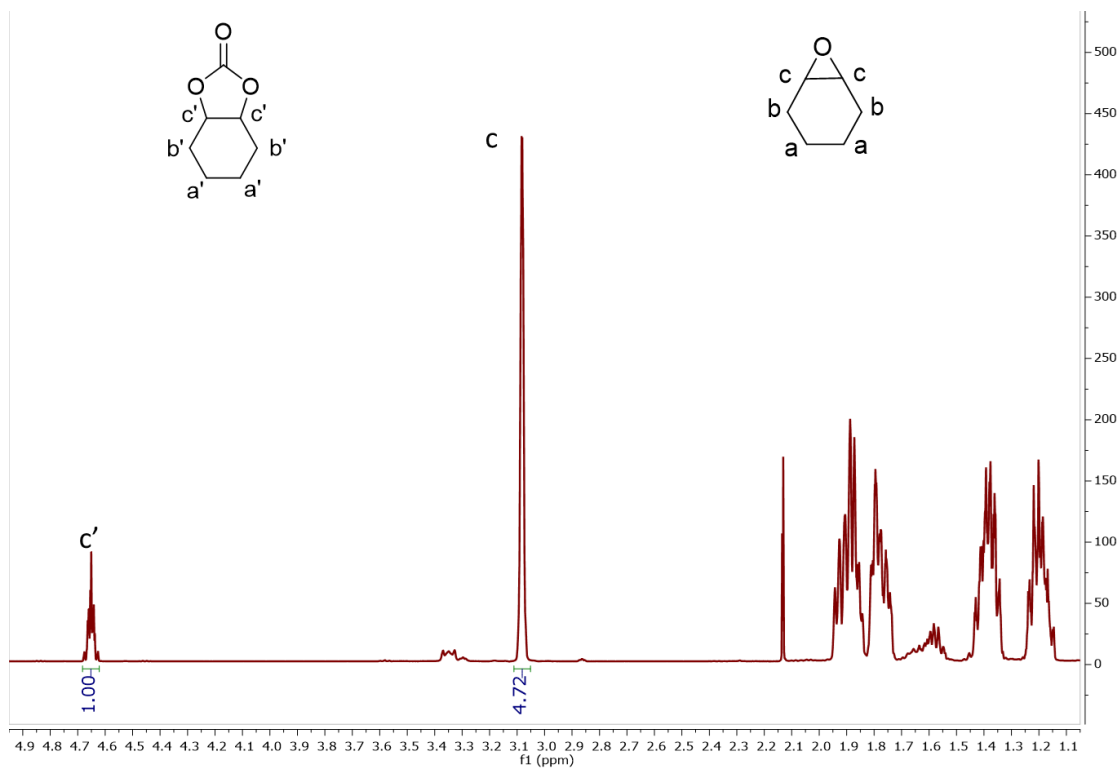


Figure S42. ^1H NMR (400 MHz, CDCl_3) spectrum of reaction mixture in Table 3 entry 5, run 3 using VPI-100 (Cu) and TBAB as catalysts. Conversion = $1/5.72 = 17.5\%$.

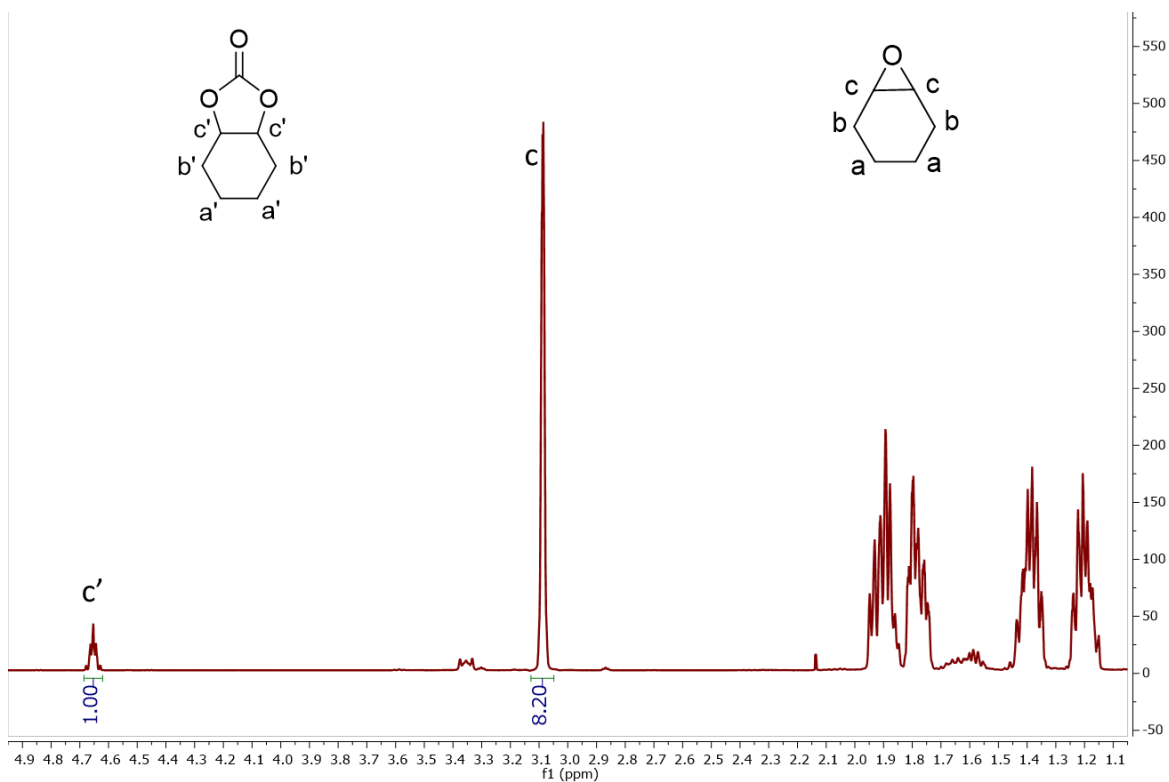


Figure S43. ^1H NMR (400 MHz, CDCl_3) spectrum of reaction mixture in Table S7 entry 9 using $[\text{NiL}](\text{ClO}_4)_2$ (**3**) and TBAB as catalysts. Conversion = $1/9.20 = 10.9\%$.

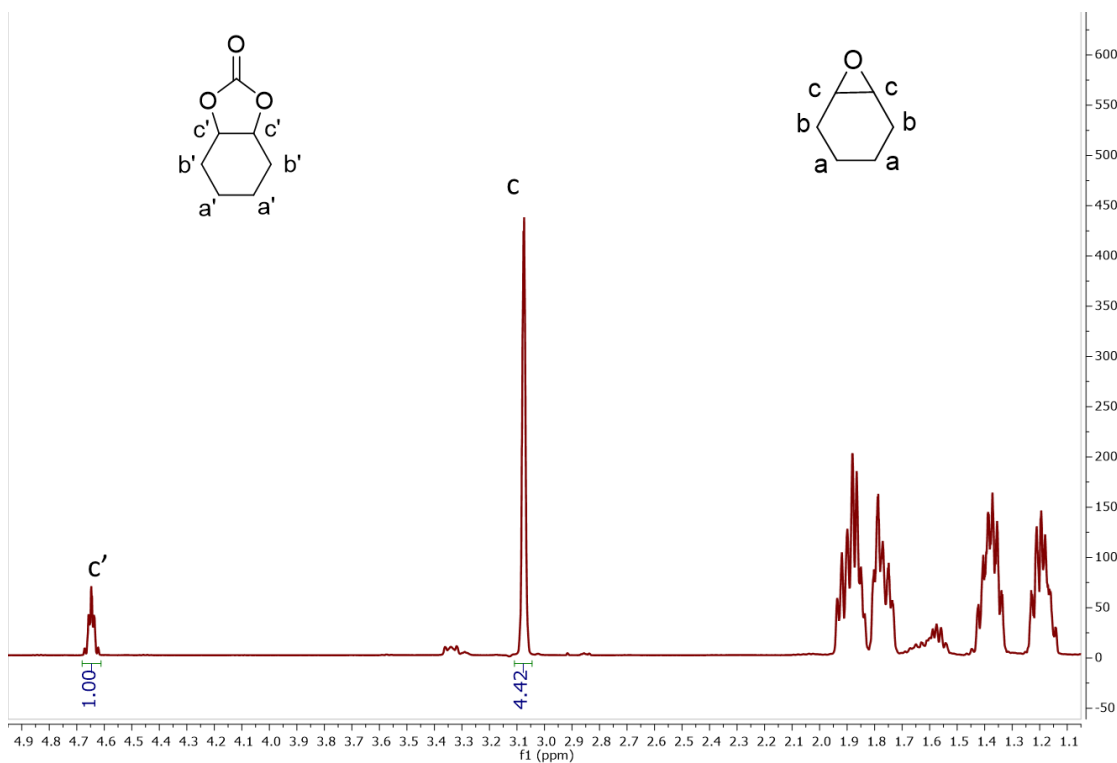


Figure S44. ^1H NMR (400 MHz, CDCl_3) spectrum of reaction mixture in Table 3 entry 6, run 1 using VPI-100 (Ni) and TBAB as catalysts. Conversion = $1/5.42 = 18.5\%$.

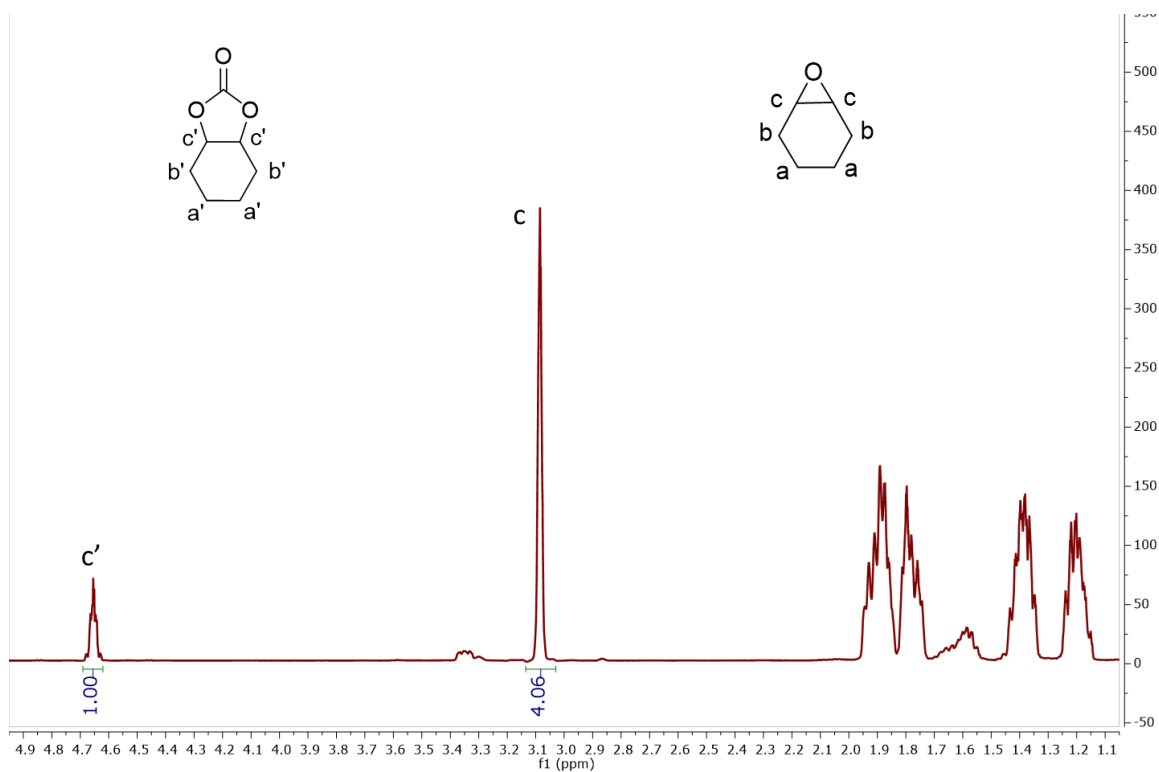


Figure S45. ^1H NMR (400 MHz, CDCl_3) spectrum of reaction mixture in Table 3 entry 6, run 2 using VPI-100 (Ni) and TBAB as catalysts. Conversion = $1/5.06 = 19.8\%$.

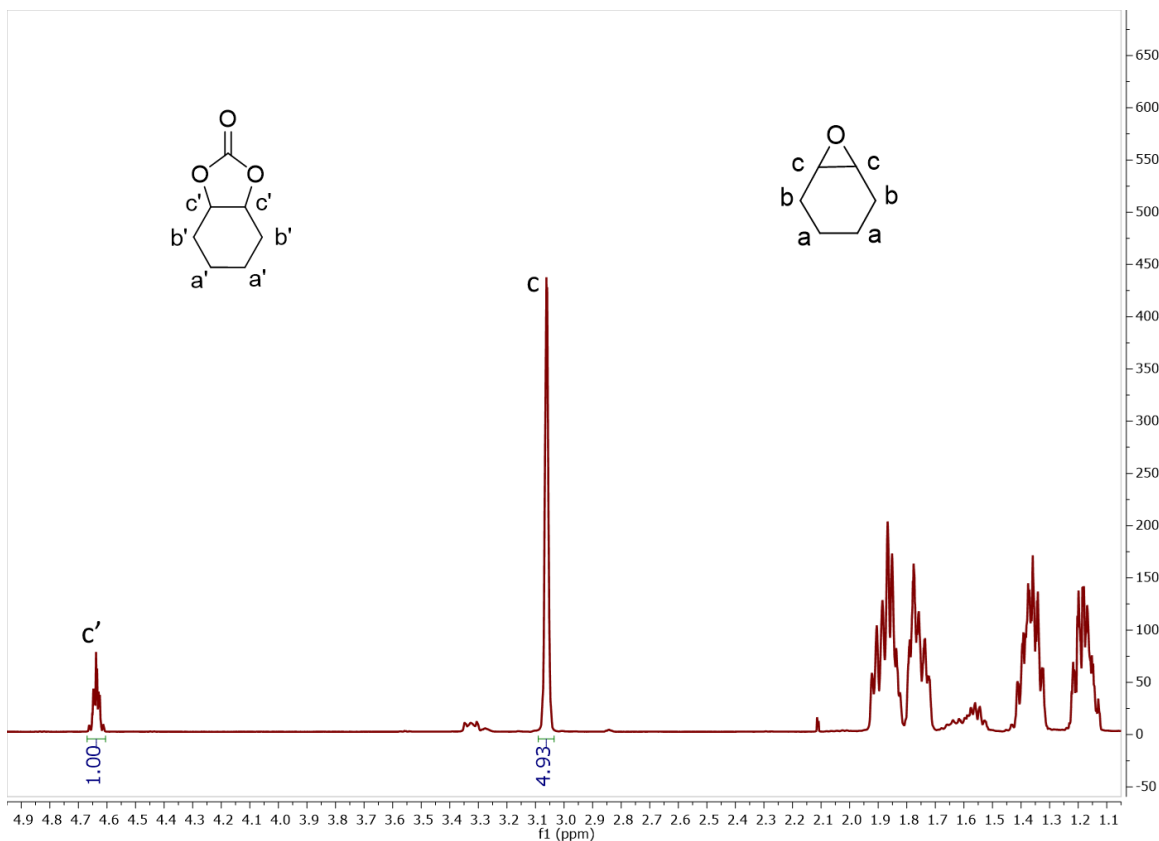
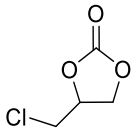
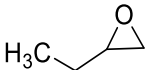
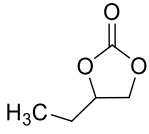
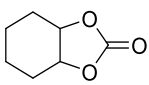


Figure S46. ^1H NMR (400 MHz, CDCl_3) spectrum of reaction mixture in Table 3 entry 6, run 3 using VPI-100 (Ni) and TBAB as catalysts. Conversion = $1/5.93 = 16.8\%$.

Table S7. Cycloaddition reaction of CO₂ with epoxide catalyzed by ligand and control.

Entry	Epoxide	Product	Catalyst	Conversion (%) ^a
1			TBAB	78.1
2			[CuL(ClO ₄) ₂] (1), TBAB	81.9
3			[NiL](ClO ₄) ₂ (3), TBAB	93.5
4			TBAB	18
5			[CuL(ClO ₄) ₂] (1), TBAB	18.9
6			[NiL](ClO ₄) ₂ (3), TBAB	21.6
7			TBAB	8.3
8			[CuL(ClO ₄) ₂] (1), TBAB	8.7
9			[NiL](ClO ₄) ₂ (3), TBAB	10.9

^aConversion evaluated from the ¹H NMR spectra by integration of epoxide versus cyclic carbonate peaks.

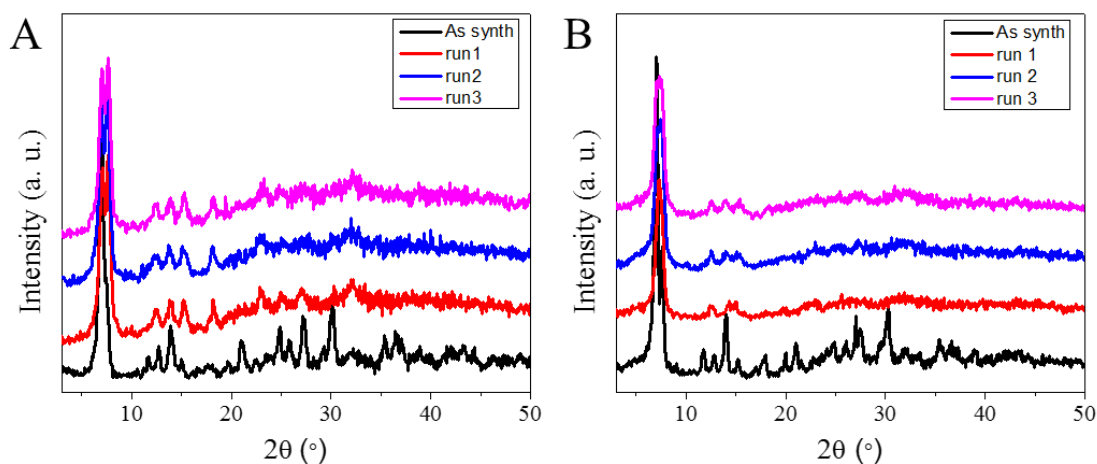


Figure S47. PXRD patterns of A) VPI-100 (Cu) and B) VPI-100 (Ni) as synthesized and after three catalytic reaction cycles from 6b to 7b.

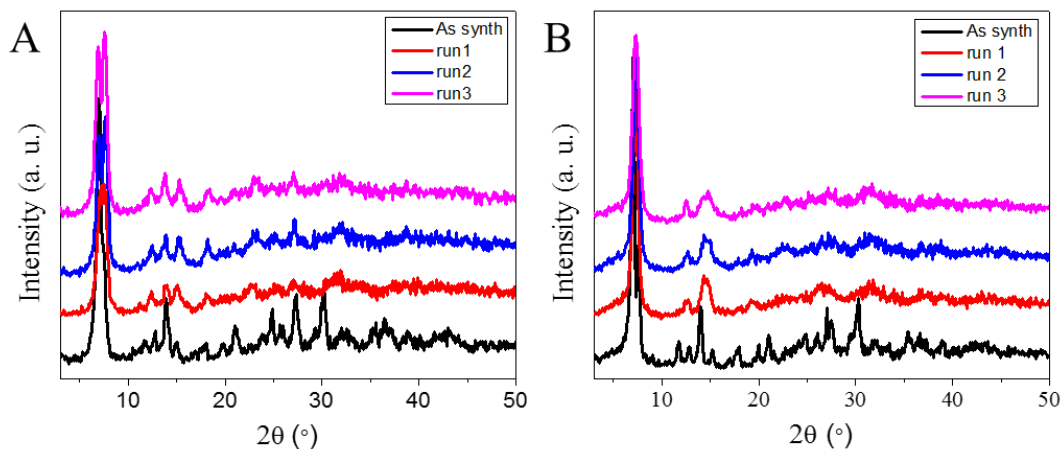


Figure S48. PXRD patterns of A) VPI-100 (Cu) and B) VPI-100 (Ni) as synthesized and after three catalytic reaction cycles from 6c to 7c.

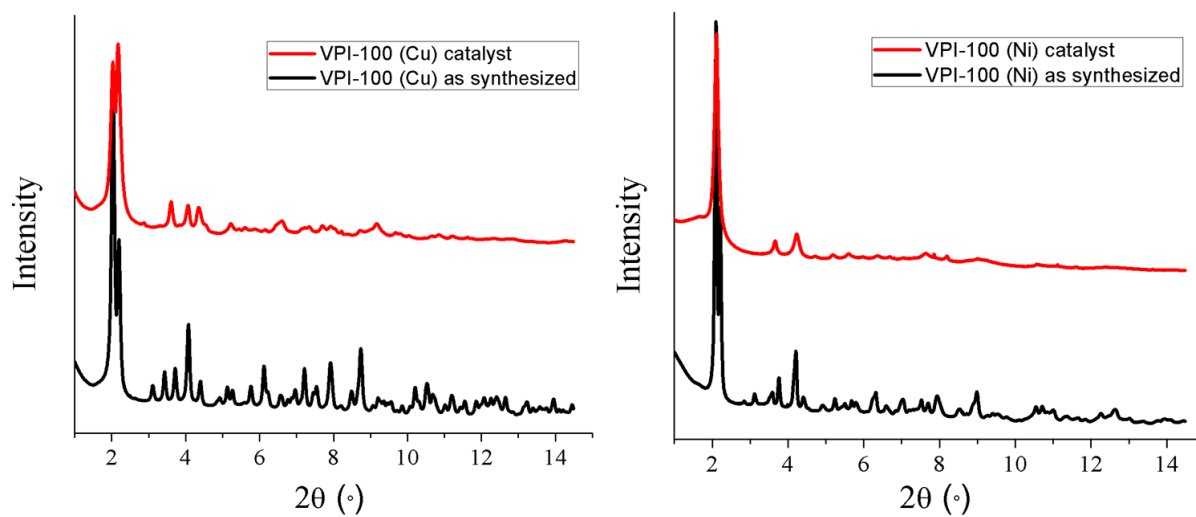


Figure S49. *in situ* synchrotron PXRD of VPI-100 after 3 catalyst cycles.

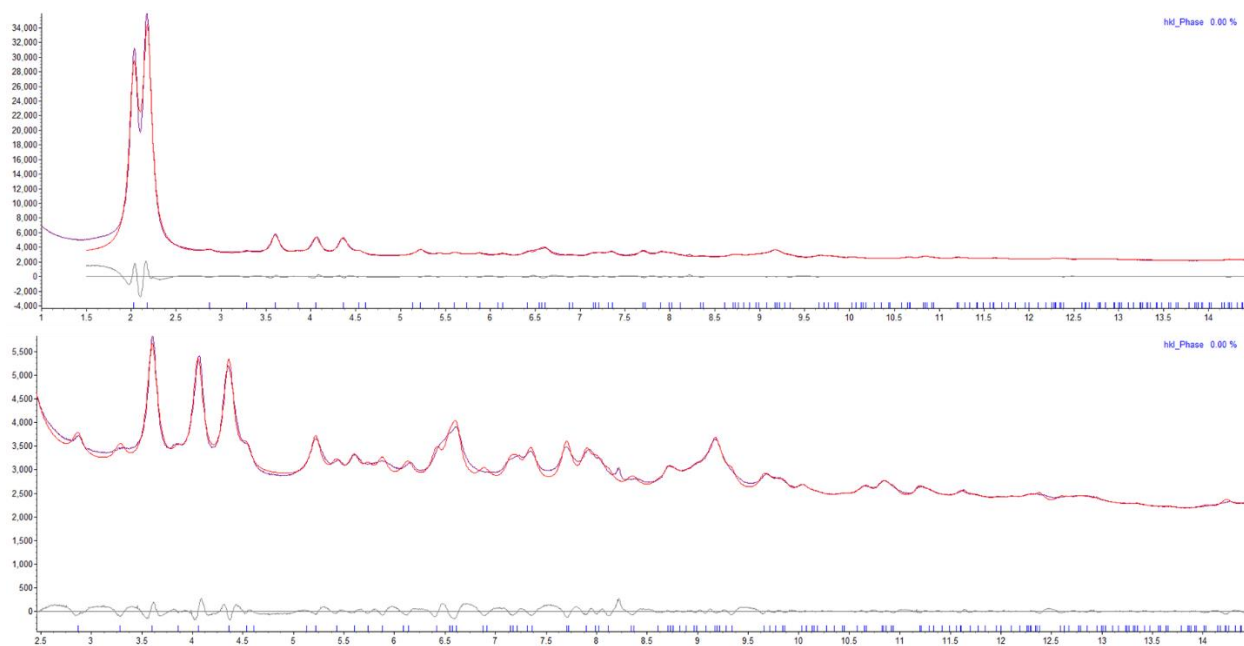


Figure S50. Le Bail refinement of VPI-100 (Cu) after 3 catalyst cycles.

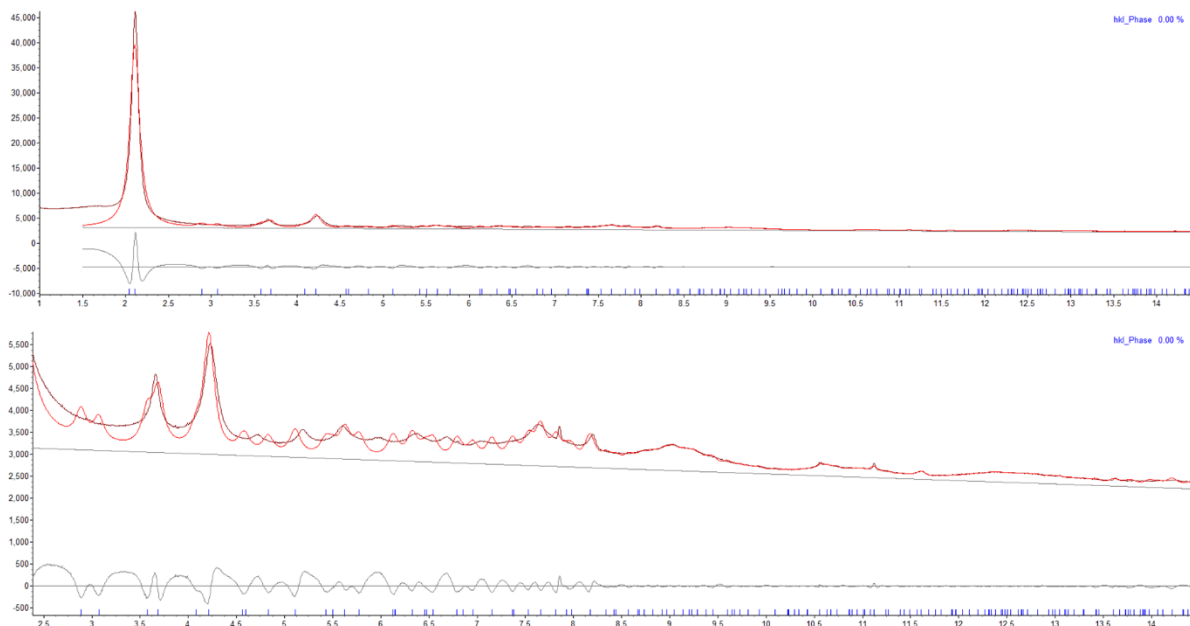


Figure S51. Le Bail refinement of VPI-100 (Ni) after 3 catalyst cycles.

Table S8. Unit cell parameter of VPI-100

	a (Å)	c (Å)
VPI-100 (Cu) as synthesis (In paper)	16.721	19.704
VPI-100 (Cu) after catalyst	18.067	15.776
VPI-100 (Ni) as synthesis (In paper)	16.510	19.811
VPI-100 (Ni) after catalyst	17.949	16.868

Table S9. Cycloaddition reaction of CO₂ with epoxide 6a catalyzed by different MOFs.

MOF	Chemical Formula (guest molecule ignored)	Co-catalyst	T, ^{a)} [K]	P, ^{b)} [atm]	Time [h]	Yield %	TO N ^{c)}	TOF ^{d)}	Ref
BIT-103	Zn ₃ (BTC) ₂	N.A	433	30	8	100	219	31	[3]
Zr(H₄L)	Zr(H ₄ L)	n-Bu ₄ NBr	373	10	10	99	2730	1365	[4]
BIT-C	CuL ₁	n-Bu ₄ NBr	333	1	6	99	-	-	[5]
UiO-67-IL	-	n-Bu ₄ NBr	363	1	3	99	-	45	[6]
1·Mn	[Mn ₅ L(H ₂ O) ₆ ·(DMA) ₂]·5DMA·4C ₂ H ₅ OH	n-Bu ₄ NBr	353	20	4	99	800	400	[7]
Gd-MOF	-	n-Bu ₄ NBr	353	20	5	99	-	-	[8]
VPI-100 (Ni)	[Zr ₆ (μ ₃ -OH) ₈ (OH) ₈ (Ni-L) ₄]	n-Bu ₄ NBr	363	10	6	98	453	76	This

										work
UTSA-16	(KCo ₃ (C ₆ H ₄ O ₇) (C ₆ H ₅ O ₇) (H ₂ O) ₂)	N.A	393	10	6	98	-	-		[9]
Zn₆(TATAB)₄(DABCO)₃	Zn ₆ (TATAB) ₄ (DABCO) ₃	N.A	373	1	16	98	158	9.9		[10]
ZIF-67	Co(mlM) ₂	N.A	393	10	6	97	-	-		[11]
VPI-100 (Cu)	[Zr ₆ (μ ₃ -OH) ₈ (OH) ₈ (Cu-L) ₄]	n-Bu ₄ NBr	363	10	6	95	439	73		This work
IL-ZIF-90	Zn(ICA) _x (IL-ICA) _{2-x}	N.A	393	10	3	94	204	68		[12]
TMOF-1	[Cu(bpy) ₂ (EDS)] _n	n-Bu ₄ NBr	r.t.	1	-	92	-	-		[13]
Gea-MOF-1	Y ₉ (μ ₃ -OH) ₈ (μ ₂ -OH) ₃ (BTB) ₆	n-Bu ₄ NBr	393	20	6	89	593	99		[2]
Cu₄MTTP	Cu ₄ MTTP	n-Bu ₄ NBr	r.t.	1	48	85	177	3.7		[14]
F-IRMOF-3	(Zn ₄ O)(BDC-NH ₂) _x (F-BDC) _{3-x}	N.A	413	20	1.5	80	-	-		[15]
UMCM-1-NH₂	(Zn ₄ O) ₉ (BDC-NH ₂)(BTB) ₅	n-Bu ₄ NBr	r.t.	12	24	78	-	-		[16]
NR₂-ZIF-8	Zn(MeIm) ₂	N.A	353	7	4	73	-	-		[17]
Cu(HIP)₂(BPY)	Cu(HIP) ₂ (BPY)	N.A	393	12	6	72	-	-		[18]
ZIF-8	Zn(MeIm) ₂	N.A	353	7	4	44	-	-		[17]
USTC-253-TFA	Al(OH)(SBPDC) _x (TFA) _{1-x}	n-Bu ₄ NBr	298	1	72	38	-	-		[19]

^aT. = temperature; ^bP.=pressure; ^cTON = Turnover number (product (mmol)/active catalytic sites or catalysts (mmol).) ^dTOF = Turnover frequency (TON/time (h)).

Table S10. Cycloaddition reaction of CO₂ with epoxide 6c catalyzed by different MOFs.

MOF	Chemical Formula (guest molecule ignored)	Co-catalyst	T. ^{a)} [K]	P. ^{b)} [atm]	Time [h]	% Yield	Ref
Ti-ZIF	Ti-ZIF	N.A.	393	1.7	8	95%	[20]
TMOF-1	[Cu(bpy) ₂ (EDS)] _n	n-Bu ₄ NBr	r.t.	1	-	39	[13]
UTSA-16	(KCo ₃ (C ₆ H ₄ O ₇) (C ₆ H ₅ O ₇) (H ₂ O) ₂)	N.A	393	10	6	26	[9]
Gd-MOF	-	n-Bu ₄ NBr	353	20	5	24	[8]
VPI-100 (Ni)	[Zr ₆ (μ ₃ -OH) ₈ (OH) ₈ (Ni-L) ₄]	n-Bu ₄ Br	363	10	6	20	This work
VPI-100 (Cu)	[Zr ₆ (μ ₃ -OH) ₈ (OH) ₈ (Cu-L) ₄]	n-Bu ₄ Br	363	10	6	18	This

							work
BIT-103	Zn ₃ (BTC) ₂	N.A	433	30	24	16	[3]
Cu(HIP)₂(BPY)	Cu(HIP) ₂ (BPY)	N.A	393	12	6	10	[18]
UMCM-1-NH₂	(Zn ₄ O) ₉ (BDC-NH ₂)(BTB) ₅	n-Bu ₄ Br	r.t.	12	24	10	[16]
IL-ZIF-90	Zn(ICA) _x (IL-ICA) _{2-x}	N.A	393	10	3	9	[12]
ZIF-67	Co(mlM) ₂	N.A	393	10	6	8	[11]

^{a)}T. = temperature; ^{b)}P.=pressure;

3.8.7 References:

- Xin, L.; Curtis, N. F.; Weatherburn, D. C. *Transition Met. Chem.* **1992**, *17*, 147-154.
- Guillerm, V.; WeselińskiŁukasz, J.; Belmabkhout, Y.; Cairns, A. J.; D'Elia, V.; WojtasŁukasz; Adil, K.; Eddaoudi, M. *Nat. Chem.* **2014**, *6*, 673-680.
- Huang, X.; Chen, Y.; Lin, Z.; Ren, X.; Song, Y.; Xu, Z.; Dong, X.; Li, X.; Hu, C.; Wang, B. *Chem. Commun.* **2014**, *50*, 2624-2627.
- Gao, C.-Y.; Ai, J.; Tian, H.-R.; Wu, D.; Sun, Z.-M. *Chem. Commun.* **2017**, *53*, 1293-1296.
- Zou, B.; Hao, L.; Fan, L.-Y.; Gao, Z.-M.; Chen, S.-L.; Li, H.; Hu, C.-W. *J. Catal.* **2015**, *329*, 119-129.
- Ding, L.-G.; Yao, B.-J.; Jiang, W.-L.; Li, J.-T.; Fu, Q.-J.; Li, Y.-A.; Liu, Z.-H.; Ma, J.-P.; Dong, Y.-B. *Inorg. Chem.* **2017**, *56*, 2337-2344.
- Jiang, W.; Yang, J.; Liu, Y.-Y.; Song, S.-Y.; Ma, J.-F. *Chem. Eur. J.* **2016**, *22*, 16991-16997.
- Xue, Z.; Jiang, J.; Ma, M.-G.; Li, M.-F.; Mu, T. *ACS Sustainable Chem. Eng.* **2017**, *5*, 2623-2631.
- Song, L.; Zhang, X.; Chen, C.; Liu, X.; Zhang, N. *Microporous Mesoporous Mater.* **2017**, *241*, 36-42.
- Han, Y.-H.; Zhou, Z.-Y.; Tian, C.-B.; Du, S.-W. *Green Chem.* **2016**, *18*, 4086-4091.
- Kuruppathparambil, R. R.; Jose, T.; Babu, R.; Hwang, G.-Y.; Kathalikkattil, A. C.; Kim, D.-W.; Park, D.-W. *Appl. Catal., B* **2016**, *182*, 562-569.
- Tharun, J.; Bhin, K.-M.; Roshan, R.; Kim, D. W.; Kathalikkattil, A. C.; Babu, R.; Ahn, H. Y.; Won, Y. S.; Park, D.-W. *Green Chem.* **2016**, *18*, 2479-2487.
- Zhang, G.; Wei, G.; Liu, Z.; Oliver, S. R. J.; Fei, H. *Chem. Mater.* **2016**, *28*, 6276-6281.
- Li, P.-Z.; Wang, X.-J.; Liu, J.; Lim, J. S.; Zou, R.; Zhao, Y. *J. Am. Chem. Soc.* **2016**, *138*, 2142-2145.
- Zhou, X.; Zhang, Y.; Yang, X.; Zhao, L.; Wang, G. *J. Mol. Catal. A: Chem.* **2012**, *361*, 12-16.
- Babu, R.; Kathalikkattil, A. C.; Roshan, R.; Tharun, J.; Kim, D.-W.; Park, D.-W. *Green Chem.* **2016**, *18*, 232-242.
- Miralda, C. M.; Macias, E. E.; Zhu, M.; Ratnasamy, P.; Carreon, M. A. *ACS Catal.* **2012**, *2*, 180-183.
- Kathalikkattil, A. C.; Kim, D.-W.; Tharun, J.; Soek, H.-G.; Roshan, R.; Park, D.-W. *Green Chem.* **2014**, *16*, 1607-1616.
- Jiang, Z.-R.; Wang, H.; Hu, Y.; Lu, J.; Jiang, H.-L. *ChemSusChem* **2015**, *8*, 878-885.
- Verma, S.; Baig, R. B. N.; Nadagouda, M. N.; Varma, R. S. *Green Chem.* **2016**, *18*, 4855-4858.

Chapter 4 Insights into Hf-VPI-100 for CO₂ Adsorption and Chemical Fixation

4.1 Abstract

Metal-organic frameworks (MOFs) have shown great promise as efficient CO₂ adsorbents, as well as an emerging class of heterogeneous catalysts for CO₂ chemical fixation. However, it is a challenge to identify the catalytic reactive sites and probe the interaction between the epoxide/CO₂ within the framework. In this work, we synthesized and characterized two isostructural hafnium-based robust MOFs as Hf-VPI-100 (Cu) and Hf-VPI-100 (Ni). Both frameworks demonstrated high CO₂ uptake and catalytic efficiency for cycloaddition of CO₂ to epoxide. Comparison of catalytic efficiency between Hf-VPI-100 and the previously reported VPI-100 revealed that the variation of the metal node does not influence the catalytic performance as expected. *In situ* PXRD, QCM and DRIFTS have been used to probe the interaction between the guest molecules (CO₂/epoxide) and Hf-VPI-100. For CO₂, no specific chemical binding sites in MOFs has been observed and the uptake of CO₂ does not change the crystal structure of Hf-VPI-100. Both QCM and DRIFTS revealed the irreversible binding between the framework and 1,2-epoxybutane. The epoxide uptake per unit cell of VPI-100 MOFs and diffusion coefficients have been calculated by QCM analysis.

4.2 Introduction

According to the BP statistical review of world energy, 85% of global energy consumption was based on fossil fuels in 2016.¹ The burning of fossil fuels leads to the rise of anthropogenic CO₂ emissions, which can cause a series of environmental problems including global climate change² and ocean acidification³. Currently, carbon capture and storage/sequestration (CCS) from point source have been proposed as a means of reducing CO₂ emission and enabling the

continued use of fossil fuels.⁴ Although the reuse of CO₂ as a reactant in chemical transformations would not be a viable long-term strategy owing to the tremendous scale of worldwide CO₂ emissions (ca. 30 Gt per year), which can easily saturate the market for any desired chemicals, converting a considerable fraction of the emissive CO₂ can offer some recompense to the development of CCS technologies.⁵ Indeed, CO₂ represents a highly functional, non-toxic, abundant, cheap and renewable C1 resource and should not be viewed as a waste material.⁶⁻⁷

One of the most effective examples of CO₂ chemical fixation is the cycloaddition reaction of CO₂ and epoxide, which is a 100% atom economic reaction. The products of those chemical transformations, cyclic carbonates, can serve as polar aprotic solvents, electrolytes for lithium-ion batteries, and valuable intermediates for polycarbonates and polyurethanes.⁸⁻⁹ Therefore, extensive research studies have focused on the development of efficient heterogeneous catalysts for cycloaddition reactions. In particular, metal-organic frameworks (MOFs) have shown outstanding catalytic activity in those reactions due to their high internal surface area, chemical and structural tunability, high density of accessible catalytic sites and high affinity for CO₂.¹⁰⁻¹³ The mechanism for the cycloaddition of CO₂ to epoxides typically involves an acid catalyst (such as a metal ion or a proton) that coordinates to the epoxide as the first step to activate the epoxide, followed by nucleophilic attack by the co-catalyst (typically a tetraalkylammonium halide) to form a halo-alkoxide. The halo-alkoxide intermediate further react with CO₂ through cycloaddition to form cyclic carbonate with regeneration of the tetraalkylammonium halide co-catalyst (Figure 4.1).^{10, 14} Therefore, the reported MOFs that catalyze CO₂ addition to epoxides usually contain structural defects, open metal sites, and/or coordinately unsaturated metal nodes to serve as Lewis acid sites. Although different active sites in MOFs have been proposed based on the mechanism mentioned above, it is hard to identify specific catalytic sites in the framework, especially when dual/multiple Lewis acid sites represented in the same material. In fact, the interaction between epoxide/CO₂ with the porous structure are rarely explored, and there are no established experimental techniques to study the distribution and diffusion of epoxide/CO₂ within the framework. Herein, we use different methods to investigate the interaction between guest molecules and MOFs, affording us an opportunity to further elucidate the mechanism insights into CO₂ chemical fixations catalyzed by MOFs.

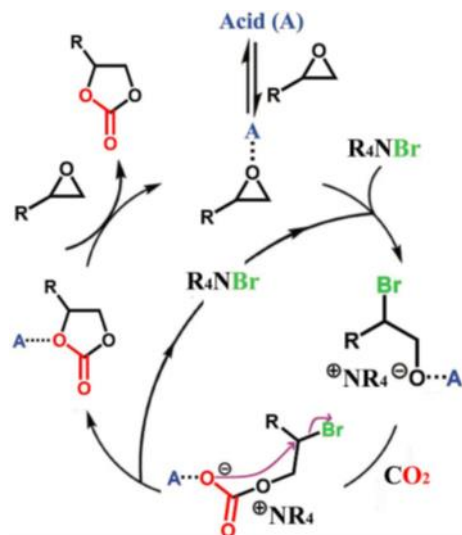


Figure 4.1 Proposed mechanism for the acid (A)-catalyzed cyclic carbonate synthesis from epoxides and CO₂ in the presence of a tetraalkyl ammonium halide (bromide).

Our group reported a new class of metal-cyclam based zirconium MOFs (VPI-100) demonstrating exceptional catalytic activity for cycloaddition of CO₂.¹⁵ In this paper, we prepared and characterized hafnium analogs of VPI-100 MOFs (Hf-VPI-100). The catalytic efficiency of Hf-VPI-100 MOFs has been investigated and the interaction between epoxide/CO₂ with the framework has been probed by *in situ* powder X-ray diffraction (PXRD), diffuse reflectance infrared Fourier transform spectroscopy (DRIFTS) and quartz crystal microbalance (QCM).

4.3 Results and discussion

4.3.1 Synthesis and characterization

Similar to reported VPI-100 MOFs, Hf-VPI-100 MOFs were prepared using modulated syntheses.¹⁶ Formic acid was used as the modulator and it is important to pre-form the hafnium oxo-cluster via a two-step solvothermal synthesis.¹⁵ Hf-VPI-100 (Cu) was obtained as violet crystalline powders, and Hf-VPI-100 (Ni) precipitated as light pink crystalline powders. SEM images revealed the morphology of the MOF samples as quasi-spherical particles with the sizes of 30-100 nm (Figure S2). Powder X-ray diffraction (PXRD) patterns (Figure 2A) collected by synchrotron radiation at Beamline 17-BM at Argonne National Laboratory (ANL) revealed that Hf-VPI-100 (Cu) and Hf-VPI-100 (Ni) are isostructural. XRD indexing and Rietveld analysis (Supporting Information, section 1) confirmed that Hf-VPI-100 (Cu) and Hf-VPI-100 (Ni) have

the same overall crystal structures (Figure 4.2), with a slight difference in unit cell parameters. Both MOFs crystallize in the space group $I4/m$ with same molecular formula, $\text{Hf}_6(\mu_3\text{-OH})_8(\text{OH})_8(\text{ML})_4$ where $\text{M} = \text{Cu}^{2+}/\text{Ni}^{2+}$, $\text{L} = 6,13\text{-dicarboxy-1,4,8,11-tetrazacyclotetradecan}$. Similar to other 8-connect Zr -MOFs such as PCN-222¹⁷ and NU-1000¹⁸, each Hf_6 cluster capped with eight $\mu_3\text{-OH}$ ligands. Eight of the twelve octahedral edges are connected to cyclam ligands, while the remaining Hf coordinate sites are occupied by eight terminal -OH ligands (Figure 4.2B). Moreover, comparison of experimental PXRD patterns between Hf-VPI-100 and parent VPI-100 has shown that the Hf and Zr analogs are isostructural (Figure S3).

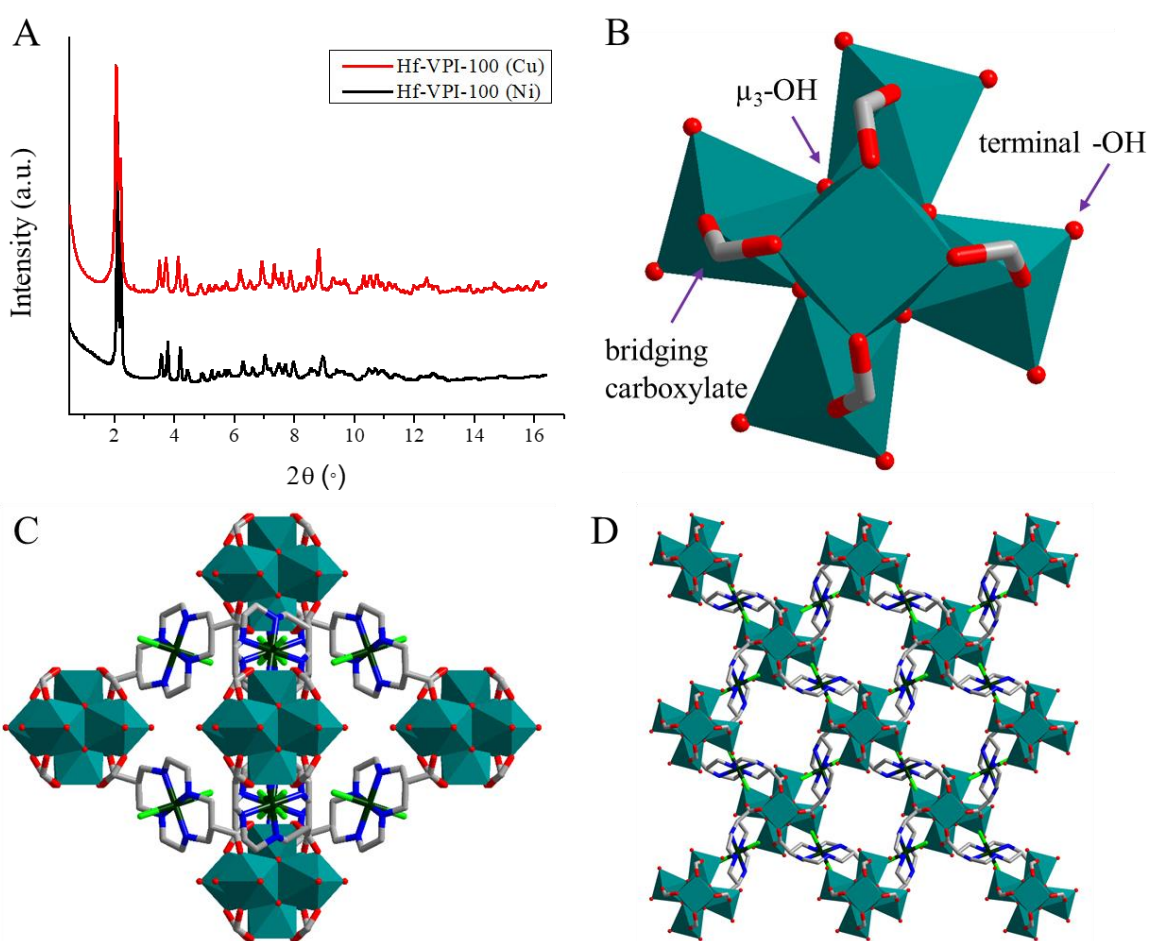


Figure 4.2 (A) PXRD patterns of as-synthesized Hf-VPI-100 MOFs collected at room temperature. (B) Polyhedral drawing of the Hf_6 cluster as view down from c axis. (C) Schematic structure of Hf-VPI-100 (Ni). (D) Packing diagram viewed down from c axis. Color scheme: Hf, light blue; C, gray; O, red; N, blue, Ni, dark green; Cl, green.

The XPS spectra revealed the oxidation states of Hf-VPI-100 MOFs to be Hf(IV), Ni(II) and Cu(II) (Figure S4 and S5), which are consistent with VPI-100. FT-IR spectra further confirmed

the overall structural similarity of Hf and Zr analogs of VPI-100 MOFs (Figure S6). Compared with metal-cyclam linkers, the carboxylic acid stretches in Hf-VPI-100 MOFs demonstrated a shift to lower wavenumbers (1614 cm^{-1} and 1585 cm^{-1} , respectively) due to the chelation of oxygen atoms to Hf_6 clusters in MOF structure. Thermogravimetric analysis (TGA) of the activated sample (Figure S7) demonstrated decomposition of the framework by ligand loss at $270\text{ }^\circ\text{C}$ for Hf-VPI-100 (Cu) and $330\text{ }^\circ\text{C}$ for the Ni analog, respectively. Hf-VPI-100 (Ni) demonstrated slightly higher thermal stability than Hf-VPI-100 (Cu), which was further confirmed variable temperature *in situ* PXRD. A similar trend has been also reported in VPI-100 MOFs. The porosity of Hf-VPI-100 MOFs was studied by N_2 adsorption-desorption experiments at 77 K and both frameworks exhibited a reversible type II isotherms (Figure S8). The Brunauer-Emmett-Teller (BET) surface areas of $396\text{ m}^2\text{ g}^{-1}$ and $399\text{ m}^2\text{ g}^{-1}$ were calculated from N_2 isotherms for Hf-VPI-100 (Cu) and Hf-VPI-100 (Ni), respectively. FT and Monte Carlo simulations revealed the pore diameters to be around 7.7 \AA and 7.2 \AA for Hf-VPI-100 (Cu) and Hf-VPI-100 (Ni).

The CO_2 capture properties of the Hf-VPI-100 MOFs were investigated at 273 K and 296 K under ambient pressure (Figure 4.3). Both MOFs exhibited characteristic type I isotherms as microporous materials. The Hf-based MOFs reached a CO_2 uptake of $42\text{ cm}^3/\text{g}$ (8.3 wt%) and $46\text{ cm}^3/\text{g}$ (9.1 wt%) at 273 K for Hf-VPI-100 (Cu) and Hf-VPI-100 (Ni), respectively. Compared with VPI-100 under same activation conditions, the hafnium analog revealed significant increase in CO_2 uptake (Table S1). This is probably because of more polarized $\mu_3\text{-OH}$ groups of Hf clusters, which strengthen the interactions between CO_2 and MOFs.¹⁹

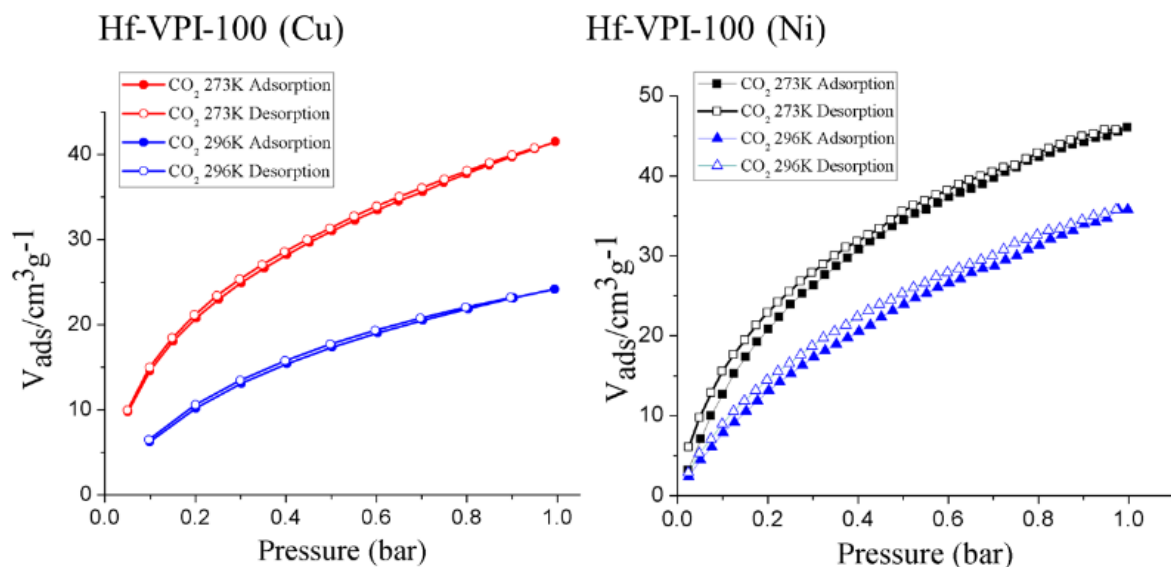


Figure 4.3 The CO₂ adsorption isotherms of Hf-VPI-100 MOFs at 273 K and 296 K, 1 atm.

4.3.2 Cycloaddition of CO₂ and epoxides

Given the high stability, porosity, and CO₂ adsorption uptake, Hf-VPI-100 (Cu) and Hf-VPI-100 (Ni) were investigated as heterogeneous catalysts for cycloaddition of CO₂ with epoxides in the presence of tetrabutylammonium bromide (TBAB) as co-catalyst. In a typical catalysis experiment, the Hf-VPI-100 catalyst (0.008 mmol), co-catalyst TBAB (0.31 mmol), and epoxides (31.3 mmol) were placed in a 25 mL stainless autoclave reactor. The reaction was carried out at 90 °C and 1.5 bar CO₂ for 6 h, and the resulting mixture was analyzed by ¹H NMR to determine the conversion yield and the selectivity of cycloaddition products (Supporting information, section 3). It is worth noting that we did not pick propylene oxide as the reactant because it is highly volatile (boiling point = 34 °C) and cannot be separated upon CO₂ decompression after the reaction. Instead, epichlorohydrin (boiling point = 117.9 °C) and 1,2-epoxybutane (boiling point = 63 °C) were used to guarantee the unreacted epoxide will not evaporate during the workup, which would not cause inaccuracy in the calculation of conversion yield.

Table 4.1 Cycloaddition of CO₂ and epichlorohydrin catalysed by different catalysts^a

Entry	Catalyst	Run	Yield (%) ^b	Selectivity (%)
-------	----------	-----	------------------------	-----------------

1	TBAB	1	16.2	94
2	[CuL(ClO ₄) ₂] and TBAB	1	90.2	99
3	Hf-VPI-100 (Cu) and TBAB	1	97.2	99
4	Hf-VPI-100 (Cu) and TBAB	2	95.6	99
5	Hf-VPI-100 (Ni) and TBAB	1	89.5	99
6	Hf-VPI-100 (Ni) and TBAB	2	86.2	99

^a Reaction conditions: 31.3 mmol epoxide, 0.008 mmol Hf-VPI-100 MOF and 0.31 mmol TBAB (1% mol) under 1.5 bar CO₂ and 90 °C for 6 h. ^b Conversion evaluated from the ¹H NMR spectra by integration of epoxide versus cyclic carbonate peaks. (Figure S9 - 14)

As shown in Table 4.1, Hf-VPI-100 demonstrated highly efficient catalytic activity for cycloaddition of epichlorohydrin and CO₂ under 1.5 bar CO₂ and 90 °C over 6 h with a yield of 97.2% (Table 4.1, entry 3) and 89.5% (Table 1, entry 5) for Cu and Ni analogs, respectively. Without the MOF catalysts, the control experiment with only TBAB (Table 4.1, entry 1) led to a low yield of 16.2%. Moreover, Hf-VPI-100 (Cu) outperformed the Cu(II)-cyclam ligand as molecular catalyst control, which exhibited 90% yield (Table 4.1, entry 2) for the formation of cyclic carbonate under same reaction conditions. We reasoned that the catalytic efficiency of molecular catalyst was limited by their low solubility under such solvent-free system.¹⁵ In contrast, the heterogeneous MOF catalyst contains more accessible active metal sites as Lewis acid sites and those catalytic centers are spatially isolated to minimize possible catalyst poisoning pathways. Moreover, the Hf-VPI-100 MOFs can be easily recycled from the reaction mixture by centrifugation and reused without substantial loss of catalytic activity (Table 4.1, entry 4 & 6). The recycled MOF powders largely retained their crystallinity evidenced by the retention of the major PXRD peaks compared with the MOF sample before catalysis (Figure S15). ICP-MS analysis revealed that the framework maintained the same Cu/Ni : Zr ratios before and after the catalysis, indicating that the metal center did not leach from the framework.

Figure 4.4 shows the influence of reaction time on the coupling reaction of CO₂ and epoxide using Hf-VPI-100 as the catalyst. At each time point, the ¹H NMR spectra of the reaction

mixture were collected to calculate the conversion yield (Figure S16). Hf-VPI-100 (Cu) was used as the catalyst, 1.5 bar CO₂ and epichlorohydrin was reacted at 90 °C with the presence of TBAB as co-catalyst. The conversion yield of cyclic carbonate increased steadily from 47% to 94% as the reaction time elapsed from 2 to 8 h. It is important to note that similar yield can be achieved in continuous reaction over the course of 6 h. Due to the sealed reaction system, the collection of the reaction mixture at each time point would interrupt the equilibrium of the reaction, thus led to a longer overall time to reach the plateau of conversion yield.

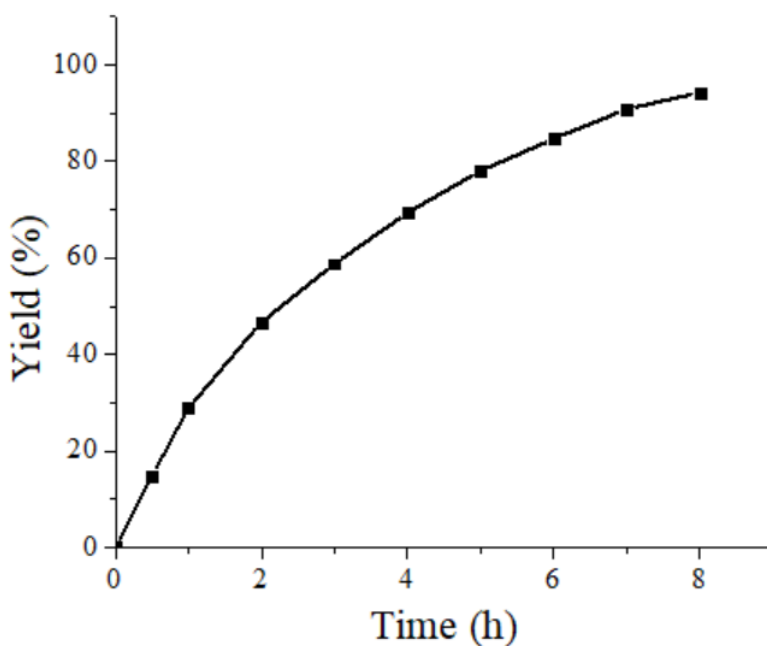


Figure 4.4 The conversion yield of epoxide to carbonate vs reaction time.

According to previous reported Hf-based MOF for CO₂ chemical fixation, it was found the Hf-NU-1000 demonstrated significant higher catalytic reactivity than Zr-NU-1000 for cycloaddition of CO₂ and epoxide. The proposed mechanism is that Hf node is more oxophilic than Zr node, thus would function as a stronger Brønsted acid to facilitate the epoxide activation.²⁰ Therefore, we also expected to observe a similar trend in the family of VPI-100 MOFs initially. In order to test the catalytic performance, the 1,2-epoxybutane was picked as the starting material since Zr-VPI-100 established moderate conversion yield as the catalyst from the pervious report.¹⁵ Interestingly, Hf-VPI-100 (Cu) and Hf-VPI-100 (Ni) was also demonstrated moderate catalytic activity towards the formation of butylene oxide at 90 °C and 1.5 bar CO₂

over 6 h with a yield of 43.8% and 39.4%, respectively (Figure S17 and 18). Higher conversion yield was obtained using Zr-VPI-100 (Cu) under the same reaction conditions (Figure S19). Considering the Lewis acidic nature of both potential accessible $\text{Cu}^{2+}/\text{Ni}^{2+}$ metal active sites in the metallocyclam and coordinatively unsaturated $\text{Hf}^{4+}/\text{Zr}^{4+}$ sites of the metal nodes in VPI-100 MOFs, it is highly possible that the dual catalytic sites may not be acted as the synergic effect under this specific conditions. In fact, for VPI-100 MOFs, Zr-VPI-100 demonstrated higher catalytic efficiency for cycloaddition of CO_2 and 1,2-epoxybutane than Hf-VPI-100. To tap the question, we decided to study the interaction between epoxide and framework using QCM, DRIFT, and PXRD as probes.

4.3.3 Quartz Crystal Microbalance (QCM)

The adsorption kinetics of 1,2-epoxybutane onto Hf-VPI-100 was uncovered by QCM-D. In Figure 4.5, 0.043 mg and 0.068 mg of Hf-VPI-100 (Cu) were drop-casted onto self-assembled monolayers terminated by carboxylic groups (SAM-COOH). In the first 10 min, pure nitrogen gas was introduced in QCM-D cells to establish a flat baseline. After diverting the nitrogen gas into a gas saturator cell containing 1,2-epoxybutane, the resulting 1,2-epoxybutane vapor was carried into the QCM-D flow cell, which allowed for gas-MOF interaction to occur. As seen from Figure 4.5, two distinct processes were associated with the adsorption of 1,2-epoxybutane. 1) A rapid decrease in frequency at the initial adsorption stage. This fast adsorption process was attributed to the non-specific binding of 1,2-epoxybutane onto the surface of Hf-VPI-100 (Cu) thin film. This first process only lasted ~ 1.5 min, but accounted for $\sim 2/3$ of the total adsorption amount. 2) A slow and steady decrease in frequency. In this process, the 1,2-epoxybutane mass-uptake slowed down and eventually saturated the Hf-VPI-100 (Cu) thin film. This slow frequency decrease was tentatively assigned to the diffusion of 1,2-epoxybutane into deeper layers of Hf-VPI-100 (Cu), due to the specific binding between 1,2-epoxybutane and the Hf-VPI-100 (Cu). After 130 min flow of the mixture of 1,2-epoxybutane and nitrogen gas, the frequency change reached a stable minimum

and QCM-D cells were purged with pure nitrogen. Irreversible adsorptions of ~18 Hz and ~34 Hz frequency changes were found for 0.043 mg and 0.068 mg of Hf-VPI-100 (Cu), respectively, resulting from the binding of 1,2-epoxybutane molecules to the active sites in Hf-VPI-100 (Cu). The irreversible adsorptions were also confirmed from dissipation graph. As 1,2-epoxybutane molecules diffused and bound to Hf-VPI-100 thin films, the larger ΔD we observed from QCM-D, suggested Hf-VPI-100 thin films became softer compared to untreated Hf-VPI-100 thin films.

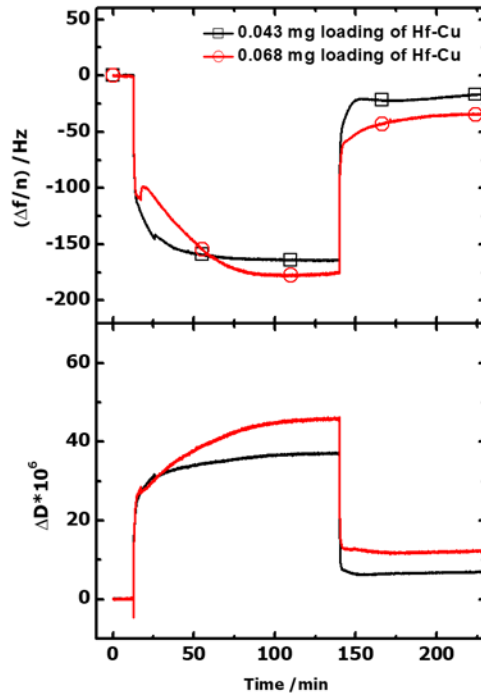


Figure 4.5 Representative adsorptions of 1,2-epoxybutane onto Hf-VPI-100 (Cu) thin films

With the application of Fickian diffusion model,²¹⁻²² we can further calculate the diffusion coefficient from two adsorption processes. In Fickian diffusion model,

$$\frac{M_f(t)}{M_\infty} = 1 - \frac{8}{\pi^2} \sum_{m=0}^{\infty} \frac{1}{(2m+1)^2} \exp\left(-\frac{4D(2m+1)^2\pi^2 t}{L^2}\right)$$

If we assume the partial pressure of 1,2-epoxybutane is far less than the nitrogen carrier gas pressure. The equation above can be simplified as

$$\frac{M_f(t)}{M_\infty} \approx \frac{8}{\sqrt{\pi}} \sqrt{\frac{Dt}{L^2}}$$

where M_∞ represents the maximum surface concentration before the final purge of nitrogen gas. $M_f(t)$ is the surface concentration at a given time t . L is the thickness of MOF thin film. Using Sauerbrey equation, one can convert the adsorption curve of 0.068 mg loading of Hf-VPI-100 (Cu) in Figure 4.5 to the curve in Figure 4.6. Two diffusion coefficients can then be derived from the slopes of linear regression for the two adsorption processes, with $1.6 \times 10^{-17} \text{ m}^2 \cdot \text{s}^{-1}$ for the initial adsorption and $4.4 \times 10^{-20} \text{ m}^2 \cdot \text{s}^{-1}$ for the second adsorption process.

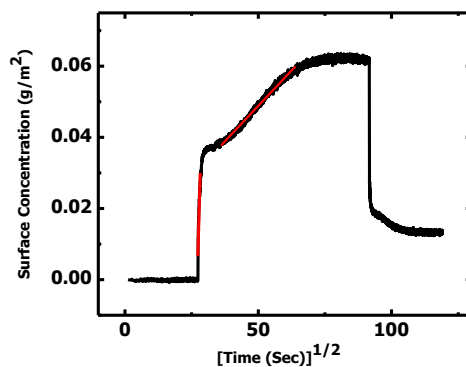


Figure 4.6 Representative surface concentration vs. square root of adsorption time.

QCM-D results are summarized in Table 2. D_1 and D_2 are the diffusion coefficients for the initial and second adsorption processes. With the loading masses of VPI-100 MOFs on QCM-D sensors and irreversible uptake-masses of 1,2-epoxybutane on VPI-100 MOF surfaces, one can readily calculate the numbers of epoxide molecules bound to a unit cell of VPI-100 MOFs. As revealed from Table 2, VPI-100 MOFs with Ni^{2+} incorporated ligands have higher 1,2-epoxybutane to unit cell ratios. This trend also holds true for the D_1 values. VPI-100 MOFs with Hf nodes have higher D_2 values. As we mentioned before, the catalytic activity of Hf-VPI-100 (Cu) is slightly higher than that of Hf-VPI-100 (Ni). Based upon epoxide molecule per unit cell data, we can deduce that the active sites on the ligands may play a more important role on catalytic activities than the active sites on the nodes.

Table 4.2 QCM-D results of epoxide molecule per unit cell, D_1 and D_2 values for VPI-100 MOF

	Hf-Cu-L MOF	Hf-Ni-L MOF	Zr-Cu-L MOF	Zr-Ni-L MOF
Epoxide molecule per unit cell	0.19	0.71	0.43	0.76
Average	0.27	0.65	0.44	0.65
Average	0.23±0.06	0.68±0.04	0.44±0.01	0.71±0.08
D_1 (m^2s^{-1})	1.6×10^{-17}	4.6×10^{-17}	3.1×10^{-18}	2.5×10^{-17}
D_1 (m^2s^{-1})	1.5×10^{-17}	6.0×10^{-17}	3.3×10^{-18}	3.9×10^{-17}
Average	$(1.6 \pm 0.1) \times 10^{-17}$	$(5.3 \pm 1.0) \times 10^{-17}$	$(3.2 \pm 0.1) \times 10^{-18}$	$(3.2 \pm 1.0) \times 10^{-17}$
D_2 (m^2s^{-1})	4.4×10^{-20}	8.5×10^{-20}	3.0×10^{-20}	2.9×10^{-20}
D_2 (m^2s^{-1})	4.3×10^{-20}	7.8×10^{-20}	3.6×10^{-20}	3.0×10^{-20}
Average	$(4.3 \pm 0.1 \times 10)^{-20}$	$(8.1 \pm 0.5) \times 10^{-20}$	$(3.3 \pm 0.5) \times 10^{-20}$	$(2.9 \pm 0.1) \times 10^{-20}$

4.3.4 *In situ* PXRD

To further probe the interaction between CO_2 and Hf-VPI-100 MOFs, *in situ* PXRD experiments under CO_2 have been performed. PXRD patterns of Hf-VPI-100 under helium and CO_2 from 1 bar to 20 bar have been collected in 298 K. As shown in Figure 4.7, no significant phase change has been observed from the diffraction patterns of both frameworks at He and 20 bar CO_2 . For Hf-VPI-100 (Cu), two small peaks (where $2\theta = 2.8$ and 3.1°) have been emerging with the presence of CO_2 at low angle region and the peak intensity has been increased with the increase of CO_2 pressure. A similar change also has been observed in the PXRD data of Hf-VPI-100 (Ni) as shown in the inset of Figure 4.7. Those two emerging peaks might simply attribute to the electronic density change after CO_2 diffused in the pore of Hf-VPI-100. Those diffraction patterns can determine no specific binding sites between CO_2 and the framework and the Hf-VPI-100 MOFs maintained their crystal structure under 20 bar CO_2 . Moreover, the PXRD patterns of Hf-VPI-100 under CO_2 at 200 K and 1 bar have also been collected. Although the framework would uptake more CO_2 at 200 K compared with those at 298 K, no notable change has been observed in PXRD data for both frameworks. DRIFTS experiments further indicated that Hf-VPI-100 MOFs maintained their well-defined structure under CO_2 atmosphere. No signal change has been observed except for the presence of vibrational peaks for CO_2 at gas phase. Therefore, no specific chemical binding sites of CO_2 in Hf-VPI-100 can be identified through those techniques.

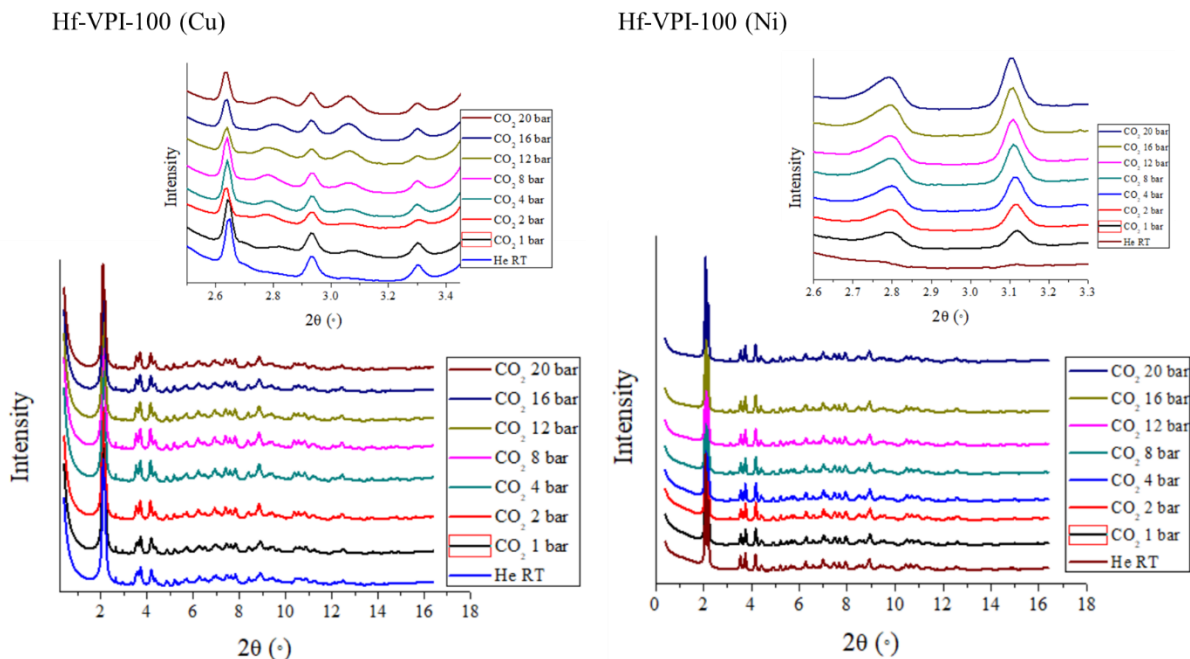


Figure 4.7 *In situ* PXRD of Hf-VPI-100 under He and CO₂ from 1 bar to 20 bar.

4.4 Experimental

4.4.1 Materials

All chemicals were purchased from commercial sources and used without further purification unless otherwise mentioned.

Caution! The perchlorate salts described are potentially explosive and should be handled with care and prepared in small quantities.

4.4.2 Synthesis

Synthesis of 6,13-dicarboxy-1,4,8,11-tetrazacyclotetradecan)-copper (II) perchlorate [CuL(ClO₄)₂] (1). Based on our reported procedure,¹⁵ the tetracarboxylate precursor [Cu(tetacH₄)](ClO₄)₂ (0.63 g, 0.99 mmol) was added to 10 mL of 0.1 M HClO₄ solution and heated at reflux for 1 h. After the reaction mixture cooled down to room temperature (R.T.), 3 mL of 60 % HClO₄ was added and the solution refrigerated overnight. The product was filtered off as red crystalline solid (0.38 g, 46 % yield).

Synthesis of 6,13-dicarboxy-1,4,8,11-tetrazacyclotetradecan (L) (2). Based on our reported procedure,¹⁵ the free-base ligand (2) was prepared by the demetallation of (1). The [CuL(ClO₄)₂] (0.32 g, 0.58 mmol) was added in 20 mL of 37 % HCl and heated to reflux for 1 h.

The resultant white solid was filtered and washed with ethanol. After drying under vacuum, white powder (0.16 g, 95 % yield) was obtained. (ESI-MS: $[M-H]^+$ $m/z = 289.19$)

Synthesis of Hf-VPI-100 (Cu). The Hf-VPI-100 (Cu) was prepared in a similar approach as reported VPI-100 MOFs.¹⁵ In an 8 mL vial, $HfCl_4$ (19 mg, 0.06 mmol) was added in 4 mL of dry DMF with 0.44 mL (200 eq.) of formic acid. The vial was heated at 80 °C in an oven for 1 h. After cooling to R.T., $[CuL(ClO_4)_2]$ (33 mg, 0.06 mmol) was added and the solution was sonicated for 10 min. Then, the mixture was heated in a 120 °C oven for 24 h. After cooling to R.T., the crystalline solid was isolated by centrifugation, rinsed with fresh DMF and acetone. The powder was dried under vacuum at 60 °C. Violet crystalline powder was obtained (30 mg, 76% yield). The phase purity of Hf-VPI-100 (Cu) was verified by PXRD.

Synthesis of Hf-VPI-100 (Ni). The Hf-VPI-100 (Ni) was prepared in a similar approach as reported VPI-100 MOFs.¹⁵ In an 8 mL vial, $HfCl_4$ (19 mg, 0.06 mmol) was dissolved in 2 mL of dry DMF with 0.44 mL (200 eq.) of formic acid. In a separate vial, $NiCl_2 \cdot 6H_2O$ (14 mg, 0.06 mmol) and free-base ligand (2) (17.3 mg, 0.06 mmol) were added to 2 mL of dry DMF, and sonicated for 10 mins. Then, both vials were heated in an 80 °C oven for 1 h. The solutions were combined into one vial and heated in a 120 °C oven for 24 h. After cooling to R.T., the resultant solid was isolated by centrifugation, washed with fresh DMF and acetone. The product was dried under vacuum at 60 °C. Light pink crystalline powders were obtained (20 mg, 51% yield). The phase purity of Hf-VPI-100 (Ni) was confirmed by PXRD.

4.4.3 Characterization and analysis

Structure determination and refinement. The structures of Hf-VPI-100 were determined by PXRD using synchrotron radiation at Beamline 17-BM at Advanced Photon Source (APS) at Argonne National Laboratory (ANL).

Powder X-ray Diffraction (PXRD). The phase purity of the synthesized MOF samples was analyzed on a Rigaku Miniflex diffractometer with a $Cu(K\alpha)$ radiation ($\lambda = 1.5418 \text{ \AA}$) over a 2θ range of 3-50° in continuous scanning mode (1.0°/min) and a resolution of 0.05°. The powder samples were loaded onto a zero-background Si (510) disk.

Attenuated Total Reflectance Fourier-Transform Infrared Spectroscopy (ATR-FTIR). ATR-FTIR spectra were obtained using a Varian 670 FT-IR Spectrometer. All spectra were an

average of 64 scans for powdered samples and were recorded from 4000 to 500 cm^{-1} with 4 cm^{-1} resolutions.

Thermogravimetric Analysis (TGA). The MOF samples (~5 mg) were placed on an aluminum pan and heated at a rate of 10 $^{\circ}\text{C}/\text{min}$ under nitrogen atmosphere over the temperature range of 25–600 $^{\circ}\text{C}$ by using a Q500 thermogravimetric analyzer from TA Instruments.

Scanning electron microscopy imaging (SEM). Images were collected by using a Leo/Zeiss 1550 Schottky field-emission scanning electron microscope.

X-ray Photoelectron Spectroscopy (XPS). The XPS spectra were collected on a PHI 5000 Vera Probe III spectrometer using an aluminum anode X-ray source (photon energy of 1486.6 eV).

N_2/CO_2 adsorption measurements. Before a gas sorption experiment, as-synthesized MOF samples (~50 mg) were washed with DMF three times and acetone three times, followed by soaking in acetone for 3 days to allow solvent exchange. The resulting exchanged frameworks were activated under vacuum for 12 h, and then degassed under vacuum for 12 h at 100 $^{\circ}\text{C}$ prior to gas adsorption/desorption measurements. The sorption isotherm data were collected with a Quantachrome Autosorb-1. The surface areas of the samples were determined by fitting the N_2 adsorption data at 77 K within a relative pressure (P/P_0) range of 0.05 to 0.25 to the BET equation.

Cycloaddition of CO_2 to epoxides. Hf-VPI-100 MOF samples (0.0045 mmol), tetrabutylammonium bromide (99 mg, 0.31 mmol), and epoxide (31.1 mmol) were added to a 20 mL stainless steel Parr reactor. The sealed vessel was heated to 90 $^{\circ}\text{C}$ in an oil bath and charged with CO_2 (1.5 bar). After 6 h, the reactor was allowed to cool to R.T. and the unreacted CO_2 was slowly released. A small aliquot was dissolved in CDCl_3 for ^1H NMR analysis to determine the conversion. The reaction solution was centrifuged to recover the catalyst. The recovered MOF powder was washed with CHCl_3 (3×1 mL) and dried under vacuum. The sample was reused three times in the catalysis experiment for each substrate. The structural stability of the framework was confirmed by PXRD.

Quartz Crystal Microbalance with Dissipation monitoring (QCM-D) The clean gold chips were immersed into 3 mM 16-mercaptohexadecanoic acid in ethanol solution for 24 hours to

allow the formation of well-defined SAM-COOH surfaces. The MOF samples (0.02~ 0.07 mg) were drop-casted on gold QCM-D sensors with –COOH terminated self-assembled monolayer (SAM-COOH). The 5th overtone frequencies before and after drop-casting were detected and recorded by QCM-D. The MOF films were held at 21 °C and purged with nitrogen gas until a flat baseline was obtained. Nitrogen gas was then diverted into a gas saturator cell containing 1,2-epoxybutane at 18 °C via a water bath. The 1,2-epoxybutane vapor was carried into the QCM–D flow cell by the nitrogen carrier gas, which allowed for gas-MOF interaction to occur. The constant flow of 1,2-epoxybutane vapor continued until the change of frequency reached a stable minimum, leading to maximum uptake at equilibrium. The flow was then switched to pure nitrogen gas until a flat frequency line was observed. The nitrogen gas flow was kept a constant flow pressure of 4 PSIG relative to the ambient pressure.

4.5 Conclusion

In summary, two metal-cyclam based Hf-MOFs have been prepared via modulated synthesis and proved to be isostructural as VPI-100 MOFs. Both frameworks demonstrated high CO₂ uptake capacity up to ~9.1 wt% adsorption at 273 K under 1 atm and excellent catalytic efficiency (up to 97.2%) for the cycloaddition of CO₂ to epichlorohydrin. QCM has been used as a unique probe to study the binding between 1,2-epoxybutane and the frameworks. The uptake of 1,2-epoxybutane and the diffusion coefficients for two adsorption processes have been obtained from quantitative analysis in QCM. Based on the comparison between Hf-VPI-100 and VPI-100, it is found that the active sites on the ligands may play a more important role in catalytic activities than the active sites on the nodes.

4.6 Acknowledgements

This material is based upon work supported by the U.S. department of Energy, Office of Basic Energy Sciences under Award Number DE-SC0012445. Use of the Advanced Photon Source, an Office of Science User Facility operated for the U.S. Department of Energy (DOE) Office of Science by Argonne National Laboratory, was supported by the U.S. DOE under Contract No. DE-AC02-06CH11357. SDS was supported by the U.S. Department of Energy, Office of Science, Office of Basic Energy Sciences, and Catalysis Science Program under contract No. DE-SC0012704.

4.7 Reference

1. Dale, S., BP Statistical Review of World Energy June 2017. BP: 2017.
2. Stocker, T., Climate Change 2013, “*The Physical Science Basis*,” Working Group I.
3. Orr, J. C.; Fabry, V. J.; Aumont, O.; Bopp, L.; Doney, S. C.; Feely, R. A.; Gnanadesikan, A.; Gruber, N.; Ishida, A.; Joos, F., Anthropogenic ocean acidification over the twenty-first century and its impact on calcifying organisms. *Nature* **2005**, *437* (7059), 681.
4. Haszeldine, R. S., Carbon Capture and Storage: How Green Can Black Be? *Science* **2009**, *325* (5948), 1647-1652.
5. Sumida, K.; Rogow, D. L.; Mason, J. A.; McDonald, T. M.; Bloch, E. D.; Herm, Z. R.; Bae, T.-H.; Long, J. R., Carbon Dioxide Capture in Metal–Organic Frameworks. *Chemical Reviews* **2012**, *112* (2), 724-781.
6. Finn, C.; Schnittger, S.; Yellowlees, L. J.; Love, J. B., Molecular approaches to the electrochemical reduction of carbon dioxide. *Chemical Communications* **2012**, *48* (10), 1392-1399.
7. Morris, A. J.; Meyer, G. J.; Fujita, E., Molecular approaches to the photocatalytic reduction of carbon dioxide for solar fuels. *Accounts of chemical research* **2009**, *42* (12), 1983-1994.
8. Cokoja, M.; Bruckmeier, C.; Rieger, B.; Herrmann, W. A.; Kühn, F. E., Transformation of Carbon Dioxide with Homogeneous Transition-Metal Catalysts: A Molecular Solution to a Global Challenge? *Angewandte Chemie International Edition* **2011**, *50* (37), 8510-8537.
9. Chen, A.; Zhang, Y.; Chen, J.; Chen, L.; Yu, Y., Metalloporphyrin-based organic polymers for carbon dioxide fixation to cyclic carbonate. *Journal of Materials Chemistry A* **2015**, *3* (18), 9807-9816.
10. Beyzavi, M. H.; Stephenson, C. J.; Liu, Y.; Karagiari, O.; Hupp, J. T.; Farha, O. K., Metal–Organic Framework-Based Catalysts: Chemical Fixation of CO₂ with Epoxides Leading to Cyclic Organic Carbonates. *Frontiers in Energy Research* **2015**, *2* (63).
11. He, H.; Perman, J. A.; Zhu, G.; Ma, S., Metal-Organic Frameworks for CO₂ Chemical Transformations. *Small* **2016**, *12* (46), 6309-6324.
12. Maina, J. W.; Pozo-Gonzalo, C.; Kong, L.; Schutz, J.; Hill, M.; Dumeénil, L. F., Metal organic framework based catalysts for CO₂ conversion. *Materials Horizons* **2017**, *4* (3), 345-361.
13. Trickett, C. A.; Helal, A.; Al-Maythaly, B. A.; Yamani, Z. H.; Cordova, K. E.; Yaghi, O. M., The chemistry of metal–organic frameworks for CO₂ capture, regeneration and conversion. *Nature Reviews Materials* **2017**, *2*, 17045.
14. North, M.; Pasquale, R.; Young, C., Synthesis of cyclic carbonates from epoxides and CO₂. *Green Chemistry* **2010**, *12* (9), 1514-1539.
15. Zhu, J.; Usov, P. M.; Xu, W.; Celis-Salazar, P. J.; Lin, S.; Kessinger, M. C.; Landaverde-Alvarado, C.; Cai, M.; May, A. M.; Sledobnick, C.; Zhu, D.; Senanayake, S. D.; Morris, A. J., A New Class of Metal-Cyclam-Based Zirconium Metal–Organic Frameworks for CO₂ Adsorption and Chemical Fixation. *Journal of the American Chemical Society* **2018**, *140* (3), 993-1003.
16. Schaate, A.; Roy, P.; Godt, A.; Lippke, J.; Waltz, F.; Wiebcke, M.; Behrens, P., Modulated Synthesis of Zr-Based Metal–Organic Frameworks: From Nano to Single Crystals. *Chemistry – A European Journal* **2011**, *17* (24), 6643-6651.
17. Feng, D.; Gu, Z. Y.; Li, J. R.; Jiang, H. L.; Wei, Z.; Zhou, H. C., Zirconium-Metalloporphyrin PCN-222: Mesoporous Metal–Organic Frameworks with Ultrahigh Stability as Biomimetic Catalysts. *Angewandte Chemie* **2012**, *124* (41), 10453-10456.
18. Mondloch, J. E.; Bury, W.; Fairen-Jimenez, D.; Kwon, S.; DeMarco, E. J.; Weston, M. H.; Sarjeant, A. A.; Nguyen, S. T.; Stair, P. C.; Snurr, R. Q.; Farha, O. K.; Hupp, J. T., Vapor-Phase Metalation by Atomic Layer Deposition in a Metal–Organic Framework. *Journal of the American Chemical Society* **2013**, *135* (28), 10294-10297.
19. Hu, Z.; Peng, Y.; Gao, Y.; Qian, Y.; Ying, S.; Yuan, D.; Horike, S.; Ogiwara, N.; Babarao, R.; Wang, Y.; Yan, N.; Zhao, D., Direct Synthesis of Hierarchically Porous Metal–Organic Frameworks with High Stability and Strong Brønsted Acidity: The Decisive Role of Hafnium in Efficient and Selective Fructose Dehydration. *Chemistry of Materials* **2016**, *28* (8), 2659-2667.

20. Beyzavi, M. H.; Klet, R. C.; Tussupbayev, S.; Borycz, J.; Vermeulen, N. A.; Cramer, C. J.; Stoddart, J. F.; Hupp, J. T.; Farha, O. K., A Hafnium-Based Metal–Organic Framework as an Efficient and Multifunctional Catalyst for Facile CO₂ Fixation and Regioselective and Enantioselective Epoxide Activation. *Journal of the American Chemical Society* **2014**, *136* (45), 15861-15864.
21. Zacher, D.; Baunemann, A.; Hermes, S.; Fischer, R. A., Deposition of microcrystalline [Cu₃(btc)₂] and [Zn₂(bdc)₂(dabco)] at alumina and silica surfaces modified with patterned self assembled organic monolayers: evidence of surface selective and oriented growth. *Journal of Materials Chemistry* **2007**, *17* (27), 2785-2792.
22. Bordiga, S.; Regli, L.; Bonino, F.; Groppo, E.; Lamberti, C.; Xiao, B.; Wheatley, P.; Morris, R.; Zecchina, A., Adsorption properties of HKUST-1 toward hydrogen and other small molecules monitored by IR. *Physical Chemistry Chemical Physics* **2007**, *9* (21), 2676-2685.

4.8 Supporting Information

4.8.1 Structure determination and refinement of Hf-VPI-100 (Cu) and Hf-VPI-100 (Ni)

XRD indexing and Rietveld analysis was performed with TOPAS version 5. Figure 2 shows the XRD profiles of Hf-VPI-100 (Cu) and Hf-VPI-100 (Ni) at room temperature. The high similarity of the diffraction patterns suggested the Cu and Ni analogues are isostructural. Indexing of the Hf-VPI-100 (Ni) patterns suggested a body-centered tetragonal lattice with unit cell parameters: $a \sim 16.6 \text{ \AA}$ and $c \sim 18.6 \text{ \AA}$. The fitted PXRD patterns are shown in Figure S1.

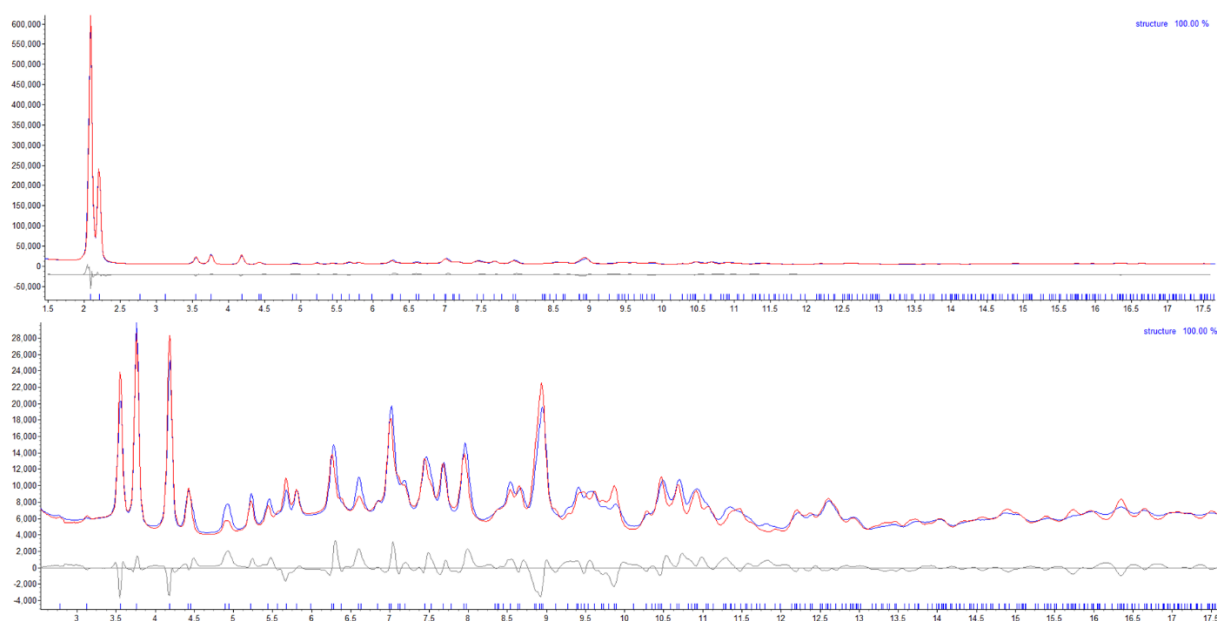


Figure S1. Refinement plots of Hf-VPI-100 (Ni) as synthesized under room temperature. The bottom panel is a zoomed-in view of the low intensity peaks in the top panel. The blue line is the observed curve, the red line is the calculated curve, the grey line is the fitted background line, and the grey line oscillating around 0 is the difference between the observed and the calculated.

4.8.2 Characterization of Hf-VPI-100 (Cu) and Hf-VPI-100 (Ni)

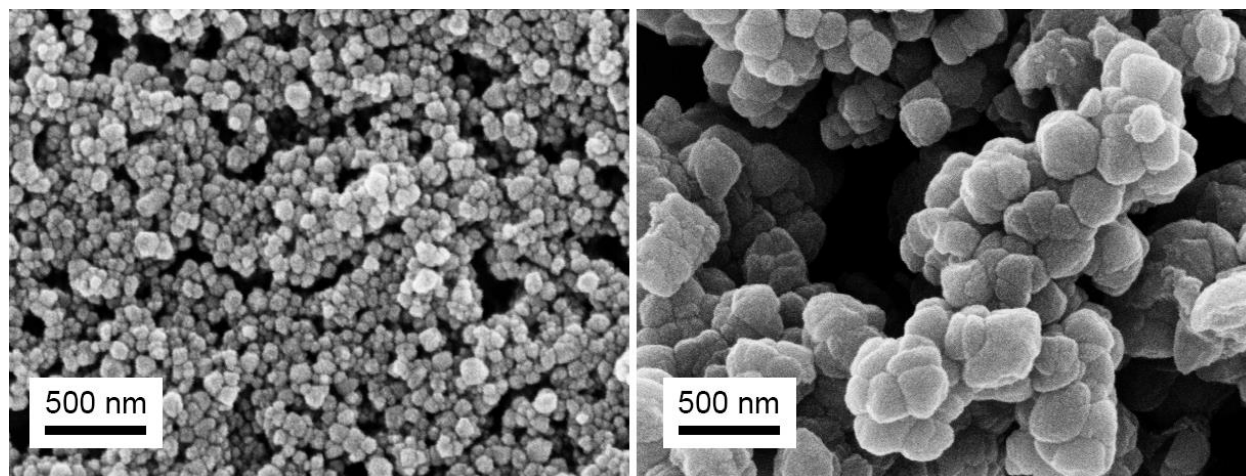


Figure S2. SEM image of the microcrystalline powder of Hf-VPI-100 (Cu) (left) and Hf-VPI-100 (Ni) (right).

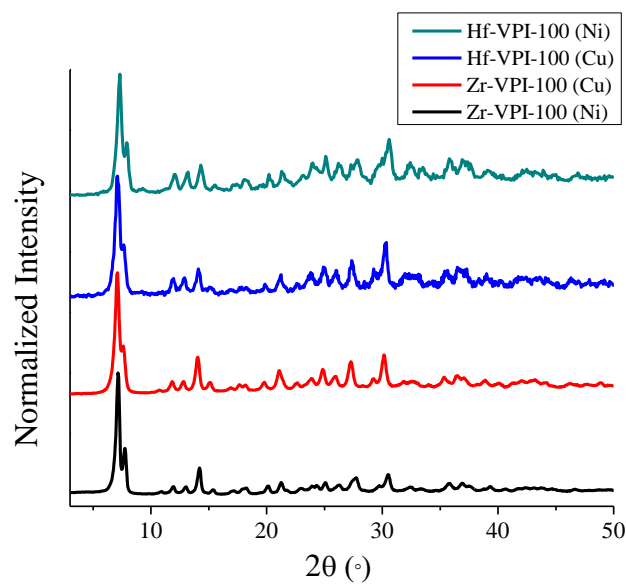


Figure S3. PXRD patterns of as synthesized Hf-VPI-100 and Zr-VPI-100 powders measured at room temperature.

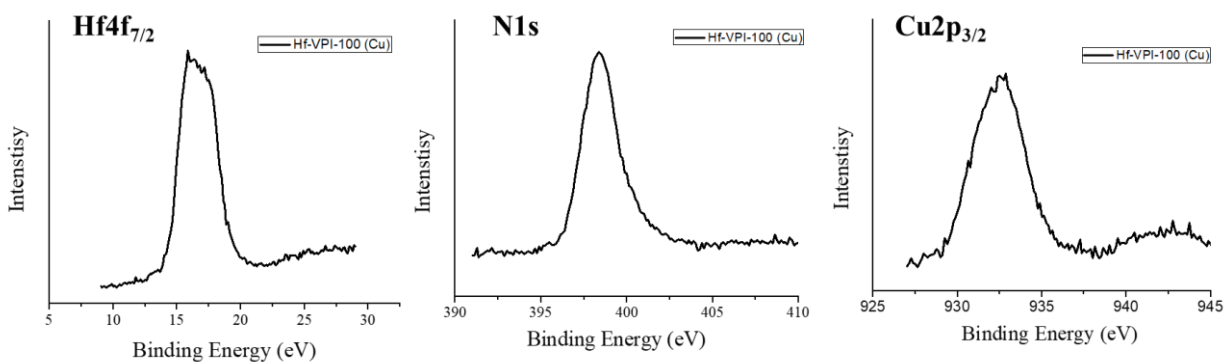


Figure S4. XPS spectrum of Hf-VPI-100 (Cu) powder displaying (left to right) Hf4f_{7/2}, N1s and Cu2p_{3/2} binding energy regions.

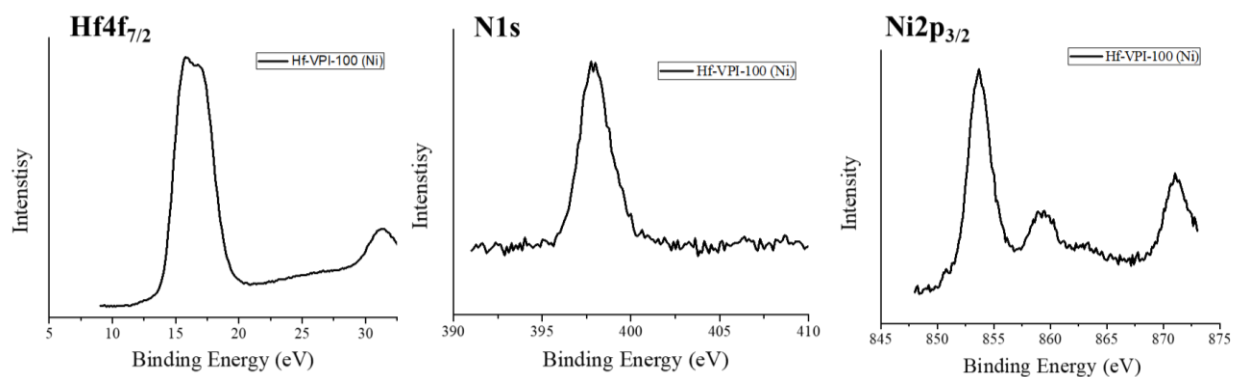


Figure S5. XPS spectrum of Hf-VPI-100 (Ni) powder displaying (left to right) Hf4f_{7/2}, N1s and Ni2p_{3/2} binding energy regions.

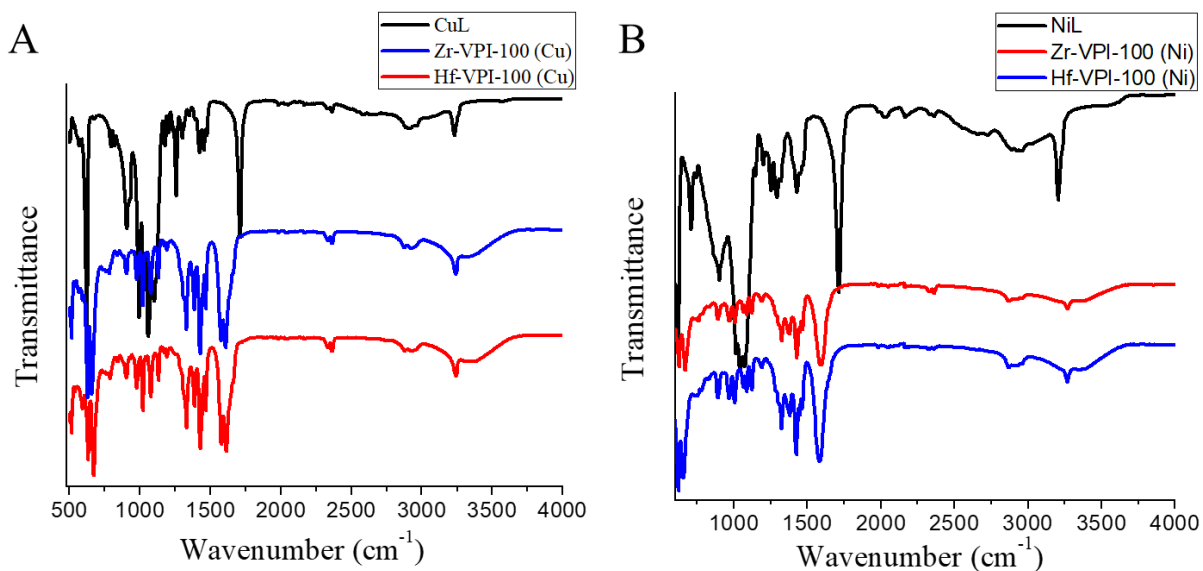


Figure S6. FTIR spectra of metal-cyclam linkers, Zr-VPI-100 MOFs and Hf-VPI-100 MOFs.

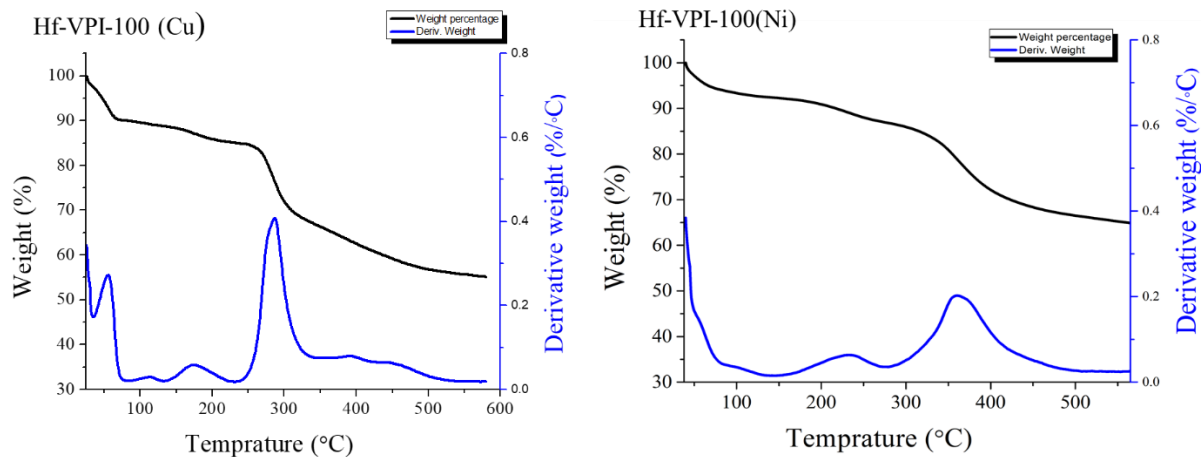


Figure S7. TGA curves of Hf-VPI-100 (Cu) and Hf-VPI-100 (Ni).

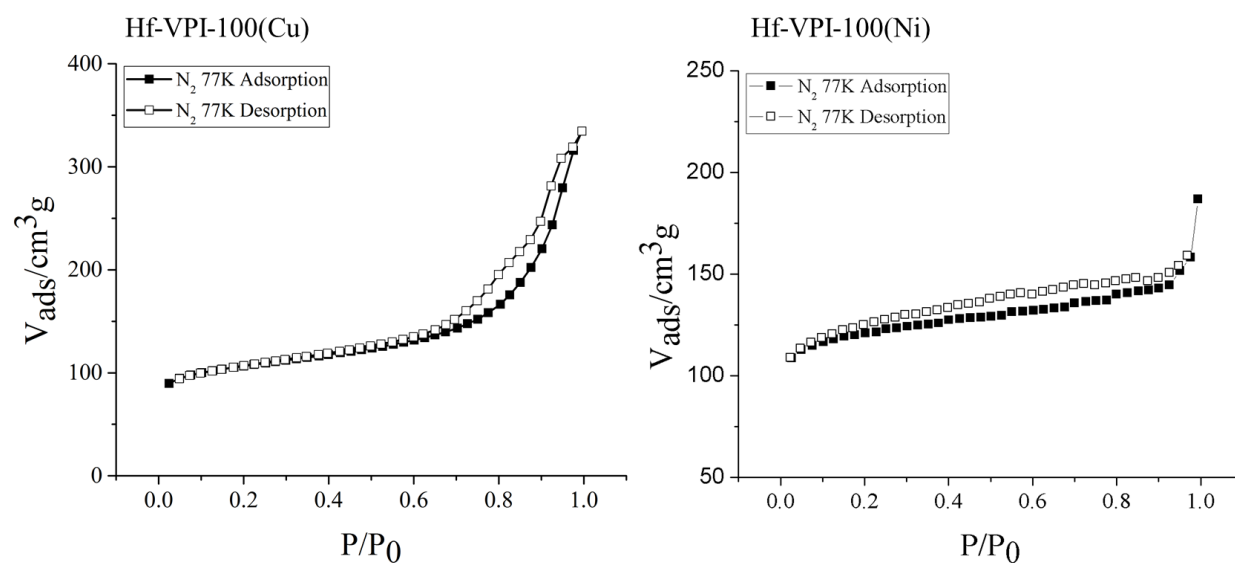


Figure S8. N₂ adsorption isotherms of (A) VPI-100 (Cu) and (B) VPI-100 (Ni) at 77 K, 1 atm after activation at 100 °C for 24 h.

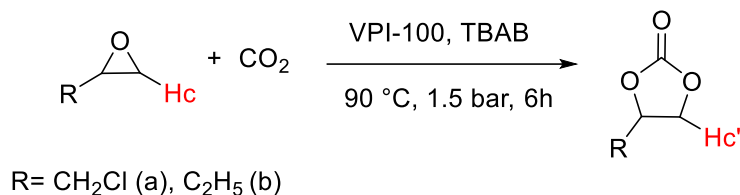
Table S1. The summary of gas sorption properties of VPI-100 and Hf-VPI-100

MOF	Activation Condition	BET surface areas (N ₂ , 77K)	Pore size	CO ₂ sorption at 273 K under 1 atm	
				STP (cm ³ /g)	wt. %
VPI-100 (Cu)	373 K	399 m ² /g	6.37 Å	33.85	6.65
VPI-100 (Ni)	373 K	344 m ² /g	5.77 Å	28.2	5.52

Hf- VPI-100 (Cu)	373 K	396 m ² /g	7.7 Å	41.60	8.25
Hf- VPI-100 (Ni)	373 K	399 m ² /g	7.2 Å	46.05	9.13

4.8.3 Catalyst studies of cycloaddition of CO₂ to epoxides using Hf-VPI-100

Determination of the conversion



Scheme S1. Synthesis of cyclic carbonates from CO₂ and epoxides catalyzed by Hf-VPI-100.

For each reaction, conversion was determined by comparison of the ¹H NMR integrals of the corresponding proton in the starting material (¹H_c) and in the product (¹H_{c'}) according to equation 1 and Table S2.

$$\text{Conversion} = \frac{I_{Hc'}}{(I_{Hc} + I_{Hc'})} \quad (1)$$

Table S2. Chemical shifts (δ, ppm) for the integrated proton in the epoxides and in the corresponding carbonates (in CDCl₃).

Epoxides	δH (CDCl ₃)(epoxide, ¹ H _c)	δH (CDCl ₃)(carbonate, ¹ H _{c'})
a	2.65	4.35
b	2.45	4.05

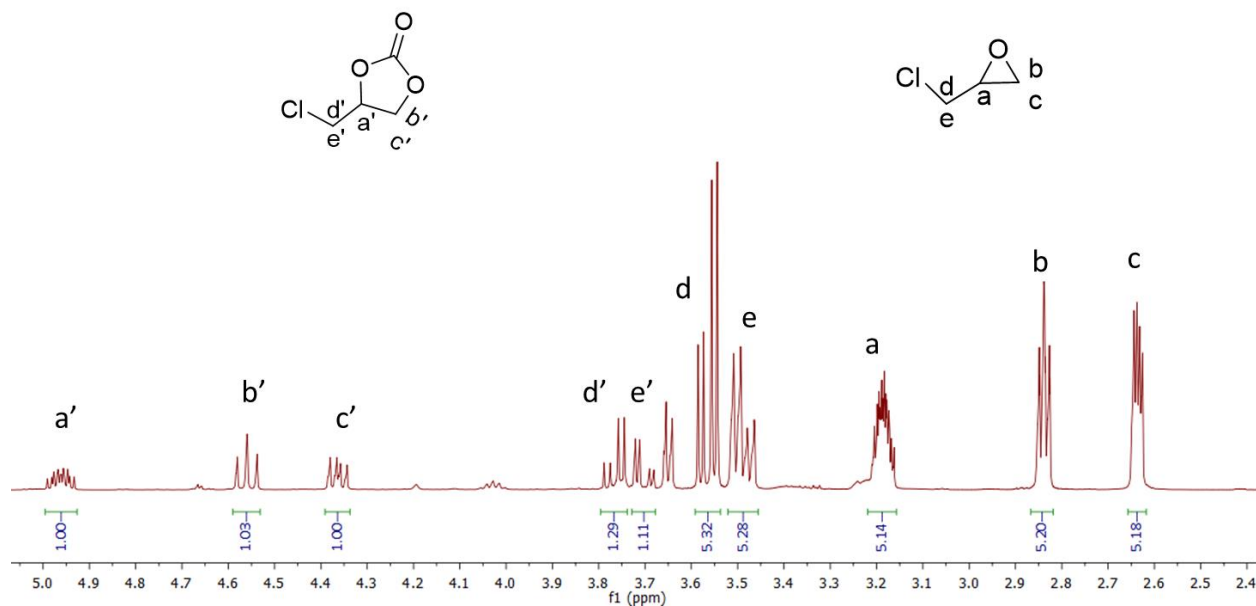


Figure S9. ^1H NMR (400 MHz, CDCl_3) spectrum of reaction mixture in Table 1 entry 1 only using TBAB as catalysts. Conversion = $1/6.18 = 16.2\%$

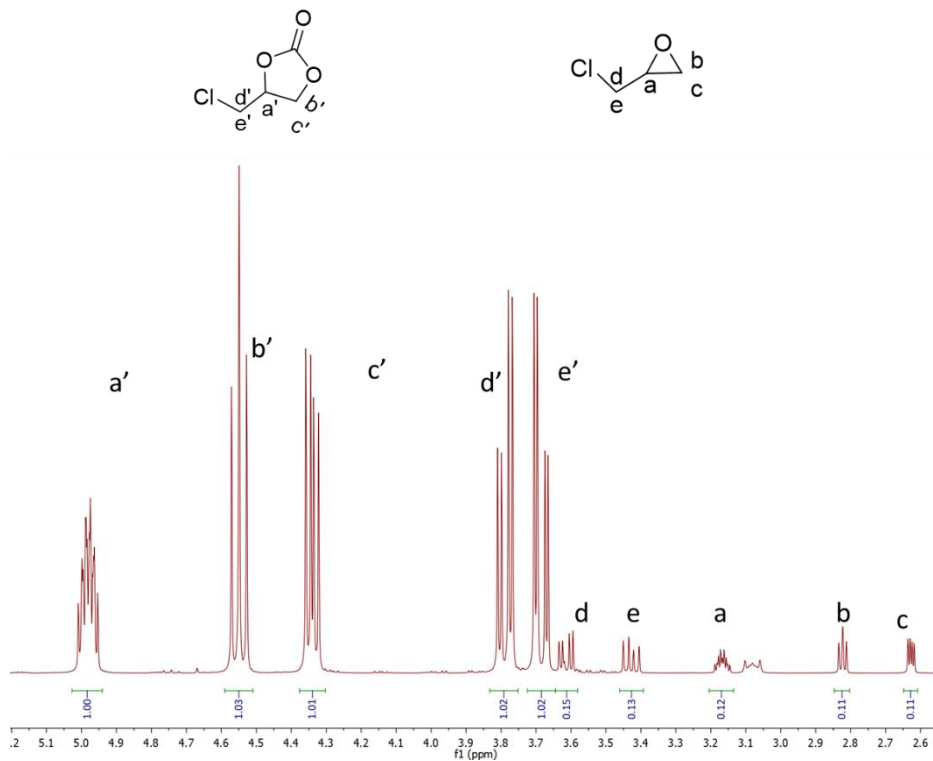


Figure S10. ^1H NMR (400 MHz, CDCl_3) spectrum of reaction mixture in Table 1 entry 2 using $[\text{CuL}(\text{ClO}_4)_2]$ (1) and TBAB as catalysts. Conversion = $1/2.12 = 90.2\%$.

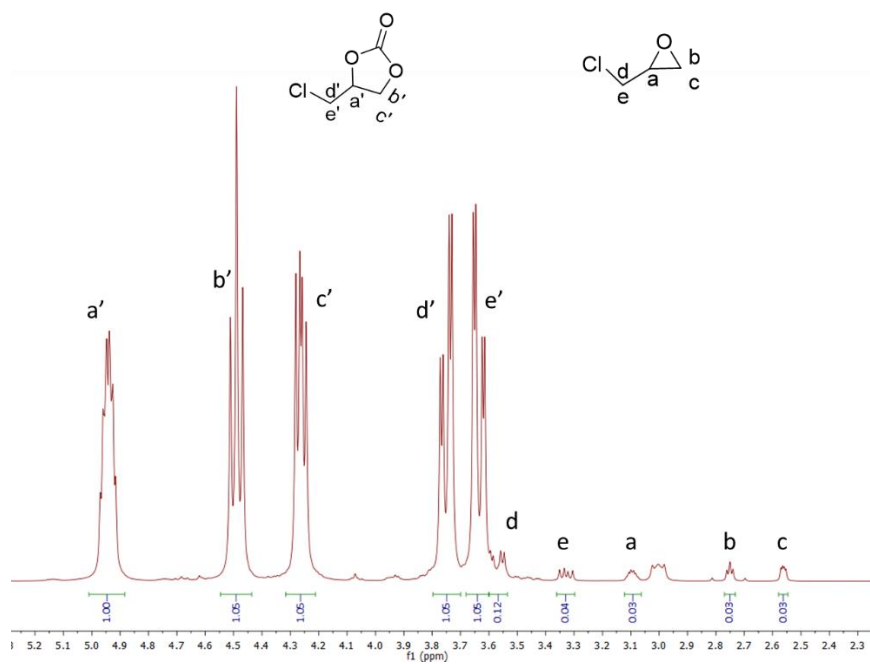


Figure S11. ^1H NMR (400 MHz, CDCl_3) spectrum of reaction mixture in Table 1 entry 3, run 1 using Hf-VPI-100 (Cu) and TBAB as catalysts. Conversion = $1.05/1.08$, = 97.2%.

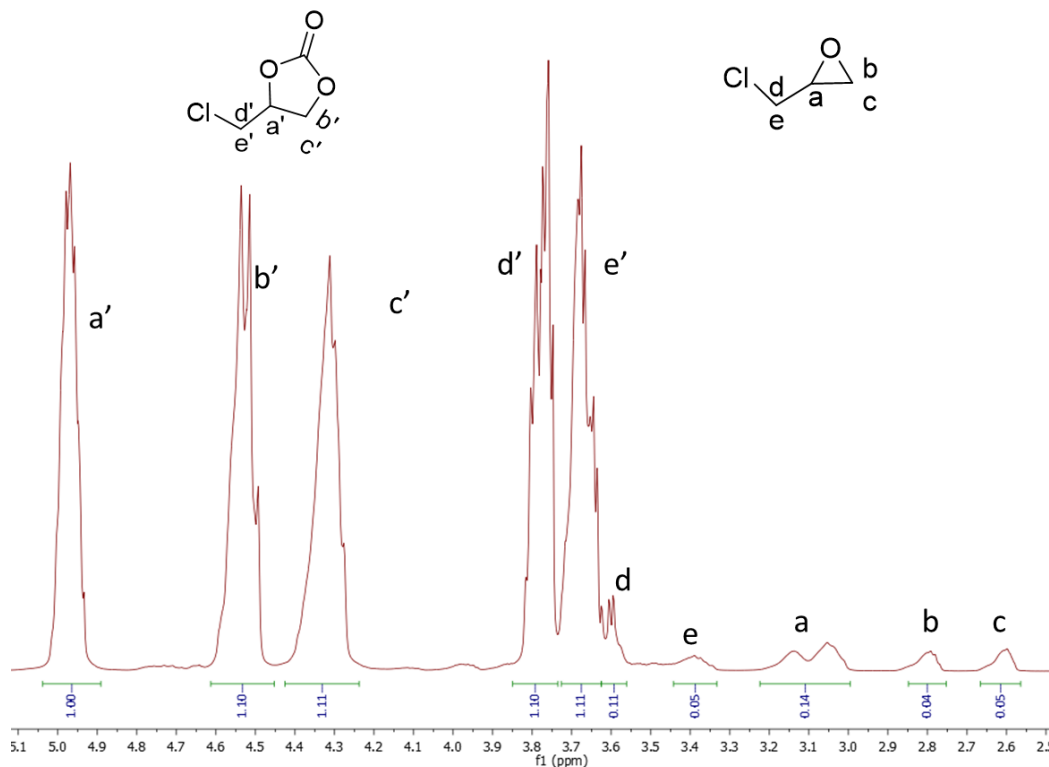


Figure S12. ^1H NMR (400 MHz, CDCl_3) spectrum of reaction mixture in Table 1 entry 4, run 2 using Hf-VPI-100 (Cu) and TBAB as catalysts. Conversion = 1.11/1.16, = 95.6%.

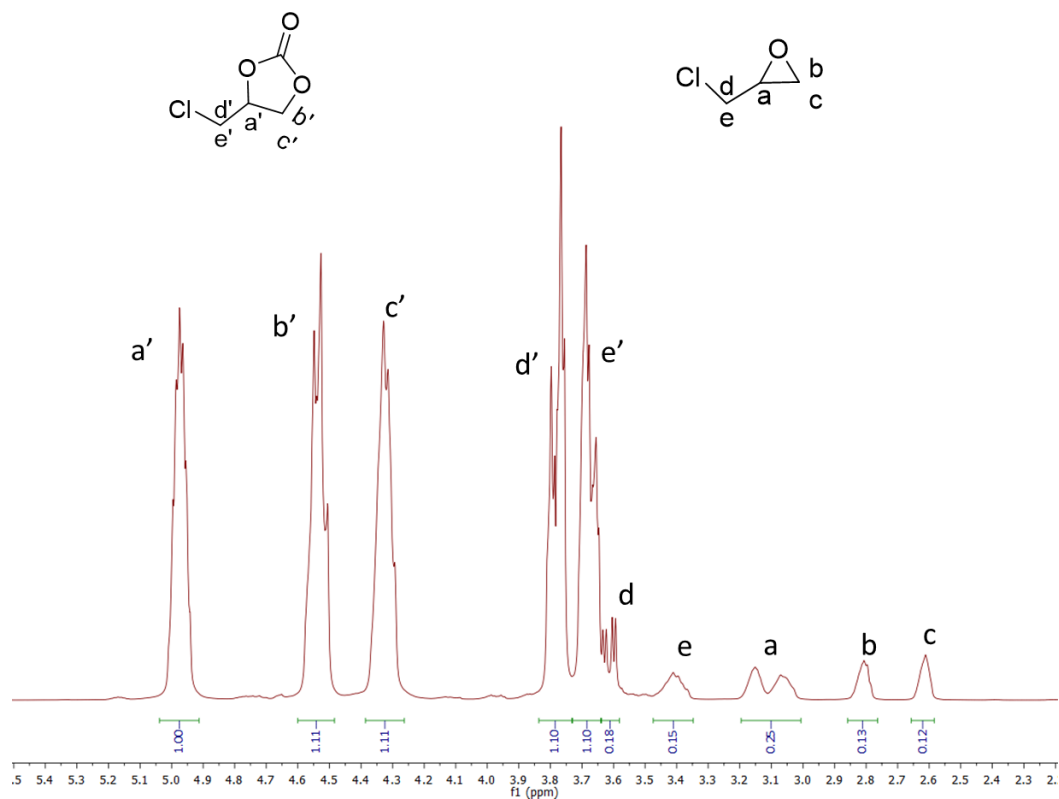


Figure S13. ^1H NMR (400 MHz, CDCl_3) spectrum of reaction mixture in Table 1 entry 5, run 1 using Hf-VPI-100 (Ni) and TBAB as catalysts. Conversion = 1.11/1.23, = 89.5%.

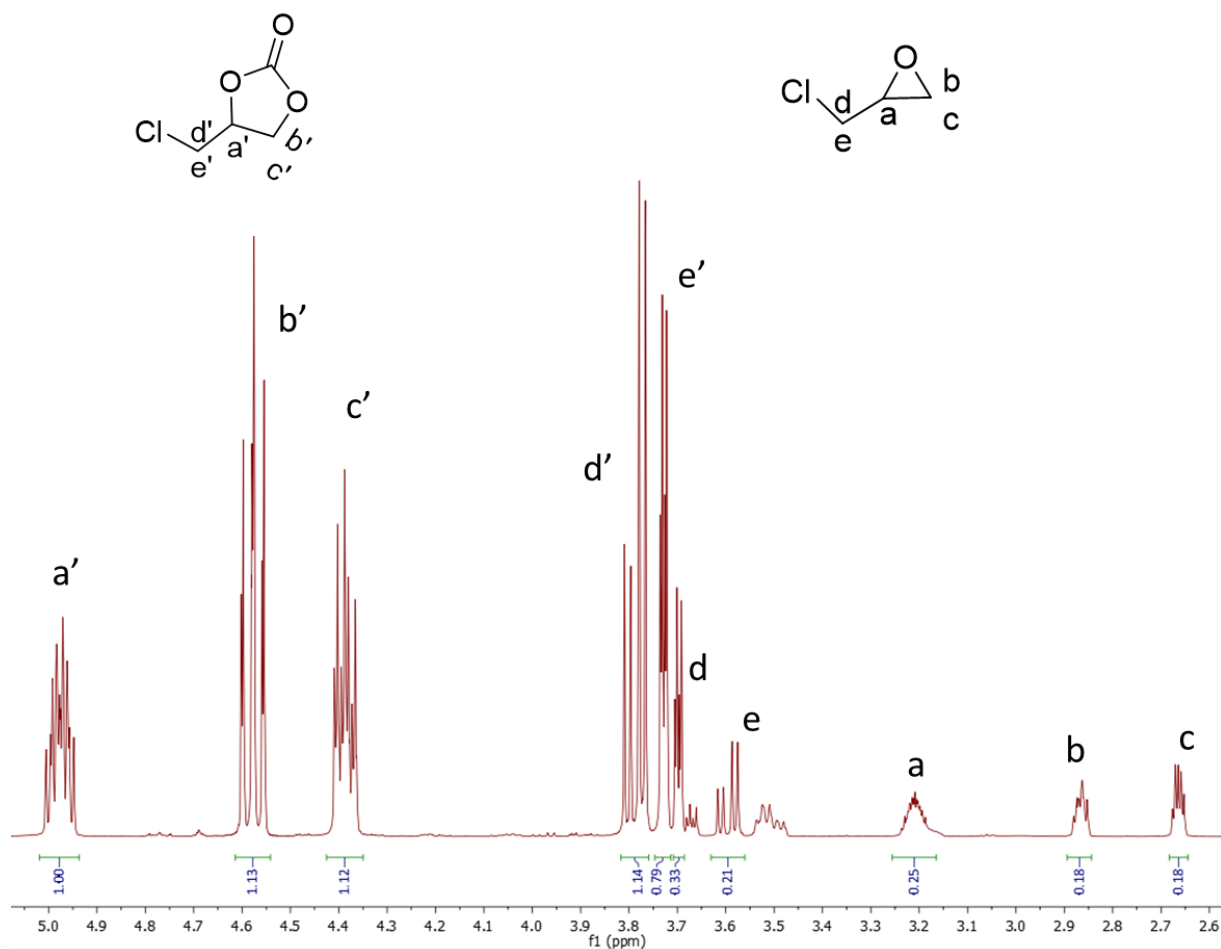


Figure S14. ¹H NMR (400 MHz, CDCl₃) spectrum of reaction mixture in Table 1 entry 6, run 2 using Hf-VPI-100 (Ni) and TBAB as catalysts. Conversion = 1.12/1.3, = 86.2%.

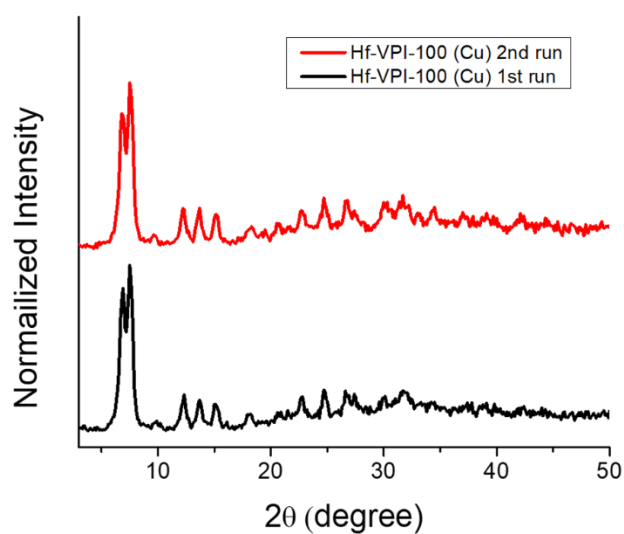


Figure S15. PXRD of Hf-VPI-100 (Cu) after catalysts.

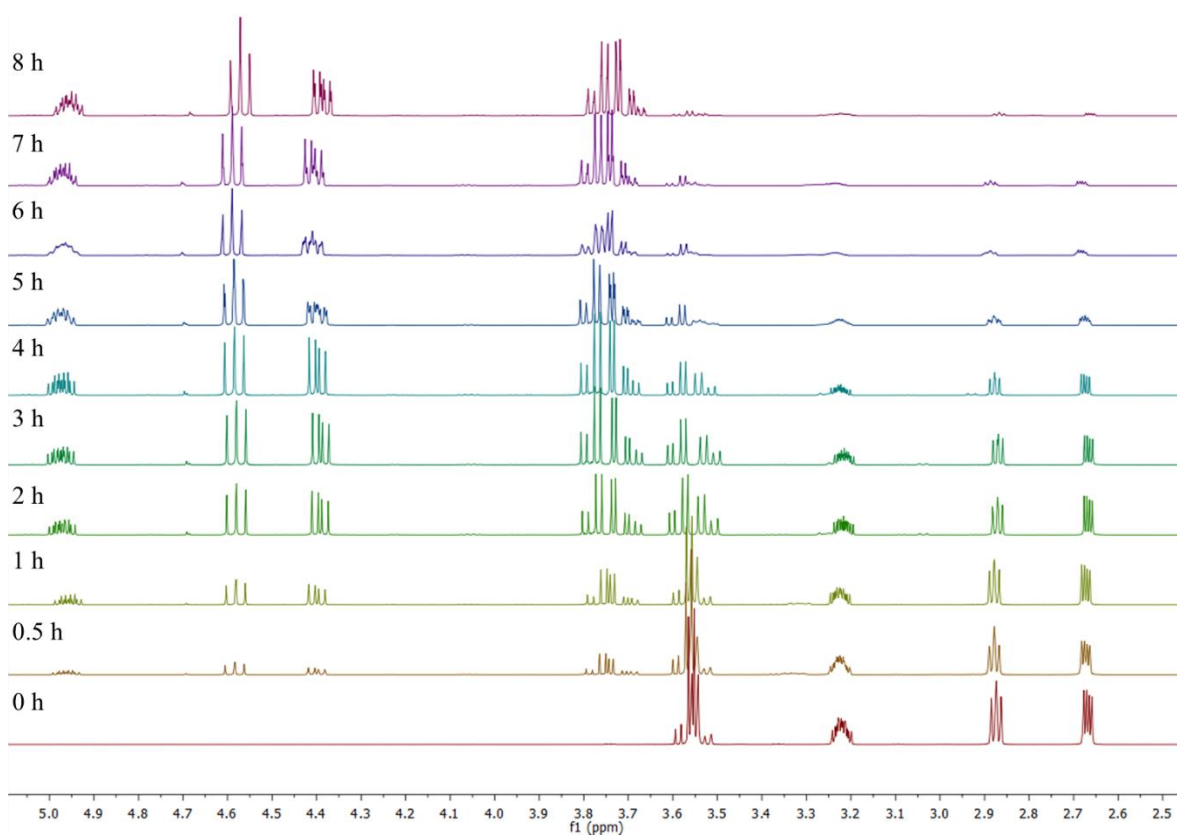


Figure S16. The monitoring of the progress of the reaction of epichlorohydrin with CO₂ (1.5 bar, 90 °C) using ¹H NMR (400 MHz, CDCl₃) from 0 to 8 h.

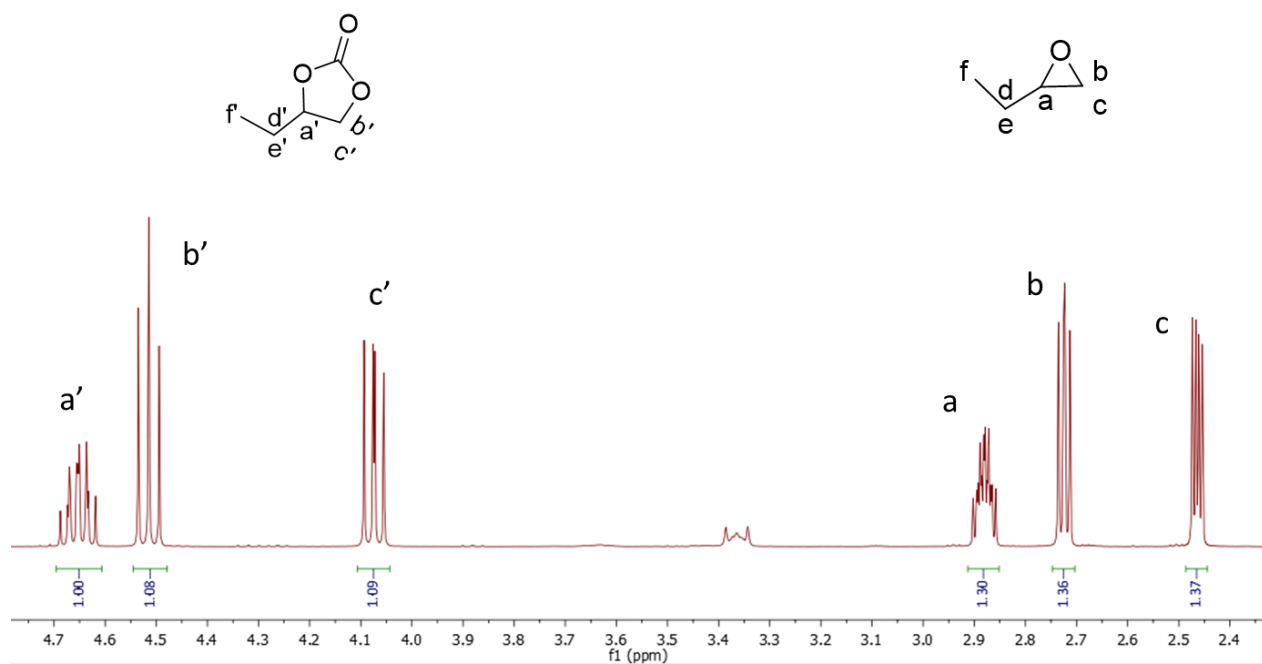


Figure S17. ^1H NMR (400 MHz, CDCl_3) spectrum of reaction mixture in run 1 using Hf-VPI-100 (Cu) and TBAB as catalysts. Conversion = $1.09/2.46$, = 43.8%.

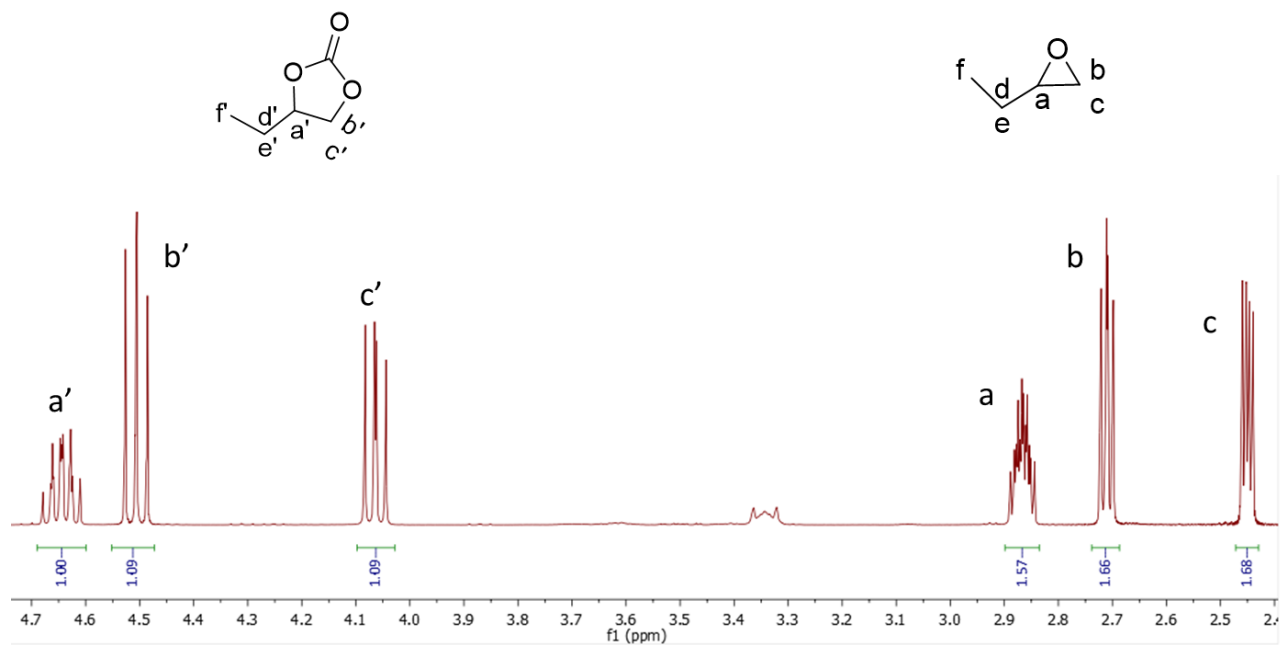


Figure S18. ^1H NMR (400 MHz, CDCl_3) spectrum of reaction mixture in run 1 using Hf-VPI-100 (Ni) and TBAB as catalysts. Conversion = $1.09/2.77$, = 39.4%.

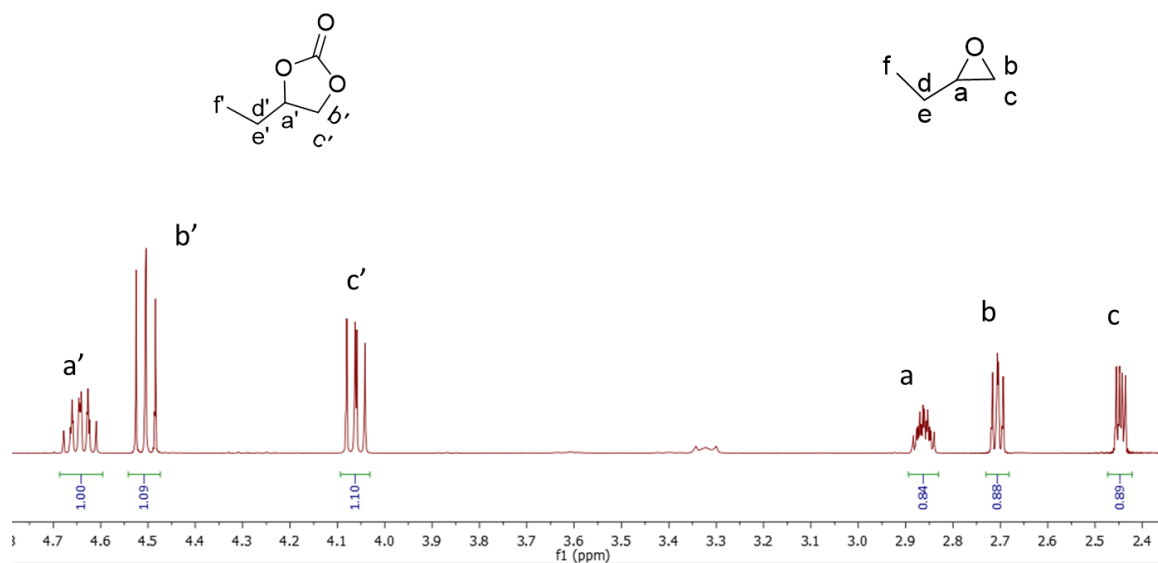


Figure S19. ¹H NMR (400 MHz, CDCl₃) spectrum of reaction mixture in run 1 using Zr-VPI-100 (Cu) and TBAB as catalysts. Conversion = 1.1/1.99, = 55.3%.

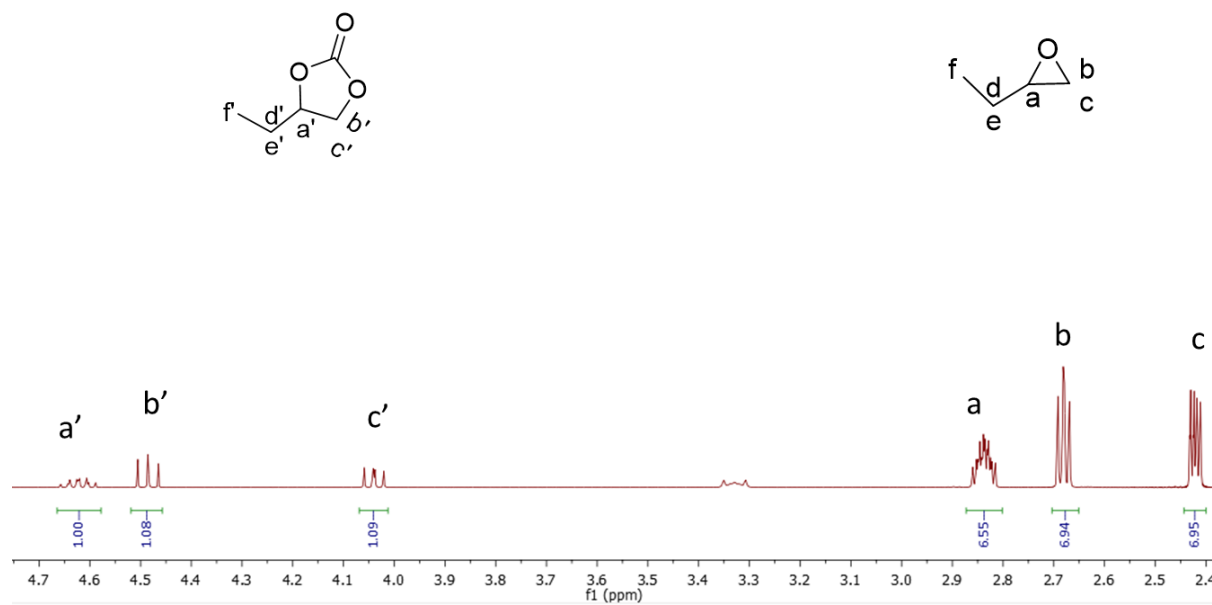


Figure S20. ¹H NMR (400 MHz, CDCl₃) spectrum of reaction mixture using only TBAB as catalysts. Conversion = 1.09/8.04, = 13.5%.

Chapter 5 Visible Light-Induced Cytotoxicity of Ru,Os-Polyazine Complexes Towards Rat Malignant Glioma

This chapter has been adapted from a published manuscript by [Zhu, J.](#); Dominijanni, A.; Rodríguez-Corrales, J. Á.; Prussin, R.; Zhao, Z.; Li, T.; Robertson, J. L.; and Brewer, K. J. from the following reference: *Inorganica Chimica Acta* **2017**, 454, 155-161. Reprinted with permission from the Elsevier copyright © 2017.

5.1 Abstract

Transition metal complexes capable of visible light-triggered cytotoxicity are appealing potential candidates for photodynamic therapy (PDT) of cancer. Two monometallic polyazine complexes, $[(\text{Ph}_2\text{phen})_2\text{Ru}(\text{dpp})]^{2+}$ (**1**) and $[(\text{Ph}_2\text{phen})_2\text{Os}(\text{dpp})]^{2+}$ (**2**) (Ph_2phen = 4,7-diphenyl-1,10-phenanthroline; dpp = 2,3-bis(2-pyridyl)pyrazine), were synthesized, characterized and studied as light activated drugs to kill rat malignant glioma F98 cells. Compounds **1** and **2** display strong absorption in visible spectrum, oxygen-mediated DNA and BSA photocleavage and significant photocytotoxicity under blue light irradiation along with negligible activity in the dark. Both compounds show approximately five-fold higher cytotoxicity than the traditional chemotherapeutic drug cisplatin. Furthermore, compound **2** shows promising photocytotoxicity in F98 rat malignant glioma cells within the phototherapeutic window with an IC_{50} value of $(86.07 \pm 8.48) \mu\text{M}$ under red light (625 nm) irradiation.

5.2 Introduction

Photodynamic therapy (PDT) is a noninvasive treatment that uses a photosensitizer (PS), low energy light, and in most cases $^3\text{O}_2$ to produce photocytotoxic reactive oxygen species (ROS) to damage neoplastic cells.¹ The generation of $^1\text{O}_2$ is believed to occur via energy transfer from the excited photosensitizer (Figure 5.1).² This minimally-invasive, light-activated therapeutic treatment allows for accurate targeting of tumor cells, and reduces side effects associated with systemic chemotherapy.³ A variety of organic PDT agents have been approved for clinical use or are undergoing clinical trials, including porphyrins, chlorins and phthalocyanines.⁴ However, these conventional PDT agents suffer from dark toxicity, prolonged skin sensitivity and hepatotoxicity, greatly limiting their widespread application.⁵ Transition metal complexes that have tunable coordination environments and varied spectral and redox properties are promising

candidates as the next generation of PDT agents.⁶ Among them, ruthenium complexes with polypyridyl ligands, such as derivatives of $[\text{Ru}(\text{bpy})_3]^{2+}$ (bpy = 2,2'-bipyridine), have been widely studied due to their active interaction with cellular components (DNA, RNA, and proteins).⁷ Ideally, PDT drugs need to be operative in the phototherapeutic window (600–900 nm), where light can efficiently penetrate bodily tissues.⁸ However, few reported metal complexes were able to be photoactivated with low energy light.⁹ Thus in this promising research area, it is still highly desirable to find novel PDT agents with enhanced activity within the phototherapeutic window and towards aggressive tumors such as high-grade malignant glioma (MG).

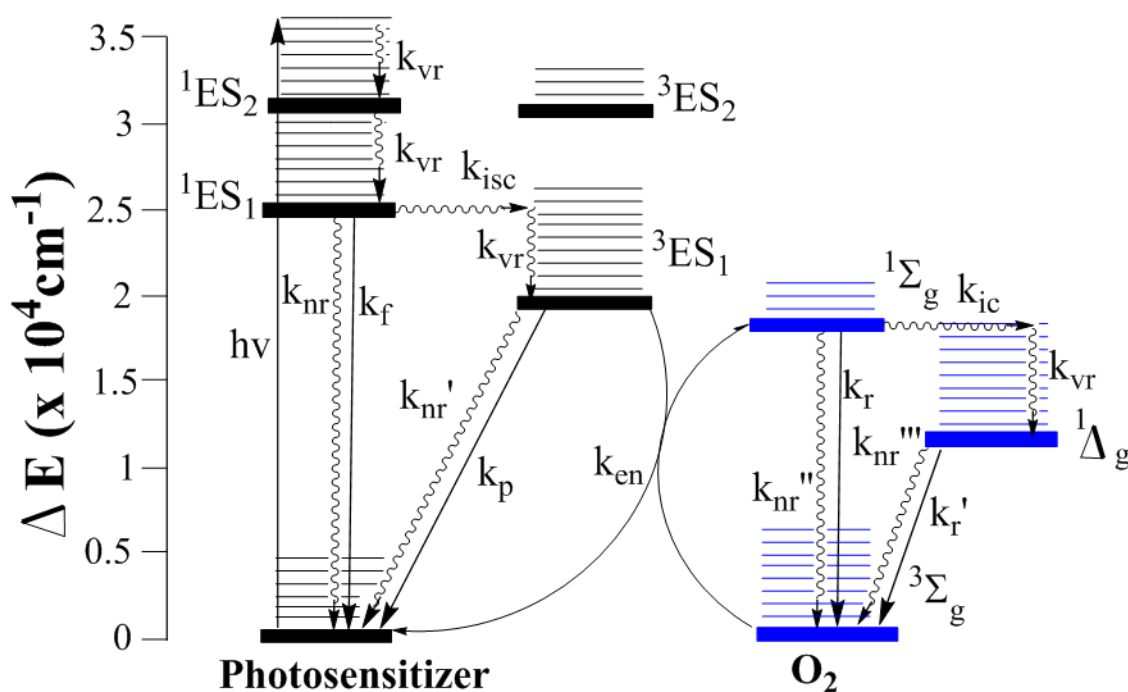


Figure 5.1 State diagram illustrating the mechanisms of action for drugs displaying oxygen-dependent photodynamic action with k 's (rate constants) for f (fluorescence), p (phosphorescence), r (radiative), nr (nonradiative), ic (internal conversion), isc (intersystem crossing), en (energy transfer) and vr (vibration). The electronic state $^1\Delta_g$ is observed at 1270 nm or 0.97 V, $^1\Sigma_g$ is estimated at 1.6–1.8 V but is short-lived.

Aggressive, infiltrative MGs make up approximately 1.35% of the total cancer cases reported in 2013.¹⁰ The survival rate for MG is extremely low, with only 17.7% living beyond 1-year of diagnosis.¹¹ The lack of external cellular growth control, infiltrative growth pattern, and resistance to host immunologic defences make MG cells a particularly aggressive therapeutic

challenge. MGs are resistant to virtually all forms of traditional cancer therapy, including radiation therapy, chemotherapy, and ablative surgical therapy as well as combinations of these procedures. Upon initial diagnosis of glioblastoma multiforme (GBM), standard treatment consists of maximal surgical resection, radiotherapy, and concomitant/adjvant chemotherapy with temozolomide (TMZ).¹² However, over 95% of all patients with MG die within two years, regardless of the type of therapy used.¹³ TMZ, as the most commonly used chemotherapeutic agent in the therapy of GBM, has an IC₅₀ (concentration resulting in cell viability of 50% of control) of approx. 200 μM towards U87-MG malignant glioma cells.¹⁴ Thus, new treatments to high-grade MG are urgently needed to address and alleviate the limitations of current therapeutic approaches and improve patient survival rates.

Transition metal complexes are actively being developed as PDT agents.¹⁵ Monometallic compounds are very attractive due to their simple synthetic approach and concise structure.¹⁶ Common approaches employed in the design of monometallic PDT agents include ligand variation/modification and metal center variation. Metal center/ligand variation allows for tuning of redox, spectroscopic and photophysical properties with ligand modification allowing for added targeting ability.^{9a, 17} Herein, we report the design of a new set of [(Ph₂phen)₂M(dpp)]²⁺ (Ph₂phen = 4,7-diphenyl-1,10-phenanthroline; dpp = 2,3-bis(2-pyridyl)pyrazine; M = Ru/Os) polyazine complexes with light-promoted cytotoxicity in rat malignant glioma F98 cells. To the best of our knowledge, compounds **1** and **2** are the first reported transition metal complexes that display PDT activity towards gliomas cells. These compounds show approximately five-fold higher cytotoxicity than the traditional chemotherapeutic drug cisplatin. Furthermore, compound **2** is the first complex to show photocytotoxicity in malignant gliomas within the phototherapeutic window. Photoactivity of the compounds was studied in DNA and bovine serum albumin (BSA) as model biomolecules, which are potential targets for these phototoxic species.

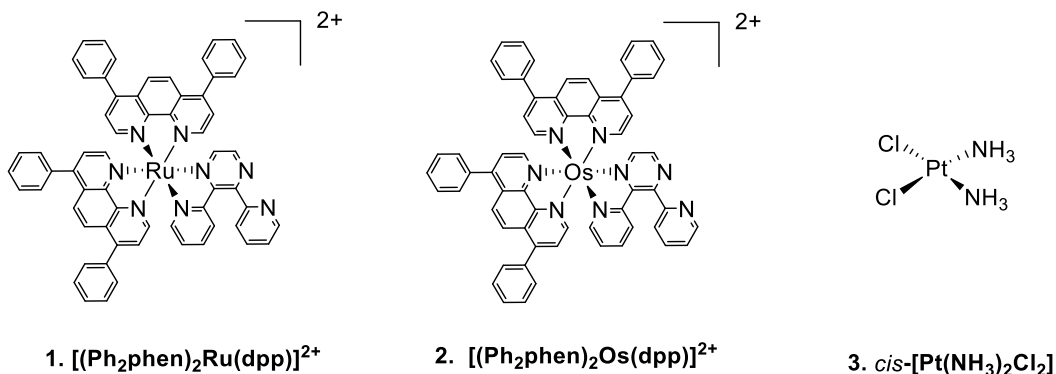


Figure 5.2 Structural representations of metal compounds in this study. Ph₂phen =4,7-diphenyl-1,10-phenanthroline;dpp =2,3-bis(2-pyridyl)pyrazine

5.3 Experimental Section

5.3.1 Materials and methods. $[(\text{Ph}_2\text{phen})_2\text{RuCl}_2]$ and $[(\text{Ph}_2\text{phen})_2\text{OsCl}_2]$ were synthesized as previously reported.¹⁸ Ph₂phen, dpp, RuCl₃·3H₂O, Bu₄NPF₆, NH₄PF₆ and cisplatin, *cis*- $[\text{Pt}(\text{NH}_3)_2\text{Cl}_2]$, were purchased from Alfa Aesar. Solvents were HPLC grade. All materials were used as received without further purification unless otherwise noted. Sephadex LH-20 was purchased from GE healthcare Biosciences Corporation. Supercoiled pUC19 plasmid DNA was purchased from Bayou Biolabs. Lamba/Hind III markers was purchased from Promega Corporation. Bovine serum albumin (BSA) was purchased from Sigma-Aldrich. NuPAGE™ Novex™ 4-12% Bis-Tris Protein Gels (1.0 mm, 15-well) was purchased from Invitrogen. F98 malignant glioma rat cancer cells were purchased from American Type Culture Collection (ATCC® CRL-2397™) and used in toxicity studies at passage 7. Cells were seeded in a Thermo Scientific 1300 Series A2 sterile hood and incubated at 37°C with 5% CO₂. Dulbecco's Modified Eagle's Medium (DMEM), Fetal Bovine Serum (FBS), penicillin-streptomycin antibiotic solutions were obtained from ATCC®. 0.05% Trypsin-EDTA and phosphate buffer solutions (PBS) were purchased from Life Technologies, while 75cm² tissue flask, serological pipettes and 15mL/50mL centrifuge tubes were obtained from Fisher Scientific. Cells were collected with a Thermo Scientific Sorvall ST 8R refrigerated centrifuge and counted in a Beckman Coulter Vi-Cell cell viability analyzer. Samples were submitted to Galbraith Laboratories, Inc., for elemental analysis.

5.3.2 Synthesis of [(Ph₂phen)₂Ru(dpp)](PF₆)₂ (1). The monometallic complex, [(Ph₂phen)₂Ru(dpp)](PF₆)₂ was synthesized as previously reported using a building block approach (Figure 5.3).¹⁸ [(Ph₂phen)₂RuCl₂] (0.56 g, 0.67 mmol) and excess dpp (0.54 g, 2.4 mmol) were heated at reflux in 30 mL of 70:30 EtOH/H₂O for ca. 2 h. The reaction mixture was cooled to R.T. and aqueous saturated NH₄PF₆ was added to induce precipitation as a PF₆⁻ salt. The solid was collected by vacuum filtration, dissolved in a minimal amount of 2:3 CH₃CN/toluene and purified by alumina chromatography using 2:3 CH₃CN/toluene eluent. The leading orange band was collected, the solvent was removed under vacuum, and the complex was flash precipitated from dry acetone in diethyl ether, with 0.69 g of desired product in 80% yield. *Anal.* Calc. for C₆₂H₄₂F₁₂N₈P₂Ru (MW =1290.07g/mol): C, 57.72%; H, 3.28%; N, 8.69%. Found: C,57.59%; H, 3.26%; N,8.82%. HPLC-MS (Figure S1) and ESI-MS: [M-2(PF₆)]²⁺, m/z=500.13.

5.3.3 Synthesis of [(Ph₂phen)₂Os(dpp)](PF₆)₂ (2). The monometallic complex, [(Ph₂phen)₂OsCl₂] was synthesized similar to compound 1, except changing the solvent to ethylene glycol (Figure 5.3). [(Ph₂phen)₂OsCl₂] (0.31 g, 0.33 mmol) and excess dpp (0.23 g, 0.99 mmol) were heated at reflux in 25 mL of ethylene glycol for ca. 2 h under Ar. The reaction mixture was cooled to R.T. and aqueous saturated NH₄PF₆ was added to induce precipitation as a PF₆⁻ salt. The solid was collected by vacuum filtration, dissolved in a minimal amount of 2:3 CH₃CN/toluene and purified by alumina chromatography using 2:3 CH₃CN/toluene eluent. The second brown band was collected; solvent was removed under vacuum, and the complex was flash precipitated from dry acetone in diethyl ether, with 0.32 g of desired product in 70% yield. *Anal.* Calc. for C₆₂H₄₂F₁₂N₈P₂Os (MW =1379.23g/mol): C, 53.99%; H, 3.07%; N, 8.12%. Found: C, 54.13%; H, 3.35%; N, 8.04%. HPLC-MS (Figure S2) and ESI-MS: [M-2(PF₆)]²⁺, m/z=545.16

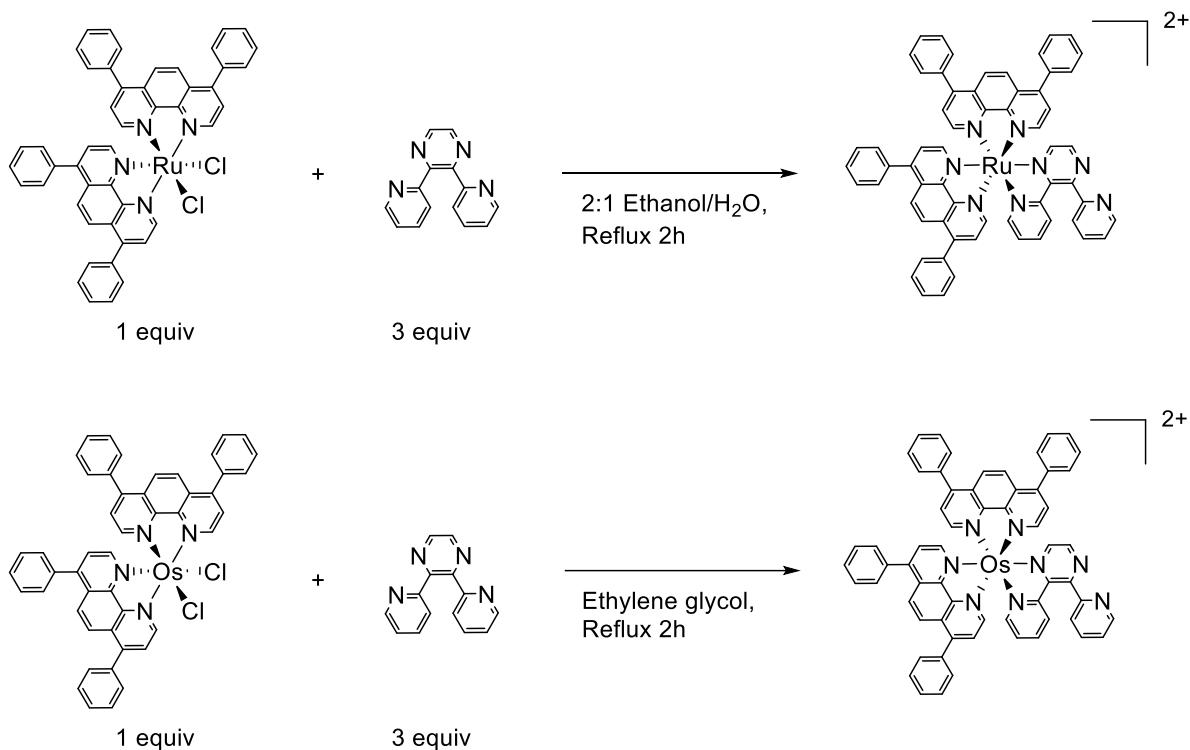


Figure 5.3 Synthetic scheme for compounds 1 and 2.

5.3.4 ESI-TOF Mass Spectrometry. ESI was performed by an Agilent Technologies 6220 Accurate-Mass TOF LC-MS with a dual ESI source to obtain high resolution mass spectral data. Samples were dissolved in HPLC grade acetonitrile.

5.3.5 High performance liquid chromatography-mass spectroscopy (HPLC-MS). A Luna C18 column (Phenomenox, Torrance, CA), 150×2.0 mm with 5 μm particles was used in all separations. The mobile phase was acetonitrile and water (containing 1% formic acid, v/v). The gradient began at 95% water for 3 min, increased to 95% acetonitrile over the next 10 min and then held for 5 min. The system was ramped down to 95%/5% (H₂O/acetonitrile) in 1 min and then equilibrated for an additional 5 min for a total analysis time of 22 min. All samples were injected using a Thermo Survey Autosampler. Injection volume was 20 μl at a concentration of 100 ng/μl. The HPLC column effluent was pumped directly without any split into a Thermo Instrument TSQ triple quadrupole mass spectrometer (Thermo Finnigan, San Jose, CA) equipped with ESI source, which was used in positive ion MS mode.

5.3.6 Electrochemistry. Cyclic voltammetry was performed in a one compartment, three electrode cell utilizing a platinum disc working electrode, platinum wire auxiliary electrode and Ag/AgCl (NaCl, 3 M) reference electrode calibrated against FeCp₂/FeCp₂⁺ (0.46 V vs Ag/AgCl) with an Epsilon potentiostat from Bioanalytical System, Inc. Measurements were recorded at 0.1 V/s in CH₃CN with 0.1 M Bu₄NPF₆ at RT degassed by bubbling with argon. The working electrode was polished with alumina paste prior to analysis.

5.3.7 Electronic Absorption Spectroscopy. Electronic absorption spectroscopy was performed using an Agilent 8453 UV-Vis spectrophotometer with a diode array having 1 nm resolution and a spectral range of 190 to 1100 nm. Spectra were measured in a 1 cm quartz cuvette in CH₃CN at RT. Extinction coefficient determination was performed in triplicate.

5.3.8 DNA Gel Shift Assay. DNA-complex solutions were prepared in aqueous 10 mM phosphate buffer (pH=7.4) with 100 μM pUC19 DNA and 20 μM tested compound (5:1 base pairs:metal complex). Photolysis was performed for 1 h with a 455 nm LED array (for blue light excitation) or a 625 nm LED array (for red excitation). Oxygen depleted samples were bubbled with argon for 20 minutes prior to photolysis and closed under an argon atmosphere. Dark controls were incubated in a dark compartment while the photolysis was being conducted. All samples were diluted with 10 mM phosphate buffer and loading dye was added. Samples were loaded into a 0.8 % w/w agarose gel with TB buffer (90 mM tris base, 90 mM boric acid), placed in a Owl Separation Systems model B1A stage and electrophoresis was conducted for 90 min at 100 V. Gels were stained in 0.5 μg/ml ethidium bromide (Biotium Inc.) for 30 min, washed using deionized water for 15 min and visualized on a Fisher Biotech UV-transilluminator. Images were captured using an Olympus SP-320 camera fitted with an ethidium bromide filter.

5.3.9 Protein Gel Shift Assay. BSA-complex solution were prepared in aqueous 10 mM phosphate buffer (pH=7.4) with 5 μM BSA and 50 μM tested compound (1:10 protein:metal complex). Photolysis was performed for 1 h and 2 h using a 625 nm LED array. Dark controls were incubated in a dark compartment while the photolysis was being conducted. Electrophoresis was performed using 1 mm 4-12 % Bis-Tris gels (Invitrogen). Gels were loaded with samples treated with Nupage LDS buffer and Nupage reducing agent according to manufacturer's instructions, followed by running in MES buffer at 200 V for 35 minutes. Gels were washed 3 times with water for five minutes before being treated with Simplyblue Safestain

(Invitrogen) for one hour. Gels were then washed overnight in water and imaged using a Bio-Rad ChemiDoc XLS system.

5.3.10 Cell Culture. F98 rat malignant glioma cells (ATCC) were maintained in DMEM supplemented with 10% fetal bovine serum (FBS, ATCC) and 1% penicillin-streptomycin and incubated at 37°C in a humidified incubator at 5% CO₂.

5.3.11 Photocytotoxicity. F98 rat malignant glioma cells were plated in triplicates in the inner 60 wells of a 96-well plate at a density of approximately 10,000 cells per well along with DMEM and incubated at 37°C and 5% CO₂ for 24 h before the treatment. Medium was removed and cells were then incubated for 1 h with desired concentrations of the compounds. After that, medium was removed, cells were washed with PBS and supplemented with fresh media. The cells were incubated for another 12-16 h prior to 1 h photolysis in a blue (470 nm) or red (625 nm) LED array. The LED array remained inside an incubator set to 37°C and 5% CO₂. A thermocouple was placed inside the LED array to monitor the temperature around the cells. Dark controls were treated under the same conditions except the photolysis step. Viability in each well was measured 48 h after photolysis with an AlamarBlue cell viability assay by monitoring absorbance at 570 and 600 nm.

5.4 Results and Discussion

5.4.1 Synthesis. Compounds **1** and **2** were synthesized by a building block method. In general, the prepared [(Ph₂phen)₂MCl₂] (M=Ru/Os) reacted with excess ligand dpp leading to the crude product, which is purified by alumina chromatography. Characterization using ESI-MS, electronic absorption and electrochemistry matches the previous reported results.¹⁸ Elemental analysis matched the theoretical composition of both compounds, while HPLC-MS confirms their high purity.

5.4.2 Electrochemistry. The electrochemical properties of monometallic complexes were studied using cyclic voltammetry (Figure 5.4). The Ru analog, [(Ph₂phen)₂Ru(dpp)](PF₆)₂, displays a reversible Ru^{II/III} oxidation at +1.42 V vs. Ag/AgCl, and reversible dpp^{0/-}, Ph₂phen^{0/-}, Ph₂phen^{0/-} reductions at -1.02 V, -1.37 V and -1.56 V, respectively, consistent with previous reports (Table 5.1).¹⁸ Upon changing the metal center from Ru to Os, a reversible Os^{II/III}

oxidation is observed at +0.96 V, and reversible dpp^{0/-}, Ph₂phen^{0/-}, Ph₂phen^{0/-} reductions at -0.99 V, -1.30 V and -1.55 V.

The redox properties of the monometallic complexes provide insight into the relative orbital energetics. For both compounds, the highest occupied molecular orbital, HOMO, is localized on the metal-based(dπ) with the lowest unoccupied molecular orbital, LUMO, localized on the dpp(π*). This predicts a lowest lying Os/Ru(dπ)→ dpp(π*) MLCT transition in the electronic absorption spectroscopy. The higher energy Os(dπ) orbital results in a smaller energy gap between HOMO and LUMO compared to the Ru congener, predicting a lower energy MLCT absorption band for the Os compound.

Table 5.1 Electrochemical Data for compound **1** and **2**^a

Complex	E _{1/2} ^{ox} (V)	E _{1/2} ^{red} (V)
1	+1.40 Ru ^{II/III}	-1.02 dpp ^{0/-}
		-1.37 Ph ₂ phen ^{0/-}
		-1.56 Ph ₂ phen ^{0/-}
2	+0.96 Os ^{II/III}	-0.99 dpp ^{0/-}
		-1.30 Ph ₂ phen ^{0/-}
		-1.55 Ph ₂ phen ^{0/-}

^aMeasurements recorded at RT under Ar in CH₃CN with 0.1 M Bu₄NPF₆ electrolyte.

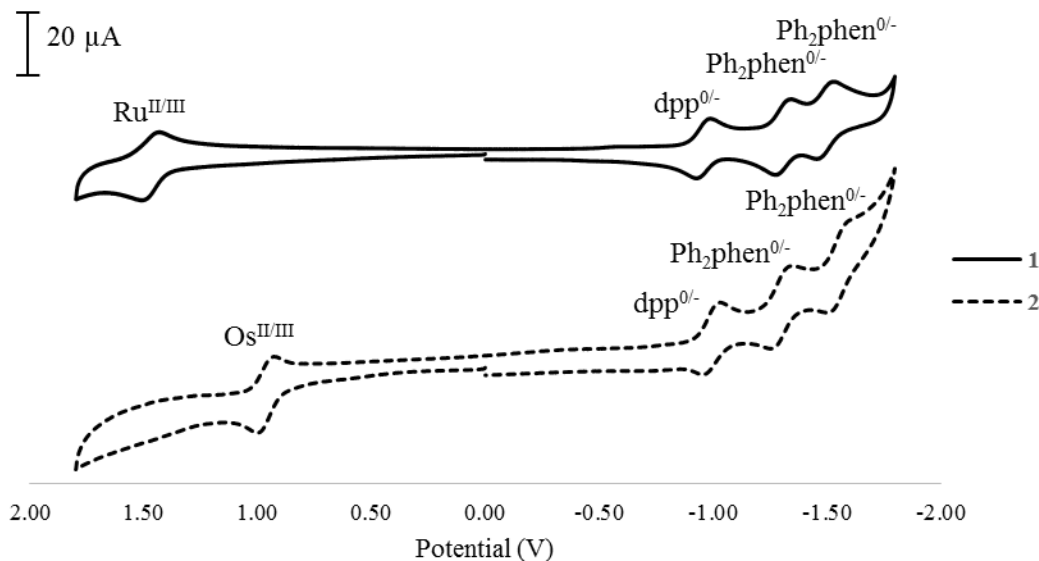


Figure 5.4 Cyclic voltammogram of **1** and **2** at RT under Ar in 0.1M Bu₄NPF₆ acetonitrile, E vs. Ag/AgCl.

5.4.3 Electronic Absorption Spectroscopy. Electronic absorption spectroscopy of the new PDT agents was investigated to evaluate their light absorbing properties. Both complexes display intense absorption through the UV and visible region (Figure 5.5). For compound **1**, the UV region is dominated by intraligand (¹IL) $\pi \rightarrow \pi^*$ transitions, with $\lambda^{\text{abs}} = 279 \text{ nm}$ ($737\,00 \text{ M}^{-1} \text{ cm}^{-1}$) for Ph₂phen $\pi \rightarrow \pi^*$ transitions and $\lambda^{\text{abs}} = 320 \text{ nm}$ ($24\,400 \text{ M}^{-1} \text{ cm}^{-1}$) for dpp $\pi \rightarrow \pi^*$ transitions. In the visible region, singlet metal-to-ligand charge transfer (¹MLCT) transitions are observed with Ru(d π) \rightarrow Ph₂phen(π^*) CT transitions occurring at 424 nm ($\epsilon = 14\,800 \text{ M}^{-1} \text{ cm}^{-1}$), followed by Ru(d π) \rightarrow dpp(π^*) CT transitions at 474 nm ($\epsilon = 15\,000 \text{ M}^{-1} \text{ cm}^{-1}$). For compound **2**, very similar intraligand transitions have been observed in the UV region, with a slightly higher molar absorptivity at 279 nm ($105\,200 \text{ M}^{-1} \text{ cm}^{-1}$) and 320 nm ($34\,900 \text{ M}^{-1} \text{ cm}^{-1}$). In the visible region, ¹MLCT red shifts to Os(d π) \rightarrow Ph₂phen(π^*) CT at 444 nm ($\epsilon = 22\,700 \text{ M}^{-1} \text{ cm}^{-1}$), followed by Os(d π) \rightarrow dpp(π^*) CT transitions at 494 nm ($\epsilon = 22\,000 \text{ M}^{-1} \text{ cm}^{-1}$). The bathochromic shift observed for **2** agrees with the trend predicted from the electrochemistry of the compounds. Also, compound **2** exhibits a broad ³MLCT absorbance centered at 650 nm ($\epsilon = 4\,829 \text{ M}^{-1} \text{ cm}^{-1}$), which is 24 times higher than the Ru congener due to a larger degree of spin-orbit coupling. This low-energy visible light absorption provides the possibility for photoactivation in the therapeutic window.

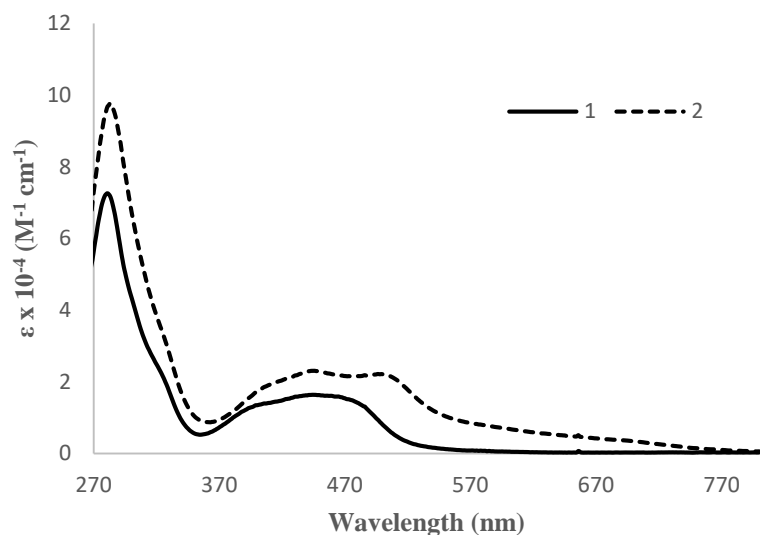


Figure 5.5 Electronic absorption spectra of **1** [(Ph₂phen)₂Ru(dpp)](PF₆)₂ (solid line) and **2** [(Ph₂phen)₂Os(dpp)](PF₆)₂ (dashed line) in DMF at RT.

Table 5.2 Summary of Light-Absorbing Properties

Compound	$\lambda^{\text{abs}}(\text{nm})$	$\epsilon \times 10^{-4} (\text{M}^{-1} \text{cm}^{-1})$	Assignment
1	279	7.37	Ph ₂ phen $\pi \rightarrow \pi^*$
	320	2.44	dpp $\pi \rightarrow \pi^*$
	424	1.48	Ru(d π) \rightarrow Ph ₂ phen(π^*) CT
	474	1.50	Ru(d π) \rightarrow dpp(π^*) CT
2	279	10.52	Ph ₂ phen $\pi \rightarrow \pi^*$
	320	3.49	dpp $\pi \rightarrow \pi^*$
	444	2.27	Os(d π) \rightarrow Ph ₂ phen(π^*) CT
	494	2.2	Os(d π) \rightarrow dpp(π^*) CT

5.4.4 DNA gel shift assay. The activity of compounds **1** and **2** towards supercoiled plasmid DNA was probed under dark and light conditions. As presented in Figure 5.6A, the untreated

pUC19 DNA (lane 2) contains mostly of the supercoiled (SC) form of the plasmid, which displays an apparent electrophoretic size of ca. 2000 bp, along with a small amount of open circular (OC) DNA, with an apparent size of 4000 bp. Incubation of this template with compounds **1** or **2** at room temperature in a dark compartment (lanes 3 and 6) for 1 hour yielded minimum to undetectable change in the electrophoretic profile of the DNA, which is attributed to negligible covalent modification of the biomolecule in the absence of light. In contrast, excitation with blue light for the same period of time (lanes 4 and 7) yielded an apparent increase in the amount of the OC form, which is attributed to single strand cleavage. Furthermore, compound **1** produced a higher degree of DNA scission than **2**. This is not surprising given that **1** has been reported to have a 20-fold higher excited state lifetime than **2** at room temperature,¹⁸ thus providing a larger spatial diffusion radius and greater probability of colliding with a DNA molecule while in the excited state. The activity of both compounds decreased when oxygen was purged from the solutions prior to photolysis, thus suggesting a predominantly oxygen-dependent mechanism for DNA scission, such as the formation of ROS. However, cleavage activity was not completely inhibited which could be attributed to either incomplete oxygen removal by the procedure herein utilized, or direct DNA scission by the excited state of the compounds.

Interestingly, the relative activity of compounds **1** and **2** under red light excitation is inversed. As observed in Figure 5.6B, photolysis of **2** with 625 nm light generated a higher amount of OC DNA than **1** (lanes 5 and 6 respectively). This behaviour is attributed to the higher extinction coefficient presented by the osmium congener at the longer excitation wavelength, due to its higher degree of spin-orbit coupling. Given that **2** absorbs light more efficiently upon irradiation, more molecules are promoted into the excited state and thus, are allowed to react either with $^3\text{O}_2$ or DNA. Irradiation time for both samples was increased to 2 hours to further proof the photodynamic effect. Once again, DNA cleavage promoted by **2** is only observed after photoactivation (lanes 2, 4 compared to lane 6 in gel B), whereas the extend of photoscission is proportional to photolysis time (lane 6 vs lane 8).

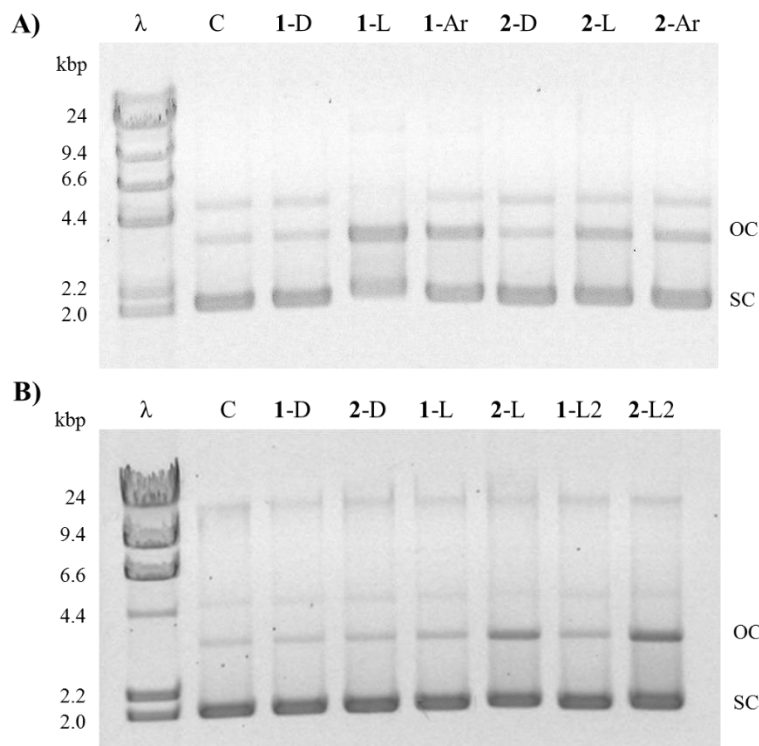


Figure 5.6 DNA gel shift assay. λ = Lamba DNA/Hind III markers. C= untreated pUC19 DNA control. D= sample incubated in dark conditions for 1 h (gel A) or 2 h (gel B). L= sample irradiated for 1 h with blue light (455 nm, gel A) or red light (625 nm, gel B). L2= sample irradiated for 2 h with red light (625 nm), Ar= oxygen depleted samples purged with argon prior to 1 h irradiation with blue light.

5.4.5 Protein gel shift assay. The activity of compounds **1** and **2** towards proteins was investigated under dark and light conditions by using BSA as a model protein. As shown in Figure 5.7A, incubation of BSA with compounds **1** and **2** in a dark compartment for 2 h yielded undetectable changes in the electrophoretic profile of BSA, probably due to the negligible interaction between the compounds and BSA in the absence of light, which agrees with the results obtained in the DNA experiments described above. In contrast, excitation with red light for 1 or 2 h resulted in apparent changes in the electrophoretic profile of BSA. To be specific, the bands were found to be less homogeneous and shift to low molecular weight positions, which may be attributed to cleavage and degradation caused by photoactivation (e.g. generation of ROS or direct photoreactivity, *vide infra*). Moreover, the profile change promoted by compound **2** was more marked than that of compound **1** in the presence of red light(625 nm), suggesting that

compound **2** had higher activity toward BSA over compound **1**, which is in consistent with the DNA and cytotoxicity data.

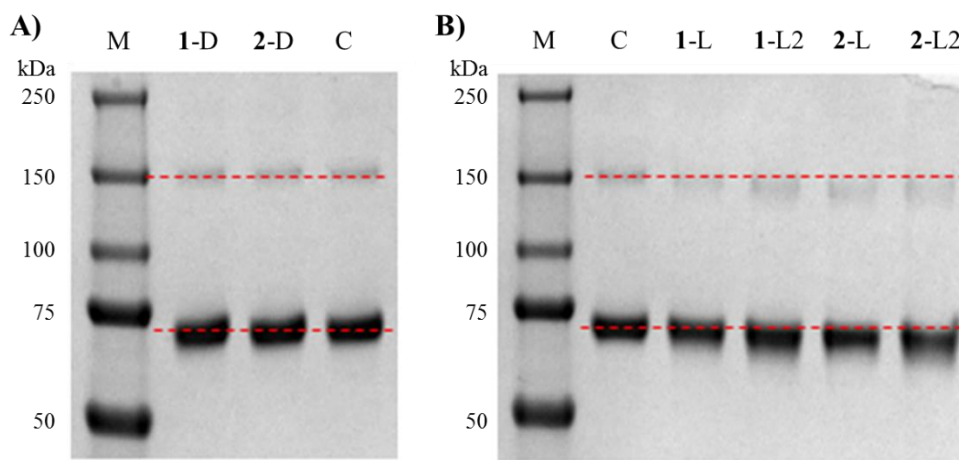


Figure 5.7 Protein gel shift assay. M=ladder. C=untreated BSA control. D=samples incubated in the dark for 2 h. L=sample irradiated for 1 h with red light (625 nm). L2=sample irradiated for 2 h with red light (625 nm).

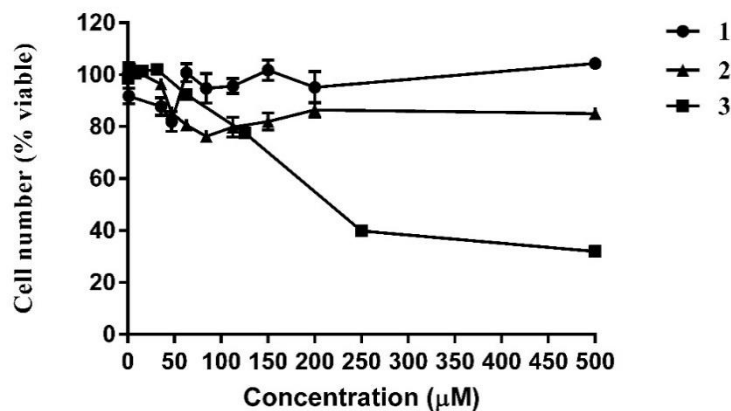
5.4.6 Cytotoxicity. The photocytotoxic activity of compounds **1** and **2** was evaluated in malignant glioma F98 rat cells in terms of its IC_{50} value by the AlamarBlue assay. Cisplatin, an FDA approved systemic chemotherapy drug, was used for comparison. Given its poor light absorption, cisplatin exhibited the same activity under light and dark conditions. The IC_{50} value stayed at (256 ± 4.0) μM under dark and blue light irradiation. As shown in Figure 5.8, compounds **1** and **2** were found to be nontoxic in the dark up to the highest concentration tested in this work (500 μM), since the viable cell percentage were higher than 80% after the treatment. In contrast, a phototoxic effect was observed upon visible light activation. For compound **1**, the IC_{50} values were calculated as (68.7 ± 1.9) and (337.1 ± 18.5) μM under blue light (470 nm) and red light (625 nm) irradiation, respectively. The lower efficacy displayed at the latter conditions was attributed to decreased light absorption at longer wavelengths, as observed in its electronic absorption spectrum (Figure 5.5). For compound **2**, the PDT effect is more significant, with IC_{50} values of (50.7 ± 2.9) μM in blue light and (86.1 ± 8.5) μM in red light. Interestingly but not surprisingly, altering the metal center from Ru to Os makes compound **2** more cytotoxic under activation within the phototherapeutic window (600–900 nm), attributed to a higher molar absorptivity at the irradiation wavelength. Upon photon absorption, the molecule populates a

reactive excited state that might lead to the generation of reactive oxygen species, as suggested by the gel electrophoresis experiment, which would favour the oxidation of molecular targets (i.e. DNA or proteins) and lead to cell death. Although the detailed cell death mechanism is still unknown and needs to be further studied, it could potentially involve ROS and oxidation or degradation of biomolecules. More prominently, both complexes show remarkably higher photocytotoxicity than cisplatin towards aggressive Rat malignant glioma F98 cells.

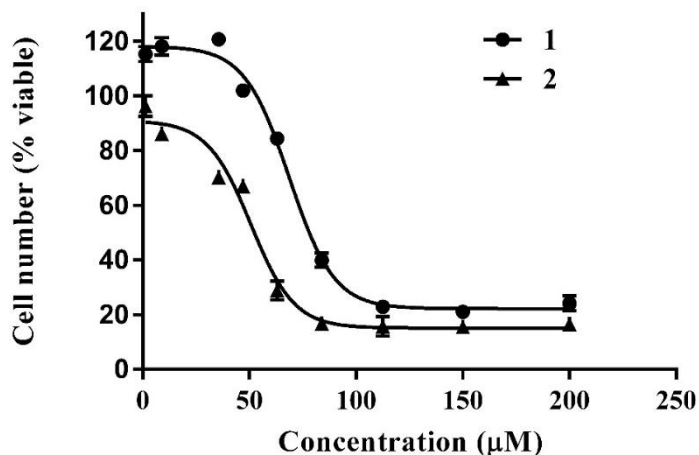
Table 5.3 Photocytotoxicity study in F98 cells

Compound	IC ₅₀ (μM)		
	Dark	Blue	Red
1	>500	68.7±1.9	337.1±18.5
2	>500	50.7±2.9	86.1±8.5
3	256±4.0	256±4.0	N.D

A)



B)



C)

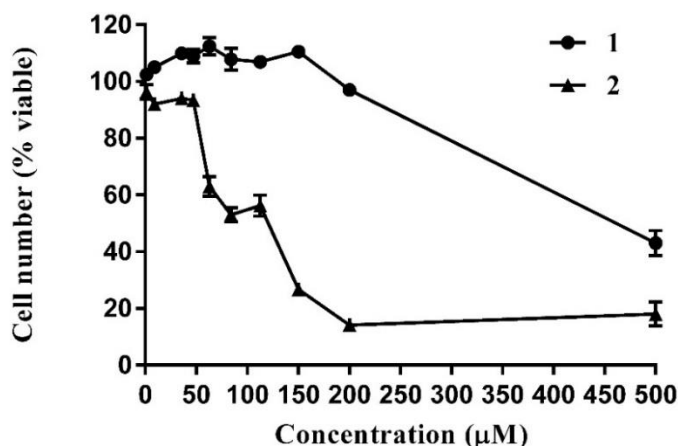


Figure 5.8 Cytotoxicity graphed as percent cell viability of F98 cells vs compound concentration (μM) 48 h after treatment. A) In the dark. B) Blue light (470 nm) irradiation for 1 h. C) Red light (625 nm) irradiation for 1 h. Each data point was performed in triplicate.

5.5 Conclusions

We present two new Ru/Os polyazine complexes as potential PDT agents towards aggressive rat malignant glioma F98 cells and photoactivated oxygen-dependent DNA and protein cleaving reagents. Both compounds have shown significant photocytotoxicity to F98 MG cells under short time (1 h) low power (3.75 mW) blue and red light activation, with relative low IC_{50} values compared to cisplatin. Metal center change from Ru to Os resulted in a higher degree of spin-orbit coupling and enhanced absorption within the phototherapeutic window, thus making compound **2** a promising PDT candidate for clinical application. This work demonstrates a simple strategy to tune transition metal complexes towards low energy light activation. Moreover, presence of the bridging ligand dpp in the reported compounds provides the possibility for further supramolecular design of multifunctional PDT agents.

5.6 Acknowledgements

The authors are grateful to the National Science Foundation (grant CHE-1301131) for funding this work. Acknowledgement is made to Dr. Amanda J. Morris and Theodore Canterbury for

helpful discussion. Special Acknowledgement is made to Prof. Karen.J.Brewer, who passed away but left precious memories and immortal inspiration as a good mentor and friend.

5.7 References

1. Celli, J. P.; Spring, B. Q.; Rizvi, I.; Evans, C. L.; Samkoe, K. S.; Verma, S.; Pogue, B. W.; Hasan, T. *Chem. Rev.* **2010**, *110* (5), 2795-2838.
2. Castano, A. P.; Demidova, T. N.; Hamblin, M. R. *Photodiagn. Photodyn. Ther.* **2004**, *1* (4), 279-293.
3. Detty, M. R.; Gibson, S. L.; Wagner, S. J. *J. Med. Chem.* **2004**, *47* (16), 3897-915.
4. (a) DeRosa, M. C.; Crutchley, R. J. *Coord. Chem. Rev.* **2002**, *233-234*, 351-371; (b) Lovell, J. F.; Liu, T. W. B.; Chen, J.; Zheng, G. *Chem. Rev.* **2010**, *110* (5), 2839-2857.
5. Bonnett, R., *Chemical aspects of photodynamic therapy*. CRC Press: 2000.
6. (a) van Rijt, S. H.; Sadler, P. J. *Drug Discovery Today* **2009**, *14* (23-24), 1089-1097; (b) Holder, A. A.; Zigler, D. F.; Tarrago-Trani, M. T.; Storrie, B.; Brewer, K. J. *Inorg. Chem.* **2007**, *46* (12), 4760-4762.
7. (a) Erkkila, K. E.; Odom, D. T.; Barton, J. K. *Chem. Rev.* **1999**, *99* (9), 2777-2796; (b) Sun, Y.; Joyce, L. E.; Dickson, N. M.; Turro, C. *Chem. Commun.* **2010**, *46* (14), 2426-2428; (c) Howerton, B. S.; Heidary, D. K.; Glazer, E. C. *J. Am. Chem. Soc.* **2012**, *134* (20), 8324-8327.
8. Zigler, D. F.; Brewer, K. J., Towards Photodynamic Therapy of Cancer with Platinum Group Metal Polyazine Complexes. In *Metal Complex-DNA Interactions*, John Wiley & Sons, Ltd: 2009; pp 235-272.
9. (a) Sun, Y.; Joyce, L. E.; Dickson, N. M.; Turro, C. *Chem. Commun.* **2010**, *46* (36), 6759-6761; (b) Wang, J.; Newman, J., Jr.; Higgins, S. L.; Brewer, K. M.; Winkel, B. S.; Brewer, K. J., *Angew. Chem., Int. Ed.* **2013**, *52* (4), 1262-5; (c) Higgins, S. L. H.; Tucker, A. J.; Winkel, B. S. J.; Brewer, K. J. *Chem. Commun.* **2012**, *48* (1), 67-69; (d) Wachter, E.; Heidary, D. K.; Howerton, B. S.; Parkin, S.; Glazer, E. C. *Chem. Commun.* **2012**, *48* (77), 9649-9651.
10. Siegel, R.; Naishadham, D.; Jemal, A. *Ca-Cancer J. Clin.* **2013**, *63* (1), 11-30.
11. Reardon, D. A.; Rich, J. N.; Friedman, H. S.; Bigner, D. D. *J. Clin. Oncol.* **2006**, *24* (8), 1253-65.
12. (a) Sathornsumetee, S.; Reardon, D. A.; Desjardins, A.; Quinn, J. A.; Vredenburgh, J. J.; Rich, J. N. *Cancer* **2007**, *110* (1), 13-24; (b) Furnari, F. B.; Fenton, T.; Bachoo, R. M.; Mukasa,

A.; Stommel, J. M.; Stegh, A.; Hahn, W. C.; Ligon, K. L.; Louis, D. N.; Brennan, C.; Chin, L.; DePinho, R. A.; Cavenee, W. K. *Genes Dev.* **2007**, *21* (21), 2683-2710.

13. Ohgaki, H.; Dessen, P.; Jourde, B.; Horstmann, S.; Nishikawa, T.; Di Patre, P. L.; Burkhard, C.; Schuler, D.; Probst-Hensch, N. M.; Maiorka, P. C.; Baeza, N.; Pisani, P.; Yonekawa, Y.; Yasargil, M. G.; Lutolf, U. M.; Kleihues, P. *Cancer Res.* **2004**, *64* (19), 6892-9.

14. Kanzawa, T.; Germano, I. M.; Komata, T.; Ito, H.; Kondo, Y.; Kondo, S. *Cell Death Differ.* **2004**, *11* (4), 448-457.

15. (a) Aguirre, J. D.; Angeles-Boza, A. M.; Chouai, A.; Pellois, J.-P.; Turro, C.; Dunbar, K. R. *J. Am. Chem. Soc.* **2009**, *131* (32), 11353-11360; (b) Basu, U.; Khan, I.; Hussain, A.; Kondaiah, P.; Chakravarty, A. R. *Angew. Chem., Int. Ed.* **2012**, *51* (11), 2658-2661; (c) Holder, A. A.; Swavey, S.; Brewer, K. J. *Inorg. Chem.* **2004**, *43* (1), 303-308.

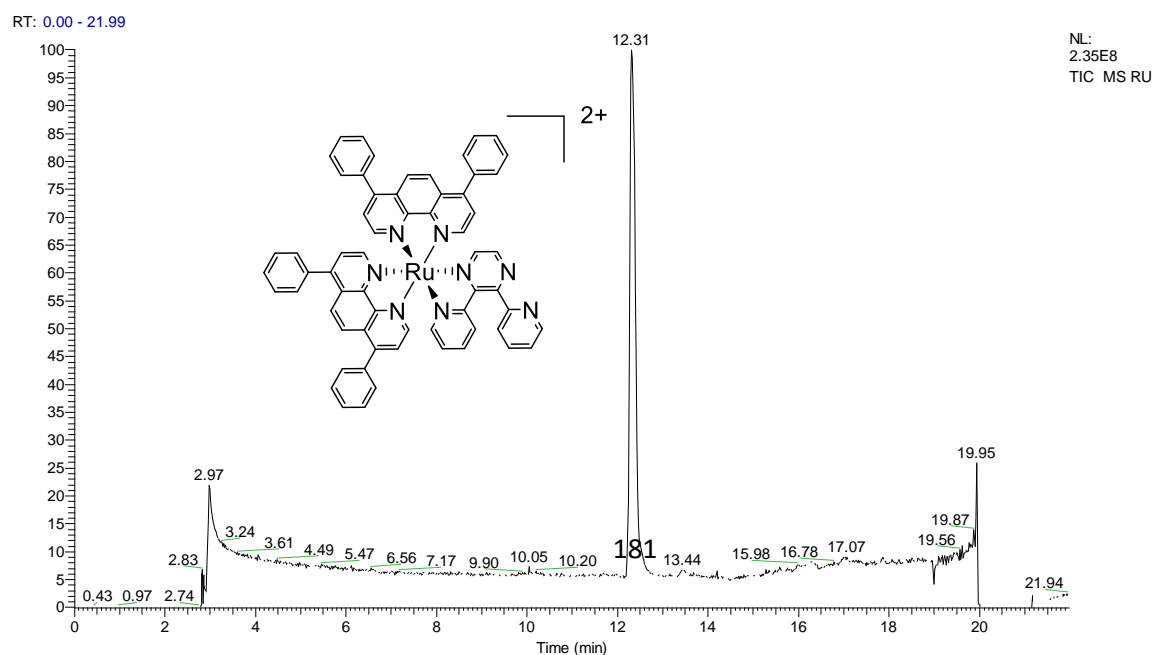
16. (a) Ye, R.-R.; Tan, C.-P.; Lin, Y.-N.; Ji, L.-N.; Mao, Z.-W. *Chem. Commun.* **2015**, *51* (39), 8353-8356; (b) Draksharapu, A.; Boersma, A. J.; Leising, M.; Meetsma, A.; Browne, W. R.; Roelfes, G. *Dalton Trans.* **2015**, *44* (8), 3647-3655.

17. (a) Dickerson, M.; Sun, Y.; Howerton, B.; Glazer, E. C. *Inorg. Chem.* **2014**, *53* (19), 10370-10377; (b) Basu, U.; Khan, I.; Hussain, A.; Gole, B.; Kondaiah, P.; Chakravarty, A. R. *Inorg. Chem.* **2014**, *53* (4), 2152-2162; (c) Yuan, Y.-X.; Chen, Y.; Wang, Y.-C.; Su, C.-Y.; Liang, S.-M.; Chao, H.; Ji, L.-N. *Inorg. Chem. Commun.* **2008**, *11* (9), 1048-1050.

18. Mongelli, M. T.; Brewer, K. J. *Inorg. Chem. Commun.* **2006**, *9* (9), 877-881.

5.8 Supporting Information

a)



b)

RU #725 RT: 12.33 AV: 1 NL: 8.40E7
T: + c ESI Q1MS [100.000-1500.000]

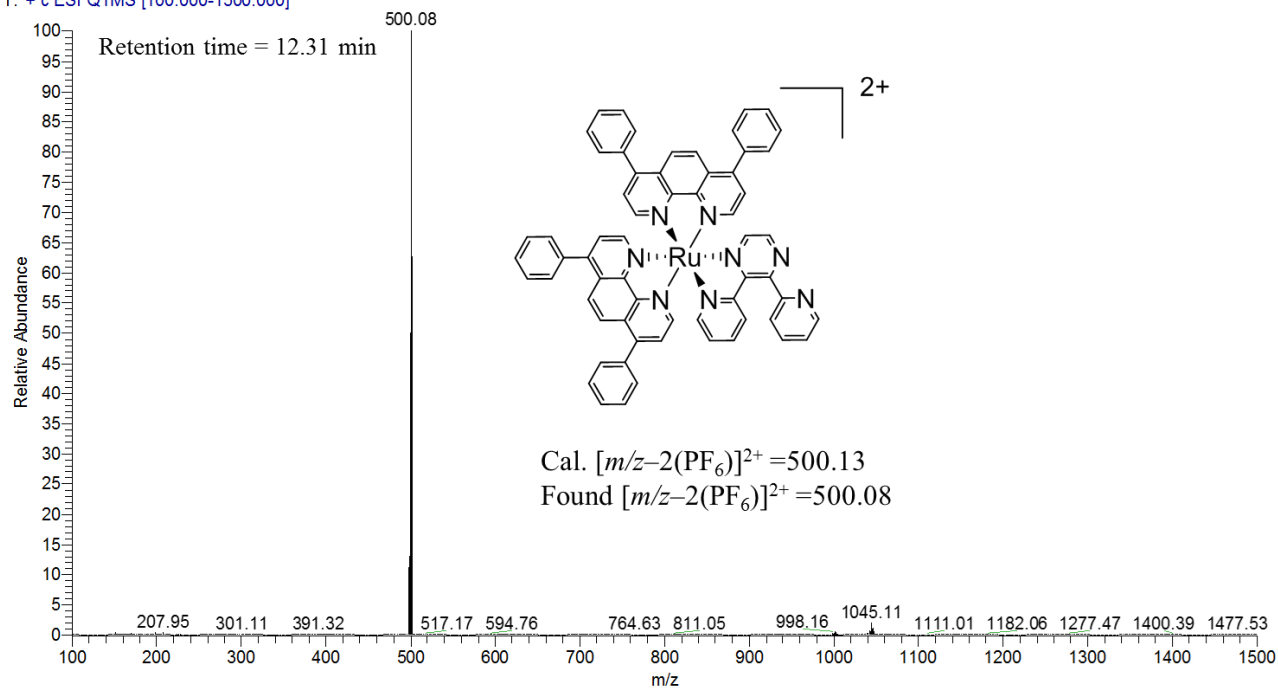


Figure S1. (a) HPLC chromatogram of $[(\text{Ph}_2\text{phen})_2\text{Ru}(\text{dpp})]^{2+}$ displaying the retention times of the compounds. (b) Total mass spectrum of the peaks at the given retention times (Ph_2phen = 4,7-diphenyl-1,10-phenanthroline; dpp = 2,3-bis(2-pyridyl)pyrazine).

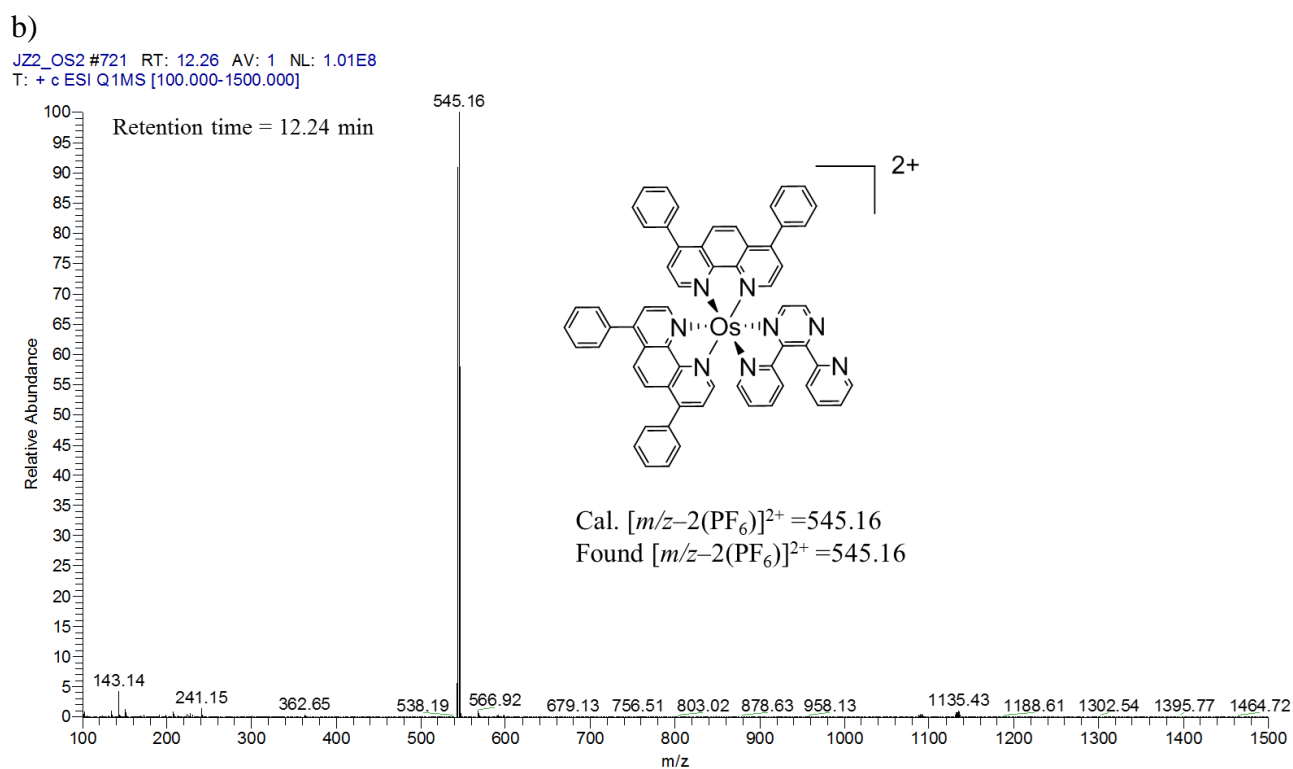
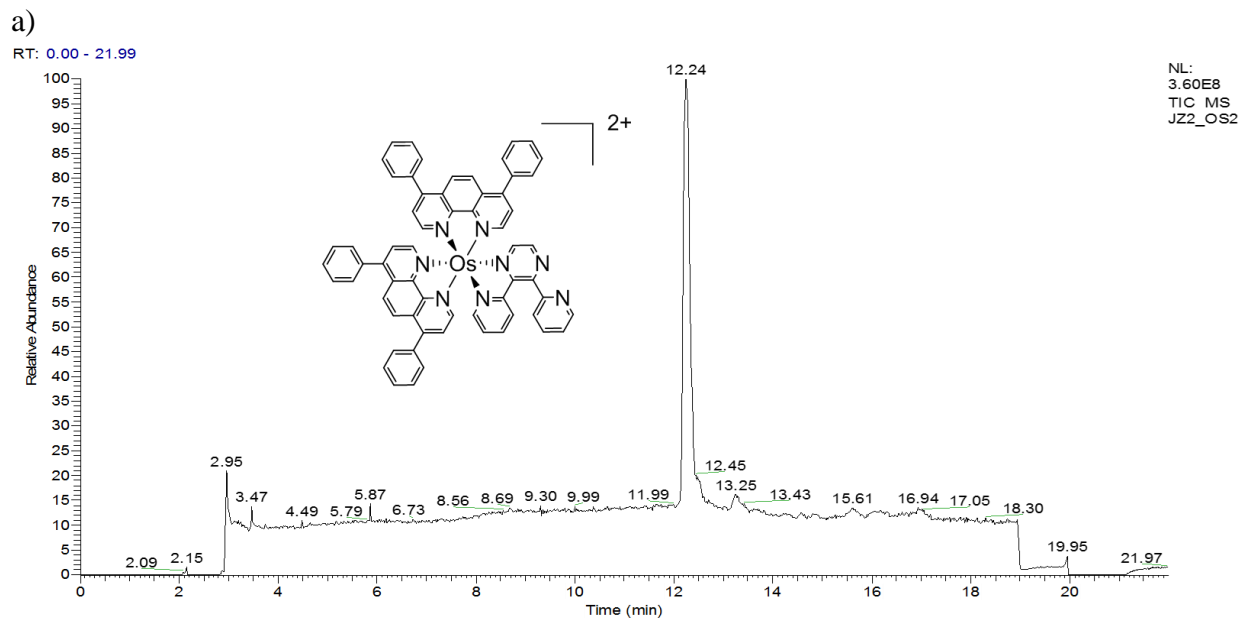


Figure S2. (a) HPLC chromatogram of $[(\text{Ph}_2\text{phen})_2\text{Os}(\text{dpp})]^{2+}$ displaying the retention times of the compounds. (b) Total mass spectrum of the peaks at the given retention times (Ph_2phen = 4,7-diphenyl-1,10-phenanthroline; dpp = 2,3-bis(2-pyridyl)pyrazine).

Chapter 6 Exploring the Activity of a Polyazine Bridged Ru(II)–Pt(II) Supramolecule in F98 Rat Malignant Glioma Cells

This chapter has been adapted from a published manuscript by [Zhu, J.](#); Rodriguez-Corrales, J. A.; Prussin, R.; Zhao, Z.; Dominijanni, A.; Hopkins, S. L.; Winkel, B. S. J.; Robertson, J. L.; and Brewer, K. J. from the following reference: *Chemical Communications* **2017**, 53 (1), 145-148. Reprinted with permission from the Royal Society of Chemistry copyright © 2017.

6.1 Abstract

The mixed-metal supramolecular complex, $[(\text{Ph}_2\text{phen})_2\text{Ru}-(\text{dpp})\text{PtCl}_2]^{2+}$, displays significant DNA modification, cell growth inhibition, and toxicity towards F98 malignant glioma cells following visible light irradiation. The design of this complex affords superior cellular uptake and antiproliferative activity compared to the classic chemotherapeutic agent, cisplatin.

6.2 Introduction

Cancer is a worldwide public health problem, a leading cause of death across all age groups.¹ Aggressive infiltrative malignant glioma (MG), which is estimated to make up approximately 1.41% of the total cancer cases in 2016,¹ is among the most devastating. The median survival rate for MG is approximately one year and less than 5% of patients diagnosed with MG live longer than five years, regardless of the type of therapy used.^{2,3} New treatments for high-grade MG are urgently needed to address and alleviate the limitations of current therapies and improve patient survival rates.

Photodynamic therapy (PDT) is a combination of chemo- and radiation therapy that uses a photosensitizer (PS), low energy light, and in some cases molecular oxygen ($^3\text{O}_2$) to produce cytotoxic reactive oxygen species (ROS) to damage neoplastic cells.^{4,5} This minimally-invasive, light-activated therapeutic treatment allows accurate targeting of tumor sites and reduces off-site effects associated with systemic chemotherapies.⁶ It is particularly promising for cancers such as MG that occur well within the 1 cm tissue penetration limit of light.

Conventional PDT agents, e.g. porphyrin-based PSs, suffer from dark toxicity, prolonged skin sensitivity, and hepatotoxicity, which limit their application as therapeutic agents.⁷ Transition metal complexes have emerged as promising candidates for the next generation of PDT agents due to their tunable coordination environments and varied spectral and redox properties.⁸⁻¹⁴ Recently, we reported two new Ru/Os polyazine monometallic complexes as photoactivated-oxygen-dependent DNA and protein cleaving reagents.¹⁵ The complexes show enhanced cytotoxicity towards F98 rat MG cells upon irradiation with visible light. However, the oxygen-dependence of these monometallic complexes limits their potential use as PDT agents due to the hypoxic environments that commonly characterize MGs and many other tumors.¹⁶

Extensive research has focused on efforts to conjugate PSs to known chemotherapeutic agents, such as cisplatin analogues, to develop a new class of potential PDT agents.¹⁷⁻²⁰ Among these, mixed-metal supramolecules stand out because of their ability to interact with biomolecules (e.g. DNA and protein) simultaneously via multiple means.^{21,22} A promising yet challenging design is the incorporation of photochemically activated bioactive sites (PAB) with thermally activated bioactive sites (TAB) through bridging ligands (BL). These novel supramolecular architectures could be triggered by multiple pathways to react with biological targets and lead to cancer cell necrosis and/or apoptosis.

Bimetallic Ru-Pt complexes are a class of PAB-BL-TAB molecules in which the ruthenium center plays a dual role as light absorber and PAB, while the cisplatin-like moiety acts as a TAB.²³⁻²⁵ It has been shown that Ru-Pt heteronuclear complexes are potential PDT agents where Ru and Pt work synergistically and in a light-dependent manner, thus leading to covalent binding to DNA (platination) through the TAB, and DNA photocleavage through the PAB.^{26,27} Furthermore, the TAB-directed binding of DNA would localize the generation of singlet oxygen ($^1\text{O}_2$) in proximity to the target biomolecule, which could circumvent the short lifetime and root mean square (RMS) diffusion distance, 4 μs and 125 nm in water.^{28,29} Recent DFT/TDDFT studies have provided further evidence that the synergistic effect between the metals makes the designed Ru-Pt complexes promising multi-target anticancer drugs.³⁰ Supramolecular Ru(II)-Pt(II) complexes thus appear to be promising new multifunctional PDT agents for the treatment of MGs and other intractable cancers.

We previously reported the synthesis and preliminary characterization of $[(\text{Ph}_2\text{phen})_2\text{Ru}(\text{dpp})\text{PtCl}_2]^{2+}$ (Ph_2phen = 4,7-diphenyl-1,10-phenanthroline; dpp = 2,3-bis(2-pyridyl) pyrazine), herein referred to as **Ru(II)-Pt(II)** (Figure 6.1).^{26, 27} This complex tethers a Ru(II) PS to a DNA targeting *cis*-Pt(II)Cl₂ motif, making it an unprecedented ³MLCT-activated DNA photobinding agent that also produces ROS. By harnessing the properties of the individual components in a supramolecular architecture, this compound opens interesting new prospects for a combined anticancer approach. In fact, we showed that excitation with visible light leads to population of a Ru($d\pi$) \rightarrow dpp(π^*) MLCT state, which affords enhanced electron density on the dpp ligand, while reducing the Lewis acidity of the platinum center with consequent photolabilization of the Pt-Cl bond.^{27,30} The photo release of such ligands is expected to facilitate its reaction with biological targets and thus represents a new pathway of activation of Pt(II) compounds to the classical hydrolysis mechanism. Furthermore, preliminary experiments using blue light activation provided evidence for DNA cleavage even after oxygen removal through six freeze-pump-thaw cycles.²⁶

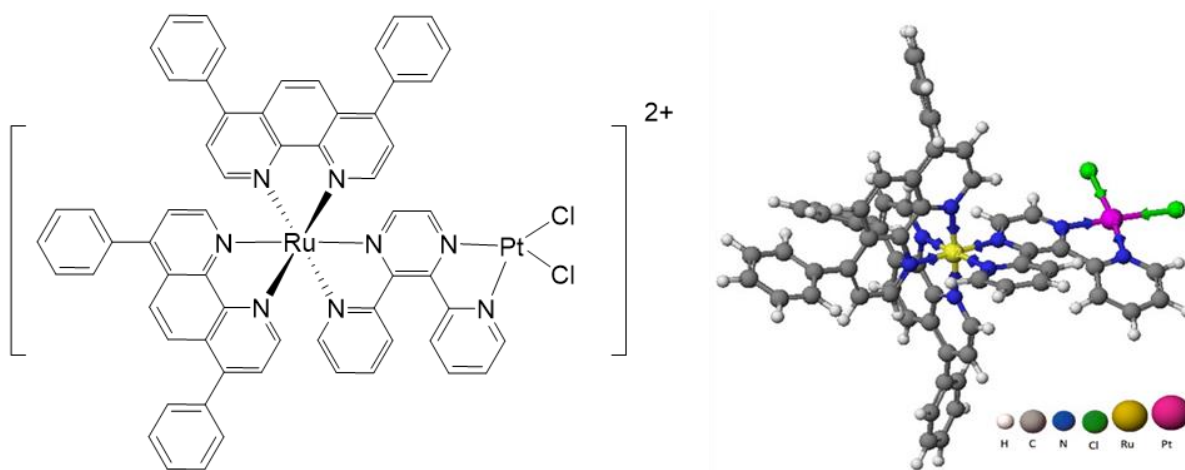


Figure 6.1 Structure of $[(\text{Ph}_2\text{phen})_2\text{Ru}(\text{dpp})\text{PtCl}_2]^{2+}$

6.3 Experimental Section

6.3.1 Synthesis and characterization of $[(\text{Ph}_2\text{phen})_2\text{Ru}(\text{dpp})\text{PtCl}_2]\text{Cl}_2$

The bimetallic complex, $[(\text{Ph}_2\text{phen})_2\text{Ru}(\text{dpp})\text{PtCl}_2]\text{Cl}_2$ was synthesized by the previously reported method using a building block strategy (Figure S1).²⁷ $[(\text{Ph}_2\text{phen})_2\text{Ru}(\text{dpp})]\text{Cl}_2$ (0.50 g, 0.47 mmol) and $[\text{PtCl}_2(\text{DMSO})_2]$ (1.0 g, 2.4 mmol) were heated at reflux in 25 mL of ethanol for ca. 2 h in the dark. The reaction mixture was cooled to room temperature and the solid was

collected by vacuum filtration. The solid was dissolved in a minimal amount of 2:1 C₂H₅OH/CH₃CN and purified by LH-20 size exclusion chromatography using 2:1 C₂H₅OH/CH₃CN eluent. The first orange-red band was collected, solvent was removed under vacuum, and the complex was flash precipitated from dry acetone into diethyl ether, with a yield of 75%.

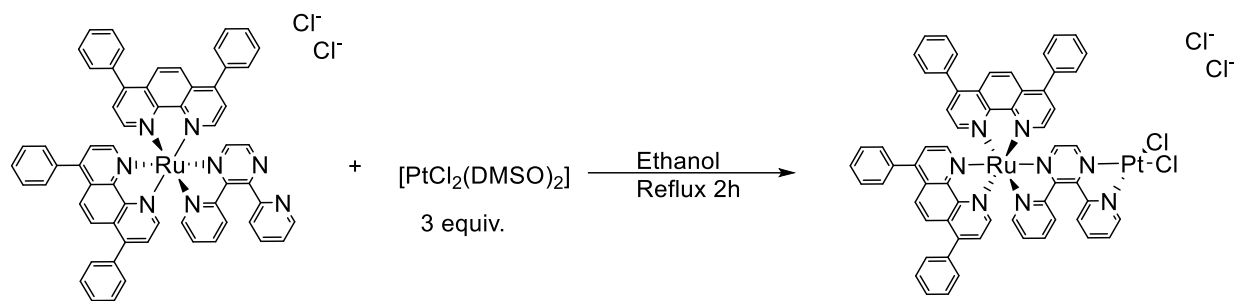


Figure S1. Synthetic scheme of $[(\text{Ph}_2\text{phen})_2\text{Ru}(\text{dpp})\text{PtCl}_2]\text{Cl}_2$.

The complex was metathesized to the PF₆⁻ salt by mixing an aqueous solution of $[(\text{Ph}_2\text{phen})_2\text{Ru}(\text{dpp})\text{PtCl}_2]\text{Cl}_2$ into a saturated solution of NH₄PF₆. $[(\text{Ph}_2\text{phen})_2\text{Ru}(\text{dpp})\text{PtCl}_2](\text{PF}_6)$ was recovered by filtration and flash precipitated from acetonitrile into diethyl ether, with a yield of 70%.

The electrochemistry of the $[(\text{Ph}_2\text{phen})_2\text{Ru}(\text{dpp})\text{PtCl}_2](\text{PF}_6)_2$ complex is shown in Figure S2. The oxidative electrochemistry shows a reversible Ru^{II/III} couple at +1.57V vs. Ag/AgCl and an irreversible oxidation of Pt^{II/IV} at +1.47V vs. Ag/AgCl, respectively, while the dpp^{0/-} is reduced at -0.50V vs. Ag/AgCl and Ph₂phen^{0/-} is reduced at -1.05V vs. Ag/AgCl.²⁶

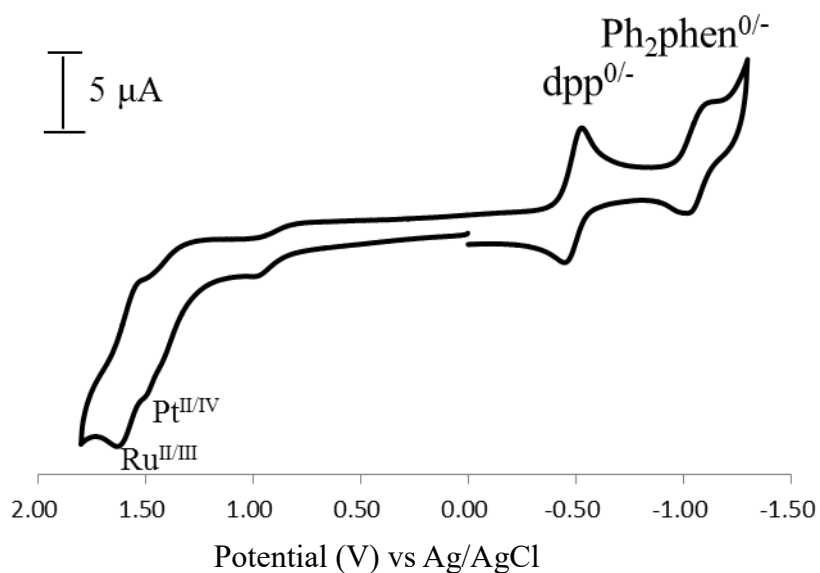


Figure S2. Cyclic voltammogram of $[(\text{Ph}_2\text{phen})_2\text{Ru}(\text{dpp})\text{PtCl}_2](\text{PF}_6)_2$ in 0.1 M TBAPF₆ acetonitrile, E vs. Ag/AgCl, $\nu = 100$ mV/s.

The electronic absorption spectrum exhibits a broad low energy Ru($d\pi$) \rightarrow dpp(π^*) metal-to-ligand charge transfer (¹MLCT) transition at 525 nm with $\epsilon = 12,100$ M⁻¹cm⁻¹, which extends throughout the visible region; while the UV region is dominated by characteristic ligand-based $\pi \rightarrow \pi^*$ transitions (Figure S3). Emission of this bimetallic complex occurs at 740 nm upon excitation at 520 nm.²⁶

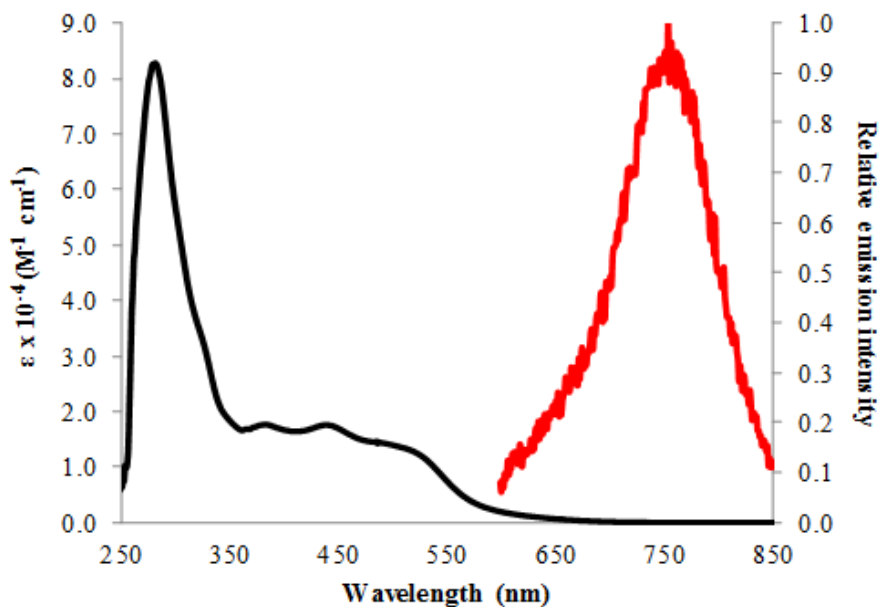


Figure S3. Electronic absorption (black) and emission (red) spectra upon excitation at 520 nm of $[(\text{Ph}_2\text{phen})_2\text{Ru}(\text{dpp})\text{PtCl}_2](\text{PF}_6)_2$ in CH_3CN at room temperature.

6.3.2 Partition coefficient

The partition coefficient of the complex relative to three well-known anticancer agents was determined as an approximation of the ability of these complexes to cross the cell membrane. The partition coefficient measures the relative concentration of a molecule in equilibrated immiscible solvents, in this case equilibrated phosphate buffer (pH 7.4) and *n*-octanol. The buffer and octanol solvents were equilibrated and separated prior to use in the experiments. The complexes were dissolved in 30 mL of buffer and 30 mL of octanol was added. The samples were stirred at 1000 rpm for 30 min and added to a separatory funnel. After 12 h of equilibration the layers were drained and the concentrations of the complexes determined based on their molar absorptivity using an electronic absorption spectrophotometer. The $\log P$ or partition coefficients were determined using equation 1,

$$\text{Log}P_{o/w} = \log \left(\frac{[\text{octanol}]}{[\text{buffer}]} \right) \quad (\text{Eq. 1})$$

where [octanol] and [buffer] are the concentrations of the compound in octanol and buffer after separation.

Partition coefficients using octanol and water are reported as $\text{Log}P_{O/W}$, where a value of 0 represents equal concentrations of the molecule in the octanol and water phases. A $\text{Log}P_{O/W}$ value greater than 0 indicates a larger concentration of the molecule in the octanol phase and therefore a more lipophilic molecule.

6.3.3 DNA Gel Shift Assay

DNA-complex solutions were prepared in aqueous 10 mM phosphate buffer (pH 7.4) with 20 μM $[(\text{Ph}_2\text{phen})_2\text{Ru}(\text{dpp})\text{PtCl}_2]\text{Cl}_2$ and 100 μM pUC19 DNA (1:5 complex:base pair molar ratio). Dark (D) and thermal (T) controls were incubated in a dark compartment at room temperature or 37 °C, respectively, while photolysis was being conducted. Photolysis was performed for 1 h with a blue (455 nm, B and B-Ar) or red (625 nm, R and R-Ar) LED array. Oxygen depleted samples (B-Ar and R-Ar) were bubbled with argon for 20 min prior to photolysis and closed under an argon atmosphere. After 1 h, 5 μL of each sample were diluted with 5 μL of 10 mM phosphate buffer and 2 μL of Type 3 loading dye (0.25% bromophenol blue, 0.25% xylene cyanol FF and 30% glycerol in water). Samples were analyzed using a 0.8 % w/w agarose gel with Tris-boric acid buffer (90 mM Tris base, 90 mM boric acid), placed in an Owl Separation Systems model B1A stage, where electrophoresis was conducted for 90 min at 100 V. Gels staining was performed using 0.5 $\mu\text{g}/\text{mL}$ ethidium bromide (Biotium Inc.) for 30 min, followed by washing with deionized water for 15 min and visualization on a Fisher Biotech UV-transilluminator. Images were captured with an Olympus SP-320 camera fitted with an ethidium bromide filter.¹⁵

6.3.4 Protein Gel Shift Assay

Bovine serum albumin (BSA)-complex solutions were prepared in aqueous 10 mM phosphate buffer (pH 7.4) with BSA: metal complex molar ratios of 1:1 or 1:10, with a fixed metal complex concentration of 20 μM . Photolysis was performed for 1 or 3 h using a blue (455 nm, B) or red (625 nm, R) LED array. Dark (D) and thermal (T) controls were incubated in a dark compartment while photolysis was being conducted. Fractionation was performed using 1 mm 4-12% Bis-Tris gels (Invitrogen). Gels were loaded with samples treated with Nupage LDS buffer and Nupage reducing agent according to the manufacturer's instructions, followed by electrophoresis in MES buffer at 200 V for 35 min. Gels were washed three times with water for

5 min before being treated with Simplyblue Safestain (Invitrogen) for 1 h. Gels were then washed overnight in water and imaged using a Bio-Rad ChemiDoc XLS system.¹⁵ (Figure S4)

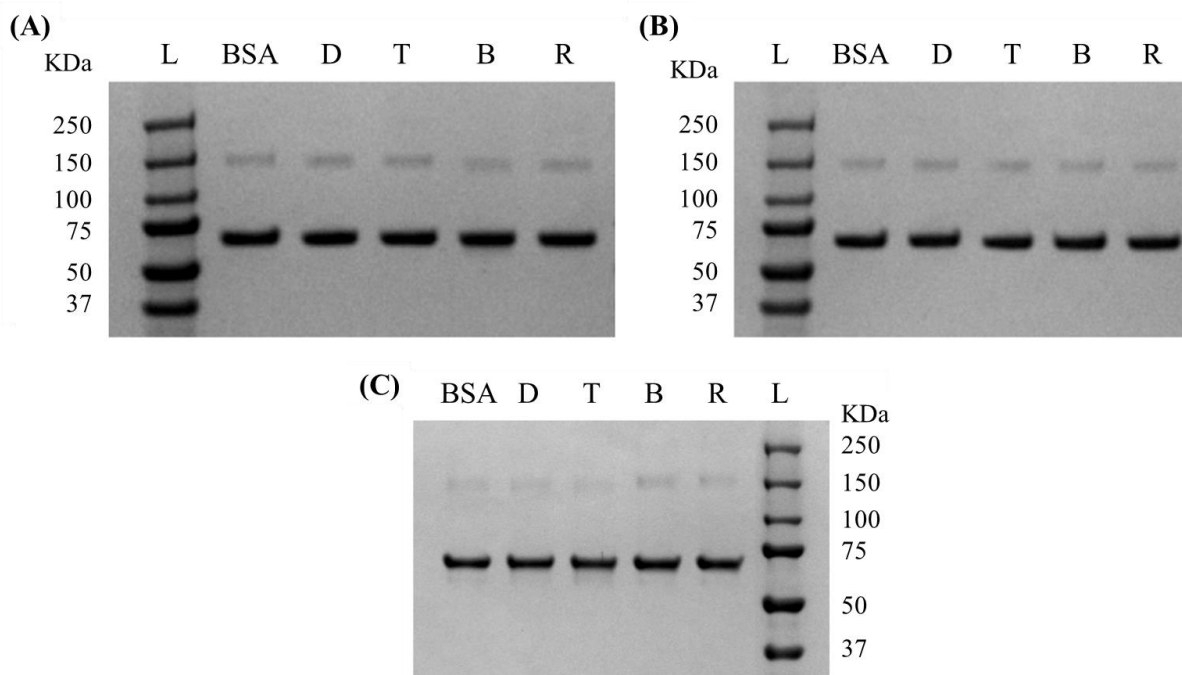


Figure S4. Protein gel shift assay. L = molecular weight ladder; BSA = untreated BSA control; D = samples incubated in the dark. T = samples incubated at 37 °C, B = samples photolyzed with blue light; R = samples photolyzed with red light. **(A)** Samples treated for 1 h at 1:1 complex:BSA molar ratio. **(B)** Samples treated for 1 h at 10:1 complex:BSA molar ratio. **(C)** Samples treated for 3 h at 10:1 complex:BSA molar ratio.

6.3.5 Cell culture

F98 rat malignant glioma cells (ATCC) were maintained in DMEM supplemented with 10% fetal bovine serum (FBS, ATCC) and 1% penicillin-streptomycin and incubated at 37 °C in a humidified incubator at 5% CO₂.

6.3.6 Cell uptake of Ru(II)-Pt(II) by F98 MG cells

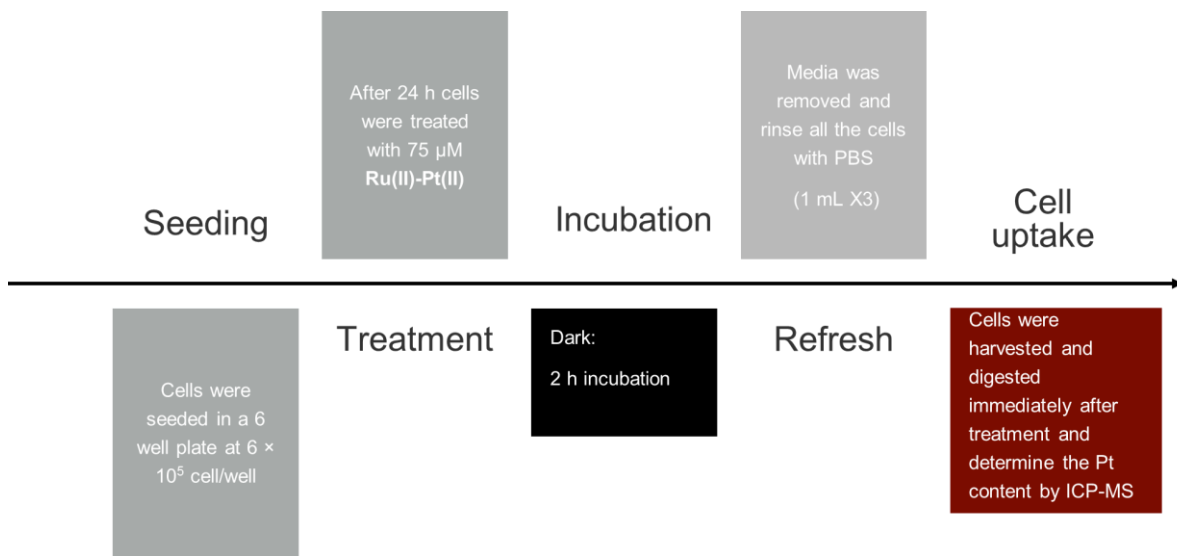


Figure S5. Protocol for **Ru(II)-Pt(II)** uptake in F98 MG cell line.

Cell uptake was quantified by inductively coupled plasma mass spectrometry (ICP-MS) analysis of intracellular platinum contents. F98 cells were grown in 6-well plates for 24 h at 37°C and 5% CO_2 before the treatment. **Ru(II)-Pt(II)** or cisplatin were dissolved in DMSO and added to cells to give a final concentration of $75 \mu\text{M}$ (final concentration of DMSO 3% v/v). Cells were incubated with either compound for 2 h at 37°C in a 5% CO_2 humidified incubator. The culture medium was discarded, and the cells were washed three times with PBS. Cells were harvested, suspended in PBS, and centrifuged at 3000 rpm for 15 min. After discarding the buffer, cell pellets were digested in 70% nitric acid at 90°C for 1 h. Samples were diluted further to a final concentration of 7% nitric acid with D.I. water containing 0.1% Triton X100. The Pt content of the cells was estimated using a Thermo Electron X-Series inductively coupled plasma mass spectrometer (ICP-MS) in accordance with Standard Method 3125-B.

6.3.7 Cytotoxicity and photocytotoxicity

The cytotoxicity of $[(\text{Ph}_2\text{phen})_2\text{Ru}(\text{dpp})\text{PtCl}_2]\text{Cl}_2$ was evaluated both under dark conditions and following photolysis to evaluate the photodynamic activity of the compound. F98 rat malignant glioma cells were plated in triplicates in the 6-well plates at a density of approximately 6×10^5 cells/well in DMEM. The cells were incubated at 37°C in a 5% CO_2 humidified atmosphere for 24 h before treatment. Medium was removed from each well and replaced with solution containing different concentrations of the complex, ranging from 25 to $75 \mu\text{M}$, dissolved in 29%

v/v phosphate buffered saline (PBS), 4% v/v dimethyl sulfoxide (DMSO), and 67% v/v RPMI 1640 (without L-glutamine and phenol red). A control sample was prepared using the same ratio of PBS, DMSO, and RPMI 1640 but without $[(\text{Ph}_2\text{phen})_2\text{Ru}(\text{dpp})\text{PtCl}_2]\text{Cl}_2$. For cytotoxicity assay, the plates were incubated in the dark for 1 h. For photocytotoxicity, the cells were incubated in the dark for 15 min and then were irradiated for 30 min using a lab-built blue light LED array (470 nm, 3.75 mW). A final 15 min dark incubation was performed after photolysis. The solutions were then aspirated and the cells were washed with fresh medium. Half of the plates were supplemented with DMEM and incubated for 48 h prior to counting cells, while cells in the rest of the wells were harvested immediately after incubation.

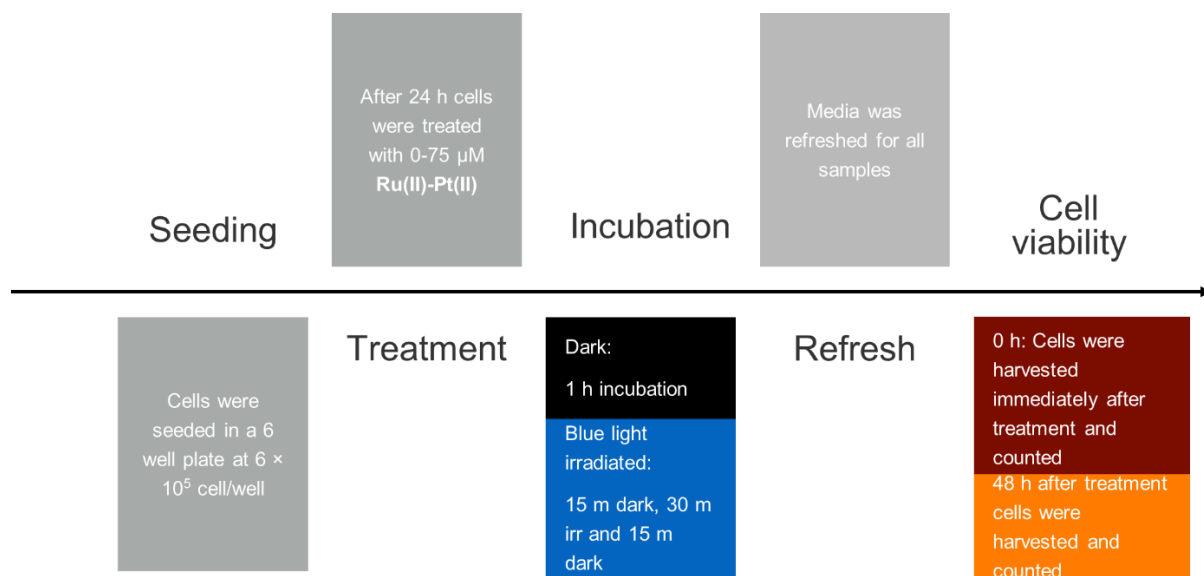


Figure S6. Protocol for F98 MG cell line photocytotoxic response to $[(\text{Ph}_2\text{phen})_2\text{Ru}(\text{dpp})\text{PtCl}_2]^{2+}$.

Cells were harvested using 0.05% trypsin in PBS/EDTA. An equivalent amount of DMEM was added to the trypsinized cells once they were visibly detached from the well. Trypan blue was used as a dye exclusion assay and cells were counted using an automated Vi-CELL[®] Cell Viability Analyzer.

Each experiment was performed in triplicate and the average values were used to calculate the final cell viability for each concentration of $[(\text{Ph}_2\text{phen})_2\text{Ru}(\text{dpp})\text{PtCl}_2]\text{Cl}_2$. The results are shown in Figure S7.

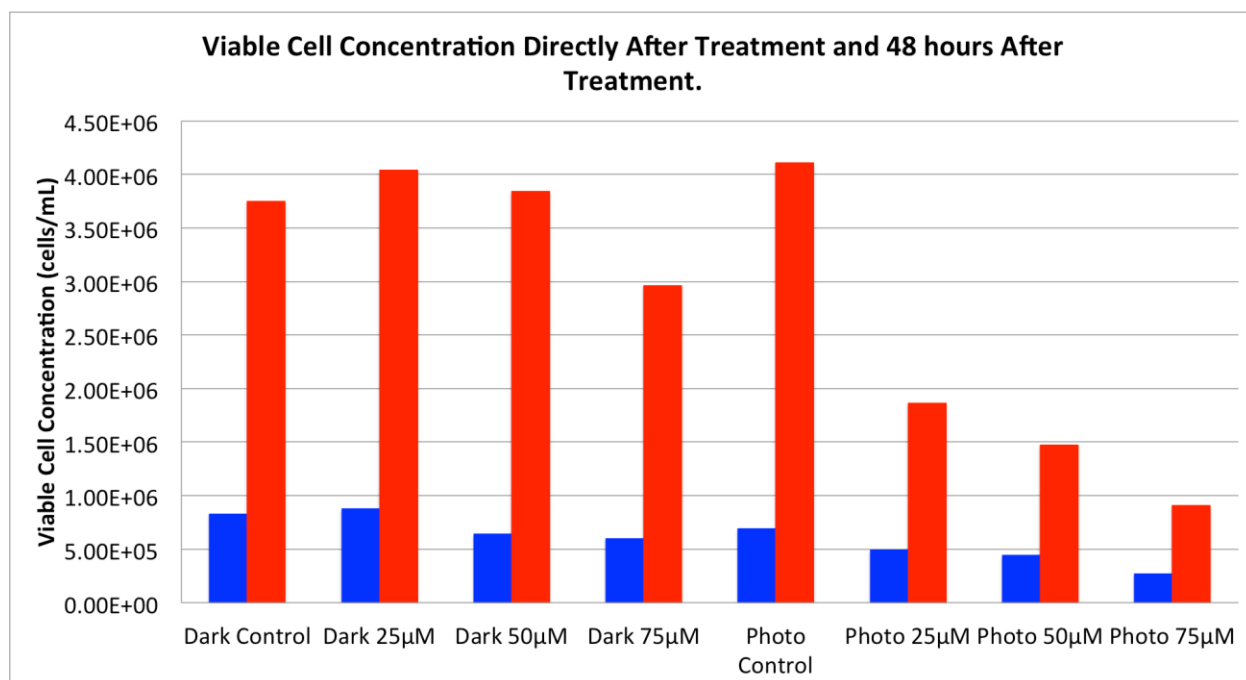


Figure S7. Viability assay of F98 MG cells after treatment with **Ru(II)-Pt(II)** for 0 h (blue) or 48 h (red). Results represent the mean value for two experiments. Photo = irradiated samples.

6.3.8 Design of LED Array

A LED array was designed to insure homogenous and controlled light delivery to the cells during treatment. The power source input was 120 V AC with an output of 13.5 V DC. A circuitry box was used to calibrate the output of each LED separately prior to the treatment. The circuitry diagram is displayed in Figure S8. Two 5 Ω resistors, wiring, a voltage controlling knob, and a LED were placed together for six LED channels, with one light source per well in the treatment containers. The six LEDs were placed on a separate board from the circuitry to avoid excessive heating of the plates during treatment. The LED head board was placed on a mount designed to fit the dimensions of the well plates used in treatment and not let light either enter or escape to interrupt the photolysis. Illumination of the cells was performed through the bottom of the plate in order to insure effective delivery of light.

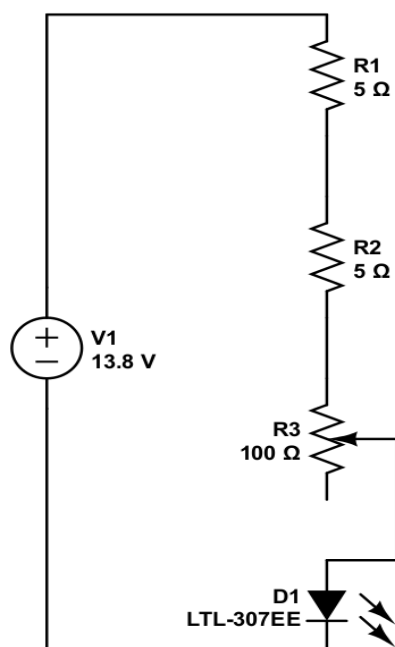
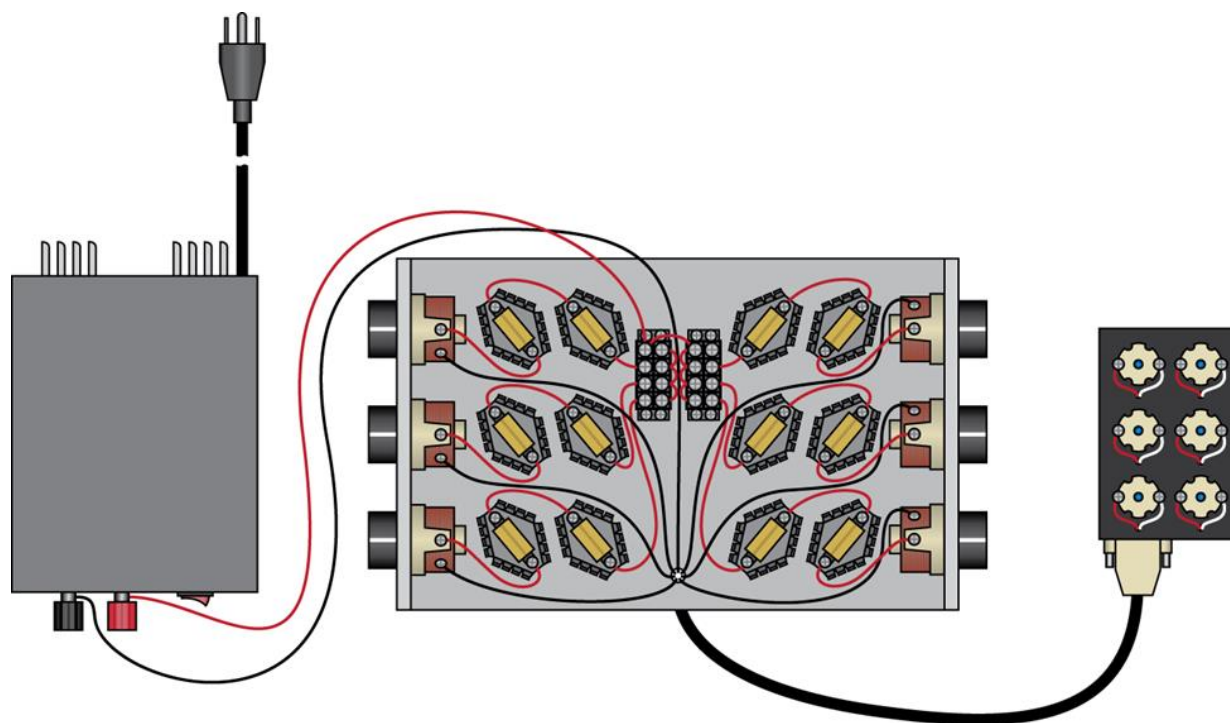


Figure S8. Circuitry diagram for calibration box

For calibration of each LED prior to the treatment, a ThorLabs sensor was used to detect the light output at the center of each well. Adjustments were made accordingly with the voltage

controlling knob and the average power delivered to those sites was 3.75 mW. This output was checked each time a plate was removed to confirm that the power remained constant throughout the treatment.

6.4 Results and Discussion

In this study we demonstrate the photodynamic activity of Ru(II)-Pt(II) both *in vitro* with purified plasmid DNA and for the first time with rat MG F98 cells, a model for human glioblastoma. The complex exhibited low toxicity in the dark, but substantially higher cytotoxicity than the classic chemotherapeutic drug cisplatin following exposure to blue light. We also uncovered evidence that the effective cytotoxicity of Ru(II)-Pt(II) at least in part reflects the higher cell membrane permeability and cellular uptake of the complex relative to cisplatin and two other classical chemotherapeutic drugs.

The Ru(II)-Pt(II) title complex was prepared using the previously described building block method and validated by electrochemical analyses (Figures S1 and S2).²⁷ To examine the bioactivity of this molecule in further detail, Ru(II)-Pt(II) was reacted with plasmid DNA *in vitro* under dark and irradiated conditions (455 and 625 nm). The samples were then examined using agarose gel electrophoresis, which provides a quick and facile evaluation of the complex for both binding and cleavage of DNA.³¹ As presented in Figure 6.2, plasmid DNA incubated with the complex in the dark (lane D) showed a slight decrease in electrophoretic mobility of the supercoiled form (SC) compared to the control containing plasmid DNA alone (lane C), likely due to covalent binding of the complex to the biomolecule. This change is enhanced upon incubation at 37°C (lane T) and is therefore attributed to thermal aquation of the *cis*-PtCl₂ moiety, a well-known behavior of cisplatin, followed by substitution of an *aquo* ligand for a purine base in DNA.³² Both blue (lane B) and red (lane R) light activation enhanced the interaction of the complex with DNA compared to dark conditions. The increase in the relative amount of open circular (OC) DNA in these samples is a clear indication of enhanced cleavage, which could arise from DNA oxidation by singlet oxygen or other ROS originating from dissolved O₂ or H₂O.²⁷ Since both cleavage and binding were promoted upon photolysis, the two metals play a synergistic role in the multifunctional modification of the biomolecule: the Ru-based PS generates oxidative stress while the Pt-based moiety promotes DNA platination. Importantly, the

ability of **Ru(II)-Pt(II)** to bind and cleave DNA was preserved in deoxygenated solutions (lanes B-Ar and R-Ar) that were purged with argon for 20 min prior to photolysis, which would deplete the majority of the dissolved oxygen in these samples. This remarkable behavior reveals that the ability of **Ru(II)-Pt(II)** to cleave DNA is not limited by its low singlet oxygen quantum yield, determined to be 0.06(7) in methanol solution.²⁶ Given the short lifetime and diffusion limited activity of $^1\text{O}_2$,^{28,29} we propose that the formation of covalent bonds between **Ru(II)-Pt(II)** and DNA may serve as a crucial localization step that leads to generation of singlet oxygen or other ROS in the immediate proximity of the biomolecule, facilitating DNA cleavage even under oxygen-depleted conditions. This postulate would explain why DNA cleavage was abolished when photolysis solution was spiked with NaN_3 ,²⁶ since it is likely that those conditions could result in substitution of the labile ligands and inhibit covalent binding to DNA.

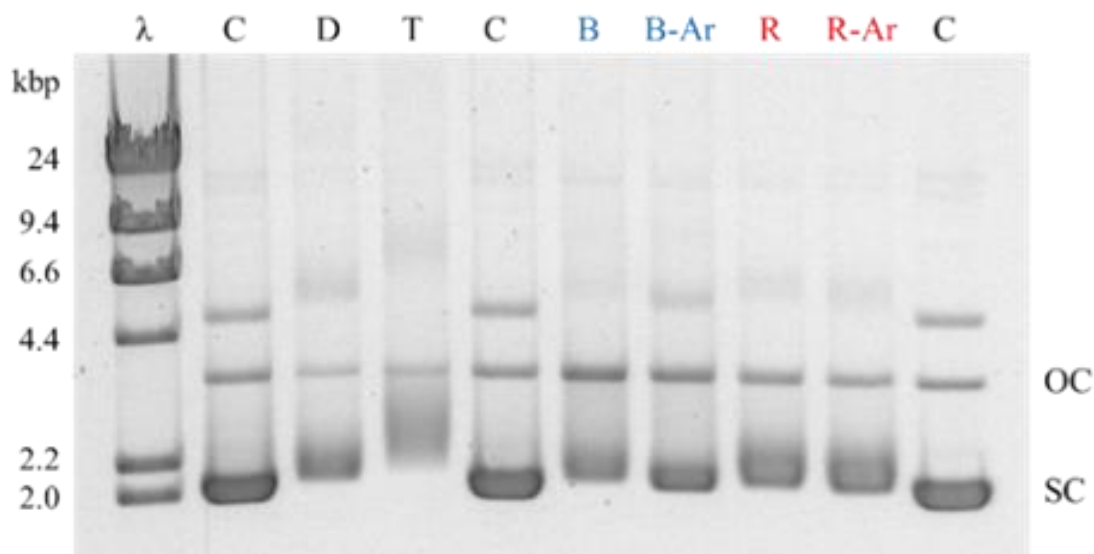


Figure 6.2 DNA gel shift assay for Ru(II)-Pt(II). λ : DNA weight marker, C: pUC19 DNA (2686 bp), D = DNA/complex incubated at room temperature in the dark, T = DNA/complex incubated at 37°C, B= DNA/complex exposed to a blue (455 nm) LED with O_2 , B-Ar = DNA/complex exposed to a blue (455 nm) LED after Ar purging, R = DNA/complex exposed to a red (625 nm) LED with O_2 , R-Ar = DNA/complex exposed to a red (625 nm) LED after Ar purging, OC = open circular DNA, SC = supercoiled DNA. All incubation steps were 1 h.

We also investigated the reactivity of **Ru(II)-Pt(II)** with bovine serum albumin (BSA), a prototypical protein. Similar to the DNA experiment, samples containing the complex and BSA

(in 1:1 and 10:1 molar ratios) were incubated in the dark or photolyzed under blue or red light for up to 3 h and analysed by electrophoresis.

Interestingly, there was no detectable difference in the electrophoretic mobility of the treated and untreated samples under any of the conditions tested, including up to 3 h of photolysis (see Figure S4). This is in striking contrast to the parent compound, $[(\text{Ph}_2\text{phen})_2\text{Ru}(\text{dpp})]^{2+}$, which cleaves BSA even with 1h of photolysis through an oxygen-dependent mechanism.¹⁵ The monometallic complex shows a 10-fold longer lived excited state than **Ru(II)-Pt(II)**, which results in a higher $^1\text{O}_2$ quantum yield and significant BSA cleavage.²⁶

The difference in activity between BSA and DNA likely reflects the number of covalent binding sites in these molecules. Covalent binding of cisplatin to DNA occurs primarily at purine bases,³² which account for 47% of the nitrogen bases in pUC19 DNA. In contrast, covalent binding to proteins occurs predominantly at exposed methionine, cysteine, and histidine residues, which make up less than 4% of the amino acids in BSA.³³ We hypothesize that without efficient covalent binding with BSA, cleavage of BSA by **Ru(II)-Pt(II)** is limited by its short-lived excited state and low $^1\text{O}_2$ quantum yield upon irradiation, while the cleavage of DNA is promoted by the highly efficient and covalent binding of **Ru(II)-Pt(II)** to this biomolecule. Although further experiments are needed to determine the affinity of **Ru(II)-Pt(II)** for protein *in vivo*, the apparent selectivity for DNA over BSA suggests that this complex could exhibit decreased drug loss and off-target toxicity due to binding to serum proteins relative to other drugs.

The octanol/water partition coefficient of **Ru(II)-Pt(II)** was determined to evaluate the hydrophobicity and lipophilicity of the complex, which are correlated with the ability to traverse and distribute throughout the body, the blood brain barrier, and cell membranes (the detailed experimental procedure presented in ESI). The complex exhibited a $\text{Log}P_{o/w}$ of 0.55, which falls in the range for optimal oral absorption and/or central nervous system penetration ($+1.5 \pm 1.0$).³⁴ Based on $\text{Log}P_{o/w}$ values (Table 6.1), the title complex demonstrates increased potential for cell membrane permeability compared to cisplatin, carboplatin, and TMZ, which are FDA approved drugs for MG treatment. This is hypothesized to arise from the lipophilicity of the aromatic ligands within the Ru(II) PS subunit.³⁵

Table 6.1 Log $P_{o/w}$ values for FDA approved anticancer agents and $[(\text{Ph}_2\text{phen})_2\text{Ru}(\text{dpp})\text{PtCl}_2]\text{Cl}_2$

Agent	Log $P_{o/w}$
Cisplatin ³⁶	-2.50
Carboplatin ³⁶	-2.30
Temozolomide ³⁷	-1.03
$[(\text{Ph}_2\text{phen})_2\text{Ru}(\text{dpp})\text{PtCl}_2]\text{Cl}_2$	0.55

The potential for enhanced permeability was further corroborated through cellular uptake studies in which ICP-MS analysis was used to quantify intracellular platinum content. After 2 h incubation of F98 MG cells with **Ru(II)–Pt(II)** or cisplatin (75 μM) in the dark, the internalization of **Ru(II)–Pt(II)** was 18.75 ± 1.25 pmol/cell, which is 10 times higher than the corresponding value for cisplatin (see ESI). Hence, coupling of the ruthenium PS dramatically increased the cellular uptake of the cisplatin moiety by F98 MG cells within a short period of exposure.

The cytotoxicity of **Ru(II)–Pt(II)** was evaluated relative to cisplatin in F98 rat MG cells by the trypan blue dye exclusion assay using an automated Vi-CELL® Cell Viability Analyzer. As shown in Figure 6.3, in the absence of light **Ru(II)–Pt(II)** displayed no detectable cytotoxicity after 48 h of exposure at up to 50 μM concentration, with approximately 20% reduction in viability remaining at 75 μM . This was in contrast to cisplatin, which exhibited detectable effects on viability even at 25 μM . The observed difference could be due to the increased steric hindrance around the Pt moiety induced by the covalently-conjugated PS $[(\text{Ph}_2\text{phen})_2\text{Ru}(\text{dpp})]^{2+}$. Additionally, the PS unit decreases electronic density at the Pt subunit, thus slowing down its aquation and allowing controlled photoactivation of the supramolecule. The low cytotoxicity of **Ru(II)–Pt(II)** in the dark is a critical feature of this molecule with regard to its potential as a PDT agent.

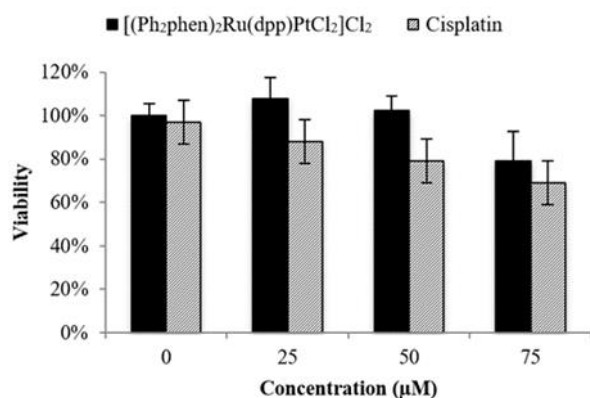


Figure 6.3 Cytotoxicity in the dark graphed as percent viability (treated/untreated control F98 MG cells) vs. concentration (μM) of Ru(II)-Pt(II) and cisplatin following 48 h incubation in the dark.

The cytotoxic activity of **Ru(II)-Pt(II)** increased dramatically after blue light irradiation (Figure 6.4). Two identical sets of samples were prepared and either incubated in the dark or irradiated in a lab-built LED array that emits blue light (470 nm, 4.35 J/cm²). For the photolysis treatment, cells were incubated for 15 min with 0 to 75 μM **Ru(II)-Pt(II)**, photolyzed for 30 min, and left in the incubator for a final 15 min before the complex solution was removed and replaced with fresh medium. Photolysis had no effect on cell growth in the absence of the complex. However, in the presence of even the lowest concentration of **Ru(II)-Pt(II)** a strong antiproliferative activity was observed starting immediately after photolysis was completed (0 h time point). Further cell growth inhibition was observed after 48 h. Cells that were treated with **Ru(II)-Pt(II)** showed 60% lower viability following photolysis than those incubated in the dark, a dramatically enhanced light-induced toxicity. The effective concentration at which 50% of the cells showed a response (EC₅₀) was approximately 20 μM under photolysis conditions, which is lower than for either [(Ph₂phen)₂Ru(dpp)]²⁺ or cisplatin alone.¹⁵ Revisiting the results from the DNA gel shift assay, we propose that photoactivation of **Ru(II)-Pt(II)** leads to population of a Ru(d π) \rightarrow dpp(π^*) ³MLCT state that produces oxidative stress and DNA platination, finally resulting in cell death. The synergistic effect between the two metals appeared to enhance the antiproliferative activities of each individual component towards aggressive MG cells. This promising result encourages further investigation on bimetallic supramolecular complexes as potential new PDT agents for cancer treatment.

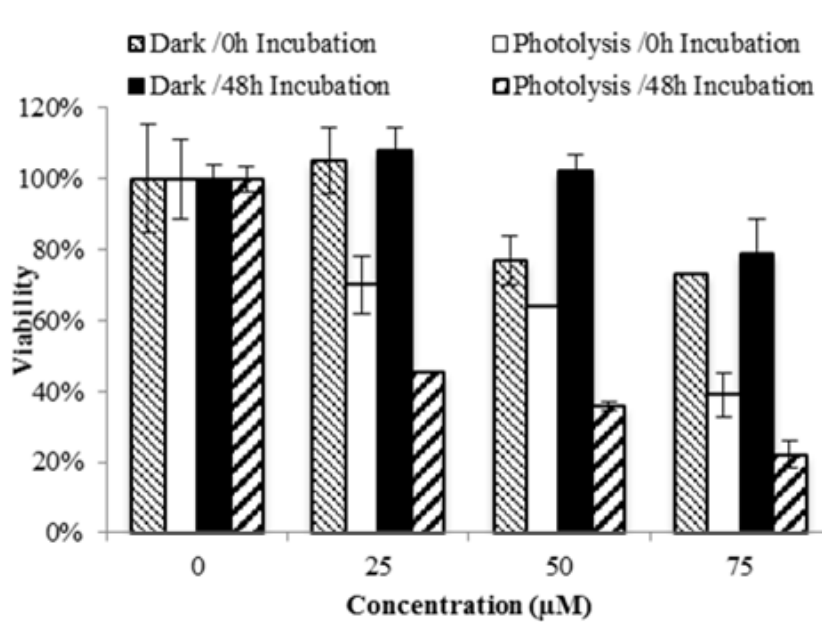


Figure 6.4 Cytotoxicity graphed as percent viability (F98 cells treated/F98 cells control) vs. concentration (μM) of $[(\text{Ph}_2\text{phen})_2\text{Ru}(\text{dpp})\text{PtCl}_2]\text{Cl}_2$ at 0 and 48 hours of incubation in darkness (dark) or after photolysis with blue light (photolysis)

6.5 Conclusions

In summary, $[(\text{Ph}_2\text{phen})_2\text{Ru}(\text{dpp})\text{PtCl}_2]\text{Cl}_2$ appears to exhibit synergistic effects between the metal centers, enabling multiple toxicity pathways (i.e. platination and oxidative stress) that lead to the enhanced cytotoxicity observed herein. *In vitro* assays showed preferential photoactivated modification of DNA, with little effect on protein under the conditions used here. This potential selective reactivity could minimize off-target binding and cytotoxic side effects *in vivo*. The present study provides the first example of a blue light photoactivated anticancer platinum (II) complex with activity against F98 rat MG cells following short-term drug exposure. These results suggest that $[(\text{Ph}_2\text{phen})_2\text{Ru}(\text{dpp})\text{PtCl}_2]\text{Cl}_2$ could provide the basis for development of an effective multifunctional PDT agent for treatment of human glioblastoma multiforme and other severe cancers.

6.6 Acknowledgements

Acknowledgement is made to VT ICTAS 119552 and the National Science Foundation (grant CHE-1301131) for funding of this work. The authors are grateful to Drs. Amanda J. Morris, Brian E. Hanson, and Roberto Padilla for helpful discussions. We thank Dr. Jeffrey L. Parks for

providing the ICP-MS data. We particularly acknowledge the late Dr. Karen J. Brewer, a great mentor and generous friend.

6.7 References

1. R. L. Siegel, K. D. Miller and A. Jemal, *CA-Cancer J. Clin.*, 2016, **66**, 7-30.
2. H. R. Kumar, X. Zhong, J. A. Sandoval, R. J. Hickey and L. H. Malkas, *Expert Rev. Neurother.*, 2008, **8**, 1497-1506.
3. D. A. Reardon, J. N. Rich, H. S. Friedman and D. D. Bigner, *J. Clin. Oncol.*, 2006, **24**, 1253-1265.
4. J. P. Celli, B. Q. Spring, I. Rizvi, C. L. Evans, K. S. Samkoe, S. Verma, B. W. Pogue and T. Hasan, *Chem. Rev.*, 2010, **110**, 2795-2838.
5. G. Stochel, A. Wanat, E. Kulis and Z. Stasicka, *Coord. Chem. Rev.*, 1998, **171**, 203-220.
6. M. R. Detty, S. L. Gibson and S. J. Wagner, *J. Med. Chem.*, 2004, **47**, 3897-3915.
7. R. Bonnett, *Chemical aspects of photodynamic therapy*, CRC Press, 2000.
8. H. Huang, B. Yu, P. Zhang, J. Huang, Y. Chen, G. Gasser, L. Ji and H. Chao, *Angew. Chem. Int. Ed.*, 2015, **54**, 14049-14052.
9. V. H. S. van Rixel, B. Siewert, S. L. Hopkins, S. H. C. Askes, A. Busemann, M. A. Siegler and S. Bonnet, *Chem. Sci.*, 2016, **7**, 4922-4929.
10. E. Wachter, D. K. Heidary, B. S. Howerton, S. Parkin and E. C. Glazer, *Chem. Commun.*, 2012, **48**, 9649-9651.
11. S. H. van Rijt and P. J. Sadler, *Drug Discovery Today*, 2009, **14**, 1089-1097.
12. S. A. Poteet, M. B. Majewski, Z. S. Breitbach, C. A. Griffith, S. Singh, D. W. Armstrong, M. O. Wolf and F. M. MacDonnell, *J. Am. Chem. Soc.*, 2013, **135**, 2419-2422.
13. C. Mari, H. Huang, R. Rubbiani, M. Schulze, F. Würthner, H. Chao and G. Gasser, *Eur. J. Inorg. Chem.*, 2016. In press.
14. U. Basu, I. Khan, A. Hussain, P. Kondaiah and A. R. Chakravarty, *Angew. Chem. Int. Ed.*, 2012, **51**, 2658-2661.
15. J. Zhu, A. Dominijanni, J. Á. Rodríguez-Corrales, R. Prussin, Z. Zhao, T. Li, J. L. Robertson and K. J. Brewer, *Inorg. Chim. Acta*, 2017, **454**, 155-161.
16. D. A. Reardon, J. N. Rich, H. S. Friedman and D. D. Bigner, *J. Clin. Oncol.*, 2006, **24**, 1253-1265.
17. C. Lottner, K.-C. Bart, G. Bernhardt and H. Brunner, *J. Med. Chem.*, 2002, **45**, 2064-2078.
18. J. Mao, Y. Zhang, J. Zhu, C. Zhang and Z. Guo, *Chem. Commun.*, 2009, **8**, 908-910.
19. I. Manet, F. Manoli, M. P. Donzello, C. Ercolani, D. Vittori, L. Cellai, A. Masi and S. Monti, *Inorg. Chem.*, 2011, **50**, 7403-7411.

20. J. T. F. Lau, P.-C. Lo, W.-P. Fong and D. K. P. Ng, *J. Med. Chem.*, 2012, **55**, 5446-5454.
21. J. D. Knoll and C. Turro, *Coord. Chem. Rev.*, 2015, **282–283**, 110-126.
22. A. G. Weidmann, A. C. Komor and J. K. Barton, *Comments Inorg. Chem.*, 2014, **34**, 114-123.
23. R. L. Williams, H. N. Toft, B. Winkel and K. J. Brewer, *Inorg. Chem.*, 2003, **42**, 4394-4400.
24. S. L. Hopkins, L. Stepanyan, N. Vahidi, A. Jain, B. S. J. Winkel and K. J. Brewer, *Inorg. Chim. Acta*, 2016. In press.
25. T. Yano, S. Hishida, M. Nakai and Y. Nakabayashi, *Inorg. Chim. Acta*, 2016. In press .
26. S. L. H. Higgins, T. A. White, B. S. J. Winkel and K. J. Brewer, *Inorg. Chem.*, 2011, **50**, 463-470.
27. S. L. H. Higgins, A. J. Tucker, B. S. J. Winkel and K. J. Brewer, *Chem. Commun.*, 2012, **48**, 67-69.
28. M. A. J. Rodgers and P. T. Snowden, *J. Am. Chem. Soc.*, 1982, **104**, 5541-5543.
29. R. W. Redmond and I. E. Kochevar, *J. Photochem. Photobiol.*, 2006, **82**, 1178-1186.
30. M. E. Alberto, N. Russo and C. Adamo, *Chem. Eur. J.*, 2016, **22**, 9162-9168.
31. A. J. Prussin II, D. F. Zigler, A. Jain, J. R. Brown, B. S. J. Winkel and K. J. Brewer, *J. Inorg. Biochem.*, 2008, **102**, 731-739.
32. S. E. Sherman and S. J. Lippard, *Chem. Rev.*, 1987, **87**, 1153-1181.
33. G. Ferraro, L. Massai, L. Messori and A. Merlino, *Chem. Commun.*, 2015, **51**, 9436-9439.
34. H. Pajouhesh and G. R. Lenz, *NeuroRx*, 2005, **2**, 541-553.
35. C. A. Puckett and J. K. Barton, *J. Am. Chem. Soc.*, 2006, **129**, 46-47.
36. D. Screnci, M. J. McKeage, P. Galettis, T. W. Hambley, B. D. Palmer and B. C. Baguley, *Br. J. Cancer*, 2000, **82**, 966-972.
37. Q. Zhou and J. M. Gallo, *Neuro. Oncol.*, 2009, **11**, 301-310.

Chapter 7 Conclusions and Future Work

7.1 Conclusions

This dissertation mainly focused on designing new metal-organic frameworks (MOFs) as efficient heterogeneous catalysts for CO₂ chemical transformations. Molecular catalyst (metal cyclam) was modified with the addition of carboxylate groups to serve as the bidentate linker, and high-valent metal ions (Zr⁴⁺/Hf⁴⁺) were used as inorganic nodes. High crystalline 3D porous frameworks have been obtained by modulated synthesis, and the structure was solved by synchrotron PXRD patterns. The first two new porous metal-cyclam based zirconium MOFs were reported as VPI-100 (Cu) and VPI-100 (Ni), where VPI stands for Virginia Polytechnic Institute. They represented the first example for the incorporation of metallocyclam-based ligands into a highly robust Zr framework. Indeed, those frameworks demonstrated good thermal stability and exceptional chemical stability, especially under harsh acid conditions. Moreover, VPI-100 MOFs established high CO₂ uptake capacity up to ~9.83 wt% adsorption under 273 K at 1 atm and excellent catalytic efficiency (up to 98% conversion) for CO₂ chemical fixations. The MOF structure featured with potential open metal sites on metallocyclam and coordinatively unsaturated metal nodes. Those accessible dual catalytic sites may both act as Lewis acid sites for cycloaddition of CO₂ to epoxide.

To further explore the potential application of VPI-100 in CO₂ chemical fixation, Hf-VPI-100 (Cu) and Hf-VPI-100 (Ni) were prepared as the isoreticular expansion of VPI-100 MOFs. Catalytic performance of Hf-VPI-100 MOFs have been investigated for the coupling reaction of CO₂ and epoxide under mild conditions (1.5 bar CO₂). More interestingly, XRD refinement indicated that only partial Cl⁻ are occupied on the axial position of metal-cyclam ligands, led to a fraction of metal cores in cyclam as open metal sites on the backbone of the framework. The QCM studies revealed the interaction between epoxide and the framework. The irreversible binding between epoxide and the MOFs further confirmed the presence of accessible open metal centers, provided thermodynamic insights for CO₂ chemical fixation using VPI-100 MOFs.

Quantitative analysis of the binding between epoxide with frameworks and the diffusion rate for epoxide revealed kinetic insights for CO₂ cycloadditions.

7.2 Future work

7.2.1 Design new metal-cyclam based MOFs.

Considering the novelty of the modified metal-cyclam linker and the framework, VPI-100 MOFs proved that it is synthetically feasible to obtain highly stable 3D framework by using flexible macrocyclic linkers. Therefore, metal-cyclam based MOFs can be easily expanded to a large family. One straightforward strategy would be the variation of the metal cluster and/or metal-cyclam. Out of the established research on metal cyclam complexes, some MOFs would be very attractive.

1. Cr-cyclam/ Ru-cyclam based MOFs as NO release materials. Ford and co-workers reported *trans*-[Cr-cyclam-(ONO)₂]⁺ as a precursor complex for light-induced NO release.¹⁻² The complexes demonstrated limited biomedical application mainly because of the low concentration of released NO. Incorporating the [Cr-cyclam-(ONO)₂]⁺ into the backbone of a framework would lead to the high density of reactive center, and more NO would be released to achieve desired biomedical activity. Similarly, *trans*-[RuCl(NO)(cyclam)]²⁺ could be the alternative complexes for NO release agent.³ It is important to note that there is few reported MOFs for the controlled release of biologically active NO.⁴⁻⁷ Even more importantly, most of those reported MOF show large hysteresis on desorption of NO, which limited the efficiency of NO release and delivery.⁸ Therefore, a photo triggered MOF system composed by NO donors can provide an excellent platform for the controlled release and delivery of pure NO.

2. Co(III)-cyclam has been used as the high selective molecular catalyst for photocatalytic CO₂ reduction.⁹ Meanwhile, metal nodes composed by Ti⁴⁺ have shown intriguing photocatalytic activity for CO₂ reduction. Therefore, the

combination of Co(III)-cyclam and Ti^{4+} inorganic node may lead to a framework with synergic effect for CO_2 photocatalytic reduction. It is important to note that the MOF backbone must be appropriately conjugated and functionalized to engineer the bandgaps and intrinsic charge carrier mobility. Preliminary data demonstrated that VPI-100 (Co^{III}) can be simply prepared by similar synthetic approach as VPI-100 (Ni) (Figure 1).

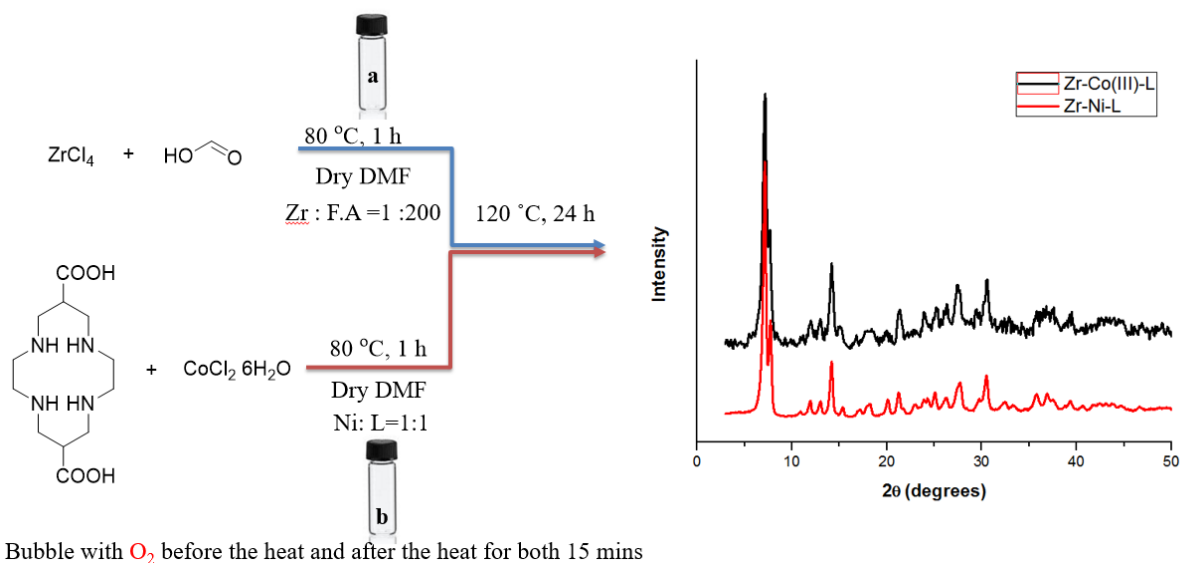


Figure 1. The synthetic scheme of VPI-100 (Co^{III}).

3. Gd^{3+} based MOF for magnetic resonance imaging (MRI). As mention in Section 1.4.3.2, azamacrocyclic ligand has been used to synthesize Gd based MOF as the potential contrast agent. In fact, the commercial available molecular contrast agents are mostly macrocyclic $Gd(III)$ chelates. Therefore, the modified cyclam linker or even the metal cyclam complexes in this work can be used as organic link to synthesize Gd^{3+} based MOF with potential application in MRI.

7.2.2 How to synthesize MOF containing free-base cyclam ligand

“Would you be able to prepare the cyclam based MOF without metal ions coordinate with the cyclam? Or Could you demetallated the metal-cyclam linkers

in the VPI-100 MOFs?” That was one of the most common questions that I have received after my seminar/talk. And the answer is not yet. So far, I have tried directly using free-base cyclam ligand (L) and zirconium salt to synthesize the desired MOF via modulated synthesis. However, the result white powder usually demonstrated low crystallinity. The key challenge is that the free-base cyclam ligand maintains several conformations with similar energy level, which made it difficult to form 3D highly ordered porous structure due to the competition between each conformation. Moreover, the Zr^{4+} metal ions coordinate with the carboxylate group too fast so that the self-assembly of the high crystalline framework is even more challenging. To solve the problem, I believe two approaches might be promising. 1. Screening different reaction conditions (especially different modulators, solvents, temperature) to obtain a similar structure as VPI-100 using free-base cyclam linker. 2. Using room temperature synthesis such as solvent vapor or slow diffusion of reactant instead of solvothermal reaction conditions. In that case, metal ions with intermediate Lewis acidity such as Cu^{2+} , Zn^{2+} should be used to get high crystalline MOFs. However, it is important to avoid the coordination between the metal ions with cyclam during the synthesis.

Demetallation of metal-cyclam in VPI-100 by post-synthetic approach could be an alternative way to get free-base cyclam MOF. Preliminary data indicated that the metal centers of VPI-100 (Cu)/(Ni) can be removed after the treatment with ethylenediaminetetraacetic acid (EDTA) or KCN in aqueous solution, evidenced by the color change from the resultant powders. However, the crystallinity of the framework cannot be conserved. The loss of crystallinity may have attributed to the conformation change in cyclam linker after the demetallation. Therefore, sequential linker installation might be a critical method to solve the problem.¹⁰ Considering the coordinatively unsaturated Zr_6 cluster in VPI-100, it is possible to install the pillar ligand such as BPDC between each Zr_6 cluster via postsynthetic

modification. After the sequential linker installation, the framework would be more robust to adjust the conformation change through demetallation process. More importantly, it is possible that the binding strength between $\text{Ni}^{2+}/\text{Cu}^{2+}$ with cyclam are too strong to remove the metal ions without collapsing the framework. Thus, MOF containing metal-cyclam complex with small binding energy between the metal center and macrocyclic ring would be more suitable for such demetallation approach.

Once the desired free-base cyclam MOF can be obtained, it would be more interesting to explore the remetallation of cyclam in MOFs via post-synthetic modification. The relationship between catalytic efficiency and loading of metal centers can be further explored. Single-crystal to single-crystal transformation may be achieved by the remetallation process. What's more, a framework with multimetallic centers in cyclam would be possible to serve as multifunctional materials. Even if the desired high crystalline materials cannot be obtained in the short term, directly using the ligand (L) to construct porous organic polymer would be an interesting area too.

7.2.3 The interaction between epoxide and MOFs

QCM has been demonstrated as an effective probe to study the uptake of the epoxide from VPI-100 MOFs. Considering the large numbers of reported MOFs as the catalyst for cycloaddition of CO_2 and epoxide, one easy following up project would be the systematic study of epoxide interaction between different MOFs. It would be interesting to compare the uptake performance from different MOFs. To be specific, it is interesting to see the effect of different metal centers in MOFs with open metal sites, such as MIL-101 series or CPO-27 MOFs. Coordinatively unsaturated nodes (NU-1000) vs. saturated nodes (UiO-67) can also be compared to study the binding between epoxide and metal nodes. Moreover, the pore size and

the size of epoxide can also be varied. Other than QCM, synchrotron PXRD can also be used to mapping the distribution of epoxide in the framework by *ex situ* treatment.

Beyond that, the modified cyclam ligand can also couple with other molecules to form supramolecular complexes. For example, the coupling between metal-cyclam and photosensitizer (e.g. Ru(bpy)₃²⁺) could generate photoactive catalytic system for desired applications. For those Ru/Os-Pt/Rh bimetallic molecules as potential PDT agents, it would be interesting to understand the cellular uptake mechanism for those complexes. The addition of glucose or peptide in those supramolecules may also be beneficial for target delivery and biological activity towards cancer cells.

7.3 Reference:

1. Ostrowski, A. D.; Absalolson, R. O.; Leo, M. A. D.; Wu, G.; Pavlovich, J. G.; Adamson, J.; Azhar, B.; Iretskii, A. V.; Megson, I. L.; Ford, P. C., Photochemistry of trans-Cr(cyclam)(ONO)₂⁺, a Nitric Oxide Precursor. *Inorganic Chemistry* **2011**, *50* (10), 4453-4462.
2. De Leo, M.; Ford, P. C., Reversible photolabilization of NO from chromium (III)-coordinated nitrite. A new strategy for nitric oxide delivery. *Journal of the American Chemical Society* **1999**, *121* (9), 1980-1981.
3. Lang, D.; Davis, J.; Lopes, L.; Ferro, A.; Vasconcellos, L.; Franco, D.; Tfouni, E.; Wieraszko, A.; Clarke, M., A controlled NO-releasing compound: synthesis, molecular structure, spectroscopy, electrochemistry, and chemical reactivity of R, R, S, S-trans-[RuCl(NO)(cyclam)]²⁺(1, 4, 8, 11-tetraazacyclotetradecane). *Inorganic chemistry* **2000**, *39* (11), 2294-2300.
4. Nguyen, J. G.; Tanabe, K. K.; Cohen, S. M., Postsynthetic diazeniumdiolate formation and NO release from MOFs. *CrystEngComm* **2010**, *12* (8), 2335-2338.
5. Miller, S. R.; Alvarez, E.; Fradcourt, L.; Devic, T.; Wuttke, S.; Wheatley, P. S.; Steunou, N.; Bonhomme, C.; Gervais, C.; Laurencin, D., A rare example of a porous Ca-MOF for the controlled release of biologically active NO. *Chemical Communications* **2013**, *49* (71), 7773-7775.
6. Harding, J. L.; Reynolds, M. M., Composite materials with embedded metal organic framework catalysts for nitric oxide release from bioavailable S-nitrosothiols. *Journal of Materials Chemistry B* **2014**, *2* (17), 2530-2536.
7. McKinlay, A. C.; Xiao, B.; Wragg, D. S.; Wheatley, P. S.; Megson, I. L.; Morris, R. E., Exceptional Behavior over the Whole Adsorption–Storage–Delivery Cycle for NO in Porous Metal Organic Frameworks. *Journal of the American Chemical Society* **2008**, *130* (31), 10440-10444.
8. Hinks, N. J.; McKinlay, A. C.; Xiao, B.; Wheatley, P. S.; Morris, R. E., Metal organic frameworks as NO delivery materials for biological applications. *Microporous and Mesoporous Materials* **2010**, *129* (3), 330-334.
9. Matsuoka, S.; Yamamoto, K.; Ogata, T.; Kusaba, M.; Nakashima, N.; Fujita, E.; Yanagida, S., Efficient and selective electron mediation of cobalt complexes with cyclam and related macrocycles in the

p-terphenyl-catalyzed photoreduction of carbon dioxide. *Journal of the American Chemical Society* **1993**, *115* (2), 601-609.

10. Yuan, S.; Lu, W.; Chen, Y.-P.; Zhang, Q.; Liu, T.-F.; Feng, D.; Wang, X.; Qin, J.; Zhou, H.-C., Sequential Linker Installation: Precise Placement of Functional Groups in Multivariate Metal–Organic Frameworks. *Journal of the American Chemical Society* **2015**, *137* (9), 3177-3180.

Appendix A Energy Transfer in Metal Organic Frameworks

Jie Zhu, Shaunak Shaikh, Nicholas Mayhall, Amanda J. Morris

1. Introduction

1.1 Background information about energy transfer

In order to create technologies based on excitation energy transfer (enhanced photovoltaic cells, more efficient photocatalytic reactors, etc.), one must first have a firm understanding of the underlying quantum mechanical mechanisms. In other words, how does energy in the form of an initially excited chromophore (donor) transfer to a different chromophore (acceptor)? To answer this question, it is helpful to first consider this as a simple two-state model. In the “initial state”, $|i\rangle$, the donor is excited, and the acceptor is in its ground-state: $|D^*A\rangle$. In the “final state”, $|f\rangle$, the acceptor is excited, while the donor is now in its ground state: $|DA^*\rangle$. This is represented schematically in Figure 1. Assuming the chromophore’s nuclei are frozen and the electronic coupling between the states is static (i.e., $V = \langle i|\widehat{H}|f\rangle \neq V(t)$), the excitation energy will simply oscillate between the two chromophores at a frequency determined by both V and the energy gap between the states, $\omega_{fi} = E_f - E_i/\hbar$. The exact solution to the time-dependent Schrödinger equation is trivially obtained, and the functional form illustrates the oscillatory behavior:

$$P_f(t) = \frac{4|V|^2}{\hbar^2\omega_{fi}^2 + 4|V|^2} \sin^2\left(\sqrt{\frac{\omega_{fi}^2}{4} + \frac{|V|^2}{\hbar^2}}t\right) \quad (1)$$

where $P_f(t)$ is the time-dependent probability that the system is in state $|f\rangle$.^{1,2,3}

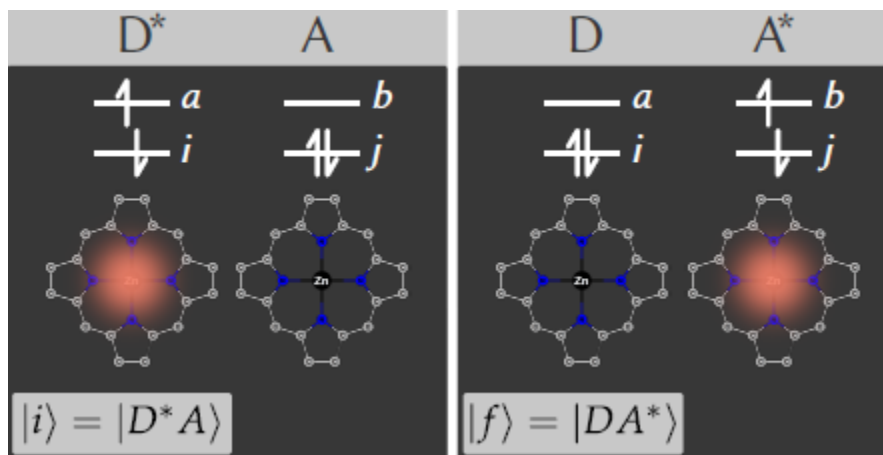


Figure 1: Schematic representation of the initial state and final states of a chromophore dimer. Note, that the actual symmetry adapted combinations of the single particle excitations have been neglected for graphical clarity. The HOMO and LUMO orbitals on Donor and Acceptor are labelled by the letters, i , a , j , and b , respectively.

1. Coupling Regimes

In reality, these two electronic states are not completely insulated from the rest of the molecule. As time evolves, so too do the chromophores' nuclei, and we must take into account the interactions between the electronic and nuclear degrees of freedom. To incorporate this nuclear motion, one usually categorizes a problem as existing in one of two limiting cases: 1) strong chromophore coupling, and 2) weak chromophore coupling.

1) Strong Coupling:

For very strong chromophore interactions, V , the oscillations occur very quickly, much quicker than the heavy nuclei move, and we say that the excitation energy transfers coherently. This language implies that it is more appropriate to describe this system as existing in coherent superpositions of the $|i\rangle$ and $|f\rangle$ states. As such, the $|i\rangle$ and $|f\rangle$ states are quantum mechanically entangled, and thus behave somewhat like a two-level system (at least at very short times), with populations oscillating quickly between the two chromophores. As a result of the coherent superposition of states occurring at different positions in space, the strongly coupled regime leads to states which are delocalized in space. In order to model the

time evolution of both the electronic and nuclear degrees of freedom, density matrix approaches are often used,^{4,5} and one attempts to numerically integrate the Louisvillie-von Neumann equation.

2) Weak Coupling:

In contrast, if the coupling between the two states is weak such that the rate of state-to-state oscillation is slow compared to the nuclear motion, we can assume that the vibrational state fully relaxes between excitation energy transfer events, and we label this excitation energy transfer as incoherent. The metal organic framework's (MOFs) discussed in this chapter are found to exist in this regime, and thus incoherent mechanisms will be solely discussed. In order to make progress towards understanding excitation energy transfer in the weakly coupled regime, we will make use of the fact that V is small and then employ perturbation theory. Applying first-order perturbation theory to the time-dependent Schrödinger equation, one finds the probability of populating the final state, $|f\rangle$, to be:

$$P_f(t) = \frac{4|V|^2}{\hbar^2\omega_{fi}^2} \sin^2\left(\frac{\omega_{fi}}{2}t\right), \quad (2)$$

which is a direct simplification of Equation 1.

This rate does not yet include any coupling to the nuclear motion, which has the effect of “smearing” out the state energies. As a consequence, at any given time the initial state $|i\rangle$ has the opportunity to transfer to an effectively different final state (since the nuclear motion continually changes the electronic environment). This probability becomes sharply peaked around values where the initial and final states

$$P_f(t) = \frac{2\pi}{\hbar^2} |V|^2 \delta(E_f - E_i)t \quad (3)$$

are degenerate, such that if we consider the long-time limit, the probability of the

system transitioning to the final state is only non-zero when the two states have equal energy. The equation which summarizes this is the state-to-state form of the famous Fermi's golden rule:

In this form, the delta function, is the resonance condition. And the rate, of this process is simply the time derivative of Equation. 3,

$$k_f = \frac{2\pi}{\hbar^2} |V|^2 \delta(E_f - E_i) \quad (4)$$

Note that one of the key features of Fermi's Golden Rule, is that the rate of transition is not a function of time. In order to obtain the actual rate from this equation, one must of course be able to compute the electronic matrix element, $V = \langle i | \hat{H} | f \rangle$. This is the topic of the next section.

2. Coupling Mechanisms

If we take Figure 1 literally and assume¹ that each chromophore's excited state involves only a pair of symmetry adapted excitations between a single occupied and a single virtual orbital, we can write the two states very simply:

$$|i\rangle = \frac{1}{\sqrt{2}} (|\psi_i^a\rangle \pm |\psi_i^{\bar{a}}\rangle) \quad (5)$$

$$|f\rangle = \frac{1}{\sqrt{2}} (|\psi_j^b\rangle \pm |\psi_j^{\bar{b}}\rangle) \quad (6)$$

where, the bar above orbital indices denote electrons with β spin. For positive and negative superpositions (spin singlet and triplet states, respectively), the Hamiltonian matrix elements are:

$$\langle i^1 | \hat{H} | f^1 \rangle = 2(ai|jb) - (ab|ji) \quad \text{Singlet Coupling} \quad (7)$$

¹ This assumption is only used to simplify discussion, and is not needed in a full treatment. However, if natural transition orbitals (instead of the canonical Hartree-Fock orbitals) are used to define these orbitals, then this minimal picture becomes much more realistic.

$$\langle i^3 | \hat{H} | f^3 \rangle = -(ab|ji) \quad \text{Triplet Coupling} \quad (8)$$

These two distinct types of electron repulsion integrals $(ai|jb)$ and $(ab|ji)$ are associated with the conceptual mechanisms illustrated in Figure 2. From here, it is clear that *singlet states have two distinct mechanisms of energy transfer*, Förster and Dexter, while *triplet states have only one mechanism*, Dexter.

2.1. Distance dependence of coupling mechanisms

As illustrated in Figure 2, the two types of integrals coupling the excited states have different qualitative interpretations. Förster type coupling involves only intra-chromophore electron transitions, whereas Dexter type coupling has only inter-chromophore electron transitions. Intuitively, we should then expect to see different behaviors between the two mechanisms when the chromophore-chromophore distance changes. This is indeed the case. We will now inspect the distance dependence of the Dexter and Förster integrals, in turn.

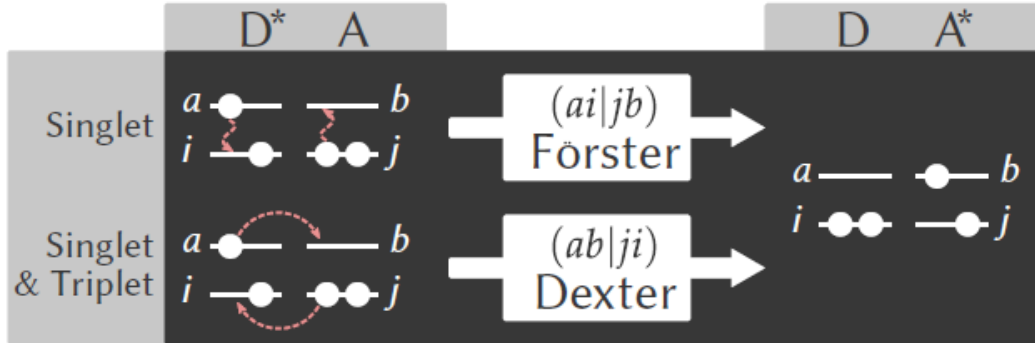


Figure 2: Connection between the conceptual transfer mechanisms and the mathematical description present in the electron repulsion integrals of the Hamiltonian matrix elements. $(ai|jb)$ contribute to Förster type coupling between singlet states, while $(ab|ji)$ contributes to Dexter type coupling between both singlet and triplets.

Dexter type integral, $(ab|ji)$: To understand the nature of the Dexter (or exchange) interaction, we write out the integral explicitly:

$$(ab|ji) = \int dr_A dr_D \phi_a(r_A) \phi_b(r_A) \frac{1}{r_{DA}} \phi_j(r_D) \phi_i(r_D) \quad (9)$$

The only time that the product of molecular orbitals, $\phi_a(r)\phi_b(r)$ or $\phi_j(r)\phi_i(r)$, can be non-zero is if there is spatial overlap between the pairs. Note, that this is not a statement about orbital orthogonality, as all orbitals are assumed orthogonal. Since orbitals i and a are on the donor, and j and b on the acceptor, this requires the two chromophores to close to one another. Because of the exponential decay of the wavefunction in free space, the overlap between these orbitals decays exponentially. Consequently, the Dexter type interaction also decays exponentially with increasing inter-chromophore distance. This means that at long distances, only singlet states can undergo excitation energy transfer, since the Dexter (or exchange) pathway is closed. However, through indirect coupling with intermediate states, more complicated Dexter pathways can also exist, which relax this constraint somewhat^{6,7}. The short-range nature of Dexter type interaction makes it strongly sensitive to the chemical structure between the chromophores and may potentially be helpful in directing energy into spatially localized energy transfer conduits or pathways. One dimensional energy transfer networks maybe particularly desirable for solar energy capture and conversion because they can direct energy in a specific direction towards a catalyst. Fine-tuning the directionality of such energy transfer pathways by manipulating the intervening molecular structure and inter-chromophore distances can enable the design of smart energy collecting materials.⁸

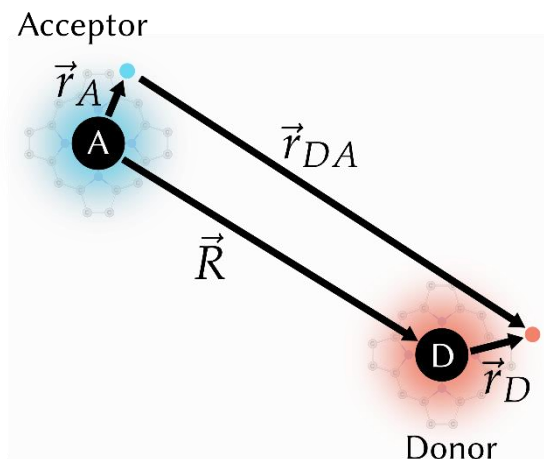


Figure 3: Illustration of the coordinate system used for expressing the two electron repulsion integrals as a dipole-dipole interaction

Förster type integral, $(ai|jb)$: Turning our attention to the Förster (or coulomb) term, the explicit forms of this integral is

$$(ai|jb) = \int dr_A dr_D \phi_a(r_A) \phi_i(r_A) \frac{1}{r_{DA}} \phi_j(r_D) \phi_b(r_D) \quad (10)$$

Unlike with the Dexter integral, the orbital products occur between orbitals on the same chromophore, and so no overlap dependence arises. To understand the distance dependence of this integral, we now need to focus on the $\frac{1}{r_{DA}}$ part. Referring to Figure 3, we can make the following substitution to remove the explicit inter-electron coordinate:

$$\begin{aligned} \vec{r}_{DA} &= \vec{R} + \vec{r}_D - \vec{r}_A \\ &= \vec{R} + \vec{r}, \end{aligned} \quad (11)$$

where, $\vec{r} = \vec{r}_D - \vec{r}_A$.

What we wish to do is take into account the fact that the inter-chromophore distance is typically much larger than the fluctuations of the electrons about each chromophore, leading to a binomial expansion,

$$\frac{1}{(1+x)^\alpha} = \sum_{k=0}^{\infty} \binom{\alpha}{k} x^k \quad (12)$$

This expansion is rapidly convergent (only a few k values needed) when $x \ll 1$, which happens to be true in our case since,

$$x = \frac{(r^2 + 2\vec{r} \cdot \vec{R})}{R^2} \quad (13)$$

and R is much larger than r . Using this expansion, we obtain,

$$\frac{1}{r_{DA}} = \frac{1}{R} - \frac{\vec{r}_D \cdot \vec{n}_R - \vec{r}_A \cdot \vec{n}_R}{R^2} + \frac{3(\vec{r} \cdot \vec{n}_R)^2 - r^2}{2R^3} + \text{Higher-order terms}, \quad (14)$$

where, \vec{n}_R is the unit vector pointing along R . It is easy to see that, because the molecular orbitals are orthogonal, the first term does not contribute to the $(ai|jb)$ integral.

$$\begin{aligned} (ai|jb) &\Leftarrow \int dr_A dr_D \phi_a(r_A) \phi_i(r_A) \frac{1}{R} \phi_j(r_D) \phi_b(r_D) \\ &= \frac{1}{R} \int dr_A \phi_a(r_A) \phi_i(r_A) \int dr_D \phi_j(r_D) \phi_b(r_D) \\ &= \frac{1}{R} (0)(0) = 0 \end{aligned}$$

The same is readily seen for the second order-term. One then finds that the first non-zero term is the third-order term, which decays with $\frac{1}{R^3}$,

$$(ai|jb) = \frac{\vec{d}_A \cdot \vec{d}_D - 3(\vec{d}_D \cdot \vec{n}_R)(\vec{d}_A \cdot \vec{n}_R)}{R^3} + \text{Higher-order terms}, \quad (15)$$

where we have introduced the definition of the *transition dipole moment*, \vec{d}_A or \vec{d}_D ,

$$\vec{d}_A = \int dr_A \phi_j(r_A) \phi_b(r_A) \vec{r}_A. \quad (16)$$

Thus, the Förster type integral, $(ai|jb)$, has an R^{-3} dependence on the *interchromophore distance*. This allows this mechanism to occur at rather long distances. For convenience, one often defines a unit vector \vec{n}_A in the direction of the dipole transition moment such that $\vec{d}_A = |\mu_A| \vec{n}_A$, to isolate all the orientational dependence into a single constant, κ :

$$\kappa = \vec{n}_A \cdot \vec{n}_D - 3(\vec{n}_D \cdot \vec{n}_R)(\vec{n}_A \cdot \vec{n}_R), \quad (17)$$

which leads to,

$$(ai|jb) \approx \frac{|\mu_A||\mu_D|\kappa}{R^3} \quad (18)$$

Substituting this into Fermi's Golden Rule, Equation 4, we see the characteristic R^{-6} distance dependence of Förster energy transfer,

$$k_{if}^{\text{Förster}} = \frac{2\pi}{\hbar^2} \frac{|\mu_A|^2 |\mu_D|^2 \kappa^2}{R^6} \delta(E_f - E_i). \quad (19)$$

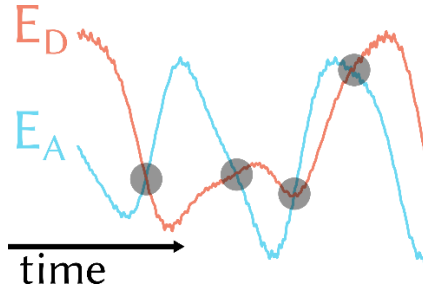


Figure 4: Cartoon representation of the time dependence of the Donor and Acceptor excitation energies. Resonance transitions only occur when the energy gap goes to zero, highlighted in grey.

This, however, is not the typical form of the rate expression used. Because the energy transfer can only occur when the energy gap $E_f - E_i$ goes to zero, a system in state $|i\rangle$ must wait until the thermal motion creates a curve crossing between the chromophore energies, as shown in Figure 4. Thus, the long-time probability of making a transition depends on how “correlated” the motion of the two chromophores is. Correlation functions are the mathematical way to quantify this “correlation”. By using the integral definition of the delta function,

$$\delta(E_f - E_i) = \frac{1}{2\pi} \int_{-\infty}^{\infty} e^{i(E_f - E_i)t} dt, \quad (20)$$

to define a time propagator and thermally average over final states, one can transform the above rate expression into one which depends on the product of transition dipole moment correlation functions on the donor and the acceptor.

Then, taking into account that the absorption or fluorescence spectrum is simply the Fourier transform of the transition dipole-moment correlation functions, and using Parsival's theorem, one can then write the Förster rate expression in terms of the experimentally available normalized absorption and emission spectra,³

$$\bar{\sigma}_A(\omega) = \frac{\sigma_A(\omega)}{|\mu_A|}$$

$$k^{\text{Förster}} = \frac{|\mu_A|^2 |\mu_D|^2 \kappa^2}{\hbar^2 R^6} \int_{-\infty}^{\infty} \bar{\sigma}_A(\omega) \bar{\sigma}_D(\omega) d\omega \quad (21)$$

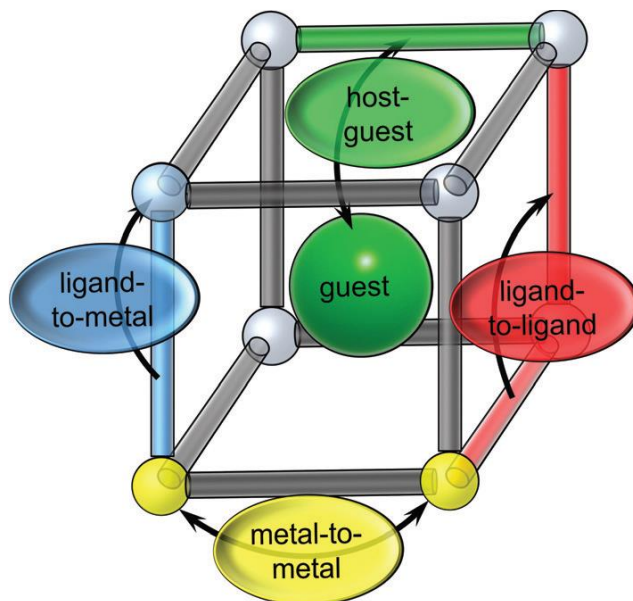
This is the equation typically used for determining the Förster rate, and which is used throughout the rest of this chapter. As can be seen from Equation 21, optimizing the rate of Förster energy transfer in materials like MOFs will require careful attention to the choice of chromophore and framework symmetry as well as other parameters like fluorescence quantum yield and chromophore oscillator strength. The key challenge is that all of this must be performed without sacrificing the integrity of MOF structure or introducing defects that may unproductively trap excitons.⁹

1.2 Why MOFs

Metal organic frameworks (MOFs), sometimes referred to as porous coordination polymers, have wide-ranging applications in light-harvesting, luminescence, artificial photosynthesis, photocatalysis and photovoltaic as hybrid materials.⁹⁻¹³ Understanding the exciton transport process within well-defined 3D solid phases will aid in the design of novel materials for highly efficient directional energy transport. MOFs offer a rich diversity of unique platforms to study energy transfer (ET). Highlighted by highly-ordered crystal structure and synthetic tunability via crystal engineering, MOFs allow for precise control of distances and angles between chromophores and their alignment by judicious choice of ligands and metal nodes. The main ET pathways observed in MOF matrices could occur

between different ligands, from ligand to metal centers (or metal to ligand), metal to metal nodes and guest to MOF skeleton, as shown in Scheme 1.¹⁴

Scheme 1. A schematic representation of different ET processes which could occur in a MOF matrix.¹⁴ Taken from Ref. 14 with the permission of Wiley Online Library.



The aim of this chapter is to give a comprehensive overview of MOF materials for energy transfer. Because the composition of bridging linkers and inorganic nodes can significantly affect the ET process within MOFs, herein, we will discuss ET mechanisms and structural motifs in MOFs based on different types of energy donor/acceptors. In general, four scenarios can be distinguished in reported studies:

1. MOFs containing lanthanide metal ion, either as the metal nodes of the framework or trapped in the MOF pores as guests.
2. Doping well-known transition-metal complexes, $\text{Ru}(\text{bpy})_3^{2+}/\text{Os}(\text{bpy})_3^{2+}$ as the chromophores in Zn/Zr based MOFs.
3. MOF materials constructed from porphyrins and metalloporphyrins as crystalline powders or thin films.
4. Using organic chromophores as bridging linkers to prepare designed MOFs.

To construct a MOF system to probe ET, several criteria need to be considered:

1. The chromophores should have intense absorption and emission bands in UV-Vis range and relatively long emission lifetimes in order for the photoexcitation and excited-state dynamics to be easily probed.
2. Good overlap between the emission spectrum of the donor and the absorption spectrum of acceptor are necessary to favor the ET process.

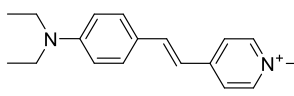
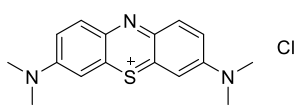
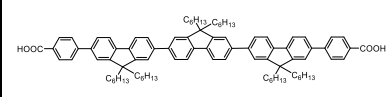
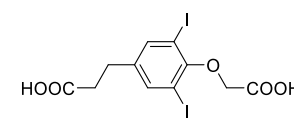
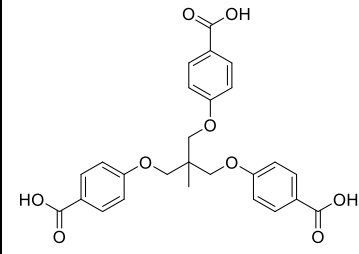
3. The energy transfer efficiency depends on the donor/acceptor ratios and highly efficient and rapid directional ET is desired for further applications.
4. It is advantageous to choose well-studied molecular chromophores, in which the photophysical and photochemical properties in solution are well established in order to model the more complicated solid-state photodynamic processes and ET mechanisms in a MOF matrix.

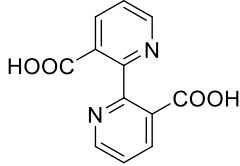
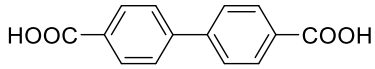
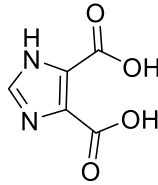
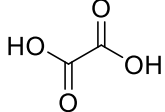
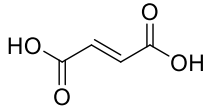
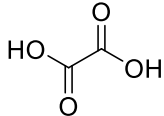
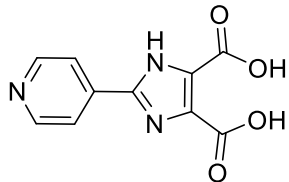
2. Lanthanide-based Luminescent MOFs

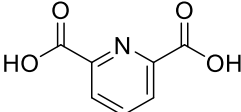
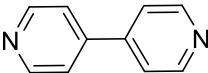
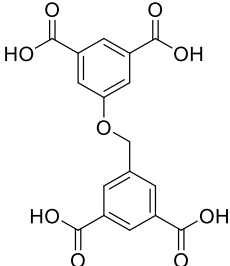
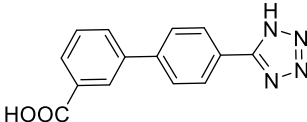
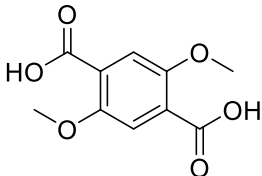
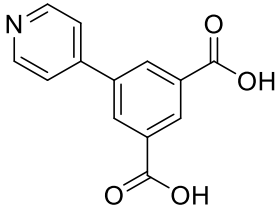
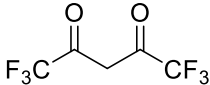
Luminescent lanthanide-based materials have been widely used in light-emitting systems and biological, environmental and clinical analysis owing to the unique luminescence that results from intra-4*f* transitions of Ln³⁺. As the 4*f* orbitals are not involved in binding Ln³⁺ emission is characterized by sharp emission bands with atom specific pure color. Gd³⁺ can emit in the UV region, Sm³⁺, Eu³⁺, Tb³⁺, Dy³⁺ and Tm³⁺ are useful luminescence centers in visible light range, while Nd³⁺, Yb³⁺, Er³⁺ and to a lesser extent Pr³⁺, Sm³⁺, Dy³⁺, Ho³⁺, Tm³⁺ in near-infrared region.¹⁵ Additionally, Ln³⁺ molecules display long excited-state lifetimes and large Stokes shifts.¹⁶ That said, the photoluminescence of lanthanide ions is an efficient process. Intra-4*f* transitions are “Laporte forbidden”, and therefore, light absorption by direct 4*f* excitation is weak and results in low intensity luminescence.¹⁶⁻¹⁷ This problem can be overcome in Ln-based MOF systems, where the organic ligands can be utilized as antennas for the metal ions. In this case, the organic chromophore absorbs light and funnels the excitation energy to the Ln³⁺ via ET, a process termed LMET. Furthermore, ET processes from metal-to-metal in heterometallic Ln-MOFs can be used to tune the photoluminescence properties, a process termed MMET. Overall, two MOF architectures have been used to probe ET in Ln³⁺-MOFs: (1) MOFs with Ln³⁺ metal nodes and (2) MOFs with encapsulated Ln³⁺ in the pores.

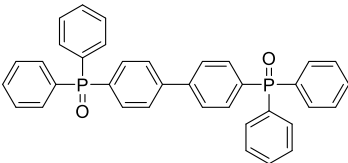
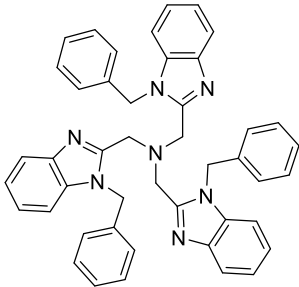
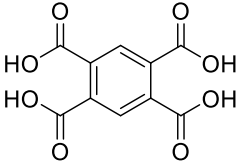
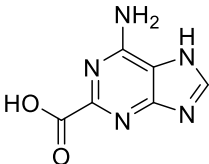
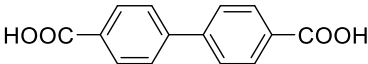
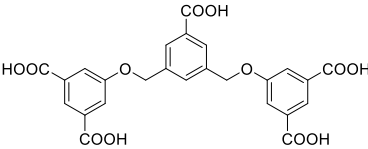
Table 1. Summary of chromophores in lanthanide-based MOFs

MOF	Chemical	Ligand Structure	Guest	Ref

	Formula			
Ln(III)-L (Ln=Gd, Eu, Yb)	Gd(L) _{1.5} ·DMF· H ₂ O	L=	D1=  D2= 	[18]
Ln ₂ (L1) ₃ ·(DMF)) _x ·(H ₂ O) _y (x,y=1-2) (Ln=Gd, Eu, Yb)	Eu(L1) _{1.5} ·(DMF) _{1.1} ·(H ₂ O) _{1.7}	H ₂ L1 =		[19]
Eu-MOF	Eu-L·5H ₂ O	L =		[20]
Ln-MOF	[Eu ₂ L ₃ (H ₂ O) ₄]·3D MF	H ₂ L =	DMF (MOF 1) H ₂ O (MOF 2)	[21]
LnL	Ln _x Gd _{1-x} L (Ln =Tb, Yb)	L =		[22]
Ln-MOFs	{ [Ln ₄ (μ ₃ - OH) ₄ (BPDC) ₃ (BP DCA) _{0.5} (H ₂ O) ₆]Cl O ₄ ·5H ₂ O}∞ (Ln = Tb ,Gd)	BPDC =		[23]

		 BPDCA = 		
	$K_5[Ln_5(IDC)_4(Ox)_4]$ (Ln = Gd, Tb, Dy)	IDC =  Ox = 		[24]
	$Eu_2(FMA)_2(OX)(H_2O)_4 \cdot 4H_2O$	FMA =  Ox = 		[25]
	$\{[Tb_3(\mu_3\text{-HPyIDC})_4(H_2O)_8] \cdot NO_3 \cdot 4H_2O\}_\infty$	H ₃ PyIDC = 		[26]
$[(Tb_{1-x}Eu_x)\text{-}(DPA)\text{-}(DPA)\text{-}]$	$[(Tb_{0.95}Eu_{0.05})(DPA)\text{-}(HDPA)]_\infty (1)$ $[(Tb_{0.5}Eu_{0.5})(DPA)\text{-}(DPA)\text{-}]$	H ₂ DPA =		[27]

(HDPa)] _∞	(HDPa)] _∞ (2)			
² [Ln ₂ Cl ₆ (bipy) ₃] ∞·2bipy	² [Gd _{2-x} Eu _x Tb _y Cl ₆ - (bipy) ₃] _∞ ·2bipy (0 ≤ x, y ≤ 0.5)	bipy = 		[30]
LnL (Ln = La, Ce, Pr, Nd, Sm, Eu, Gd, Tb, Ho, Er)	{[Ln ₂ (L) ₂](H ₂ O) ₃ · (Me ₂ NH ₂) ₂] _∞	H ₄ L = 		[31]
Ln-Zn (Ln = Eu, Tb)	{[LnOH(H ₂ O) ₆][Zn ₂ Ln ₄ (H-Htbca) ₂ -(4- tbca) ₈ (H ₂ O) ₁₂] _∞ · 6nH ₂ O	4-H ₂ tbca = 		[32]
Ln-DMBDC (Ln = Tb, Eu)	(Eu _x Tb _{1-x}) ₂ (DMBDC) ₃ (H ₂ O)) ₄ ·DMF· H ₂ O	DMBDC = 		[33]
LnPIA (Ln = Tb, Eu)	(Eu _x Tb _{1-x}) ₂ (PIA)(HPIA)(H ₂ O) _{2.5}	H ₂ PIA = 		[34]
[Ln(hfa) ₃ (dpbp)] _n (Ln = Tb, Eu)	[Tb _{0.99} Eu _{0.01} (hfa) ₃ (dpbp)] _∞	hfa = 		[35]

		dpbp = 		
2-Ln-Ag (Ln=Gd, Eu)	$[\text{LnAg}_3(3\text{-TPyMNTB})_2(\text{H}_2\text{O})(\text{MeCN})](\text{ClO}_4)_6 \cdot 4\text{MeCN}$ Ln=Gd, Eu	TPyMNTB = 		[36]
	$[\text{NH}_4]_2[\text{ZnL}] \cdot 6\text{H}_2\text{O}$	L = 	Ln = Eu ³⁺ , Tb ³⁺	[37]
Ln ³⁺ @bio-MOF-1 Ln=Tb, Sm, Eu, Yb	$[\text{Zn}_8(\text{ad})_4(\text{BPDC})_6 \text{O} \cdot 2\text{Me}_2\text{NH}_2, 8\text{DMF}, 11\text{H}_2\text{O}]$	ad =  BPDC = 	Ln=Tb, Sm, Eu, Yb	[38]
Ln ³⁺ @Zn(II)-MOF Ln = Tb, Eu	$\{[\text{Zn}_2(\text{L}) \cdot \text{H}_2\text{O}] \cdot 3\text{H}_2\text{O} \cdot 3\text{DMAc} \cdot \text{NH}_2(\text{C}_6\text{H}_3)_2\}_\infty$	L = 	Ln = Tb, Eu	[39]

2.1 Energy transfer in Ln-node based MOF

amount can be controlled by reaction temperature. For example, in the Gd^{3+} -L MOF, the guest loading amount based on ligand L can be up to ~ 6.7 mol% for D1 and ~ 2.8 mol% for D2 at 140°C . More interestingly, the guest encapsulated in MOFs at 140°C can be released gradually at room temperature in DMF and this process is reversible (Scheme 2)¹². Photoluminescence and fluorescence lifetime decay studies showed that the D1-loaded MOFs exhibit efficient light harvesting with ET from the framework to the guest molecule. As shown in Figure 5, the emission peak of L has large overlap with the absorption spectrum of D1. When L mixed with D1 in a homogeneous DMF solution at a molar ratio of 1:2, the emission of L was quenched but no ET could be observed (Figure 5, curve b). The authors postulate that this was due to favorable collisional electron transfer and/or the formation of non-emissive aggregates. With the addition of $\text{Gd}(\text{OAc})_3$ and MOF self-assembly, emission from D1 at ~ 580 nm appeared upon MOF excitation at 365 nm, which is optimal excitation of L (Figure 5, curve c & d). Therefore, MOF incorporation and chromophore isolation led to efficient ET between the donor L with the acceptor D1, not observed in homogeneous solution. It is important to note that in this case the Gd^{3+} did not play an active role in the ET chain. The main role of the Gd^{3+} was to organize and isolate the chromophores in 3D space, thus preventing electron transfer and/or the formation of non-emissive aggregates.

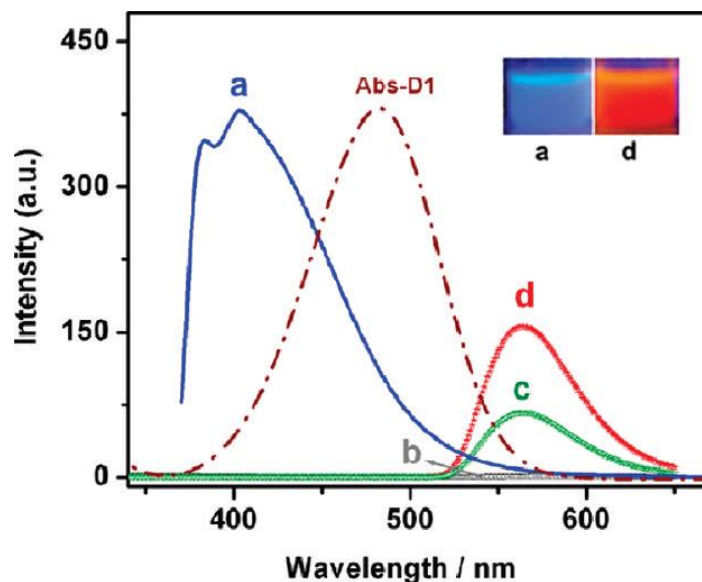


Figure 5. PL spectra of L (a), L + D1 (b), and L + D1 + Gd(OAc)₃ prepared at 20 °C (c) and 140 °C (d) in DMF. All of the samples have the same concentrations of L; samples b, c, and d have the same concentration of D1. The dotted line is a UV-vis spectrum of D1 in DMF. Inset: photo images of samples (a) and (d) under UV light (365 nm). Taken from Ref. 18 with the permission of American Chemical Society.

LLET is not only limited in the host-guest system, but also can be observed in frameworks with mixed ligands. Compared with encapsulation, which occurs by weak non-covalent interactions, strong coordination between metal and ligand can preferentially orient the linker components to enhance ET efficiency. Stable 3D networks were constructed with Ln³⁺ (Ln³⁺ = Gd, Eu, Yb) and a series of different π -conjugated dicarboxylate ligands with different side-chain lengths (Figure 6).¹⁹ The long alkyl chains on the ligand prevented aggregation of the nanometer MOF particles, while the absorption and fluorescence of the MOFs can be tuned by using different chemical speciation of the monomeric units. The structural similarity in the main chain of the ligands ensured that the forces between dicarboxylate linkers and Ln³⁺ ions were approximately similar and led to the same crystal structure for designed MOFs. Doping H₂L2 into Ln-L1 MOFs afforded efficient Förster resonance ET (FRET) from L1 to L2 within the framework, and did not alter the MOF structure (Figure 7). The excitation spectrum and time-resolved fluorescence

decay of Gd-L1-L2 nanoparticle dispersions in DMF confirmed the ET from L1 to L2 under the photo-irradiation at 365/370 nm. The ET from L1 to L2 is evidenced by the quenching of the Gd-L1 emission and the concomitant increase in the acceptor emission (L2) at 550 nm when excited at the 360 nm (the absorption maximum of donor L1) (Figure 7d). A similar FRET process from L3 to L4 can be observed in Gd-L3-L4 system where 1% mol of H₂L4 was doped in Gd-L3 MOF (Figure 8b). Perhaps more important than the demonstration of *in*-MOF LLET, the authors also investigated LMET through the antenna effect between the organic chromophores and Eu³⁺. Indeed, very efficient sensitization of Eu³⁺ was observed when the Gd was replaced with Eu in the L3-based MOF. In the Eu-L3 MOF, the emission of L3 was quenched with the concomitant observation of Eu³⁺ emission. In the mixed Ln³⁺ MOF, Gd(III)_{0.95}-Eu(III)_{0.05}-L3_{1.47}-L4_{0.03}, the acceptor ligand, L4, and the Eu³⁺ ion can be co-sensitized by the same donor, L3, revealed by multiband emissions (Figure 8d).

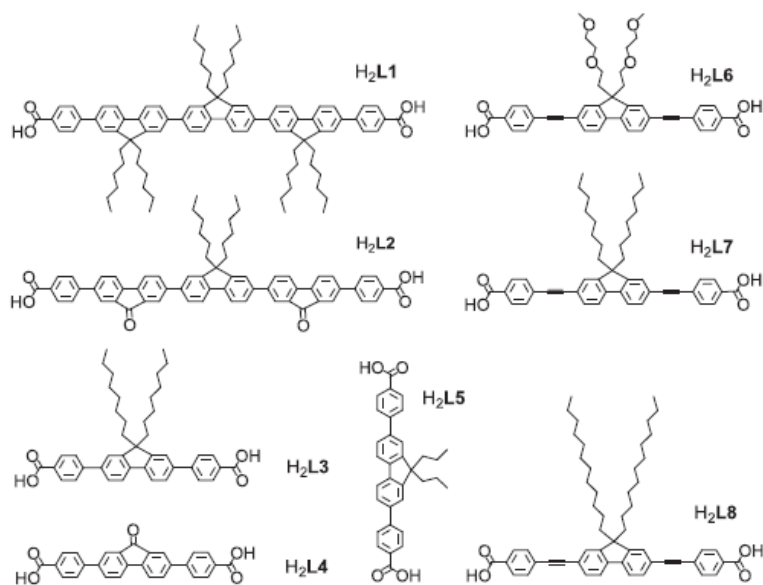


Figure 6. Chemical structures of the ligands with different -conjugation lengths and differing side chains. Taken from Ref. 19 with the permission of Wiley Online Library.

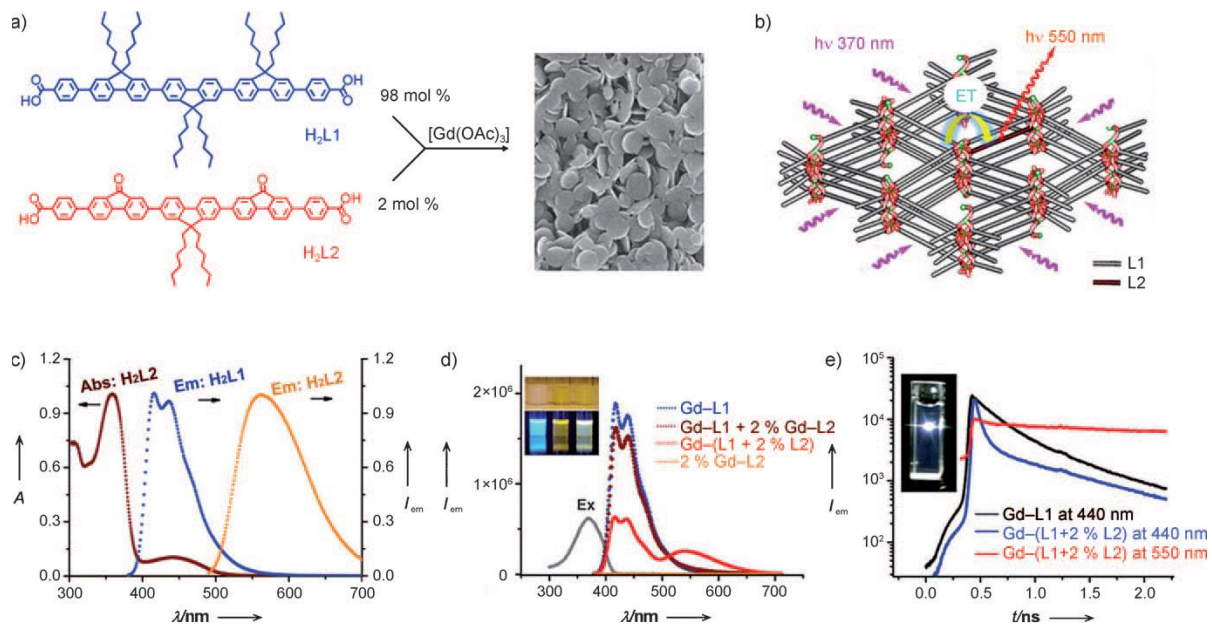


Figure 7. Synthesis and light harvesting study of multicomponent nanoparticles: a) Illustration showing the preparation of Gd–L1–L2 multicomponent nanoparticles. b) Schematic representation of the energy transfer in long-range ordered MOFs. c) Normalized absorption and emission spectra of H₂L1 and H₂L2 in DMF. d) Emission spectra of Gd–L1, Gd–L1 mixed with 2 mol% Gd–L2, Gd–(L1+2 mol% L2), and Gd–L2 nanoparticles. The gray curve is the excitation spectrum of Gd–(L1+2 mol% L2) nanoparticles; inset (from left to right): photo-images of Gd–L1, Gd–L2, and Gd–L1–L2 nanoparticles in daylight (upper row) and under an ultraviolet lamp (365 nm; bottom row). e) Time-resolved fluorescence decay of Gd–L1, Gd–L2, and Gd–(L1+2 mol% L2). Inset: photo-image of Gd–(L1+2 mol% L2) nanoparticles under excitation by laser (370 nm). Reprinted from Ref. 19 with the permission of Wiley Online Library.

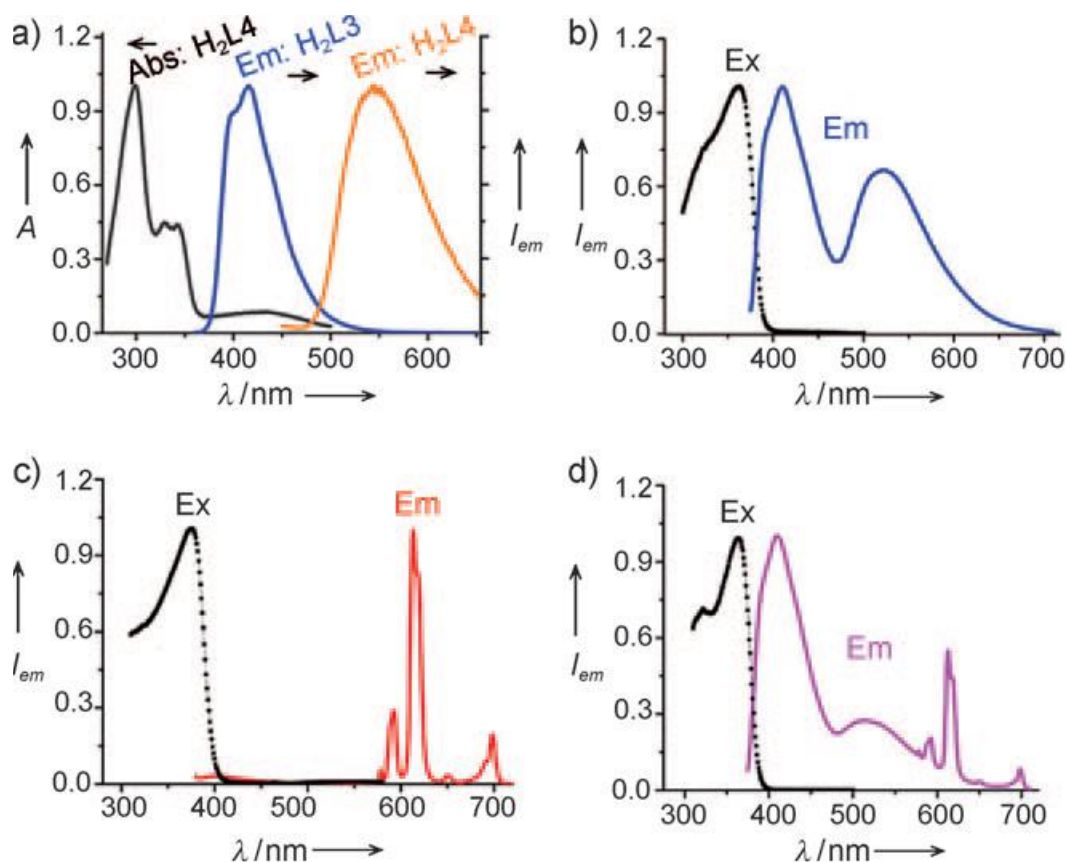


Figure 8. a) Normalized UV/Vis absorption and emission spectra of H_2L3 and H_2L4 in DMF. b) Excitation and emission spectra of Gd-(L3+1% mol L4) nanoparticles. c) Excitation and emission spectra of Eu-L3 nanoparticles. d) Excitation (detected at 590 nm) and emission spectra of Gd(III)_{0.95}-Eu(III)_{0.05}-L3_{1.47}-L4_{0.03} multicomponent nanoparticles dispersed in DMF. Reprinted from Ref. 19 with the permission of Wiley Online Library.

To further enhance the efficiency of LMET, photophysical properties can be modulated through the heavy atom effect (HAE). To briefly introduce this concept, the spin configuration of ligand and Ln^{3+} excited states must be considered. Upon the irradiation of light, organic chromophores form singlet excited states. The excited states of Ln^{3+} ions are formally triplets. Therefore, to promote efficient ET between spin-conserved states, the organic chromophore must first intersystem cross (ISC) to its triplet state. When the energy gap between singlet excited and triplet excited states of the ligand is greater than 5000 cm^{-1} , the intersystem crossing (ISC) process will be effective according to Reinholdt's empirical rule. The HAE enhances spin-orbit coupling between the singlet and triplet states.

Therefore, ISC is favored in the presence of heavy atoms, such as iodine or bromine. Jayakannan and coworkers investigated the HAE concept in using iodo-substituted carboxylic ligands to build one and three-dimensional MOFs with Eu^{3+} .²⁰ Close packing of the bisiodo ligand in the solid state through π - π stacking restricted vibrational relaxation, reduced the radiative decay through S_1 to S_0 transition and promoted the population of triplet states by ISC, which further facilitated LMET from the ligand triplet excited state (T) to the metal ion (5D_0 for Eu^{3+}) in the Eu-MOFs (Figure 9).

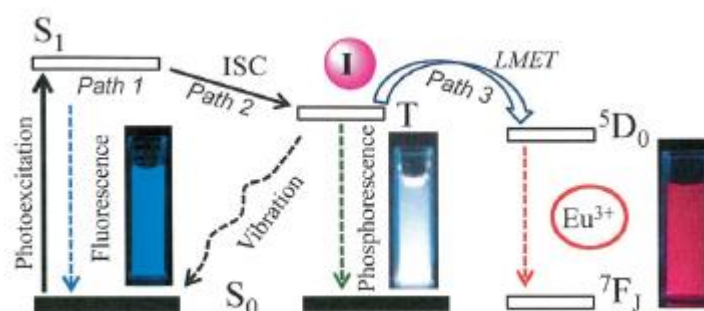


Figure 9. The HAE-assisted ligand to metal energy transfer (LMET) concept. Reprinted from Ref. 20 with the permission of Wiley Online Library.

With sensing applications in mind, the efficiency of LMET in Ln-based MOFs has also been modulated by the encapsulation of small guest molecules and ions in the pores of the MOF matrix. Interactions between the guest molecules and the MOF have been shown to both enhance and quench the luminescence of different MOF constructs. Therefore, enabling both turn-on and turn-off sensing of molecules of interest. As an alternative strategy, the encapsulation of guests that competitively absorb light in the range of the antenna ligand have also effectively decreased the luminescence observed from LMET.

Song and coworkers prepared a luminescent lanthanide MOF, which can selectively detect DMF vapor. The 3D MOF $[\text{Eu}_2\text{L}_3(\text{H}_2\text{O})_4] \cdot 3\text{DMF}$ was synthesized by heating of 2',5'-bis(methoxymethyl)-[1,1':4',1''-terphenyl]-4,4''-

dicarboxylate and $\text{Eu}(\text{NO}_3)_3$ in DMF/ H_2O .²¹ As shown by X-ray crystal analysis, DMF is located in the solvent channel along the a-axis in 3D framework, which can be replaced by water to form an isostructural MOF. The MOF with H_2O in pores exhibited fast response rates to DMF, revealed by the significant increase of luminescence intensity. This DMF effect is caused by DMF-ligand interactions that presumably shifts the energy levels of excited ligand and facilitates the LMET process. In a similar fashion, Ln-MOF $\{[\text{Tb}_4(\mu_3\text{-OH})_4(\text{BPDC})_3(\text{BPDCA})_{0.5}(\text{H}_2\text{O})_6]\text{ClO}_4 \cdot 5\text{H}_2\text{O}\}_\infty$, where $\text{BPDC}^{2-} = 3,3'$ -dicarboxylate-2,2'-dipyridine anion and $\text{BPDCA}^{2-} =$ biphenyl-4,4'-dicarboxylate anion, could sensitively detect small molecules and ions especially benzene, acetone, Cu^{2+} and CrO_4^{2-} .²² An anionic MOF $\text{K}_5[\text{Tb}_5(\text{IDC})_4(\text{ox})_4]$ (IDC = imidazole-4,5-dicarboxylate, ox = oxalate) had a selective response with enhanced emission when guest K^+ exchanged with Ca^{2+} .²³ Qian, Chen and coworkers reported a microporous luminescent MOF, $\text{Eu}_2(\text{FMA})_2(\text{OX}) \cdot (\text{H}_2\text{O})_4 \cdot 4\text{H}_2\text{O}$ (FMA = fumarate; OX = oxalate), that exhibited highly selective and sensitive sensing of Cu^{2+} in aqueous solution (Figure 10).²⁴ Zhang and coworkers prepared Tb(III)-based MOF using a blue emitting ligand 2-(4-pyridyl)-1H-imidazole-4,5-dicarboxylic acid (H_3PyIDC), which showed good selectivity and sensitivity toward Fe^{3+} in water.²⁵ Lastly, as an example of competitive absorption, a family of Ln-MOFs has been shown to effectively sense acetone molecules based on fluorescence attenuation caused by the overlap absorption between acetone and the ligand.²⁶

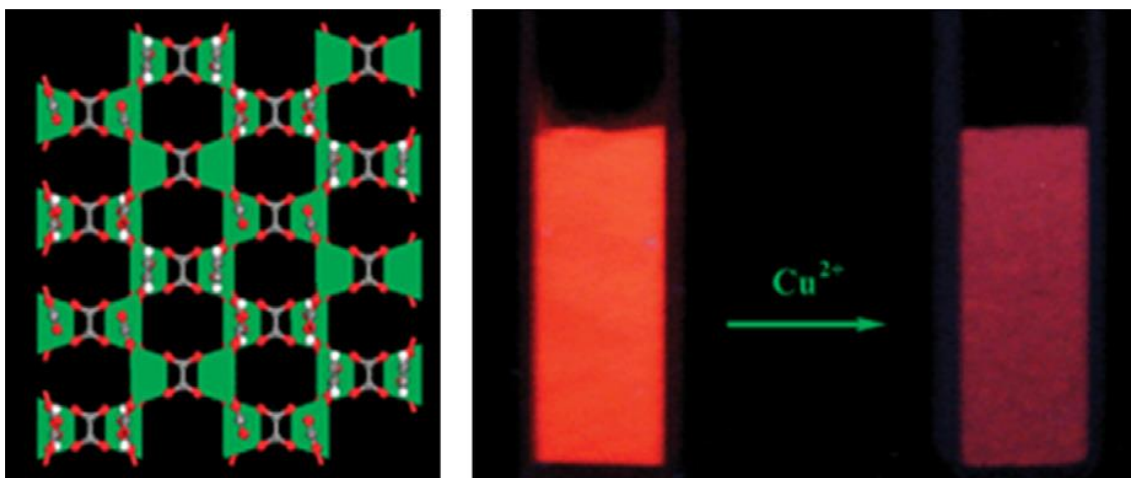


Figure 10. (Left) X-ray single crystal structure of MOF $\text{Eu}_2(\text{FMA})_2(\text{OX})(\text{H}_2\text{O})_4 \cdot 4\text{H}_2\text{O}$. (Right) The luminescence change after the addition of Cu^{2+} (10^{-2} M) on MOF under UV light. Adopted from Ref. 24 with the permission of Royal Society of Chemistry.

Synthetically, the formation of isostructural Ln-based MOF using single component and mixed Ln^{3+} ions is straight forward. Therefore, metal-to-metal energy transfer (MMET) has been widely used to tune the emission color of designed MOFs without altering the structure. Indeed, changing the doping ratio of mixed- Ln^{3+} ions significantly influences both the color and the intensity of observed emission by tuning the efficiency of MMET. The ability to control emission profile and intensity directly relates to the development of white light emitting materials. White emitting materials have broad applications such as displays and lighting. Although emitting coordination complexes have been extensively investigated, only a small number of MOFs with direct white emission have been reported. The emission color can be quantitatively characterized by using the color coordinates according to the Commission Internationale de L'Eclairage (CIE) 1931 diagram.²⁷⁻²⁸ The CIE XYZ color space was derived from a series of experiments done in the late 1920s by William²⁷ and John²⁸, and the coordinates x and y represent red and green color components, respectively. For ideal white light, the CIE coordinates are (0.333, 0.333). Comparison of the CIE coordinates of the following MOFs and the ideal coordinates highlights the

potential for MOFs in this application space. Near ideal white light emission has been achieved through the following examples of MOF MMET.

Rodrigues *et al.* reported a complementary experimental and theoretical investigation of the ET mechanism between $\text{Tb}^{3+} \rightarrow \text{Eu}^{3+}$ in two isomorphous 2D hetero-metallic lanthanide-organic frameworks,²⁹ $[(\text{Tb}_{0.95}\text{Eu}_{0.05})(\text{DPA})-(\text{HDPA})]_{\infty}$ (1) and $[(\text{Tb}_{0.5}\text{Eu}_{0.5})(\text{DPA})(\text{HDPA})]_{\infty}$ (2), where H_2DPA is pyridine 2,6-dicarboxylic acid). Steady-state emission spectra of both MOF samples showed the high quenching effect on Tb^{3+} emission caused by Eu^{3+} ion, indicating efficient $\text{Tb}^{3+} \rightarrow \text{Eu}^{3+}$ ET. The $\text{Tb}^{3+} \rightarrow \text{Eu}^{3+}$ ET rates (k_{ET}) for (1) and (2) and rise rates (k_r) of the Eu^{3+} ion for (1) were investigated at different temperatures. k_r and k_{ET} for (1) were on same order of magnitude, indicating that the sensitization of the $\text{Eu}^{3+} {}^5\text{D}_0$ level is driven by the ET from ${}^5\text{D}_4$ of Tb^{3+} ion. The $\text{Tb}^{3+} \rightarrow \text{Eu}^{3+}$ ET efficiency η_{ET} and R_0 values in (1) varied between 67~79% and 7.15~7.93 Å. For (2), the ET occurs on average with η_{ET} and R_0 of 97% and ca. 31 Å, respectively. The differences in efficiency are simply a result of the loading percentage which increased by 45% from (1) to (2). The role of the dipole–dipole (d–d), dipole–quadrupole (d–q), quadrupole–quadrupole (q–q), and exchange (Ex) mechanisms in ET processes were estimated by Malta’s model. The ET processes investigated were predominantly governed by d–d and d–q mechanisms.

In a series of isotopic, 2D MOFs, $[\text{Gd}_{2-x-y}\text{Eu}_x\text{Tb}_y\text{Cl}_6(\text{bipy})_3]_{\infty} \cdot 2\text{bipy}$, (Figure 11A), where $0 \leq x, y \leq 0.5$, $\text{bipy} = 4,4'$ -bipyridine, the emission color in-between green and red can be tuned.³⁰ Specifically, 4,4'-bipyridine functions as an antenna, providing the $\text{T}_1 \rightarrow 4f$ LMET to Eu^{3+} and Tb^{3+} , giving a red luminescence for Eu^{3+} and a green luminescence for Tb^{3+} , respectively (Figure 12). Different ratios of Eu^{3+} and Tb^{3+} can be incorporated into the MOF by mixing their metal salts with GdCl_3 under solvent-free melt conditions of 4,4'-bipyridine. The combination of

Eu³⁺ and Tb³⁺ led to MMET from Tb³⁺→Eu³⁺, which could tune the emission color (Figure 11D).

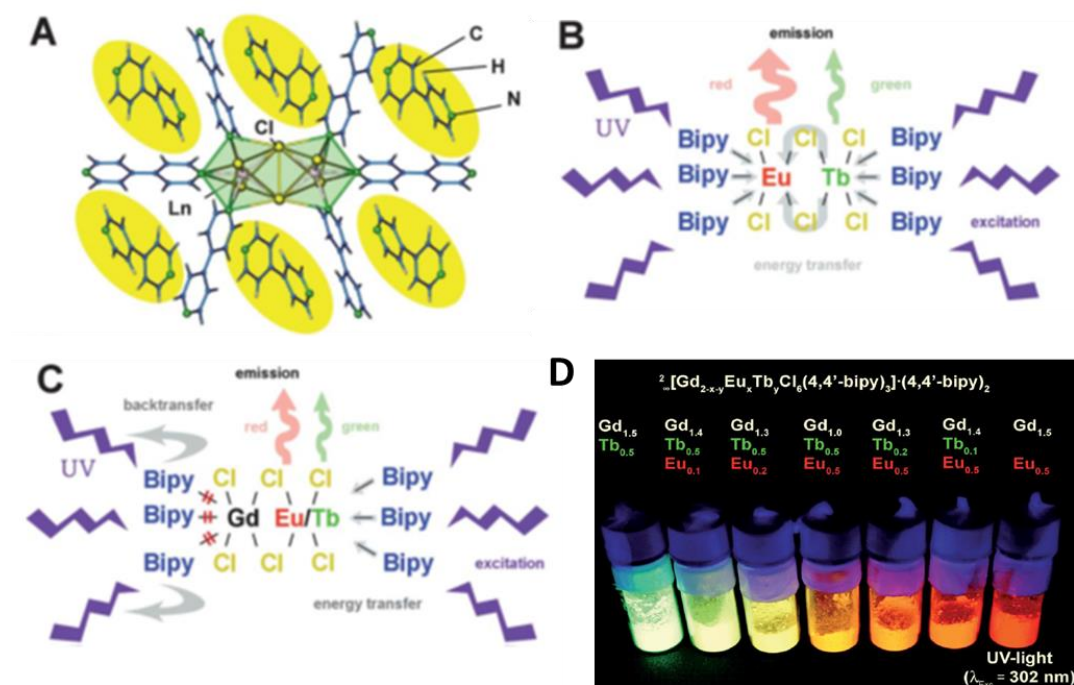


Figure 11. A. Depiction of the connectivity in the 2D layer structure of ${}^2_{\infty}[\text{Ln}_2\text{Cl}_6(\text{bipy})_3]\cdot 2\text{bipy}$. B & C. Schematic depiction of the energy transfer processes between metal ions and ligands. D. Photoluminescence of the series of solid solutions of ${}^2[\text{Gd}_{2-x-y}\text{Eu}_x\text{Tb}_y\text{Cl}_6(\text{bipy})_3]\cdot 2\text{bipy}$ under UV light ($\lambda = 302\text{ nm}$). Adopted from Ref. 30 with the permission of Royal Society of Chemistry.

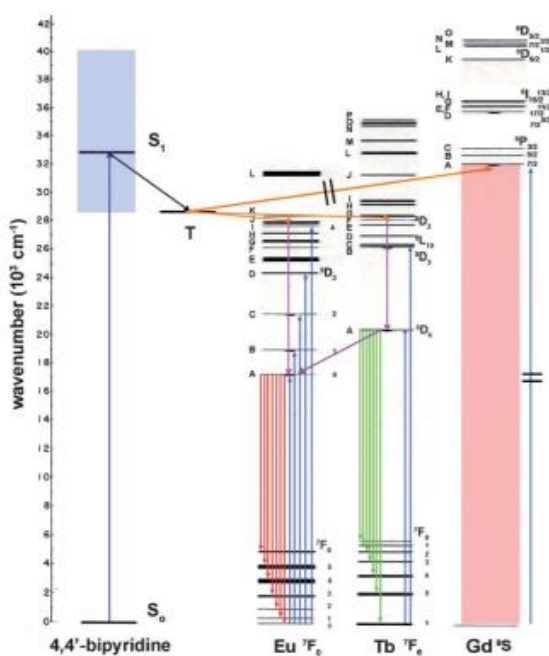


Figure 12. Excitation and emission process between metal ions and ligands in $^2[\text{Gd}_{2-x-y}\text{Eu}_x\text{Tb}_y\text{Cl}_6(\text{bipy})_3]_{\infty} \cdot 2\text{bipy}$. Reproduced from Ref. 30 with the permission of Royal Society of Chemistry.

Zang's group synthesized a series of isostructural lanthanide MOFs, LnL ($\text{Ln} = \text{La, Ce, Pr, Nd, Sm, Eu, Gd, Tb, Ho, Er}$), under solvothermal conditions using flexible multicarboxylic acid ($\text{H}_4\text{L} = 5\text{-(3,5-dicarboxybenzyloxy)-isophthalic acid}$). Efficient ET from the ligand to Tb^{3+} or Eu^{3+} was observed.³¹ Additionally, the emission spectrum was controlled by adjusting the Tb/Eu molar ratio. White light emission was achieved by combination of the blue emission of the ligand and the intense emissions of lanthanide ions (Figure 13). The corresponding CIE coordinates of the MOFs, (0.330, 0.334) and (0.332, 0.338), for $\text{Eu}_{0.17}\text{Tb}_{0.18}\text{La}_{0.65}\text{L}$ and $\text{Eu}_{0.16}\text{Tb}_{0.19}\text{La}_{0.65}\text{L}$, respectively, are very close to the coordinates for ideal white-light (0.333, 0.333).

Similarly, two novel isostructural Ln-Zn ($\text{Ln} = \text{Eu}$ and Tb) hetero-metallic frameworks were prepared by reaction with 4-(1H-tetrazol-5-yl)-biphenyl-3-carboxylic acid (4- H_2tbca) under hydrothermal conditions.³² Both Eu-Zn and Tb-Zn MOFs showed characteristic red and green luminescence, respectively, due to antenna effect from the ligand. Remarkably, the photoluminescence spectra indicated that, not only can the ligand in Tb-Zn MOF transfer energy to Tb^{3+} centers to emit green emission, but it can also maintain effective blue luminescent properties of the 4- H_2tbca ligand. Therefore, additional doping of Eu^{3+} into Tb-Zn MOF can tune the luminescence from green and red to white. The CIE coordinates of the emission spectra of 0.4% to 1.5% Eu^{3+} -doped Tb^{3+} MOFs fall in the white-region. When the percentage of Eu^{3+} dopant is 0.5%, nearly ideal white light emission with the CIE coordinate of (0.331, 0.328) was achieved.

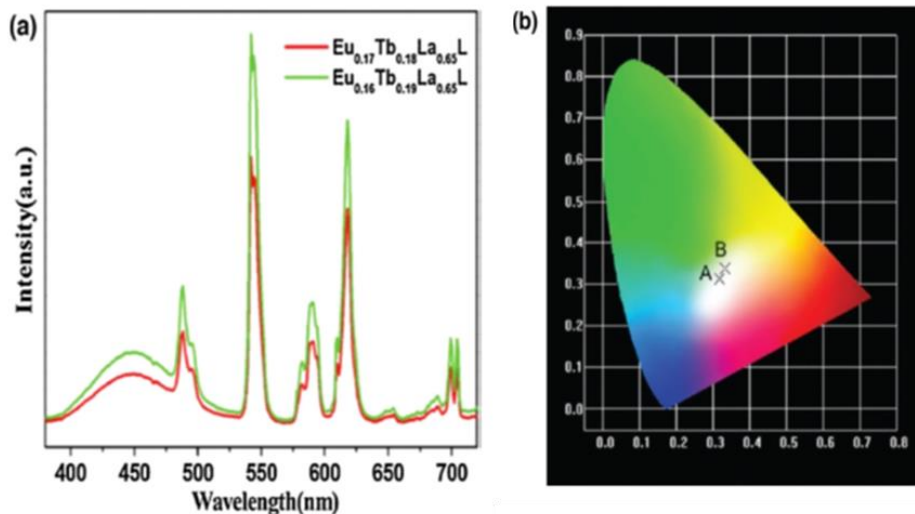


Figure 13. (a) PL emission spectra of the Eu/Tb doped La compound ($\lambda_{\text{ex}}=367$ nm, solid samples). (b) CIE chromaticity diagram for $\text{Eu}_{0.17}\text{Tb}_{0.18}\text{La}_{0.65}\text{L}$ (A) and $\text{Eu}_{0.16}\text{Tb}_{0.19}\text{La}_{0.65}\text{L}$ (B). Reprinted from Ref. 31 with the permission of Royal Society of Chemistry.

Mixed lanthanide MOFs can also act as luminescent thermometers since some of the frameworks exhibited a strong temperature dependence to their luminescence intensity. Qian, Chen and coworkers reported two isostructural 3D MOFs Tb-DMBDC and Eu-DMBDC using 2,5-dimethoxy-1,4-benzene-dicarboxylate (DMBDC) as the organic linker.³³ Owing to the sensitization effect from DMBDC, LMET to Tb^{3+} lead to green emission at 545 nm and LMET to Eu^{3+} lead to red emission at 613 nm. By increasing the temperature from 10 K to 300 K, the emission intensities gradually decreased due to the thermal activation of non-radiative decay. Intriguingly, the mixed doped MOF $\text{Eu}_{0.0069}\text{Tb}_{0.9931}\text{-DMBDC}$ exhibited unique temperature-dependent luminescence behaviors that differed from Tb-DMBDC and Eu-DMBDC. With the increase of temperature, the probability of $\text{Tb}^{3+} \rightarrow \text{Eu}^{3+}$ ET was significantly enhanced. Therefore, at 10 K, the emission band of Eu^{3+} and Tb^{3+} have comparable intensity, while at 300 K, the emission of Eu^{3+} dominates the overall luminescence color. Additionally, a linear correlation between temperature and emission intensity ratio in $\text{Eu}_{0.0069}\text{Tb}_{0.9931}\text{-DMBDC}$ was observed from 50 to 200 K, which indicated that the MOF is an excellent candidate

for self-referencing luminescent thermometers (Figure 14). A follow up study reported $\text{Tb}_{0.9}\text{Eu}_{0.1}\text{PIA}$ ($\text{H}_2\text{PIA} = 5\text{-(pyridin-4-yl)isophthalic acid}$) as luminescent thermometer whose sensitivity is more than nine times higher than $\text{Eu}_{0.0069}\text{Tb}_{0.9931}\text{-DMBDC}$ in an even boarder temperature range of 100 to 300 K, due to the higher triplet-state energy of the ligand.³⁴ Similarly, Hasegawa and coworkers reported $[\text{Tb}_{0.99}\text{Eu}_{0.01}(\text{hfa})_3(\text{dpbp})]_n$ (dpbp: 4,4'-bis(diphe-nylphosphoryl) biphenyl) as a novel thermosensor over a wide range of 200 to 500 K with high sensitivity ($0.83\% \text{ } ^\circ\text{C}^{-1}$).³⁵

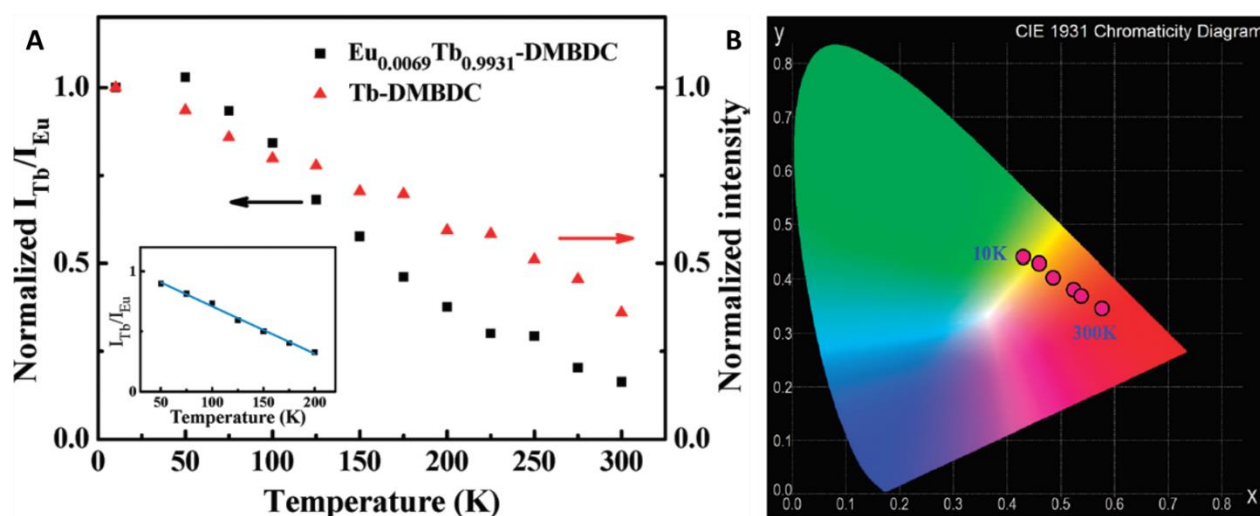


Figure 14. A. Temperature dependence of the integrated intensity ratio of Tb^{3+} (545 nm) to Eu^{3+} (613 nm) for $\text{Eu}_{0.0069}\text{Tb}_{0.9931}\text{-DMBDC}$ (black squares), and temperature dependence of integrated intensity of Tb^{3+} (545 nm) for Tb-DMBDC (red triangles). (Inset) Fitted curves of the integrated intensity ratio for $\text{Eu}_{0.0069}\text{Tb}_{0.9931}\text{-DMBDC}$ from 50 to 200 K. B. CIE chromaticity diagram showing the luminescence color of $\text{Eu}_{0.0069}\text{Tb}_{0.9931}\text{-DMBDC}$ at different temperatures. Adopted from Ref. 33 with the permission of American Chemical Society.

As a demonstration of yet another method to yield white light emission, a hetero-metallic Eu-Ag MOF (2-Eu-Ag) that exhibited dual emission was synthesized.³⁶ In the purely homo-metallic Eu analog, the ligand acts as an antenna to transfer absorbed energy to the Eu^{3+} center, resulting in characteristic red luminescence, via the oft-observed LMET process. Remarkably, upon addition of Ag^+ in a step-wise fashion to form 2-Eu-Ag, ligand-centered emission was observed in addition to

Eu³⁺ emission via LMET. This resulted in white-light emission from a single crystal (Figure 15). It is likely that the 3D structural changes imparted by Ag⁺ inclusion decreased the efficiency of LMET, leading to radiative relaxation of the linker.

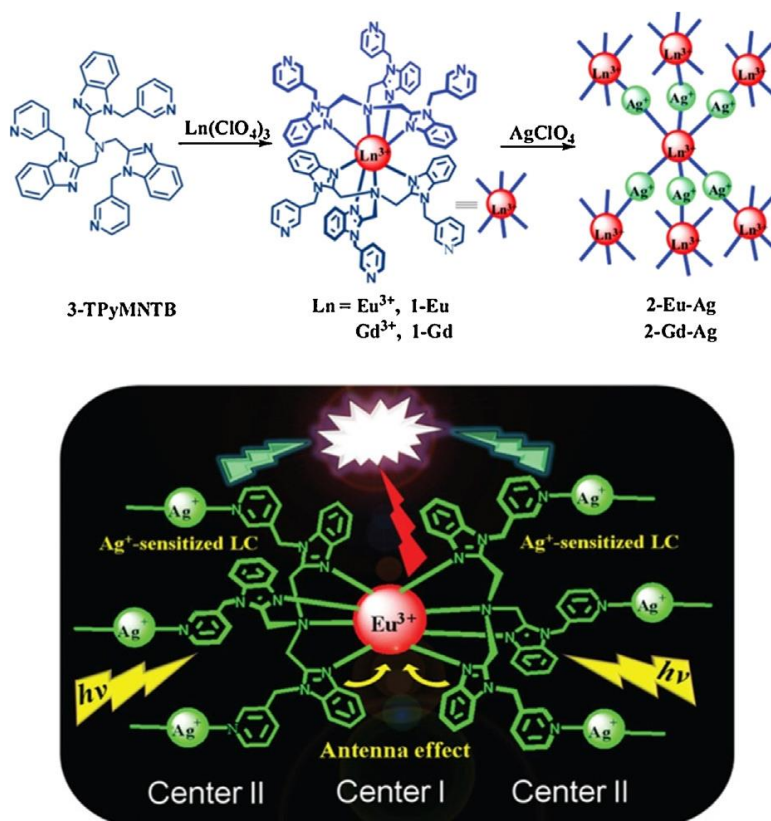


Figure 15. Stepwise assembly of MOFs 2-Ln-Ag (top) and representation of dual-emitting pathways in 2-Eu-Ag generating white-light emission (bottom). Adopted from Ref. 36 with the permission of American Chemical Society.

2.2 Ln@MOF

There is a wealth of Ln³⁺ molecular compounds that have been synthesized. However, the use of these molecular analogs in luminescence-dependent applications (for example, sensing or biomedical imaging) has been limited to the well-known quenching of the Ln³⁺ emission by aqueous media. MOFs provide a rigid scaffold that can serve as the host for protecting the Ln³⁺ ions from such solvent quenching. For example, Luo *et al.* prepared microporous MOF,

$[\text{NH}_4]_2[\text{ZnL}] \cdot 6\text{H}_2\text{O}$ ($\text{L} = 1,2,4,5\text{-benzenetetra-carboxylate}$), with regular one dimensional channels, which were occupied by $[\text{NH}_4]^+$ counter ions.³⁷ The Ln^{3+} -encapsulated MOF can be simply generated through a cation exchange process (Ln^{3+} for $[\text{NH}_4^+]$) in water. The original blue emission of MOF was tuned by doping the framework with Eu^{3+} or Tb^{3+} to produce red or green emission, respectively, through LMET. The framework was explored as a sensor for transition metal ions and the emission intensity was found to be quenched in the presence of Cu^{2+} and Co^{2+} .

Rosi, Petoud and coworkers prepared a porous anionic MOF, bio-MOF-1 with the structure $[\text{Zn}_8(\text{ad})_4(\text{BPDC})_6\text{O} \cdot 2\text{Me}_2\text{NH}_2^+, 8\text{DMF}, 11\text{H}_2\text{O}]$ ($\text{ad} = \text{adeninate}$; $\text{BPDC} = \text{biphenyldicarboxylate}$; $\text{DMF} = \text{dimethylformamide}$, Me_2NH_2^+ is the oxidation form of DMF), that acts as a scaffold for hosting and sensitizing several visible (Sm^{3+} , Tb^{3+} , Eu^{3+}) and near-infrared (NIR) emitting (Yb^{3+}) Ln^{3+} cations.³⁸ The loading of Ln^{3+} cations into the pore of bio-MOF-1 can be achieved by a simple cation exchange process between Me_2NH_2^+ and Ln^{3+} . The loading was confirmed by the luminescence properties of the resulting host-guest materials (Figure 16 A, B and C). Excitation and emission spectra of $\text{Ln}@$ bio-MOF-1 revealed the energy migration from MOF chromophoric structure (BPDC based) to Ln^{3+} guest cation under irradiation at 340 nm (Figure 16 B). Although water is a highly quenching solvent for the emission of Ln^{3+} ions, bio-MOF-1 was found to serve as a “lantern” to protect the Ln^{3+} cations and enhance their luminescence in water. Moreover, preliminary O_2 detection experiments using $\text{Yb}^{3+}@$ bio-MOF-1 demonstrated that $\text{Ln}^{3+}@$ bio-MOF-1 materials can potentially be used as versatile high surface area sensors for small molecules, such as dioxygen.

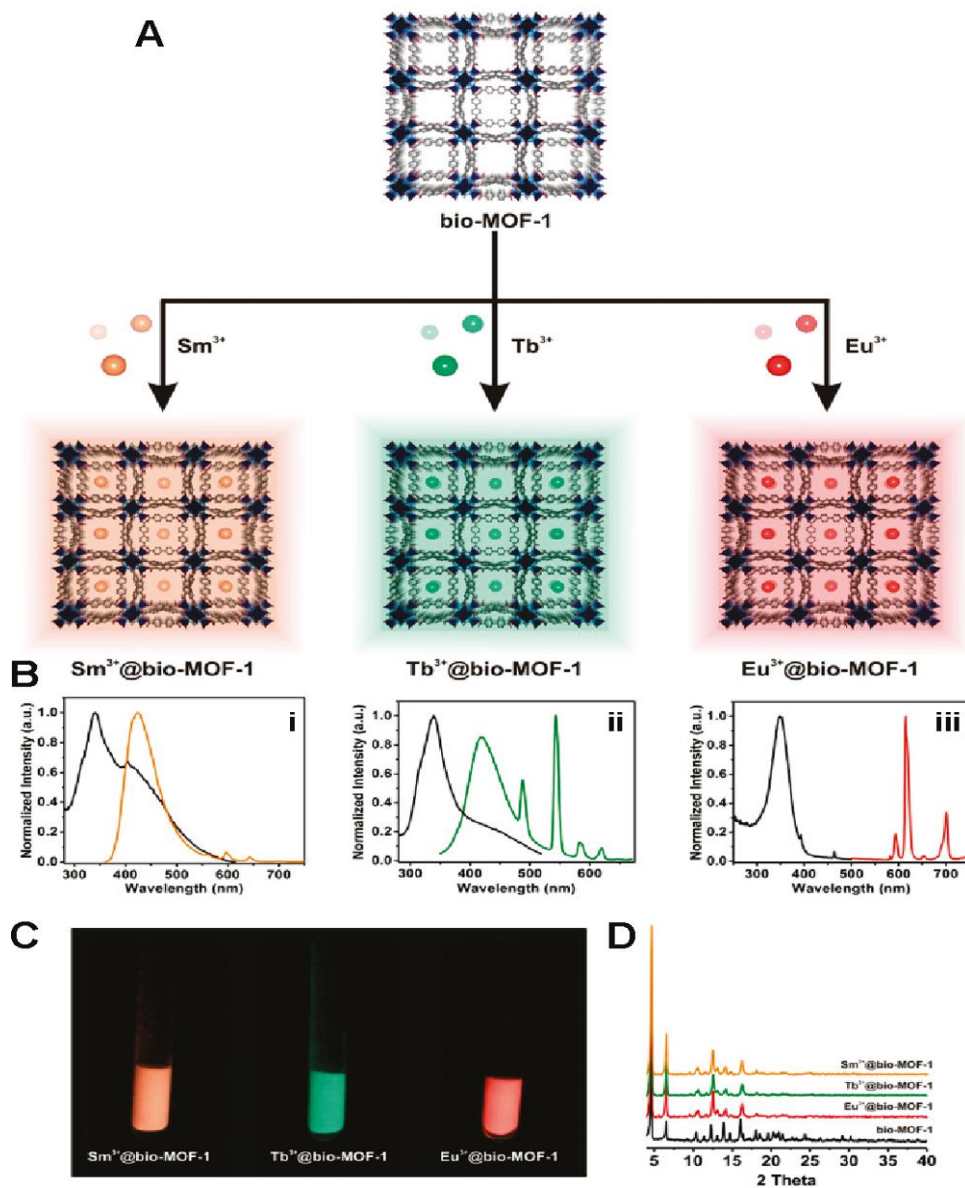


Figure 16. Bio-MOF-1 encapsulation and sensitization of lanthanide cations. (A) Schematic illustration of Ln³⁺ incorporation into bio-MOF-1 and subsequent Ln³⁺ sensitization by the framework. (B) Excitation and emission spectra of Sm³⁺@bio-MOF-1 (i), Tb³⁺@bio-MOF-1 (ii), and Eu³⁺@bio-MOF-1 (iii). (C) Samples of Ln³⁺@bio-MOF-1 illuminated with 365 nm laboratory UV light. (D) PXRD patterns of Ln³⁺@bio-MOF-1. Reprinted from Ref.38 with permission of American Chemical Society.

Ln³⁺ encapsulation has also been explored in the application space of white-light emitting materials. Using a similar cation exchange process to that described above, Ln³⁺ ions were exchanged for Me₂NH₂⁺ cations present in the 1D channels of the 3D MOF, {[Zn₂(L)·H₂O]·3H₂O·3DMAc·NH₂-(CH₃)₂}_∞ (Zn(II)-MOF),

where H₅L = (3,5-bis(1-methoxy-3,5-benzene dicarboxylic acid)benzoic acid) and DMAc = *N,N'*-dimethylacetamide.³⁹ Eu³⁺ and Tb³⁺ were co-encapsulated in the pores in varying ratios to tune the emission of the MOF. The best performing combination of Eu³⁺ and Tb³⁺ concentration in the Ln³⁺-exchanged materials for white light emission is Eu³⁺_{0.127}/Tb³⁺_{0.432}@Zn(II)-MOF (the quantum yield is $\eta = 7\%$) and Eu³⁺_{0.183}/Tb³⁺_{0.408}@Zn(II)-MOF (the quantum yield is $\eta = 8\%$) with the corresponding CIE coordinates being (0.312, 0.335) and (0.339, 0.327), respectively (Figure 17).

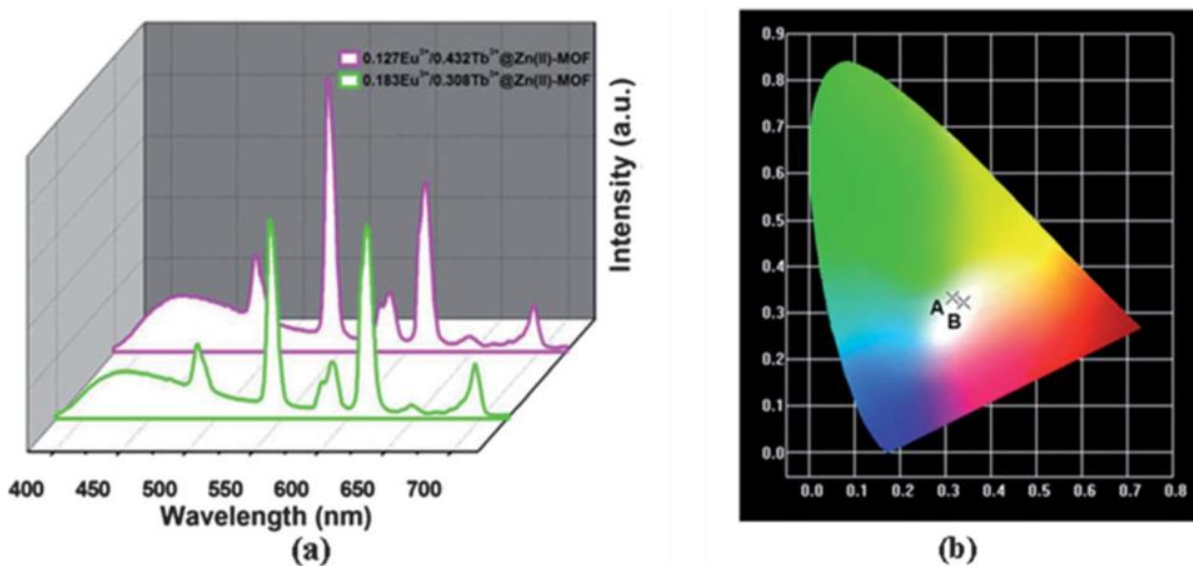


Figure 17. (a) Emission spectra of 0.127Eu³⁺/0.432Tb³⁺@Zn(II)-MOF and 0.183Eu³⁺/0.408Tb³⁺@Zn(II)-MOF excitation at 359 nm. (b) CIE chromaticity diagram for the xEu³⁺/yTb³⁺@Zn(II)-MOF monitored under 359 nm ((A) x = 0.127, y = 0.432 and (B) x = 0.183, y = 0.408). Reprinted from Ref.39 with permission of Royal Society of Chemistry.

2.3 Summary

Lanthanide MOFs provide a versatile platform to exploit different ET processes to tune the resultant luminescent properties. Indeed, ET tuning has led the demonstration of Ln-MOF utility in sensing, luminescence thermometers, and solid state lighting. Key findings are summarized below:

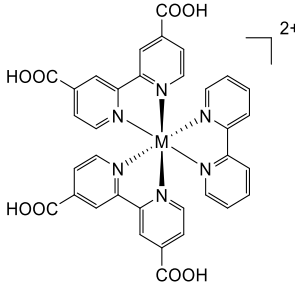
- LLET, LMET and MMET have been demonstrated in Ln-MOFs.

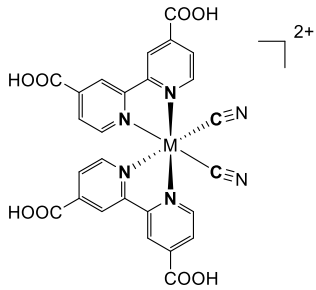
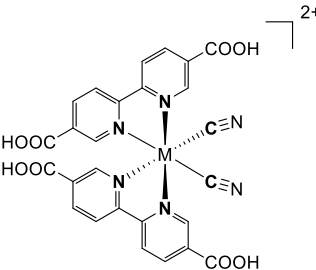
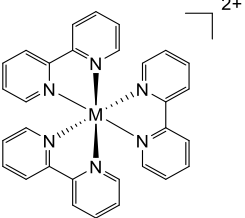
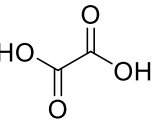
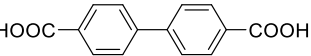
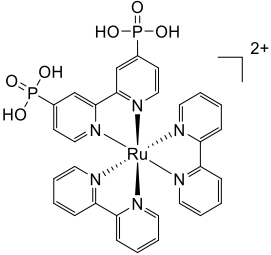
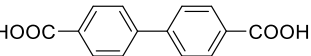
- The well-known heavy atom effect is transferrable to MOF systems and can enhance the efficiency of LMET in MOF constructs.
- Near ideal, white-light emission can be achieved through a combination of ligand based sensitization of Ln^{3+} ions (antenna effect/LMET and MMET).
- Encapsulation of Ln^{3+} ions can attenuate the effect of solvent-based luminescence quenching and opens Ln^{3+} materials to application in aqueous media.

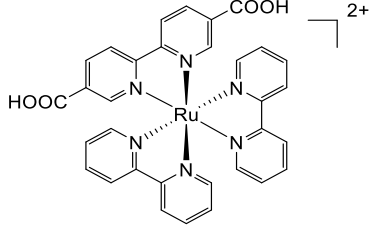
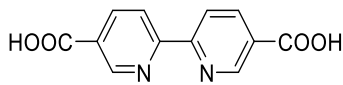
3. Ru/Os based MOF

$\text{Ru}(\text{bpy})_3^{2+}$ and $\text{Os}(\text{bpy})_3^{2+}$ (bpy = bipyridine) are ideal photoactive compounds to dope into a MOF matrix due to their relative long-lived excited states and redox activity. There is rich scientific literature for the study of the photochemical and photophysical behavior of $\text{Ru}(\text{bpy})_3^{2+}$ and $\text{Os}(\text{bpy})_3^{2+}$ in homogeneous solution. Comparison between MOF studies and homogeneous approaches can elucidate the effects of MOF incorporation and/or encapsulation on photophysics. Additionally, the well-defined crystal structure of MOFs allows for precise control over inter-chromophore distances and angles via crystal engineering. Therefore, the potential to tune photophysics through 3D orientation presents itself. Current Ru/Os MOF studies have focused on the incorporation and/or encapsulation of Ru/Os chromophores MOFs with Zn- or Zr- based nodes. The reported MOFs containing Ru/Os chromophores are shown in Table 2.

Table 2. Summary of MOFs containing Ru/Os chromophores

MOF	Chemical Formula	Ligand Structure	Guest	Ref
MOF-1	$[\text{ZnL}_1] \cdot 2\text{DMF} \cdot 4\text{H}_2\text{O}$	$\text{L}_1 =$  $\text{M}=\text{Ru or Os}$		[44]

MOF-2	$[\text{Zn}(\text{H}_2\text{L}_2)] \cdot 3\text{H}_2\text{O}$	$\text{L}_2 =$  $\text{M} = \text{Ru or Os}$		[45]
MOF-3	$[\text{Zn}_5(\text{L}_3)_2 \cdot (\mu\text{-OH}) \cdot (\text{HCOO}) \cdot \text{DMF} \cdot 2\text{H}_2\text{O}] \cdot 6\text{H}_2\text{O}$	$\text{L}_3 =$  $\text{M} = \text{Ru or Os}$		[46]
MOF-4	$[\text{M}(\text{bpy})_3]^{2+} [\text{Zn}_2(\text{C}_2\text{O}_4)_3]$	Oxalate =	 $\text{M} = \text{Ru or Os}$	[47]
MOF-5	$[\text{M}(\text{bpy})_3]^{2+} [\text{NaAl}(\text{C}_2\text{O}_4)_3]$			
Ru@IRMOF-10	$\text{Ru}(\text{bpy})_2(\text{dpbpy})@ \text{Zn}_4\text{O}(\text{bpdC})_3$	$\text{BpdC} =$ 		[48]
RuDCBPY-Uio67	$\text{Zr}_6\text{O}_4(\text{OH})_4(\text{RuDCBPY})_x(\text{BPDC})_{6-x}$	$\text{BpdC} =$  $\text{RuDCBPY} =$		[52]

			
RuDCBPY-UiO-67-DCBPY	$Zr_6O_4(OH)_4(RuDCBPY)_x(DCBPY)_{6-x}$	DCBPY = 	[53]

3.1 Ru/Os in Zn-node based MOFs

Energy flow from polypyridyl-based metal-to-ligand charge transfer (MLCT) excited states of Ru(II) to Os(II) has been studied in a variety of systems, such as ligand-bridged complexes, supramolecular assemblies,⁴⁰ polymers⁴¹ and crystalline molecular solids,⁴²⁻⁴³ in order to elucidate the energy transfer dynamics. The Lin and Meyer groups first investigated this classic Ru-to-Os energy transfer process in 2D bilayer MOF structures using the derivatives of $Ru(bpy)_3^{2+}/Os(bpy)_3^{2+}$ as the ditopic linkers.⁴⁴ As shown in Scheme 3, the phosphorescent MOF-1, based on $Ru(II)(bpy)(4,4'-dcbpy)_2$ (L_{1-Ru} , where 4,4'-dcbpy = 2,2'-bipyridine-4,4'-dicarboxylic acid), has strong absorption in the visible region. Upon doping $Os(II)(bpy)(4,4'-dcbpy)_2(L_{1-Os})$ into the framework structure, the mixed-metal MOF-1 was obtained with 0.3, 0.6, 1.4 and 2.6 mol % Os loading. Time-resolved emission studies were performed with two-photon excitation at 850 nm and energy migration from photo-excited Ru to Os trap sites was observed (Figure 18a). The lifetimes of Ru(II) excited states decreased progressively with the increasing doping of Os from 0.3 to 2.6 mol % (Figure 18b). The sensitization of Os loading was proposed to occur via a Ru-to-Ru energy hopping followed by Ru-to-Os energy cascade due to the lower energy state of Os acting as a trap site (Figure

18c). Assuming 3D energy hopping, it was calculated that an Os site could effectively quench Ru excitons that originated within a 40 Å radius.

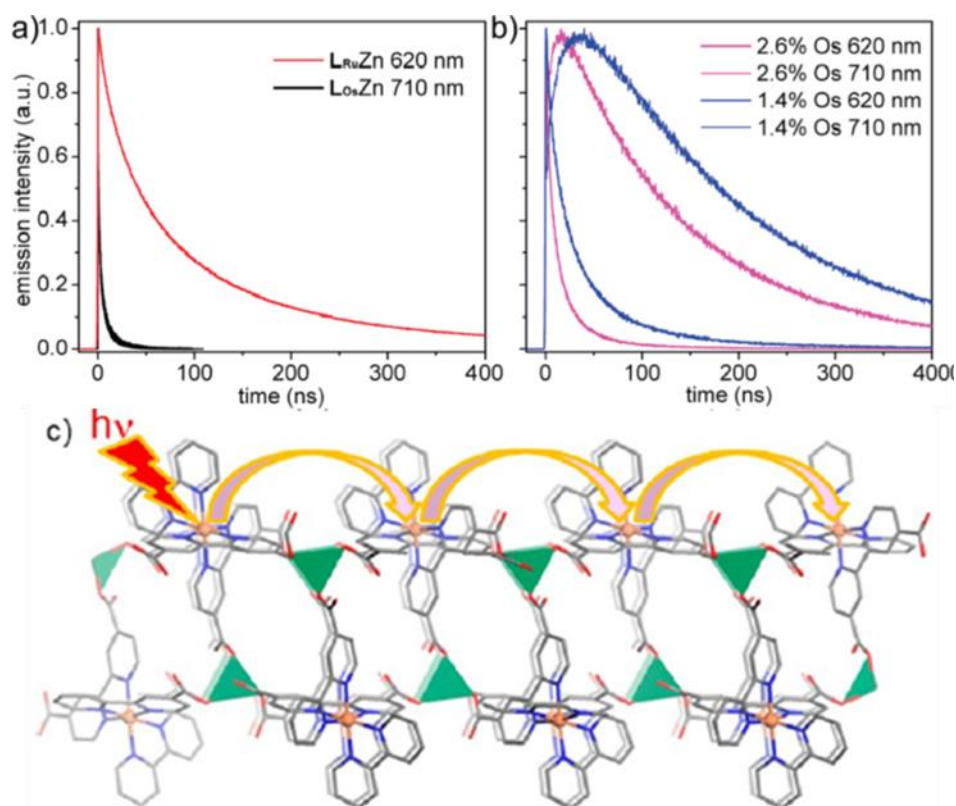
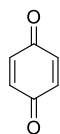
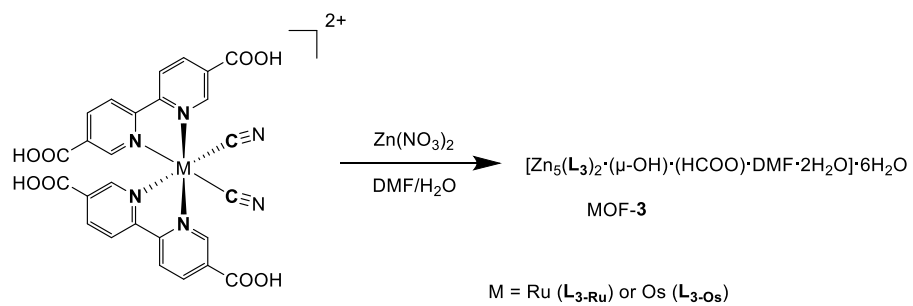
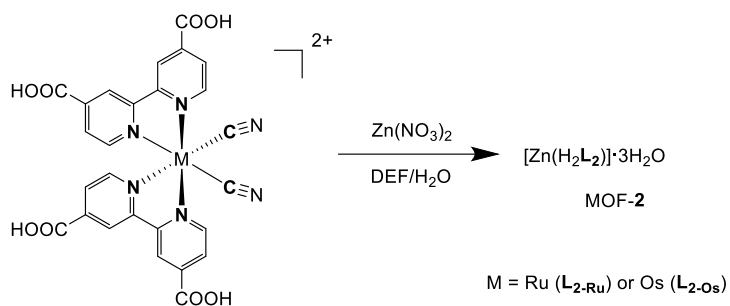
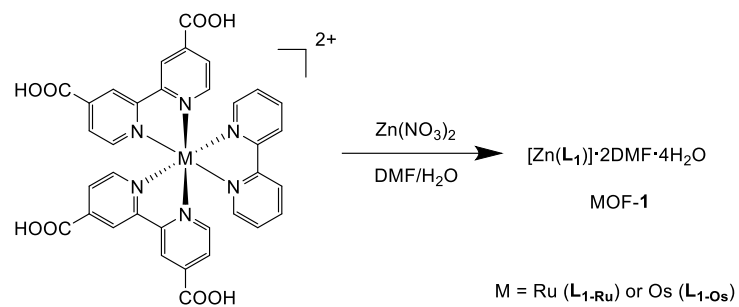


Figure 18. (a) Transient emission decay profiles for L_{Ru} and L_{Os} MOF-1 monitored at 620 and 710 nm respectively following two-photon excitation at 850 nm. (b) Transients for 1.4 and 2.6 mol % Os-doped MOF-1 at 620 and 710 nm with emission at 620 nm dominated by Ru(II)* and at 710 nm by Os(II)*. (c) Schematic depicting the hopping of the Ru(II)*-bpy excited states in MOF-1. Reprinted from Ref.44 with permission from American Chemical Society.

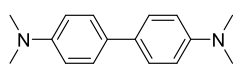
Following the energy migration studies, Lin, Meyer and co-workers used redox luminescence quenching to probe the charge separation ability of MOF-1 and MOF-2, which is built from a similar ruthenium-based bridging ligand ($L_{2-Ru} = Ru(4,4'-dcbpy)_2(CN)_2$).⁴⁵ The quenching experiments were performed with stirred suspension of the MOF microcrystals in degassed acetonitrile in the presence of an oxidative quencher (1,4-benzoquinone, BQ) or a reductive quencher (N,N,N',N'-tetramethylbenzidine, TMBD). Both MOFs showed that the extent of Ru(II)* emission quenching increases as the quencher concentration is increased. Up to

98% quenching was achieved for MOF-2, with either BQ or TMBD, as a result of rapid energy migration over several hundred nanometers followed by efficient electron transfer quenching (Figure 19). The quenching process was proposed to take place at the MOF/solution interface as the MOF channels are too small to allow the diffusion of quencher molecules. Another study from the same groups demonstrated an amplified luminescence quenching for MOF-2 with methylene blue (MB^+) as quencher.⁴⁶ Strong non-covalent interactions between the MOF surface and cationic quencher molecules coupled with rapid energy transfer through the MOF microcrystal lead to a 7000-fold enhancement of Stern-Völmer quenching constant compare with the ligand ($\text{L}_{2\text{-Ru}}$) in solution. It is important to mention that the rate of energy transfer through MOF plays a very important role in changing the quenching efficiency. MOF-3 was synthesized with $\text{L}_{3\text{-Ru}}$ by changing the $\text{Ru}(4,4\text{'-dcbpy})_2(\text{CN})_2$ in MOF-2 to $\text{Ru}(5,5\text{'-dcbpy})_2(\text{CN})_2$, resulting in a three-dimensional framework. Although similar ionic interaction between the quencher and MOF surface would be expected, emission quenching efficiency saturates at 80% with methyl viologen (MV^{2+}) for MOF-3, mainly due to the competition between excited-state decay process with energy transfer via hopping mechanism. However, for MOF-2, the intra-MOF energy transfer is more rapid than MOF-3, so that the complete emission quenching was achieved with $[\text{MV}^{2+}]$. These results highlight the effect of 3D structure of ET efficiency. The chromophores in MOF-2 and MOF-3 differ only in the position of the carboxylic acid units. However, the ET efficiency is drastically different, which may be in part due to the change in angles between interacting chromophores.

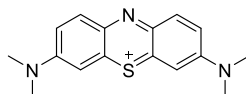
Scheme 4. Synthesis of phosphorescent MOF-1, MOF-2 and MOF-3 and chemical structure of various redox quenchers.



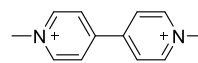
BQ



TMBD



MB⁺



MV²⁺

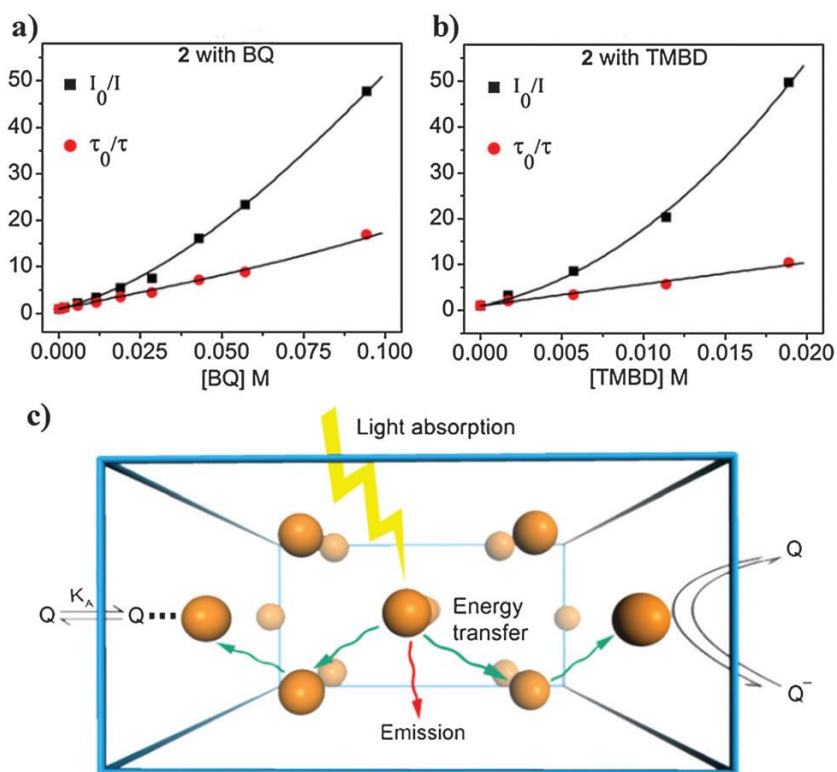


Figure 19. (a,b) Steady-state (black) and time-resolved (red) Stern–Volmer quenching analysis of MOF-2 with BQ (a) or TMBD (b). (c) Schematic showing the light-harvesting process in MOF microcrystals as a result of a rapid energy migration over several hundred nanometers followed by efficient electron transfer quenching at the MOF/solution interface. Reprinted from Ref.45 with permission from American Chemical Society.

Due to their porosity and aperture size tunability, photoactive Ru/Os polypyridyl complexes can also be encapsulated into the MOFs as guest molecules to probe energy transfer. The Lin and Meyer groups synthesized two non-porous MOFs with caged $\text{Ru}(\text{bpy})_3^{2+}/\text{Os}(\text{bpy})_3^{2+}$ chromophores, $[\text{M}(\text{bpy})_3^{2+}]@[\text{Zn}_2(\text{C}_2\text{O}_4)_3]$ (MOF-4) and $[\text{M}(\text{bpy})_3^{2+}]@[\text{NaAl}(\text{C}_2\text{O}_4)_3]$ (MOF-5).⁴⁷ Long-lived ³MLCT excited states with lifetimes of 760 and 1305 ns were observed in Ru-MOF-4 and Ru-MOF-5, respectively, under anaerobic conditions. With the presence of trace amount oxygen, the lifetimes were significantly shortened to 92 ns for MOF-4 and 144 ns for MOF-5, due to energy transfer from $\text{Ru}(\text{II})^*$ to O_2 . Similar to MOF-1 and MOF-2, $\text{Os}(\text{bpy})_3^{2+}$ could act as energy trap sites at doping level of 0.2-1.0%. Kinetic studies showed that the entrapped chromophores in MOF-4 and MOF-5

provided a network for rapid excited state energy transfer migration among $\text{Ru}(\text{bpy})_3^{2+}$ units, ultimately, finding an $\text{Os}(\text{bpy})_3^{2+}$ trap site.

The aforementioned experimental results were complemented with a theoretical analysis of ET in MOF-1 and MOF-4. The goal of the study was to elucidate how the MOF structure influences the pathways for exciton flow.⁸ The analysis showed that the exciton states are localized on single $\text{Ru}(\text{bpy})_3^{2+}$ or $\text{Os}(\text{bpy})_3^{2+}$ sites, as opposed to delocalized in a semiconductor-like material. Additionally, the mechanism of ET was dominated by a Dexter exchange process. Both MOFs (MOF-1 and MOF-4) exhibited ~ 10 ns calculated exciton hopping times between adjacent Ru-polypyridyl sites separated by 8-10 Å. Therefore, the excitons can make 3-6 hopping steps (~ 30 -60 Å distances) within their lifetimes, depending on the dimensionality of the hopping network (1D along a linear chain, 2D within one MOF layer or plane, or 3D throughout the entire framework). The computed Dexter couplings in the MOFs showed that the exciton transport takes place in 1D network in MOF-1, while ET in MOF-4 occurs through a 3D network. The kinetic analysis allowed direct comparison of ET efficiency between the two MOFs and indicated that the higher dimensionality coupling pathways weakly enhance the quenching efficiencies. In summary, the dominance of the weak Dexter coupling interactions leads to ET that is highly sensitive to metal-metal distance and the distribution of encapsulated chromophores in 3D space. One possible approach to improve the speed of ET in the Dexter coupling mechanism is to enhance Dexter coupling interactions by constructing MOFs with shorter intermetallic distances or more highly conjugated bridging units.

Yan and coworkers reported the encapsulation of $\text{Ru}(\text{bpy})_2(\text{dpbpy})$ ($\text{dpbpy} = 4,4'$ -diphosphonate-2,2'-bipyridine) into the biphenyl-based MOF (referred to as $\text{Ru}@$ IRMOF-10).⁴⁸ The designed material exhibited well-defined blue/red luminescence at the crystal interior and exterior as detected by 3D confocal

fluorescence microscopy. By controlling the amount and location of the Ru chromophores, the intensity ratio of blue to red emission can be varied at different regions within the MOF crystal. Specifically, at a low loading percentage of Ru@MOF (2.25%), the crystal interior exhibited blue luminescence, which was assigned to IRMOF-10 emission, while the surface of crystal exhibited emission at 600 nm, which can be attributed to the luminescence of the Ru chromophore. Those observations indicated the non-uniform distribution of Ru complex within the nano-channel, which is consistent with the gradual diffusion process of the Ru(bpy)₂(dpbpy) molecules into the MOF matrix. Moreover, the decrease in the intensity ratio of blue to red emission in the selected region close to the MOF surface suggests the occurrence of energy transfer between the MOF host and Ru chromophore guest. A higher population of Ru(bpy)₂(dpbpy) molecules close to crystal exterior leads to more efficient energy transfer from the MOF matrix to Ru chromophore compared with that in the center of MOF. The energy transfer processes from host to guest molecule and the intramolecular MLCT process were further confirmed by DFT calculations, which were consistent with the experimental results. Upon attaching the MOF to a rutile TiO₂ nano-array, the Ru@MOF system showed enhanced incident photon-to-current conversion efficiency (IPCE) relative to the pristine Ru-based complex directly anchored to the semiconductor surface (Figure 20). Therefore, by the appropriate choice of MOF and photoactive complex with suitable energy levels, host-guest photo-functional materials have potential applications in luminescent and optoelectronic materials, including solar cells.

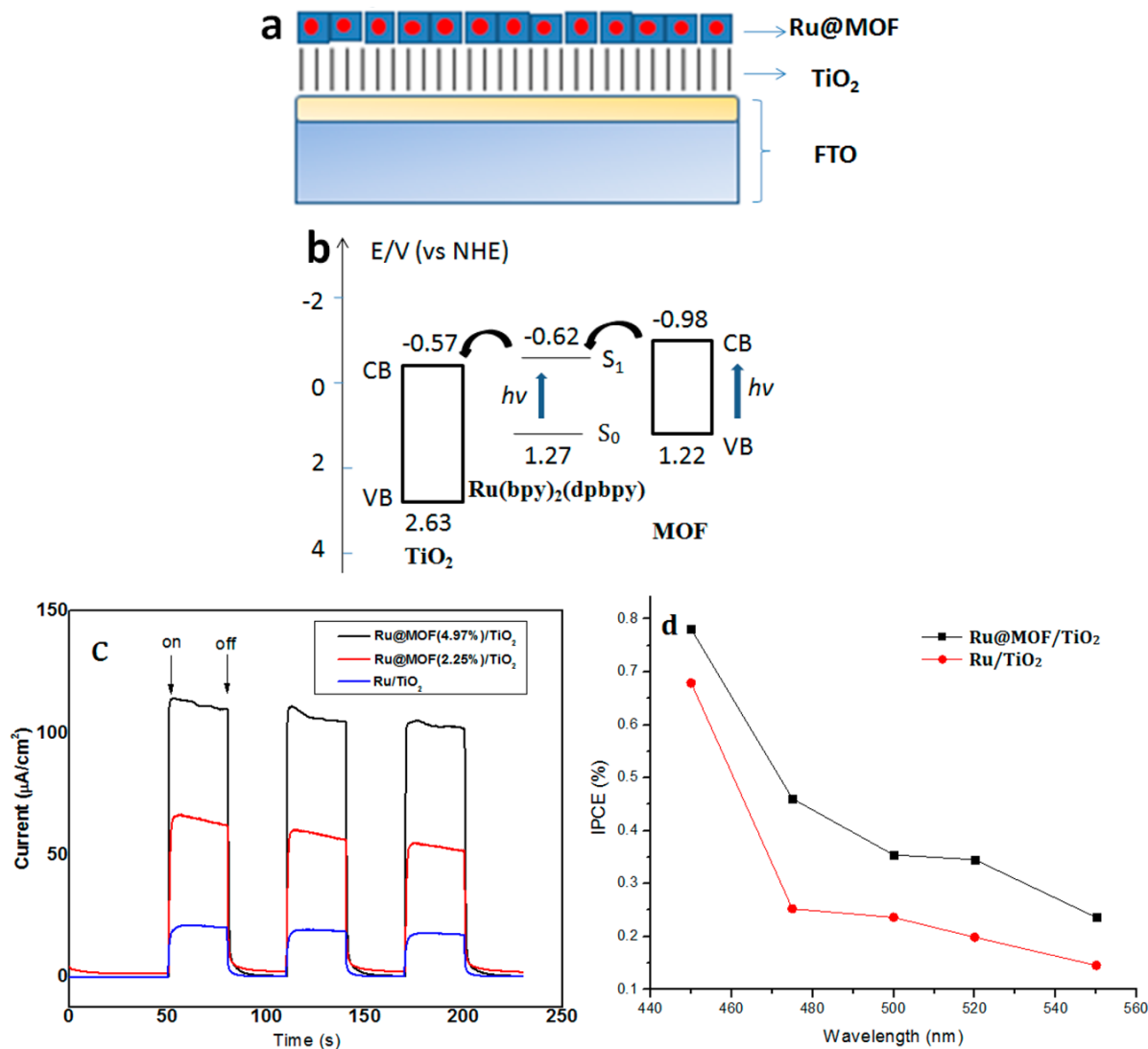


Figure 20. (a) Schematic structure of Ru@MOF/TiO₂ as photoelectrode. (b) Energy level positions of Ru complex, MOF, and TiO₂ relative to the NHE. (c) Photocurrent–time measurements with a chopped light from a Xe lamp light source (100 mW/cm²) and at an external bias (0 V vs Ag/AgCl) for Ru@MOF (2.25%)/TiO₂, Ru@MOF (4.97%)/TiO₂, and Ru/TiO₂ (0.1 M phosphate buffer, pH 7). (d) Dependence of IPCE values on incident wavelength for Ru@MOF (4.97%)/TiO₂ and Ru/TiO₂. Reprinted from Ref.48 with permission from American Chemical Society.

3.2 Ru(bpy)₃²⁺ doped zirconium(IV) MOFs

UiO-67 is a water-stable framework containing Zr₆(μ₃-O)₄(μ₃-OH)₄ nodes connected by twelve 4,4'-biphenyldicarboxylate (BPDC) linkers (Figure 21A).⁴⁹ The structure contains pores with two distinct geometric environments: an octahedral pore of 23 Å diameter and a tetrahedral pore of 11.5 Å diameter (Figure

21B).⁵⁰ UiO-67 provides a unique platform for incorporation of inorganic photosensitizers, such as $[\text{Ru}(\text{dcbpy})(\text{bpy})_2]^{2+}$ (RuDCBPY), by the simple replacement of one the bipyridine ligands with 2,2'-bipyridyl-5,5'-dicarboxylic acid (DCBPY) (Figure 21B).⁵¹ Lin and co-workers were the first to report this mix-and-match synthetic strategy to dope different transitional-metal molecular catalysts, including RuDCBPY, into the UiO-67 framework.⁵¹ The dependence of the photophysical behavior on $\text{Ru}(\text{bpy})_3^{2+}$ loading was later probed by the Morris group.⁵²⁻⁵³ The changes in excited-state lifetimes and spectral differences observed with increasing dye concentration were attributed to dipole-dipole homogeneous resonance energy transfer (RET) and loading-dependent differences in incorporation/ encapsulation environments (*vide infra*).⁵²⁻⁵³

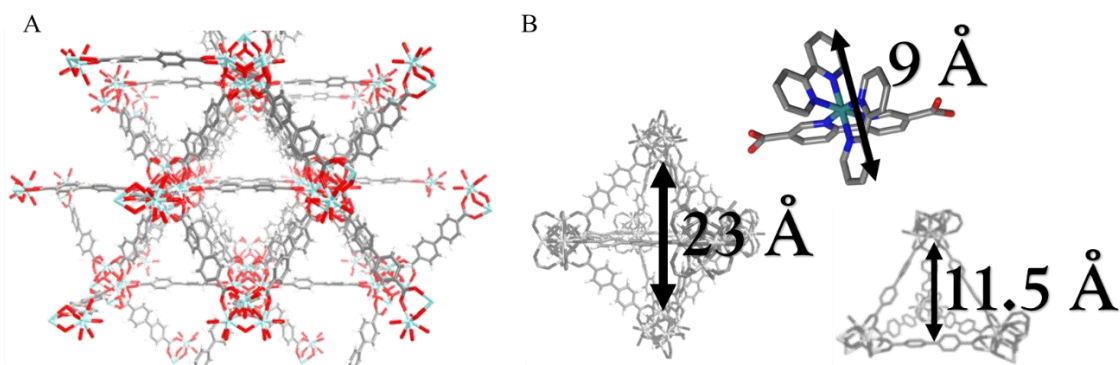


Figure 21. A) Crystal structure of UiO-67, $\text{Zr}_6(\mu_3\text{-O})_4(\mu_3\text{-OH})_4(\text{BPDC})_{12}$, where BPDC = biphenyldicarboxylic acid: black, carbon; red, oxygen; cyan, zirconium. B) Octahedral cavity (left), the tetrahedral cavity (right), RuDCBPY (middle). Reprinted from Ref.52 with permission from American Chemical Society.

The photophysical properties of RuDCBPY-UiO-67 were first probed as a function of the doping concentrations. The steady-state diffuse reflectance of the RuDCBPY-UiO-67 powder showed an absorption maximum at 455 nm, which was attributed to a singlet metal-to-ligand charge transfer ($^1\text{MLCT}$) characteristic of $\text{Ru}(\text{bpy})_3^{2+}$ and its derivatives.^{52, 54} This absorption band broadened with increased loading percentage, while the absorption maximum remained constant at all doping concentrations. However, the energy of the emission maxima and excited-state

lifetimes were found to be quite sensitive to the concentration of RuDCBPY incorporated into UiO-67. At low doping concentrations (≤ 16.4 mm), the excited-state properties of RuDCBPY in the MOF deviate markedly from those in aqueous solution, but resemble those in DMF. Specifically, the emission maximum centered around 630 nm, was slightly bathochromically shifted relative to RuDCBPY in DMF (625 nm).⁵² The emission decay can be adequately modeled using a single discrete exponential decay function with an observed lifetime of 1.4 μ s, which is longer lived excited state compared to RuDCBPY in DMF (890 ns). This increased lifetime is due to the fact that vibrational decay pathways are hindered when the chromophore is incorporated into a rigid matrix. Interestingly, at higher doping concentrations (> 16.4 mm), the emission spectra demonstrated a bathochromic shift relative to the low doping materials, displaying an emission maximum around 650 nm. The observed emission decays at high loadings were biphasic with a concentration-dependent long lifetime component ($\tau \sim 165$ -210 ns) and a concentration independent short lifetime component (~ 24 ns) resembling the lifetime of RuDCBPY in water (~ 38 ns).

A two-state model was proposed to explain the biphasic nature of the decay at high doping concentration (Figure 22). At low doping concentrations, RuDCBPY was said to preferentially occupy the larger octahedral cages of UiO-67 by incorporation into the backbone of the cage. As a result of residual solvothermal reaction solvent (i.e. DMF) in the pore, this population experiences a dimethylformamide (DMF)-like solvation environment. However, at higher doping concentrations, in addition to the RuDCBPY *incorporated* into the backbone of UiO-67, populations of RuDCBPY were found to be *encapsulated* in separate octahedral cavities of the MOF (Figure 22). Encapsulation is assumed to restrict the solvent (DMF) occupancy within the pore and the μ -O and μ -OH bridges of the Zr-nodes were thought to impose a polar water-like dielectric on RuDCBPY so that

the solvation environment resembles that of bulk water. The result was emission spectra and lifetimes dominated by water-like photophysical properties. RuDCBPY has shorter emission lifetime (~ 38 ns) in water than in DMF, mainly due to the sensitivity to solvent (particularly solution pH) arising from preferred localization of the $^3\text{MLCT}$ on the DCBPY ligand.

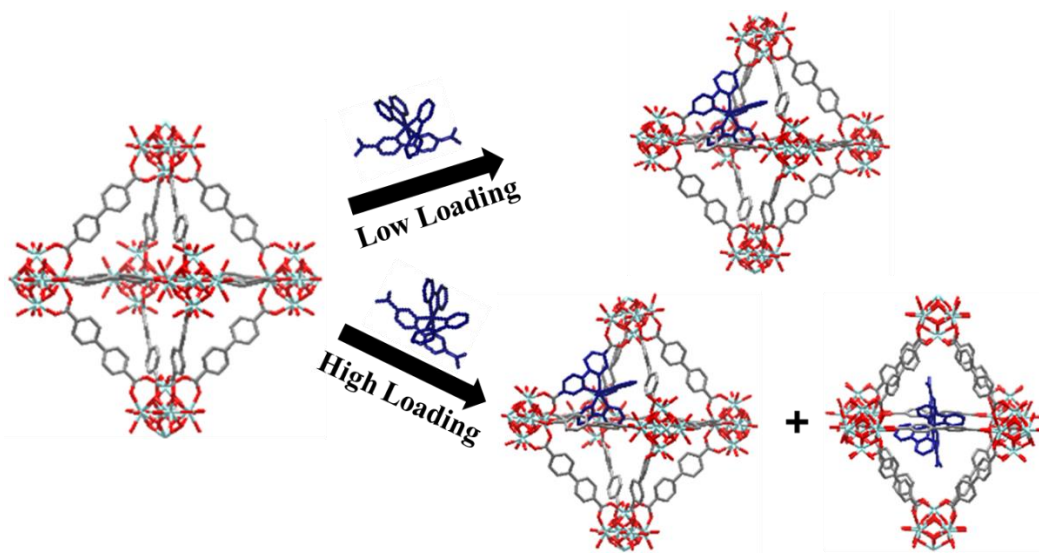


Figure 22. Two-state model of concentration dependent RuDCBPY doping behavior

The concentration dependence of the long lifetime component observed for RuDCBPY-UiO-67 was attributed to RET between RuDCBPY $^3\text{MLCT}$ states. The emission lifetime data for RuDCBPY-UiO-67 at the doping concentration between 3 mm and 21 mm was fit to the Inokuti-Hirayama function, which lead to $1/r^4$ distance dependence for the energy transfer rate. This suggests a dipole-dipole RET process lying on a continuum between the Perrin weak coupling and Förster very weak coupling regimes, which has been proposed by Kenkre and Knox.⁵⁵ This indicates that the framework imparts a stronger dipole coupling between the incorporated RuDCBPY chromophores. The RuDCBPY incorporated in the MOF are locked into a specific geometry dictated by the crystal structure of the UiO framework. Such preferential orientation of chromophores enables dipole alignment, stronger dipole-dipole coupling, and longer range energy transfer.

To further probe the two-state hypothesis, a post-synthetic approach was used to incorporate the transition metal complex directly into the backbone of UiO-67 MOF *in situ*, forming the iso-structural MOF termed RuDCBPY-UiO-67-DCBPY.⁵³ The post-synthetic method removes the potential for an encapsulated emissive RuDCBPY and indeed, the fast lifetime component observed previously was not present in the photophysics of RuDCBPY-UiO-67-DCBPY. Thus, further evidence for the two-state model was provided. That said, the emission decay of RuDCBPY-UiO-67-DCBPY was dramatically quenched at low dopant concentrations. To explore the origin of such behavior the data was fit to the Klafter and Blumen model, which indicated concentration-dependent dimensionality to the observed RET. At low loading of RuDCBPY ($< 10 \text{ mm}$), RET was one-dimensional. At concentrations between ~ 10 and $\sim 50 \text{ mm}$, the RET was two-dimensional. And at a concentration above 50 mm at which point a percolation limit was met, the RET was then three-dimensional. The cartoon representation of concentration-dependent dimensionality is shown in Figure 23 and was confirmed through confocal microscopy studies.

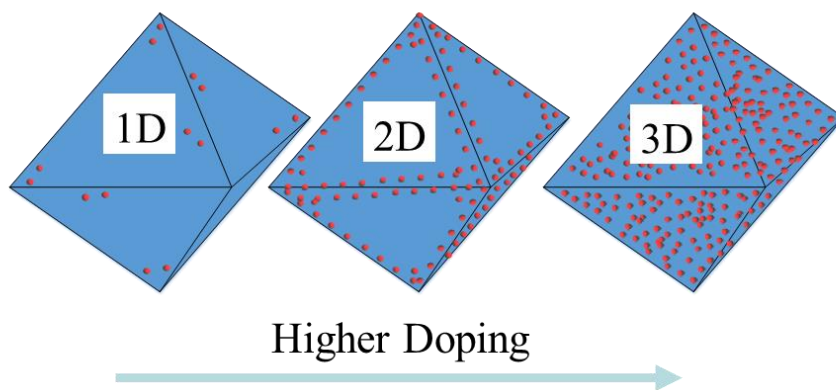


Figure 23. The assumption of FRET mechanism on dependence of RuDCBPY loading. Reprinted from Ref.53 with permission from American Chemical Society.

3.3 Summary

Comparison between the photophysical behavior of $\text{Ru}(\text{bpy})_3^{2+}/\text{Os}(\text{bpy})_3^{2+}$ chromophores in homogeneous solution to those incorporated or encapsulated in MOFs provide insight into the effects of scaffolding on observed behavior. The work summarized here provides some critical information regarding ET in MOFs that can be used as design principles for further study:

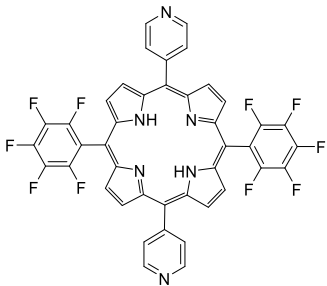
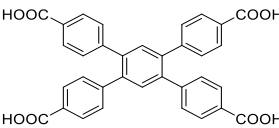
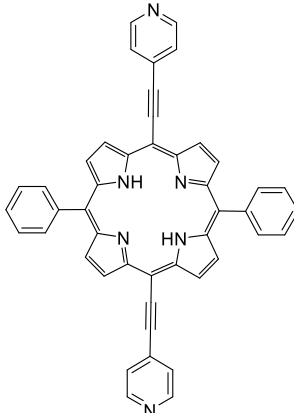
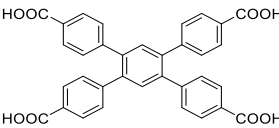
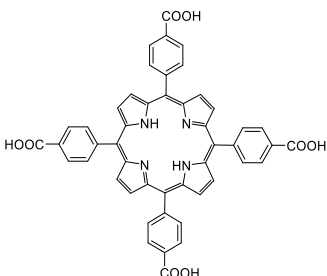
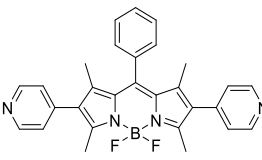
- The lifetime of chromophores can be significantly increased through either incorporation or encapsulations into MOF scaffolds. This results from a decrease in the vibrational freedom of the molecule. Thus, non-radiative pathways for energy dissipation are attenuated and both lifetime and quantum yield enhanced.
- The structure of the MOF plays a critical role in the efficiency of energy transfer. Inter-chromophore distance should be minimized to enable stronger Dexter coupling between the $^3\text{MLCT}$ states responsible for ET.
- The synthetic approach – one-pot vs. post-synthetic – results in isostructural materials with potentially vastly differing photophysics.
- Finally and perhaps most importantly, MOF incorporation or encapsulation leads to chromophore alignment enabling long-distance ET.

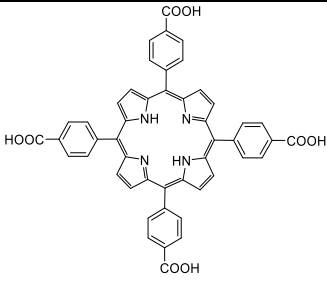
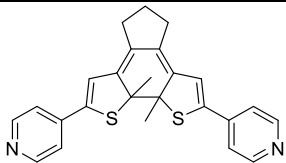
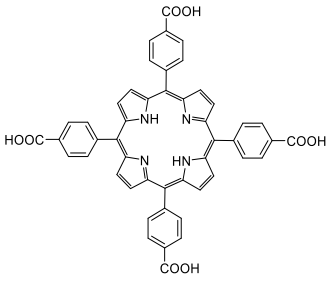
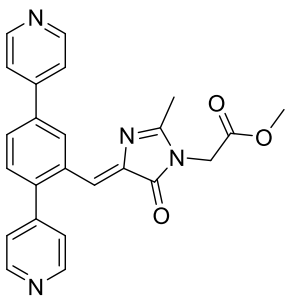
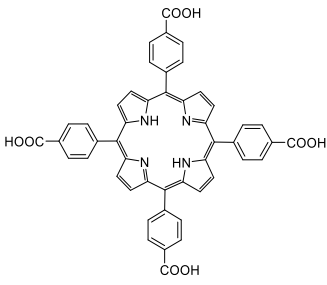
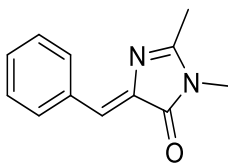
4. Porphyrin and metalloporphyrins based MOFs materials

Porphyrins and their derivatives are a class of well-known molecular chromophores that typically have strong light absorption in the UV-visible region of the electromagnetic spectrum. Indeed, porphyrins have been widely utilized in MOFs designed for solar harvesting applications.⁹ Table 3 summarizes the porphyrin-based MOFs that have been reported in the literature.

Table 3. Summary of MOFs containing porphyrin-based ligands

MOF	Chemical Formula	Porphyrin based Ligand Structure	Co-ligand/Guest	Ref

F-MOF		<p>F-H₂P =</p> 		[56]
DA-MOF		<p>DA-H₂P</p> 		[56]
BOP MOF	C ₇₇ H ₄₉ BF ₂ N ₈ O ₉ Zn ₃	<p>TCPP =</p> 		[57]
[Zn ₂ (ZnTCPP)(BPMT) _{0.85} (DEF) _{1.15}]		<p>TCPP =</p>	<p>BPMT=</p>	[58]

				
DBP-PI-1 DBP-PI-1'	$[\text{Zn}_2(\text{ZnTCPP})(\text{DPB-BI})_{0.86}(\text{DMF})_{1.14}] \cdot (\text{DMF})_{8.86}(\text{H}_2\text{O})_{20}$ $[\text{Zn}_2(\text{ZnTCPP})(\text{DPB-BI})_{0.64}(\text{DEF})_{0.36}] \cdot (\text{DEF})_{6.94} \cdot (\text{H}_2\text{O})_{12.55}$	TCPP = 	DPB-BI = 	[59]
BI@2	$\text{Pb}_2(\text{TCPP}) \cdot 4\text{DMF}$	TCPP = 	BI = 	[59]

4.1 Porphyrin-based MOFs as crystalline powders

In natural photosynthesis, energy (exciton) migration primarily occurs in highly ordered porphyrin-like pigments (chlorophylls). Hupp, Wiederrecht, Farha and their co-workers designed two Zn-porphyrin based MOFs (DA-MOF and F-MOF) to mimic the light-harvesting behavior of natural photosynthetic systems (Figure 24).⁵⁶ Photo-generated exciton migration was investigated based on fluorescence quenching experiments and theoretical calculations. Pyridyl-ferrocene, FcPy, was incorporated in the MOF through axial coordination to the porphyrinic linkers

(Figure 26). Concentration-dependent studies of the effect of FcPy on the emission lifetime allowed for characterization of the ET processed. In F-MOF, a photo-generated exciton only migrates over a net distance up to ~ 3 porphyrin struts (8 hops) within its lifetime. Remarkably for DA-MOF, the exciton migrates up to ~ 45 porphyrin struts (2025 hops) with a high anisotropy along a specific direction. This implied that the molecular structure of the porphyrins plays a significant role in exciton hopping. As shown in Figure 25, the addition of two acetylene moieties in the porphyrin molecule enhances the π -conjugation in DA-H₂P ligand, which leads to higher absorption and red-shifted of Q-band, better absorption/emission overlap, greater dipolar coupling and much faster exciton hopping compared with the F-ZnP ligand. DA-MOF provided the first example of long distance and directional energy migration in MOF materials and afforded useful guidelines for the development of efficient ligand-harvesting and energy-transport materials.

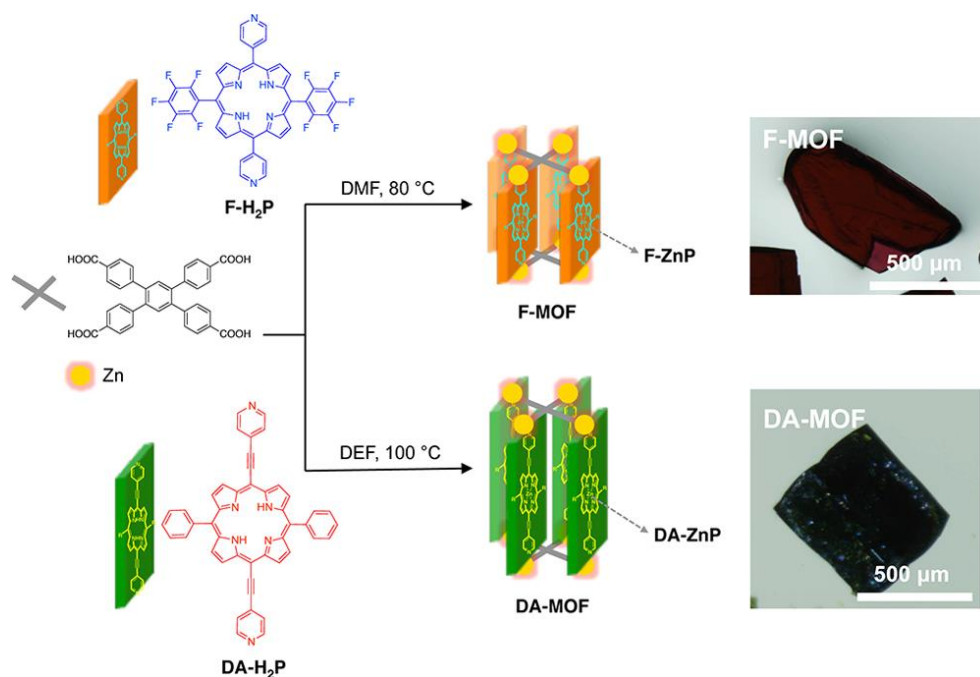


Figure 24. Synthesis Routes of the Isostructural DA-MOF and F-MOF Compounds. Reprinted from Ref.56 with permission from American Chemical Society.

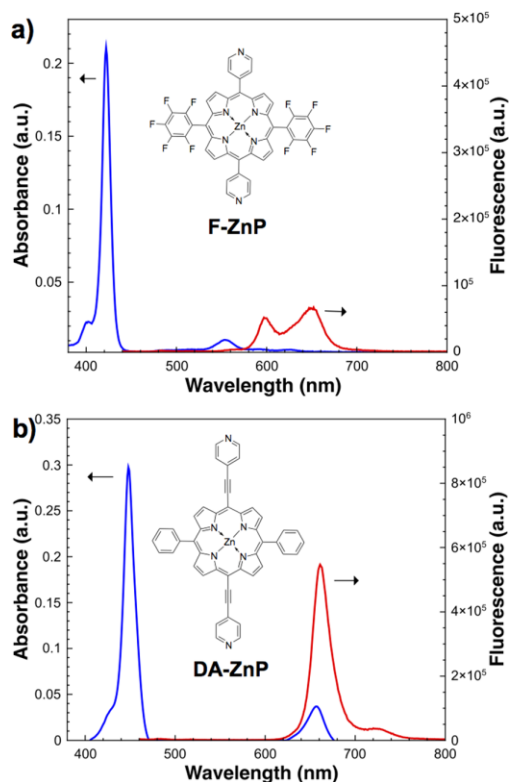


Figure 25. UV-vis absorption (blue) and emission (red) spectra of F-ZnP (a) and DA-ZnP (b) molecules in DMF. Their chemical structures are shown in the inset. Reprinted from Ref.56 with permission from American Chemical Society.

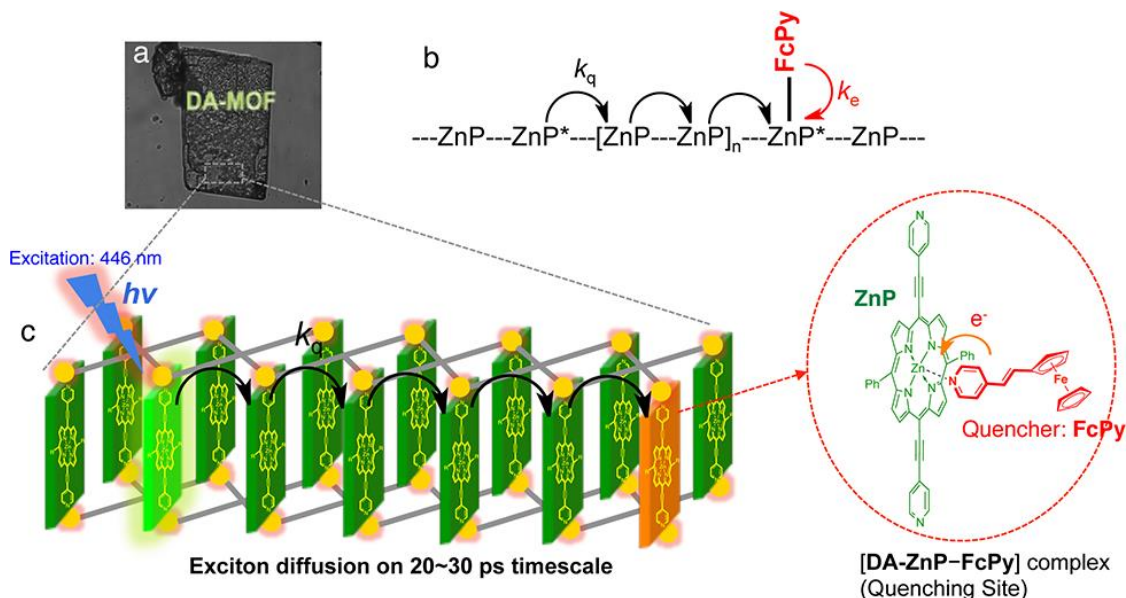


Figure 26. (a) Photograph of a DA-MOF particle from which fluorescence is recorded based on laser excitation at 446 nm. Luminescence quenching measurements are conducted to probe the energy (exciton) migration dynamics. (b,c) Schematic representation of the exciton migration and quenching processes. Reprinted from Ref.56 with permission from American Chemical Society.

Hupp and co-workers also explored energy transfer in mixed porphyrin donor-acceptor MOFs, similar to the studies of Lin and Meyer with Ru/Os MOF assemblies. In BOP MOF, boron dipyrromethene (bodipy) and tetracarboxyphenylporphyrin complementary chromophore pairs formed a pillared-paddlewheel type MOF (Figure 27).⁵⁷ The complementary absorption spectra of the chromophores enables panchromatic absorption over the visible region of the electromagnetic spectrum, such that the BOP MOF crystals appear black to the eye. Excitation at 543 nm of the control MOF, BOB MOF, formed with bodipy and 1,4-dibromo-2,3,5,6-tetrakis(4-carboxyphenyl)benzene, results in typical bodipy fluorescence behavior with the emission maxima at 596 nm (Figure 28). Excitation of same strut in BOP MOF at 543 nm is emissive in the 650-710 nm range. Thus, the bodipy linkers served to absorb light and funnel the excited energy to the porphyrinic struts via ET, akin to the antenna effect previously discussed for Ln³⁺ MOFs.

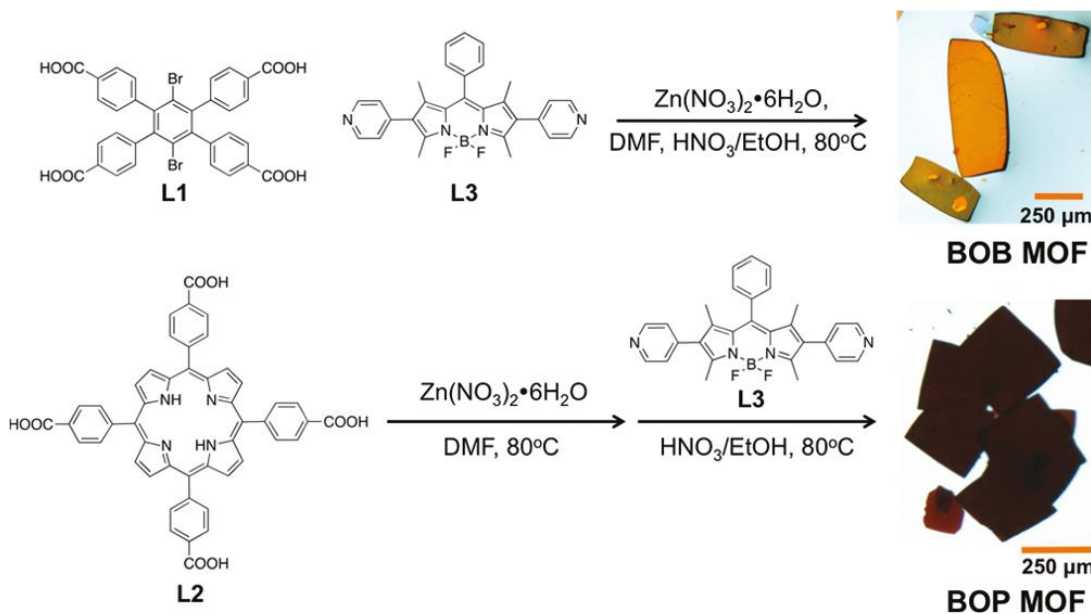


Figure 27. Synthesis of the Isostructural BOB MOF and BOP MOF. Reprinted from Ref.57 with permission from American Chemical Society.

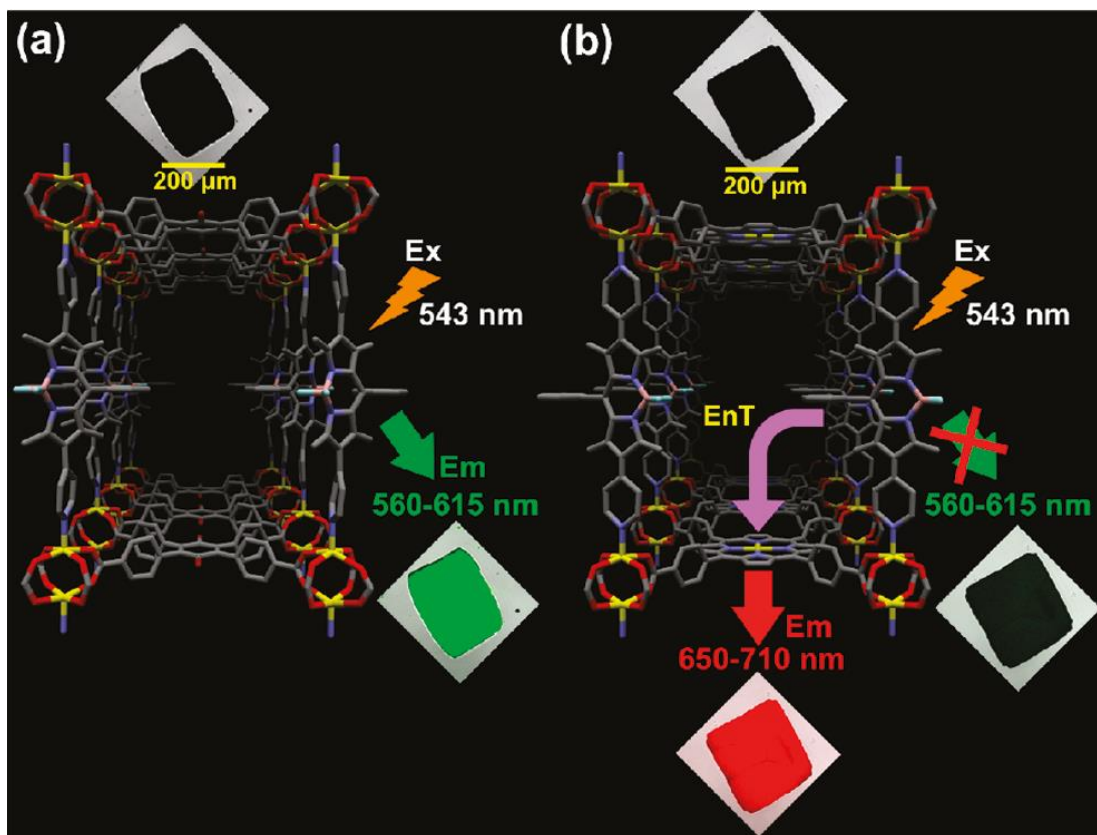


Figure 28. Confocal laser scanning microscopy (CLSM) images of crystals of: (a) BOB MOF and (b) BOP MOF. Reprinted from Ref.57 with permission from American Chemical Society.

As an extension of mixed porphyrin linker approach, the Shustova group explored turn-on, turn-off ET in a mixed diarylethene/porphyrin MOF, $[\text{Zn}_2(\text{ZnTCPP})(\text{BPMT})_{0.85}(\text{DEF})_{1.15}]$.⁵⁸ Diarylethene is a photochromic switch that under UV excitation exhibits a “closed” arrangement and absorbs broadly from 425-700 nm. Upon visible light excitation, the switch “opens” to a form that only absorbs in the UV region of the electromagnetic spectrum. Due to this change in absorption behavior, Shustova postulated that in the closed form the diarylethene would act as a sufficient energy transfer acceptor and quench the porphyrin emission. However, in the open form, which has very poor spectral overlap with the emission spectrum of the porphyrin strut, ET would not occur. Upon MOF incorporation, the diarylethene derivative, BPMT, maintained its photo-switchable behavior and indeed, directed the excited-state decay pathway of the

host. Specifically, the porphyrin-based linker acts as the donor and transfers excitation energy to the acceptor BPMTc (Figure 29). Irradiation of the MOF at 365 nm led to the “closed” form of BPMTc, which quenched the photoluminescence of the MOF through FRET with an estimated R_0 (Föster radius) of ~ 30 Å. When irradiated at 590 nm, BPMTc isomerization to the open form successfully eliminates the ET pathway and the PL response of the porphyrin was observed.

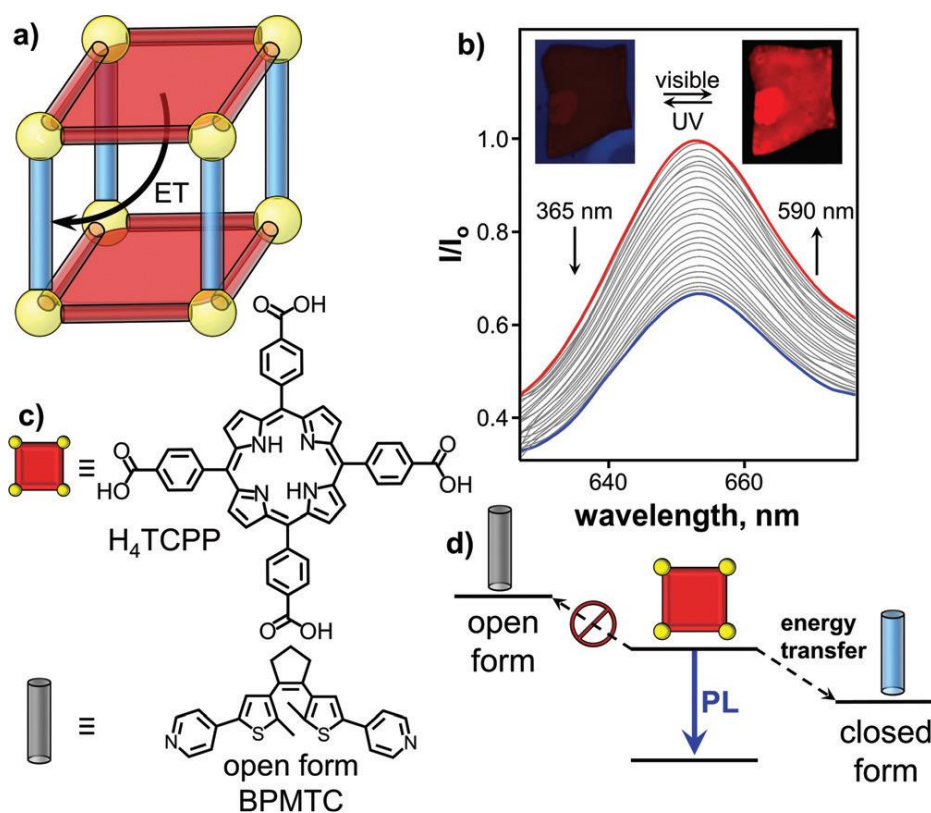


Figure 29. a) Förster ET between porphyrin-based ligand and photochromic BPMTc inside the MOF matrix. b) Emission spectra recorded for the porphyrin photo-switch MOF, scaled to give intensity (I_0) of 1.0 on the first scan at $\lambda_{ex}=590$ nm. The inset shows the epifluorescence microscopy images of the photo-switchable MOF crystal. c) Porphyrin-based donor and BPMTc acceptor (the latter is shown in the open form). d) A simplified diagram demonstrating the transitions responsible for fluorescence and FRET. Adopted from Ref.58 with permission from American Chemical Society.

Harkening back to the bio-inspired nature of porphyrin light harvesters, the Shustova group extended their mixed ligand MOF studies to explore a MOF mimic of a highly efficient ET process observed between green fluorescent protein and a

heme-binding cytochrome. Two approaches to explore ET in a MOF mimic were explored including (1) direct incorporation of the donor and acceptor species as the linkers in a 3D framework and (2) the encapsulation of the donor in the pores of the MOF, termed BI@2 (Figure 30). Two unique MOFs with the donor (BI = 4-hydroxybenzylideneimidazolinone) and acceptor (tetracarboxyphenylporphyrin) incorporated into the backbone were achieved upon changing the solvothermal reaction conditions, $[\text{Zn}_2(\text{ZnTCPP})(\text{DPB-BI})_{0.86}(\text{DMF})_{1.14}] \cdot (\text{DMF})_{8.86}(\text{H}_2\text{O})_{20}$ (**1**) and $[\text{Zn}_2(\text{ZnTCPP})(\text{DPB-BI})_{0.64}(\text{DEF})_{0.36}] \cdot (\text{DEF})_{6.94} \cdot (\text{H}_2\text{O})_{12.55}$ (**1'**).⁵⁹ All three materials (**1**), (**1'**), and BI@2 showed efficient energy transfer indicated by the complete disappearance of donor emission. Combining the time-resolved PL studies with spectral overlap function calculations, quantitative values of ET efficiency Φ_{ET} , ET rate constant, k_{ET} , and the Förster radius were determined and summarized in Table 4. Although, the efficiency of energy transfer did not match that of the protein pair, the Φ_{ET} BI@2 was 72%. There were slight differences between the photophysical behaviors of (**1**) and (**1'**), which was attributed to the differences in interlayer stacking observed via single crystal X-ray diffraction.

Table 4. The amplitude-weighted average lifetimes (τ_{av}), ET rate constants (k_{ET}), Förster critical radii (R_0), ET efficiency (Φ_{ET}), and spectral overlap functions (J) for DPB-BI, DPB-BI-1, DPB-BI-1', BI, and BI@2 samples. Reprinted from Ref.59 with permission from Wiley Online Library.

	DPB-BI	DPB-BI-1	DPB-BI-1'	BI	BI@2
$\langle \tau_{av} \rangle$ [ns] ^[a]	1.09	0.38	0.51	1.89	0.53
k_{ET} [$\times 10^{10} \text{ s}^{-1}$]	–	1.71	1.04	–	1.36
R_0 [Å]	–	23	23	–	21
Φ_{ET} [%]	–	65	53	–	72
J [$\times 10^{-14} \text{ cm}^3 \text{ M}^{-1}$]	–	6.25	6.25	–	4.57

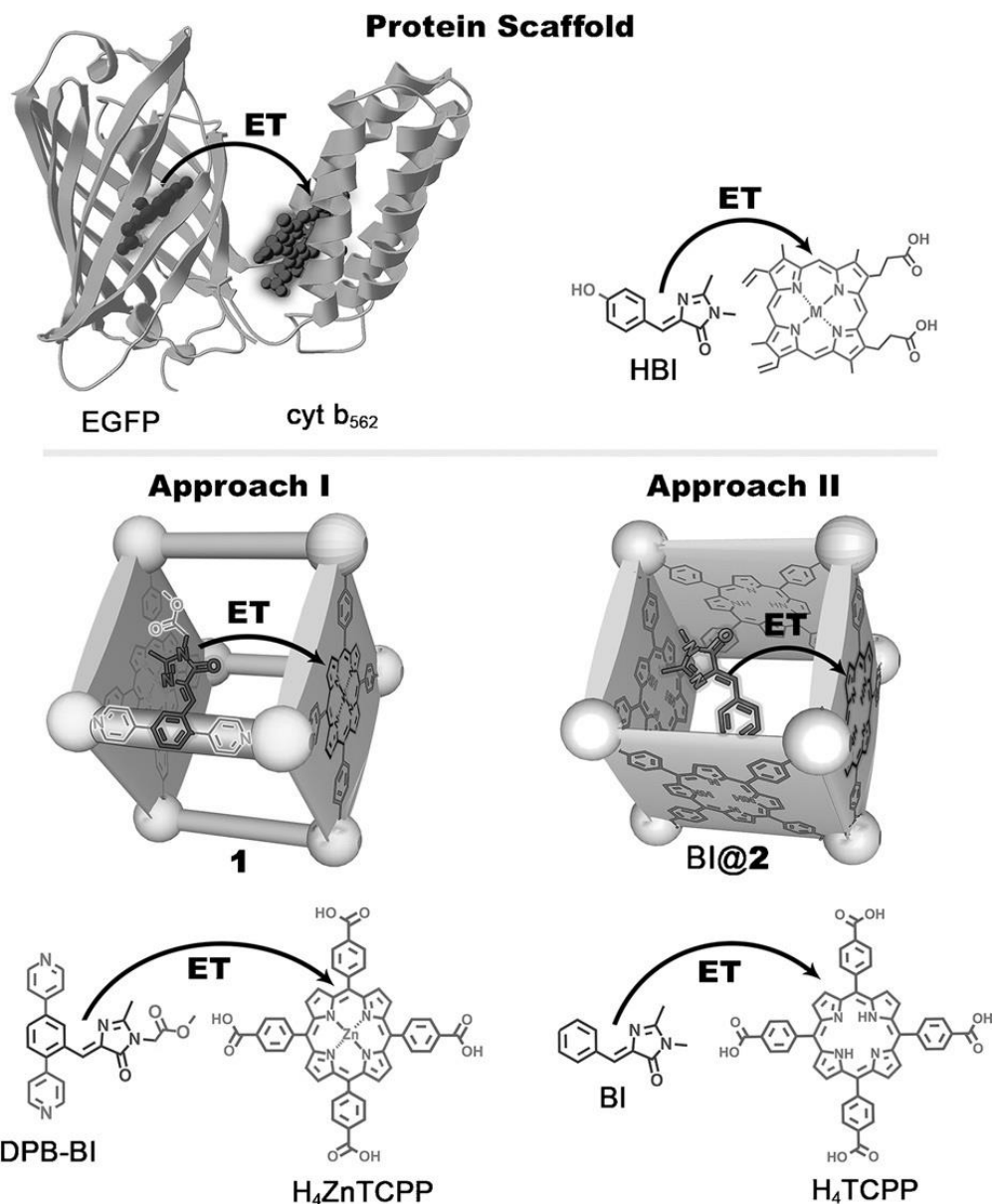


Figure 30. (Top) Representation of ET between the two coupled chromophore cores of a green fluorescent protein variant (EGFP) and the electron-transfer protein, cytb₅₆₂. (bottom) Approaches I and II involved incorporation of chromophores with HBI- and porphyrin- based cores inside the rigid scaffold. Approach I focused on coordinative immobilization of both chromophores in crystalline scaffolds 1 and 1' while Approach II is based on inclusion of the BI donor in the porphyrin-based framework 2. Reprinted from Ref.59 with permission from Wiley Online Library.

4.2 Porphyrin-based MOFs as thin films

After mimicking the light harvesting in the natural photosystem using highly ordered porphyrin chromophores in MOFs, the next challenge is how to direct

excitation-energy funneling along a predesigned pathway. One attractive strategy is to build an energy transfer cascade through the use of a series of chromophores built into MOFs as struts or pillars via layer-by-layer assembly. The aforementioned photophysics, including long range ET up to 45 porphyrin units makes porphyrins ideal candidates for thin film assemblies of this nature. Preferably, the designed MOF thin-films should meet certain criteria for practical application:

1. The thickness of films should be able to be precisely controlled by synthetic approach.
2. Directed exciton migration should be achieved with high efficiency and fast ET rate.
3. The exciton propagation distance should meet or exceed the MOF film thickness in order to move the exciton toward either an underlying electrode or external redox phase.

Following the study of DA-MOF in the powder form, So *et al.* grew DA-MOF as thin films on functionalized surfaces using layer-by-layer (LBL) approach.⁶⁰ The thickness of the film increased systematically with the number of assembly cycles. Polarization excitation and fluorescence measurements indicated that the porphyrin units are preferentially oriented in the MOF film. A far-red emitting squaraine dye (S1), which exhibits a high overlap integral with the DA-MOF, was deposited onto the surface of the MOF film. Exclusive emission from S1 was observed following selective excitation of Zn-porphyrin units in a 50-cycle film (Figure 31). These results suggest that the films can be used as antennae for light harvesting and efficient Förster energy transfer is possible within the film, considering the long-distance exciton propagation.⁹

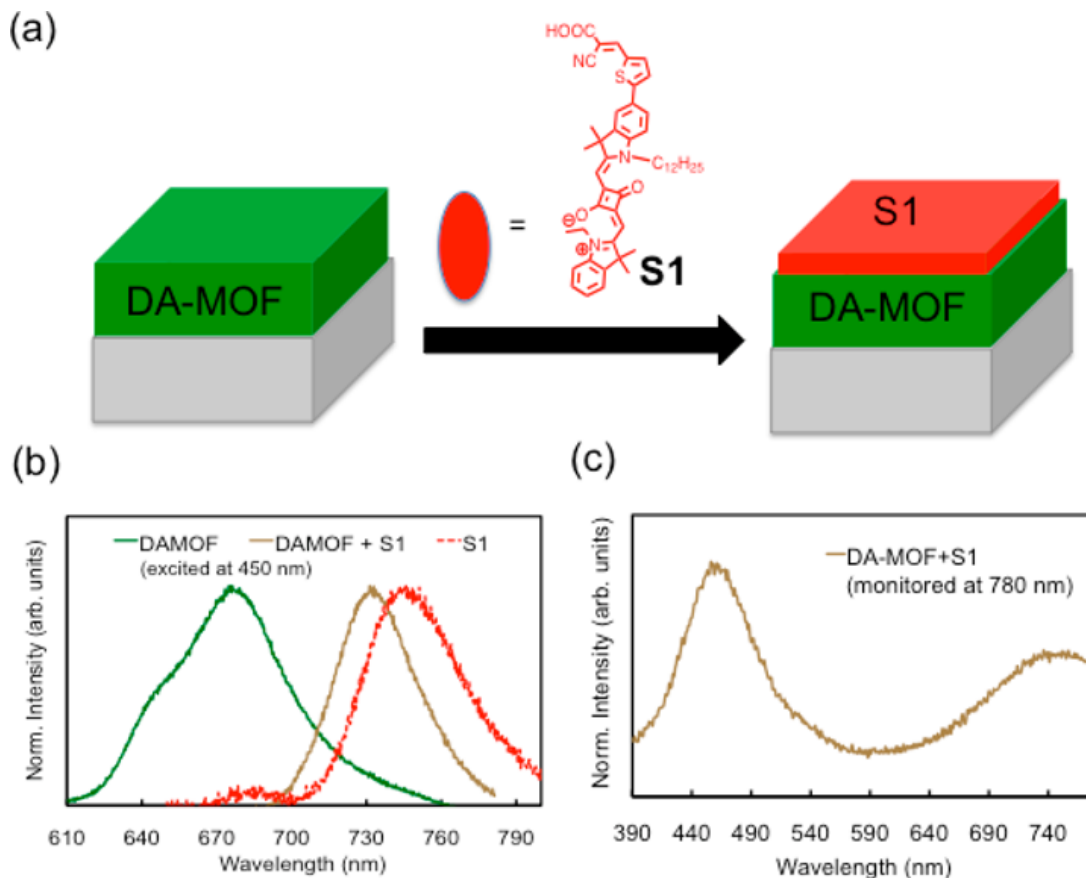


Figure 31. (a) Schematic diagram of preparation of sensitized DA-MOF film. (b) Comparison of emission profiles of DA-MOF (green solid), S1 (red solid), and DA-MOF sensitized with S1 (light-green dotted) upon excitation at 450 nm. (c) Excitation profile of the DA-MOF+S1 film monitored at 780 nm, where the emission from DA-MOF is negligible. Reprinted from Ref.60 with permission from American Chemical Society.

In order to increase the interlayer exciton hopping efficiency along the direction perpendicular to the substrate, Hupp's group converted a pillared paddlewheel porphyrin containing 3D MOF thin film to a 2D framework by solvent-assisted linker exchange (SALE).⁶¹ As shown in Figure 32, the pillar ligand 4,4'-bipyridine was replaced by non-bridging ligand pyridine, leading to the collapse of the 3D MOF structure to a layered 2D coordination polymer. The distance between inter-layer chromophores significantly decreased due to the structural change, which resulted in enhanced energy transfer through the 2D MOF film. Pd-TCPP (P2) was used as an efficient, non-fluorescent energy acceptor (quencher) sited at the

terminus of the film. Steady-state emission spectroscopy combined with time-resolved emission spectroscopy indicated that excitons can travel through about 9-11 porphyrin layers in the 2D films whereas, in the 3D films, exciton propagation only occurs through 6-8 chromophore layers. Considering the effective elimination of void space between porphyrin layers by SALE, one would expect a decrease in donor-acceptor separation distance, r , which should result in an enhancement in exciton migration through the 2D MOF films, from the simplest Förster energy transfer theory consideration. However, SALE-induced MOF collapse is accompanied by the lateral shifting of alternating 2D layers, which resulting in a non-ideal porphyrin-porphyrin configuration from the perspective of the dipole-dipole coupling. Therefore, future direction for this strategy should focus on extending exciton propagation by diminishing chromophore interlayer spacing without also affecting the chromophore alignment and dipole-dipole coupling as a consequence.

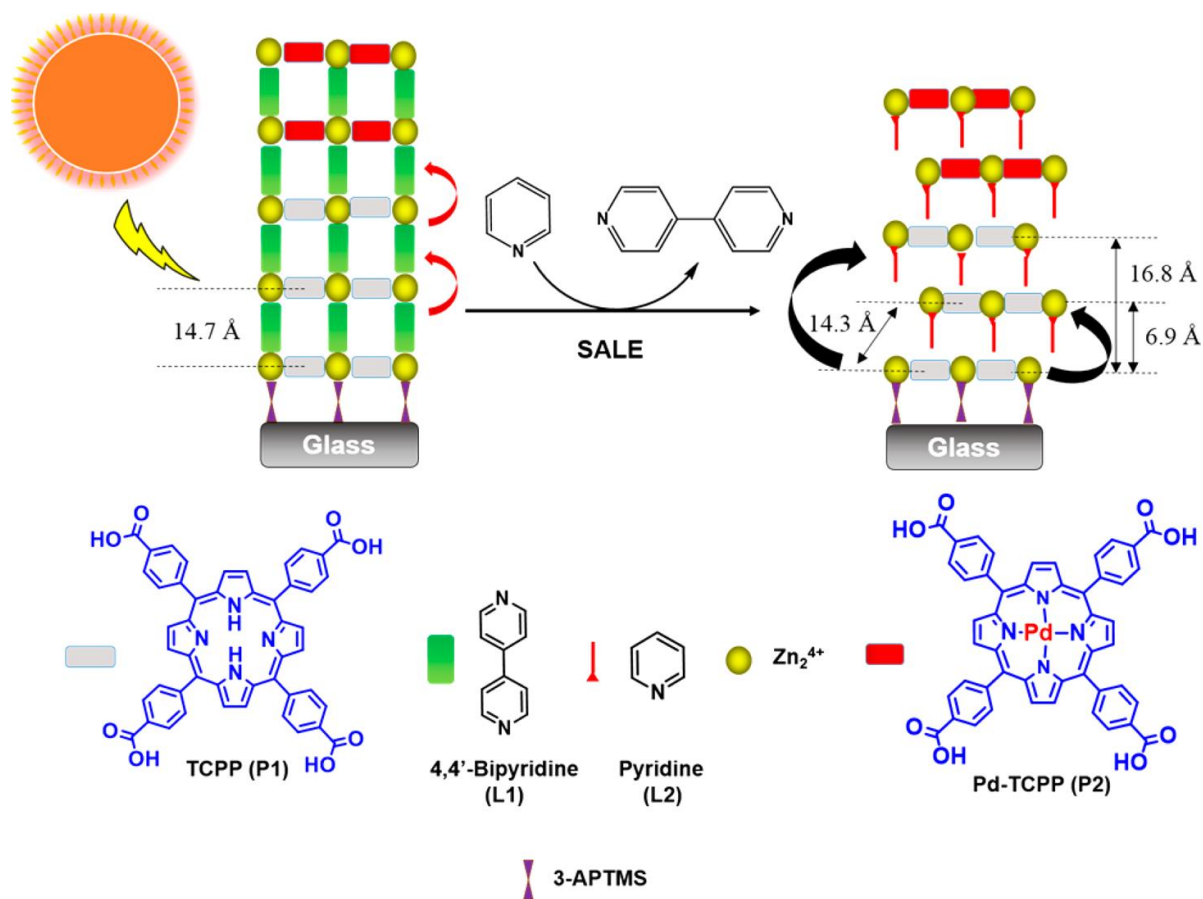


Figure 32. Free-base porphyrin P1 and linker L1 were used to fabricate N (number of cycles) cycles of MOF thin films followed by N + 1 and N + 2 cycles by palladium porphyrin P2 and linker L1. Reprinted from Ref.61 with permission from American Chemical Society.

4.3 Summary

The use of porphyrin linkers in MOF assemblies not only mimics the molecular speciation of natural systems but also provides a scaffold for 3D control of orientation similar to the protein environment. While the pioneering examples here do not directly match the efficiency of biological approaches, critical information has been gained to guide future study:

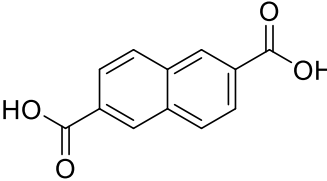
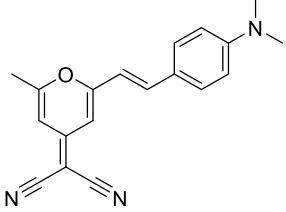
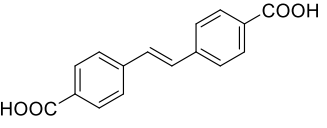
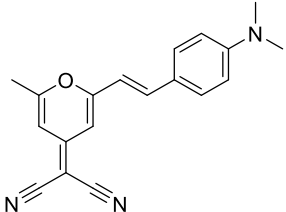
- Long-range energy transfer comprised of approximately 2000 hops can be achieved between porphyrin chromophores.
- The inter-porphyrin spacing is critical to efficient energy transfer. Indeed, a factor of 2 in terms of number of hops can be achieved by collapsing parent MOF structures.

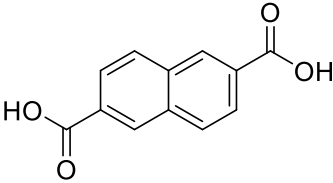
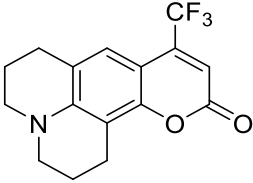
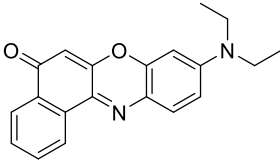
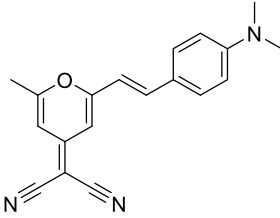
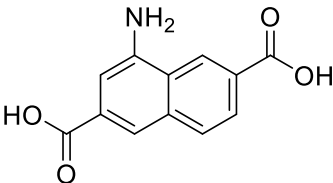
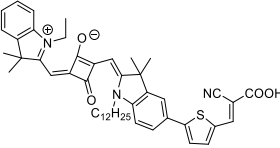
- Photo-isomerizable linkers can be used as molecular switches to turn-on and turn-off photoluminescence via ET quenching.
- Layer-by-layer thin films of MOFs can result in efficient ET cascade assemblies, providing the potential for directional ET and charge separation at interfaces.

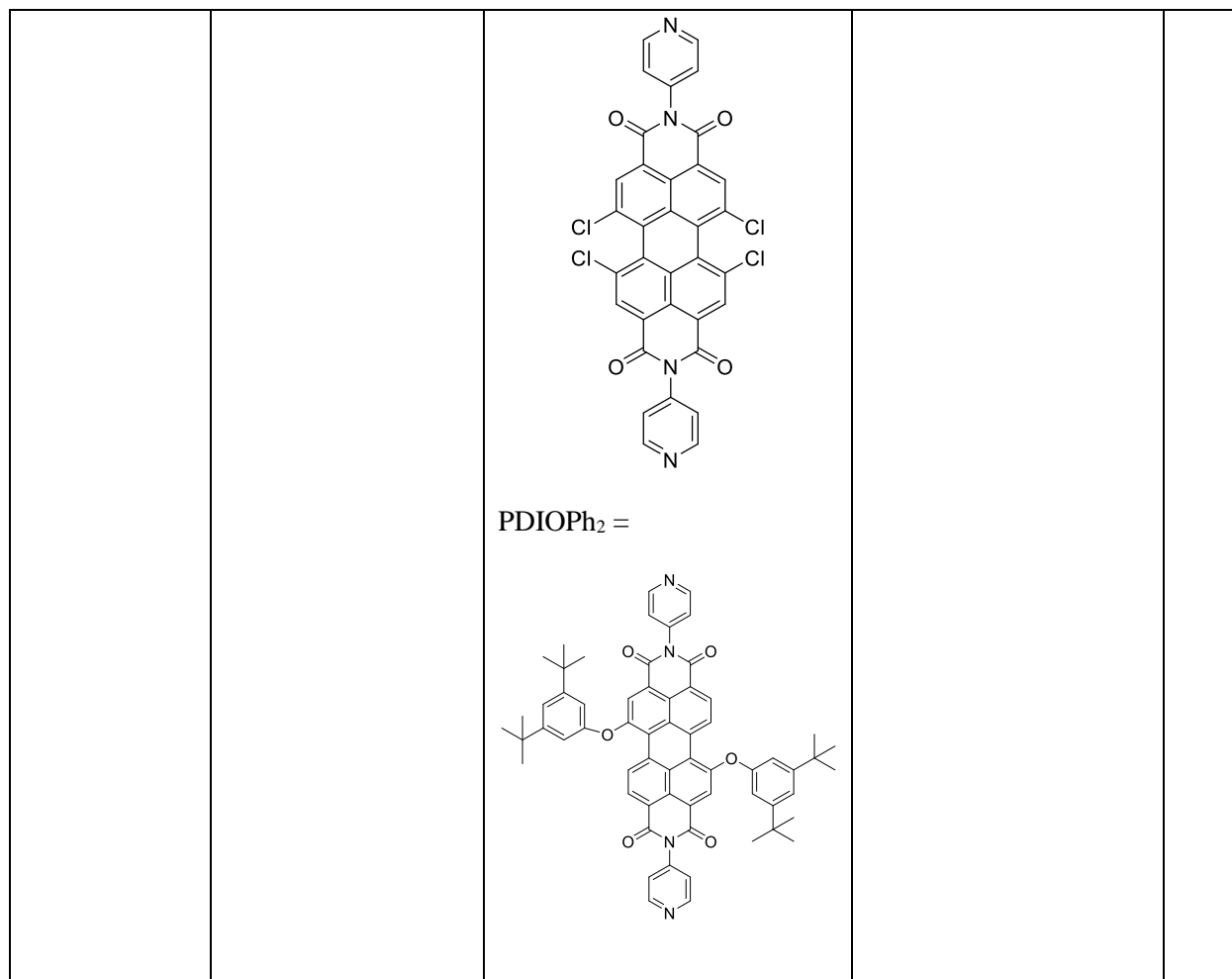
5. Non-Porphyrinic, Organic Chromophore -based MOFs

Organic chromophores such as naphthalene, stilbene, and perylene diimides have also been used to study ET in MOF materials. Using different chromophores as ligands to construct hetero-linker MOFs or assembling chromophore guests with MOF as host matrices are two common approaches that have been reported. Table 5 summarizes the reported MOFs that contain ligands based on organic chromophores.

Table 5. MOFs constructed from ligands containing organic chromophores

MOF	Chemical Formula	Ligand Structure	Guest	Ref
DCM@IRMOF-8	$Zn_4O(C_{12}H_6O_4)$		DCM = 	[62]
DCM@stilbene-MOF	$Zn_4O(C_{16}H_{10}O_4)_3$		DCM = 	[63]
Zr-NDC	$Zr_6O_4(OH)_4(C_{12}H_6O_4)_6$	NDC =	C153 =	[64]

			 NR =  DCM = 	
Zr-NADC	$Zr_6O_4(OH)_4(C_{12}H_6O_4)_6$ $\cdot x(C_{12}H_7NO_4)_x$	NADC = 		[65] [66]
MOF-like thin films		PDICl ₄ =	S1= 	[67]



Yan and coworkers reported the incorporation of a laser dye, 4-(dicyanomethylene)-2-methyl-6-(4-dimethylaminostyryl)-4H-pyran (DCM), into stilbene-based and naphthalene-based (IRMOF-8) MOF systems (Figure 33).⁶² The resulting materials exhibit blue/red two color emission, corresponding to the MOF emission and DCM emission, respectively. Probed by 3D confocal fluorescence microscopy, the intensity ratio of blue to red fluorescence varies in different planes within the MOF single crystals (Figure 34). The ratio is a function of the different degrees of energy transfer between the MOF hosts and guest molecules due to the non-uniform distribution of DCM within the MOF matrix. The population of DCM molecules is highest at the edges of the MOF crystallites, thus the energy transfer from the host matrix to DCM is more effective in those regions. DFT calculations

also indicate that host-guest energy transfer occurs for two the DCM@MOF systems. Moreover, the luminescence response of the DCM@MOF systems is sensitive to volatile organic solvents (methanol, acetone and toluene), in that both the emission wavelength and the intensity ratio of blue to red emission vary after exposure, showing that the materials have potential applications in the fabrication of luminescent sensors.

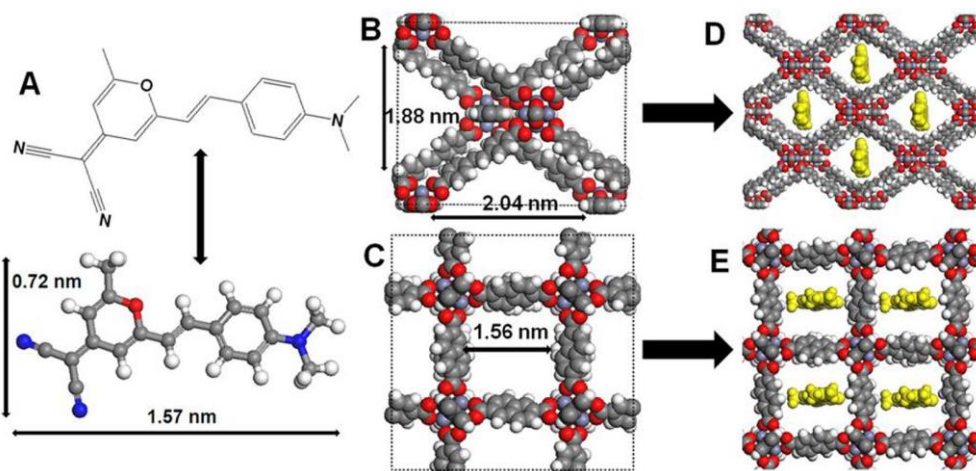


Figure 33. Incorporation of DCM guests into the nano-channels of MOFs. (A) The molecular structure of DCM; the host structures of stilbene-MOF (B) and IRMOF-8 (C); the schematic host-guest structures of DCM@stilbene-MOF (D) and DCM@IRMOF-8 (E). Reprinted from Ref.62 with permission from Nature.

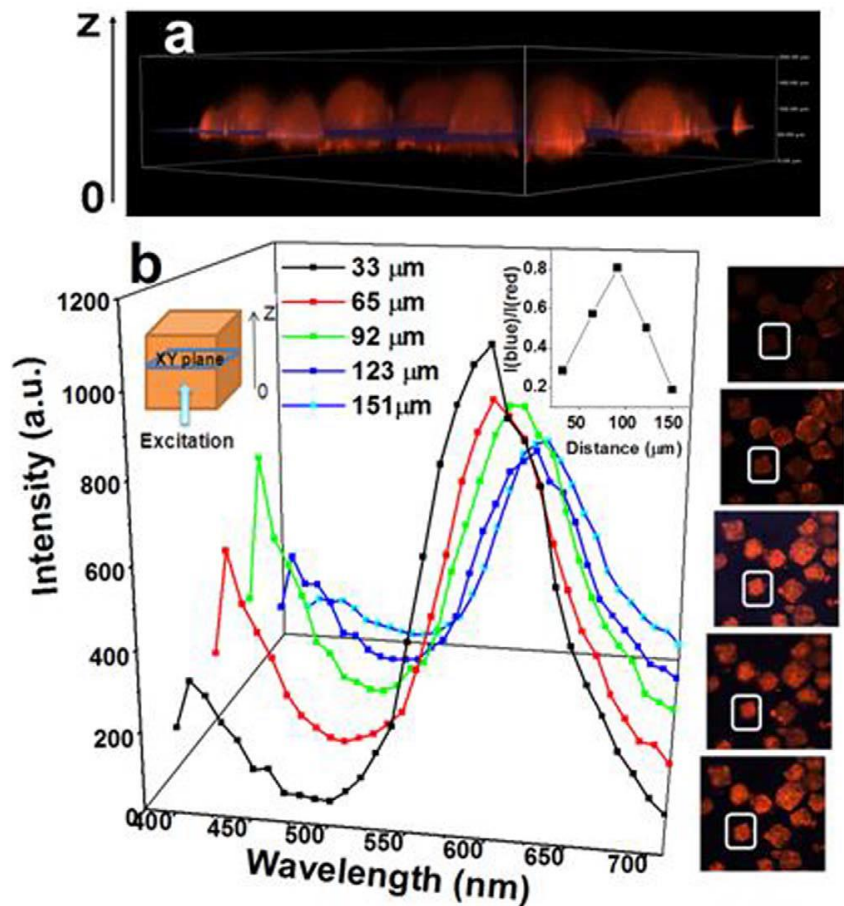


Figure 34. (a) 3D fluorescence image of the selected single crystal MOFs; (b) the two-color fluorescence spectra and intensity ratios of blue to red emission (inset) of an individual DCM@stilbene-MOF single crystal (outlined by the white color in the inset of b) in different xy-planes based on z-axis scanning. Inset photographs show the fluorescence images in focal planes at different distances (33, 65, 92, 123, and 151 μm) from the excitation laser (372 nm). Reprinted from Ref.62 with permission from Nature.

A more comprehensive study to probe the ET between MOF host with dye guest molecules has been reported by Douhal *et al.*⁶³ Three different laser dyes, Coumarin 153 (C153), Nile Red (NR) and DCM, were trapped into a Zr-naphthalene dicarboxylic acid (Zr-NDC) MOF. By trapping these dyes into the Zr-NDC porous structure, the emission of the dye@MOF materials can be tuned due to energy transfer photo-events. For example, encapsulating C153 or NR, the original blue emission from MOF could be changed to green (C153) or red (NR). Moreover, the white-light-emitting composite materials can be obtained by simultaneously doping C153 and NR, or DCM, with quantum yields up to 41%.

The obtained white light has CIE coordinates (0.32, 0.34), which are very close to the ideal (0.33, 0.33). Additionally, the studies provided evidence for *in*-MOF excimer formation between MOF incorporated ligands. Excimers are dimeric species of interacting chromophore that when excited have drastically different photophysical behavior from their monomers, red-shifted absorption/emission and longer-lived emission lifetimes. In the case of NR and DCM, energy transfer to the encapsulated dyes occurs from MOF excimer states. However, for C153, only energy transfer from MOF monomers (electronically isolated ligands) to the dye was observed.

Douhal and Sánchez reported the spectral and dynamic properties of two Zr-based MOFs, Zr-2,6-naphthalenedicarboxylate (Zr-NDC) MOF and 4-amino-2,6-naphthalenedicarboxylate (Zr-NADC) MOF.⁶⁴⁻⁶⁶ They first observed intra-particle excimer formation between neighboring naphthalene organic linkers in a diluted Zr-NDC MOF suspension.⁶⁴ Excimer formation was reflected by a broad red-shifted band in the Zr-NDC emission spectrum and also by its dynamics composed of three components; $\tau_1 = 650$ ps (excimer formation process), $\tau_2 = 3.7$ ns (monomer lifetime) and $\tau_3 = 13.9$ ns (excimer lifetime). By increasing the polarity of the solvent, blue shifts in both the absorption and the emission spectrum were observed. Furthermore, the excimer formation time changed significantly from 490 ps in ACN to 840 ps in DCM. The authors attributed the solvent polarity dependent behavior to a breathing effect within the MOF structure induced by the filling of solvent. Such breathing would change the spacing between the chromophores and disrupt excimer formation. Interestingly, at higher concentrations of MOF particles in suspensions of THF, fs-dynamic studies showed an ultrafast inter-crystal excimer formation occurring in ~ 5 ps. The observation was attributed to the interaction between naphthalenes of closely associated MOF particles (Figure 35).

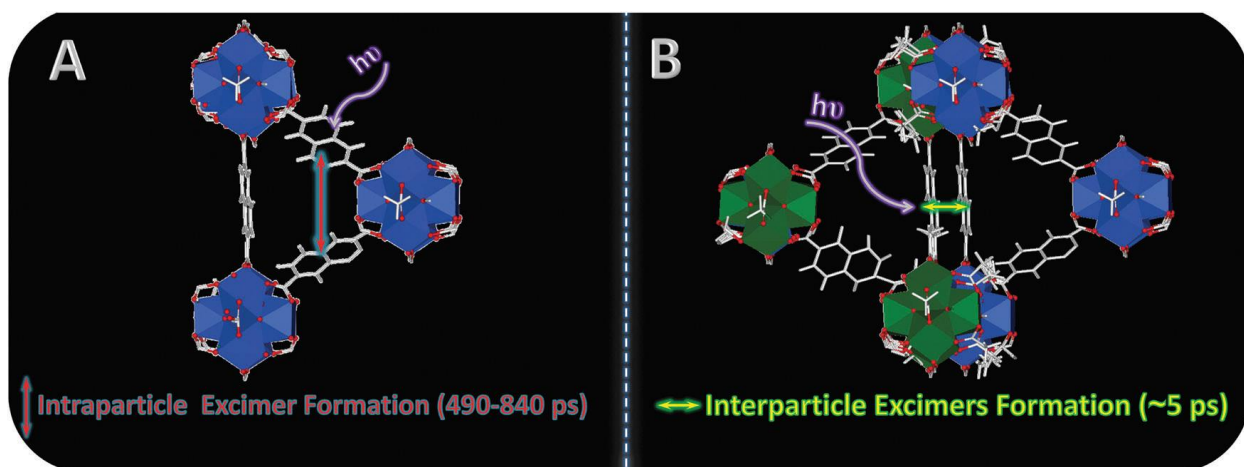


Figure 35. Representation of the excimer photo-formation in (A) diluted suspensions, due to the interaction between naphthalenes of the same MOF crystal and (B) concentrated THF suspension, owing to interactions between naphthalenes of closely associated MOF crystals. Reprinted from Ref.64 with permission from Royal Society of Chemistry.

A follow-up study constructed a Zr-NADC MOFs by using hetero-linker, a mixture of 2,6-naphthalenedicarboxylate (NDC) and 4-amino-2,6-naphthalenedicarboxylate (NADC). The fraction of NADC relative to NDC varied from 2% to 35% in these MOFs.⁶⁵ Increase percentages of NADC linkers in the MOF led to a decrease in the lifetime of NDC excimer formation, which can be explained by an increase in energy-transfer probability between NDC and NADC. Meanwhile, the emission intensity of NADC experienced a drop at the highest doping percentage in the MOF, mainly due to the ultrafast charge transfer assisted by the amino group. Specifically, at the lowest NADC doping concentration (2%), the photo-dynamics are similar to Zr-NDC, mainly dominated by NDC-excimer photo-formation. With increase of NADC linkers in Zr-NADC MOFs (5 and 10%), the lifetime of excimer is decreased because of higher probability for ET between NDC and NADC. For NADC fractions of 20 and 35%, we observed a very fast rise component (1.2 ps) in the emission signal due to the related ET between the hetero-linkers. These results showed that by using MOFs with hetero-linkers, it is possible to trigger and tune excimer formation and ET processes.

Extending their work on directional energy transfer in LBL thin films, Hupp and coworkers synthesized three-component LBL MOF-like thin films containing two perylenediimides (PDICl₄, PDIOPh₂) and a squaraine dye (S1).⁶⁷ As shown in Figure 36, 1,2,4,5-tetrakis(4-carboxyphenyl)benzene (L1) units as tetratopic linkers coordinate pairs of Zn(II) ions in paddlewheel fashion, and either (or both) N,N'-di(4-pyridyl)-1,7-di(3,5-ditert-butylphenoxy)-3,4,9,10-perylenetetracarboxylic diimide (PDIOPh₂) and N,N'-di(4-pyridyl)-1,6,7,12-tetrachloro-3,4,9,10-perylenetetracarboxylic diimide (PDICl₄) linkers serve as Zn(II)-ligating spacers/pillars between the L1-defined layers. The thickness of each layer with different building blocks can be precisely controlled through LBL assembly. Interestingly, the multicomponent MOF-like films can absorb light across visible light region and slightly beyond (350-750 nm) based on the functionalized perylenediimide- and squaraine-type chromophores. Due to the high spectral overlap and oriented transition dipole moments of the donor (PDICl₄ and PDIOPh₂) and acceptor (S1) components, directional long-range energy transfer from the bluest to reddest absorber was successfully achieved. The observed panchromatic absorption and cascade-type transport and delivery of molecular excitons over tens of nanometers to the film exterior have significant implications for the application in solar energy conversion.

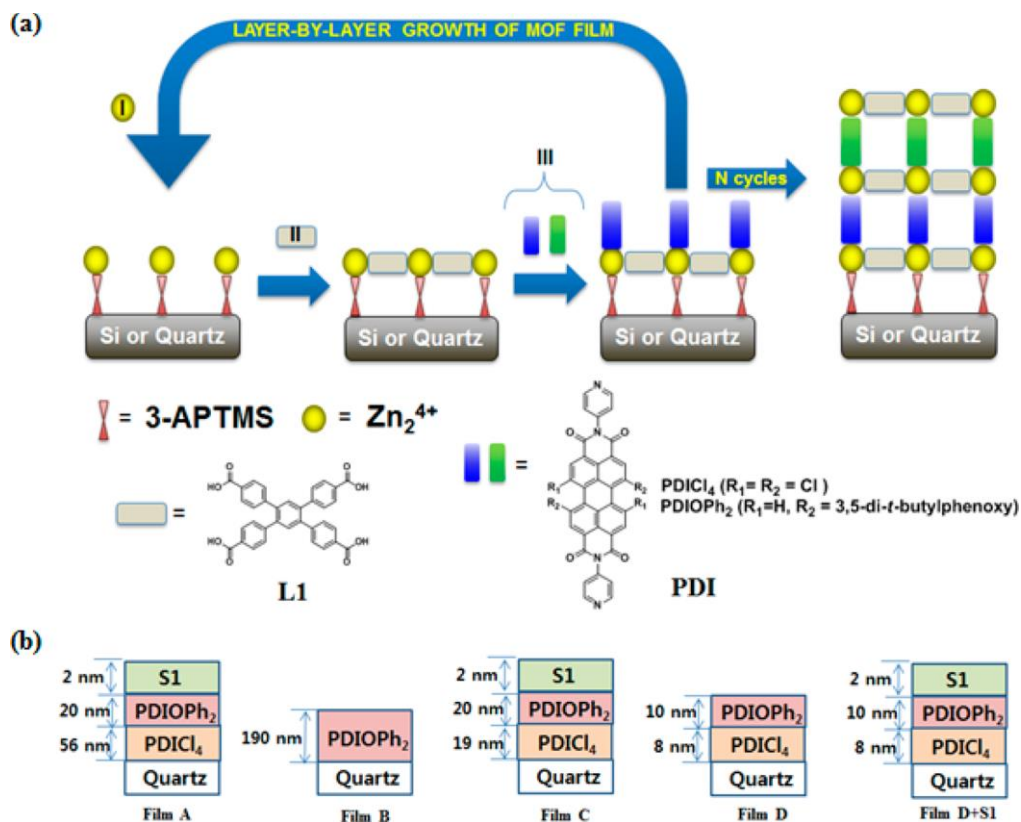


Figure 36. (a) Schematic diagram for sequential deposition of the MOF-like film via LBL assembly. Over N cycles, the thin MOF-like film is formed on silicon platform functionalized with 3-APTMS. Introduction of $\text{Zn}(\text{II})$ is followed by L1, and then PDICl_4 or PDIOPh_2 . Note that the bay positions of the PDI are functionalized with either chlorine or 3,5-di-*t*-butylphenoxy groups. (b) Prepared thin MOF-like films of film A, film B, film C, film D, and film D+S1. Reprinted from Ref.67 with permission from American Chemical Society.

5.1 Summary

While organic chromophores typically exhibit short lived excited states, they have still found utility in MOF energy transfer studies. Of particular interest is the work on *in*-MOF excimer formation and the effect on observed photophysics. There appears to be a moderate effect of encapsulation species on the formation of these excimers and further study is needed to uncover the guiding principles behind this phenomenon. Additionally, the use of perylenediimides led to the first example of a multi-component energy transfer cascade in MOF-like thin film assemblies.

6. Conclusions

The use of MOFs to manipulate ET photophysics is a relatively new field with immense potential. With the body of work summarized in this chapter, MOF energy transfer was applied to such fields as solid state light and displays, sensing, and light-harvesting with impressive results. The 3D orientation and structuring of chromophores leads to long-range energy transfer not exhibited in homogeneous solution. Couple this to the immense synthetic diversity of the chromophores that have been incorporated into MOFs and the tunable range of photophysical properties seems boundless. The fundamental studies described herein provide some guiding principles for future studies. For example, the effect of 3D structure on the ET rate is clear. Synthetic strategies to decrease chromophore spacing and increase dipole coupling should be explored. Additionally, energy transfer processes should be further exploited to produce panchromatic absorbers that exhibit directional ET. This may be accomplished through the extension of the pioneering LBL synthesis methods described herein. Of course, these three concepts ET distance, chromophore absorption, and directional ET are inextricably linked. Without long range ET, sufficient absorption within the critical distance may not be possible even with judicious choice of chromophores. Additionally, in constructing energy transfer cascades, the small changes required to promote transfer from one layer to another will ultimately effect the critical distance over which energy transfer can occur as well. The MOF community will need to play with this delicate balance to produce materials with applications in actual devices.

7. Reference

1. Atkins, P. W.; Friedman, R., *Molecular quantum mechanics*. Oxford University Press: 2011; p 537-537.
2. Schatz, G.; Ratner, M., *Quantum Mechanics in Chemistry*. Dover Publications, Inc.: 1993.
3. Tokmakoff, A., *Introductory Quantum Mechanics II*. 2009.

4. Greyson, E. C.; Vura-Weis, J.; Michl, J.; Ratner, M. A., Maximizing singlet fission in organic dimers: theoretical investigation of triplet yield in the regime of localized excitation and fast coherent electron transfer. *J. Phys. Chem. B* **2010**, *114* (45), 14168-77.
5. Parkhill, J. A.; Tempel, D. G.; Aspuru-Guzik, A., Exciton coherence lifetimes from electronic structure. *J. Chem. Phys.* **2012**, *136* (10), 104510-104510.
6. Lin, S. H.; Xiao, W. Z.; Dietz, W., Generalized Förster-Dexter theory of photoinduced intramolecular energy transfer. *Phys. Rev. E* **1993**, *47* (5), 3698-3706.
7. Skourtis, S. S.; Liu, C.; Antoniou, P.; Virshup, A. M.; Beratan, D. N., Dexter energy transfer pathways. *Proc. Natl. Acad. Sci. U. S. A.* **2016**, *113* (29), 8115-20.
8. Lin, J.; Hu, X.; Zhang, P.; Van Rynbach, A.; Beratan, D. N.; Kent, C. A.; Mehl, B. P.; Papanikolas, J. M.; Meyer, T. J.; Lin, W.; Skourtis, S. S.; Constantinou, M., Triplet Excitation Energy Dynamics in Metal–Organic Frameworks. *The Journal of Physical Chemistry C* **2013**, *117* (43), 22250-22259.
9. So, M. C.; Wiederrecht, G. P.; Mondloch, J. E.; Hupp, J. T.; Farha, O. K., Metal-organic framework materials for light-harvesting and energy transfer. *Chemical Communications* **2015**, *51* (17), 3501-3510.
10. Heine, J.; Muller-Buschbaum, K., Engineering metal-based luminescence in coordination polymers and metal-organic frameworks. *Chemical Society Reviews* **2013**, *42* (24), 9232-9242.
11. Zhang, T.; Lin, W., Metal-organic frameworks for artificial photosynthesis and photocatalysis. *Chemical Society Reviews* **2014**, *43* (16), 5982-5993.
12. Zhang, X.; Wang, W.; Hu, Z.; Wang, G.; Uvdal, K., Coordination polymers for energy transfer: Preparations, properties, sensing applications, and perspectives. *Coordination Chemistry Reviews* **2015**, *284*, 206-235.
13. Dhakshinamoorthy, A.; Asiri, A. M.; García, H., Metal–Organic Framework (MOF) Compounds: Photocatalysts for Redox Reactions and Solar Fuel Production. *Angewandte Chemie International Edition* **2016**, *55* (18), 5414-5445.
14. Williams, D. E.; Shustova, N. B., Metal–Organic Frameworks as a Versatile Tool To Study and Model Energy Transfer Processes. *Chemistry – A European Journal* **2015**, *21* (44), 15474-15479.
15. Binnemans, K., Lanthanide-Based Luminescent Hybrid Materials. *Chemical Reviews* **2009**, *109* (9), 4283-4374.
16. Eliseeva, S. V.; Bunzli, J.-C. G., Lanthanide luminescence for functional materials and bio-sciences. *Chemical Society Reviews* **2010**, *39* (1), 189-227.
17. Bünzli, J.-C. G., Lanthanide Luminescence for Biomedical Analyses and Imaging. *Chemical Reviews* **2010**, *110* (5), 2729-2755.
18. Zhang, X.; Ballem, M. A.; Ahrén, M.; Suska, A.; Bergman, P.; Uvdal, K., Nanoscale Ln(III)-Carboxylate Coordination Polymers (Ln = Gd, Eu, Yb): Temperature-Controlled Guest Encapsulation and Light Harvesting. *Journal of the American Chemical Society* **2010**, *132* (30), 10391-10397.
19. Zhang, X.; Ballem, M. A.; Hu, Z.-J.; Bergman, P.; Uvdal, K., Nanoscale Light-Harvesting Metal–Organic Frameworks. *Angewandte Chemie International Edition* **2011**, *50* (25), 5729-5733.
20. Balamurugan, A.; Gupta, A. K.; Boomishankar, R.; Lakshmi Reddy, M.; Jayakannan, M., Heavy Atom Effect Driven Organic Phosphors and Their Luminescent Lanthanide Metal–Organic Frameworks. *ChemPlusChem* **2013**, *78* (7), 737-745.
21. Li, Y.; Zhang, S.; Song, D., A Luminescent Metal–Organic Framework as a Turn-On Sensor for DMF Vapor. *Angewandte Chemie International Edition* **2013**, *52* (2), 710-713.
22. Zhou, J.-M.; Shi, W.; Li, H.-M.; Li, H.; Cheng, P., Experimental Studies and Mechanism Analysis of High-Sensitivity Luminescent Sensing of Pollutational Small Molecules and Ions in Ln₄O₄ Cluster Based Microporous Metal–Organic Frameworks. *The Journal of Physical Chemistry C* **2014**, *118* (1), 416-426.
23. Lu, W.-G.; Jiang, L.; Feng, X.-L.; Lu, T.-B., Three-Dimensional Lanthanide Anionic Metal–Organic Frameworks with Tunable Luminescent Properties Induced by Cation Exchange. *Inorganic Chemistry* **2009**, *48* (15), 6997-6999.

24. Xiao, Y.; Cui, Y.; Zheng, Q.; Xiang, S.; Qian, G.; Chen, B., A microporous luminescent metal-organic framework for highly selective and sensitive sensing of Cu²⁺ in aqueous solution. *Chemical Communications* **2010**, 46 (30), 5503-5505.
25. Cai, S.-L.; Zheng, S.-R.; Fan, J.; Xiao, T.-T.; Tan, J.-B.; Zhang, W.-G., A new sensor based on luminescent terbium-organic framework for detection of Fe³⁺ in water. *Inorganic Chemistry Communications* **2011**, 14 (6), 937-939.
26. Dang, S.; Min, X.; Yang, W.; Yi, F.-Y.; You, H.; Sun, Z.-M., Lanthanide Metal-Organic Frameworks Showing Luminescence in the Visible and Near-Infrared Regions with Potential for Acetone Sensing. *Chemistry – A European Journal* **2013**, 19 (50), 17172-17179.
27. Wright, W. D., A re-determination of the trichromatic coefficients of the spectral colours. *Transactions of the Optical Society* **1929**, 30 (4), 141.
28. Guild, J., The Colorimetric Properties of the Spectrum. *Philosophical Transactions of the Royal Society of London. Series A, Containing Papers of a Mathematical or Physical Character* **1932**, 230 (681-693), 149-187.
29. Rodrigues, M. O.; Dutra, J. D. L.; Nunes, L. A. O.; de Sá, G. F.; de Azevedo, W. M.; Silva, P.; Paz, F. A. A.; Freire, R. O.; A. Júnior, S., Tb³⁺→Eu³⁺ Energy Transfer in Mixed-Lanthanide-Organic Frameworks. *The Journal of Physical Chemistry C* **2012**, 116 (37), 19951-19957.
30. Matthes, P.; Höller, C. J.; Mai, M.; Heck, J.; Sedlmaier, S. J.; Schmiechen, S.; Feldmann, C.; Schnick, W.; Müller-Buschbaum, K., Luminescence tuning of MOFs via ligand to metal and metal to metal energy transfer by co-doping of 2∞[Gd 2 Cl 6 (bipy) 3]· 2bipy with europium and terbium. *Journal of materials chemistry* **2012**, 22 (20), 10179-10187.
31. Ma, M.-L.; Ji, C.; Zang, S.-Q., Syntheses, structures, tunable emission and white light emitting Eu³⁺ and Tb³⁺ doped lanthanide metal-organic framework materials. *Dalton Transactions* **2013**, 42 (29), 10579-10586.
32. Liu, Z.-F.; Wu, M.-F.; Wang, S.-H.; Zheng, F.-K.; Wang, G.-E.; Chen, J.; Xiao, Y.; Wu, A. Q.; Guo, G.-C.; Huang, J.-S., Eu³⁺-doped Tb³⁺ metal-organic frameworks emitting tunable three primary colors towards white light. *Journal of Materials Chemistry C* **2013**, 1 (31), 4634-4639.
33. Cui, Y.; Xu, H.; Yue, Y.; Guo, Z.; Yu, J.; Chen, Z.; Gao, J.; Yang, Y.; Qian, G.; Chen, B., A Luminescent Mixed-Lanthanide Metal-Organic Framework Thermometer. *Journal of the American Chemical Society* **2012**, 134 (9), 3979-3982.
34. Rao, X.; Song, T.; Gao, J.; Cui, Y.; Yang, Y.; Wu, C.; Chen, B.; Qian, G., A Highly Sensitive Mixed Lanthanide Metal-Organic Framework Self-Calibrated Luminescent Thermometer. *Journal of the American Chemical Society* **2013**, 135 (41), 15559-15564.
35. Miyata, K.; Konno, Y.; Nakanishi, T.; Kobayashi, A.; Kato, M.; Fushimi, K.; Hasegawa, Y., Chameleon Luminophore for Sensing Temperatures: Control of Metal-to-Metal and Energy Back Transfer in Lanthanide Coordination Polymers. *Angewandte Chemie International Edition* **2013**, 52 (25), 6413-6416.
36. Liu, Y.; Pan, M.; Yang, Q.-Y.; Fu, L.; Li, K.; Wei, S.-C.; Su, C.-Y., Dual-Emission from a Single-Phase Eu-Ag Metal-Organic Framework: An Alternative Way to Get White-Light Phosphor. *Chemistry of Materials* **2012**, 24 (10), 1954-1960.
37. Luo, F.; Batten, S. R., Metal-organic framework (MOF): lanthanide(iii)-doped approach for luminescence modulation and luminescent sensing. *Dalton Transactions* **2010**, 39 (19), 4485-4488.
38. An, J.; Shade, C. M.; Chengelis-Czegan, D. A.; Petoud, S.; Rosi, N. L., Zinc-Adeninate Metal-Organic Framework for Aqueous Encapsulation and Sensitization of Near-infrared and Visible Emitting Lanthanide Cations. *Journal of the American Chemical Society* **2011**, 133 (5), 1220-1223.
39. Ma, M.-L.; Qin, J.-H.; Ji, C.; Xu, H.; Wang, R.; Li, B.-J.; Zang, S.-Q.; Hou, H.-W.; Batten, S. R., Anionic porous metal-organic framework with novel 5-connected vbk topology for rapid adsorption of dyes and tunable white light emission. *Journal of Materials Chemistry C* **2014**, 2 (6), 1085-1093.
40. Ward, M. D.; Barigelletti, F., Control of photoinduced energy transfer between metal-polypyridyl luminophores across rigid covalent, flexible covalent, or hydrogen-bonded bridges. *Coordination Chemistry Reviews* **2001**, 216, 127-154.

41. Fleming, C. N.; Maxwell, K. A.; DeSimone, J. M.; Meyer, T. J.; Papanikolas, J. M., Ultrafast excited-state energy migration dynamics in an efficient light-harvesting antenna polymer based on Ru (II) and Os (II) polypyridyl complexes. *Journal of the American Chemical Society* **2001**, *123* (42), 10336-10347.
42. Tsushima, M.; Ikeda, N.; Yoshimura, A.; Nozaki, K.; Ohno, T., Solid-state photochemistry: energy-transfer and electron-transfer of 3 CT in crystals of $[\text{Os}_x \text{Ru}_{1-x}(\text{bpy})_3]_2$ ($x = 0-0.23$). *Coordination Chemistry Reviews* **2000**, *208* (1), 299-308.
43. Yersin, H.; Kratzer, C., Energy transfer and harvesting in $[\text{Ru}_{1-x}\text{Os}_x(\text{bpy})_3](\text{PF}_6)_2$ and $\{\Delta-[\text{Ru}(\text{bpy})_3]\Delta-[\text{Os}(\text{bpy})_3]\}(\text{PF}_6)_4$. *Coordination chemistry reviews* **2002**, *229* (1), 75-93.
44. Kent, C. A.; Mehl, B. P.; Ma, L.; Papanikolas, J. M.; Meyer, T. J.; Lin, W., Energy transfer dynamics in metal-organic frameworks. *Journal of the American Chemical Society* **2010**, *132* (37), 12767-12769.
45. Kent, C. A.; Liu, D.; Ma, L.; Papanikolas, J. M.; Meyer, T. J.; Lin, W., Light harvesting in microscale metal-organic frameworks by energy migration and interfacial electron transfer quenching. *Journal of the American Chemical Society* **2011**, *133* (33), 12940-12943.
46. Kent, C. A.; Liu, D.; Meyer, T. J.; Lin, W., Amplified luminescence quenching of phosphorescent metal-organic frameworks. *Journal of the American Chemical Society* **2012**, *134* (9), 3991-3994.
47. Kent, C. A.; Liu, D.; Ito, A.; Zhang, T.; Brennaman, M. K.; Meyer, T. J.; Lin, W., Rapid energy transfer in non-porous metal-organic frameworks with caged Ru (bpy)₃²⁺ chromophores: oxygen trapping and luminescence quenching. *Journal of Materials Chemistry A* **2013**, *1* (47), 14982-14989.
48. Tang, Y.; He, W.; Lu, Y.; Fielden, J.; Xiang, X.; Yan, D., Assembly of Ruthenium-Based Complex into Metal-Organic Framework with Tunable Area-Selected Luminescence and Enhanced Photon-to-Electron Conversion Efficiency. *The Journal of Physical Chemistry C* **2014**, *118* (44), 25365-25373.
49. Cavka, J. H.; Jakobsen, S.; Olsbye, U.; Guillou, N.; Lamberti, C.; Bordiga, S.; Lillerud, K. P., A New Zirconium Inorganic Building Brick Forming Metal Organic Frameworks with Exceptional Stability. *Journal of the American Chemical Society* **2008**, *130* (42), 13850-13851.
50. Bon, V.; Senkovska, I.; Weiss, M. S.; Kaskel, S., Tailoring of network dimensionality and porosity adjustment in Zr- and Hf-based MOFs. *CrystEngComm* **2013**, *15* (45), 9572-9577.
51. Wang, C.; Xie, Z.; deKrafft, K. E.; Lin, W., Doping Metal-Organic Frameworks for Water Oxidation, Carbon Dioxide Reduction, and Organic Photocatalysis. *Journal of the American Chemical Society* **2011**, *133* (34), 13445-13454.
52. Maza, W. A.; Morris, A. J., Photophysical Characterization of a Ruthenium(II) Tris(2,2'-bipyridine)-Doped Zirconium UiO-67 Metal-Organic Framework. *The Journal of Physical Chemistry C* **2014**, *118* (17), 8803-8817.
53. Maza, W. A.; Padilla, R.; Morris, A. J., Concentration dependent dimensionality of resonance energy transfer in a postsynthetically doped morphologically homologous analogue of uiO-67 mof with a ruthenium (ii) polypyridyl complex. *Journal of the American Chemical Society* **2015**, *137* (25), 8161-8168.
54. Meyer, T. J., Photochemistry of metal coordination complexes: metal to ligand charge transfer excited states. In *Pure and Applied Chemistry*, 1986; Vol. 58, p 1193.
55. Kenkre, V. M.; Knox, R. S., Theory of Fast and Slow Excitation Transfer Rates. *Physical Review Letters* **1974**, *33* (14), 803-806.
56. Son, H.-J.; Jin, S.; Patwardhan, S.; Wezenberg, S. J.; Jeong, N. C.; So, M.; Wilmer, C. E.; Sarjeant, A. A.; Schatz, G. C.; Snurr, R. Q., Light-harvesting and ultrafast energy migration in porphyrin-based metal-organic frameworks. *Journal of the American Chemical Society* **2013**, *135* (2), 862-869.
57. Lee, C. Y.; Farha, O. K.; Hong, B. J.; Sarjeant, A. A.; Nguyen, S. T.; Hupp, J. T., Light-Harvesting Metal-Organic Frameworks (MOFs): Efficient Strut-to-Strut Energy Transfer in Bodipy and Porphyrin-Based MOFs. *Journal of the American Chemical Society* **2011**, *133* (40), 15858-15861.

58. Williams, D. E.; Rietman, J. A.; Maier, J. M.; Tan, R.; Greytak, A. B.; Smith, M. D.; Krause, J. A.; Shustova, N. B., Energy Transfer on Demand: Photoswitch-Directed Behavior of Metal–Porphyrin Frameworks. *Journal of the American Chemical Society* **2014**, *136* (34), 11886-11889.
59. Dolgoplova, E. A.; Williams, D. E.; Greytak, A. B.; Rice, A. M.; Smith, M. D.; Krause, J. A.; Shustova, N. B., A Bio-inspired Approach for Chromophore Communication: Ligand-to-Ligand and Host-to-Guest Energy Transfer in Hybrid Crystalline Scaffolds. *Angewandte Chemie International Edition* **2015**, *54* (46), 13639-13643.
60. So, M. C.; Jin, S.; Son, H.-J.; Wiederrecht, G. P.; Farha, O. K.; Hupp, J. T., Layer-by-Layer Fabrication of Oriented Porous Thin Films Based on Porphyrin-Containing Metal–Organic Frameworks. *Journal of the American Chemical Society* **2013**, *135* (42), 15698-15701.
61. Goswami, S.; Ma, L.; Martinson, A. B.; Wasielewski, M. R.; Farha, O. K.; Hupp, J. T., Toward Metal-Organic Framework Based Solar Cells: Enhancing Directional Exciton Transport by Collapsing Three-Dimensional Film Structures. *ACS Applied Materials & Interfaces* **2016**.
62. Yan, D.; Tang, Y.; Lin, H.; Wang, D., Tunable Two-color Luminescence and Host–guest Energy Transfer of Fluorescent Chromophores Encapsulated in Metal-Organic Frameworks. *Scientific reports* **2014**, *4*.
63. Gutiérrez, M.; Sánchez, F.; Douhal, A., Efficient multicolor and white light emission from Zr-based MOF composites: spectral and dynamic properties. *Journal of Materials Chemistry C* **2015**, *3* (43), 11300-11310.
64. Gutiérrez, M.; Sánchez, F.; Douhal, A., Spectral and dynamical properties of a Zr-based MOF. *Physical Chemistry Chemical Physics* **2016**, *18* (7), 5112-5120.
65. Gutiérrez, M.; Sánchez, F.; Douhal, A., Competitive Excimer Formation and Energy Transfer in Zr-Based Heterolinker Metal–Organic Frameworks. *Chemistry-A European Journal* **2016**, *22* (37), 13072-13082.
66. Gutierrez, M.; Cohen, B.; Sánchez, F.; Douhal, A., Photochemistry of Zr-based MOFs: ligand-to-cluster charge transfer, energy transfer and excimer formation, what else is there? *Physical Chemistry Chemical Physics* **2016**, *18* (40), 27761-27774.
67. Park, H. J.; So, M. C.; Gosztola, D.; Wiederrecht, G. P.; Emery, J. D.; Martinson, A. B. F.; Er, S.; Wilmer, C. E.; Vermeulen, N. A.; Aspuru-Guzik, A.; Stoddart, J. F.; Farha, O. K.; Hupp, J. T., Layer-by-Layer Assembled Films of Perylene Diimide- and Squaraine-Containing Metal–Organic Framework-like Materials: Solar Energy Capture and Directional Energy Transfer. *ACS Applied Materials & Interfaces* **2016**, *8* (38), 24983-24988.